Insights into the nature of climate and vegetation changes over the last 28,000 years using combined pollen and leaf-wax biomarker analyses from the SW Iberian Margin

by

Anna Victoria Cutmore

Thesis submitted to University College London

for the degree of Doctor of Philosophy

2021

Supervised by Professor Polychronis Tzedakis (University College London)

Professor Mark Maslin (University College London)

Professor Timothy Eglinton (ETH, Zurich)

Natural Environment Research Council

Declaration

I, Anna Victoria Cutmore, confirm that the work presented in this thesis is my own. This work has not been submitted in whole or in part for any other degrees or professional qualifications. Where information has been derived from other sources, I confirm that this has been clearly indicated in the thesis.

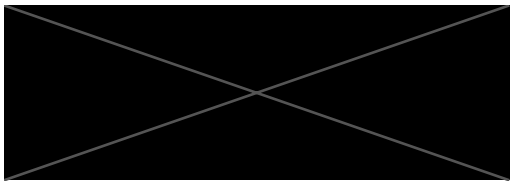

A.V. Cutmore

Abstract

This thesis aims to enhance the current understanding of the response of SW Iberian ecosystems to abrupt and orbital-scale climate changes. The last ~28 thousand years can provide such insight, containing several abrupt North Atlantic climate events superimposed on orbital-scale global changes. This study presents new high-resolution pollen and leaf-wax *n*-alkane records combined with palaeoceanographic proxies from the same deep-sea cores (SHAK06-5K and MD01-2444) on the Southwestern (SW) Iberian Margin. The chronology of these records is based on high-resolution Accelerator Mass Spectrometry radiocarbon dating of planktonic foraminifer *Globigerina bulloides* from cores SHAK06-5K and MD01-2444.

Changes in temperate and steppe records during the Last Glacial Maximum and subsequent deglaciation are closely coupled with changes in sea surface temperatures (SSTs), and global ice volume. This coupling continues during the onset of the Holocene, with the peak in thermophilous woodland lagging the boreal insolation maxima by ~2 kyr. This possibly arises from the persistence of residual high-latitude ice-sheets into the Holocene. A close correlation between rapid oscillations in pollen percentages and millennial/centennial-scale variations in SSTs, planktonic $\delta^{18}O$, and lithology suggests extrinsically-forced SW Iberian ecosystem changes in response to abrupt North Atlantic climate events. In contrast, the abrupt thermophilous woodland decline at ~7.8 thousand years before present (cal ka BP) indicates an intrinsically-mediated abrupt vegetation response to the gradually declining boreal insolation, resulting in the crossing of an ecological threshold.

The leaf-wax *n*-alkane $\delta^{13}C$ record from SHAK06-5K combined with the pollen record from the same core and modern leaf-wax *n*-alkane $\delta^{13}C$ data from SW Iberia suggest that this geochemical proxy is directly or indirectly driven by SW Iberian climate variations. Two

potential mechanisms are proposed: i) *n*-alkane $\delta^{13}C$ is directly controlled by changes in regional moisture availability; or ii) climate change leads to a turnover of plant species with inherently different *n*-alkane $\delta^{13}C$ signatures.

Keywords:

Last Glacial Maximum, Deglaciation, MIS 2, Holocene, SW Iberian Margin, Portuguese Margin, Western Iberia, Climate change, Abrupt events, Vegetation change, Pollen, Leaf-wax biomarkers, *n*-alkanes, $\delta^{13}C$, Shackleton site

Impact Statement

The western Mediterranean is already experiencing significant, tangible effects of anthropogenic climate change. Rising temperatures in this region have exceeded the global mean over the past few decades and drought stress is projected to increase in future (Lionello *et al.,* 2014 and references therein). These climate changes will impact western Mediterranean vegetation, which is cause for both ecological and socio-economic concern. Consequently, there is an urgent need for better understanding of the response and sensitivity of western Mediterranean vegetation to changing background conditions.

To better understand the dynamics of Mediterranean ecosystem responses to anthropogenic climate change, this research explores the response and sensitivity of Southwest (SW) Iberian vegetation communities to changing background conditions on (sub)millennial-to-orbital timescales. These dynamics are investigated with complementary high-resolution palaeoenvironmental records: high-resolution pollen records from SW Iberian Margin sediment cores SHAK06-5K and MD01-2444, and high-resolution leaf-wax *n*-alkane records from core SHAK06-5K, spanning the last ~28 kyr within which several abrupt changes occurred (including the cold events of Heinrich Stadials 1 & 2, the Younger Dryas, and the 8,200 year event, and the warm event at the onset of the Bølling-Allerød interstadial) superimposed onto orbital-scale global changes. The fossil leaf-wax *n*-alkane palaeoenvironmental reconstructions were ground-truthed through molecular and isotopic ($\delta^{13}C$) assessment of leaf-wax *n*-alkanes in contemporary plants of SW Iberia as a means to explore down-core signatures of these proxies as a (hydro)climate signal within a C_3-vegetation environment. The overarching goal is to use fossil leaf-wax *n*-alkane records in combination with the pollen record and existing palaeoceanographic records from within the same core to provide further insight into the response and sensitivity of SW Iberian vegetation to changing background conditions.

This work is also a crucial part of a wider research project on sediments from core SHAK06-5K (JC089 James Cook cruise), led by an international interdisciplinary team of scientists at the University of Cambridge, ETH Zürich, and University College London. SW Iberian marine sediment cores provide continuous and high-fidelity records due to its unique geographical features which allow for direct correlation of marine and terrestrial records with ice-core records from Greenland and Antarctica. This project's overall aim is to produce coeval high-resolution records of marine and terrestrial proxies from within a single marine core, enabling an *in situ* exploration of the relative timing of climate change in marine and terrestrial environments of SW Iberia over the past ~28 kyr.

Gaining insights into the response and sensitivity of SW Iberian vegetation to gradual and abrupt climate change will contribute towards the development of an empirical knowledge that can help assess the future ecological impacts and socio-economic consequences of anthropogenic climate change in the Mediterranean region.

Acknowledgements

To my supervisors, Professor Chronis Tzedakis, Professor Mark Maslin, and Professor Timothy Eglinton, thank you all for your constant support, expert advice, and training throughout the last four years. I am so grateful that you gave me this opportunity and for everything you have taught me. Chronis, thank you for introducing me to the world of Palaeoclimatology and Palynology, for having faith in my ability to complete a PhD, and providing me with the continued support to undertake this project.

I am appreciative for all the expert advice, training and support I received from Dr Blanca Ausin, Dr Julia Krawielicki, Dr David Thornalley, and Professor Anson MacKay. I am indebted to Dr Clayton Magill, without whose support, the isotope analysis would not have been possible; I am extremely grateful for all his time, effort, and guidance. Sincere thanks to Daniel Montluçon, Janet Hope, Kevin Roe and Bonnie Atkinson for their laboratory support and to the following individuals for their contribution to this research: Dr. Negar Haghipour for assistance with the ^{14}C measurements; Dr Francesco Muschitiello for his contribution to the alignment of the cores used in the production of the age-model; Simon Crowhurst for assistance with the Gaussian Interpolation of the simulated and climate records; and Dr Laurie Menviel for providing the simulated western Iberian climate records.

This research was made possible by a research grant from the Natural Environment Research Council (NERC grant NE/L002485/1). The authors recognise the critical role of the 2013 James Cook JC089 expedition, led by David Hodell and supported by the UK Natural Environment Research Council (NERC grant NE/J00653X/1), in providing the high-quality SHAK06-5K core for this research. I also acknowledge the 2001 R/V Marion Dufresne cruise in providing the high-quality core of MD01-2444, led by Nick McCave on behalf of Nick Shackleton, made possible by EU funding for the POP project ENV 2000 008. Thanks go to Nick McCave, Luke Skinner for

kasten core operations and collection of SHAK06-5K, and to Daniel Montluçon, and Clayton Magill for their assistance processing core SHAK06-5K. Funding from the QRA's New Researchers Award Scheme made the isotope analysis at The Lyell Centre possible, while the fieldwork in Portugal was supported by the MEAD Travel Fund and Frank Carter Award. I also acknowledge the role of the QRA INQUA fund in enabling me to present my research at the 2019 INQUA conference.

Thank you to my friends and colleagues who have brought so much fun to the last four years and have provided constant support: Bethan, Kat, Harriet, Ellie, Annie, Zoe, Sophie, Jenna, Becky, Emily, Akida, Ellen, David, Adrienne, Liam, Lily, and Azra. Abdul Bhanji OBE, I will forever be indebted to you for your encouragement and support and for having faith in my ability to take on this challenge. Grandma and Grandad, and Grandad Hugh, thank you for all your wisdom and encouragement- you all helped me achieve this. Mum, Dad, and Ben- you're the most fun, supportive, and encouraging team and have never put any pressure on me. Dad, thanks for telling me to get in the car. Mum, thanks for driving me back to London. Alex, thank you for everything.

i. Table of Contents

ii. List of Figures

5K; e. temperate pollen (%) from SHAK06-5K; f. steppe pollen (%) from SHAK06-5K; g. Ericaceae pollen (%) from SHAK06-5K; h. June boreal insolation (40°N; Wm^2).

Fig. 8.1: From core SHAK06-5K: a. Sediment accumulation rate (cm ka^{-1}); b. bulk density (g cm^{-3}); c. *ln*(Ca/Ti); d. *n*-alkane concentration (C_{27} – C_{33}; ng g^{-1}); e. *n*-alkane mass accumulation rate (C_{27} – C_{33}) (ng cm^{-2} ka^{-1}); f. pollen concentration (grains g^{-1}); g. pollen mass accumulation rate (grains cm^{-2} ka^{-1}); and h. pollen concentration of core MD01-2444 (grains g^{-1}); i. pollen concentration of core D1385 (grains g^{-1}); j. ice rafted debris from core SHAK06-5K (grains g^{-1}).

Fig. 8.2: Climate records over the past 27.4 kyr (cal yrs BP) of: a. North Greenland $\delta^{18}O_{ice}$ (‰ VSMOW); b. Zr/Sr from SHAK06-5K; c. $\delta^{18}O$ planktonic foraminifera from SHAK06-5K (‰ VPDB); d. $\delta^{18}O$ benthic foraminifera from MD95-2042 (‰ VPDB); e. UK'37 -derived sea surface temperature (°C) from SHAK06-5K and MD01-2444; f. temperate pollen from SHAK06-5K and MD01-2444 (%); g. Mediterranean pollen from SHAK06-5K and MD01-2444 (%); h. steppe pollen from SHAK06-5K and MD01-2444 (%); i. Ericaceae pollen from SHAK05-5K and MD01-2444 (%); j. *n*-alkane $\delta^{13}C_{C31}$ from SHAK06-5K (‰ VPDB); k. boreal insolation at 40°N (Wm^2); l. ice-rafted debris (grains g^{-1}).

Fig. 8.3: In SW Iberian Margin cores over HS1 and HS2, changes in: a. Zr/Sr from SHAK06-5K; b. *ln*(Ca/Ti) from SHAK06-5K; c. UK'37 -derived sea surface temperature (°C) from SHAK06-5K and MD01-2444; d. Eurosiberian pollen from SHAK06-5K (%); e. Mediterranean pollen from SHAK06-5K (%); f. pioneer pollen from SHAK06-5K (%); g. steppe pollen from SHAK06-5K (%); h. Ericaceae pollen from SHAK06-5K (%); i. *n*-alkane $\delta^{13}C_{C31}$ from SHAK06-5K (‰ VPDB); j. ice rafted debris (IRD; grains g^{-1}).

Fig. 8.4: Changes over time (cal ka BP) in the normalised rates of change and resampled climate and vegetation records of simulated annual precipitation (cm yr^{-1}) (a. & b.); simulated December to February surface air temperature (°C) (c. & d.); $U^{K'}_{37}$-derived sea surface temperatures from MD01-2444 (°C) (e. & f.); temperate taxa from SHAK06-5K (%) (g. & h.); and

steppe taxa from SHAK06-5K (%) (i. & j.); and changes over time of: k. boreal insolation at 40°N (Wm^2); l. ice-rafted debris (IRD; grains g^{-1}).

Fig. 8.5: SW Iberian pollen records of temperate, steppe, and Ericaceae vegetation change over MIS2 and the Holocene, from cores MD95-2042, MD01-2444, U1385, SHAK06-5K, D13882, and Charco da Candieira.

iii. List of Tables

iv. List of Equations

iv. Abbreviations

AABW	*Antarctic Bottom Water*
ACL	*Average chain length*
AMOC	*Atlantic Meridional Ocean Circulation*
AMS	*Accelerator mass spectrometry*
AP	*Arboreal pollen*
asl	*Above sea level*
BA	*Bølling Allerød*
Be	*Beryllium*
BD	*Bulk density*
Ca	*Calcium*
CH_4	*Methane*
Cl	*Chlorine*
CL	*Cuticular layer*
CP	*Cuticle proper*
CPI	*Carbon preference index*
CO_2	*Carbon dioxide*
C_3	*Hatch-Slack photosynthetic pathway*
C_4	*Calvin-Benson photosynthetic pathway*
DCM	*Dichloromethane*
D-O	*Dansgaard-Oeschger*
$F^{14}C$	*Fraction modern*
GC-FID	*Gas chromatography with flame ionisation detector*
GC-IRMS	*Gas chromatography with isotope-ratio mass spectrometry*
GCR	*Galactic Cosmic Ray*
GDGT	*Glycerol dibiphytanyl glycerol tetraether*
GICC05	*Greenland Ice Core Chronology 2005*
GS	*Greenland Stadial*
HCl	*Hydrochloric acid*
HE	*Heinrich Event*
HF	*Hydrofluoric acid*
HL	*Heinrich layer*
HS	*Heinrich stadial*
HNO_3	*Nitric acid*
H_3PO_4	*Phosphoric acid*
IRD	*Ice-rafted debris*
ITCZ	*Intertropical convergence zone*
ka/kyr	*Thousand years*
KOH	*Potassium hydroxide*
LDW	*Lower Deep Water*
LGM	*Last Glacial Maximum*
LIS	*Laurentide ice-sheet*
ln	*Natural logarithm*
LSW	*Labrador Sea Water*
MAR	*Mass accumulation rate*
MCMC	*Markov-chain Monte Carlo*
MeOH	*Methanol*
MICADAS	*Mini Carbon Dating System*
MIS	*Marine isotope stage*

mm/m/km	*Millimetre/metre/ kilometre*
MOW	*Mediterranean Overflow Water*
MSW	*Mediterranean Sea water*
MWP1a	*Meltwater Pulse 1a*
n-alkane	*'Normal' straight-chain alkane*
NADW	*North Atlantic Deep Water*
NAO	*North Atlantic Oscillation*
NAP	*Non arboreal pollen*
NEADW	*Northeastern Atlantic Deep Water*
ng/µg/g	*Nanogram/ microgram/gram*
NGRIP	*North Greenland Ice Core Project*
NW	*Northwestern*
PAZ	*Pollen assemblage zone*
PCA	*Principal component analysis*
PC	*Portugal current*
PCC	*Portugal Coastal Counter Current*
pCO_2	*Partial pressure of CO_2*
r	*Coefficient of correlation*
R-age	*Reservoir age*
RoC	*Rate of change*
s	*Second*
SLR	*Sea level rise*
SPM	*Suspended particulate matter*
SW	*Southwestern*
t	*Tonne*
TBA	*Tertiary-butary alcohol*
Th	*Thorium*
Ti	*Titanium*
U	*Uranium*
VSMOW	*Vienna Standard Mean Ocean Water*
VPDB	*Vienna Pee Dee Belemnite*
XRF	*X-ray fluorescence*
YD	*Younger Dryas*
$\delta^{13}C$	*Measure of the ratio of carbon-13 to carbon-12*
δD	*Measure of the ratio of hydrogen-2 to hydrogen-1*
$\delta^{18}O$	*Measure of the ratio of oxygen-18 to oxygen-16*
σ	*Standard deviation*
µl/ml	*Microlitre/millilitre*
°C	*Degrees Celsius*
^{12}C	*Carbon-12*
^{13}C	*Carbon-13*
^{14}C	*Carbon-14*

Chapter 1: Introduction

Palaeoclimate science provides critical insight into past changes in global circulation systems, hydrological patterns, and the biosphere. While no previous geological period can serve as a direct analogue for anthropogenic climate change due to the unprecedented rate and nature of today's global warming (Haywood *et al.,* 2011), palaeoclimate records provide insight into the direct and indirect impacts of rising temperatures on the Earth's system. One region that is already seeing significant effects of anthropogenic climate change is the western Mediterranean. Temperature rise in this region has exceeded the global mean over the past couple of decades (Giorgi, 2006; Diffenbaugh *et al.,* 2007; Lionello *et al.,* 2014; Dubrovsky *et al.,* 2014; Cramer *et al.,* 2018) and the future projections of enhanced heat stress and increasingly severe and regular droughts is cause for ecological and socio-economic concern (Giorgi, 2006; Giorgi & Lionello, 2008; Lionello, 2012; Lionello *et al.,* 2014). Situated in a transition zone between temperate central Europe and arid North Africa, the western Mediterranean experiences hot/dry summers and cool/wet winters. This region is heavily affected by mid-latitude and sub-tropical interactions making it particularly sensitive to variations in the general circulation (Giorgi & Lionello, 2008; Lionello, 2012). Consequently, there is a need for greater knowledge of the response of western Mediterranean vegetation to changing background conditions, both on orbital and millennial timescales. Marine isotope stage 2 (MIS 2; 26 – 11.7 ka) and the Holocene (11.7 ka – present) can provide this understanding, as they contain the Last Glacial Maximum (LGM) and several abrupt North Atlantic climate events superimposed onto orbital-scale global changes that include expansion of Northern Hemisphere ice sheets, deglaciation, and the establishment of interglacial conditions. This time period includes the abrupt cold events of Heinrich Stadials 1 & 2 (HS2; HS1), the Younger Dryas (YD), and the 8,200 year (8.2 ka) event, and the abrupt warm onset of the Bølling-Allerød (BA) period.

The Southwest (SW) Iberian Margin has emerged as one of the most important locations for investigating orbital- and millennial-scale changes in the coupled ocean-land system, where analyses of palaeoceanographic and terrestrial proxies from the same marine samples enable the relative timing of changes to be explored *in situ* (e.g. Shackleton *et al.,* 2000, 2003; Sanchez Goñi *et al.,* 2000; Tzedakis *et al.,* 2004, 2018; Margari *et al.,* 2010; 2020). This is a direct consequence of the region's geography. The combined effects of two major rivers, the Tagus and the Sado, which have supplied the SW Iberian Margin throughout glacial and interglacial

periods (Jouanneau *et al.,* 1998), and a narrow continental shelf (30 – 50 km wide) with a steep slope into the abyssal plain lead to the rapid transport of terrestrial material to deep-water environments (Vanney and Mougenot, 1981; Naughton *et al.,* 2007). This enables a direct correlation with marine proxies (Hodell *et al.,* 2013a; Hodell *et al.,* 2015). Additionally, on millennial timescales, planktonic and benthic foraminifera isotope records from the Iberian Margin are closely correlated with ice core temperature records from Greenland and Antarctica, respectively (Blunier *et al.,* 1998; Petit *et al.,* 1999; Shackleton *et al.,* 2000), with millennial-scale variability in planktonic $\delta^{18}O$ ($\delta^{18}O_{planktonic}$) from this region closely related to changes in SST (Shackleton *et al.,* 2000; Skinner & Shackleton, 2005; Skinner *et al.,* 2007).

This research will explore SW Iberian vegetation changes over the past 28,000 years (28 kyr), using Iberian Margin sediment cores SHAK06-5K and MD01-2444 from within the vicinity of the Shackleton site (Shackleton *et al.,* 2000), a location that has provided continuous and high-fidelity records due to its unique geographical features (Hodell *et al.,* 2013a; Hodell *et al.,* 2015).

1.1. Aims and objectives

The aim of this research is to better understand the ecological responses of SW Iberian vegetation to both orbital and millennial/centennial-scale climate change over the past 28 kyr, in order to assess the sensitivity of these ecosystems to different climate forcings. To address this research aim, the key objectives are as follows:

1. Generate two high-resolution pollen records from cores SHAK06-5K and MD01-2444 and a detailed ^{14}C chronology to assess the absolute timing of SW Iberian vegetation changes on orbital and millennial timescales over the LGM, last deglaciation and Holocene.
2. Generate a high-resolution leaf-wax *n*-alkane $\delta^{13}C$ record from SHAK06-5K, interpret the climate/physiological drivers of this signal using modern leaf-wax *n*-alkane $\delta^{13}C$ records from dominant SW Iberian vegetation, and explore the potential use of this proxy as a climate change signal.
3. Use these records alongside existing palaeoceanographic analyses from the same cores to assess the relative timing of changes in these records and the response and sensitivity of SW Iberian vegetation to orbital-scale climate variability and abrupt climate events over the past 28 kyr.

1.2.Thesis structure

This thesis is organised as follows:

Chapter 2 presents the physical setting of the research area: SW Iberia and the SW Iberian Margin. Chapter 3 discusses the existing palaeoclimate knowledge of global and regional mechanisms responsible for western Mediterranean climate, oceanographic and vegetation conditions over the past 28 kyr. Chapter 4 describes the laboratory methods of the pollen preparation and analysis from cores SHAK06-5K and MD01-2444, and presents and describes the results, referring to changes with depth. Chapter 5 describes the laboratory methods of the leaf-wax *n*-alkane preparation and analysis from core SHAK06-5K, and presents and describes the results, referring to changes with depth. Chapter 6 presents the chronology of the records, produced using existing ^{14}C dates from core SHAK06-5K (n = 40) and new ^{14}C dates from MD01-2444 (n = 7). Chapter 7 describes the field and laboratory methods used to produce the modern leaf-wax *n*-alkane record from the Tagus catchment basin in Portugal. These results are then presented and interpreted, and subsequently used in the interpretation of the SHAK06-5K fossil *n*-alkane record. Chapter 8 discusses the overall interpretation of terrestrial vegetation records (pollen and *n*-alkane) from SHAK06-5K and MD01-2444 and compares these to existing SW Iberian vegetation and palaeoceanographic records. Chapter 9 draws together the main conclusions and limitations of this research and suggests future directions following on from this work.

1.3.Conventions

Ages are given in calendar years before present (cal yrs BP), with 'ka' used for thousand years before present and 'kyr' used for durations. Uncalibrated radiocarbon ages are presented as '^{14}C'. The terms glacial/stadial refer to relatively cold and/or arid periods, while the terms interglacial/interstadial refer to relatively warm and/or humid periods. Botanical nomenclature follows *Mabberley's Plant-book* (Mabberley, 2017). δ^{13}C is the ratio of carbon-13 (^{13}C) to carbon-12 (^{12}C), calibrated using the Vienna Pee Dee Belemnite (VPDB) reference standard, while δ^{18}O is the ratio of oxygen-18 (^{18}O) to oxygen-16 (^{16}O), with ice core records calibrated using the Vienna Standard Mean Ocean Water (VSMOW) reference standard and carbonate records calibrated using VPDB reference standard (Coplen, 1994). Both isotope ratios are reported in parts per thousand (per mil; ‰). The 'n-' prefix in *n*-alkane refers 'normal' meaning the isomers are straight-chain. *n*-Alkane homologues are distinguished by the number of carbon atoms present in the compound, prefixed by 'C'.

This chapter provides the present-day environmental setting for the marine sediment cores SHAK06-5K and MD01-2444. A brief site description and outline of the scientific importance of this location is followed by the present-day oceanographic, climatic, and terrestrial conditions. The present-day sediment transport to the core sites is explored, with particular reference to the changes in this transport over MIS 2 and the Holocene. The potential impact of resuspension, redeposition, and *allochthonous* lateral transport on sediment delivered to SHAK06-5K and MD01-2444 are also discussed.

2.1. Sites SHAK06-5K and MD01-2444

The 3.44 m long SHAK06-5K kasten core was recovered from 2,646 m water depth on the SW Iberian Margin, in the vicinity of the Shackleton sites during the 2013 James Cook cruise JC089 (37°34 N, 10°09 W) (Hodell *et al.,* 2014). The site is located on the Promontório do Príncipe de Avis spur, ~115 km east of the Portuguese coast and southwest of the Tagus and Sado river mouths (Fig. 2.1). The MD01-2444 27.5 m long Calypso piston core was retrieved from the same area (37°34 N, 10°09 W) at a depth of 2,637 m during the 2001 R/V *Marion Dufresne II* Geosciences Cruise (Vautravers & Shackleton, 2006; Hodell *et al.,* 2013a).

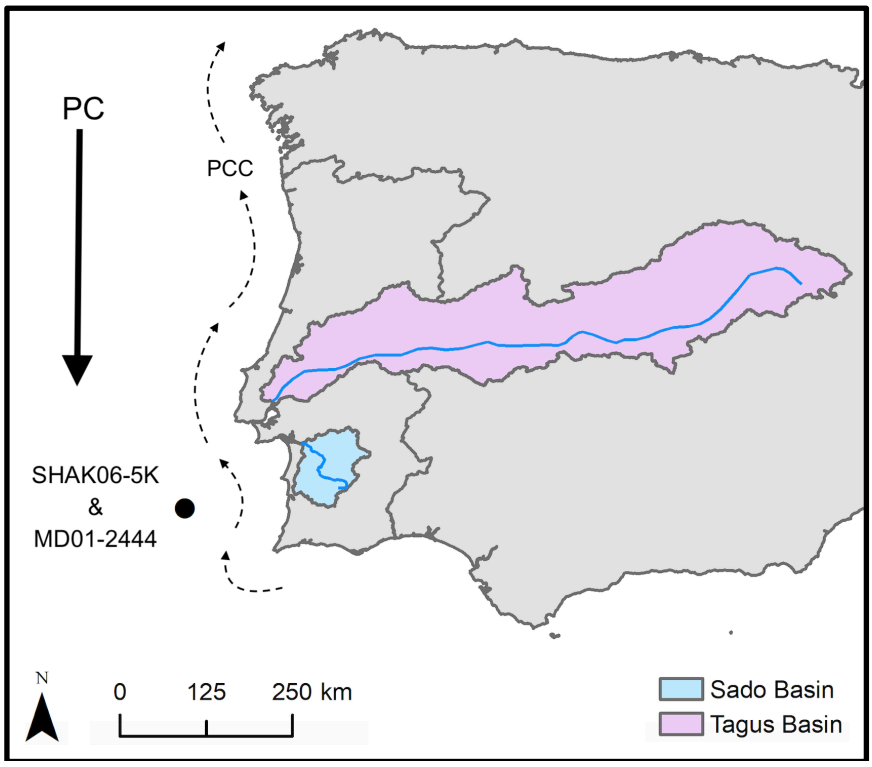

Fig. 2.1: Site of cores SHAK06-5K and MD01-2444, highlighting the Tagus (pink) and Sado (blue) river catchments. PC = Portugal Current ; PCC = Portugal Coastal Counter Current.

Basemap sourced from: https://www.arcgis.com/home/item.html?id=ed712cb1db3e4bae9e85329040fb9a49

2.2. Present-day western Iberian climate

Western Iberia has an oceanic climate. The Tagus and Sado basins in SW Iberia are characterized by the high-seasonality of the Mediterranean climate, with warm, dry summers and mild winters, where mean annual precipitation is <600 mm, while mean winter temperature is ~10°C and mean summer temperature is ~23°C (Fick & Hijmans, 2017). Annual precipitation in this region has a slight bimodal pattern, with high winter precipitation from October-January, declining February-March, rising again in April-May, before decreasing from June-September (IAEA/WISER; http://nucleus.iaea.org/wiser). Annual temperature has a strong unimodal pattern, with high summer temperatures peaking in July and coinciding with lowest precipitation levels (Quezel, 1985). Although the Tagus and Sado rivers have a continuous discharge throughout the year, (with a mean of 400 $m^3 s^{-1} yr^{-1}$ and 10 $m^3 s^{-1} yr^{-1}$, respectively), the flow is highly seasonal (Vale & Sundby, 1987; Vale *et al.,* 1993; Jouanneau *et al.,* 1998). During winter months, the discharge increases substantially, reducing in Spring through to Autumn.

Western Iberian climate is heavily influenced by the North Atlantic Oscillation (NAO), although this influence is highest in SW Iberia, decreasing eastwards across the Peninsula, (Alcara Ariza *et al.,* 1987; Vicente-Serrano & Heredia-Laclaustra, 2004). Inter-annual climate variability, particularly winter precipitation, is heavily influenced by NAO changes, caused by pressure gradient fluctuations between the Icelandic Low and Azores High (Hurrell, 1995). A positive NAO index sees an increased pressure gradient which strengthens and displaces the westerly winds northwards, reducing Iberian Peninsula winter precipitation; a negative NAO sees this gradient reduced, resulting in the opposite effect which increases river discharge (Trigo *et al.,* 2004). A positive winter NAO trend has been seen over the past 30 years (Gouveia *et al.,* 2008).

Although this region's dominant winds are northerly and westerly sourced (Fig. 2.2; Hurrell, 1995), winds can occasionally be sourced from the south, transporting Saharan dust to western Iberia (Rodríguez *et al.,* 2001).

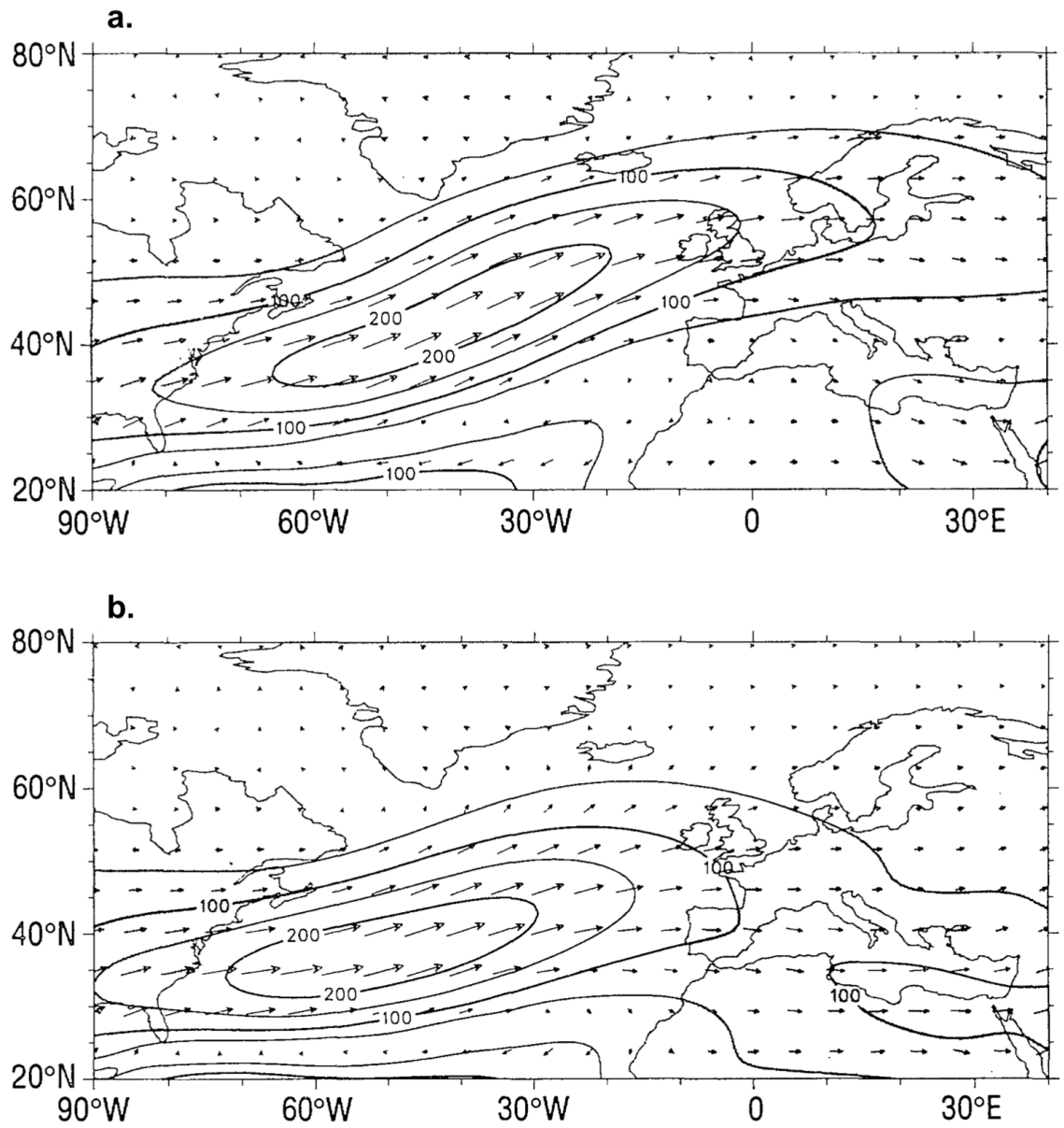

Fig. 2.2: Vertically integrated dominant moisture transport during: **a.** positive NAO; and **b.** negative NAO modes (Hurrell, 1995)

2.3. Present-day western Iberian oceanography

The Portugal Current (PC) is the dominant surface current (Fig. 2.1), transporting cold surface waters equatorward (Pérez *et al.,* 2001). Between June and September this is enhanced with the summer strengthening of the Azores anticyclonic cell and weakening of the Icelandic low, intensifying northerly and northwesterly winds along the Portuguese Coast (Fiúza *et al.,* 1982; Relvas *et al.,* 2007). This drives strong upwelling of cold nutrient-rich waters from 60 – 120 m depth promoting primary productivity (Abrantes, 1992), whilst low energy waves lead to upper-level stratification in the summer months (Jorge da Silva, 1992). Between October and March, the strengthened Icelandic low and weakened Azores High result in southward-shifted

westerlies; these dominant and strong south-westerly winds create down-welling over the Iberian Margin continental shelf (Ambar & Fiuza, 1994; Vitorino *et al.,* 2002), and drives the poleward Portugal Coastal Counter current (PCC) which flows between the continent and the PC (Fig. 2.1). This winter cooling of surface waters combined with high energy waves creates well mixed homogenised surface waters to ~100 m (Vitorino *et al.,* 2002). These surface currents are therefore directly linked to atmospheric circulation and are extremely sensitive to rapid atmospheric changes. Tides on the SW Iberian margin are semi-diurnal and their currents are weak (Jouanneau *et al.,* 1998).

Wind strength and therefore upwelling has a positive relationship with NAO due to the northerly winds (Oschlies, 2001), whilst mean-grain size of riverine material transported via the Tagus increases during negative NAO phases due to increased precipitation (Alt-Epping *et al.,* 2009).

At mid-depth (500 – 1700 m), the western Iberian Margin is dominated by warm and salty northward flowing Mediterranean Overflow Water (MOW), formed by the mixing of Mediterranean Sea water (MSW) and Atlantic Ocean water in the Gulf of Cadiz (van Aken, 2000a). Under this, flows the North Atlantic Deep-water's (NADW) upper component, Labrador Sea Water (LSW), at ~1600 m, with Northeastern Atlantic Deep Water (NEADW) and Lower Deep Water (LDW) (derived from Antarctic Bottom Water (AABW)) flowing below this (van Aken, 2000b; Voelker & de Abreu, 2011). Today, deep-water is dominated by NADW components with Antarctic originated LDW below 4000 m. During the Last Glacial, however, the contribution of AABW sourced water was more significant (Skinner *et al.,* 2003; Martrat *et al.,* 2007).

2.4. Present-day western Iberian geomorphology

2.4.1. Terrestrial

The dominant sediment supply to the south-west Iberian Margin is from the Tagus river, followed by the Sado (Jouanneau *et al.,* 1998). The former has a catchment area of 80,600 km^2 and is 1,110 km in length (Vale, 1990), while the latter has a catchment area of 7,640 km^2 and is 175 km in length (Loureiro *et al.,* 1986). The discharge of both rivers has a strong dry/wet signal, which strongly relates to the suspended sediment load (Vale & Sundby, 1987; Vale et al., 1993; Jouanneau *et al.,* 1998). Although the annual suspended sediment load is 0.4 - 1 x 10^6 t for the Tagus river and ~15 x 10^3 t for the Sado river, the highest proportion of this sediment

discharge occurs during winter months when the river's flow is highest (Vale & Sundby, 1987; Vale *et al.,* 1993). The valley of the Tagus river has been incised during numerous glacial sea-level low stands over the Quaternary (Vis *et al.,* 2016). Its source is in the Iberian Mountains, east of the Peninsula; these are old crystalline fold mountains formed during Late Palaeozoic Hercynian folding and are predominantly composed of Jurassic and Cretaceous limestones (Polunin & Smythies, 1973). Another group of these old-fold mountains, the Central Sierras, are to the north of the Tagus basin, with the Estremadura plateau to the south. In central Iberia, the Tagus flows through the New Castile plateau which is flat and featureless in the east but more undulating in the west (Polunin & Smythies, 1973). The river itself has formed a large low flat fertile plain, flooded with Tertiary deposits. It forms a dividing line between Mediterranean flora to the south and Atlantic vegetation to the north. The Sado basin is made up of tertiary deposits with the region's topography determined by a number of fault systems that cross the drainage basin (Pimental & Azevedo, 1994; Pimental, 2002). In the south of the basin where the river's source is located (in the Ourique hills) Quaternary terraces formed, while in the north of the basin, Tertiary deposits are overlain with Pliocene fluvial sands making terraces harder to identify (Pimental & Azevedo, 1994; Pimental, 2002). The mouths of the Tagus and Sado basins have formed lowlands and coastal plains but are bordered by prominent sea cliffs on the rocky Atlantic coastline (Polunin & Smythies, 1973).

2.4.2. Ocean

The western Iberian continental shelf is narrow, on average 20 – 30 km wide, composed of Cenozoic sediments >1000 m thick, and dissected by a number of submarine canyons (Jouanneau *et al.,* 1998; Arzola *et al.,* 2008). Two canyons incise the continental shelf in an east-west direction, the Cascais and Lisbon-Sebútal canyons (Fig. 2.3), transporting sediment from the narrow continental shelf to the deep ocean of the Tagus Abyssal Plain. The Lisbon-Sebutal canyon meets the abyssal plain at 4800 m depth and is formed of two branches: the main Sebutal channel starts 6 km from the Sado river mouth and is 175 km in length, while the Lisbon canyon is 167 km in length, commencing 13 km from the mouth of the Tagus (Lastras *et al.,* 2009). The Cascais canyon is shorter and steeper, with its canyon head at 175 m depth, 27 km from the Tagus, meeting the abyssal plain at 4600 m (Lastras *et al.,* 2009). The canyons are bordered by the Estremadura Spur, connected to the Lisbon Margin to the north, and the Promontório do Príncipe de Avis spur, connected to the Alentejo Margin, to the south (Fig. 2.3).

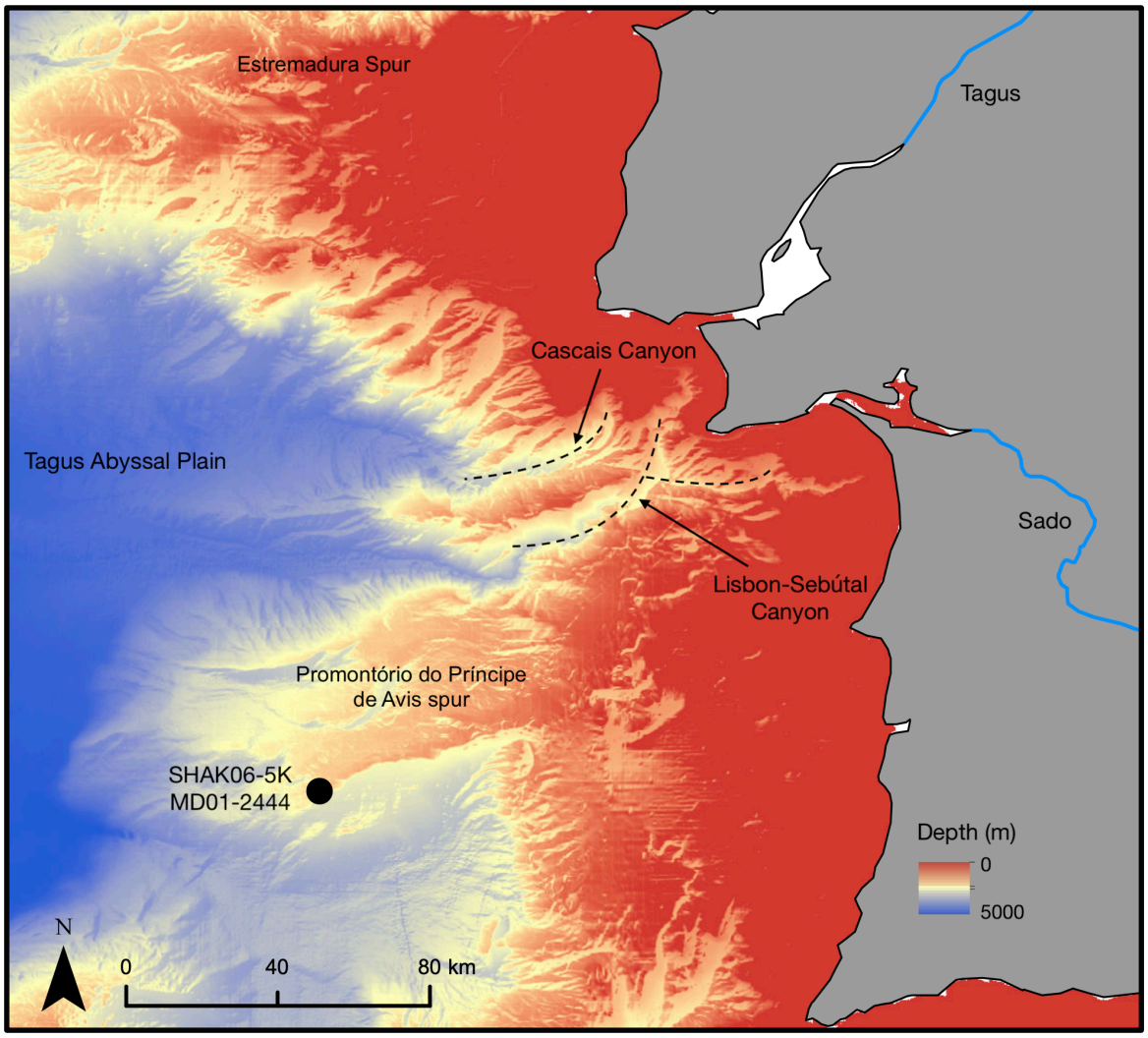

Fig. 2.3: Bathymetric map of the western Iberian Margin showing sites SHAK06-5K and MD01-2444. Bathymetry data sourced from: www.emodnet-bathymetry.eu

2.4.3. Present-day sediment transport to the Shackleton site

The Tagus river is the SW Iberian Margin's dominant sediment source, delivering an annual suspended sediment load of 0.4 – 1 x 10^6 t, four times that of the Sado (Jouanneau *et al.,* 1998). The Sado river also transports sediment to this region, but its sediment load is a quarter of that of the Tagus (Jouanneau *et al.,* 1998). Additionally, this material is primarily trapped in the Sado's estuary, making this river's supply to the margin far less significant (Jouanneau *et al.,* 1998).

Northerly winds are predominantly responsible for transporting Tagus sediment across the shelf in summer, while in winter, high variability in wind patterns and downwelling from southerly winds cause fine sediment transport offshore (Vitorino *et al.,* 2002; Oliveira *et al.,* 2002). Surface and benthic nepheloid layers transport this material across the shelf, depositing

courser, more organic carbon matter closer to the river mouth, which decreases offshore (Jouanneau *et al.,* 1998; Oliveira *et al.,* 2002; de Stigter *et al.,* 2011). The changing suspended particulate matter (SPM) concentration in the benthic nepheloid layer with distance from the Tagus river mouth is summarised in Table 2.1, with organic matter being of predominantly marine origin outside of the close vicinity of the Tagus river mouth (Alt-Epping *et al.,* 2007). The benthic nepheloid layer is considerable, reaching depths up to 150 m due to strong bottom currents resuspending and preventing sediment deposition; this layer is usually directed southward towards the Lisbon-Sebutal canyons (Jouanneau *et al.,* 1998). The surface nepheloid layer is smaller, restricted to the river mouth in the winter and extending 30 km westward in the summer due to increased biogenic material and northerly winds (Jouanneau *et al.,* 1998). Although these layers transport a large proportion of this sediment supply across the shelf, a significant quantity is deposited near the Tagus estuary, rather than transported to the deep-ocean (Jouanneau *et al.,* 1998).

Location		SPM concentration
Tagus river mouth		3 g m^{-3}
Open slope		0.1 g m^{-3}
Upper Canyon	*Lisbon & Setubal Canyons*	1 g m^{-3}
	Cascais Canyon	0.5 g m^{-3}

Table 2.1: Suspended particulate matter (SPM) concentration in bottom nepheloid layer of difference regions of the SW Iberian Margin (de Stigter *et al.,* 2011).

Sediment that reaches the outer shelf can then be transported onto the continental slope or deep-ocean. Transport to the deep-ocean primarily occurs via the Cascais and Lisbon-Sebutal canyons which act as a sink for terrestrial material, although it has been acknowledged that there are limited sediment gravity flows in these canyons and a substantial quantity of material accumulates in the upper sections, not reaching the deep-ocean due to bottom water up-flows (de Stiger *et al.,* 2011). Today, these canyons do not transport significant quantities of sediment to the Tagus Abyssal Plain, with the upper canyon acting as a depocenter (de Stiger *et al.,* 2011; Vis *et al.,* 2016). At the outer shelf, high turbulence and currents keep fine sediments suspended, meaning this material is not permanently deposited in these areas, instead transported onto the continental slope (Stanley & Wear, 1978; Dias, 1987). Although today's

SPM deposition on continental slopes south of the canyons (where SHAK06-5K is situated) is significantly lower than that of the inner shelf and upper canyons, it is similar to the lower Cascais and Sebutal-Lisbon canyons (de Stiger *et al.,* 2011), with the benefit of being away from the influence of turbidites (Hodell *et al.,* 2013b).

2.4.4. LGM and deglacial sediment transport to the Shackleton site

Although the dominant terrestrial sediment supply to the south-west Iberian Margin over the last 28 kyr was from the Tagus catchment basin, with a smaller contribution from the Sado, the depocenters of terrestrial sediment on this margin changed over the last deglaciation (Jouanneau *et al.,* 1998).

During the LGM, sediment supply to the Tagus Abyssal Plain was significantly higher than that of the Holocene, heavily influenced by the lowered sea-levels of this period (Vis *et al.,* 2008; 2016; Lebreiro *et al.,* 2009). LGM sea level was -130 – -140 m above present sea level (asl), just 30 – 70 m above shelf break (Dias *et al.,* 2000; Waelbroeck *et al.,* 2002; Vis *et al.,* 2008). The Tagus, a braided channel at this time, extended deep into the shelf, meaning sediment was directly and rapidly transported via the Cascais and Sebutal-Lisbon canyons into the deep-sea, with gravity flows and turbidites common in both canyons (Vis *et al.,* 2008; de Stigter *et al.,* 2011; Vis *et al.,* 2016).

Sea level rose steadily until 16 ka to -100 m asl, stabilising until 13 ka (Dias *et al.,* 2000; Waelbroeck *et al.,* 2002), with the braided Tagus forming a single channel around ~14 ka (Vis & Kasse, 2009), but sea levels continued to be low enough for sediment to bypass the shelf with the Tagus Abyssal Plain still acting as the depocenter. As sea levels rose to -60 m asl between 13 – 12 ka (Lambeck et al., 2014), these canyons became disconnected from the direct continental sediment supply, flooding the shelf and moving the depocenter landwards, with high fluvial sediment deposition on the shelf during this period (Vis *et al.,* 2008; 2016).

Present-day sea level was reached by ~7 ka, with the Lower Tagus valley completely submerged by this time, resulting in an inland depocenter as sediment was trapped within the lower valley (Vis *et al.,* 2008; 2016). Once this area was filled, increasing quantities of sediment were transferred back to the shelf from 5.5 ka (Vis *et al.,* 2016), with cores from the Tagus mud patch showing a rise in sediment input from ~3.5 ka (Rodrigues *et al.,* 2009). The quantity of sediment reaching the core sites SHAK06-5K and MD01-2444 has therefore varied over the deglaciation

and Holocene, although the catchment area has been relatively constant. The close proximity of these river mouths and narrow SW Iberian Margin continental shelf (Vanney & Mougenot, 1981) means terrestrial material is rapidly delivered to deep-marine environments, enabling direct correlation with co-occurring marine proxies and other terrestrial sequences (Hodell *et al.,* 2013b). Therefore, the pollen and *n*-alkane records from SHAK06-5K should provide a clearer understanding of this region's vegetation composition over the last 28 kyr. As pollen and leaf-wax biomarkers, however, have unique production, transportation, and taphonomy, these processes and their impact on each proxy's geographical source area will be explored in more detail in Chapters 4 and 5.

2.4.5. SW Iberia sediment resuspension, redeposition, and allochthonous lateral transport

In the marine environment, age discrepancies between different co-occurring (i.e. from the same sediment depth) sedimentary components have been demonstrated, highlighting the impact of lateral transport, resuspension, and redeposition on different grain-size fractions (Ohkouchi *et al.,* 2002; Mollenhauer *et al.,* 2005; Magill *et al.,* 2018; Ausin *et al.,* 2019b). Fine sediment fractions (alkenones, TOC, and long-chain fatty acids) have been shown to be considerably older than co-occurring planktonic foraminifera over the Late Quaternary. One of the most significant is a 7000 year discrepancy in Bermuda Rise sediments (Ohkouchi *et al.,* 2002), while ~1000, 1000 – 4500 and 2000 – 3000 year age offsets have been shown on the Chilean Margin, Namibian Margin, and in the South China Sea, respectively (Mollenhauer *et al.,* 2005). This has been attributed to lateral transport of pre-aged allochthonous material.

The significance of potential age offsets at our site has been studied in the SHAK06-5K core over the deglaciation (Magill *et al.,* 2018; Ausin *et al.,* 2019b). Magill *et al.* (2018) showed organic fractions (<63 μm) to be ~1000 – 3500 years older than planktonic foraminifera from the same depth, with these offsets varying over the deglaciation; decreasing during the LGM, BA, and early to mid-Holocene and increasing during HE1, the BA-YD transition, and late Holocene. In core SHAK06-5K, these offsets have been attributed to lateral transport of pre-aged material as there is little evidence of bioturbation in the upper 10 cm of the core and limited impact of diagenetic alteration/downslope remobilisation of foraminifera, as planktonic foraminiferal radiocarbon ages continuously increase downcore (Magill *et al.,* 2018). The magnitude of this offset implies the lateral transport of allochthonous material, as local resuspension would not have this impact on ^{14}C age (Ausin *et al.,* 2019b). MOW is suggested to play a role in transporting this pre-aged material from the western Mediterranean to our core

site via intermediate nepheloid layers associated with this water mass (Magill *et al.,* 2018). This water mass flows uninterrupted along the Alentejo margin until it reaches the Setubal canyon (de Stigter *et al.,* 2011). At the Gulf of Cadiz, MOW has a large 0.25g m^{-3} turbidity signal, predominantly from outflow water eroding material south of Cadiz. By the time this water mass reaches our site, however, this concentration reduces to 0.05g m^{-3} due to particle fallout and mixing with the NADW below (McCave & Hall, 2002).

Although the addition of pre-aged material impacts the ^{14}C ages of different components at the same depth in the core, the impact of pre-aged material on the proxy signal will be limited as the fraction of older allochthonous material has been shown to be small (Ausin *et al.,* 2019b). While between 15 and 20% of alkenones at this site could be sourced from pre-aged material (Ausin *et al.,* 2019b), the reworking of nannofossils within core SHAK06-5K is also small (mean of 4.4%, Appendix 1; Magill *et al.,* 2018). Furthermore, the synchronous changes in the pollen and palaeoceanographic records from core SHAK06-5K during abrupt events (presented in Chapter 8 of this thesis) indicate that there is a minimal influence of pre-aged material in this core over the past 28 kyr.

2.5. Present-day western Iberian vegetation

Mediterranean flora on the Iberian Peninsula has undergone complex and profound changes over geological time which have contributed to the rich diversity of taxa found in this region today, with the Iberian Peninsula containing a high biodiversity and a considerable number of endemic species (Greuter, 1991; Médail & Quezel, 1997; Médail *et al.,* 2019). Iberia contains >9000 plant species, with 19.1 and 4.4% of these endemic to Spain and Portugal, respectively (Médail & Quezel, 1997). This rich diversity has been created through a number of processes: glacial refugia of Tertiary species; proximity to Africa enabled northward migration of species; geographical isolation allowed for the evolution of endemic species; while a significant range of climatic conditions across the region created numerous niches for plants with ranging tolerances (Polunin & Smythies, 1973). Today, land-use across Iberia is highly varied (Fig. 2.4), influenced heavily by geological, climatic, and anthropogenic conditions. Much of the landscape is dedicated to farming, including a multifunctional agrosilvopastoral system characterised by low density trees combined with agriculture or pastoral farming, known as a 'Montado' in Portugal and a 'Dehesa' in Spain. This type of agroforestry eliminates shrubs typically in favour of evergreen *Quercus* (primarily *Q. suber or Q. ilex*) and grasses.

In the Tagus and Sado basins, the coastal region is dominated by thermophilous woodland, Mediterranean pines and maquis shrubs, which includes *Pinus pinaster, Pinus pinea, Quercus coccifera, Q. suber, Pistacia lentiscus, Phillyrea latifolia, Arbutus unedo, Olea europea, Ceratonia siliqua*, and *Erica arborea* (Morales-Molino *et al.,* 2020). The vegetation of the western and central Tagus basin and the inner Sado basin is primarily composed of scrub, orchards, vineyards, and woodland. The latter is dominated by *Q. ilex* and *Q. suber* forests and 'montados', with a considerable presence of Mediterranean pines and deciduous oaks, as well as other Mediterranean elements including *Phillyrea angustifolia* and *Pistacia terebinthus* (Blanco Castro *et al.,* 1997; Morales-Molino *et al.,* 2020). At mid-elevation (700 – 1000 m above sea-level (a.s.l)) forest composition is dominated by deciduous *Quercus* species, including *Q. pyrenaica* and *Q. faginea*, along with sub-Mediterranean and Eurosiberian elements *Pinus sylvestris, Pinus nigra, Juniperus thurifera*, and *Taxus baccata* (Blanco Castro *et al.,* 1997; Morales-Molino *et al.,* 2020). Where woodland degradation occurs, two types of matorral communities (a Mediterranean shrubland or heath ecosystem) can form: Cistaceae scrublands in regions with annual rainfall between 600 – 1000mm, and Ericaceae communities where precipitation is higher (Blanco Castro *et al.,* 1997). In the highest elevation regions of the central and eastern Tagus basin, *P. sylvestris* and *P. nigra* forests dominate, with deciduous *Q. pyrenaica* woodland also present. In areas where human interference has reduced soil cover matorral scrub occurs which includes Cistaceae, *Erica, Calluna,* Genisteae, and Lamiaceae (Polunin & Smythies, 1973; Blanco Castro *et al.,* 1997; Morales-Molino *et al.,* 2020). Although greatly disturbed by anthropogenic activity, particularly olive groves and vineyards on the fertile river soils (Aguiar & Ferreira, 2005), riparian woodland in the Tagus basin is dominated by *Fraxinus angustifolia*, *Alnus glutinosa*, *Populus nigra*, *Salix alba*, and *Salix salviifolia*, with the edge of these forest environments often surrounded by *Rubus ulmifolius*, *Crataegus monogyna*, and *Erica arborea* (Aguiar *et al.,* 2000). The Sado basin is predominantly woodland and scrub, with large *Q. suber* forests planted for cork in the south, although a substantial proportion of the land is used for arable purposes (Polunin & Smythies, 1973). On the coast where these rivers meet the Atlantic, Maritime Pines (*Pinus pinaster*) have been planted and are the dominant trees, alongside a significant proportion of heathland species such as *Erica*, *Cistus*, *Halimium*, and Leguminosae (Polunin & Smythies, 1973).

Vegetation productivity in this region is heavily influenced by the NAO. Analysis of this relationship has demonstrated that the highest impact of winter NAO on vegetation activity is during the growth phase of the following spring, with positive (negative) winter NAO resulting

in reduced (increased) vegetation productivity (Gouveia *et al.,* 2008). Additionally, the growth period productivity peaks earlier (later) following negative (positive) winter NAO, indicating the dependence of vegetation productivity on water availability from the previous winter (Gouveia *et al.,* 2008; Gouveia & Trigo, 2011).

Fig. 2.4: Land use map of present-day Iberia (Polunin & Smythies, 1973)

2.6. Conclusions

The present-day oceanographic, climatic, and geological setting provides insight into the natural drivers of western Mediterranean vegetation composition and a preliminary framework for exploring changes in SW Iberian vegetation over the past 28 kyr and the influence of terrestrial and oceanographic conditions. This chapter also explored the processes by which marine and terrestrial proxies are currently deposited at the Shackleton site, providing a background for how changing terrestrial and oceanographic conditions over the past 28 kyr may have influenced SW Iberian Margin sedimentary processes.

Palaeoclimatic knowledge is critical for understanding the response of different components of the Earth's system to anthropogenic climate change (Lea, 2015). Fundamental to this understanding is the exploration of how the global climate shifted into and out of glacial-interglacial cycles, with abrupt millennial/centennial-scale climate changes superimposed on longer trends. This chapter will firstly explore the general mechanisms and processes of global glacial-interglacial variability and abrupt climate changes throughout the Quaternary, before exploring the end of the last glacial period and current interglacial (specifically the last 28 kyr) and the abrupt climate jumps punctuating this period. These include the cold events of Heinrich Stadial 2 (HS2; 24.3 – 23.3 ka; Barker *et al.,* 2009) and Heinrich Stadial 1 (HS1)/Mystery Interval (17.5 – 14.5 ka; Denton *et al.,* 2006) which bracketed the LGM (22 – 19 ka; Yokoyama *et al.,* 2000), the warm BA (14.7 – 12.9 ka; Hartz & Milthers, 1901; Magny *et al.,* 2003a; Rasmussen *et al.,* 2006), the cold YD (12.9 – 11.7; Watts, 1977, 1980; Mott *et al.,* 1986; Magny *et al.,* 2003a; Rasmussen *et al.,* 2006), and 8.2 ka event (Alley *et al.,* 1997; Bond *et al.,* 1997; Magny *et al.,* 2003b). Finally, as a particularly sensitive region to past climate variability (e.g. Cacho *et al.,* 1999; Shackleton et al., 2000; Pailler & Bard, 2002; Combourieu Nebout *et al.,* 2002; 2009), the existing knowledge of the impact of these events on Iberian climate and vegetation will be assessed.

3.1. Orbital-scale climate change: Global Patterns

During the Quaternary period (2.588 million years ago – present), glacial-interglacial cycles have dominated the Earth's climate occurring every ~41 kyr in the Early Pleistocene and ~100 kyr in the Middle and Late Pleistocene (Imbrie *et al.,* 1984; Shackleton *et al.,* 1990; Ruddiman, *et al.* 1986). Hays *et al.* (1976) showed that changes in the Earth's orbital geometry and axial inclination, modifying the amount of summer insolation received at northern high latitudes, are the pacemaker of Quaternary ice ages, thus providing support for the Milankovitch hypothesis (1941). Although there is no consensus on the origin and mechanism of the 100-kyr cycle, with a range of proposed non-linear processes and climate feedbacks, a key element appears to be the critical size of ice-sheets in triggering deglaciations (e.g. Raymo, 1997; Paillard, 1998; Tzedakis *et al.,* 2017).

The glacial-interglacial cycles are reflected in records of global ice volume (Shackleton & Opdyke, 1973; Hays *et al.,* 1976; Imbrie *et al.,* 1984; Ruddiman *et al.,* 1989), sea level variations

(Broecker *et al.,* 1968; Mesolella *et al.,* 1969; Lambeck and Chappell, 2001), atmospheric carbon dioxide (CO_2) and methane (CH_4) trends (Petit *et al.,* 1999), sea surface and air temperature variations (Cuffey *et al.,* 1995; McManus *et al.,* 1999; NGRIP Members, 2004; Jouzel *et al.,* 2007; Martrat *et al.,* 2007), and changes in the strength of global monsoon systems (Rossignol-Strick, 1983; Wang *et al.,* 2001; Larrasoaña *et al.,* 2003). Compared to present, sea levels were on average 130 m lower during the LGM (Lambeck *et al.,* 2014) while the $\delta^{18}O$ of the global ocean was 1.1‰ higher (Adkins *et al.,* 2002).

Vegetation responds to climatic variability over orbital timescales, altering geographical distribution, range and abundance, with migratory routes and rates, and genetic adaptation varying according to species (Bennett *et al.,* 1986; Davis & Shaw, 2001). During glacial periods, many taxa in the temperate Northern Hemisphere were confined to glacial refugia in southern regions (Beug, 1968; van der Hammen *et al.,* 1971; Huntley & Birks, 1983; Bennett *et al.,* 1991; Tzedakis, 1993). Then, in response to interglacial warming, northward migration and range expansion occurred.

Palaeoarchives from Iberian Margin marine sediments show glacial-interglacial variability was synchronous with changes in global ice volume (Roucoux *et al.,* 2006; Martrat *et al.,* 2007). During interglacial (glacial) periods, western Iberian sea surface temperatures (SSTs) increase (decrease), the strength of deep-ocean ventilation increases (decreases), the influence of Arctic surface waters reduces (increases), and the proportion of NADW to AABW increases (decreases) (Skinner et al., 2003; Martrat *et al.,* 2007). Vegetation shifts demonstrate this orbital tempo, with an expansion (contraction) of woody taxa during interglacial (glacial) periods (Tzedakis et al., 2004; Roucoux *et al.,* 2006).

3.2. Abrupt Climate Change: Global Patterns

Warm-cold oscillations are not only restricted to orbital time-scales, with strong millennial and multi-centennial-scale changes shown in ice-core, marine, and terrestrial records, particularly during the Last Glacial period, ie. Marine Isotope Stage 3 (MIS 3) (Bond *et al.,* 1993; Allen *et al.,* 1999; NGRIP Members, 2004). Dansgaard *et al.* (1982), first showed the presence of abrupt millennial-scale events throughout the Last Glacial period in Greenland ice-cores. Several ice-core records across Greenland have since corroborated the occurrence of large oscillations in air temperatures (Dansgaard *et al.,* 1993; Grootes *et al.,* 1993; NGRIP Members, 2004; NEEM Community Members, 2013), known as Dansgaard-Oeschger (D-O) cycles. A typical cycle is

characterized by a decadal-scale warming (the so-called D-O event) ranging from 5 to 16°C (Kindler *et al.,* 2014) leading into a warm Greenland interstadial, followed by a gradual cooling into stadial conditions and a final fast cooling (Wolff *et al.,* 2010). The temperature variations were accompanied by changes in snow accumulation rates, atmospheric CH_4, and terrestrial dust and sea salt concentrations (Wolff *et al.,* 2010), implying that the climate changes were at least hemispheric in scale. 24 D-O cycles are recorded over Last Glacial period (Grootes *et al.,* 1993) and have been closely matched with abrupt changes in North Atlantic SSTs, linking atmospheric and oceanic processes in the region (Bond *et al.,* 1993).

Despite significant research into D-O cycles, their cause is still widely debated. Freshwater forcing and associated changes in the strength of the Atlantic Meridional Overturning Circulation (AMOC) has often been invoked as the trigger for D-O cycles (Broecker *et al.,* 1985; Bond & Lotti, 1995; Rind *et al.,* 2001; Ganopolski & Rahmstorf, 2001; Clark *et al.,* 2001; Zhang *et al.,* 2017). The AMOC is widely acknowledged to be highly sensitive to freshwater forcing, and it has been proposed that alterations in the ocean-atmosphere system trigger jumps between stable modes of operation (Broecker & Denton, 1989; Dokken & Jansen, 1999), with different modes of deep-water production and alternative ocean circulation states existing during specific climate conditions (Broecker *et al.,* 1985). Depending on the extent of disruption of the AMOC caused by freshwater forcing, three modes of circulation have been proposed: an 'on' mode during interglacial/D-O interstadials, a 'weak/cold' mode during glacials/D-O stadials, and an 'off' mode during Heinrich Events (Sarnthein *et al.,* 1994; Sarnthein, 2000; Rahmstorf, 2002). Models have investigated the stability of these different ocean circulation modes (Wright & Stocker, 1991; Stocker & Wright, 1991; Marotzke & Willebrand, 1991) resulting in the hypothesis of a non-linear hysteresis mechanism (Ganopolski & Rahmstorf, 2001).

Ice-rafted debris (IRD) in North Atlantic sediment, however, has been shown to occur after the onset of cooling (Barker *et al.,* 2015), leading to suggestions of an atmospheric, rather than freshwater trigger which alters sea-ice cover and consequently changes northern North Atlantic sub-surface salinity and temperatures, therefore driving changes in the AMOC (Dokken *et al.,* 2013; Menviel *et al.,* 2014; Li & Born, 2019). A competing argument suggests that Nordic Sea convection was continuous over the last glacial, but different mechanisms were responsible for deep-water formation: convection during interglacials, and brine rejection from sea-ice freezing during glacials (Dokken & Jansen, 1999).

3.2.1. Heinrich Events

In parallel, research on North Atlantic sediment cores showed that there were distinct layers of terrestrial sourced IRD during the last glacial period, with these layers of enhanced IRD and low foraminifera termed 'Heinrich layers' (HL) (Heinrich, 1988; Broecker *et al.,* 1992; Bond *et al.,* 1992). These layers were attributed to the discharge and subsequent melting of large icebergs, termed a Heinrich Event (HE), caused by the surging of the Laurentide ice-sheet (LIS), occurring at the end of a ~7 – 13 kyr cooling cycle of several D-O events (known as a Bond cycle), when atmospheric temperatures over Greenland had reached a minimum (Broecker *et al.,* 1992; Bond *et al.,* 1993). With HEs occurring after the stadial cooling has started, the freshwater input continued to reduce deep-water formation, further weakening the AMOC (Bond *et al.,* 1992). Although these Heinrich Events are not apparent in the Greenland ice-core temperature record, North Atlantic sediment records bear the imprint of D-O and Heinrich events, indicating a link between ice-sheet behaviour and ocean-atmosphere temperatures (Bond *et al.,* 1993).

Although in the literature 'Heinrich Stadial' (HS) has been used interchangeably with Heinrich Event' (HE), a HS is the entire cold North Atlantic interval, while HE applies to the period of IRD deposition at the end of the HS, confined to the North Atlantic Ocean; associated with these events are HLs, the physical manifestation of the HE (Barker *et al.,* 2009; Sanchez Goñi & Harrison, 2010; Hodell *et al.,* 2017). Imprints of HSs are shown in global records over the last glacial (Broecker, 1994), with reduced temperatures and glacier advance in Europe (Ivy-Ochs *et al.,* 2006), weakened East Asian and Indian Monsoon systems (Schulz *et al.,* 1998; Wang *et al.,* 2001; Higginson *et al.,* 2004; Deplazes *et al.,* 2014), and increased moisture availability in tropical South American and African records (Arz *et al.,* 1998; Wang *et al.,* 2006; Hessler *et al.,* 2010).

Both internal ice-sheet mechanisms and ice volume responses to external climate change mechanisms have been suggested as the cause of HEs. The Binge-Purge model is one of the most prominent internal ice-sheet mechanisms that has been proposed (MacAyeal, 1993). The binge phase is the LIS growth on the rigid sediment bed of the Hudson Bay and Strait. As this sediment thaws under increasing basal temperatures, the large volumes of ice are 'purged', resulting in a rapid iceberg discharge into the North Atlantic Ocean. This internal ice-sheet mechanism, however, does not account for IRD of different origins found within the same layers, indicating synchronised iceberg pulses from Canada, Europe, and Iceland (Broecker *et*

al., 1992; Grousset *et al.,* 1993), which imply the existence of an external climate control. Additionally, models have been unable to reproduce this mechanism without additional parameters (Calov *et al.,* 2002; Papa *et al.,* 2006) and SST decline has been shown to precede IRD peaks, indicating that increased iceberg calving is the response of colder conditions, not the cause (Bond & Lotti, 1995; Barker *et al.,* 2015).

Several ice-sheet responses to external climate mechanisms have been proposed. The first of these is sea level rise (SLR). When D-O stadial temperatures fell below a critical threshold, ice-calving from the Gulf of St Lawrence was enhanced, raising sea-levels and subsequently causing HE iceberg discharge from the LIS (Bond & Lotti, 1995; Flückiger *et al.,* 2006). The second suggested external mechanism is the forcing of climate-controlled meltwater. Warming summer temperatures (possibly resulting from intrastadial variability, or the end of the extreme cold conditions) are suggested to have enhanced meltwater accumulating on ice-sheet fringing and collecting in crevasses on the ice, leading to catastrophic break-up of the Labrador Sea ice-shelf which expanded substantially during extreme cold D-O temperatures (Hulbe *et al.,* 2004). The third suggestion is a change in the AMOC. SST records have indicated subsurface ocean warming prior to HEs (Peck *et al.,* 2007), which is in agreement with simulated results indicating that a weakened AMOC warmed the subsurface ocean, destabilising ice-sheets (Shaffer *et al.,* 2004; Alvarez-Solas *et al.,* 2010; Marcott *et al.,* 2011). This is caused by the weakened AMOC increasing stratification which breaks down convection and gradually warms northern North Atlantic subsurface water masses (Shaffer *et al.,* 2004; Mignot *et al.,* 2007).

Bassis *et al.* (2017) suggests this subsurface warming due to weakened AMOC enhanced underwater glacier melt, which increased iceberg discharge. Ice-sheet models support this, indicating that this mechanism can explain both timing and magnitude of HEs (Bassis *et al.,* 2017). Furthermore, after a significant ice discharge, the subsequent bed uplift (isostatic adjustment) isolates the glacier from the ocean forcing, enabling regrowth over the course of a Bond cycle which then culminates in a HE event. Consequently, this explains why each D-O event does not end equivalently (Bassis *et al.,* 2017).

3.2.2. Bipolar Seesaw

During periods of abrupt Greenland warming (D-O events), alignment of Vostok CH_4 records have been used to show a contemporaneous gradual Antarctic cooling. This is followed by

gradual Antarctic warming, coeval with strong North Atlantic cooling (Blunier *et al.,* 1998). This antiphase relationship has been termed the bipolar see-saw, with the strength and stability of the AMOC determining the interhemispheric heat transfer (Stocker & Johnson, 2003; Barker *et al.,* 2009). Temperature maxima in Greenland have been shown to lead Antarctica by 200 years (WAIS, 2015).

The thermal bipolar seesaw model (Stocker & Johnsen, 2003) attempts to explain the differing signals of the two regions, suggesting a southern sourced heat reservoir is responsible for the timing and dampening of the northern hemispheric signal, leading to gradual Antarctic changes. The interior ocean north of the Antarctic Circumpolar Current has been a suggested location of this heat reservoir (Pedro *et al.,* 2018).

Global records bear the imprint of these abrupt events which include a weakening of west African and Asian monsoons during stadials and HEs (Wang *et al.,* 2001; Peck *et al.,* 2004; Itambi *et al.,* 2009), reduced global CH_4 and nitrogen oxide levels, and enhanced dust and sea-salt transport (Thomas *et al.,* 2009). Increased global atmospheric CO_2 concentrations during stadial events, particularly HEs (Bauska *et al.,* 2016; Eggleston *et al.,* 2016), have been associated with the bipolar seesaw (Ahn & Brook, 2008). Increased CO_2 ventilation during HS1 and the YD is linked to enhanced Southern Ocean degassing (Skinner *et al.,* 2014) caused either by enhanced Antarctic air-sea gas exchange or upwelling from alterations in stratification (Schmittner & Galbraith, 2008), sea-ice extent (Skinner *et al.,* 2010), or winds (Anderson *et al.,* 2009).

A region which bears the imprint of this interhemispheric heat transport and plays an important role in assessing rapid climate change is the Iberian Margin. The systematic offset between the $\delta^{18}O$ of planktonic and benthic foraminifera records from a marine core southwest of the Iberian Peninsula have suggested the simultaneous presence of different climatic signals in surface and deep-water masses (Shackleton *et al.,* 2000). The former correlated with the $\delta^{18}O$ of Greenland and the latter with the 'triangular-wave' of Antarctic $\delta^{18}O$ (Blunier *et al.,* 1998; Petit *et al.,* 1999). Shackleton *et al.* (2000) attributed benthic $\delta^{18}O$ fluctuations to ice volume variations, but Skinner *et al.* (2007) have shown that the Iberian Margin deep-water signal was also influenced by local hydrographic and temperature changes, reflecting the isotopic composition of southern-sourced water, therefore tracking Antarctic temperature variations. Iberian Margin marine cores can, therefore, provide insight into north-south asynchrony

beyond the timeframe of ice-core records (de Abreu *et al.,* 2003; Tzedakis et al., 2004; Martrat *et al.,* 2007; Margari et al., 2010; 2014; Hodell *et al.,* 2013a; Hodell *et al.,* 2015).

3.3. Abrupt climate change: End of the Last Glacial period to present

This study focuses on the transition from the last glacial period to the Holocene. This includes a number of key millennial scale events; HS2 and HS1 which bracketed the LGM, the onset of the BA, YD, and 8.2 ka event, all of which have been attributed to freshwater forcing from ice-sheet meltwater altering the AMOC strength (McManus *et al.,* 2004; Thornalley *et al.,* 2010) with a total of 100 m SLR during the last deglaciation (Fairbanks, 1989). The impact of this meltwater on the AMOC during the deglaciation, however, varied between these events and is hypothesised to be the result of the location the freshwater entered the ocean (Clark *et al.,* 2001; Carlson & Clark, 2012). The cause of HEs has already been discussed, so the trigger of the BA, YD, and 8.2 ka event will be discussed here.

Traditionally the BA is thought to result from AMOC recovery following HS1 (Broecker *et al.,* 1990; Dokken & Jansen, 1999; Knorr & Lohmann, 2007; Liu *et al.,* 2009). The conundrum is the timing of meltwater pulse 1a (MWP1a) which was coeval with BA Greenland warming and led to ~18 m SLR in ~350 years (Fairbanks, 1989; Deschamps *et al.,* 2012). This has led to suggestions that MWP1a was the trigger of the BA, entering the Atlantic from the Mississippi river or Southern Ocean, which invigorated NADW production and caused the warming event (Clark *et al.,* 2001; Weaver *et al.,* 2003). The hemispheric source of this meltwater, however, is debated. A substantial proportion is suggested to have entered through the Mississippi river (Keigwin *et al.,* 1991; Peltier, 2005; Gregoire *et al.,* 2012), with model simulations demonstrating that the separation of the Laurentide and Cordilleran ice domes produced MWP1a (Gregoire *et al.,* 2012). Other models, however, have indicated that the AMOC would have been weakened if significant meltwater entered at this location (Manabe & Stouffer, 1997; Roche *et al.,* 2007, 2010). As this weakening is unsupported by existing fossil records and research indicates that the LIS could not be the source of such a considerable freshwater input, alternative theories of a rapid Antarctic freshwater pulse have been proposed (Clark *et al.,* 1996; 2002; Weaver *et al.,* 2003; Bassett *et al.,* 2005; Carlson, 2009). There are also suggestions, however, that during stadials the strengthened, highly saline MOW entering the Atlantic played a key role in the switch of the AMOC from stadial to interstadial conditions resulting in the abrupt warming at the start of the BA (Voelker *et al.,* 2006; Rogerson *et al.,* 2006).

For the YD, meltwater entering the Atlantic from an eastern/northern source is suggested to have weakened the AMOC through the reduction of NADW production (Clark *et al.,* 2001). Although this stadial has global impacts, with warming in the Southern Hemisphere and cooling in the Northern Hemisphere (Shakun & Carson, 2010; Stenni *et al.,* 2011; Heiri *et al.,* 2014), the cause of this event is debated. Meltwater (Broecker, 1985) and bolide impact (Firestone *et al.,* 2007) have been proposed as drivers, with some studies indicating the cause is more complex, involving a combination of factors (Renssen *et al.,* 2015). The meltwater hypothesis is the most widely discussed. One branch of this theory is the rerouting of Lake Agassiz freshwater from the Mississippi to the St. Lawrence river which shut down the AMOC (Rooth, 1982; Broecker *et al.,* 1985, 1989; Broecker, 2006). Others, however, have proposed that LIS meltwater entered the Arctic Ocean via the McKenzie river (Tarasov & Peltier, 2005; Murton *et al.,* 2010; Keigwin *et al.,* 2018).

The 8.2 ka event has also been attributed to an abrupt meltwater event that resulted in AMOC weakening in the early Holocene. This is suggested to be the result of the catastrophic drainage of Lakes Agassiz and Ojibway entering the North Atlantic Ocean through the Hudson Strait (Barber *et al.,* 1999), which led to a northern hemispheric temperature reduction (Rensenn *et al.,* 2001) coeval with a 160-year Greenland temperature decline (Thomas *et al.,* 2007). Models indicate that the separation of the Labrador and Baffin ice domes may have caused this meltwater pulse (Gregoire *et al.,* 2012).

3.3.1. The Holocene

Early research considered the Holocene climate to be relatively stable. Boreal insolation reached its maximum at 11.6 ka as obliquity and precession peaks coincided, declining through the course of the interglacial; this led to a southward migration of the intertropical convergence zone (ITCZ) and overall cooling of the North Atlantic Ocean and northern landmasses (Wanner *et al.,* 2008). Three main phases of the Holocene have been proposed (Nesje & Dahl, 1993; Walker *et al.,* 2018): the early Holocene (the Greenlandian; 11.7 – 8.3 ka), a period that still had the cooling influence of North American ice-sheets, despite the boreal insolation maxima; the mid-Holocene (the Northgrippian; 8.3 – 4.2 ka), where these ice-sheets had retreated, yet insolation was still high and a NAO-like system was established (Fletcher *et al.,* 2013); and the late Holocene (the Meghalayan; 4.2 ka – present), a period of declining summer insolation.

The Holocene also contains many abrupt centennial-scale climate changes. Although smaller than the magnitude of those during the last deglaciation, six periods of abrupt change (cooling/drying and atmospheric circulation change) have been shown in global Holocene records (Mayewski *et al.,* 2004). Bond *et al.* (2001) suggested a 1,500-year cyclicity of these events, corresponding with IRD peaks in North Atlantic Ocean marine records, although this cyclicity is disputed (Moros *et al.,* 2016), with suggestions of continuous 2,500-year cycles throughout the Holocene, a 1,000-year periodicity in the Early Holocene, and 1,600-year cycles during the Late Holocene (Debret *et al.,* 2007; 2009). In turn, these have been shown to be coeval with Greenland ^{10}Be and tree-ring ^{14}C records, leading to suggestions that variations in solar forcing was responsible (Mayewski *et al.,* 2004). Internal cycles, however, have also been suggested as drivers (Schulz *et al.,* 2007; Jongma et al., 2007) including temperature and salinity changes in the surface subpolar North Atlantic Ocean (Thornalley *et al.,* 2009) and changes in the strength and position of the westerlies (Giraudeau *et al.,* 2010).

3.4. Iberian climate and vegetation change: LGM to present

There are many existing records reconstructing Iberian climate change over the last 28 kyr, with the locations of those mentioned in the text shown in Fig. 3.1 and outlined in Table 3.1. These studies have contributed greatly to our understanding of climatic shifts and the response of vegetation in this region to these changes (Hooghiemstra *et al.,* 1992; van der Knaap & van Leuween, 1995, 1997; Boessenkool *et al.,* 2001; Turon *et al.,* 2003; Chabaud *et al.,* 2014; Oliveira *et al.,* 2018; Naughton *et al.,* 2019). There remains, however, conflicting evidence with regards to the western Iberian hydrological conditions over the last 28 kyr. This section will outline what is already known about this region's climate over the past 28 kyr, where the gaps in our knowledge still remain, and how this study can contribute to this area of research.

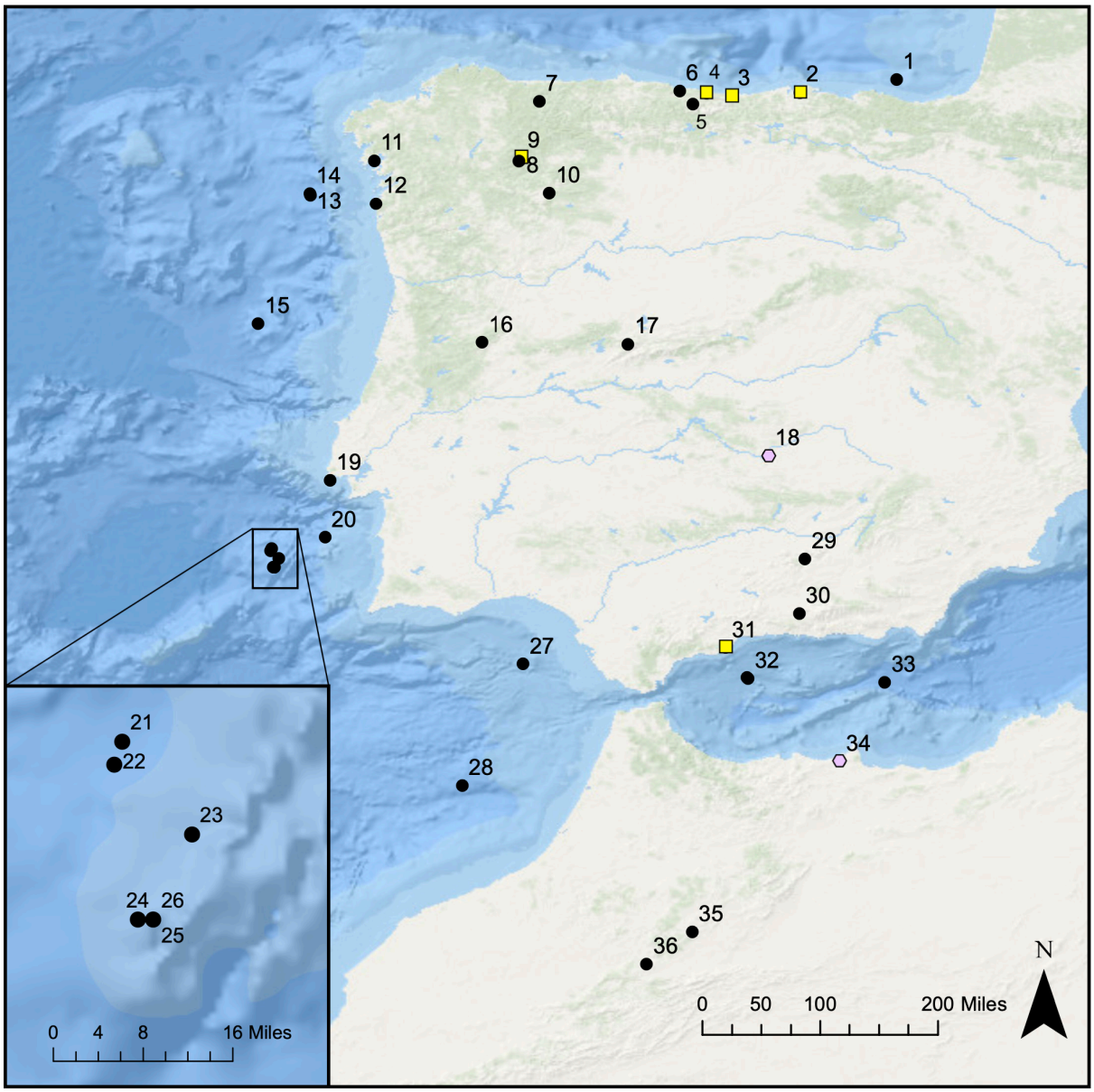

Fig. 3.1: Sites of Iberian climate reconstructions over the past 28 kyr. 1. KS05-10; 2. La Garma Cave; 3. Pindal Cave; 4. La Vallina Cave; 5. Lago Enol; 6. Cueva Rosa; 7. Lago de Ajo; 8. Laguna Lucenza; 9. Cova de Arcoia; 10. Lago de Sanabria area; 11. A14-VC15; 12. Mougás lagoon; 13. MD99-2331; 14. MD03-2697; 15. MD95-2039; 16. Serra da Estrela; 17. Navamuno peat bog; 18. Fuentillejo maar; 19. D13882; 20. SO75- 6KL; 21. MD95-2042; 22. SU 81-18; 23. 8057B; 24. SHAK06-5K (this study); 25. MD01-2444 (this study); 26. U1385; 27. GeoB5901-2; 28. M 15669-1; 29. Padul 15-05 & 13-01; 30. Padul peat bog; 31. El Refugio Cave; 32. ODP-161-976A & ODP 976; 33. MD95-2043; 34. Kert river; 35. Lake Sidi Ali; 36. AI.13. Vegetation (black circles), speleothem (yellow squares) and sedimentological/geochemical (pink hexagons) records. Details and references outlined in Table 3.1.

Ocean basemap sourced from: https://www.arcgis.com/home/item.html?id=5ae9e138a17842688b0b79283a4353f6

Region	Archive	Site	Time period	Reference	No. on map
Bay of Biscay	Marine core: Pollen	KS05-10	9 ka – present	Oliveira, 2012	1
Cantabrian coast, N Iberia	Speleothem	La Garma Cave	13.5 ka – present	Baldini *et al.,* 2015; 2019	2
Cantabrian coast, N Iberia	Speleothem	Pindal Cave	25 – 11.6 ka 14 – 4 ka	Moreno *et al.,* 2010a Stoll *et al.,* 2013	3
Cantabrian coast, N Iberia	Speleothem	La Vallina Cave	10 ka – present	Stoll *et al.,* 2013	4
Cantabrian coast, N Iberia	Terrestrial core: Pollen, Sedimentological, Geochemical	Lago Enol	40 ka – present	Moreno *et al.,* 2010b; 2012	5
Cantabrian coast, N Iberia	Speleothem	Cueva Rosa	14 – 5 ka	Stoll *et al.,* 2013	6
Cantabrian Mtns, NW Iberia	Terrestrial core: Pollen	Lago de Ajo	14.5 ka – present	Allen *et al.,* 1996	7
Cantabrian Mtns, NW Iberia	Terrestrial core: Pollen	Laguna Lucenza	9.8 ka – present 17 ka – present	Santos *et al.,* 2000 Muñoz-Sobrino *et al.,* 2001	8
Galician *Massif*, NW Iberia	Speleothem	Cova de Arcoia	9.3 ka – present	Railsback *et al.,* 2011	9
Galician *Massif*, NW Iberia	Terrestrial core: Pollen	Laguna de la Roya; Sanabria Marsh Laguna de las Sanguijuelas; Lleguna	14.5 ka – present 18 ka – present	Allen *et al.,* 1996 Muñoz-Sobrino *et al.,* 2004	10
Coastal NW Iberia	Terrestrial core: Pollen & Sedimentological	A14-VC15	14.4 – 9.4 ka	Garcia-Moreiras *et al.,* 2019	11
Coastal NW Iberia	Littoral core: Pollen	Mougás lagoon	16 ka – present	Gómez-Orellana *et al.,* 1998	12
NW Iberian Margin	Marine core: Pollen	MD99-2331	25 ka – present 40 – 16 ka	Naughton *et al.,* 2007 Naughton *et al.,* 2009	13
NW Iberian Margin	Marine core: Pollen	MD03-2697	25 ka – present 20 ka – present	Naughton *et al.,* 2007 Naughton *et al.,* 2016	14
Central Portugal	Marine core: Pollen	MD95-2039	10 – 65 ka	Roucoux *et al.,* 2005	15
Serra da Estrela, C. Portugal	Terrestrial: Pollen	10 cores from 8 sites (lagoons, lakes and ponds)	10.3 ka – present 14.8 – 9.5 ka	Van der Knaap & Van Leeuwen, 1995 Van der Knaap & Van Leeuwen, 1997	16
Central Iberia	Terrestrial core: Pollen, Sedimentological, Geochemical	S3	15.6 – 10.6 ka	López-Sáez *et al.,* 2020	17
Central Iberia	Terrestrial core: Sedimentological & Geochemical	Fuentillejo maar	50 ka – present	Vegas *et al.,* 2010	18
SW Iberian Margin	Marine core: Pollen	D13882	13.4 – 11.4 ka	Naughton *et al.,* 2019	19
SW Iberian Margin	Marine core: Pollen	SO75- 6KL	21 ka – present	Boessenkool *et al.,* 2001	20

SW Iberian Margin	Marine core: Pollen	MD95-2042	14.2 ka – present	Chabaud *et al.,* 2014	21
SW Iberian Margin	Marine core: Pollen	SU 81-18	25 ka – present	Turon *et al.,* 2003	22
SW Iberian Margin	Marine core: Pollen	8057B	19.1 – 2.9 ka	Hooghiemstra *et al.,* 1992	23
SW Iberian Margin	Marine core: Pollen	U1385	17.5 ka – present	Oliveira *et al.,* 2018	26
Gulf of Cadiz	Marine core: *n*-Alkane & Sedimentological	GeoB5901-2	6 – 2.5 ka	Schirrmacher *et al.,* 2019	27
NW Moroccan Margin	Marine core: Pollen	M 15669-1	121.7 – 6.3 ka	Hooghiemstra *et al.,* 1992	28
Padul, Southern Spain	Terrestrial core: Pollen, Sedimentological, Geochemical	Padul 15-05	11.6 ka – present	Ramos-Roman *et al.,* 2018a	29
			4.7 ka – present	Ramos-Roman *et al.,* 2018b	
	Terrestrial core: Pollen	Padul 13-01	200 ka – present	Camuera *et al.,* 2018	
			4.7 ka – present	Ramos-Roman *et al.,* 2018b	
Padul, Southern Spain	Terrestrial core: Pollen	Padul peat bog	30 – 4.5 ka	Pons & Reille, 1988	30
Southern Spain coast	Speleothem	El Refugio Cave	9.3 – 2.9 ka	Walczak *et al.,* 2015	31
Alboran Sea	Marine core: *n*-Alkane & Sedimentological	ODP-161-976A	6 – 2.5 ka	Schirrmacher *et al.,* 2019	31
Alboran Sea	Marine core: Pollen	ODP 976	25 ka – present	Combourieu Nebout *et al.,* 2009	32
			15 – 4 ka	Dormoy *et al.,* 2009	
Alboran Sea	Marine core: Pollen	MD95-2043	48 ka – present	Fletcher & Sanchez Goñi, 2008	33
			20 – 6 ka	Fletcher *et al.,* 2010	
Northern Morocco	River channel: Sedimentological	Kert river	30 ka – present	El Amrani *et al.,* 2008	34
Middle Atlas, Morocco	Terrestrial core: Pollen, Sedimentological, Geochemical	Lake Sidi Ali	12.3 ka – present	Zielhofer *et al.,* 2017	35
				Zielhofer *et al.,* 2018	
Middle Atlas, Morocco	Terrestrial core: Pollen, Sedimentological, Geochemical	AI.13	25 ka – present	Tabel *et al.,* 2016	36

Table 3.1: Details of Iberian climate research over the past 28 kyr and position on map (Fig. 3.1).

The Mediterranean lies in a transition zone that is influenced by both mid- and low-latitude climate dynamics (Raicich *et al.,* 2003). On orbital timescales, precession has been a key driver of Mediterranean climate, strengthening the African summer monsoons at precession minima (boreal insolation maxima) linked to reduced dust transport and increased freshwater input into the Mediterranean Sea via northward draining catchments along the North African coast and the Nile, leading to the quasi-periodic deposition of organic-rich sapropel layers as a result of increased surface water freshening, reduced deep water ventilation and increased export production (Rossignol-Strick et al. 1982; Lourens *et al.,* 1992; Tuenter *et al.,* 2003; Rohling *et al.,* 2015). As the African Summer monsoonal precipitation did not affect the Mediterranean region directly extending only to 24°N (Tzedakis *et al.,* 2007), increased Mediterranean SSTs and Iberian Margin upwelling changes are thought to be the direct effect of precessional insolation, shifting the ITCZ northward and enhancing wind driven processes in the Mediterranean (Lourens *et al.,* 1992; Tuenter *et al.,* 2003; Hodell *et al.,* 2013a). Obliquity has a smaller control, driving Mediterranean SST changes, sapropel thickness, and to a lesser extent, ocean productivity; this corresponds with ice volume changes demonstrating a high-latitude control over this region (Lourens *et al.,* 1992; Lourens *et al.,* 1996). Mediterranean vegetation changes have been shown to be coeval with atmospheric CH_4 concentrations on orbital and millennial timescales (Tzedakis *et al.,* 2009). This has been explained by the coupling of low- and mid-latitude hydrological processes which are thought to be influenced by the movement of the ITCZ.

In addition to these influences, Iberia is also highly sensitive to changes in NADW production on millennial and centennial timescales due to a direct atmospheric link between the North Atlantic Ocean and Iberia (Cacho *et al.,* 1999; 2001; Rohling *et al.,* 1998; 2002; Frigola *et al.,* 2007), with Iberian vegetation changes over the last 28 kyr shown to be synchronous with North Atlantic variability (Combourieu Nebout *et al.,* 2002; 2009). During the LGM and subsequent deglaciation, the presence of large Northern Hemisphere ice-sheets brought western Iberia under North Atlantic influence. This was the result of an enhanced equator to pole temperature gradient which displaced the westerlies southwards, making flow more zonal which consequently strengthened winds over Iberia (Harrison *et al.,* 1992; Kageyama *et al.,* 1999; Cacho *et al.,* 2000; Laine *et al.,* 2009; Beghin *et al.,* 2016). The polar front is suggested to have reached western Iberia at 40°N during HS1 and the YD, reducing Iberian Margin SSTs (Ruddiman & McIntyre, 1981; Bard *et al.,* 1987; Boessenkool *et al.,* 2001). Increased aeolian activity in Central Iberia occurred between 29 – 19 ka and during the YD (Bateman & Diez

Herrero, 2001; Rebollal & Pérez-González, 2007), while in SW Iberia, the maximum strength of the westerlies occurred at 17.5 ka, during HS1 (Costas *et al.,* 2016). In northern Iberia, maximum activity occurred from the YD to the early Holocene, indicating a northward movement of the westerlies at this time (Rebollal & Pérez-González, 2007).

As a consequence of the enhanced westerlies, deep-water production and ventilation in the western Mediterranean Sea was enhanced during stadials, which, when combined with the reduced NADW production, led to enhanced water exchange through the Gibraltar Strait (Cacho *et al.,* 2000; Voelker *et al.,* 2006; Rogerson *et al.,* 2006). It has been argued, however, that this mechanism was disrupted when icebergs reached the entrance of the Mediterranean during HEs, reducing surface-water salinity and western Mediterranean deep-water productivity (Sierro *et al.,* 2005). On the SW Iberian Margin, at multi-centennial timescales, reduced productivity and upwelling strength and a deeper nutricline depth have been linked to cold stadial periods during the deglaciation due to water column stratification (Ausin *et al.,* 2020).

The impact of the strengthened and southward displaced westerlies on Iberian hydrology during the last glacial is more complex. Models demonstrate an increase in winter precipitation resulting from the southward movement and intensification of the westerlies (Laine *et al.,* 2009; Beghin *et al.,* 2016), while palaeoclimatic reconstructions generally show an expansion of steppe taxa and lower lake levels indicating reduced precipitation (Boessenkool *et al.,* 2001; Turon *et al.,* 2003; Roucoux *et al.,* 2005; Naughton *et al.,* 2007; 2009; El Amrani *et al.,* 2008; Vegas *et al.,* 2010). These discrepancies between the simulated and proxy data are suggested to result from models overestimating the temperatures experienced in this region (Jost *et al.,* 2005), because with colder Iberian temperatures, less evaporation and consequently, precipitation would be expected, despite stronger and more southward storm tracks.

The picture emerging from the palaeoclimatic reconstructions is much more complex than just reduced precipitation during the last glacial. The vegetation and climatic shifts of this region are both spatially and temporally variable across Iberia as outlined in Table 3.2. The mechanisms controlling the hydrology of this region need to be better understood as there continue to be discrepancies between the interpretations of proxy and simulated data.

Over the Holocene, the climate shifts are also complex, as shown in Table 3.2, with significant spatial variability shown in water availability patterns across the Iberian Peninsula. During the YD, arid conditions are shown to have prevailed across the region; however, at the transition into the early Holocene (until ~10 ka), humidity increased in Atlantic-influenced northwestern sites but decreased in southeastern regions due to summer insolation maxima reducing summer water availability in Mediterranean-influenced areas (Morellón *et al.,* 2018). From 9.3 ka onwards, the influence of the changing position of the Azores High and westerlies on the spatial variability of humidity patterns across the Iberian Peninsula has also been explored (Walczak *et al.,* 2015). During the early Holocene, a northward migration of the Azores High, coinciding with the boreal insolation maximum, resulted in increased year-round aridity in northern Iberia. The steady year-round precipitation in southern Iberia was therefore likely to be Mediterranean sourced. Over the mid-Holocene, the Azores High migrated southward, likely located year-round over southern Iberia resulting in continued aridity. Northern Iberia also experienced mid-Holocene summer aridity, however, as the Azores High remained below this region in winter, wintertime precipitation was enhanced. In the late Holocene, after 5 ka, with northern high-latitude ice-sheets no longer determining the strength and position of the ITCZ, the modern-day NAO system is suggested to have been established (Walczak *et al.,* 2015). With the Azores High moving further southward, this resulted in significantly wetter winters in both northern and southern Iberia, while in summer, northern Iberia experienced enhanced rainfall with southern Iberia becoming drier.

	Northwestern Iberia	Central/SW Iberia	Southern Iberia/Northern Morocco
LGM	Herbaceous taxa dominated, but the occurrence of deciduous elements indicate that cool-dry conditions are less severe than in the HSs bracketing this period (Roucoux *et al.,* 2005; Naughton *et al.,* 2007). Speleothem records indicate higher precipitation compared to the HSs, but conditions were drier than present (Moreno *et al.,* 2010a).	Although cold conditions prevailed, aridity decreased in SW Iberia, shown by the steppe taxa reduction and expansion of ferns, Cyperaceae, Ericaceae, and some deciduous elements (Turon *et al.,* 2003). Lake levels rose from the end of HS2 and peaked at ~20 ka before declining into HS1 (Vegas *et al.,* 2010).	High southern Iberian lake levels are suggested to have resulted from reduced evaporation rather than precipitation rise (Camuera *et al.,* 2018). In North Africa, steppe and heathland contracted, indicating cold-humid conditions (Combourieu Nebout *et al.,* 2009), while sediment analysis shows increased humidity between 30 – 20 ka (El Amrani *et al.,* 2008). Peaks in aquatic taxa in the Atlas Mountains suggest regional snow precipitation increased during the LGM (Tabel *et al.,* 2016).
HS1 & 2	Both stadials show two distinct stages: An initial SST decrease, southward westerly displacement and heathland expansion, indicating cold, relatively wet conditions followed by northward westerly displacement, cool-arid conditions and steppe expansion (Naughton *et al.,* 2007; 2009). High resolution records show HS1 to be warmer/wetter (Naughton *et al.,* 2016), while speleothem growth hiatus & lake records indicate increased HS1 aridity (Moreno *et al.,* 2010a; 2010b).	Steppe taxa expansion occurred during both events, inferring reduced evaporative moisture to Iberia (Boessenkool *et al.,* 2001; Turon *et al.,* 2003). However, maximum steppe expansion and the coldest most arid conditions of the past 28 kyr occurred during HS1, corresponding with strong SST decline and IRD deposition at the SW Iberian Margin (Turon *et al.,* 2003). Lacustrine geochemical/sedimentary records show cold and arid conditions in Central Iberia with low lake levels (Vegas *et al.,* 2010).	Reduction in forests, with an expansion of steppe taxa correspond with reduced SSTs and cold, arid conditions during both periods, although HS1 was the most extreme (Pons & Reille, 1988; Combourieu Nebout *et al.,* 2009; Fletcher *et al.,* 2010). Reduced lake levels are shown during HS1 in southern Iberia reflecting increased aridity (Camuera *et al.,* 2018).
BA	Throughout this stadial, pioneer vegetation and deciduous *Quercus* forests expanded while semi-desert elements contracted, corresponding with increased Iberian Margin SSTs showing higher temperatures and moisture availability (Naughton *et al.,* 2002; 2007; 2016). Increased water availability is also shown in speleothem records (Moreno *et al.,* 2010a).	Iberian Margin records show Ericaceae expanded while *Quercus* forests increased towards the end of the BA, indicating warmer-wetter conditions (Turon *et al.,* 2003; Chabaud *et al.,* 2014; Oliveira *et al.,* 2018). Central Portuguese records show complex forest expansions and contractions (Van der Knaap & Van Leuween, 1997; López-Sáez *et al.,* 2020) and increased lake levels & water availability (Vegas *et al.,* 2010).	Two periods of deciduous forest expansion at ~14 and 13.3 ka, correspond with the Bølling and Allerød warm periods (Fletcher *et al.,* 2010; Combourieu Nebout *et al.,* 2009). Increased lake levels and lacustrine deposition of carbonate facies indicate increased water availability (Camuera *et al.,* 2018).
YD	Reduced Eurosiberian elements and increased grassland/*Pinus* and *Betula* open forests indicate cold/dry conditions. Despite	Steppe taxa expanded, with a reduction in deciduous *Quercus* (Boessenkool *et al.,* 2001; Turon *et al.,* 2003; Chabaud *et al.,* 2014;	Steppe taxa increase, with forest decline prior to SST decrease, indicating an initial vegetation response to

	this, there was sufficient winter precipitation for heathland to survive (Naughton *et al.,* 2016; Garcia-Moreiras *et al.,* 2019). Lake records show reduced moisture (Moreno *et al.,* 2012), while speleothem records indicate wetter summers and drier winters during the early YD, moving to wetter than average winters in the latter part of this period (Baldini *et al.,* 2019).	Oliveira *et al.,* 2018; Naughton *et al.,* 2019; López-Sáez *et al.,* 2020). SST changes on the SW Iberian Margin occurred over 400 years, with expanding steppe taxa responding rapidly (Boessenkool *et al.,* 2001). Central Iberian lacustrine records show low lake levels, indicating cold/arid conditions (Vegas *et al.,* 2010).	atmospheric change (Fletcher *et al.,* 2010). Early in the YD, an increase in *Artemisia* is followed by an increase in deciduous and *Cedrus* forests, indicating warmer/wetter conditions at the end of the stadial (Pons & Reille, 1988; Combourieu Nebout *et al.,* 2009). Reduced Alboran SSTs (Cacho *et al.,* 2001) and lower lake levels in Northern Morocco suggest reduced regional precipitation (Zielhofer *et al.,* 2017).
Early Holocene	Deciduous forest expansion indicates increased temperature and precipitation, while reduced heathland show increased hydroclimate seasonality corresponding with boreal insolation maximum (Naughton *et al.,* 2007; 2016; Garcia-Moreiras *et al.,* 2019). Different speleothem records highlight regional spatial variability, showing both increased aridity (Railsback *et al.,* 2011) and humidity (Stoll *et al.,* 2013). Lake records, however, indicate wetter conditions (Moreno *et al.,* 2012).	Prominent woodland expansion parallels the increased boreal insolation. Marine records show maximum levels are reached between ~11.8 – 8 ka, declining abruptly thereafter (Chabaud *et al.,* 2014; Oliveira *et al.,* 2018; Gomes *et al.,* 2020), although terrestrial records show a more gradual forest decline (Van der Knaap & Van Leuween, 1995). A number of short cold arid events, including the 8.2 ka event, are shown by low lake levels in Central Iberia (Vegas *et al.,* 2010).	Deciduous forests with Mediterranean elements expanded during the warm, humid Holocene Climate Optimum (9-7 ka), interrupted by forest contraction at ~8.2 ka (Combourieu Nebout *et al.,* 2009; Fletcher *et al.,* 2010; Ramos-Roman *et al.,* 2019a). Southern Iberian speleothem records indicate evenly distributed rainfall (Walczak *et al.,* 2015), while in northern Morocco, warmer conditions (Tabel *et al.,* 2016) and enhanced winter rainfall were punctuated by abrupt cool/arid events at 8.2 and 10.2 ka (Zielhofer *et al.,* 2017).
Mid to Late Holocene	Steady deciduous tree decline, replaced by heathland, reflect increased annual water availability/reduced hydroclimate seasonality as boreal insolation decreased (Naughton *et al.,* 2007; 2016). Speleothem and lake records show spatial & temporal variation with a wetter mid-Holocene moving to late Holocene aridity (Stoll *et al.,* 2013) and vice versa (Railsback *et al.,* 2011; Moreno *et al.,* 2012). Between the mid & late Holocene, precipitation seasonality changed from summer dominance to winter (Baldini *et al.,* 2019).	Deciduous *Quercus* forests declined, while Ericaceae expanded indicating a reduced hydroclimate seasonality (Turon *et al.,* 2003; Chabaud *et al.,* 2014; Oliveira *et al.,* 2018; Gomes *et al.,* 2020). In addition to natural drivers of vegetation change, anthropogenic deforestation & grazing had an increasing influence from ~5.7 ka (Van der Knaap & Van Leuween, 1995).	Forest contraction occurred from 7 ka, with anthropogenic influence on vegetation from ~1.5 ka (Combourieu Nebout *et al.,* 2009; Ramos-Roman *et al.,* 2019a). Unlike northern & central Iberia, speleothem and lake records show increased aridity during the mid-Holocene, although spatial variability is apparent (Walczak *et al.,* 2015; Zielhofer *et al.,* 2017). After 5 ka, speleothem records show increased seasonality, reduced annual precipitation and multi-decadal variability indicating the NAO establishment (Walczak *et al.,* 2015).

Table 3.2: Spatial variability in vegetation and climatic shifts over the past 28 kyr across Iberia. Climate interpretations are of cited authors.

3.4.1. SW Iberian vegetation change

Looking specifically at SW Iberia, there are a number of high-resolution records that cover sections of the past 28 kyr period, which when combined provide an insight into the millennial and multi-centennial climatic changes in this region.

- *HS1&2:* During both HS1&2, steppe vegetation expanded prior to the arrival of IRD at SW Iberian Margin sites at the second half of both stadials, with records showing the fast response of vegetation to HS1 cooling (Boessenkool *et al.,* 2001; Turon *et al.,* 2003).
- *LGM:* This period sees the dominance of steppic taxa, although proportions are lower than the neighbouring stadials (Boessenkool *et al.,* 2001; Turon *et al.,* 2003). Increased humidity is shown by the expansion of Ericaceae and smaller increase in deciduous *Quercus*, Cyperaceae, and ferns, although the representation of *Empetrum*-type indicates continued cold conditions (Turon *et al.,* 2003).
- *BA:* Warm humid conditions are indicated by the vegetation of the BA. Marine records demonstrate the dominance of deciduous woodland with some evergreen elements; by the end of this interstadial, deciduous *Quercus* and Cyperaceae reach their maximum values coinciding with a with contraction of steppe elements (Boessenkool *et al.,* 2001; Turon *et al.,* 2003; Chabaud *et al.,* 2014).
- *YD:* Steppe taxa became dominant after the onset of SW Iberian Margin SST cooling (Boessenkool *et al.,* 2001). In Central/SW Iberia, this stadial was composed of complex centennial-scale variations (van der Knaap & van Leuween, 1995; Chabaud *et al.,* 2014; Naughton *et al.,* 2019). Multi-centennial scale vegetation changes have been shown throughout this stadial, controlled by the coupling of this region with complex North Atlantic ocean-atmosphere variations (Naughton *et al.,* 2019). An initial contraction of forest elements and expansion of steppe taxa indicate the coldest and driest conditions of the stadial, albeit with sufficient winter precipitation to sustain some forest and heath elements. Naughton *et al.* (2019) suggest this vegetation change is the consequence of sea-ice expansion and AMOC weakening, leading to the southward displacement of the westerlies and reduction in Iberian Margin SSTs. The mid-YD saw a forest expansion, reflecting warming and increased precipitation, resulting from reduced sea-ice, increased convection, and therefore strengthened AMOC, causing the weakening and northward displacement of the westerlies. The final phase of the YD was marked by vegetation composition fluctuations (expansion and contraction of semi-desert taxa, with heath and arboreal elements increasing towards the Holocene transition), indicating changes between cool-wet and cold-dry phases; this complexity

stems from unsteady variation in AMOC strength, sea-ice extent, and intensity and position of the westerlies as the climate moved into the interglacial (Naughton *et al.,* 2019).

- *Holocene:* In SW Iberia, during the Holocene, xerothermic forest components (adapted to dry, hot climates) expanded more rapidly than mesothermic elements (adapted to warm-temperate conditions), indicating a more Mediterranean-type climate, corresponding with the boreal insolation maximum resulting in hot dry summers and cooler wetter winters (Van der Knaap & Van Leuween, 1997; Chabaud *et al.,* 2014; Oliveira *et al.,* 2018). SW Iberian marine records show woodland expansion is interrupted at 8.2 ka by a brief and abrupt forest contraction and steppe expansion, indicating a cooling/drying over SW Iberia (Chabaud *et al.,* 2014). The timing of which corresponds with the outflow of freshwater from Lake Agassiz/Ojibway which caused AMOC slowdown (Barber *et al.,* 1999; Rensenn *et al.,* 2001). Terrestrial central Portuguese records, however, show a more gradual and later decline (Van der Knaap & Van Leuween, 1997), as do Alboran Sea (Combourieu Nebout *et al.,* 2009) and northwestern (NW) Iberian records (Naughton *et al.,* 2007). As the interstadial progresses, low initial values of Ericaceae increase from the mid-Holocene to their peak in the late Holocene, corresponding to reduced boreal summer insolation, indicating a reduced hydroclimate seasonality due to lower summer aridity and increased annual moisture availability (Rodríguez-Rajo *et al.,* 2005; Chabaud *et al.,* 2014; Oliveira *et al.,* 2018; Margari *et al.,* 2014). At a multi-centennial scale, Holocene vegetation records from SW Iberia show numerous forest contractions indicating cool/dry episodes, coeval with reduced SW Iberian margin SSTs (Chabaud *et al.,* 2014). These multi-centennial forest contractions are also shown in Alboran Sea (Fletcher *et al.,* 2010) and NW African records (Zielhofer *et al.,* 2017). It has been suggested that during the early Holocene, SST decreases as a result of meltwater discharges were responsible for these drying events across Iberia , particularly a reduction in winter precipitation, but after the mid-Holocene, with no large ice-sheets remaining, NAO-like variability is suggested to have been the dominant driver of abrupt events in this region, with positive NAO stages corresponding with Iberian drying events, paced by centennial-scale solar minima (Fletcher et al., 2013; Zielhofer *et al.,* 2017; 2018; Schirrmacher *et al.,* 2019). Overall, the close coupling of Iberian vegetation change with the strength of the AMOC and the position and strength of the westerlies, shows the sensitivity of this region to oceanic-atmospheric changes. Finally, anthropogenic pressures, including deforestation,

agricultural land-use, over-grazing, soil erosion, and increasing freshwater exploitation, had an important impact on the region's vegetation after 3.2 ka, but most severely after 0.96 ka (Van der Knaap & Van Leeuwen, 1995).

Taken together, these records provide an overview of the vegetation variations in SW Iberia over the last 28 kyr, but a lack of robust chronologies means that detailed comparison of millennial and multi-centennial scale vegetation changes are not straightforward. Additionally, substantial uncertainty remains around SW Iberian hydrology since the LGM. To date, no continuous high-resolution pollen record combined with hydrological indicators from the same core exists to reconstruct precisely western Iberian hydrology. To clarify these uncertainties, new long multi-proxy high-resolution continuous records with adequate chronological control are needed.

3.5. Conclusions

Overall, there is good understanding of the general controls of Iberian climate over the last 28 kyr, including the strength and position of the westerlies, atmospheric and SST changes, and the general shifts in vegetation composition. There are, however, aspects of the region's palaeoclimate over the last 28 kyr that need further exploration. The first is a need to enhance the current knowledge of the ecological sensitivity of SW Iberian vegetation to orbital and millennial scale climate changes with different background conditions. The second area that requires better understanding is Iberian hydrology over the past 28 kyr, including changes in hydroclimate seasonality and water availability. This will allow for further exploration into the impact of changing background conditions, both on orbital and millennial timescales, on SW Iberian hydrology and consequently the influence of hydrological variations on SW Iberian vegetation. This research aims to address these two issues by producing high-resolution pollen records from SHAK06-5K and MD01-2444 to explore the response and sensitivity of SW Iberian vegetation to gradual and abrupt climate changes over the last 28 kyr, and by producing a high-resolution *n*-alkane $\delta^{13}C$ record from the same core and exploring its use as a climate change indicator.

4.1. Introduction

Accurate interpretation of pollen records requires robust understanding of differential pollen production, pollination methods and taphonomy, as well as the geographical location of the source area of the core site. This chapter will, therefore, address the principles and limitations of marine palynology and determine the location of the pollen source area of SHAK06-5K and MD01-2444. The methods used to prepare, identify, analyse and present these pollen records will then be outlined, before providing the results of this analysis using pollen percentage diagrams against depth. Each diagram will be divided into pollen assemblage zones (PAZs) which will form the basis of the descriptions of SW Iberian vegetation change with depth.

4.1.1. Principles of Pollen Analysis

Derived from local vegetation, pollen and spores are a powerful tool for providing palaeoenvironmental information (von Post, 1916; Faegri & Iverson, 1950; Seppa & Bennett, 2003; Birks, 2019). Due to pollen's strong exine walls which are composed of the relatively chemically inert polymer sporopollenin, grains have been preserved for up to 240 million years (Hochuli & Feist-Burkhardt, 2013). The exine's structure is adapted to the transport mechanism of the grain, making its appearance characteristic of its taxonomic group. This means its parent plant can be identified to family, genus or sometimes species level (Faegri & Iverson, 1950). As the taxonomic structure of an ecosystem is dependent on the surrounding environment, the resulting pollen composition in a sediment archive is sensitive to climatic changes (von Post, 1916; Seppa & Bennett, 2003; Birks, 2019).

Quaternary pollen analysis formally started with von Post's 1916 lecture which introduced pollen as a technique for understanding past climates (von Post, 1916). Palynology then spread primarily as a tool for dating and assessing vegetation history, advancing significantly by the late 1940's/early 1950's. Firstly, the introduction of radiocarbon dating provided an independent dating technique (Libby *et al.,* 1949), enabling the timing of vegetation changes and anthropogenic impacts to be assessed. Then, in 1950, Faegri & Iverson (1950) provided a foundation for using pollen analysis in reconstructing past environmental dynamics.

Today, due to prominent developments in the field, laboratory and in data analysis, palynology is an advanced palaeoclimatic reconstruction technique which enables vegetational and

climatic history to be reconstructed at a range of spatial and temporal scales (Seppa & Bennett, 2003; Birks & Berglund, 2018; Birks, 2019). Field and laboratory advances include improved coring techniques, preparation methodologies, and the introduction of light, electron and scanning microscopy (Faegri & Iverson; 1964; Berglund & Ralska-Jasiewiczowa, 1986). Ecological and climatic interpretation of pollen records have been improved by advances in concentration estimations, reference collections, understanding of pollen taphonomy, pollen dispersal and accumulation rate modelling, statistical analysis, and summarisation of pollen stratigraphical data (Anderson, 1970; Stockmarr, 1971; Birks & Birks, 1980; Birks & Gordon, 1985; Reille, 1999; Beug, 2004; Xu *et al.,* 2016).

Pollen analysis has significantly enhanced our ecological knowledge, with Birks (2019) grouping these into four key contributions: 1. improved understanding of the ecology of interglacial/glacial periods, including glacial refugia and soil variations; 2. enhanced insight into vegetation responses to environmental change, including expansion, extinction, and adaptation; 3. development of key ecological concepts including potential niche theory, realised environmental spaces, assemblages lacking modern analogues, long-term forest dynamics, and the nature of vegetation; and 4. the advancement in the application of Quaternary botany to ecology/biogeography, including anthropogenic impacts, biodiversity/conservation, and flora-fauna interactions. The contribution of Quaternary botany to ecological and biodiversity science is reviewed in detail in Birks (2019).

4.1.2. Limitations of pollen as a palaeoenvironmental indicator

An awareness of the limitations of pollen as a palaeoclimatic indicator should proceed any ecological and climatic interpretations of such records. These result from the complexities and uncertainties in the life-cycle of a pollen grain from its production through to fossilisation.

The first element to consider is the production of pollen. A simple relationship does not exist between the composition of pollen rain and the abundance of surrounding taxa. The quantity and timing of pollen production varies between species and is affected by the surrounding environment (eg. van der Knaap *et al.,* 2001; Sugita *et al.,* 2010; Xu *et al.,* 2007; 2016). The pollen dispersal mechanism of a plant is one such factor which determines the quantity of pollen produced. While many herbaceous plants rely on insect pollination (entomophily), the majority of trees, grasses and sedges are dependent upon wind dispersal (anemophily) which typically produces significantly more grains (Pacini *et al.,* 1992).

Pollen is transported to marine sediments by two key mechanisms: aeolian (short- and long-distance) transport, and waterborne (fluvial and marine) transport (Muller, 1959; Rossignol-Strick, 1973; Xu *et al.,* 2016).

Aeolian transportation is strongly influenced by environmental factors (ie. wind speed, topography), the dispersal mechanism of the plant, and the morphological characteristics of the grain (Hopkins, 1950; Fall, 1987). Although distribution >100 km is possible, dependent on pollen morphology, site openness, canopy structure, and wind intensity/direction (Hevly, 1981; Birks & Birks, 2000), a prominent fall in pollen dispersal is shown >10 m away from its source (House, 1985; Kershaw & Strickland, 1990).

Over long distances, fluvial flow has a greater transport capacity than wind (Chmura & Liu, 1990; Zhu *et al.,* 2003). Distortion of the pollen signal due to the effects of mixing, sorting, and resuspension must, however, be considered. It has been argued that sorting occurs during fluvial transport, due to the association of certain taxa to different grain-size fractions (Fall, 1987; Brush & Brush, 1972). The effect of this sorting, however, is debated, with some suggesting that the impact is relatively minor, particularly where there is high flow rate and carrying capacity (Hall, 1989; Holmes, 1990; Zhu *et al.,* 2003).

Upon reaching the marine environment, aggregation of pollen grains in algal masses and faecal pellets is an important transport mechanism to bottom sediments (Hooghiemstra, 1988; Dupont, 1999). The lamination and stratigraphy of samples can be affected by re-deposition, bioturbation, or lags during transportation (Stanley, 1966; Hevly, 1981), but reworked old pollen grains may be distinguished under the microscope as they accept safranin differently, either giving a yellow tinge or staining more readily (Muller, 1959; Stanley, 1966). In marine areas, while lowest pollen concentrations are found in high-energy environments, maximum pollen concentrations are found in alluvial deposits near river mouths, with concentrations decreasing offshore with distance from the vegetation source (Heusser & Balsam, 1977; Heusser, 1983).

Preservation issues can occur due to both intrinsic characteristics of the grain, such as size, exine thickness, and structure, as well as external factors, such as pH, oxidation, and microbial breakdown (Havinga, 1967; Hevly, 1981). Both issues can cause some species to be underrepresented. Due to its susceptibility to degradation under oxic conditions, pollen is not

well preserved in dust or soil (Havinga *et al.,* 1967). In fluvial environments, finer sediments generally allow for better pollen preservation than coarse sediments (Cushing, 1967).

These limitations must be accounted for when interpreting the environmental signal provided by marine core pollen assemblages. The pollen proportions are not directly related to the abundance of the source taxa and biases can occur due to transportation and preservation issues. Despite these limitations, marine core pollen records can capture major transitions while largely reflecting the dominant taxa of the source area. *Pinus*, however, is overrepresented in marine sediments due to productivity and susceptibility to long-distance transport (Heusser & Balsam, 1977; Heusser, 1983).

4.1.3. Source area of SHAK06-5K and MD01-2444

The first crucial step to understanding the pollen signal is to distinguish the source area of pollen to our core sites (Fig. 2.1). Complex models aimed at simplifying source areas are restricted primarily to terrestrial cores, as well as in the accuracy of their application due to the spatial and temporal variability of sites (eg. Prentice, 1985, 1988; Sugita, 1993, 1994).

Pollen representation is dependent on the size of the sample area. Small lakes are acknowledged to be highly sensitive to the local vegetation composition, while the pollen signal of larger lakes and marine environments have a greater regional component (Jacobson & Bradshaw, 1981; Prentice, 1985, 1988; Sugita, 1993, 1994; Davis, 2000; Seppa & Bennett, 2003; Naughton *et al.,* 2007; Morales-Molino *et al.,* 2020). Marine cores provide an understanding of vegetation change over a significantly larger geographical area, representing an integrated image of the hydrographic source area. With modern records highlighting the heterogeneity of western Iberian vegetation, the granularity of these records provides an understanding of the different plant communities contributing to the marine pollen record (Naughton *et al.,* 2007; Morales-Molino *et al.,* 2020). Present-day marine pollen from the Iberian Margin strongly reflects the adjacent continent's regional vegetation, correlating with the general modern pollen signatures from terrestrial sites (Naughton *et al.,* 2007; Morales-Molino *et al.,* 2020).

As the dominant supply of organic terrestrial material to the SW Iberian Margin is from the Tagus river (section 2.5), it is assumed that the principal supply of pollen to our core sites is from vegetation growing within the Tagus basin, with the Sado river contributing a small quantity of pollen from within its basin. Short-distance wind transport will play a role in

transferring pollen into these rivers, directly from the plant and from top-soils, but as the Iberian Margin's dominant wind source is northerly and westerly over the Atlantic (Hurrell, 1995), significant oceanward transport from the continent is likely to be limited (Sanchez Goñi, 1999; Naughton *et al.,* 2007). It must also be acknowledged that the changes in the rate and direction of sediment transport into the Tagus Abyssal Plain over the deglaciation and Holocene (outlined in section 2.5) will have also affected the quantity of pollen delivered to our site; this will be discussed further in Chapter 8.

Although most grains do not travel far from their source, long-distance wind transport >100 km is also possible (Hevly, 1981; Guerzoni *et al.,* 1997; Schefuss *et al.,* 2003). Again, due to northerly and westerly winds, long-distance transport will play a modest role in this region (Sanchez Goñi, 1999; Naughton *et al.,* 2007), but during occasional periods of strong southerly winds, North African pollen grains, such as *Cedrus*, will have reached this site (Lamb & van der Kaars, 1995; Magri & Parra, 2002; Bell & Fletcher, 2016). Previous work, however, shows the contribution of North African grains to be limited (Fletcher, 2008). Additionally, due to the poor preservation of pollen in soil and dust under oxic conditions (Havinga *et al.,* 1967) any pre-aged NW African grains may be identified.

The dominant pollen transport mechanisms to our core site are therefore likely to be fluvial and short-distance wind transport. The latter is primarily confined to the continent, transferring pollen to the Tagus and Sado rivers from within the basin. Hence, the catchment of the Tagus river represents the main pollen source area for this marine core, with a minor contribution from the Sado basin (Sanchez Goñi *et al.,* 1999; 2000; Roucoux *et al.,* 2006; Naughton *et al.,* 2007).

4.2. Materials and Methods

4.2.1. Pollen preparation procedure

For each sample, 6-7 g of dry marine sediment was weighed in order to extract sufficient pollen grains from cores SHAK06-5K and MD01-2444. SHAK06-5K samples were taken at 2 cm intervals (n = 165; 0-329 cm), increasing the resolution to every 1 cm between 46 and 64 cm due to reduced sediment accumulation rate (SAR) in this section of the core (section 6). In MD01-2444 samples were taken at 3 cm intervals, with additional depths of 161 and 164 cm (n = 42; 121-238 cm). To each sample, one *Lycopodium* spike was added to quantify the absolute pollen concentration (Stockmarr, 1971). Pollen extraction was conducted using the UCL Department of Geography Marine Fossil Pollen Preparation Method (Table 4.1; Margari, 2016). This elutes calcium carbonate, humic acids, organic material, silicates, and sulphides and pyrites from the sediment, using 10% hydrochloric acid (HCl), 10% Potassium hydroxide (KOH), a 180 µm sieve, 40% hydrofluoric acid (HF), and 10% Nitric acid (HNO_3), respectively. Microsieving was not used due to concerns over loss of differential pollen types. Tertiary-butyl alcohol (TBA) was used as a dehydrating agent, enabling pollen residue to be stained with safranin to ensure clear identification, before combining with silicone oil to suspend grains for turning during identification (Matthews, 1969). Prior to identification, each pollen sample was prepared on microscope slides with 22x50 mm cover slips and sealed with clear nail varnish (Traverse, 2007).

4.2.2. Pollen identification procedure

Using a compound microscope (x400 magnification), 100 grains (excluding *Pinus*, *Cedrus*, aquatics, pteridophytes, algae, and indeterminate grains) were counted and identified for each sample. This is considered an adequate quantity to represent taxa diversity reliably (Birks & Birks, 1980; Moore *et al.,* 1991; Kotthoff *et al.,* 2008). Each traverse was separated by 2 mm to prevent grain recounting. Pollen was identified to its lowest possible taxonomic levels using the pollen identification manual for European & Middle Eastern flora (Reille, 1999; Beug, 2004), with nomenclature following *Mabberley's Plant-book* (Mabberley, 2017). Generally, taxa are identifiable to family, or genus level, but identification to sub-family or sub-genus level is sometimes possible. For the Asteraceae family, grains not identifiable to genus level were identified by subfamily: Cichorioideae and Asteroideae. *Quercus* pollen grains were categorised into three groups (Smit, 1973): deciduous-type (*Q. robur, Q. petraea, Q. pubescens*, and *Q. pyrenaica*), evergreen-type (*Q. ilex* and *Q. coccifera*), and *Quercus suber*-type (*Q. suber* and *Q. crenata*). Both scanning electron microscopy (Smit, 1973) and light microscopy (Jarvis *et al.,*

1992) enable differentiation of different *Quercus* groups, assisted by the availability of extensive identification keys (Van Benthem *et al.,* 1984; Reille, 1999; Beug, 2004). Here, *Quercus* grains were differentiated using the following criteria. Deciduous-type grains are identifiable by their rounded scabrate-verrucate surface structure and larger equatorial and polar axis (Smit, 1973; Van Benthem, 1984; Beug, 2004). Evergreen-type grains have an irregular regulate surface structure with elongated elements, a smaller equatorial and polar axis, and sometimes a poroid/constriction of the colpus (Smit, 1973; Van Benthem, 1984; Beug, 2004). *Quercus suber*-type pollen is distinguishable by its scabrate surface structure which combines rounded and elongated elements (Smit, 1973; Van Benthem, 1984). Indeterminate grains were categorised into broken, concealed, crumpled, corroded, and degraded, following Cushing's (1967) definitions.

Stage	Method	Justification
1. Sample preparation	a. 6 g of dry sediment measured & placed in three 50 ml centrifuge tubes b. One *Lycopodium* tablet added to each 6 g sample	a. After preparing a number of preliminary samples at different depths of the core, 6 g of sediment was deemed sufficient for our palynological analysis. b. Exotic spikes enable the calculation of absolute pollen content
2. Calcium carbonate removal	a. 50 ml 10% HCl added b. 1 hour in water bath[1]; centrifuged[2], decanted[3] c. 50 ml distilled H_2O added, centrifuged[2], decanted[3]	a. Extracts calcium carbonate from the sample b. Assists with the action of the HCl on the calcium carbonate c. Removes previously added chemicals and excess calcium
3. Humic acid removal	a. 35 ml 10% KOH b. 4 minutes in water bath	a. Makes the solution alkaline (pH14), mobilising humic acids & clays into the solution b. Assists with the action of the KOH on the humic acids & clays within the sample
4. Organic removal	a. Samples sieved (180 µm) into 1l beakers; transferred into centrifuge tubes using H_2O; centrifuged[2], decanted[3] b. 50ml H_2O; centrifuged[2], decanted[3] (repeated until liquid is clear) c. 2 drops of 10% $(NaPO_3)_6$ after KOH removal ($1^{st}/2^{nd}$ wash)	a. Removes organic and non-organic matter >180 µm b. Extracts organic particles <180 µm c. Breaks electrostatic bonds to remove remaining humic acids & clays, preventing low pollen concentrations (Bates *et al.,* 1978)
5. Silicate removal	a. 50 ml HCl; centrifuged[2], decanted[3] b. 30 ml 40% HF; 1 hour in water bath; centrifuged[2], decanted[3] c. 35 ml 10% HCl; 40 minutes in water bath; centrifuged[2], decanted[3] d. Repeat step b; then c, but with 40 ml 10% HCl & 1 hour water bath e. Sample examined under compound microscope at x400 magnification f. Steps a to e repeated if large pieces remain	a. Acidifies the sample to assist with residual carbonate removal by HF b. Removes silicates from the sample c. Extracts silicate residues and fluorosilicates d. Removes remaining silicates e. Checks for any remaining silicates and whether this procedure requires repeating
6. Sulphide and pyrite removal	a. Black debris removal from tube walls using tissue and glass rod b. 3ml 10% HNO_3 & 30 ml H_2O c. 1ml pipette of methylated spirit d. 4 minutes in water bath; centrifuged[2], decanted[3] e. 50ml distilled H_2O; centrifuged[2], decanted[3]	a. Removes pyrites from the tube wall b. Extracts sulphides and pyrites from the sample c. Removes any sample attached to tube walls d. Assists with the action of the HNO_3 on the sulphides and pyrites within the sample e. Removes any remaining chemicals, sulphides, and pyrites
7. Staining & mounting	a. 2 ml 1% KOH & 20 ml H_2O; centrifuged[2], decanted[3] b. 50 ml H_2O; centrifuged[2], decanted[3] (repeated until liquid is clear) c. 2 safranin drops & 50 ml H_2O; centrifuged[2], decanted[3] d. 10 ml TBA; centrifuged[2], decanted[3]; transferred into labelled vials e. Silicon oil added in equal quantity to remaining residue f. Vial left open for 24 hours, adding labelled caps after this period	a. Takes the sample to an alkaline so safranin can turn the sample red b. Washes sample of KOH c. Stains the pollen, enabling clearer viewing under compound microscope (Traverse, 2007) d. Dehydrates residue, enabling the addition of silicate oil for mounting on slides (Matthews, 1969) e. Silicon oil is a low refractive medium, helping grain examination & movement (Traverse, 2007) f. Enables TBA evaporation; stirring stops drying out; covering with tissue prevents contamination

Table 4.1: Method for marine fossil pollen preparation for extraction of pollen from core SHAK06-5K (Margari, 2016)

[1] Water bath at 70°C
[2] Sample centrifuged at 3000 rpm for 5 minutes
[3] Excess liquid decanted from the sample
[4] Samples centrifuged for 3 minutes

4.2.3. Pollen diagram construction

Pollen sum and percentages:

The main pollen sum represents all grains encountered in each sample (excluding *Pinus*, *Cedrus*, aquatics, pteridophytes, algae, and indeterminate grains). Aquatic, algal, and pteridophyte grains were removed to focus on broad regional changes, while *Pinus* pollen is produced in high quantities and susceptible to long-distance transport, making it overrepresented in marine samples (Bradshaw & Webb, 1985; Cheddadi, 1988; Reille & Lowe, 1993). It is likely that *Cedrus* was present in North Africa, but not SW Iberia, during the Last Glacial period and Holocene, so its presence in SW Iberian marine cores may reflect periods of strengthened southerly wind activity (Lamb & van der Kaars, 1995; Magri & Parra, 2002; Bell & Fletcher, 2016). Nonetheless, all are included in the pollen diagrams as they can be important climate indicators (Prentice *et al.,* 1996). Pollen diagrams produced from this data are plotted as a function of depth, with all taxa presented in pollen percentages (%).

Taxa within the main pollen sum (e.g. *Betula*) were calculated as follows:

$$\left(\frac{\sum Betula}{\sum \text{main pollen}}\right) * \ 100 = \%Betula$$

Taxa outside the main sum (e.g. *Pinus*, *Cedrus*, aquatics, pteridophytes, algae, and indeterminate grains) were calculated as follows:

$$\left(\frac{\sum Pinus}{(\sum \text{main pollen} + \ \sum Pinus)}\right) * \ 100 = \%Pinus$$

Subsequently, percentages (%) of arboreal pollen (AP) were calculated, to show key data trends. AP includes all trees and shrubs minus *Pinus* and *Cedrus*. This was split into a further three groups (pioneer, Mediterranean & Eurosiberian taxa) defined by the tolerance levels of the species included within them. In line with other publications from the western Iberian Margin, Mediterranean and Eurosiberian percentages are combined as 'Temperate tree taxa'. Heliophilous pioneer species are slow to decline, yet rapid to recover when conditions return to their tolerance levels, therefore *Betula, Hippophae, Juniperus,* and *Salix* are included in this sum (Roucoux *et al*., 2011). Mediterranean taxa are adapted to a high seasonality climate of hot, dry summers and mild, wet winters. *Phillyrea, Pistacia, Olea*, and evergreen *Quercus*

included within this group. Eurosiberian species represent the sum of all tree and shrubs found in SHAK06-5K and MD01-2444 excluding *Pinus*, *Cedrus*, pioneer, and Mediterranean taxa. These species require year-round humidity and can tolerate lower winter temperatures. Herbaceous taxa (non-arboreal pollen; NAP) is divided into semi-desert (Amaranthaceae and *Artemisia*), steppe (Amaranthaceae, *Artemisia*, Poaceae and *Ephedra*), and ubiquitous herbs. Semi-desert taxa are able to withstand extreme temperatures and aridity, while less extreme cold/arid conditions are tolerated by xerophilic steppe taxa. The remaining ubiquitous herbs include a number of thermophilous (Lamiaceae and Fabaceae), heliophilous (*Plantago*, *Urtica*, *Helianthemum*, *Centaurea*, Cichorioideae and Asteroideae), hygrophytic (Cyperaceae, *Polygonum*, and *Thalictrum*) and psammophilous (*Calligonum*) species. The pollen percentages of these summary groups are shown in Appendix 2 (SHAK06-5K) and Appendix 3 (MD01-2444).

Pollen Concentration Calculation:

Each sample's pollen concentration (C_{pollen}) was calculated using Stockmar's exotic marker technique (1971), quantifying grains per gram of sediment (grains g^{-1}; Equation. 4.1) (Appendix 4 and 5). One *Lycopodium* tablet of a known quantity was added to each sample (L_{total}). In SHAK06-5K samples, the spores per tablet were 9666 (spike batch no. 3862), while in MD01-2444 samples, spores per tablet were 13911 (spike batch: 710961).

$$C_{pollen} = \frac{P_{slide}}{L_{slide}} * \frac{L_{total}}{W_{total}}$$

Equation. 4.1: Pollen Concentration (C_{pollen}; grains g^{-1} of dry weight sediment) calculated using; quantity of pollen grains (P_{slide}) and *Lycopodium* spores (L_{slide}) counted in the slide; total *Lycopodium* spores added to sample (L_{total}), and total weight of sample (W_{total}; grams) (Stockmarr, 1971).

Ordering of Taxa:

Within the diagram, taxa are ordered according to Mediterranean succession (Fig. 4.1; van der Hammen *et al.,* 1971; Tzedakis, 2007). As temperatures warm after a cold period, an open woodland forms (pioneer vegetation with other deciduous elements), moving to Mediterranean sclerophyllous taxa when seasonality is high. Subsequently, with increased annual moisture availability, deciduous broad-leaf vegetation dominates, replaced by coniferous trees as temperatures cool, then reverting back to open woodland as moisture availability decreases (Tzedakis, 2007). As a result, tree taxa in the pollen diagrams are ordered

according to this succession, commencing with pioneer vegetation, followed by Mediterranean then temperate taxa (tree and shrub).

Pollen diagram & zonation:

Pollen diagrams permit vast quantities of pollen data to be visualised, assessed, and interpreted (Birks & Birks, 1980). Within these diagrams the ordering of taxa can visually demonstrate similar or opposing trends from specific groups of taxa, which may imply a climatic signal. Temporal changes across these groups can also be displayed using PAZs. These represent an assemblage of taxa with analogous characteristics, corresponding to a distinct stage of vegetational succession (Birks & Gordon, 1985). This simplifies interpretations and establishes key vegetation transitions over the depth of the core (Grimm, 1987), facilitating identification of vegetation events independently of marine data.

Numerical zonation has the advantage of being able to determine a consistent formulation of the zonation criteria (Birks & Gordon, 1985). Additionally, with so many varying factors in palynological datasets, large quantities of data can be retained and balanced, whilst also rapidly obtaining the zonation results (Birks & Gordon, 1985). Here, PSIMPOLL software was used to construct the pollen zonation diagrams (Bennett, 2011; http://chrono.qub.ac.uk/psimpoll/psimpoll.html). For the creation of the PAZs, numerical zonation played a key role (using the scheme 'optimal splitting using information content'), as it is neither hierarchical nor constrained by the fixed position of earlier boundaries (Birks & Gordon, 1985; Birks, 1987). The variance over the data set was reduced by minimising the information content (Grimm, 1987; Birks & Gordon, 1985; Bennet, 1996). Taxa greater than or equal to 1% were included in the zonation. The positioning and number of zones was then manually reviewed and edited. Although this adds an element of subjectivity, it allows data trends to be examined qualitatively, taking into account both the intuition of the researcher and features of ecological importance (Gordon & Birks, 1972). For the pollen diagram of SHAK06-5K, 12 PAZs were constructed, and assigned the prefix "SHAK06-", while in the MD01-2444 pollen diagram, 8 PAZs were constructed and assigned the prefix "MD01-".

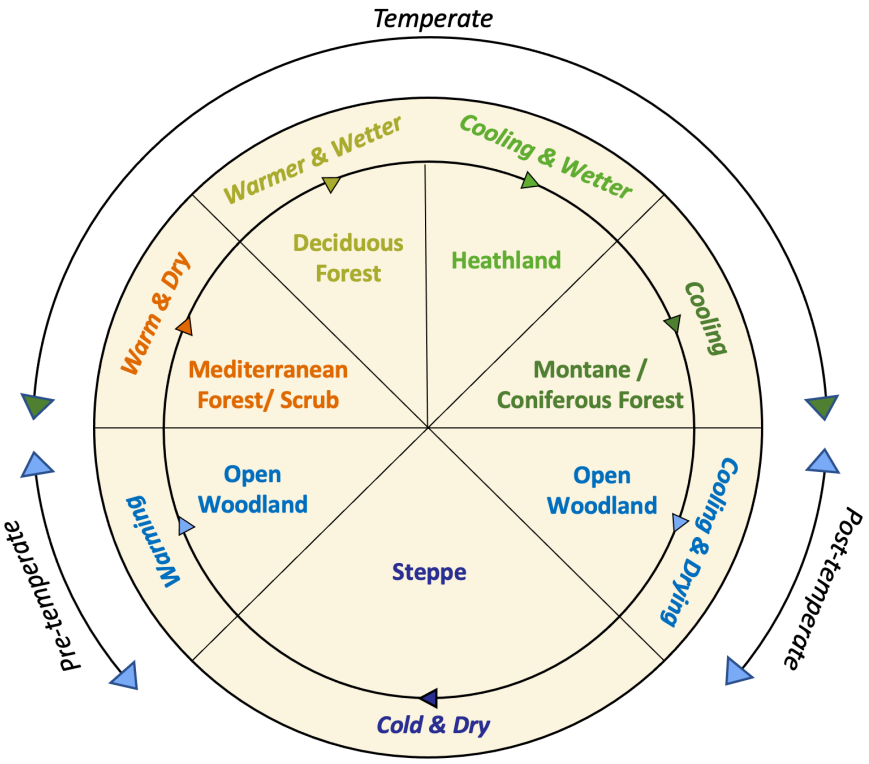

Fig. 4.1: Southern European vegetation succession cycle (adapted from Tzedakis, 2007).

4.2.4. Methods of published records

SHAK06-5K $\delta^{18}O$ of G. bulloides (Ausin et al., 2019a):

High-resolution $\delta^{18}O$ of the planktonic foraminifer *G. bulloides* ($\delta^{18}O_{G.\ bulloides}$) were produced from SHAK06-5K spanning the last 27.4 cal ka BP. Samples were taken every 2cm (n = 170), isolating *G. bulloides* specimens from ~15 g of wet sediment, firstly by diluting the sediment with deionised water and disaggregating using a centrifuge tube rotator on a slow speed. Then, using 300 – 250 µm sieves and a high-pressure deionised water stream, the solution was wet sieved, washed, and oven dried (at 60°C). From this fraction six to 12 *G. bulloides* specimens were picked and used for stable isotope measurements, performed at the Stable Isotope Laboratory of Climate Geology, ETH Zurich, using a Gas Bench II coupled to a Delta V Plus isotope ratio mass spectrometer. Stable isotope ratios are expressed in ‰ and calibrated using the Vienna Pee Dee Belemnite (VPDB) standard, defined in respect to two in-house standards calibrated previously against two international standards: NBS-18 and NBS-19. The long-term standard deviation of the measurements (1σ) is <0.07‰.

MD01-2444 $\delta^{18}O$ of G. bulloides (Vautravers & Shackleton, 2005):

Stable isotope measurements ($\delta^{18}O$) from core MD01-2444 were performed at the University of Cambridge using a VG SIRA mass spectrometer using an acid bath at 90°C. Samples were

taken every 3 cm along the length of the core, performing stable isotope analysis on 30 *G. bulloides* specimens from each sample, taken from the 300 – 355 µm size fraction. Stable isotope ratios are expressed in ‰ and calibrated using the Vienna Pee Dee Belemnite (VPDB) standard, defined in respect to the international NBS-19 standard.

SHAK06-5K X-ray fluorescence (Ausin et al., 2020):

Core SHAK06-5K was sub-sampled along its length, onboard the ship, using three u-channels (plastic core-length boxes; 2 cm x 2 cm cross section; 150 cm maximum length). To reduce desiccation and prevent contamination, each channel's surface was scraped clean and covered with SPEXCertiPrep Ultralene foil (4mm thickness). The semi-quantitative elemental data was measured using an Avaatech X-ray florescence (XRF) core scanner at the Godwin Laboratory, University of Cambridge. A rhodium X-ray source (0.2 mA tube current) irradiated each section at three voltages: 10 kV (no filter), 30 kV (thin lead filter), and 50 kV (copper filter). XRF data were collected at 0.5 cm resolution along each u-channel's length. The width and length of the irradiated surface (down-core by cross-core) was 0.25 cm by 1.2 cm, using a 60 second count time. Element intensities (dependent on element concentrations) were obtained using Canberra WinAxil software with standard software settings and spectrum-fit models. To provide a more accurate and precise reflection of chemical composition changes, natural logarithm (*ln*) ratios of element intensities are used to present the XRF data (Weltje & Tjallingii, 2008). For this research, this is applied to calcium/titanium ratios (*ln*(Ca/Ti)) and zirconium/strontium ratios (*ln*(Zr/Sr)). Both reflect variations in the proportion of biogenic (Ca and Sr) to detrital (Ti and Zr) sediment and can be used as a proxy to infer stadial/ interstadial conditions (Hodell *et al.,* 2013b; Freeman et al., 2016).

MD01-2444 X-ray fluorescence (Hodell et al., 2013a):

Using an Avaatech X-ray florescence (XRF) core scanner at the Godwin Laboratory, University of Cambridge, archive halves of 19 sections of core MD01-2444 were analysed. The core's surface was scraped clean and covered with SPEXCertiPrep Ultralene foil (4mm thickness). Measurements were made using a 0.2 mA current at three voltages: 10 kV (no filter), 30 kV (thin lead filter), and 50 kV (copper filter). XRF data were collected at 0.25 cm resolution along the length of the entire core. The width and length of the irradiated surface (down-core by cross-core) was 0.25 cm by 1.2 cm, using a 40 second count time. Results are presented in *ln* ratios of element intensities.

4.3. Results

4.3.1. Features of the whole sequences

A range of pollen and spores were identified in SHAK06-5K and MD01-2444, which includes angiosperms, gymnosperms, pteridophytes, and bryophytes. The list of all identified taxa is outlined in Table 4.2. Of the taxa used in the pollen sums, 69 different taxa were identified in the SHAK06-5K record (excluding *Pinus*, *Cedrus*, aquatics, pteridophytes, and algae). This includes 24 trees and shrubs, Ericaceae, and 44 herbaceous taxa, with the main features of the record shown in Table 4.3. In MD01-2444, 52 different taxa were identified (excluding *Pinus*, *Cedrus*, aquatics, pteridophytes, and algae). This includes 18 trees, Ericaceae, and shrubs and 33 herbaceous taxa, with the main features of the record shown in Table 4.4. Although 42 samples were prepared from MD01-2444, five of these were barren of pollen (127, 130, 136, 139 and 142 cm).

Nomenclature	Common name	Growth habit	Group	Presence
ADOXACEAE				
Viburnum		Shrub	Ag	SHAK
ALISMATACEAE				
Alisma	Water-plantain	Aquatic	Ag	SHAK & MD01
AMARANTHACEAE	Amaranth family	Herb	Ag	SHAK & MD01
AMARYLLIDACEAE		Herb	Ag	SHAK
ANACARDIACEAE				
Pistacia		Tree	Ag	SHAK & MD01
APIACEAE	Carrot family	Herb	Ag	SHAK
AQUIFOLIACEAE				
Ilex	Holly	Shrub	Ag	SHAK
ARALIACEAE				
Hedera	Ivy	Shrub	Ag	SHAK
ASTERACEAE	Daisy family			
Cichorioideae		Herb	Ag	SHAK & MD01
Asteroideae		Herb	Ag	SHAK & MD01
Artemisia		Herb	Ag	SHAK & MD01
Centaurea		Herb	Ag	SHAK & MD01
BETULACEAE				
Alnus	Alder	Tree	Ag	SHAK & MD01

Betula	Birch	Tree	Ag	SHAK & MD01
Carpinus betulus	Hornbeam	Tree	Ag	SHAK & MD01
Carpinus orientalis		Tree	Ag	SHAK & MD01
Corylus	Hazel	Shrub	Ag	SHAK & MD01
Ostrya	Hop hornbeam	Tree	Ag	SHAK & MD01
BORAGINACEAE	Forget-me-not family	Herb	Ag	SHAK & MD01
BRASSICACEAE	Cabbage family	Herb	Ag	SHAK & MD01
BUXACEAE				
Buxus	Box	Shrub	Ag	SHAK & MD01
CAMPANULACEAE	Bellflower family			
Campanula		Herb	Ag	SHAK
CARYOPHYLLACEAE	Carnation family	Herb	Ag	SHAK & MD01
CISTACEAE	Rock-rose family			
Cistus		Herb	Ag	SHAK & MD01
Helianthemum		Herb	Ag	SHAK & MD01
CUPRESSACEAE				
Juniperus	Juniper	Shrub	Gy	SHAK & MD01
CYPERACEAE	Sedge family	Herb	Gy	SHAK & MD01
ELAEAGNACEAE				
Hippophae	Sea buckthorn	Shrub	Ag	SHAK
EPHEDRACEAE				
Ephedra fragilis		Herb	Ag	SHAK & MD01
Ephedra distachya		Herb	Ag	SHAK & MD01
ERICACEAE	Heather family	Herb	Ag	SHAK & MD01
EUPHORBIACEAE	Spurge family	Herb	Ag	SHAK & MD01
FABACEAE	Pea family	Herb	Ag	SHAK & MD01
FAGACEAE				
Deciduous – type *Quercus*	Deciduous oak	Tree	Ag	SHAK & MD01
Evergreen – type *Quercus*	Evergreen oak	Tree	Ag	SHAK & MD01
Quercus suber	Cork oak	Tree	Ag	SHAK & MD01
GENTIANACEAE		Herb	Ag	SHAK & MD01
GERANIACEAE		Herb	Ag	SHAK
HYPERICACEAE				
Hypericum		Herb	Ag	SHAK & MD01
HALORAGACEAE				

Myriophyllum	Watermilfoil	Aquatic	Ag	SHAK
ISOETACEAE	Quillworts			
Isoetes		Lycophyte	Pt	SHAK & MD01
LAMIACEAE	Mint family	Herb	Ag	SHAK & MD01
LENTIBULARIACEAE				
Utricularia		Aquatic	Ag	SHAK
LILIACEAE		Herb	Ag	SHAK & MD01
MALVACEAE	Mallow family	Herb	Ag	SHAK
MYRTACEAE				
Myrtus	Myrtle	Shrub	Ag	SHAK & MD01
NYMPHAEACEAE	Water lily family			
Nuphar		Aquatic	Ag	SHAK
Nymphaea		Aquatic	Ag	SHAK
OLEACEAE				
Fraxinus excelsior	Common ash	Tree	Ag	SHAK & MD01
Fraxinus ornus	Manna ash	Tree	Ag	SHAK & MD01
Olea	Olive	Tree	Ag	SHAK & MD01
Phillyrea		Tree	Ag	SHAK & MD01
OPHIOGLOSSACEAE				
Botrychium	Moonworts	Fern	Pt	SHAK
OSMUNDACEAE				
Osmunda		Fern	Pt	SHAK & MD01
PAPAVERACEAE	Poppy family	Herb	Ag	SHAK & MD01
PINACEAE				
Cedrus	Cedar	Tree	Gy	SHAK & MD01
Pinus	Pine	Tree	Gy	SHAK & MD01
PLANTAGINACEAE	Plantain family			
Plantago		Herb	Ag	SHAK & MD01
PLUMBAGINACEAE	Leadwort family			SHAK & MD01
Armeria		Herb	Ag	MD01
POACEAE	Grass family	Herb	Ag	SHAK & MD01
POLYGONACEAE	Knotweed family			
Calligonum		Herb	Ag	SHAK
Polygonum		Herb	Ag	SHAK
Rumex		Herb	Ag	SHAK & MD01
POLYPODIACEAE		Fern	Pt	SHAK & MD01

Polypodium				
POTAMOGETONACEAE				
Potamogeton	Pondweed	Aquatic	Ag	SHAK & MD01
PRIMULACEAE	Primrose family	Herb	Ag	SHAK
RANUNCULACEAE				
Helleborus	Hellebore	Herb	Ag	SHAK
Ranunculus	Buttercups	Herb	Ag	SHAK & MD01
Thalictrum	Meadow – rue	Herb	Ag	SHAK & MD01
RHAMNACEAE	Buckthorn family	Herb	Ag	SHAK
ROSACEAE	Rose family	Herb	Ag	SHAK & MD01
RUTACEAE				
Ruta	Rue	Herb	Ag	SHAK
SALICACEAE				
Salix	Willow	Shrub	Ag	SHAK & MD01
SAXIFRAGACEAE		Herb	Ag	SHAK & MD01
SCROPHULARIACEAE	Figwort family	Herb	Ag	SHAK & MD01
SPHAGNACEAE				
Sphagnum	Peat moss	Moss	Br	SHAK & MD01
TYPHACEAE				
Sparganium	Bur – reed	Aquatic	Ag	SHAK & MD01
Typha	Bulrush	Aquatic	Ag	SHAK & MD01
ULMACEAE				
Ulmus	Elm	Tree	Ag	SHAK & MD01
URTICACEAE	Nettle family			
Urtica		Herb	Ag	SHAK & MD01

Table 4.2: Nomenclature, common names, and growth habit of all identified land plants in cores SHAK06-5K and MD01-2444. The plant groups are highlighted as follows: angiosperm (Ag), gymnosperms (Gy), bryophytes (Br), and pteridophytes (Pt).

Both cores have good pollen preservation, with the percentage of indeterminate grains ranging between 4 – 16% (mean = 12%; n = 165) and 2 – 26% (mean = 10%; n = 37) in SHAK06-5K and MD01-2444, respectively. Degraded grains make up the majority of indeterminate grains (with a mean of 8% in SHAK06-5K and 7% in MD01-2444), while broken and crumpled grains make up a smaller percentage (with a mean of 1% and 3%, respectively, in SHAK06-5K and 2% each in MD01-2444).

In SHAK06-5K, the pollen concentration is highly variable (Fig. 4.2a) with the highest values in the lower part of the core (SHAK–8 to SHAK–1; 80.5 – 329 cm; Fig. 4.3), averaging 2,512 grains g^{-1}. These values, however, are highly variable, ranging between 242 and 40,619 grains g^{-1}. This reduces substantially in zones SHAK– 9 to SHAK– 12 (0 – 80.5 cm) where the mean concentration is 480 grains g^{-1} and the lowest concentration of the core is reached at 56 cm (133 grains g^{-1}). The record has several extreme pollen concentration values (n = 3; 96, 168, and 314 cm). These are only included and highlighted in Fig. 4.2 and have been removed from all other diagrams in this section so as not to distort the summary curves and to facilitate the assessment of the overall pollen concentration pattern. These three separate anomalously high pollen concentrations could result from an anomalously low SAR or the uncertainty resulting from the relatively low pollen count (Maher, 1981). Alternatively they could result from improved preservation conditions, but as isolated samples, they cannot be used to draw palaeoclimatic inferences. Further up the core, there is a section of the record where the concentration declines significantly. The possible climatic explanation for this will be discussed in Chapter 8 once the core's chronology has been presented in Chapter 6.

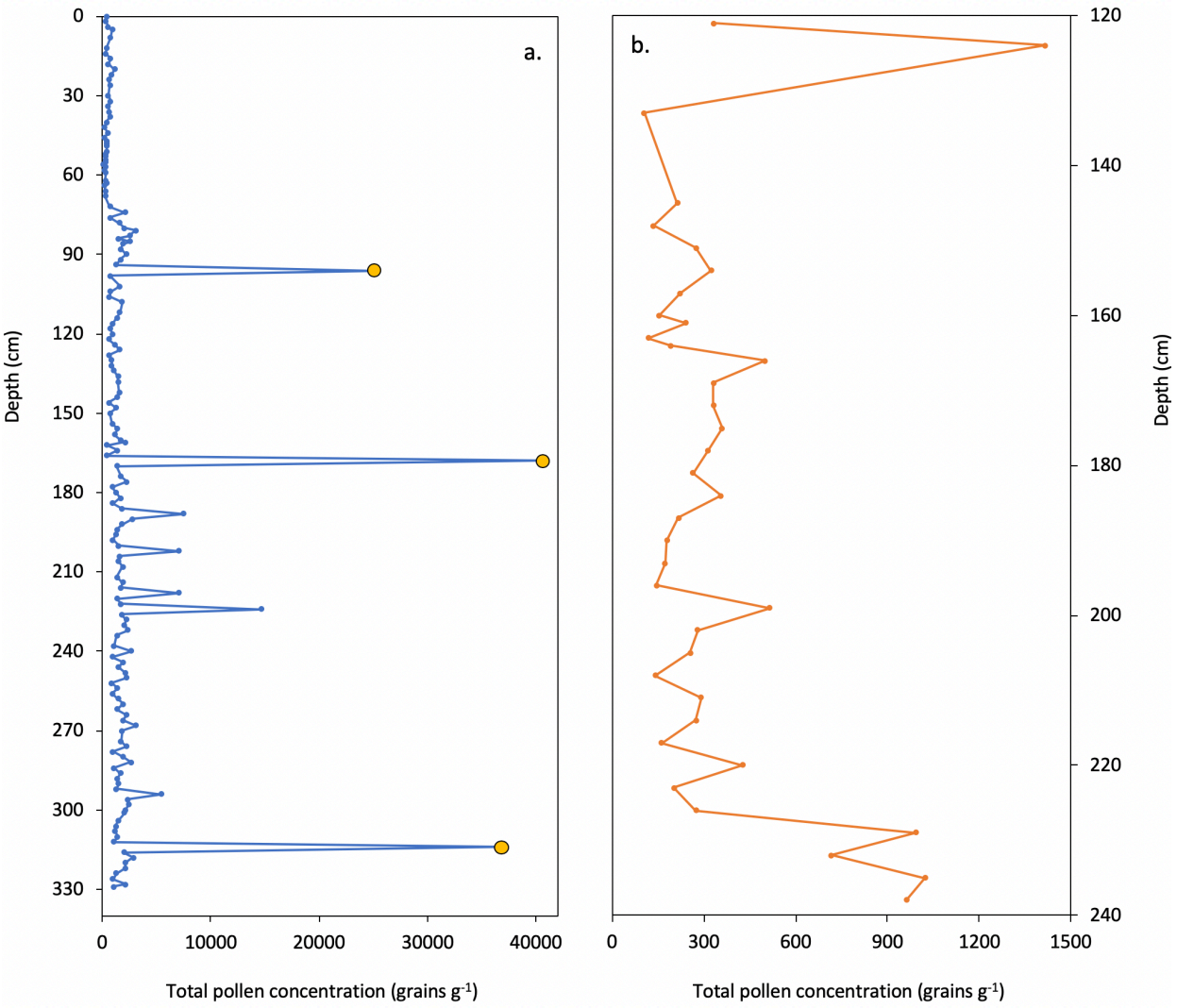

Fig. 4.2: Total pollen concentration (grains g^{-1}) in cores **a.** SHAK06-5K, highlighting the three peaks in concentration in yellow (which are removed from further concentration diagrams); and **b.** MD01-2444.

In MD01-2444, the pollen concentration (Fig. 4.2b; Fig. 4.4) is higher in the lower part of the core (238 – 229 cm; averaging 924 grains g^{-1}), declining to 274 grains g^{-1} at 226 cm. The concentration remains low, ranging between 105 – 516 grains g^{-1} until 124 cm where the concentration spikes to 1,400 grains g^{-1} before declining again to 334 grains g^{-1} at 121 cm. The peak at 124 cm could result from increased SAR or enhanced preservation, but again, as an isolated sample, climatic inferences cannot be made.

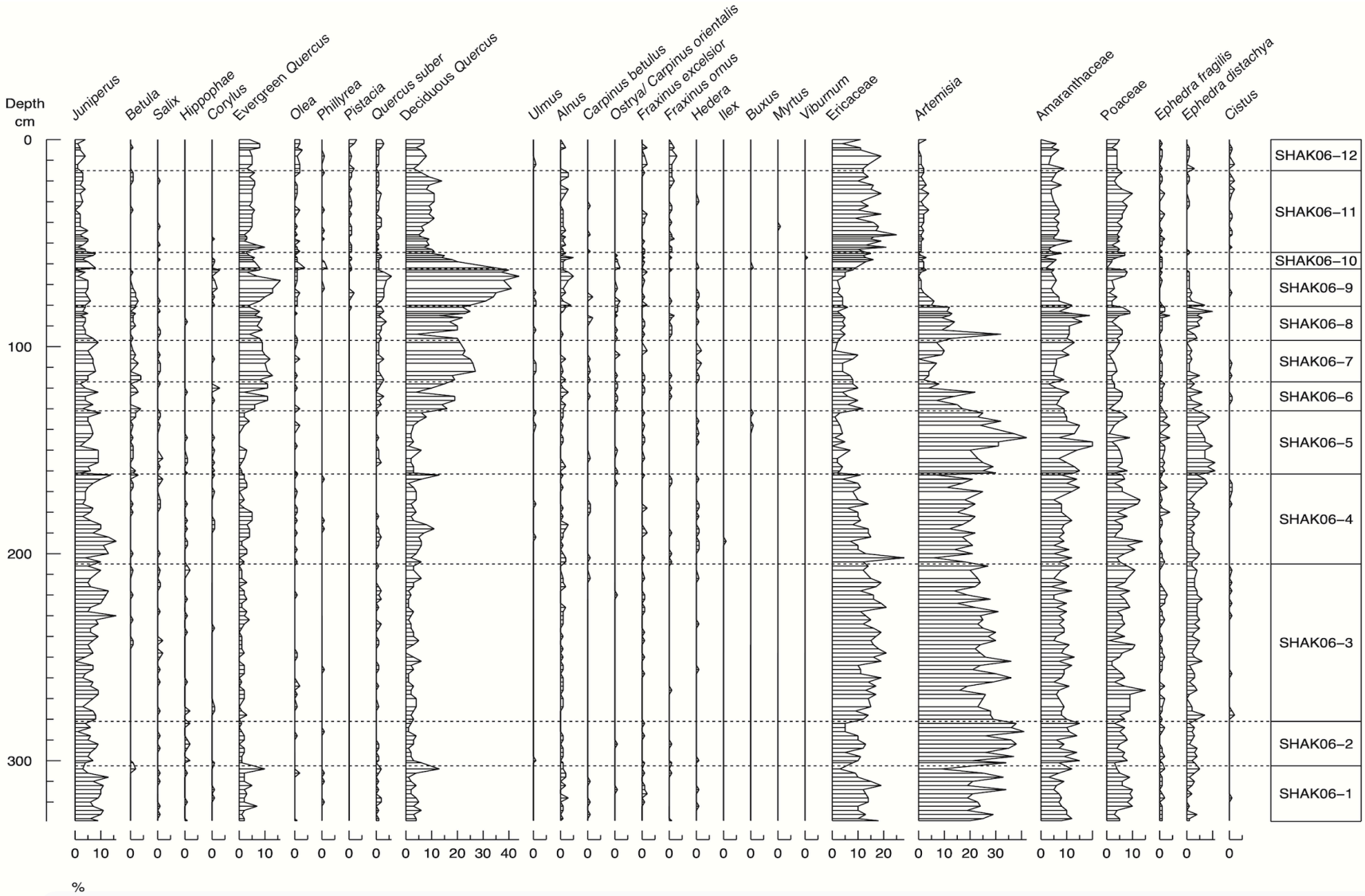

Fig. 4.3: Full pollen diagram showing change in pollen percentages (%) with depth in core SHAK06-5K. The total pollen concentration (x10^3 grains g^{-1}), $\delta^{18}O$ of *G. bulloides* (x10^{-1} ‰ VPDB), and *ln(*Ca/Ti) are also illustrated.

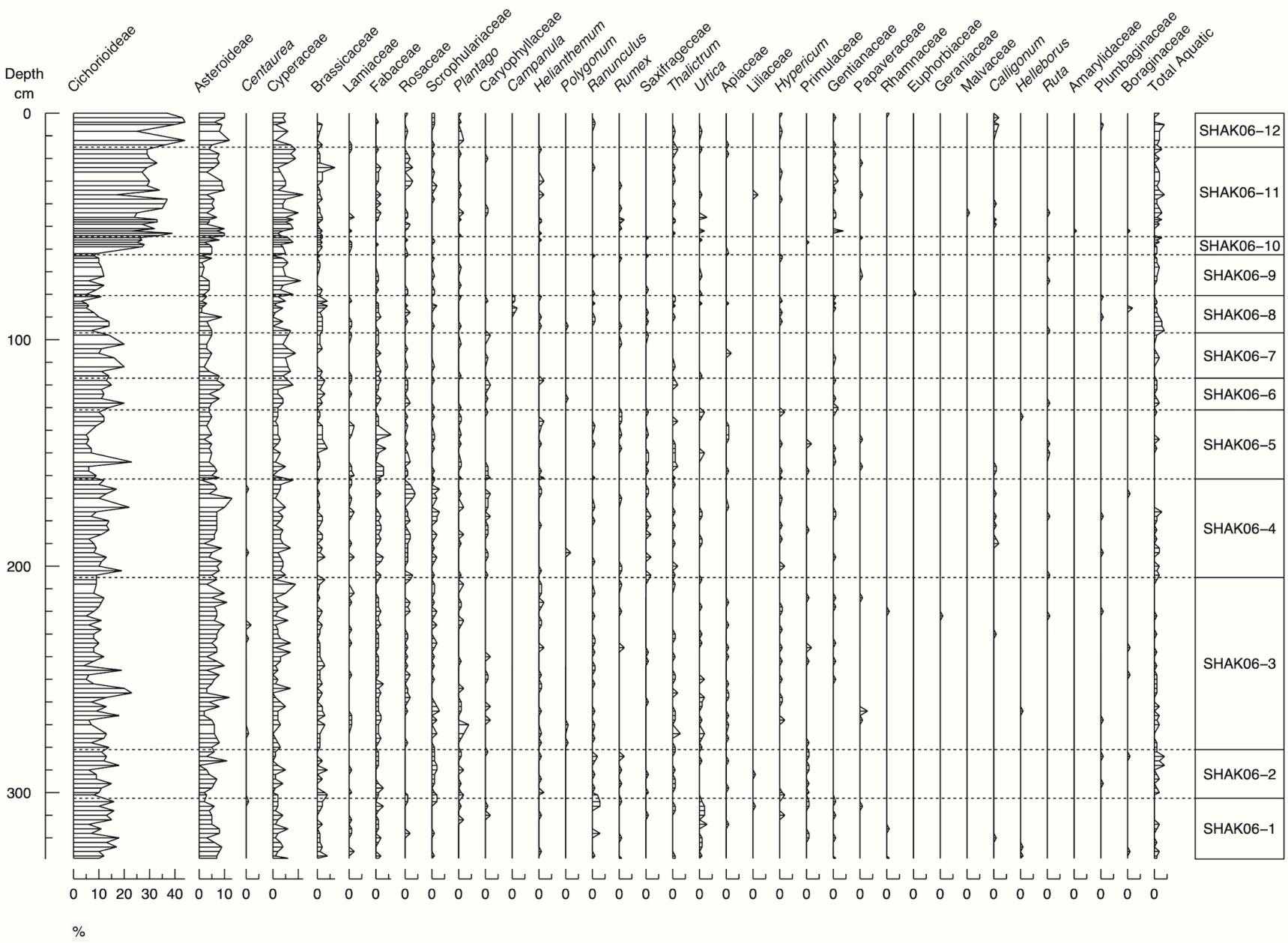
Depth
cm
0
100
200
300
Cichorioideae
Asteroideae
Centaurea
Cyperaceae
Brassicaceae
Lamiaceae
Fabaceae
Rosaceae
Scrophulariaceae
Plantago
Caryophyllaceae
Campanula
Helianthemum
Polygonum
Ranunculus
Rumex
Saxifrageceae
Thalictrum
Urtica
Apiaceae
Liliaceae
Hypericum
Primulaceae
Gentianaceae
Papaveraceae
Rhamnaceae
Euphorbiaceae
Geraniaceae
Malvaceae
Calligonum
Helleborus
Ruta
Amarylidaceae
Plumbaginaceae
Boraginaceae
Total Aquatic
SHAK06–12
SHAK06–11
SHAK06–10
SHAK06–9
SHAK06–8
SHAK06–7
SHAK06–6
SHAK06–5
SHAK06–4
SHAK06–3
SHAK06–2
SHAK06–1
0 10 20 30 40
0 10
0
0
0
0
0
0
0
0
0
0
0
0
0
0
0
0
0
0
0
0
0
0
0
0
0
0
0
0
0
0
0
0
%

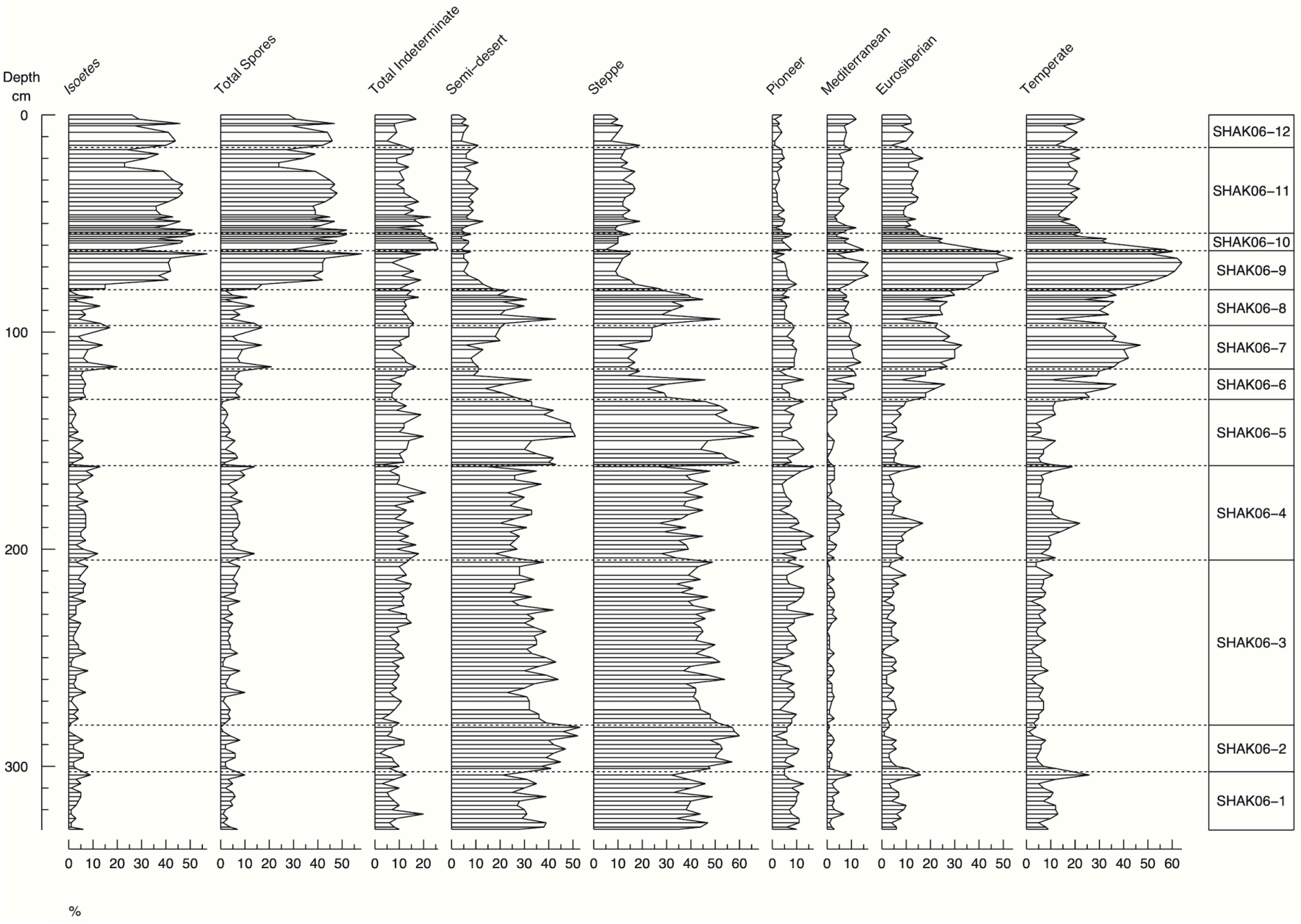
Depth
cm
Isoetes
Total Spores
Total Indeterminate
Semi–desert
Steppe
Pioneer
Mediterranean
Eurosiberian
Temperate
0
100
200
300
SHAK06–12
SHAK06–11
SHAK06–10
SHAK06–9
SHAK06–8
SHAK06–7
SHAK06–6
SHAK06–5
SHAK06–4
SHAK06–3
SHAK06–2
SHAK06–1
0 10 20 30 40 50
0 10 20 30 40 50
0 10 20
0 10 20 30 40 50
0 10 20 30 40 50 60
0 10
0 10
0 10 20 30 40 50
0 10 20 30 40 50 60
%

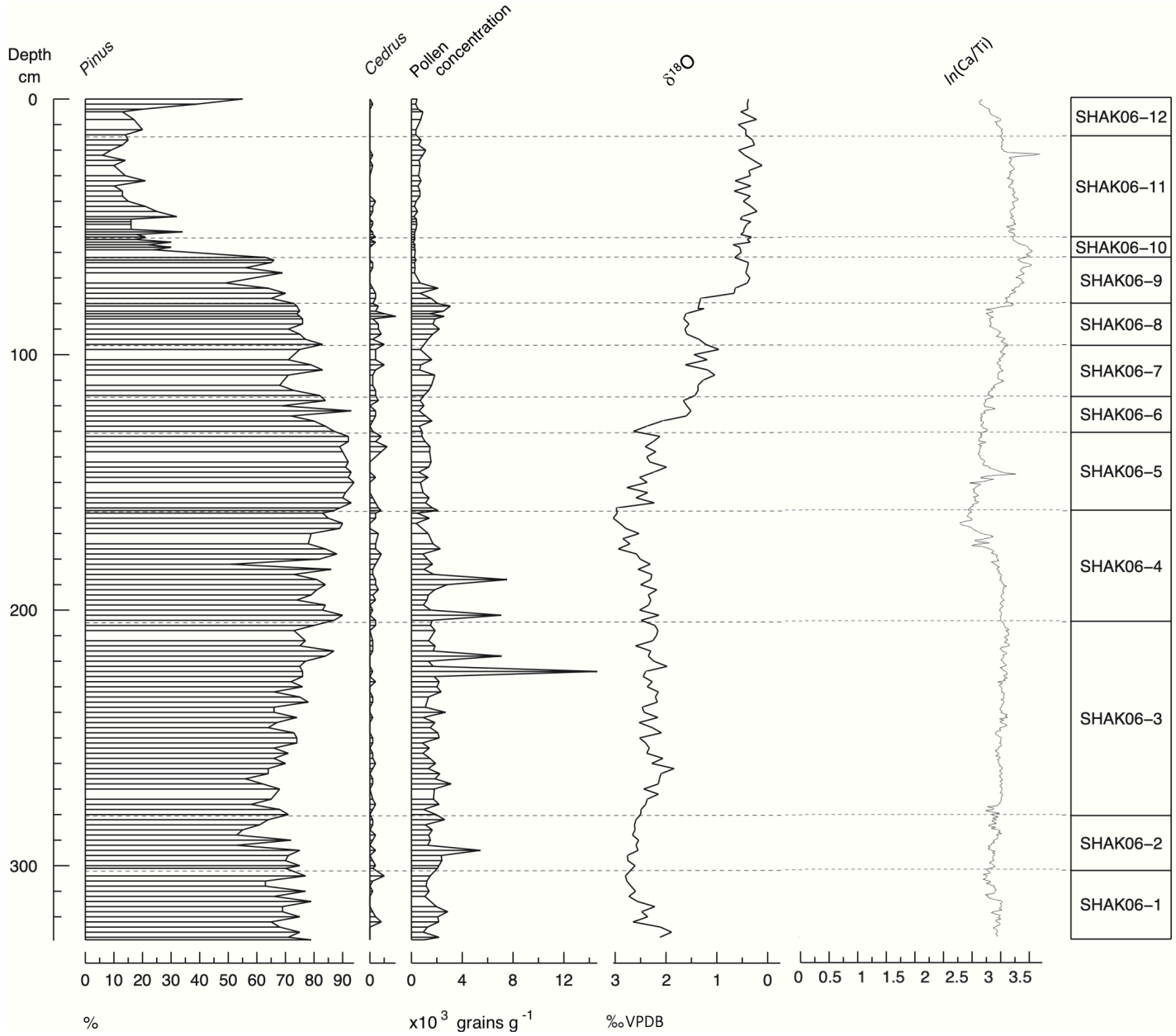
Depth
cm
0
100
200
300
Pinus
Cedrus
Pollen
concentration
δ18O
ln(Ca/Ti)
SHAK06–12
SHAK06–11
SHAK06–10
SHAK06–9
SHAK06–8
SHAK06–7
SHAK06–6
SHAK06–5
SHAK06–4
SHAK06–3
SHAK06–2
SHAK06–1
0 10 20 30 40 50 60 70 80 90
%
0
0 4 8 12
x10 3 grains g -1
3 2 1 0
‰VPDB
0 0.5 1 1.5 2 2.5 3 3.5

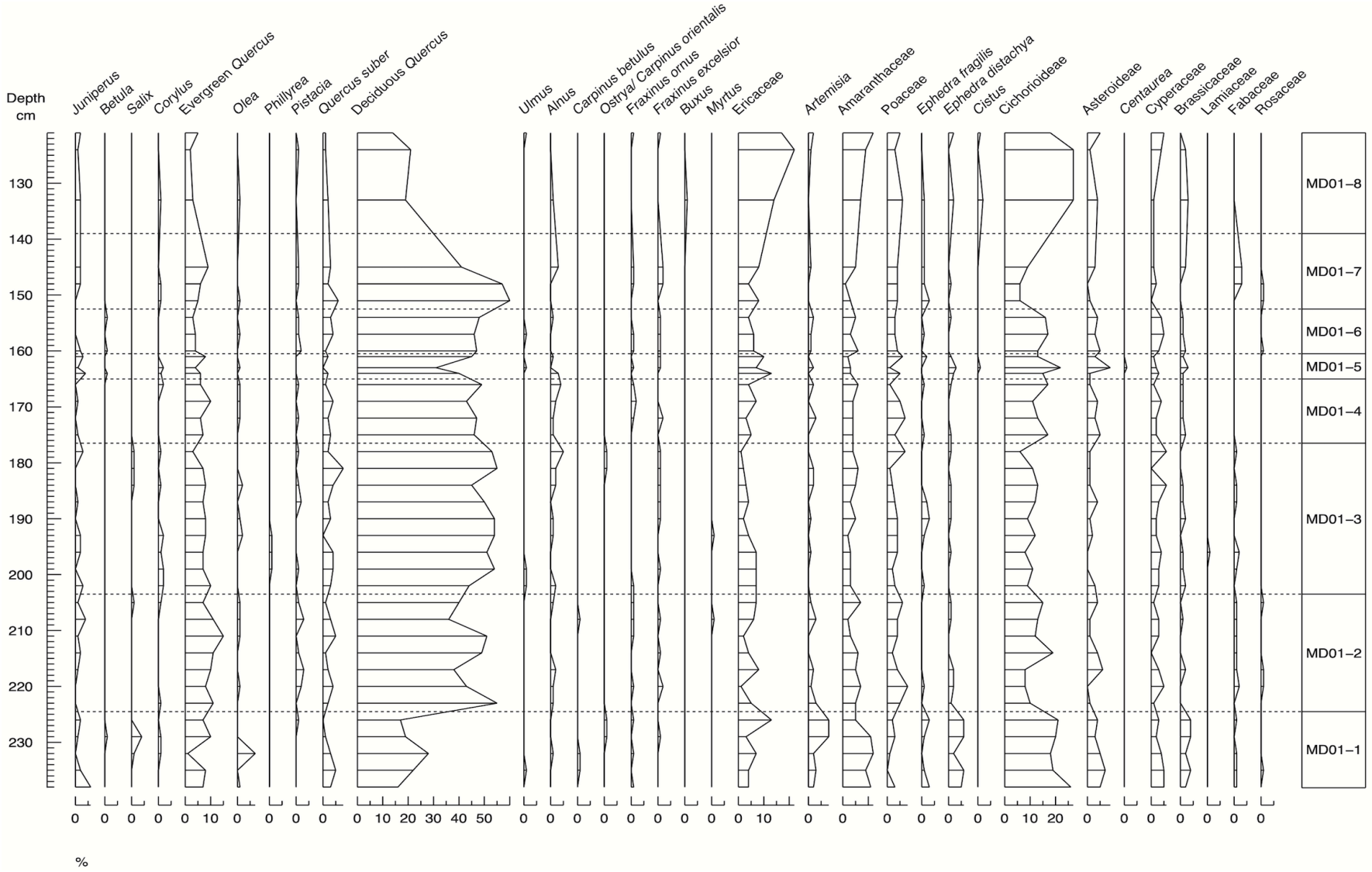

Fig. 4.4: Full pollen diagram showing change in pollen percentages (%) with depth in core MD01-2444. The total pollen concentration (x10^2 grains g^{-1}), $\delta^{18}O$ of *G.bulloides* (x10^{-1} ‰ VPDB), and *ln(*Ca/Ti) are also illustrated.

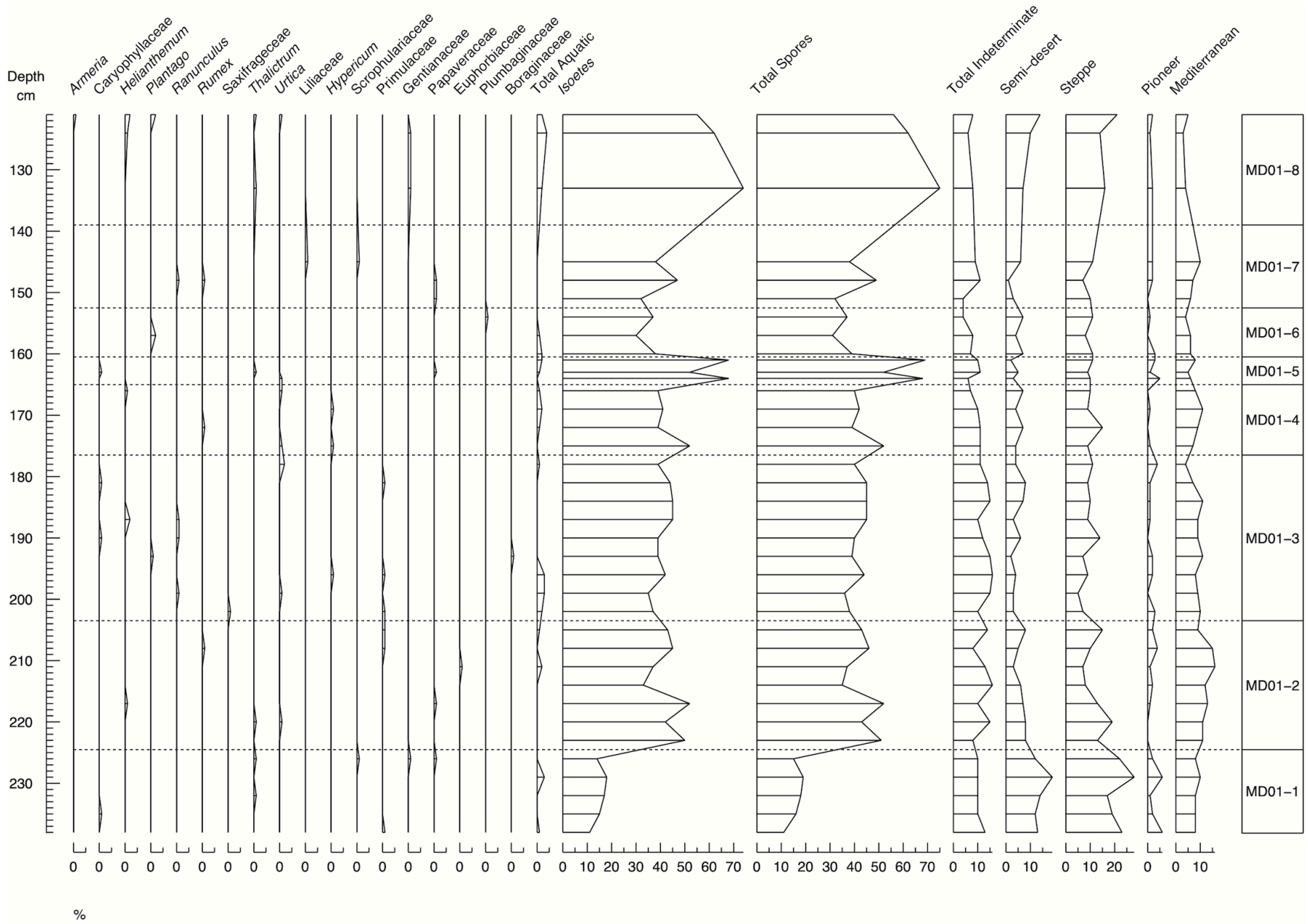
Depth
cm
Armeria
Caryophyllaceae
Helianthemum
Plantago
Ranunculus
Rumex
Saxifrageceae
Thalictrum
Urtica
Liliaceae
Hypericum
Scrophulariaceae
Primulaceae
Gentianaceae
Papaveraceae
Euphorbiaceae
Plumbaginaceae
Boraginaceae
Total Aquatic
Isoetes
Total Spores
Total Indeterminate
Semi-desert
Steppe
Pioneer
Mediterranean
130
140
150
160
170
180
190
200
210
220
230
MD01-8
MD01-7
MD01-6
MD01-5
MD01-4
MD01-3
MD01-2
MD01-1
%

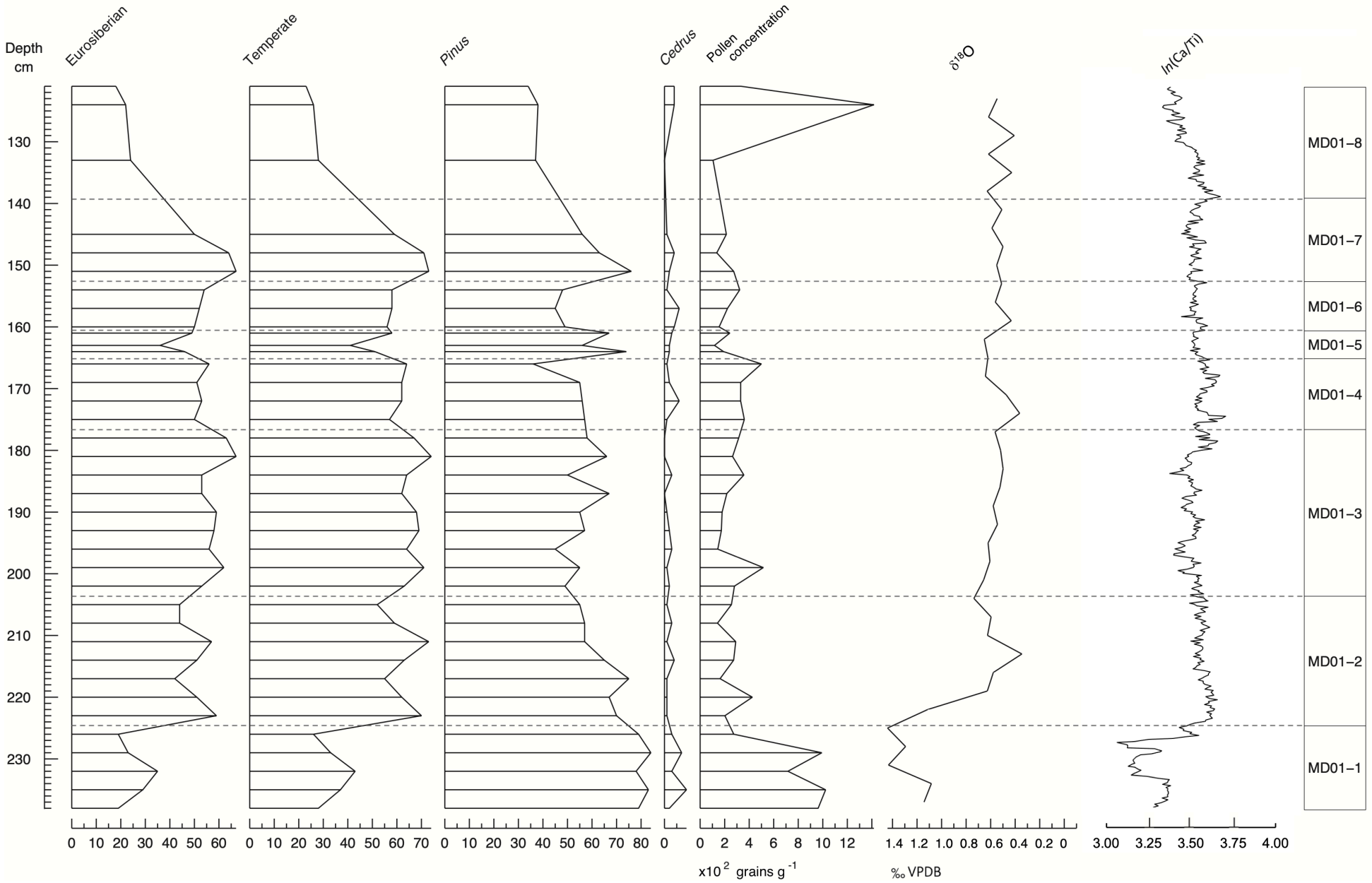
Depth
cm
Eurosiberian
Temperate
Pinus
Cedrus
Pollen
concentration
δ18O
ln(Ca/Ti)
130
140
150
160
170
180
190
200
210
220
230
MD01–8
MD01–7
MD01–6
MD01–5
MD01–4
MD01–3
MD01–2
MD01–1
0 10 20 30 40 50 60
0 10 20 30 40 50 60 70
0 10 20 30 40 50 60 70 80
0
0 2 4 6 8 10 12
x10 2 grains g -1
1.4 1.2 1.0 0.8 0.6 0.4 0.2 0
‰ VPDB
3.00 3.25 3.50 3.75 4.00

4.3.2. SHAK06-5K pollen record description by zone

Zone	Depth (cm)	Vegetation	Main pollen signature
SHAK06 – 1	329 – 302.5	Steppe	Highest percentages of steppe taxa (~40%), primarily composed of *Artemisia* (~23%)
SHAK06 – 2	302.5 – 281	Semi-desert/Steppe	Rise in percentages semi-desert taxa (reaching 52%), primarily *Artemisia* (~33%)
SHAK06 – 3	281 – 205	Steppe	Reduced semi-desert values (~33%), primarily Artemisia (~25%) and increase in Ericaceae (~15%)
SHAK06 – 4	205 – 161.5	Steppe/Open mixed woodland	Rise in temperate percentages (reaching 22% at 188 cm), primarily composed of deciduous *Quercus*, followed by a decline (reaching 5% at 170 cm). High steppe taxa values (~40%)
SHAK06 – 5	161.5 – 131	Semi-desert/Steppe	Steppe taxa values rise to highest values of the record (reaching 68%), primarily composed of *Artemisia* (reaching 42%)
SHAK06 – 6	131 – 117	Steppe/Open mixed woodland	Early rise in temperate taxa values (26 – 37%) to 124 cm, with deciduous *Quercus* (16% to 19%) and evergreen *Quercus* (6% to 11%) contributing most significantly. Decline in deciduous *Quercus* at 122 cm (to 10%), recovering towards the upper boundary
SHAK06 – 7	117 – 97	Mixed woodland	Increased temperate taxa percentages (peaking at 47%), primarily made up of deciduous *Quercus* (~22%) with a rise in Mediterranean elements (~11%)
SHAK06 – 8	97 – 80.5	Steppe/Open mixed woodland	Prominent rise in steppe taxa values (~36%), primarily *Artemisia* and Amaranthaceae (~14% and ~12%, respectively) and reduced temperate taxa percentages (~30%)
SHAK06 – 9	80.5 – 62.5	Mixed forest	Increase in temperate values to highest of the record (reaching 64%); predominately deciduous *Quercus* (~36%) and evergreen *Quercus* (~9%)
SHAK06 – 10	62.5 – 54.5	Open mixed woodland	Transitional zone of increased Ericaceae percentages (~13%), decreasing temperate values (~33%) and significant increase in Cichorioideae (~24%)
SHAK06 – 11	54.5 – 15	Open mixed woodland	Highest Ericaceae values of the record (reaching 25%), high Cichorioideae (~30%) and temperate taxa, dominated by deciduous *Quercus* (~9%) and evergreen *Quercus* (~5%)
SHAK06 – 12	15 – 0	Open mixed woodland	Highest percentages of Cichorioideae of the record (reaching 44%), increasing temperate values (12% to 19%) and initial rise, then decline (19% to 4%) in Ericaceae

Table 4.3: The main vegetation features of each PAZ in the SHAK06-5K record (Fig. 4.3).

SHAK06–1 (329 – 302.5 cm)

The major characteristic of this zone is the dominance of steppe taxa (pollen percentages ranging between 32 – 49%) which declines up the core. Of this group, *Artemisia* is the dominant taxon (~23%), with high values of Amaranthaceae and Poaceae (~8% and ~7%, respectively). Pollen percentages of temperate taxa range between 5 – 26%, increasing towards the upper boundary, composed principally of deciduous *Quercus* (~4%) with a continuous presence of evergreen *Quercus* (~3%), *Alnus* (~1%), and *Quercus suber* (~1%). There are high values of pioneer taxa (5 – 13%), primarily *Juniperus* (~8%). Heliophilous herbs are present, predominantly Cichorioideae and Asteroideae (~12% and ~6%, respectively). Ericaceae values increases until the mid-zone (reaching 19%), declining to 3% at the upper boundary. *Pinus* pollen percentages are high throughout (~71%) with peaks of *Cedrus* (~5%) at the bottom of the core and at the transition into SHAK– 2. The pollen concentration is variable with a mean value of 1,598 grains g^{-1}.

SHAK06– 2 (302.5 – 281 cm)

This zone is marked by a substantial rise in semi-desert taxa percentages (37 – 53%), primarily *Artemisia* (~33%). Semi-desert elements increase significantly from the preceding zone to 41% at the lower SHAK– 2 boundary and continue to increase up the core, peaking at 282 cm (53%). Although slightly lower than the preceding zone, prominent values of Poaceae, Cichorioideae, and Asteroideae are still present (~6%, ~11%, and ~5%, respectively). Percentages of *Juniperus* decline from the preceding zone (~5%), as do those of temperate taxa (~6%), with low deciduous *Quercus* values (~2%) and a low but continuous presence of Mediterranean taxa (~1%). Two declines in percentages of temperate taxa are seen at ~298 cm and ~286cm, respectively, separated by a small recovery which coincides with a decline in Amaranthaceae and Cichorioideae. During both contractions of temperate taxa percentages, values of pioneer vegetation (primarily *Juniperus*) also decline but recover earlier than temperate elements (dominated by deciduous *Quercus*). Ericaceae percentages are lower (ranging between 5 – 13%), increasing until the mid-zone and declining thereafter. This coincides with the second decline in temperate taxa values. *Pinus* values remain high early in the zone, declining to 53% at 288cm, before rising towards the upper transition. The pollen concentration is higher with a mean of 1,847 grains g^{-1}. Early concentration values are higher but decline from the mid to upper zone.

SHAK06–3 (281 – 205 cm)

This zone is marked by a reduction in semi-desert taxa percentages (ranging between 23 – 44%), primarily *Artemisia* (~19%) and an expansion of Ericaceae percentages (~15%). Values of semi-desert taxa decline until 266 cm (from 39% to 23%), coinciding with an increase in Poaceae percentages (from 7 to 15%), followed by a short recovery and then a gradual decline towards the top of the zone. There are low values of pioneer taxa (~8%), primarily composed of *Juniperus* (~7%), and low steady temperate taxa values (~6%), primarily composed of deciduous *Quercus* (~2%), with a small presence of *Alnus* (~1%), and evergreen *Quercus* (~1%). Overall, *Pinus* percentages increase (~71%), rising towards the top of the core, while *Cedrus* percentages remain low but relatively steady throughout the zone (~1%). *Isoetes* continues to be present at low levels (~6%), rising through the core. The pollen concentration is variable with a lower mean than the preceding zone (~1,732 grains g^{-1}).

SHAK06–4 (205 – 161.5 cm)

The main characteristic of this zone is the overall decline in *Artemisia* percentages (~19%) and the initial rise, then decline in temperate taxa values. *Juniperus* percentages peak at 194cm reaching 16%, before the peak in temperate taxa percentages at 188 cm (to 22%). These temperate elements are primarily deciduous *Quercus* (11%), with evergreen *Quercus* values continuing to increase (to 5%) until 180 cm. As percentages of temperate taxa decline to 5% at 176 cm, Amaranthaceae values also decline, coinciding with a rise in percentages of heliophilous taxa: Poaceae, Cichorioideae, and Asteroideae (13%, 22% and 13%, respectively). This is followed by a rise in Amaranthaceae and *Ephedra distachya* percentages (to 15% and 3%, respectively) which then reduce at the SHAK–2/3 transition coinciding with a rise in temperate taxa values (to 19%), primarily composed of *Juniperus* and deciduous *Quercus* (reaching 14% and 13%, respectively). Ericaceae percentages decline steadily over the zone, averaging 10%. Overall, there is a rise in *Pinus* percentages (~83%) and a slight increase in *Isoetes* (~6%) and *Cedrus* (~2%) values. Overall, the pollen concentration of this zone is lower, averaging 1,414 grains g^{-1}, with two peaks at 190 and 176 cm.

SHAK06–5 (161.5 – 131 cm)

This zone is marked by overall rise in steppe taxa percentages (ranging between 44 – 68%), with a small early peak at 160 cm, reaching 60%, and a larger second peak at 144 cm, reaching 68%. The

initial rise is primarily due to an increase in semi-desert elements as well as a rise in *Ephedra distachya*. This coincides with a reduction in the percentages of pioneer and Eurosiberian taxa (~6% and ~5%, respectively) and little to no presence of Mediterranean elements (≤1%). This is followed by a recovery in pioneer taxa values which reach 13%, and a smaller and slightly later peak in values of Eurosiberian and Mediterranean taxa (reaching 9% and 3%, respectively). The second expansion in steppe percentages is greater than the first, dominated by *Artemisia* and Amaranthaceae (reaching 32% and 15%, respectively). *Ephedra distachya* values remains high throughout the zone (~8%). Synchronously, *Juniperus* percentages decline, values of Eurosiberian elements are low, and pollen of Mediterranean taxa is absent. After this, percentages of semi-desert elements decline, coinciding with an expansion of arboreal pollen values; percentages of pioneer taxa rise first, followed by those of Eurosiberian and Mediterranean elements. Ericaceae percentages remain low (0 – 7%) while *Pinus* percentages increase and reach the highest levels of the record (87 – 94%). *Cedrus* values increase early (reaching 6%) and late (reaching 4%) in the zone, while *Isoetes* reaches the lowest values of the record (~3%). Overall, the pollen concentration is lower with a mean of 1,254 grains g^{-1}. The concentration peaks at 2,102 grains g^{-1} at the lower boundary, declining to 593 grains g^{-1} at 146 cm. This then rises to 1,548 grains g^{-1} before a decline towards the upper boundary.

SHAK06–6 (131 – 117 cm)

The key characteristic of this zone is the initial increase in values of Eurosiberian and Mediterranean taxa, peaking at 25% and 10%, respectively, followed by a decline in values of Eurosiberian taxa (to ~8%). The initial increase in arboreal pollen percentages is dominated by deciduous and evergreen *Quercus* (reaching 19% and 11%, respectively), coinciding with reduced steppe and pioneer percentages (to 13% and 4%, respectively). Values of Eurosiberian taxa then decline while those of steppe taxa increase to 46%. This is followed by a rise in Asteroideae and Cyperaceae percentages (to 13% and 8%, respectively). Overall, percentages of Ericaceae and *Isoetes* rise (~8% and ~6%, respectively), *Cedrus* remains low (~1%), and *Pinus* declines (69 – 93%). The pollen concentration has a lower mean value than the preceding zone of ~924 grains g^{-1}.

SHAK06–7 (117 – 97 cm)

This zone is characterised by a substantial rise in values of Eurosiberian taxa (ranging between 22 – 33%) and a reduction in those of steppe taxa (9 – 24%). The increase in arboreal pollen

percentages is primarily due to a rise in values of deciduous *Quercus*, peaking at 27% at 112 cm and gradually declining towards the upper boundary. There is a smaller rise in evergreen *Quercus* and *Juniperus* percentages (8 – 13% and 5 – 9%, respectively), with a small presence of *Quercus suber* and *Betula* (both ~2%). Cichorioideae and Cyperaceae values increase (~13% and ~6%, respectively), with reduced percentages of semi – desert taxa and Poaceae, which rise slightly throughout this zone, reaching 20% and 5%, respectively. For the first time in the record, Artemisia is not the dominant semi-desert pollen taxon (~5%), with values of Amaranthaceae reaching ~8%. On average, *Pinus* percentages are lower (~75%), decreasing early in the zone before increasing to 83%, coinciding with a peak in Ericaceae percentages (10%). Values of both taxa decline towards the upper boundary. *Cedrus* pollen is continuously present (~2%) while *Isoetes* pollen percentages have a higher mean (10%), despite being highly variable, ranging between 4% and 20%. The pollen concentration is variable with a mean value of 1,185 grains g^{-1}.

SHAK06–8 (97 – 80.5 cm)

This zone is dominated by a rise in percentages of steppe taxa (ranging between 28 – 52%), a strong decline in percentages of temperate taxa (12 – 37%), and low values of Ericaceae (~4%). Although *Artemisia* is the most dominant taxon (~14%), Amaranthaceae, Poaceae, and *Ephedra* percentages are also significant (with a mean of 12%, 6%, and 5% of taxa, respectively). Percentages of heliophilous ubiquitous herb are low, with Cichorioideae, Asteroideae, and Cyperaceae representing 7%, 4%, and 3% of taxa, respectively. Percentages of temperate taxa, although lower than the preceding zone, are dominated by deciduous *Quercus* (~19%), rising through the zone. Evergreen *Quercus* values (~7%) decline towards the top of the core, while *Quercus suber* values are steady (~2%). Percentages of pioneer taxa, principally *Juniperus*, decline through the zone (8% to 6%). *Pinus* values rise (ranging between 71 – 83%), with a higher, continuous presence of *Cedrus* (1 – 9%). *Isoetes* percentages decline (~6%), while the pollen concentration rises towards the upper boundary, with a mean value of 2,043 grains g^{-1}.

SHAK06–9 (80.5 – 62.5 cm)

This zone is characterised by an increase in percentages of temperate taxa, reaching 64% at 68 cm, the highest values of the record. Of this, Eurosiberian taxa are dominant (ranging between 35 – 54%), primarily composed of deciduous *Quercus*, *Quercus suber*, and *Alnus* (36%, 3% and 2%, respectively), all reaching their highest values of the record. Percentages of Mediterranean taxa

also increase to their highest values (4 – 17%), with a continuous occurrence of evergreen *Quercus* (~9%) and *Olea* (~1%) and an intermittent occurrence of *Pistacia* and *Phillyrea* (<1%) pollen. Despite a constant presence of pioneer taxa pollen (~5%), *Juniperus* and *Betula* decrease as values of Eurosiberian taxa peak. Between 63 – 66 cm, percentages of both Mediterranean and pioneer taxa decline, recovering at the transition into SHAK– 10. This coincides with a rise in Poaceae percentages, reaching 7%. Overall, values of steppe taxa decrease (~15%), with *Artemisia* declining from 12% at the lower boundary to 0% at 66 cm. The reduction in Amaranthaceae and Poaceae percentages is less prominent (~6% and 4%, respectively). Ericaceae values remain low (around 4%) until the transition into SHAK– 10, where they rise to 8%. *Pinus* percentages decline, reducing over the zone to ~64%. *Cedrus* pollen is not continuously present, reaching maximum values of 2%, while *Isoetes* values increase from 15 – 41% at the start of this zone, with values remaining high. The pollen concentration declines from 2,061 grains g^{-1} at the lower boundary to 374 grains g^{-1} at the upper boundary, with a mean value of 915 grains g^{-1}.

SHAK06–10 (62.5 – 54.5 cm)

A substantial decline in Eurosiberian taxa percentages (from 41% to 15%), reduction in Mediterranean taxa (from 15% to 4%), and rise in Cichorioideae values (from 9% to 26%) characterises this zone. The Eurosiberian pollen decline is primarily due to a reduction in deciduous *Quercus* values (~19%), although there is a minor presence of *Alnus* (~2%), *Quercus suber*, *Ostrya/Carpinus orientalis*, and *Fraxinus excelsior* (~1%). Reduced percentages of Mediterranean taxa are primarily caused by a reduction in evergreen *Quercus*, although there remains an intermittent occurrence of *Olea*, *Phillyrea*, and *Pistacia* pollen. Meanwhile, *Juniperus* percentages are higher (~6%) than at the end of the preceding zone. Overall, steppe percentages are lower (~15%), with values of Amaranthaceae and Poaceae increasing towards the upper boundary. However, percentages of *Artemisia* are higher (~2%) than at the end of SHAK– 9. Over this zone, Ericaceae percentages increase from 9 – 15%, while *Pinus* values decline from 63 – 18%. The presence of *Cedrus* pollen is discontinuous, not exceeding 2%. *Isoetes* values vary but remain high (~43%), while the mean pollen concentration is the lowest of the core at 247 grains g^{-1}.

SHAK06–11 (54.5 – 15 cm)

This zone is characterised by an expansion of Ericaceae values, which reach the highest percentages of the core (25%) at 46 cm. Heliophilous Cichorioideae reach high values (~30%), while

percentages of temperate taxa decline (~19%). Of the temperate elements, deciduous *Quercus* remains dominant (~9%), with a continuous steady presence of evergreen *Quercus* pollen (~5%). *Alnus* (~1%), *Quercus suber* (~1%), *Pistacia* (~1%), *Olea* (~1%), and *Fraxinus ornus* (~1%) are frequently, but discontinuously present. There is a low but continuous occurrence of pioneer taxa pollen, with *Juniperus* averaging values of 3% over the zone. Amaranthaceae and Poaceae values increase (~6% and ~5%, respectively), while those of *Artemisia* are considerably reduced (~2%). Percentages of *Pinus* reach a minimum (~17%), ranging between 6 – 34%. *Cedrus* pollen is present at low levels until the middle of this zone, with intermittent low values towards the upper core. *Isoetes* percentages remain high, with peak values around 47%, although there is a decline to 23% at 24 cm. The pollen concentration remains low, increasing up the core, with a mean value of 520 grains g^{-1}.

SHAK06–12 (15 – 0 cm)

This zone is marked by high values of Cichorioideae and Asteroideae (~38% and ~9%, respectively), reduced Eurosiberian and steppe percentages (~10% and ~10%, respectively), a slight rise in Mediterranean taxa (~8%), and a decline in Ericaceae percentages towards the top of the core (ranging between 4 – 19%). Percentages of Eurosiberian taxa are dominated by deciduous *Quercus* (~6%), while pollen of *Quercus suber* (~1%), *Fraxinus ornus* (~1%), and *Fraxinus excelsior* (~1%) are also present. Percentages of Mediterranean taxa remain steady early in the zone, rising towards the top of the core, primarily due to a rise in values of evergreen *Quercus*, reaching 8%. *Olea* and *Pistacia* pollen are also present throughout the zone (~2% and ~1%, respectively). *Juniperus* percentages remain low throughout the zone (~2%). Amaranthaceae and Poaceae are the dominant steppe taxa (~4% and ~4%, respectively), with a reduced, intermittent presence of *Artemisia* (~1%). *Pinus* percentages remain low early in the zone (14%), increasing significantly to 55% at the top of the core. *Cedrus* pollen is only present (<1%) at the top of this zone, while *Isoetes* percentages remain high (~36%) but decline to 26% up the core. With relatively low variability and a mean pollen concentration of 522 grains g^{-1}, this zone sees an initial decline in concentration which gives way to a rise mid-zone, before declining towards the top of the core.

4.3.3. MD01-2444 pollen record description by zone

Zone	Depth (cm)	Vegetation	Main pollen signature
MD01 – 1	238 – 224.5	Open mixed woodland	Highest values of herbaceous taxa, particularly Cichorioideae (~20%) and steppe taxa (~21%), particularly Amaranthaceae (~9%), with presence of temperate taxa (~33%).
MD01 – 2	224.5 – 203.5	Mixed forest	Rise in temperate taxa percentages (~62%), primarily deciduous *Quercus* (~44%) and increase in Mediterranean taxa percentages, primarily evergreen *Quercus* (~10%) and Pistacia (~1%)
MD01 – 3	203.5 – 176.5	Mixed forest	Decline in evergreen *Quercus* percentages (~7%), but rise in deciduous *Quercus* (~50%)
MD01 – 4	176.5 – 165	Mixed forest	Slight decline in percentages of temperate taxa (~61%), primarily due to a decline in deciduous *Quercus* (~45%)
MD01 – 5	165.5 – 160.5	Mixed forest	Overall decline in percentages of temperate taxa (~50%) due to significant reduction in deciduous *Quercus* (~38%) and rise in Ericaceae (~10%) and some herbaceous elements including Cichorioideae and Asteroideae
MD01 – 6	160.5 – 152.5	Mixed forest	Overall increase but steady temperate taxa percentages (~57%), dominated by deciduous *Quercus* (~45%)
MD01 – 7	152.5 – 139	Mixed forest	Rise in temperate values (~68%) dominated by Eurosiberian elements (reaching 68%), followed by a later rise in Mediterranean taxa (~10%) and rising Ericaceae percentages (~7%)
MD01 – 8	139 – 121	Open mixed woodland	Decline in temperate taxa percentages (~25%) primarily deciduous *Quercus* (~17%) and rise in Ericaceae, reaching 21%, the highest of the record, and a rise in Cichorioideae, reaching 27%

Table 4.4: The main vegetation features of each PAZ in the MD01-2444 record (Fig. 4.4).

MD01 – 1 (238 – 224.5 cm)

This zone is characterised by moderate percentages of temperate taxa (ranging between 26 – 43%), steppe taxa (17 – 28%), and Cichorioideae (18 – 26%). Temperate taxa percentages are dominated by deciduous *Quercus* (~20%) and *Quercus suber* (~2%), rising until 232 cm, and declining towards the upper part of the zone. Values of Mediterranean taxa remain steady, dominated by evergreen *Quercus* (~6%) with the intermittent occurrence of *Olea*. Pioneer pollen values are low throughout the zone (~3%). Steppe taxa are primarily composed of Amaranthaceae

(~10%), *Ephedra distachya* (~5%), and *Artemisia* (~4%). There is a continuous presence of pollen of Cichorioideae (~21%), Asteroideae (~5%), Brassicaceae (~3%), and hygrophytic Cyperaceae (~4%). Ericaceae percentages remains low (~6%), while *Pinus* reaches the highest percentages of the record (~81%). *Cedrus* pollen is continuously present, reaching 9%, while *Isoetes* declines to the lowest values of the record (~15%). The pollen concentration of this zone is highly variable, but has the highest mean value of the record, peaking at 1,023 grains g^{-1}, but declining significantly to 274 grains g^{-1} at the upper boundary.

MD01 – 2 (224.5 – 203.5)

This zone is marked by a rise in temperate taxa percentages (ranging between 52 – 73%), primarily composed of Eurosiberian elements, and a decline in steppe taxa (7 – 19%) and Cichorioideae (8 – 19%). Values of deciduous *Quercus* (~45%) and *Quercus suber* (~2%) show an initial rise before declining until 217 cm. Both then increase until 211 cm but decline towards the upper boundary. Percentages of evergreen *Quercus* rise through the zone, before declining towards the transition. Pollen of *Pistacia* (reaching 3%), *Juniperus*, *Olea*, *Alnus*, *Fraxinus excelsior*, and *Fraxinus ornus* (all ~1%) is intermittently present. The decline in steppe percentages results from a reduction in Amaranthaceae, *Artemisia*, and *Ephedra* (~5%, ~1%, and ~1%, respectively). Poaceae values, however, increase from the preceding zone (~5%). Although Ericaceae percentages remain low (~5%), they peak twice, both coinciding with the decline in Eurosiberian taxa values. *Pinus* percentages decrease throughout the zone (~64%), while those of *Cedrus* are low but continuous (~2%). This zone sees a major rise in *Isoetes* (~43%) and a reduction in the pollen concentration which has a mean value of 250 grains g^{-1}.

MD01 – 3 (203.5 – 176.5 cm)

The vegetation composition of this zone is relatively stable, characterised by an overall rise in percentages of Eurosiberian taxa (ranging between 53 – 67%) and reduced levels of steppe taxa (5 – 14%) and Cichorioideae (6 – 13%). This rise in values of Eurosiberian taxa is primarily composed of deciduous *Quercus* (~51%), with a small rise in *Quercus suber* (~3%), and a low discontinuous presence of *Fraxinus excelsior* (~1%). Percentages of Mediterranean taxa are lower than the preceding zone (~9%), primarily composed of evergreen *Quercus* (~7%), although there are low and intermittent *Pistacia* and *Olea* values (both ~1%). Steppe taxa are primarily composed of Amaranthaceae and Poaceae (~4% and ~3%, respectively), with intermittent, low *Artemisia*,

Ephedra distachya, and *Ephedra fragilis* values (all ~1%). There is a near continuous presence of Cyperaceae (~3%), while Ericaceae percentages decline through the zone, from 7% to 1%. *Pinus* percentages are variable, but lower overall (~56%). *Cedrus* values are both lower and sporadic (~1%), while *Isoetes* percentages are high and steady (~41%). After an early decline, the pollen concentration rises slightly towards the upper boundary, averaging 272 grains g^{-1}.

MD01 – 4 (176.5 – 165 cm)

A small decline in Eurosiberian taxa percentages (ranging between 57 – 64%) characterises this zone, primarily due to a decline in deciduous *Quercus* (~46%). There are low values of *Quercus suber* (~3%) and *Alnus* (~2%), and low intermittent values of *Fraxinus excelsior* and *Fraxinus ornus* (<2%). Percentages of Mediterranean taxa remain relatively steady (~9%), dominated by evergreen *Quercus* (~7%), while *Pistacia* and *Olea* percentages are low and discontinuous (<1%). Pollen of pioneer taxa is intermittently present and does not exceed 1%. Percentages of steppe taxa remain relatively steady (~11%), although there is a change in contributing taxa, with a rise in Poaceae (~4%). Values of Cichorioideae (~14%), Ericaceae (~5%), and Asteroideae (~3%) rise. *Pinus* percentages decline throughout the zone, reaching ~36% by the upper boundary, while *Cedrus* pollen remains continuously present (~3%). *Isoetes* values remain high (~43%), and overall, the pollen concentration is higher in this zone, averaging 380 grains g^{-1}.

MD01 – 5 (165.5 – 160.5 cm)

This zone is characterised by a decline in percentages of temperate taxa reaching 41% at 163 cm. This contraction is primarily due to a prominent decline in deciduous *Quercus* and a smaller reduction in evergreen *Quercus* (reaching 39% and 6%, respectively). At the same time, there is a small presence of *Alnus* and *Quercus suber* pollen, which also decline at 163 cm. Percentages of temperate taxa then rise towards the upper boundary, reaching 58%. Overall, values of pioneer taxa are higher than the preceding zone (~3%), along with increased *Corylus* percentages (~1%) and a rise in Cichorioideae (~17%) and Asteroideae (~4%) values. Although overall steppe percentages remain relatively steady (~10%), those of Amaranthaceae decline (~3%), while *Ephedra* values rise (~3%). Percentages of Ericaceae (~10%) and *Pinus* (~66%) increase and there continues to be a low presence of *Cedrus* pollen (~2%). *Isoetes* percentages rise substantially (~63%). The pollen concentration declines towards the middle of this zone, reaching 118 grains g^{-}

^{1}, before rising slightly at the upper transition. On average, this zone's pollen concentration is the lowest of the record at 184 grains g^{-1}.

MD01 – 6 (160.5 – 152.5 cm)

This zone is marked by an overall increase in percentages of Eurosiberian taxa which remain relatively steady throughout (ranging between 50 – 54%). These are dominated by deciduous *Quercus* (~47%), with a continuous presence of *Quercus suber* (~3%) and *Fraxinus excelsior* pollen (~1%). Values of Mediterranean and pioneer elements are low (~5% and ~1%, respectively), declining throughout the zone. Steppe values remain steady (8 – 11%), primarily composed of Poaceae and Amaranthaceae. There is an overall decline in Cichorioideae percentages (~15%), a rise in Cyperaceae (~4%), and a continuous Asteroideae pollen presence (~4%). Percentages of Ericaceae show a slight decline (~5%) as do those of *Pinus* (~47%), while *Cedrus* pollen shows a low but continuous present (~4%). *Isoetes* values decline significantly (~35%) and the pollen concentration increases from 155 grains g^{-1} at the lower boundary to 323 grains g^{-1} at the upper transition.

MD01 – 7 (152.5 – 139 cm)

The main characteristic of this zone is a substantial early rise in percentages of Eurosiberian taxa, reaching 67% at 151 cm, before declining towards the upper boundary. Eurosiberian taxa are dominated by deciduous *Quercus* (~53%), with *Quercus suber* (~4%), *Fraxinus excelsior*, and *Fraxinus ornus* pollen (both ~1%) also present. Values of Mediterranean taxa also increase, peaking later at 145 cm (reaching 10%), dominated by values of evergreen *Quercus* (~7%) with a low presence of *Pistacia* and *Olea*. Low, steady steppe values (ranging between 7 – 11%) are primarily composed of Poaceae and Amaranthaceae, while overall percentages of Cichorioideae (~7%), Asteroideae, and Cyperaceae (both ~1%) decline, and Fabaceae levels rise (~2%). Pinus percentages increase significantly at the start of the zone, reaching 76%, before declining up the core (to 56%). Ericaceae values rise slightly (~7%), *Isoetes* percentages increase (~39%), and *Cedrus* pollen is continuously present (~2%). The pollen concentration remains low throughout, averaging 208 grains g^{-1}.

MD01 – 8 (139 – 121 cm)

This zone is dominated by a considerable rise in Cichorioideae and Ericaceae values, both reaching the highest percentages of the record (27% and 22%, respectively). Percentages of temperate taxa decline from 28% to 23%, primarily composed of deciduous *Quercus* (~18%) with a small presence of evergreen *Quercus* (~3%). There is a low continuous occurrence of *Juniperus* pollen (~2%). Percentages of steppe taxa increase (ranging between 14 – 21%), dominated by Amaranthaceae (~9%) and Poaceae (~5%), with low intermittent *Artemisia* and *Ephedra* values (both ~1%). *Pinus* percentages reach the lowest values of the record (~36%), while *Cedrus* pollen is not present early in the zone but reaches values of 4% at the top of the core. Percentages of *Isoetes* rise, reaching 64%, the highest of the record, while the pollen concentration is the most variable of the record, ranging between 105 and 1,417 grains g^{-1}.

4.4. Inferred vegetation trends

This chapter presented the results of the pollen analysis in cores SHAK06-5K and MD01-2444. When comparing the SHAK06-5K pollen and $\delta^{18}O_{G.\ bulloides}$ records (Fig. 4.3), the high $\delta^{18}O_{G.\ bulloides}$ values between 329 to ~126 cm (~2.5‰) and lower *ln*(Ca/Ti) values (~3.1) indicate glacial conditions (Adkins *et al.,* 2002; Lisiecki & Raymo, 2005). At this time, SW Iberian vegetation was dominated by steppe elements, associated with cool/dry conditions. The dominant taxa were *Artemisia* and Amaranthaceae, with a low but continuous presence of woodland elements, primarily *Juniperus* and deciduous and evergreen *Quercus*. The decreasing $\delta^{18}O_{G.\ bulloides}$ values between ~ 126 to 78 cm (declining from ~2 – 1.3‰) and increasing *ln*(Ca/Ti) values reflect a transitional period, with the expansion of arboreal elements and decline of steppe taxa. Over this period, steppe vegetation was gradually replaced by woodland, dominated by deciduous *Quercus* and some Mediterranean elements, pointing to increasingly warm/wet conditions. The interval from 76 to 0 cm reflects interglacial conditions, indicated by the low $\delta^{18}O_{G.\ bulloides}$ values (~0.5‰) and higher *ln*(Ca/Ti) values (~3.4). At the onset of this interval, there was a further expansion of woodland, primarily composed of deciduous and evergreen *Quercus*, dominating until ~62 cm. After 62 cm woodland contracted and heathland expanded.

Comparing the MD01-2444 pollen and $\delta^{18}O_{G.\ bulloides}$ records (Fig. 4.4), it is apparent that these records cover the transition to the interglacial and the early part of the interglacial. Early in the record $\delta^{18}O_{G.\ bulloides}$ levels are high (~1.3‰ between ~238 and 222 cm) with presence of steppe vegetation alongside woodland communities (primarily deciduous *Quercus*) indicating cooler conditions with moderate moisture levels, where steppe levels were high despite woodland dominating (primarily composed of deciduous *Quercus*). After this, $\delta^{18}O_{G.\ bulloides}$ declined, remaining around 0.6 ‰ until the end of the record at 121 cm, indicating interglacial conditions. Over this period, woodland expanded, dominated by deciduous *Quercus* and a continuous presence of evergreen *Quercus* and *Quercus suber.* At this time, steppe communities declined, indicating increasingly warm/wet conditions. At the end of the record, between 133 and 121 cm, woodland elements contracted and heathland expanded.

In summary, our records show the vegetation transition from glacial to interglacial conditions, with large fluctuations in vegetation composition. In the SHAK06-5K record, deciduous *Quercus* is the dominant taxon in the pollen spectra. *Pinus* and Cichorioideae are omnipresent (although the

former is removed from the pollen sums). Steppe taxa and Cichorioideae are the dominant non-arboreal pollen in the sequence, with the former dominating earlier in the record (SHAK06-1 to -9), and the latter dominating towards the top of the core (SHAK06-10 to -12). Of the steppe elements, *Artemisia* dominates earlier in core SHAK06-5K, but its proportions reduce and are surpassed by Amaranthaceae and Poaceae later in the record (SHAK06-9 to -12). Although levels fluctuate throughout, MD01-2444 has a constant presence of *Pinus*, deciduous and evergreen *Quercus*, Ericaceae, Amaranthaceae and Cichorioideae. The majority of the record is dominated by deciduous *Quercus* (MD01-2 to -7), although at the start and end of the record (MD01-1 and MD01-8), Cichorioideae is the dominant taxon. A more thorough assessment of the nature and timing of vegetation changes in relation to other proxies from the same cores and to other records will be provided in Chapter 8, after a detailed chronology is developed in Chapter 6.

5.1. Introduction

Leaf cuticular waxes of vascular plants are the primary interface between a plant and its surrounding environment, performing an essential role in regulating gas exchange and water loss, and protecting against both biotic and abiotic threats (Jetter *et al.,* 2008). One critical component of these waxes is the existence of long-chain n-alkyl lipids; *n*-alkanes, *n*-alcohols, *n*-alkanoic acids and wax esters (Fig. 5.1) (Chibnall *et al.,* 1934; Eglinton *et al.,* 1962; Eglinton & Hamilton, 1967). As these compounds can be preserved for millions of years in the sedimentary record, they can be used to better understand the influence of climate change on terrestrial vegetation over geological timescales (Eglinton & Hamilton, 1967; Cranwell, 1981; Poynter *et al.,* 1989; Pancost & Boot, 2004; Eglinton & Eglinton, 2008; Freeman & Pancost, 2013; Diefendorf & Freimuth, 2017). Although these compounds are found on other plant organs, the highest concentrations are produced on the leaf surface (Gamarra & Kahmen, 2015; Diefendorf & Freimuth, 2017), consequently, waxes delivered to sediments will be referred to as leaf-waxes. Of these leaf-waxes, *n*-alkanes have been the most widely researched (Diefendorf & Freimuth, 2017). Typically, their chain lengths range between C_{25} – C_{35} (names, molecular and structural formulas outlined in Table 5.1), and a strong odd-over-even carbon homologue predominance exists (Eglinton *et al.,* 1962; Eglinton & Hamilton, 1967).

This chapter presents the fossil *n*-alkane record from core SHAK06-5K, firstly outlining the current understanding of leaf-wax *n*-alkanes as palaeoclimatic indicators, before explaining the methods used to prepare and analyse the leaf-wax *n*-alkanes from core SHAK06-5K. Finally, the leaf-wax *n*-alkane distribution and carbon isotope records will be presented against depth.

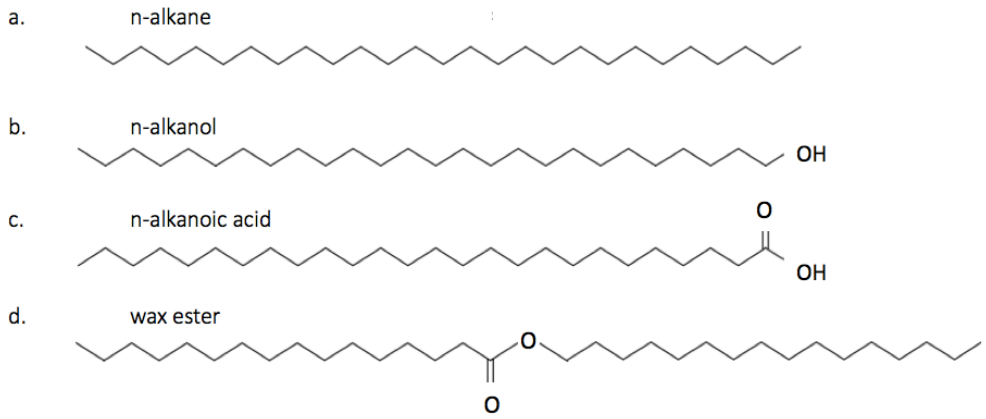

Fig. 5.1: Structure of straight-chain terrestrial leaf-wax *n*-alkyl lipids: **a.** *n*-alkanes; **b.** *n*-alkonols; **c.** *n*-alkanoic acids; and **d.** wax esters (Pancost and Boot, 2004)

No. of carbon atoms	Name	Molecular formula	Structural formula
C_{25}	n-pentacosane	$C_{25}H_{52}$	$CH_3(CH_2)_{23}CH_3$
C_{27}	n-heptacosane	$C_{27}H_{56}$	$CH_3(CH_2)_{25}CH_3$
C_{29}	n-nonacosane	$C_{29}H_{60}$	$CH_3(CH_2)_{27}CH_3$
C_{31}	n-hentriacontane	$C_{31}H_{64}$	$CH_3(CH_2)_{29}CH_3$
C_{33}	n-tritriacontane	$C_{33}H_{68}$	$CH_3(CH_2)_{31}CH_3$
C_{35}	n-pentatriacontane	$C_{35}H_{72}$	$CH_3(CH_2)_{33}CH_3$

Table 5.1: Molecular and structural formula of the dominant chain lengths in terrestrial leaf-waxes (Eglinton *et al.,* 1962; Eglinton & Hamilton, 1967).

5.1.1. Leaf-wax n-alkane production, transport and residence time

Leaf-wax ablation occurs primarily by abrasion from wind, dust, and precipitation; wet and dry deposition then transfer these compounds from the atmosphere into soils, fluvial systems and marine environments (Gagosian & Peltzer, 1986; Rogge *et al.,* 1993; Shepherd & Wynne Griffiths, 2006). The molecular composition of these leaf-wax aerosols has been shown to be reflective of the vegetation of the source region of these particles (Conte & Weber, 2002). As the greatest biosynthesis of leaf-waxes occurs after leaf unfurling, the most significant leaf-wax aerosol production, transportation, and subsequent accumulation in sediments occurs at the start of the growing season (Tipple *et al.,* 2013; Nelson *et al.,* 2018), although in evergreen species, *n*-alkane synthesis continues up to 4 months after leaf flush, and considerably longer than that in many deciduous species (Sachse *et al.,* 2015). Leaf-wax transport also occurs during leaf-fall, where they can be incorporated into soils or transported into lake, river, or marine environments (Diefendorf & Freimuth, 2017).

Transport of these terrestrial compounds to the ocean can occur by both atmospheric and fluvial mechanisms. Leaf-waxes from fresh vegetation and soils can also be transported atmospherically, reaching the open ocean over days to weeks, causing the leaf-wax signal to reflect vegetation of the neighbouring continents (Gagosian *et al.,* 1981; Huang *et al.,* 2000; Conte & Weber, 2002; Eglinton *et al.,* 2002; Schefuss *et al.,* 2003). These leaf-waxes are typically reflective of the relative

input from both arboreal and herbaceous vegetation (Diefendorf & Freimuth, 2017). *n*-Alkanes entering the marine environment via fluvial transport are reflective of the vegetation of the river's catchment basin (Haggi *et al.,* 2016), although degradation and replacement of organic matter during transport means the *n*-alkane signal is dominated by vegetation closer to the deposition site (Galy *et al.,* 2011). Despite rapid fluvial and atmospheric transport of terrestrial biomarkers to the marine environment over days to months (Conte & Weber, 2002), upon reaching the ocean, the transit time across continental shelves before burial in marine sediments can be thousands of years (Eglinton & Eglinton, 2008; Bröder *et al.,* 2018; Bao *et al.,* 2018). Grain size also influences transit times across continental shelves. Particles < 20 µm and > 65 µm demonstrate older ages compared to the sortable silt fraction which undergoes the most remobilisation and resuspension (Bao *et al.,* 2018).

Both in soils and the water column (fluvial and marine), terrestrial lipids become adsorbed onto mineral particles (Mayer *et al.,* 1994). *n*-Alkanes are suggested to have the highest association with finer fractions, with long-chain terrestrial *n*-alkanes the most abundant in clays, followed by the silt fraction (Quenea *et al.,* 2004). Clays and fine silts are not significantly affected by gravitational settling and are, therefore, transported further (Eglinton *et al.,* 2002). In the water column, terrestrial lipids can also become incorporated within faecal pellets and transported vertically into marine sediments (Gagosian & Peltzer, 1986).

Significant uncertainty and regional variation surround the residence times of biomarkers in continental reservoirs. Consequently the contribution of pre-aged leaf-wax material to marine sediments from intermediate reservoirs, such as soils and terrestrial watersheds, must be considered. In soils, the residence times of leaf-wax can be thousands of years (Huang *et al.,* 1996; Kusch *et al.,* 2010), while in the Red Sea, leaf-waxes sourced from paleolakes have led to radiocarbon age offsets of ~5000 years (Eglinton *et al.,* 1997). In many regions, the contribution of pre-aged material is significant; in the Saanich Inlet, in western Canada, the pre-aged contribution is greater than 80% (Smittenberg *et al.,* 2006), while in the Bay of Bengal, 79 – 83% of leaf-waxes have been stored in continental reservoirs for ~1000 years prior to deposition (French *et al.,* 2018). These trends, however, are not common to all sites. In the Black Sea, the Santa Monica, and the Santa Barbara Basins, continental residence times of vascular biomarkers entering marine environments were found to be < 100 years, with 80 – 87% of biomarkers in Santa Monica Basin

marine sediments suggested to be sourced from contemporary terrestrial material (Eglinton *et al.,* 1997; Pearson & Eglinton, 2000; Mollenhauer & Eglinton, 2007). The continental residence time of leaf-waxes is therefore dependent on regional geology, hydrology, and climate. Steep topography and annual flood deposits can enhance the young pool of carbon, while aridity and colder temperatures can increase carbon storage and continental residence time (Drenzek *et al.,* 2007; Galy & Eglinton, 2011; Vonk *et al.,* 2019).

5.1.2. Leaf-wax n-alkane preservation and degradation

With a compound structure of over 20 carbon atoms, terrestrial long-chain *n*-alkanes are chemically inert, insoluble in water, relatively resistant to biodegradation, and have minimal volatility, meaning they are highly conserved in lacustrine and marine sediments (Cranwell, 1981; Eglinton & Eglinton, 2008).

These long-chain compounds are still at risk of degradation from microbial and chemical processes during the transport process and after deposition (Gagosian & Peltzer, 1986; Meyers & Eadie, 1993; Galy *et al.,* 2011). In the water column, lipids have been shown to make up 20% of organic carbon, which reduces to 0.2% in marine sediments as a result of microbial degradation and oxidation (Wakeham *et al.,* 1997). This degradation, however, primarily impacts short-chain *n*-alkanes, as the increased stability of long-chain *n*-alkanes means these compounds are less readily degraded and better preserved in sediments (Rieley *et al.,* 1991a; Meyers & Eadie, 1993; Wakeham *et al.,* 1997). Furthermore, degradation of leaf-waxes in the water column is small as exposure to degradation processes, such as oxidation, has already occurred during atmospheric transport (Gagosian & Peltzer, 1986). Additionally, the close association of plant biomarkers with mineral surfaces is suggested to protect particles from degradation (Mayer *et al.,* 1994), while remineralisation of long-chain *n*-alkanes in fluvial systems has not been shown to be extensive (Haggi *et al.,* 2016).

The input of petrogenic organic matter (material formed by the decomposition of organic material under extreme temperatures and pressure) can significantly influence the leaf-wax signal (Lichtfouse & Eglinton, 1995; Jeng, 2006), although in some marine sediments, the contribution is relatively minor (Pearson & Eglinton, 2000). As both degraded and petrogenic material demonstrate no carbon preference, it is possible to assess the contribution of these materials by calculating the carbon preference index (CPI) (outlined in section 5.2). As higher plant cuticular

waxes demonstrate an odd-over-even chain length preference (Eglinton & Hamilton, 1967), a CPI above one suggests a terrestrial plant source of the *n*-alkanes, rather than a significant input from petrogenic or degraded material (Bray & Evans, 1961; Kennicutt *et al.,* 1987). CPI in fresh leaves is usually > 4 (Collister *et al.,* 1994).

5.1.3. Leaf-wax n-alkanes as palaeoclimatic indicators

Climatic inferences have been made extensively using leaf-waxes from sedimentary sequences, with long-chain *n*-alkanes (C_{27} – C_{33}) one of the most widely used of these plant biomarkers (e.g. Eglinton & Hamilton, 1963; Cranwell, 1973; Rommerskirchen *et al.,* 2003; Vogts *et al.,* 2009; Bush & McInerney, 2013).

5.1.3.1. n-Alkane concentrations and average chain length

Leaf-wax concentrations vary considerably among plant types, although long-chain leaf-wax *n*-alkane concentrations are generally higher in angiosperms than gymnosperms (Sachse *et al.,* 2006; Diefendorf *et al.,* 2011; Bush & McInerney, 2013; Diefendorf & Freimuth, 2017). The distribution of long-chain *n*-alkanes also varies considerably among plant types, with the climatic and biological controls of average chain length (ACL) still relatively unknown. Many have suggested that *n*-alkane ACL in the sedimentary record can be used to determine dominant vegetation composition, based on the assumption that longer chain-lengths (C_{31} – C_{33}) are derived from graminoid-type taxa and shorter dominant chain-lengths (C_{27} – C_{29}) are sourced from woody plants (Cranwell, 1973; Meyers & Ishiwatari, 1993; Rieley *et al.,* 1995; Schwark *et al.,* 2002; Bai *et al.,* 2009; Bliedtner *et al.,* 2018). This view is opposed by many studies, which demonstrate ACL variations within the same species/taxa group (Schwark *et al.,* 2002; Rao *et al.,* 2011; Bush & McInerney, 2013; Hoffmann *et al.,* 2013). Other suggested ACL controls include temperature (Poynter *et al.,* 1989; Poynter & Eglinton, 1990; Hoffmann *et al.,* 2013; Tipple & Pagani, 2013; Bush & McInerney, 2015) and water stress (Huang *et al.,* 2000; Schefuss *et al.,* 2003), although climate has been shown to impact ACL in opposing ways for two species along the same climate transect (Hoffmann *et al.,* 2013). Consequently, ACL should be used cautiously as a climate and vegetation proxy (Wang *et al.,* 2015; Diefendorf & Freimuth, 2017).

5.1.3.2. $\delta^{13}C$ of plant biomass

Plants discriminate against ^{13}C during photosynthesis, producing plant biomass that is ^{13}C depleted relative to the atmosphere (Melander & Saunders, 1979; O'Leary, 1981). Plants using the C_4 (Hatch-Slack) photosynthetic pathway (an adaptation to reduce photorespiration) produce higher plant $\delta^{13}C$ ($\delta^{13}C_{plant}$) compared to those using the C_3 (Calvin-Benson) pathway, due to less isotopic fractionation in the former (Hayes, 1993; Collister *et al.,* 1994; Cernusak *et al.,* 2013; Freenman & Pancost, 2014). Plants using the Crassulacean acid metabolism (CAM) pathway (used by plants in extreme hot/dry environments) have intermediate fractionation (O'Leary, 1981; Diefendorf & Freimuth, 2017). In C_3 plants, ribulose bisphosphate carboxylase/oxygenase (RuBisCo), a critical enzyme involved in carbon assimilation, is the primary cause of carbon isotope fractionation during photosynthesis, discriminating against the heavier and less reactive ^{13}C (O'Leary, 1981). The magnitude of a plant's carbon isotope fractionation is also influenced by surrounding environmental conditions, with the major physiological and environmental controls of $\delta^{13}C_{plant}$ summarised in Equation 5.1 (Farquhar *et al.,* 1982) and illustrated in Fig. 5.2.

$$\delta^{13}C_{plant} = \delta^{13}C_{atmos} - a - b\ (b - a)C_i/C_a$$

Equation. 5.1: Formula for calculating $\delta^{13}C_{plant}$ (‰) where: $\delta^{13}C_{atmos}$ is the isotope ratio of the ambient CO_2; C_i/C_a ratio is the intercellular leaf space CO_2 concentration against the atmospheric CO_2 concentration; *a* is the fractionation between intercellular leaf space and atmosphere (constant parameter of 4.4‰); and *b* is fractionation of CO_2 during photosynthetic carbon fixation.

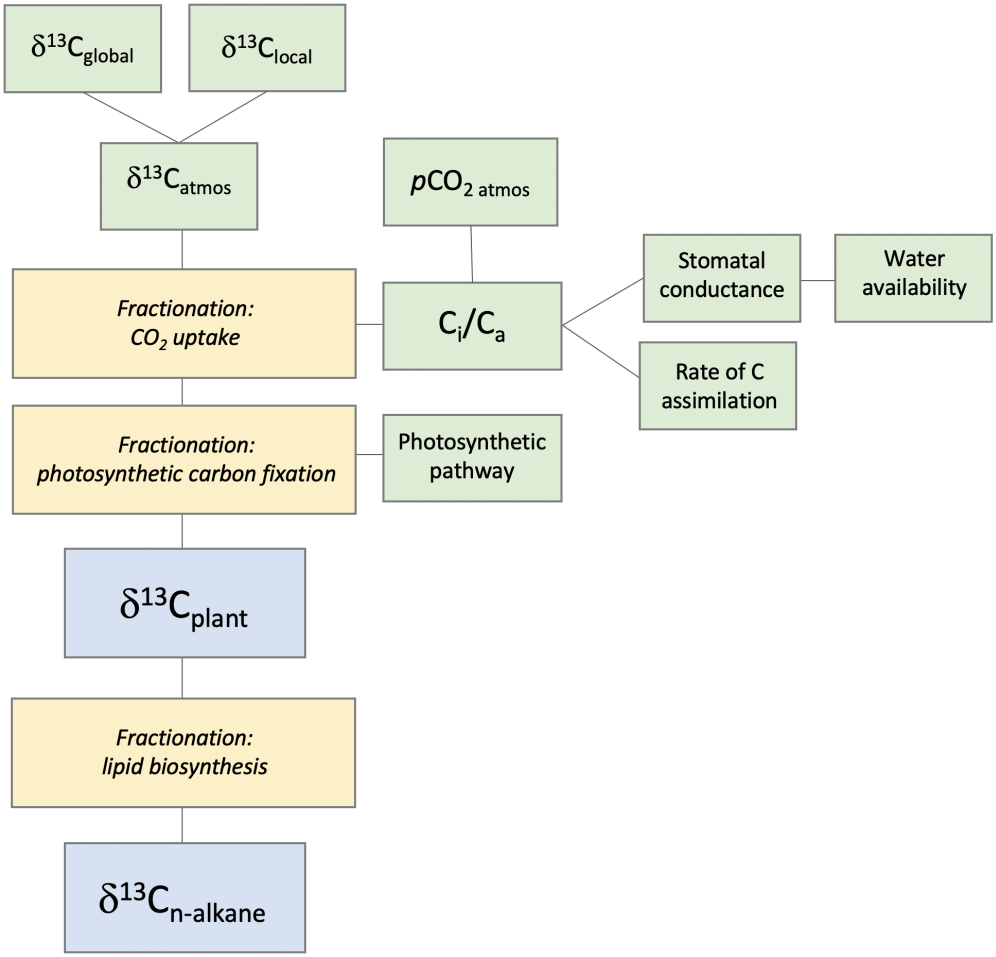

Fig. 5.2: The main controls of $\delta^{13}C_{plant}$ and $\delta^{13}C_{n\text{-alkane}}$ (‰; blue boxes). Yellow boxes show stages where carbon isotope fractionation occurs and green boxes show the environmental and physiological variables that influence this fractionation. Created using literature sources (Pancost & Boot, 2004; Freeman & Pancost, 2013).

One key environmental variable influencing $\delta^{13}C_{plant}$ is atmospheric $\delta^{13}C$ ($\delta^{13}C_{atmos}$), which is dependent on both the isotopic composition of the global atmosphere ($\delta^{13}C_{global}$) and local conditions ($\delta^{13}C_{local}$) (Farquhar *et al.,* 1982; Arens *et al.,* 2000; Pancost & Boot, 2004). While $\delta^{13}C_{global}$ can vary temporally over orbital timescales (Leuenberger *et al.,* 1992; Marino *et al.,* 1992; Eggleston *et al.,* 2016), $\delta^{13}C_{local}$ can vary spatially, depending on local biogeochemical conditions such as the canopy effect, whereby $\delta^{13}C_{local}$ is influenced by the isotopic composition of carbon respired by surrounding plants (Grinstead, 1977; Broadmeadow & Griffiths, 1993; Bush *et al.,* 2017). Another important control of $\delta^{13}C_{plant}$ is C_i/C_a; the CO_2 concentration of the leaf's

intercellular space (C_i) compared to the concentration of the atmosphere (C_a) (Farquhar *et al.,* 1982). C_i/C_a can be influenced by a number of factors. These include water availability, whereby the plant alters their stomatal conductance to ensure efficient water use (Farquhar *et al.,* 1982; Farquhar & Sharkey, 1982; Ehleringer *et al.,* 1992; Diefendorf *et al.,* 2010; Kohn *et al.,* 2010; Liu & An, 2020), atmospheric CO_2 concentration (pCO_2) which has changed over geological timescales (Popp *et al.,* 1989), and the rate of carbon assimilation in the plant (Lockheart *et al.,* 1997; Pancost & Boot, 2004). Further fractionation occurs during lipid biosynthesis. While the range of $\delta^{13}C_{plant}$ in C_3 vegetation falls between -25 and -30‰, $\delta^{13}C$ of epicuticular *n*-alkanes ($\delta^{13}C_{n\text{-alkane}}$) ranges between -30.9 and -35.9‰ (Rieley *et al.,* 1991b; Collister *et al.,* 1994; Chikaraishi *et al.,* 2004).

The physiology of a plant also influences carbon isotope fractionation. In addition to C_3 and C_4 photosynthetic pathways driving variations in $\delta^{13}C_{plant}$, studies have found $\delta^{13}C_{plant}$ and $\delta^{13}C_{n\text{-alkane}}$ to also vary between taxa groups and genera. While gymnosperms typically demonstrate higher $\delta^{13}C_{plant}$ and $\delta^{13}C_{n\text{-alkane}}$ than angiosperms (Brooks *et al.,* 1997; Chikaraishi & Naraoka, 2003; Diefendorf *et al.,* 2010; Norström *et al.,* 2017), carbon isotope fractionation also varies between trees, graminoids, forbs and shrubs (Norström *et al.,* 2017; Diefendorf & Friemuth, 2017). This indicates that in addition to a plant's photosynthetic pathway and external environmental conditions, physiological mechanisms at a taxonomic level also drive variations in carbon isotope fractionation.

Despite challenges and uncertainties, $\delta^{13}C_{plant}$ (including $\delta^{13}C$ of cuticular lipids) has been successfully applied to numerous paleoclimate studies to explore past changes in C_3 vs C_4 vegetation (ie. Huang *et al.,* 1999; 2000; Freeman & Colarusso, 2001; Maslin *et al.,* 2012a; Hoetzel *et al.,* 2013; Jiang *et al.,* 2019) and regional hydrological conditions (ie. Maslin *et al.,* 2012b; Sikes *et al.,* 2013).

5.1.4. n-Alkane signal in SHAK06-5K

An accurate quantification of biomarker production, transport, preservation, and isotopic climate signal is yet to be determined for SW Iberia. Based on existing research, however, we assume that the dominant transport method of *n*-alkanes to our marine site is from the Tagus and Sado rivers systems (Jouanneau *et al.,* 1998), sourced from vegetation and soils in the catchment basins which enter fluvial systems via both wet and dry deposition (Gagosian & Peltzer, 1986; Rogge *et al.,* 1993;

Shepherd & Wynne Griffiths, 2006). As northerly and westerly winds are dominant on the Iberian Margin (Hurrell, 1995), there is likely to be limited aeolian transport of terrestrial material from the continent (Sanchez Goñi, 1999; Naughton *et al.,* 2007). Consequently, the delivery of leaf-waxes to the marine environment on the SW Iberian Margin is likely to be primarily associated with finer sediment fractions (Eglinton *et al.,* 2002; Quenea *et al.,* 2004). Additionally, the relative resistance of *n*-alkanes to degradation in marine environments (Cranwell, 1981; Rieley *et al.,* 1991a; Wakeham *et al.,* 1997; Eglinton & Eglinton, 2008; Haggi *et al.,* 2016) is hoped to prevent bias in the preservation of different homologues and will be explored in this research.

As $\delta^{13}C_{plant}$ can be used to assess the photosynthetic pathway used by a plant (Collister *et al.,* 1994), which can then be used to distinguish C_3 and C_4 vegetation in the fossil record (Pancost & Boot, 2004; Diefendorf & Freimuth, 2017), our research will assess the dominant photosynthetic pathway of vegetation from SW Iberia over the past 28 kyr. Based on existing SW Iberian vegetation reconstructions over the last 28 kyr (van der Knaap and van Leuween; 1995; 1997; Chabaud *et al.,* 2014; Oliveira *et al.,* 2018; Gomes *et al.,* 2020), we expect our $\delta^{13}C_{n\text{-alkane}}$ signal to be within the C_3 range of -30.9 to -35.9‰, indicating the dominance of C_3 vegetation. If this is the case, after accounting for deglacial changes in $\delta^{13}C_{atmos}$, the potential climatic and/or biological drivers of $\delta^{13}C_{n\text{-alkane}}$ in this record can be explored.

5.2. Materials and Methods

All fossil *n*-alkane preparation was performed at the Biogeoscience Laboratory, ETH, Zürich. The isotope analysis was performed at the Biogeoscience Laboratory, ETH, Zürich, and the Lyell Centre, Heriot-Watt University, Edinburgh.

5.2.1. Standard preparation

To accurately measure *n*-alkane concentration of SHAK06-5K samples using gas chromatography with a flame ionisation detector (GC-FID), an external standard was first produced. By comparing the known retention time and peak area of the *n*-alkanes in the external standard with the peaks in the SHAK06-5K samples, the fossil long-chain leaf-wax *n*-alkanes (C_{25} – C_{35}) were identified and their concentration calculated.

The initial stock solution was created using three odd *n*-alkanes; two at either end of the scale for higher *n*-alkanes (C_{21} and C_{37}) and one in the range of the most abundant *n*-alkane lengths for terrestrial vegetation (C_{27}) (Eglinton & Hamilton, 1963; Pancost & Boot, 2004). A glass weighing boat measured *n*-alkane quantity to the nearest two decimal points, which was combined with solvent to produce a stock solution of ~10mg ml^{-1} (exact weights and concentrations shown in Table 5.2). The external standard was produced from the stock solution (with exact measurements shown in Table 5.2). Isooctane was chosen as the solvent for both solutions due to its low volatility which prevents both rapid evaporation and extreme concentration changes.

	***n*-Alkane**			**Stock**			**Standard**
	Compound	Catalogue no.	Lott no.	Solute (mg)	Solvent (ml)	Concentration (mg ml^{-1})	Concentration (ng μl^{-1})
C_{21}	Heneicosane	286052-1G	MKBC5373V	10.85	10	1.085	10.85
C_{27}	Heptacosane	51559-1G	BCB2936V	10.83	10	1.083	10.83
C_{37}	Heptatriacontane	51848-1G	1434205V	10.47	10	1.047	10.47

Table 5.2: *n*-Alkane weight in stock solution and resulting concentration of both the stock and standard.

A calibration curve was produced for each GC-FID used in this study (instrumentation details shown in Table 5.3). This was created by repeating standard injections at volumes of 1, 2, 4 and 5 µl, to assess the limit of quantification (below this volume, concentrations cannot be reliably detected), and limit of linearity (above this volume, a linear relationship no longer exists between the instrument response and concentration) (Armbruster & Pry, 2008). As Fig. 5.3a and b show, neither the limit of quantification nor the limit of linearity lie between this range, therefore, the standard injections for this research were set between these bounds.

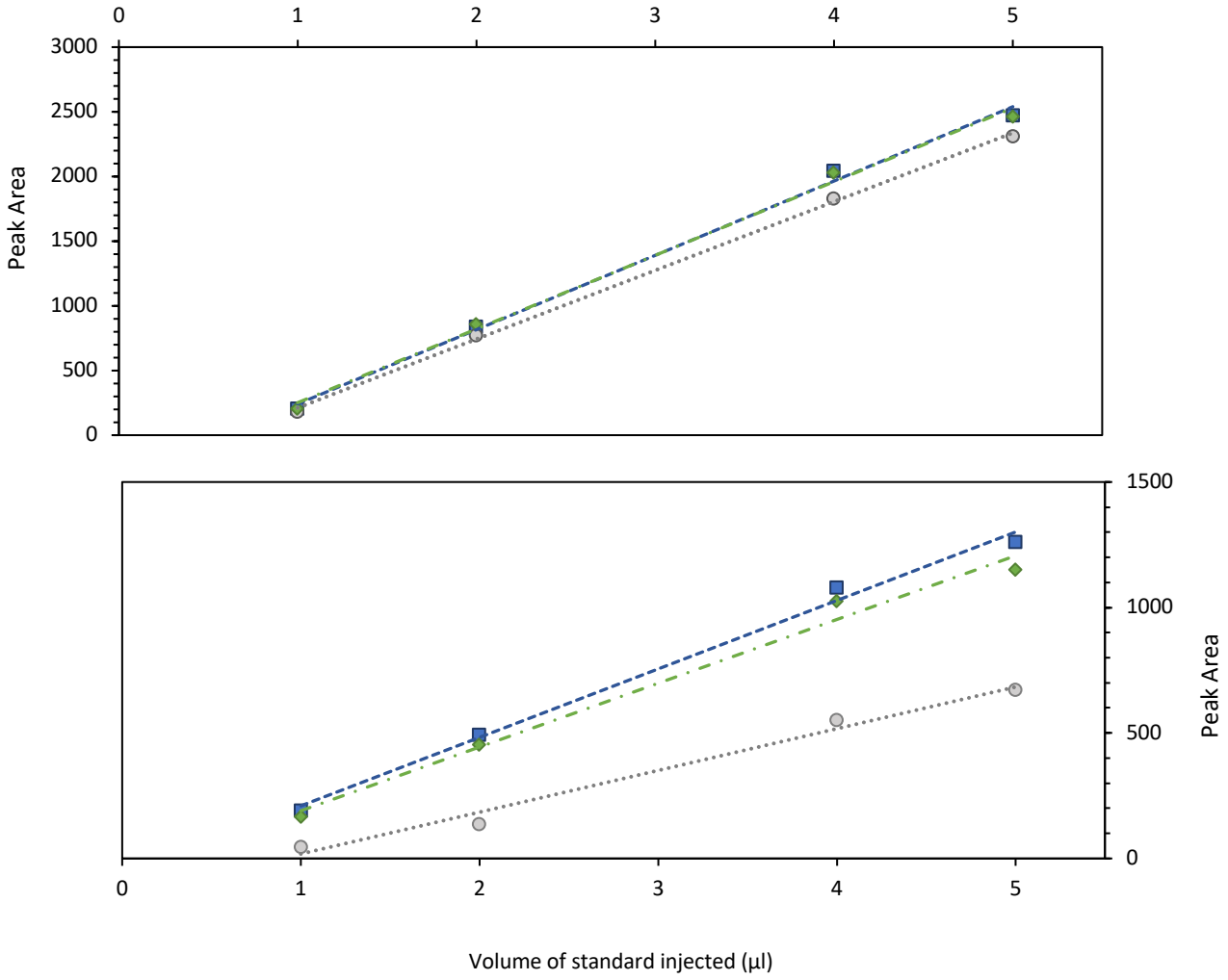

Fig. 5.3: Calibration curve showing response of peak area to changes in external standard injection volume (µl) **a.** for *n*-alkane chain length C_{21} (blue) (y = 574.55x - 333.43), C_{27} (orange) (y = 569.4x - 317.98) and C_{37} (grey) (y = 531.25x - 319.72), run on GC-FID 1; and **b.** for *n*-alkane chain lengths C_{21} (blue) (y = 272.76x - 62.98), C_{27} (orange) (y = 254.04x - 63.87) and C_{37} (grey) (y = 166.3x - 148.08), run on GC-FID 2.

5.2.2. n-Alkane preparation

To isolate the *n*-alkanes from the dry sediment of core SHAK06-5K, a three-stage procedure was used. This is explained below and illustrated in Fig. 5.4.

Stage 1. *Total Lipid Extraction:*

The inner Teflon tubes of the microwave carousel cells were cleaned with Dichloromethane:Methanol (DCM:MeOH), 9:1 which was heated in a microwave (80°C for 40 mins) to remove polar and non-polar molecules. A maximum of 20 g of dry sediment from a single depth was placed into each tube and covered with enough DCM:MeOH, 9:1 to saturate the mixture. Cells were then heated in the microwave (80°C for 50 minutes) to ensure the complete transfer of all lipids into the solvent. Once complete, the solvent was extracted into a 40 ml vial using a glass Pasteur pipette. DCM:MeOH, 9:1 was added to cover the sediment, before repeating the extraction process twice to ensure the complete removal of all lipid fractions from the sediment. The extracted solvent was blown down to ~10 ml, using a nitrogen evaporator and heat block.

Stage 2. *Saponification:*

Fatty acids (acid fraction) were isolated from the triglycerides (Metcalfe *et al.,* 1966) using saponification. KOH in MeOH 0.5M (5 ml) was added to each sample, along with three drops of milli-Q® water, then heated in 40 ml vials on a heat block (70°C) for two hours.

a. *Neutral Fraction Extraction:*

   After saponification, the neutral fraction was extracted. Milli-Q® water (5 ml) and hexane (5 ml) were added and vortex mixed to assist with the dissolution of the neutral fraction into the non-polar solvent. The solvent was transferred into a 40 ml glass vial before adding hexane (5 ml) to the original vial, vortexing, then transferring the solvent into the neutral vial. This step was repeated once more to ensure the transfer of all neutral fractions. The neutral fraction was then blown down and transferred into a 2 ml vial using hexane. The vial was cleaned twice with hexane to ensure the complete transfer of the neutral fraction.

b. *Acid Fraction Extraction:*

   Ten drops of HCl were added to the saponified solution to bring the pH to 1 (tested on litmus paper). Hexane:DCM, (4:1, 5 ml) was added and vortex mixed to transfer the acid fraction into the solvent. Using the steps outlined above, the Hexane:DCM solvent containing the acid fraction was transferred first into a 40 ml vial, then a 2 ml vial.

Stage 3. *Column Chromatography:*

Chromatography columns were set up using an iron stand to hold small glass Pasteur pipettes vertically. Combusted glass wool was inserted and compressed at the bottom of each pipette before 4 cm of silica gel dissolved in hexane was added to each column. The columns were then cleaned with hexane.

To separate the *n*-alkanes from the neutral fraction, two drops of hexane were added to the solution, dissolving the *n*-alkanes within the solvent. The hexane solution was added to the column, transferring the dissolved *n*-alkanes into the first 4 ml vial, while the other fractions remained trapped in the silica gel. The vial was cleaned twice with hexane to ensure the complete transfer of all *n*-alkanes through the column. This method was repeated using Hexane:DCM, 1:3, to transfer n-alkenones into a second 4 ml vial, and then using DCM:MeOH, 1:1 to transfer glycerol dialkyl glycerol tetraethers (GDGTs) into the final 4 ml vial.

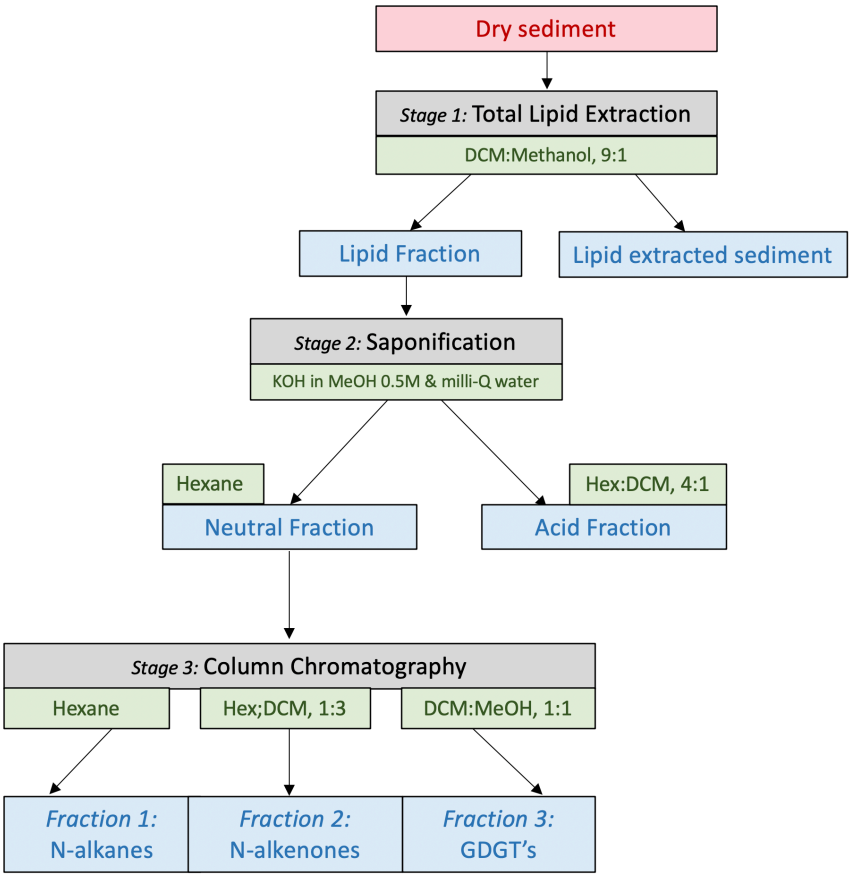

Fig. 5.4: Method for extracting *n*-alkanes from SHAK06-5K sediment. Dry sediment input (red), the three key method stages (black), the major chemicals used (green), and the fractions extracted from the sediment during the process (blue) are outlined.

5.2.2.1. Sediment quantities

Following the preparation of each sample, the *n*-alkane concentration (ng g^{-1} dry sediment) was measured. Existing solvent was blown down before adding isooctane (100 µl). One of two GC-FID's was used to quantify the *n*-alkane concentration (Table 5.3), with both instruments following the same method (50°C to 320°C at 5°C/ min). The typical sequence involved one isooctane blank and one standard injection, followed by the SHAK06-5K *n*-alkanes samples which were interposed by an isooctane blank every three/four vials. The blanks assessed the working of the instruments and traced any artificial contamination. The output of each sample was a chromatograph (example shown in Fig. 5.5) from which the peak area for odd and even long-chain homologues between C_{25} and C_{35} were calculated. The peak area was used to calculate the *n*-alkane concentration of each long-chain homologue in the dry sediment samples (ng g^{-1}) using the following equation:

$$\text{a.} \quad C_{inj} = \frac{(P_{sample} * C_{std} * J_{std})}{(P_{std} * J_{sample})}$$

$$\text{b.} \quad K_{vial} = C_{inj} * V_{solvent}$$

$$\text{c.} \quad K_{sed} = K_{vial} / W_{sed}$$

Equation. 5.2 a. Concentration of injection (C_{inj}; ng μl^{-1}) calculated using peak area of sample (P_{sample}) and standard (P_{std}), concentration of standard (C_{std}; ng μl^{-1}), and injection volume of the standard (J_{std}; µl) and sample (J_{sample}; µl); **b.** *n*-alkane quantity in vial (K_{vial}; ng) quantified with C_{inj} and the volume of solvent in the vial ($V_{solvent}$; µl); **c.** *n*-alkane quantity in dry sediment (K_{sed}; ng g^{-1}) calculated using K_{vial} and dry weight of sediment (g).

Initially, the amount of sediment used for the *n*-alkane preparation method ranged from 1.0 g to 5.3 g, with 160 samples prepared along the depth of SHAK06-5K with a mean weight of 2.3 g. When assessing the concentration of the long-chain *n*-alkanes within these samples, it became apparent that the detection limits were reached due to the low *n*-alkane concentration in the SHAK06-5K samples (Appendix 6 and 7). Consequently, larger aliquots of sediment were required to accurately measure the *n*-alkane concentrations and carbon isotope ratios. 71 large concentration samples were prepared, with weights ranging from 30.9 g to 179.9 g and a mean weight of 88.7 g (Appendix 8 and 9).

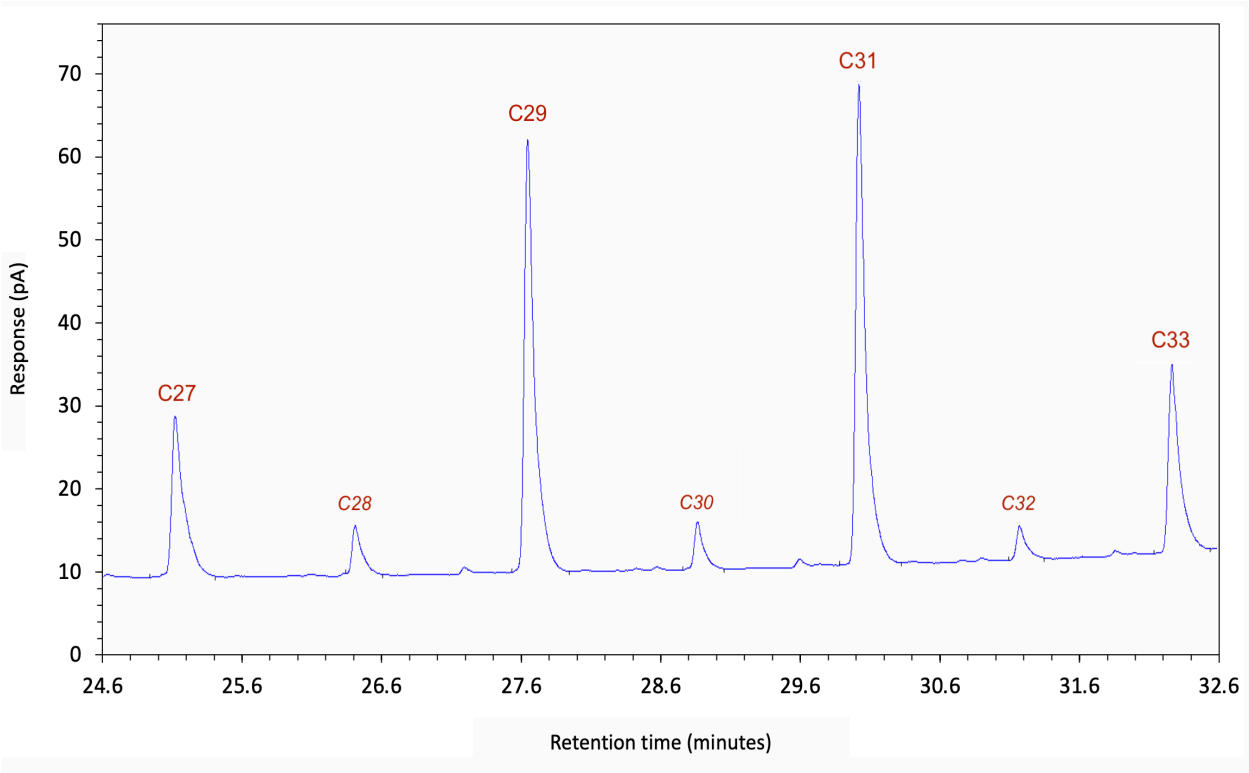

Fig. 5.5: Chromatograph illustrating the response (pA) and retention time (minutes) of long-chain *n*-alkanes from sample 270 cm from SHAK06-5K, highlighting the *n*-alkane chain-lengths.

5.2.2.2. Carbon preference index and average chain length

Using the concentration data, the CPI and ACL of each sample was calculated using Equation. 5.3a and b. CPI assesses the source of the *n*-alkanes, with a CPI greater than 1 illustrating an odd-over-even chain length dominance and a terrestrial plant source (Bray & Evans, 1961; Kennicutt *et al.,* 1987). Here, the revised CPI equation of Marzi *et al.* (1993) was used, as it prevents the unfavourable averaging previously encountered by the original CPI equation (Bray & Evans, 1961). ACL was calculated to assess changes in dominant chain length with depth. The four odd chain-lengths with the highest concentrations in the SHAK06-5K samples were inserted into the formulas of both equations: C_{27}, C_{29}, C_{31} and C_{33}. These homologues are the major constituents of terrestrial leaf-wax *n*-alkanes (Cranwell, 1973; Eglinton & Hamilton, 1963; Pancost & Boot, 2004).

a. $$\mathrm{CPI} = \frac{([C_{27}] + [C_{29}] + [C_{31}]) + ([C_{29}] + [C_{31}] + [C_{33}])}{2 * ([C_{28}] + [C_{30}] + [C_{32}])}$$

b. $$\mathrm{ACL}_{27-33} = \frac{(27[C_{27}] + 29[C_{29}] + 31[C_{31}] + 33[C_{33}])}{([C_{27}] + [C_{29}] + [C_{31}] + [C_{33}])}$$

Equation. 5.3: Formula to calculate: **a.** the carbon preference index (CPI) (Marzi *et al.,* 1993); and **b.** the average chain length (ACL) (Poynter *et al.,* 1989)

5.2.2.3. Sample cleaning

Prior to performing isotopic analysis using Gas Chromatography with isotope-ratio mass spectrometry (GC-IRMS), SHAK06-5K samples required further cleaning to completely isolate all odd long-chain *n*-alkane peaks (C_{25} – C_{35}) and prevent other compounds with similar retention times from interfering with the isotopic signal. Two cleaning methods were applied to different samples to investigate which technique showed the best *n*-alkane recovery rate: these were the zeolite and the urea methods (Fig. 5.6 and Fig. 5.7, respectively). While the zeolite technique had a 47% recovery rate (n = 53) (Appendix 10), the urea method had a lower recovery rate of 38% and was therefore applied to fewer samples (n = 11) (Appendix 11). Fig. 5.8 shows example chromatographs before and after applying the zeolite cleaning method to the sample.

Zeolite Cleaning Method

Stage 1. *Zeolite:*

A column was assembled holding glass Pasteur pipette's vertically in an iron stand. Compacted glass wool was inserted into each pipette before 100 mg of combusted zeolite was placed on top. This was flushed with hexane to clean the column before transferring the solvent containing the *n*-alkanes into the pipette. While cyclic compounds and the solvent passed through the pipette into the 4 ml vial below, long straight-chain *n*-alkanes were trapped within the zeolite. The collected solvent was then transferred back into the column twice more to ensure all straight-chain compounds were trapped within the column. The zeolite was then left to dry (~12 hours) before transferring the contents into a small Teflon vial.

Stage 2. *Hydrofluoric acid:*

HF was used to remove the zeolite from the *n*-alkane fraction. 40% aqueous HF (1 ml) was added to the Teflon tube, allowing it to react with the zeolite. After dissolution, an excess of silica gel was added to neutralise the solution.

Stage 3. *Extraction:*

Hexane was added to the Teflon tube (~2 ml) to extract the *n*-alkanes and placed in a vibrating water bath to transfer the *n*-alkanes into the solvent. The hexane was extracted into a 2 µl vial, before the solvent was blown down. This stage was repeated six times to ensure the removal of all *n*-alkanes. Finally, all samples were run on the GC-FID to assess the concentration and measure the *n*-alkane recovery rate.

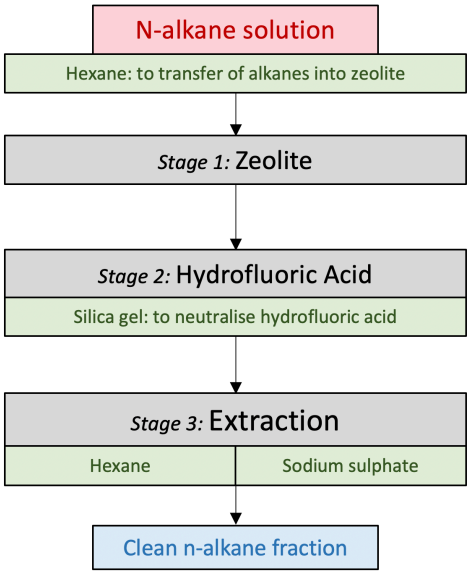

Fig. 5.6: Zeolite cleaning method, outlining the three method stages (black) and the chemicals used (green) to remove cyclic chains from the solution (red), resulting in the clean fraction of straight-chain compounds (blue).

Urea Adduction Cleaning Method

Stage 1. *Urea crystal formation:*

The urea methanol solution (300 mg urea to 300 ml MeOH) was sonicated (5 minutes) for full dissolution and added to the blown down *n*-alkane vial. This trapped straight-chain compounds within the urea crystal structures, separating the *n*-alkanes from highly branched or cyclic structures. The vial was then placed in the freezer (10 minutes) to assist with urea crystal formation.

Stage 2. *Non-adducted fraction:*

Hexane was added to the sample (1 ml), before shaking and whirl mixing the vial. The solvent containing the free highly branched and cyclic structures (non-adducted fraction) was transferred into a separate vial. Hexane was added to the original vial (1 ml) before freezing the vial (5 minutes) and washing again with hexane. This step was repeated three times to remove all non-adducted compounds.

Stage 3. *Adducted fraction:*

Finally, Milli-Q® water was added (2 ml), before shaking and whirl mixing the solution to dissolve all urea crystals. Hexane was added (2 ml) and the vial was shaken and whirl mixed to transfer all straight-chain *n*-alkanes into the non-polar solvent, before removing the hexane and dissolved *n*-alkanes (adducted fraction) into a vial. This final step was repeated three times to ensure the thorough transfer of all *n*-alkanes. Samples were run on the GC-FID to measure the concentrations and assess the recovery rate.

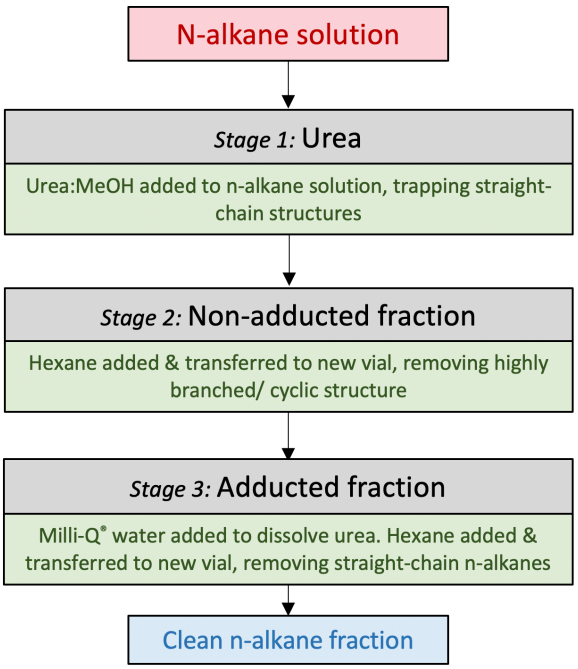

Fig. 5.7: Urea adduction cleaning method, outlining the three stages (black) and the chemicals (green) used to remove cyclic chains from the solution (red), resulting in the clean fraction (blue) of straight-chain compounds.

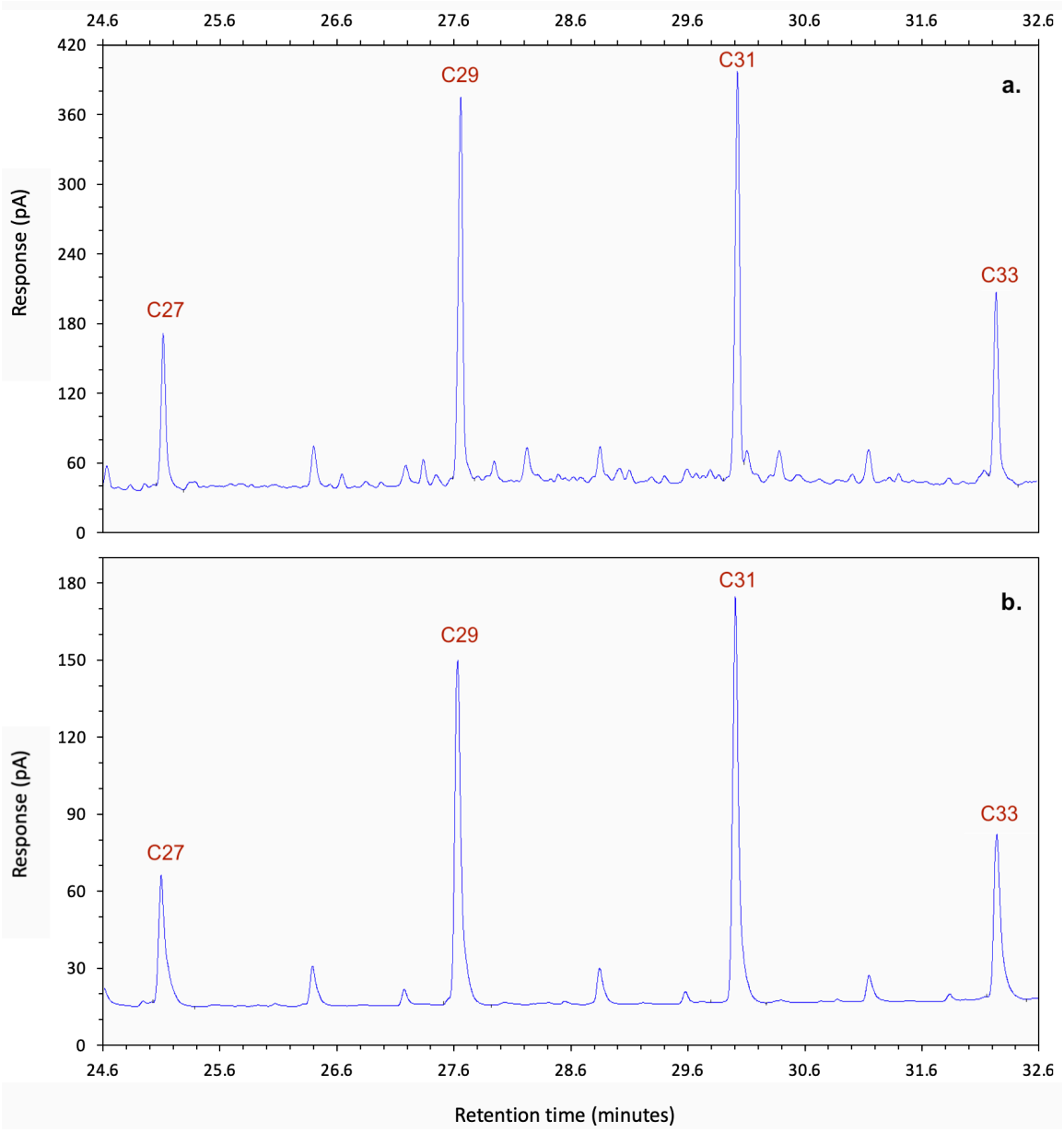

Fig. 5.8: Chromatographs illustrating the response (pA) and retention time (minutes) of long-chain *n*-alkanes from sample 300 cm from core SHAK06-5K, showing: **a.** sample prior to zeolite cleaning; **b.** sample after zeolite cleaning. *n*-Alkane chain-lengths are illustrated.

5.2.3. Biomarker Isotope Analysis

Using the *n*-alkane concentration, each sample's optimum injection volume was calculated to ensure an accurate isotope reading on the GC-IRMS. Carbon isotope analysis was performed at ETH, Zürich and Heriot-Watt University (details in Table 5.3). Measurements were made following CO_2 gas formation in a combustion reactor at 1000°C and the GC measurement method was as

follows: 45°C to 130°C at 40°C min^{-1}, then to 300°C at 6°C min^{-1} and held for 31.46 minutes. All isotopic measurements are defined relative to a reference gas. Carbon isotopes were calibrated to VPDB and values are expressed in permil (‰) units.

Once the carbon isotope composition was known for each sample (R_{sample}), it was inserted into the following formula, which required the known isotopic composition of the reference gas ($R_{standard}$) (detailed in Table 5.3). The resulting output is the stable isotope ratio of each sample (Equation. 5.4a) expressed with the delta notation (δ) (Sachse *et al.,* 2012). The weighted mean of the dominant long-chain *n*-alkane homologues (C_{27} – C_{33}) was calculated for each sample using Equation. 5.4b.

$$\textbf{a}. \quad \delta^{13}\mathrm{C} = \frac{\mathrm{R_{sample}} - \mathrm{R_{standard}}}{\mathrm{R_{standard}}}$$

$$\textbf{b}. \quad \delta^{13}\mathrm{C}_{WA} = (\delta^{13}C_{27} \times W_{27}) + (\delta^{13}C_{29} \times W_{29}) \ldots / (W_{27} + W_{29} \ldots)$$

Equation. 5.4: a. Formula to calculate stable isotope ratios (‰ VPDB); and **b.** the *n*-alkane $\delta^{13}C$ weighted mean of terrestrial long-chain *n*-alkane homologues in the sample (C_{27} – C_{33}), calculated using the $\delta^{13}C$ of each dominant *n*-alkane homologue present in the sample, and the weight (W) given to each homologue, calculated using its concentration in the sediment sample (ng g^{-1}).

In total, 65 of the 71 prepared *n*-alkane samples had sufficient *n*-alkane concentrations to measure their carbon isotope composition. Each sample was measured in duplicates or triplicates. Eight samples were removed due to potential contamination: 96, 126, 148, 156, 176, 194, 250, and 288 cm. All were measured in the same run and demonstrated extreme values and/or high standard deviation greater than 1 ‰ (± 1σ). Of the final 57 samples included in our $\delta^{13}C_{n\text{-alkane}}$ record, the measurements showed high precision, with the average standard deviation (± 1σ) of the $\delta^{13}C_{n\text{-alkane}}$ replicates as follows: 0.17‰ for C_{27}, 0.14‰ for C_{29}, 0.14‰ for C_{31}, and 0.25‰ for C_{33} (Appendix 12).

Laboratory	Name	Type	Details	Standard
Biogeoscience, ETH, Zürich	**GC-FID 1**	Agilent Technologies 7890A; GC with FID detectors	**Flow:** Hydrogen carrier gas at 5 mL/ min **Column type:** Agilent HP-5 **Column details:** 30 m length**;** 0.32 mm inside diameter; 0.25 µm film thickness	External standard: C_{21}, C_{27}, C_{37} (see Table 5.2 for details)
Biogeoscience, ETH, Zürich	**GC-FID 2**	Agilent Technologies 7890A; GC with FID detectors	**Flow:** Hydrogen carrier gas at 3 mL/ min **Column type:** Agilent VF-1ms **Column details:** 60 m length; 0.25 mm inside diameter; 0.25 µm film thickness	External standard: C_{21}, C_{27}, C_{37} (see Table 5.2 for details)
Biogeoscience, ETH, Zürich & Lyell Centre, Heriot-Watt, Edinburgh	**GC-IRMS**	GC: Thermo Trace GC Ultra IRMS: Thermo Delta V Plus	**Flow:** Helium carrier gas 1 mL/ min **Column type:** Agilent GC column VF-1MS **Column details:** 60 m length; 0.25 mm inside diameter; 0.25 µm film thickness	External standard ($\delta^{13}C$ measurements): Carbon isotope standard: A5 from the University of Indiana

Table 5.3: Details of the instrumentation and external standards used during the biomarker method.

5.3. Results and Discussion

5.3.1. n-Alkane distributions in SHAK06-5K

In the SHAK06-5K samples (n = 71), the long-chain *n*-alkanes are dominated by the odd homologues C_{27}, C_{29}, C_{31} and C_{33}. When analysing the CPI, all samples exceed a value of 1 (with a mean of 6.2) and demonstrate a strong odd-over-even chain-length dominance. The CPI, therefore, signifies that the higher molecular weight *n*-alkanes in these samples are biogenically sourced, while the dominant chain-lengths (C_{27} – C_{33}) indicate a vascular plant origin (Bray & Evans, 1961; Eglinton & Hamilton, 1963; Kennicutt *et al.,* 1987). As CPI does not decline towards the base of the core, diagenesis is not visibly increasing over time. The CPI of this record, therefore, indicates that the leaf-wax physiological/climate signal has not been exceeded by the input of degraded or petrogenic material; however, no clear pattern is seen in the variation of the CPI values, which range from 2.6 to 9.2 (Fig. 5.9a).

The total concentration of the odd long-chain *n*-alkanes (C_{27}-C_{31}) (ng g^{-1}) varies significantly throughout the core (Fig. 5.9b), ranging between ~40 and 2700 ng g^{-1}. Of these, the C_{33} homologue has the highest range in concentration (1171.40 ng g^{-1}), while the highest mean concentration is demonstrated by C_{31} (258.94 ng g^{-1}), followed closely by C_{29} (238.32 ng g^{-1}) (Table 5.4). This mirrors the pattern seen in existing fossil *n*-alkane records from the Mediterranean which show C_{29} and C_{31} to be the most abundant homologues in the sedimentary record (Norström *et al.,* 2017; Sabino *et al.,* 2020). While this could indicate bias in the preservation of the shorter C_{27} homologue, this *n*-alkane homologue is also the least abundant in modern Mediterranean plants (Schäfer et al., 2016; Norström *et al.,* 2017). This suggests that the concentrations of long-chain homologues in the sedimentary record are reflective of the source vegetation rather than significant preservation bias. The concentration of the four long-chain homologues covaries with depth (Fig. 5.9b), and all show a significant positive correlation with the other three homologues ($p < 0.05$) (Fig. 5.10). While C_{27} & C_{29}, C_{27} & C_{31} and C_{29} & C_{31} demonstrate the strongest relationships (r= 0.94, 0.90 and 0.93, respectively), C_{33} has a slightly weaker correlation with C_{27}, C_{29} and C_{31} (r= 0.79, 0.80, and 0.79, respectively).

Concentration (ng g^{-1})	C_{27}	C_{29}	C_{31}	C_{33}
Mean	126.82	238.32	258.94	180.60
Std dev (± 1σ)	77.39	143.32	148.93	170.85
Range	366.11	708.66	726.78	1171.40

Table 5.4: Total *n*-alkane concentration (ng g^{-1}) of terrestrially sourced *n*-alkane homologues from SHAK06-5K.

Throughout the core, ACL shows rapid and continuous variation with values ranging from 29.48 to 31.06, with a mean of 30.19 (Fig. 5.9c). ACL is slightly lower between 0 and 220 cm (with an exception at 38 cm), demonstrating a general decline, before increasing after 220 cm and remaining higher towards the base of the core. No significant relationship is shown between *n*-alkane ACL and vegetation records of SHAK06-5K (Fig. 5.9c-e), with a weak correlation demonstrated between ACL and arboreal taxa (r = 0.23; p = > 0.05), and ACL and non-arboreal taxa (r = -0.16; p = > 0.05). While previous research has assumed a relationship between leaf-wax ACL and the surrounding vegetation structure (woody vs herbaceous taxa), using this proxy as a signal of a region's dominant vegetation structure (e.g. Cranwell, 1973; Meyers & Ishiwatari, 1993; Schwark *et al.,* 2002; Bai *et al.,* 2009; Bliedtner *et al.,* 2018), our results suggest that ACL cannot be reliably used to distinguish the dominant vegetation structure of SW Iberia. While these results may indicate that no relationship exists between *n*-alkane ACL and the surrounding vegetation structure, another possibility is that *n*-alkane ACL in the fossil record reflects vegetation change on a different spatial/temporal scale to that of the pollen record. While present-day marine pollen from the Iberian Margin is strongly reflective of the regional vegetation from the adjacent continent (Naughton *et al.,* 2007; Morales-Molino *et al.,* 2020), the understanding of transport modes of terrestrial *n*-alkanes to SW Iberian Margin sediments is less well understood. Consequently, the *n*-alkane record could be influenced by different transport vectors and consequently demonstrate time lags or represent different plant communities. Another consideration is the contribution of pre-aged material which has been shown to influence fossil *n*-alkane records in other regions (Huang *et al.,* 1996; Eglinton *et al.,* 1997; Pearson & Eglinton, 2000; Smittenberg *et al.,* 2006; Mollenhauer & Eglinton, 2007; Kusch *et al.,* 2010; French *et al.,* 2018). This is yet to be quantified on the Iberian Margin. Until the source of *n*-alkanes in SHAK06-5K is explored further, ACL cannot reliably be used in this record to distinguish the dominant vegetation structure of this region (woody vs herbaceous taxa), despite this method having previously been applied to other locations.

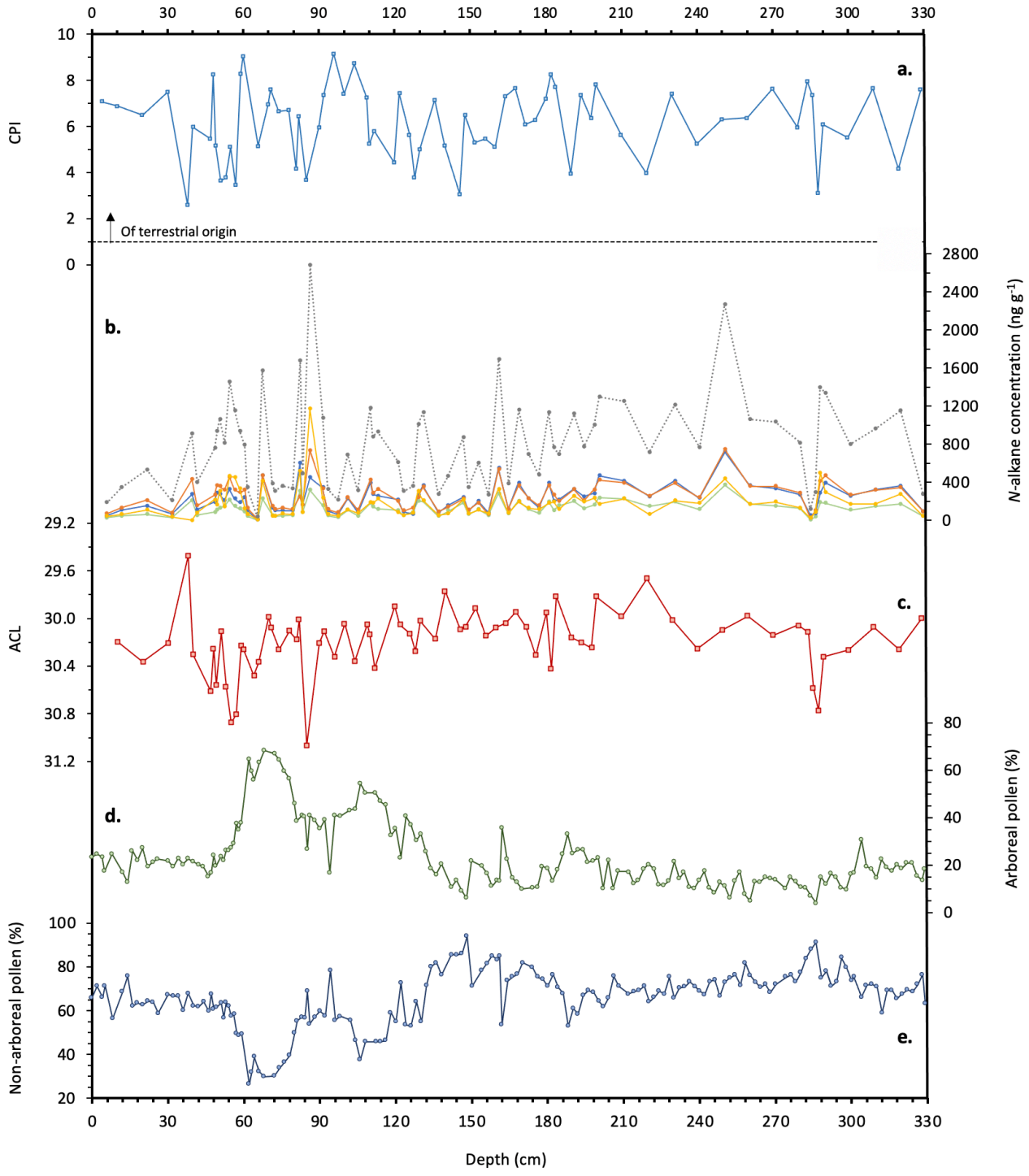

Fig. 5.9: From core SHAK06-5K, changes with depth (cm) in: **a.** carbon preference index (CPI) of long-chain *n*-alkanes - the grey dashed line shows the value above which *n*-alkanes are assumed to be of terrestrial origin (Bray & Evans, 1961; Eglinton & Hamilton, 1963; Kennicutt *et al.,* 1987); **b.** concentration of odd long-chain terrestrially sourced *n*-alkane homologues (ng g^{-1}); C_{27} (green), C_{29}

(blue), C_{31} (orange), C_{33} (yellow), and total concentration (C_{27} – C_{33}; grey dashed line); **c.** average chain-length (ACL) of odd long-chain terrestrially sourced *n*-alkanes (C_{27} – C_{33}); **d.** arboreal taxa (%); and **e.** non-arboreal taxa (%).

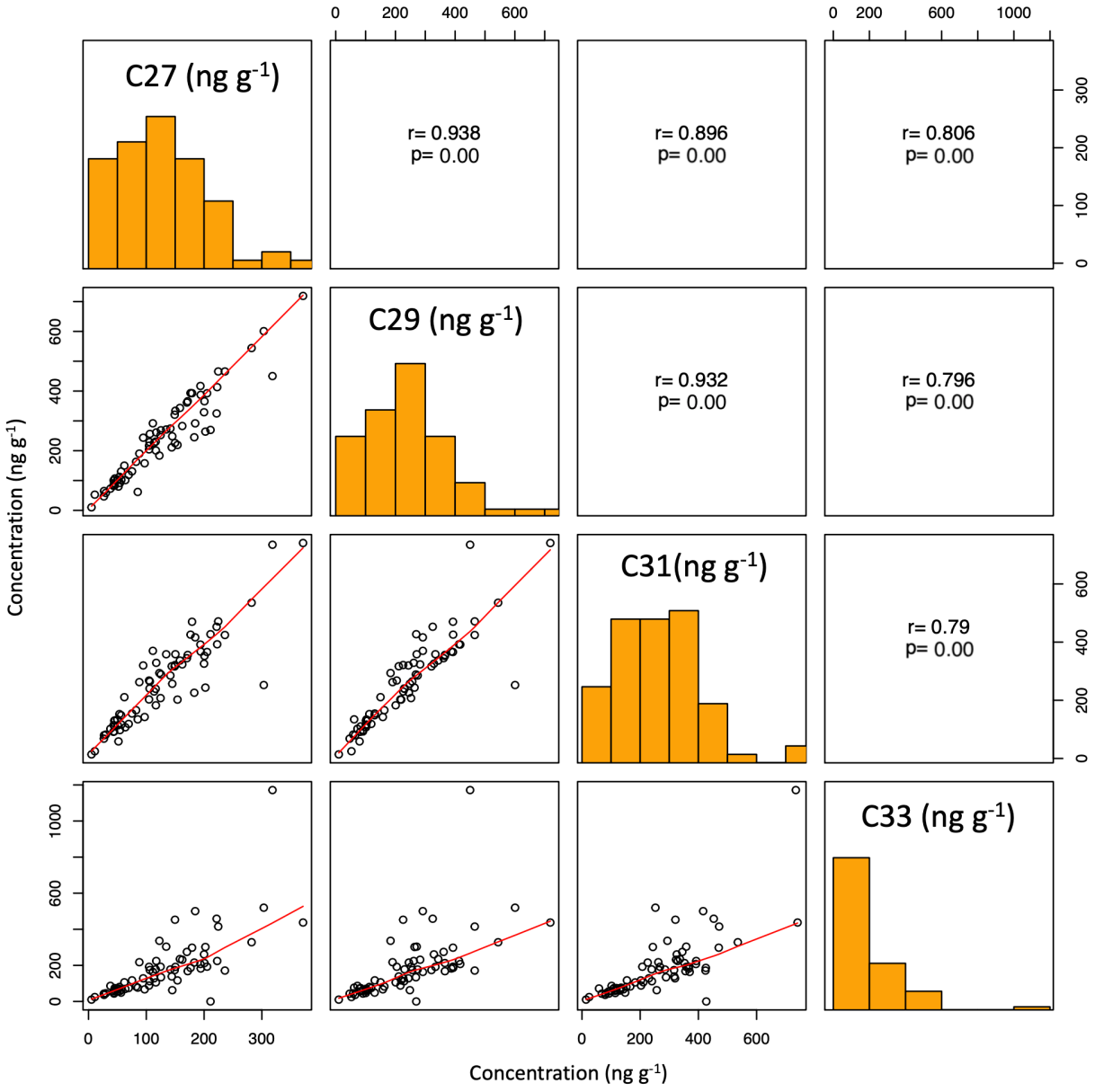

Fig. 5.10: Correlogram of homologue concentrations (ng g^{-1}) (C_{27} – C_{33}). Diagonally central squares display histograms of each homologue's concentration distribution in the core, while bottom squares show scatter plots of the datasets, including a local polynomial regression curve (red). Upper squares illustrate the correlation between the variables (r ; applying Spearman's Rank correlation), and the significance of the correlation ($p < 0.05$).

5.3.2. n-Alkane $\delta^{13}C$ in SHAK06-5K

In the $\delta^{13}C_{n\text{-alkane}}$ record (n = 57) (Fig. 5.12), $\delta^{13}C$ of the four most dominant long-chain homologues in SHAK06-5K, C_{27} - C_{33} ($\delta^{13}C_{C27} - \delta^{13}C_{C33}$), ranges between -32.9 and -29.28‰. This is within the range of the C_3 photosynthetic pathway, demonstrating the dominance of C_3 vegetation in SW Iberia over the depth of core SHAK06-5K (Rieley *et al.,* 1991b; Collister *et al.,* 1994; Chikaraishi *et al.,* 2004; Pancost & Boot, 2004). On average, C_{33} was the most depleted in ^{13}C, followed by C_{31}, and C_{29} (with mean δ $\delta^{13}C_{n\text{-alkane}}$ values of -31.85‰, -31.82‰, and -31.75‰, respectively). Because the *n*-alkane concentration of the C_{27} homologue was exceptionally low in many of the samples, an accurate reading of $\delta^{13}C$ in C_{27} was only made on 34 datapoints; despite this, the C_{27} homologue has the highest $\delta^{13}C$, averaging -30.62‰. Existing records have also shown $\delta^{13}C$ of longer chain-lengths to be more negative in sedimentary records from a number of locations (Yamada and Ishiwatari, 1999; Zhao *et al.,* 2000), including the Mediterranean region (Norström *et al.,* 2017; Schäfer *et al.,* 2018). All $\delta^{13}C_{n\text{-alkane}}$ homologue values are significantly correlated with each other (Fig. 5.11), with the strongest relationships occurring between adjacent odd homologues: $\delta^{13}C_{C27}$ and $\delta^{13}C_{C29}$ (r = 0.69), $\delta^{13}C_{C31}$ and $\delta^{13}C_{C33}$ (r = 0.68), and $\delta^{13}C_{C29}$ and $\delta^{13}C_{C31}$ (r = 0.67). The weakest relationship is between the most distant chain-lengths: $\delta^{13}C_{C27}$ and $\delta^{13}C_{C33}$ (r = 0.30), followed by $\delta^{13}C_{C29}$ and $\delta^{13}C_{C33}$ (r = 0.47) and $\delta^{13}C_{C27}$ and $\delta^{13}C_{C31}$ (r = 0.48). In SHAK06-5K, while the $\delta^{13}C_{n\text{-alkane}}$ pattern of each homologue covaries over the depth of the core (Fig. 5.12), the variability of the records increase with chain-length. While $\delta^{13}C_{C27}$ shows the smallest variability, $\delta^{13}C_{C33}$ demonstrates significant variation over the depth of the core. In the lower part of the core (329 – 168 cm), all homologues have relatively stable $\delta^{13}C$. Above ~168 cm, $\delta^{13}C_{C29}$ shifts to slightly higher but relatively stable values, while $\delta^{13}C_{C31}$ gradually increases. The $\delta^{13}C_{C33}$ record shows increased variability after ~200 cm, declining at ~198 cm and ~128 cm, before increasing after ~120cm. All homologues have higher $\delta^{13}C_{n\text{-alkane}}$ between ~74 – 55 cm, before decreasing and reaching low values at ~53 cm. Increased variability is demonstrated by all homologues towards the top of the core, but $\delta^{13}C_{n\text{-alkane}}$ remains relatively high. When assessing the weighted mean of the dominant long-chain *n*-alkane homologues (C_{27} – C_{33}) in the sedimentary record (Fig. 5.12e), $\delta^{13}C_{WA}$ values are lower at the lower part of the core, and higher after 128 cm. When comparing $\delta^{13}C_{WA}$ to the pollen records (Fig. 5.12f and g), similar overall patterns are demonstrated by all records. Lower (higher) $\delta^{13}C_{WA}$ coincides with low (high) levels of AP and high (low) NAP values, and the highest $\delta^{13}C_{WA}$ values of the record (~60 cm) coincide with the peak in AP.

While the C_{29} and C_{33} homologues are most abundant in the fossil record (Table 5.1) and have the lowest mean standard deviation of the replicate measurements (±0.13‰), the mean concentration of C_{31} is slightly higher than that of C_{29} and has slightly less noise. Consequently, $\delta^{13}C_{C31}$ will be used for comparison with the other fossil records from SHAK06-5K.

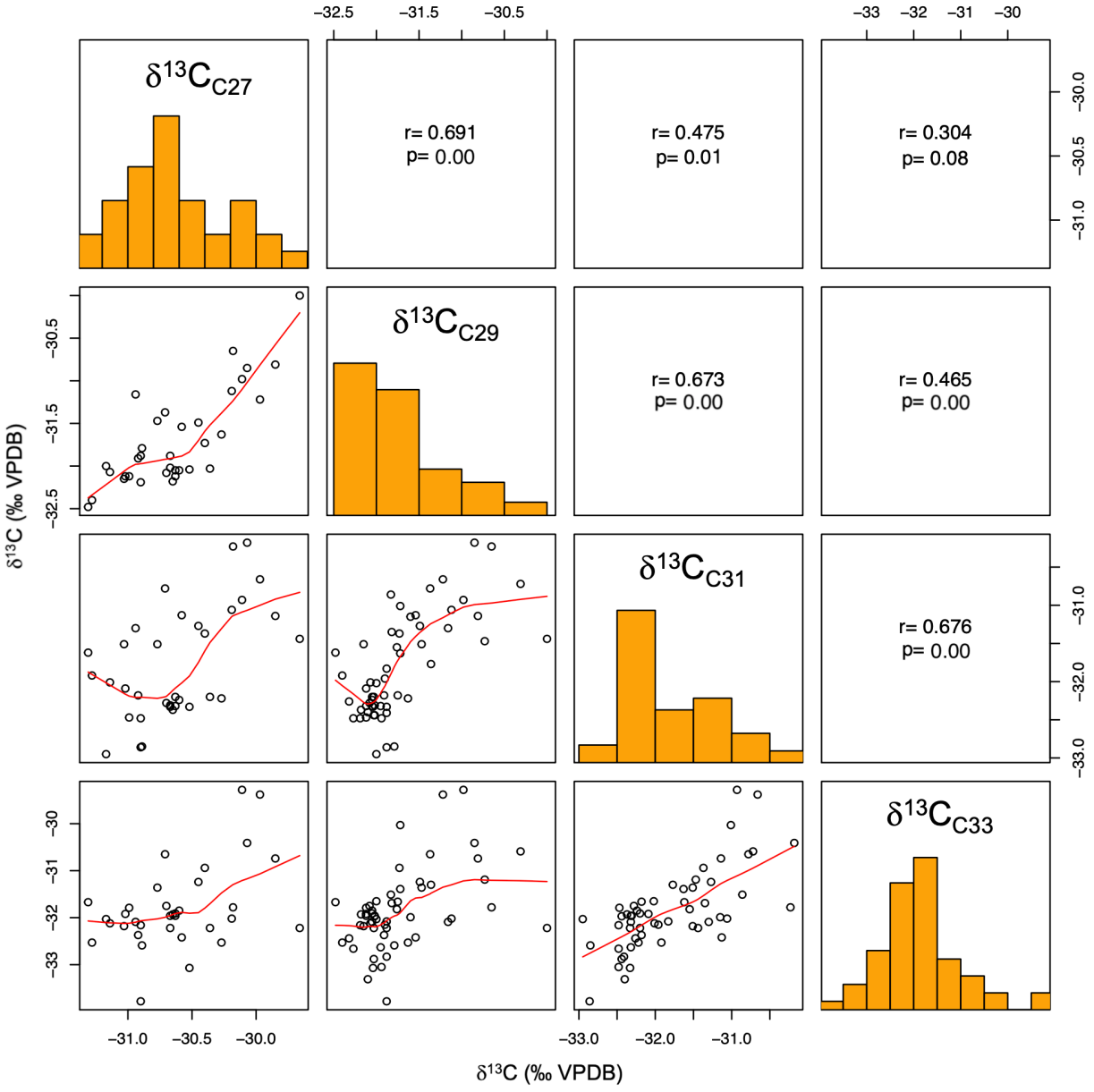

Fig. 5.11: Correlogram of $\delta^{13}C$ (‰ VPDB) of the four dominant terrestrial long-chain homologues in SHAK06-5K (C_{27} – C_{33}). Diagonally central squares display histograms of each homologue's $\delta^{13}C$ distribution in the core, while bottom squares show scatter plots of the data, including a local polynomial regression curve (red). Upper squares illustrate the correlation between the variables (r ; applying Spearman's Rank correlation), and the significance of the correlation ($p < 0.05$).

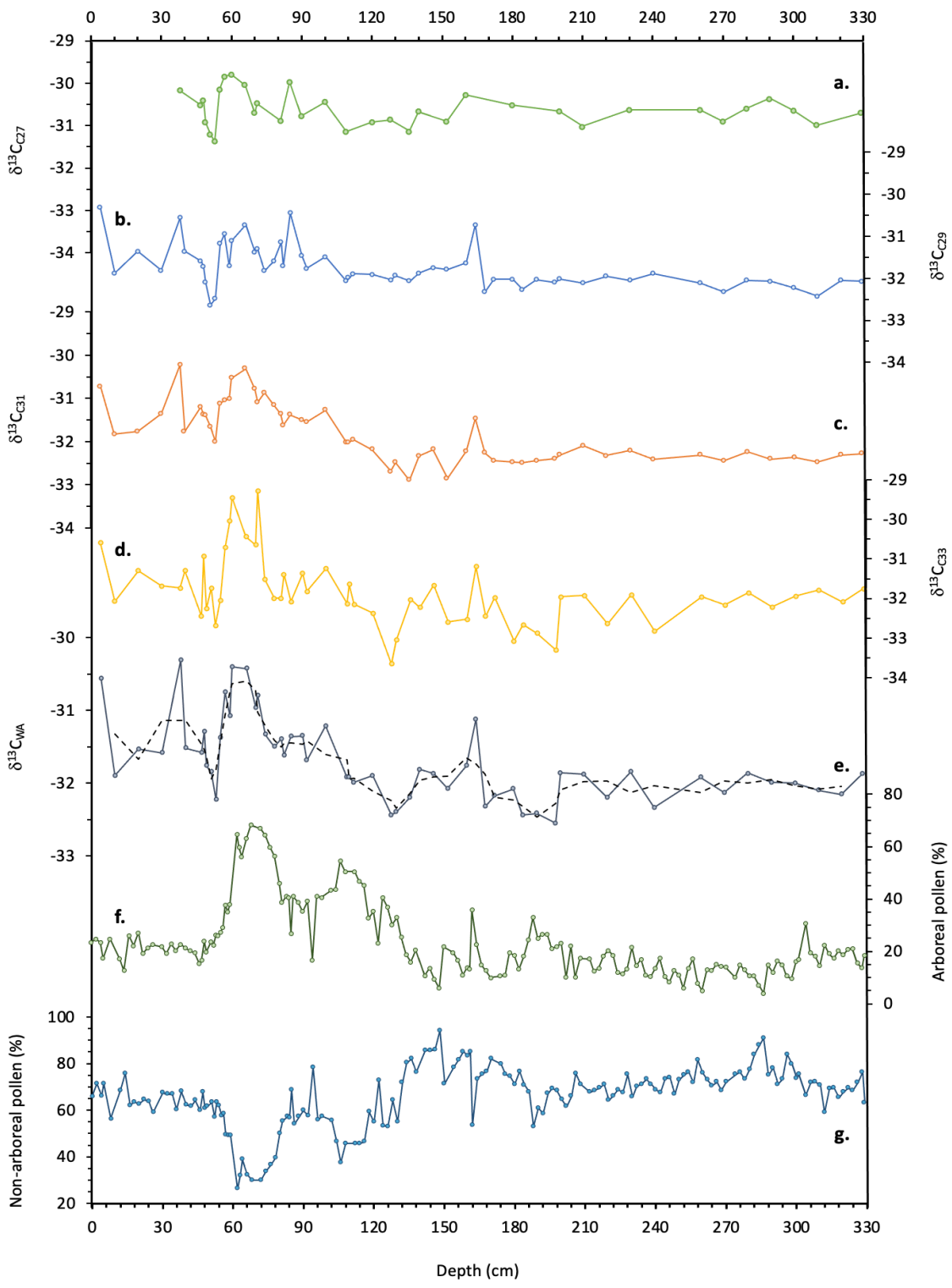

Fig. 5.12: From core SHAK06-5K, changes with depth (cm) in *n*-alkane $\delta^{13}C$ (‰ VPDB) in terrestrially sourced long-chain homologues: **a.** $\delta^{13}C$ of C_{27} ($\delta^{13}C_{C27}$); **b.** $\delta^{13}C$ of C_{29} ($\delta^{13}C_{C29}$); **c.** $\delta^{13}C$ of C_{31} ($\delta^{13}C_{C31}$); **d.** $\delta^{13}C$ of C_{33} ($\delta^{13}C_{C33}$); **e.** Weighted mean of C_{27} – C_{33} $\delta^{13}C$ ($\delta^{13}C_{WA}$) (grey line) and 3-point running mean of $\delta^{13}C_{WA}$ (black dashed line); **f.** arboreal pollen (%); and **g.** non-arboreal pollen (%).

5.3.3. Relationship between n-alkane properties in SHAK06-5K

There appears to be no significant relationships between the majority of the *n*-alkane properties in the SHAK06-5K record (Fig. 5.13). There are two exceptions: total *n*-alkane concentration and CPI demonstrate a significant but weak negative correlation (r = -0.44; $p < 0.05$), while ACL and $\delta^{13}C_{C31}$ demonstrate a significant but weak positive relationship (r = 0.34; $p < 0.05$). ACL and $\delta^{13}C_{C29}$, however, do not demonstrate a significant relationship, despite a relatively strong positive relationship between $\delta^{13}C_{31}$ and $\delta^{13}C_{C29}$. This suggests that different properties of *n*-alkanes in the fossil record (ACL, $\delta^{13}C$, CPI and total concentration) may have different climatic/biological controls, despite the source of these lipids being SW Iberian terrestrial vegetation.

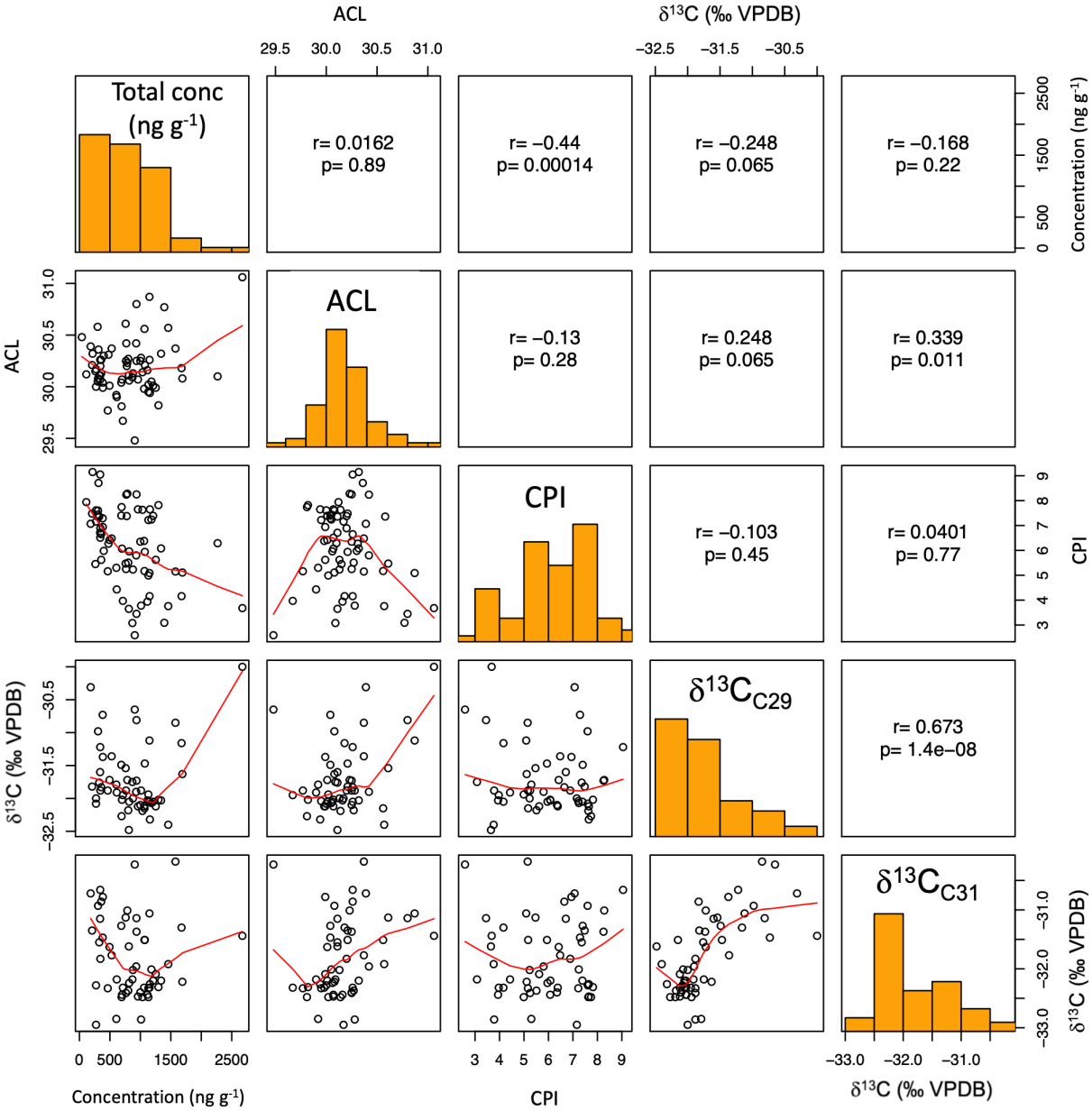

Fig. 5.13: Correlogram of the different *n*-alkane properties, including total *n*-alkane concentration (ng g^{-1}), ACL, CPI, and $\delta^{13}C$ of C_{29} and C_{31} homologues ($\delta^{13}C_{C29}$ and $\delta^{13}C_{C31}$) (‰ VPDB). Diagonally central squares display histograms of each variable's distribution in the core, while bottom squares show scatter plots of the datasets, including a local polynomial regression curve (red). Upper squares illustrate the correlation between the variables (r ; applying Spearman's Rank correlation), and the significance of the correlation ($p < 0.05$).

5.4. Conclusions

- The strong odd over even chain-length dominance in long-chain *n*-alkanes throughout the SHAK06-5K record, with CPI values > 1, demonstrates that the core's fossil *n*-alkane record is not significantly impacted by diagenesis or petrogenic input.
- The *n*-alkane ACL record from SHAK06-5K demonstrates no correlation with the AP/NAP pollen records from the same core. While this may show that no relationship exists between *n*-alkane ACL and the regional vegetation structure, it could indicate that *n*-alkane ACL reflects vegetation change on a different spatial/temporal scale to the pollen record, or it may reflect different plant types, or vegetation sources.
- The abundance and $\delta^{13}C_{n\text{-alkane}}$ of long-chain odd *n*-alkane homologues (C_{27}-C_{33}) in SHAK06-5K samples covary over the depth of the core. C_{29} and C_{31} are the most abundant chain-lengths in the fossil record, while $\delta^{13}C_{n\text{-alkane}}$ demonstrates more negative values with increasing chain-length.
- In SHAK06-5K, $\delta^{13}C$ values are more negative in the lower part of the core, while in the upper part of the core (after 128 cm), values are higher. The SHAK06-5K $\delta^{13}C$ record demonstrates a similar long-term pattern to the AP record in the same core, with higher (lower) $\delta^{13}C$ corresponding with higher (lower) AP values. By applying a high-resolution age model to these records (presented in Chapter 6), and using a modern leaf-wax *n*-alkane record from SW Iberia to better understand the fossil *n*-alkane signal, the palaeoclimatic interpretation of these records will be explored in Chapters 7 and 8.
- No long-term trends are shown in the *n*-alkane ACL, CPI, or concentration records from SHAK06-5K. Additionally, no strong relationship is shown between any of the *n*-alkane properties (ACL, CPI, concentration, and $\delta^{13}C_{n\text{-alkane}}$), indicating that these variables in SW Iberian vegetation may be influenced by different biological/environmental controls.

6.1. Introduction

Palaeoclimatic inferences and comparison between archives rely on an accurate chronostratigraphical and, ideally, absolute chronological framework. Radiocarbon (^{14}C) dating has been undertaken on both the SHAK06-5K and MD01-2444 cores to provide two independently dated records. This chapter will outline a new master chronology, created using the published ^{14}C dates of SHAK06-5K (Ausin *et al.,* 2019a; 0 – 329 cm; n = 40) and 7 new ^{14}C dates from MD01-2444 (121 – 223 cm). The method for the alignment of these records will also be outlined. The principles and limitations of ^{14}C dating in marine environments will briefly be discussed before outlining the methods used to create the master chronology, which will then be presented and discussed.

6.1.1. Principles of ^{14}C dating in marine environments

Since the discovery of ^{14}C dating (Libby *et al.,* 1949) this technique has been widely applied to palaeoclimatic research. First performed in 1977, the Accelerator Mass Spectrometry (AMS) method quantifies the number of carbon atoms present and calculates the number of ^{14}C isotopes relative to their stable carbon isotope counterparts (^{12}C and ^{13}C) (Gove *et al.,* 1992; Jull *et al.,* 2013). Since then, AMS has become the most widely used ^{14}C dating technique; benefitting from the method's rapid counting time, high sensitivity, and ability to measure sub-milligram samples (Gove *et al.,* 1992; Tuniz *et al.,* 1998; Jull *et al.,* 2013).

In marine environments, fossil planktonic foraminifera are an invaluable dating tool, widely used to construct marine chronostratigraphic frameworks dating back to 50 ka by determining the ^{14}C ages of their fossilised calcium carbonate shells. Planktonic foraminifera ages are also used in comparison with those of benthic foraminifera to infer variations in water mass ages, the strength of ocean ventilation (Broecker *et al.,* 1984, 2004; Adkins & Boyle, 1997; Sikes *et al.,* 2000; Skinner *et al.,* 2010) and changes in ocean circulation (Ingram & Kennett, 1995; Robinson *et al.,* 2005). There are, however, significant drawbacks to ^{14}C dating in marine environments. Low sedimentation rate, bioturbation, diagenetic alteration, downslope remobilisation, winnowing, calcite dissolution, and variable reservoir ages can produce ^{14}C age offsets amongst co-occurring proxies of the same depth (Mekik, 2014).

6.1.2. Calibration of ^{14}C records

Unlike its naturally occurring stable counterparts, radioactive carbon (^{14}C) emits beta particles as a result of its nucleus imbalance (6 protons and 8 neutrons). This causes ^{14}C to decay to nitrogen-14 with a half-life of 5,730 years (Godwin, 1962). ^{14}C is naturally produced in the upper troposphere and stratosphere by galactic cosmic rays (GCR) entering the atmosphere (Montgomery & Montgomery, 1939; Libby, 1946). As GCRs are modulated by the strength of solar winds and variations in the magnetic field of the Sun and Earth, these variables influence ^{14}C production (Elsasser *et al.,* 1956; Stuiver, 1961; Stuiver & Quay, 1980; Castagnoli & Lal, 1980; Voelker *et al.,* 2000). In addition, the proportion of atmospheric ^{14}C fluctuates with changes in the global carbon cycle as its distribution between reservoirs changes (Damon *et al.,* 1978; Stuiver & Braziunas, 1993; Edwards *et al.,* 1993; Stocker & Wright, 1996; Hughen *et al.,* 2000; Beck *et al.,* 2001).

Over time, centennial and millennial-scale variations in ^{14}C production and the global carbon cycle have altered the proportion of ^{14}C in the atmosphere relative to its stable carbon counterparts (Damon *et al.,* 1978; Reimer *et al.,* 2020). As a result, the conventional ^{14}C age of a sample must be calibrated using true calendar ages provided by independent measurements. A wealth of records are used to produce this calibration. Continuous and overlapping tree rings are the primary method for calibration of the Holocene (Stuiver, 1982; Stuiver *et al.,* 1998; Friedrich *et al.,* 2004; Hogg *et al.,* 2016; Capano *et al.,* 2020), while a range of longer records go beyond this, spanning the last 60 ka. These records include: paired ^{14}C and uranium/thorium (U/Th) on corals (Bard *et al.,* 1990; Edwards *et al.,* 1993; Bard *et al.,* 1998; Fairbanks *et al.,* 2005) and stalagmites (Beck *et al.,* 2001; Hoffmann *et al.,* 2010; Southon *et al.,* 2012); lacustrine records using ^{14}C dating of macrofossils and lake varves (Goslar et al. 1995; 2000; Bjorck *et al.,* 1996; Kitagawa & Van Der Plicht, 1997); cosmogenic chlorine-36 (^{36}Cl) and beryllium-10 (^{10}Be) in ice cores (Wagner *et al.,* 2000; Muscheler *et al.,* 2000; 2005) and marine sediments (Frank *et al.,* 1997); and foraminifera ^{14}C ages cross calibrated with ice core (Voelker *et al.,* 2000; Hughen *et al.,* 2004) and speleothem records (Hughen *et al.,* 2006; Bard *et al.,* 2013; Hughen & Heaton, 2020). At present, the most up to date internationally agreed calibration curve for Northern Hemispheric records is provided by IntCAL20 (Reimer *et al.,* 2020), while for Southern Hemispheric and marine records, SHCal20 and Marine 20 are available, respectively (Hogg *et al.,* 2020; Heaton *et al.,* 2020a).

Analysis of changes in atmospheric ^{14}C ($\Delta^{14}C$) over the Last Glacial and last deglaciation show abrupt centennial and millennial-scale shifts, superimposed onto a long-term trend of declining

atmospheric ^{14}C (Bard *et al.,* 1998; Beck *et al.,* 2001; Reimer *et al.,* 2020). Between 13 – 12 ka (corresponding with the YD period) there was a substantial and rapid excursion of ^{14}C into the atmosphere (Edwards *et al.,* 1993; Goslar *et al.,* 1995; Capano *et al.,* 2020), while annual records have highlighted numerous rapid shifts during the Holocene, including ^{14}C excursions between 774 – 775 AD, 993 – 994 AD and ~660 BC (Miyake *et al.,* 2012; 2013; Büntgen *et al.,* 2018; O'Hare *et al.,* 2019).

Despite decades of significant advances in ^{14}C calibration, errors arise from climatological/biological characteristics of individual datasets, laboratory methods and statistical integration of records (Reimer *et al.,* 2020). Beyond the tree-ring record (before 13.9 ka), there are substantially fewer high-precision data available, resulting in less precise calibration of records earlier than the YD (Reimer *et al.,* 2020). The most recent calibration curve, however, uses a greater quantity of records, a higher precision of AMS dating, and a Bayesian spline approach to statistically integrate records beyond 13.9 ka (Reimer *et al.,* 2020; Heaton *et al.,* 2020b).

6.1.3. Marine reservoir age offsets

Conventional ^{14}C ages (and therefore calibration curves such as IntCal20) do not account for ^{14}C age offsets that occur between different carbon reservoirs. Understanding the reservoir age offset between the atmosphere and surface ocean (R-age) is essential when creating an accurate chronology using fossils of the surface ocean dwelling planktonic foraminifera, *G. bulloides*, as the surface ocean is continuously exchanging carbon with the atmosphere and deep waters below. Consequently, a marine calibration curve that is corrected for R-age is applied to marine samples, with Marine20 being the most recently published curve (Heaton *et al.,* 2020a).

Although today the average R-age is ~400 years, there is significant spatiotemporal variation that must be acknowledged when applying a marine correction (Heaton *et al.,* 2020a). While the globally averaged R-age of the Holocene is ~500 years (Heaton *et al.,* 2020a), the changing strength of the AMOC during the deglaciation altered the ventilation rate and consequently the offset between the atmosphere and the surface and deep ocean (Skinner & Shackleton, 2004; Barker *et al.,* 2010; Thornalley *et al.,* 2011; 2015; Skinner *et al.,* 2010; 2014; 2015a; Sikes *et al.,* 2016). It is widely accepted that North Atlantic surface and deep-ocean reservoir ages were magnified during the cold LGM, HS1 and YD, and reduced during the warm BA and Holocene (Waelbroeck *et al.,* 2001; Thornalley *et al.,* 2011; Skinner *et al.,* 2014).

Unlike earlier calibration curves which have applied a static reservoir correction beyond the Holocene (Reimer *et al.,* 2013), Marine20 acknowledges and accounts for the globally averaged temporal variation in R-age beyond 11.7 ka, caused by changes in the AMOC which have long been documented (Skinner & Shackleton, 2004; Barker *et al.,* 2010; Thornalley *et al.,* 2011; 2015; Skinner *et al.,* 2010; 2014; 2015a; Sikes *et al.,* 2016), but not previously quantified in the calibration curve. The R-age correction in Marine20 is a 'global-average' of the non-polar ocean located between 40°S and 50°N in the Atlantic Ocean. It is produced using 500 simulations created by a box model of the global isotopic carbon cycle (BICYCLE model), incorporating terrestrial, oceanic and atmospheric modules. An external specification of atmospheric CO_2 and ^{14}C are used, obtained from ice core reconstructions and the IntCal20 curve, respectively. The propagated uncertainty is quantified using a Monte Carlo approach. The Marine20 calibration curve shows a large R-age between 15 – 28 ka (750-1000 years), a significant decline between 14 – 15 ka (~400 years) and a rise between 12 – 13 ka (~750 years).

In addition to this temporal variability over the last deglaciation, there are local/regional deviations in the surface reservoir age (ΔR) that must be acknowledged (Stuiver *et al.,* 1986). While regional upwelling of ^{14}C depleted deep-ocean water (Stuiver *et al.,* 1986; Bard, 1988; Toggweiler *et al.,* 1991; Southon *et al.,* 2002; Monges Soares *et al.,* 2016) can cause spatial variations in R-age, during cold events, high-latitude R-ages were of greater amplitude than those of mid-latitude areas (Bard, 1988; Sikes & Guilderson, 2016; Skinner *et al.,* 2019). It has been acknowledged that circulation changes over the Last Glacial and subsequent deglaciation led to local R-age variations over this period (Waelbroeck *et al.,* 2001; Stern and Lisiecki, 2013; Skinner *et al.,* 2015b; Freeman *et al.,* 2016; Skinner *et al.,* 2019) with suppressed upwelling on the Iberian Margin during abrupt cold events (Voelker *et al.,* 2009; Ausin *et al.,* 2020). The synchroneity of temperature changes recorded in Greenland $\delta^{18}O_{ice}$ with planktonic foraminifera $\delta^{18}O$ from Iberian Margin cores (Shackleton *et al.,* 2004; Skinner & Shackleton, 2005) has allowed Iberian Margin R-ages over the Last Glacial and subsequent deglaciation to be estimated by integrating the stratigraphy of marine records using the absolute age constraints of Greenland ice core records (Martrat *et al.,* 2007; Skinner *et al.,* 2008). There are suggestions that during HS1 and HS2, Iberian Margin R-ages exceeded 1000 years (Skinner *et al.,* 2015b; Freeman *et al.,* 2016; Skinner *et al.,* 2019), however, an accurate quantification of this region's spatiotemporal variability in R-ages over the Last Glacial and subsequent deglacial is yet to be determined (Skinner *et al.,* 2019).

6.2. Materials and Methods

AMS ^{14}C ages of monospecific samples of the planktonic foraminifera *G. bulloides* were measured from cores SHAK06-5K (n = 40) and MD01-2444 (n = 7) to create a master chronology on the SHAK06-5K depth scale. Existing Iberian Margin records have used *G. bulloides* AMS ^{14}C ages to produce reliable age models for this region (Bard et al., 2004; Chabaud et al., 2014; Oliveira et al., 2018). While the 40 AMS ^{14}C measurements from core SHAK06-5K have previously been published in Ausin *et al.* (2019a), for this research, seven new AMS ^{14}C dates have been measured from core MD01-2444. The two cores were aligned using an automated stratigraphical alignment method. The alignment served to transfer the MD01-2444 dates onto the SHAK06-5K stratigraphy in order to create a combined 'Master' Bayesian age model.

6.2.1. Radiometric dating

While a similar preparation approach was taken to isolate *G. bulloides* specimens from samples in SHAK06-5K and MD01-2444, preparation of the former was conducted at ETH Zürich and is outlined in Ausin *et al.* (2019a), while the latter took place at the UCL Department of Geography. 10 regularly spaced samples were taken from MD01-2444, with ~15 g of wet sediment weighed for each depth. This was then diluted with deionised water and disaggregated using a centrifuge tube rotator on a slow speed (to avoid shell breakage) for ~2 hours. Using 300 – 250 μm sieves and a high-pressure deionised water stream, the solution was wet sieved, washed, and left to dry overnight in a 60°C oven. From this fraction ~200 well preserved *G. bulloides* specimens were picked.

The AMS ^{14}C measurements ($^{14}C/^{12}C$) for both the SHAK06-5K and MD01-2444 samples were determined using a Mini Carbon Dating System (MICADAS) with a gaseous ion source (Synal *et al.,* 2007; Wacker *et al.,* 2013), at the ETH Zürich Laboratory of Ion Beam Physics. Firstly, atmospheric CO_2 was removed from the septa sealed glass vial (4.5 ml exetainer vials from Labco Ltd, UK) containing the sample, using a 60 ml min^{-1} He flow for 10 minutes. Surface contaminants were then leached (referred hereafter as the leachate) from the foraminifera using 100 μl of ultrapure HCl (0.02 M) inserted by an automated syringe. The CO_2 released from the leachate was transported to a zeolite trap using helium and subsequently transferred to the ion source for ^{14}C measurement. This step removes any possible contamination from secondary calcite or exogenous carbon

introduced during sample collection/preparation (Wacker *et al.,* 2013). After measuring the leachate, the remaining sample (referred to as the main fraction) was acidified using 100 µl ultrapure phosphoric acid (H_3PO_4; 85%) and heated (75°C) for 1 hour. The CO_2 released from the main fraction was then transferred into the zeolite trap, injected into the ion source, and again, measured for ^{14}C for at least 15 minutes on two gas targets.

IAEA standards C1 and C2 were used; the former as a blank and the latter as an internal standard. For fractionation correction and normalization, Oxalic acid II NIST SRM 4990 standard was used. The measured $^{14}C/^{12}C$ ratios are corrected and reported as fraction modern ($F^{14}C$) according to Stuiver & Polach (1977) and Reimer *et al.* (2004). The measurement precision is better than 5‰ for modern samples, with the data processing conducted using BATs Software (Wacker *et al.,* 2010). ^{14}C values and errors were not rounded in order to prevent propagated errors and artificial offsets; although they have been rounded in the following section (6.3) to follow convention.

6.2.2. Alignment of the SHAK06-5K and MD01-2444 records

The stratigraphical alignment of the cores was modelled using an automated algorithm based on Bayesian Markov-chain Monte Carlo (MCMC) inversion using the mathematical formulation of Muschitiello *et al.* (2020) which has been successfully applied to a variety of palaeoclimate records (Muschitiello *et al.,* 2015; 2019; Wohlfarth *et al.,* 2018; Sessford *et al.,* 2019; West *et al.,* 2019). A robust multi-parameter alignment was performed that simultaneously correlated the input and target stratigraphies using two independent proxy signals, applying XRF calcium/titanium (Ca/Ti) and ^{14}C records from core MD01-2444 (Hodell *et al.,* 2013a) as inputs and their counterpart records from core SHAK06-5K (Ausin et al., 2020) as targets. The data from both records were pre-normalised between -1 and 1 and the algorithm was run for 10^6 iterations after discarding the initial 10^5 MCMC samples ("burn-in"). The median of the MCMC alignment sample was used to infer the posterior optimal correlation between MD01-2444 and SHAK06-5K, while its variability was used to estimate the posterior uncertainty of the synchronisation of the records. This algorithm is grounded on the assumption that variations in the Ca/Ti records and *G. bulloides* AMS ^{14}C ages were near synchronous at both sites at the resolution of our records. This removes the subjective nature of visual alignment, providing a reproducible and continuous alignment that accounts for potential uneven compaction/expansion in the sediment cores.

6.2.3. Age-depth model

In SHAK06-5K, planktonic foraminiferal ^{14}C ages continuously increase downcore. This is generally the case in MD01-2444, although one ^{14}C age was rejected (151 cm) as reflecting older material (see next section). The automated stratigraphical alignment also highlighted two further ^{14}C age reversals, which were removed from the age model. This decision is explained in more detail in section 6.3.

Seven new ^{14}C dates MD01-2444 transferred onto the SHAK06-5K stratigraphy and 40 ^{14}C dates from SHAK06-5K were used in the production of the master age model. A Bayesian depositional age-depth model (*P_sequence*) was created using the calibration package Oxcal 4.4 (Bronk Ramsey, 2009). As previously discussed, planktonic foraminifera ^{14}C ages must be corrected to account for the R-age. With a range of R-age correction methods available, three different corrections were applied to the calibration of our ^{14}C dates to assess the alignment of our SHAK06-5K records with the resulting age models. These were: i) the Marine13 calibration curve which uses a static R-age correction beyond the Holocene (Reimer *et al.,* 2013); ii) the Marine20 calibration curve which uses a temporally variable R-age beyond the Holocene (Heaton *et al.,* 2020a); and iii) the Marine20 calibration curve with an added temporally variable ΔR correction for the YD and HS1 to bring these stadials into sync with the corresponding stadials in the Greenland Ice Core Chronology 2005 (GICC05) (Rasmussen *et al.,* 2014). The suitability of the resulting age models was assessed by comparing the calendar ages of the abrupt cold to warm transitions in our records (the YD into the Holocene; HS1 into the BA; and HS2 into the LGM) with those of the North Greenland ice core project (NGRIP) $\delta^{18}O$ record (Greenland Stadial (GS)-1 into the Holocene; GS-2.1a to Greenland Interstadial (GI)-1e; GS-3 to GI-2.2), established by the Greenland Ice Core Chronology 2005 (GICC05) (Vinther *et al.,* 2006; Andersen *et al.,* 2006; Svensson *et al.,* 2006; Rasmussen *et al.,* 2006; 2014). The timing of these abrupt transitions has previously been demarcated in core SHAK06-5K by Ausin et al. (2019a; 2019b) using SST and $\delta^{18}O_{\textit{G. bulloides}}$ records; these timings will be followed here.

The application of the Marine13 calibration curve to our age model results in an asynchrony of the timing of the cold to warm abrupt events (Table 6.1), with these periods in the SHAK06-5K records leading those of the NGRIP $\delta^{18}O$ record (Fig. 6.1). This offset is ~600 years for the end of the YD, and ~900 and ~500 years for the end of HS1 and HS2, respectively. With the exception of the end of HS2, this offset falls outside of the combined estimated uncertainty of the Marine13 calibrated master age model and the GICC05 timescale (± 2σ; Table 6.2).

Transition on the GICC05 timescale	Age on GICC05 timescale (cal ka BP)	Cold to warm transition	Age using Marine13 age model (cal ka BP)	Age using Marine20 age model (cal ka BP)	Age using Marine20 calibration curve with variable ΔR (cal ka BP)
GS-1 to the Holocene	11.7	End of YD	12.3	12	11.7
GS-2.1a to GS-1e	14.7	End of HS1	15.6	15.2	14.7
GS-3 to GI-2.2	23.3	End of HS2	23.8	23.3	23.3

Table 6.1: The age (cal ka BP) of the cold to warm transitions on the GICC05 timescale, and the age of the corresponding event in the SHAK06-5K record when applying the Marine13 age model (shown in Fig. 6.1), the Marine20 age model (shown in Fig. 6.2) and the Marine20 calibration curve with variable ΔR (shown in Fig. 6.3).

Cold to warm transition	GICC05 timescale error (± 2σ)	Age model error (years; ± 2σ)		Offset between NGRIP $\delta^{18}O$ and SHAK06-5K records (years)	
		Marine13 calibration curve	Marine20 calibration curve	Marine13 age model	Marine20 age model
End of YD	~120	~290	~320	~600	~300
End of HS1	~250	~320	~330	~900	~500
End of HS2	~630	~380	~380	~500	0

Table 6.2: For the cold to warm transitions at the end of YD, HS1 and HS2, the mean error (± 2σ) of the GICC05 timescale and SHAK06-5K age models produced using the Marine13 and Marine20 calibration curves, and the calendar age offset (years) between these events in NGRIP $\delta^{18}O$ record and the SHAK06-5K records with the respective age models. Error for the SHAK06-5K age models calculated using the mean of the uncertainties of the depths of the high resolution XRF record. The offset between the records is calculated using the ages in Table 6.1 and is visually illustrated in Figures. 6.1 and 6.2.

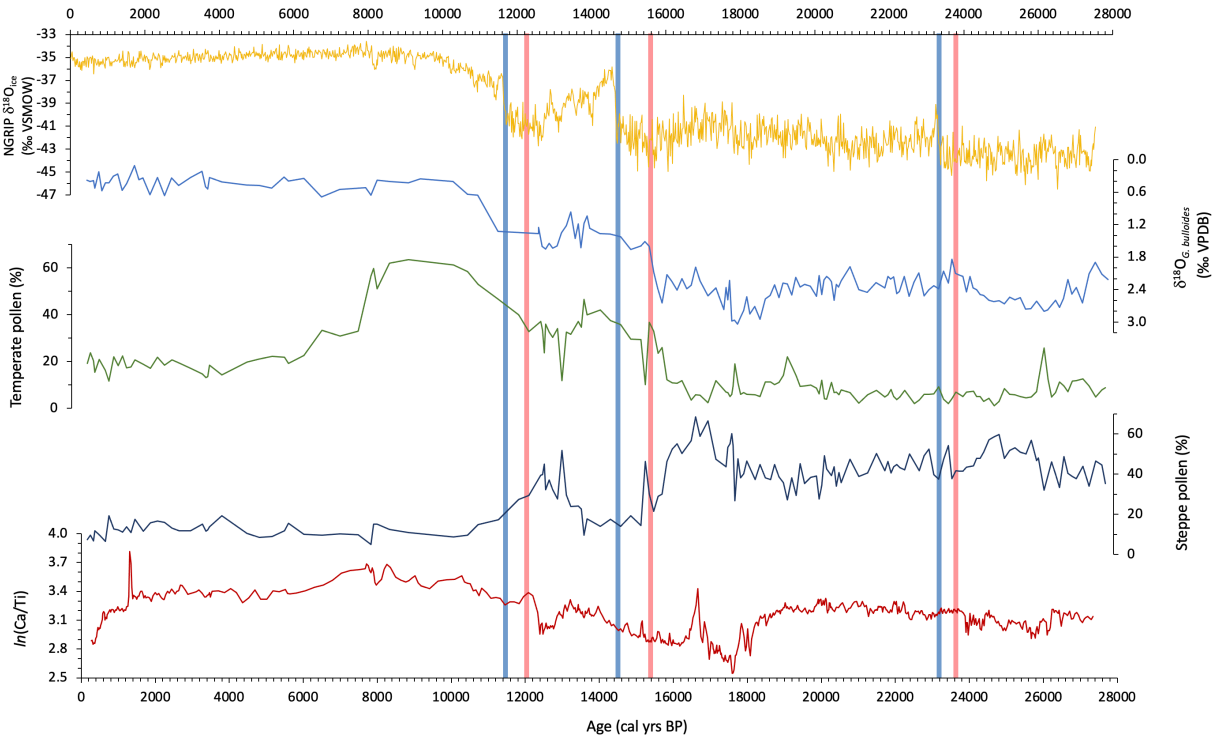

Fig. 6.1: Master age model produced using the Marine13 calibration curve: **a.** NGRIP $\delta^{18}O$ ice core record plotted using the GICC05 timescale (‰ VSMOW); and SHAK06-5K records plotted against the master age model (cal yrs BP) of: **b.** $\delta^{18}O$ from *G. bulloides* (‰ VPDB); **c.** temperate pollen (%); **d.** steppe pollen (%); and **e.** *ln*(Ca/Ti). Blue bands show the position of the abrupt warming events at the transition from GS-1 to the Holocene, GS-2.1a to GI-1e and GS-3 to GI-2.2 (Rasmussen *et al.,* 2014) (correlative with the end of the YD, the end of HS1 and the end of HS2, respectively) in the NGRIP $\delta^{18}O$ record according to the GICC05 timescale, while the red bands show the position of the cold to warm transitions in the SHAK06-5K records according to the master age model.

By applying the Marine20 calibration curve to the age model, the cold to warm transitions in our core are closer aligned with the NGRIP $\delta^{18}O$ record (Fig. 6.2), although there is still an apparent offset of the cold to warm transitions for both the end of the YD and the end of HS1 of ~300 and ~500 years, respectively. Both offsets, however, fall within the combined estimated uncertainty of the Marine20 calibrated age model and the GICC05 timescale (± 2σ; Table 6.1). The transition at the end of HS2 does not display a significant offset when applying this age model.

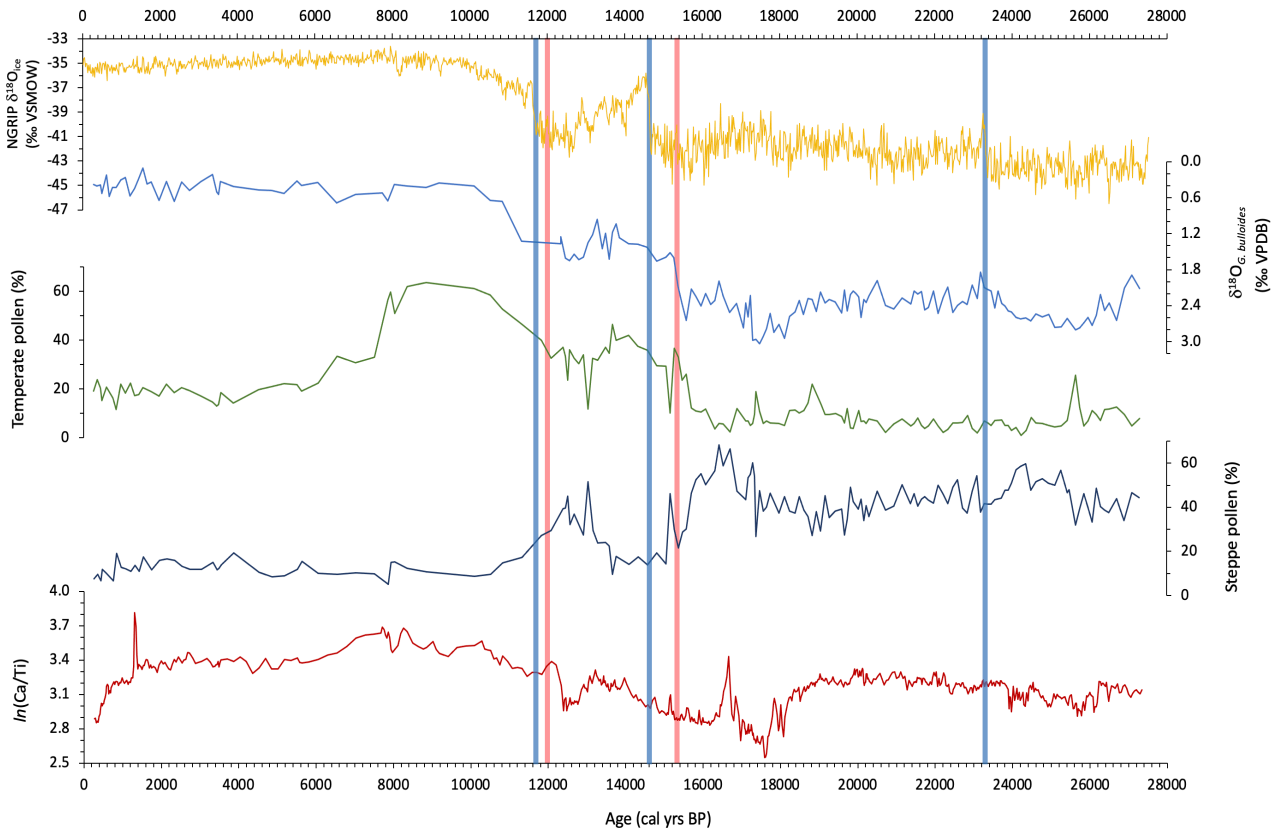

Fig. 6.2: Master age model produced using the Marine20 calibration curve: **a.** NGRIP $\delta^{18}O$ ice core record plotted using the GICC05 timescale (‰ VSMOW); and SHAK06-5K records plotted against age (cal yrs BP) of: **b.** $\delta^{18}O$ from *G. bulloides* (‰ VPDB); **c.** temperate pollen (%); **d.** steppe pollen (%); and **e.** *ln*(Ca/Ti). Blue bands show the position of the abrupt warming events at the transition from GS-1 to the Holocene, GS-2.1a to GI-1e and GS-3 to GI-2.2 (Rasmussen *et al.,* 2014) (correlative with the end of the YD, the end of HS1 and the end of HS2, respectively) in the NGRIP $\delta^{18}O$ record according to the GICC05 timescale, while the red bands show the position of the cold to warm transitions in the SHAK06-5K records according to the master age model.

In order to test adding a local R-age correction to the Marine20 calibration curve, a variable ΔR correction was applied to the cold stadials of the YD and HS1 (of 300 and 500 years, respectively) to align these periods with the corresponding stadials in the GICC05 (Rasmussen *et al.,* 2014). The resulting alignment of the abrupt changes in the SHAK06-5K records and NGRIP $\delta^{18}O$ record is better than that of the previous models (Fig. 6.3), but despite the fit of the stratigraphy of these records, there are a number of issues with using this correction for the master age model. Although research has acknowledged the spatiotemporal variability in the Iberian Margin's R-age over the

Last Glacial and subsequent deglaciation (Waelbroeck *et al.,* 2001; Stern and Lisiecki, 2013; Freeman *et al.,* 2016; Skinner *et al.,* 2019), an accurate quantification of this is yet to emerge (Skinner *et al.,* 2019). Thereby, the addition of a variable ΔR correction (based on the stratigraphic links between corresponding cold to warm transitions in the SHAK0605K and NGRIP $\delta^{18}O$ records) means that an assumption is being made that no time lag exists between the abrupt temperature changes in Greenland and the abrupt events in SW Iberia, highlighted by our records. Additionally, this ΔR correction assumes that the error lies fully in the R-age at the Iberian Margin, when in reality the error could result, to some degree, from both timescales.

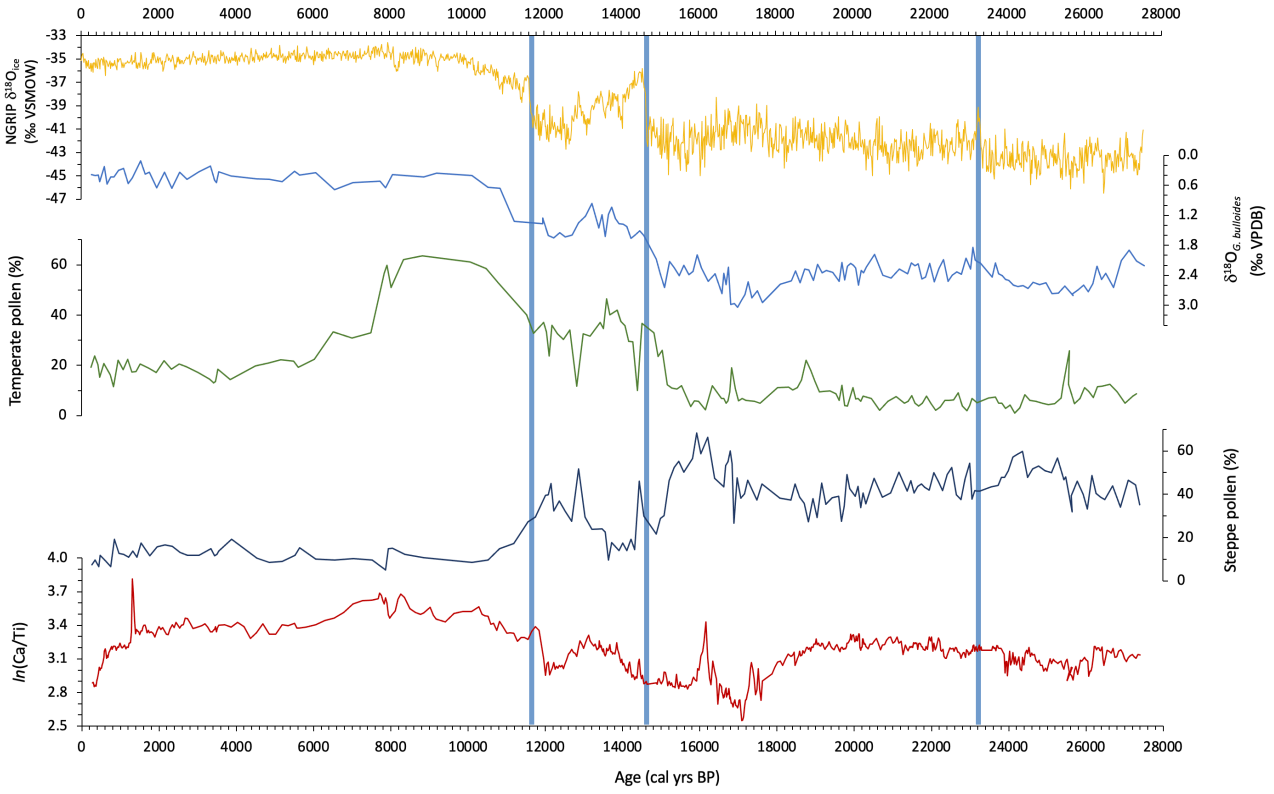

Fig. 6.3: Master age model produced using the Marine20 calibration curve with variable ΔR correction added to the cold stadials of YD, HS1 and HS2: **a.** NGRIP $\delta^{18}O$ ice core record plotted using the GICC05 timescale (‰ VSMOW); and SHAK06-5K records plotted against age (cal yrs BP) of: **b.** $\delta^{18}O$ from *G. bulloides* (‰ VPDB); **c.** temperate pollen (%); **d.** steppe pollen (%); and **e.** *ln*(Ca/Ti). Blue bands show the position of the abrupt warming events at the transition from GS-1 to the Holocene, GS-2.1a to GI-1e and GS-3 to GI-2.2 (Rasmussen *et al.,* 2014) (correlative with the end of the YD, the end of HS1 and the end of HS2, respectively) in the NGRIP $\delta^{18}O$ record according to the GICC05 timescale.

This exercise suggests that there is significant scope for future improvement of the precision and quantification of the R-age correction at the Iberian Margin to account for this region's spatiotemporal variability over the deglaciation. The Marine20 calibration curve, providing a baseline for the global surface ocean reservoir, is here considered as the most suitable for producing a master age model. The features of Marine20 enable a more accurate calculation of R-age, accounting for the globally averaged temporal variation in marine reservoir age beyond the Holocene, while the calculation of propagated uncertainty using a Monte Carlo approach provides a more reliable precision of the ^{14}C calibration of our marine records (Heaton *et al.,* 2020a). Finally, given its distance from high-latitude regions where R-ages are both large and variable (Waelbroeck, 2001; Bard *et al.,* 2004), the SW Iberian Margin is within a suitable latitudinal range for this calibration curve (Heaton *et al.,* 2020a). The marine ^{14}C ages from both cores used in the master age model were therefore corrected using a temporally variable R-age, applied using the Marine20 curve (Heaton *et al.,* 2020a). All reported ages are in calendar years before present (cal yrs BP), with present corresponding to 1950 AD.

The final master age-model is created using 47 AMS ^{14}C dates from SHAK06-5K and MD01-2444. The sediment accumulation rate (SAR) of the master sequence has been calculated for the depths of the high-resolution XRF records of SHAK06-5K and MD01-2444 providing a sample resolution of 0.5 cm for the majority of the core, increasing to ~0.1 cm between 55 and 102 cm. This is calculated using the Bayesian *P_sequence* model in Oxcal 4.4, which assumes random deposition (Bronk Ramsey, 2007).

6.3. Results and Discussion

6.3.1. Master Age Model ^{14}C dates

While the 40 ^{14}C dates of SHAK06-5K and associated uncertainties (± 1σ) have been published in Ausin *et al.* (2019a), those of MD01-2444 are presented for the first time below (Table 6.3).

6.3.1.1. MD01-2444: Main fraction vs leachate

The difference between the ^{14}C ages of the leachate and main fraction of the MD01-2444 samples is < 8%. The leachate shows younger values than the main fraction in all but two samples (Table 6.3); a trend that is demonstrated in other studies (Bard *et al.,* 2015; Ausin *et al.,* 2019a). The two samples that do not follow this trend are the shallowest depth (121 cm; Table 6.3, highlighted in grey) and the outlier (151 cm; Table 6.3, highlighted in red). In sample 121 cm, the difference between the values of the leachate and main fraction is still within the margin of error (± 1σ), while that of 151 cm, is not. As previous research shows leached material to be younger than that of the main fraction (Bard *et al.,* 2015), the differences between the two values are proposed to be the result of successful surface contaminant removal (Ausin *et al.,* 2019a).

		Main fraction			Leachate			
SHAK06-5K aligned depth (cm)	'Real' MD01-2444 depth (cm)	Lab Code	Radiocarbon age (^{14}C yr BP)	± 1σ	Lab Code	Radiocarbon age (^{14}C yr BP)	± 1σ	Age difference (yrs)
55.2	**121**	**102679.1.1**	**5,501**	**± 65**	**102679.2.1**	**5,556**	**± 75**	**55**
59.3	136	102678.1.1	7,322	± 80	102678.2.1	7,019	± 80	304
61.9	**151**	**102677.1.1**	**7,810**	**± 80**	**102677.2.1**	**7,596**	**± 90**	**214**
63.7	163	102676.1.1	7,683	± 95	102676.2.1	7,274	± 90	409
65.8	178	102675.1.1	8,012	± 85	102675.2.1	7,709	± 90	303
67.3	193	102674.1.1	8,378	± 95	102674.2.1	7,996	± 90	382
69.5	211	102673.1.1	8,603	± 85	102673.2.1	7,990	± 95	613
72.4	223	102672.1.1	9,553	± 95	102672.2.1	9,016	± 95	537
86.9	232	102671.1.1	11,742	± 115	102671.2.1	11,161	± 110	581
102.2	238	102670.1.1	11,851	± 115	102670.2.1	11,341	± 105	510

Table 6.3: MD01-2444 ^{14}C age differences between the main fraction and leachate. Both the 'real' depth in the MD01-2444 core (cm) and the SHAK06-5K aligned depth (cm) (using the automated proxy-to-proxy stratigraphical alignment method) is shown. Values in bold represent depths where the leachate is older than the main fraction, with grey representing a difference within the margin of error and red representing an age reversal outside the margin of error and therefore removed from the age-model. Associated error have been rounded according to convention.

6.3.1.2. MD01-2444 ^{14}C dates

Of the 10 ^{14}C dates sampled from MD01-2444, three were not included in the master age-model; 151cm, 232cm, and 238cm. The outlier at 151 cm was removed prior to running the automated stratigraphical alignment algorithm as it was clear that this sample (both the main fraction and leachate) does not follow the decline in ^{14}C age with increasing depth. Additionally, the age uncertainty (± 1σ) falls outside of the margin of error of the two neighbouring samples. Consequently, this sample is likely reflecting older material. Although high SAR has been shown to minimise the influence of bioturbation (Bard, 2010), age offsets between coexisting planktonic foraminifera (Ausin *et al.,* 2019a) and ichnofabric analysis (Dorador & Rodríguez-Tovar, 2016) during this period in records close to core MD01-2444 indicate that bioturbation may well have influenced the age of the material at this site. Downslope remobilisation and calcite dissolution may have also played a role in these age reversals. The precision of the main fraction of the remaining nine ^{14}C values is relatively high (quoted at 68.3%; ± 1σ), ranging between ± 65 and ± 115 years, with values generally increasing up the core.

6.3.2. Alignment of SHAK06-5K and MD01-2444 records

During the automated stratigraphical alignment of MD01-2444 with SHAK06-5K, it became apparent that the MD01-2444 ^{14}C dates at 232 cm and 238 cm also reflected age reversals. Even when accounting for the uncertainty of the alignment (± 2σ), the ^{14}C age of 232 cm reflected older material than the SHAK06-5K samples up the core, and 238 cm demonstrated younger ^{14}C age than SHAK06-5K samples down the core (Fig. 6.4). Both were consequently removed from the master age model. The result of the synchronisation is shown in Fig. 6.5, with the MD01-2444 record aligning to the SHAK06-5K depth scale between 55 – 102 cm. The alignment has relatively high precision (± 2σ), with a mean of ±1.35 cm. The smallest uncertainties are seen at the beginning and end of the record (reaching a minimum of ±1 cm). The variability increases from 74 cm, peaking at 227.5 cm (±2.94 cm), and reducing thereafter.

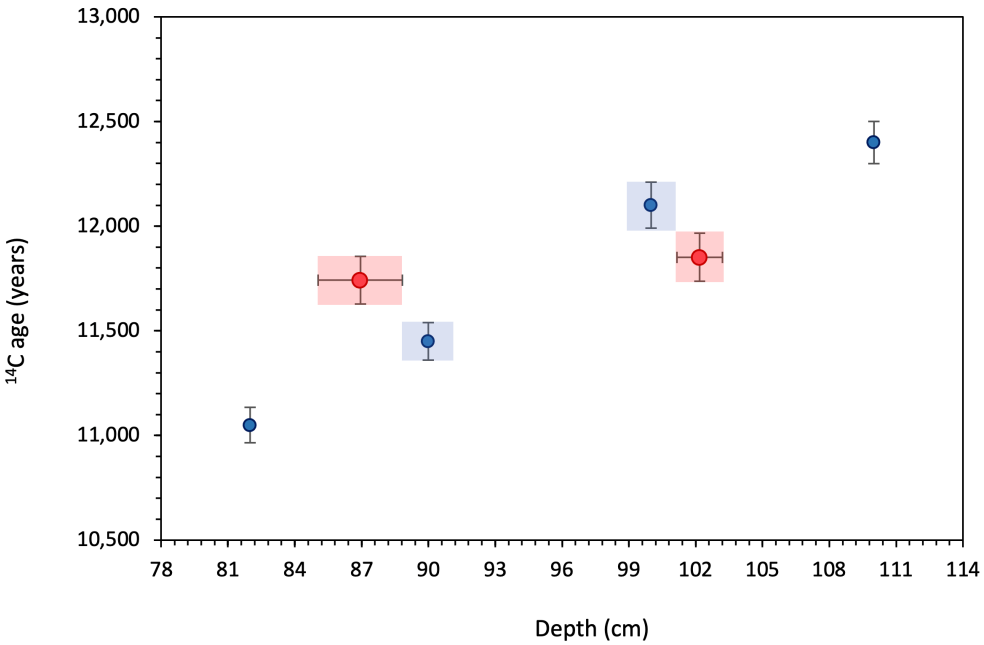

Fig. 6.4: Alignment of the SHAK06-5K (blue dots) and MD01-2444 (red dots) ^{14}C records on the SHAK06-5K depth scale (cm), produced by the automated stratigraphical alignment method. The two outliers from MD01-2444 are highlighted (232 and 238 cm). These samples reflect older/younger material and are consequently not used in the age model. Horizontal error bars (MD01 samples) show the uncertainty of the model alignment on the SHAK06-5K depth scale; vertical error bars show ^{14}C age uncertainties (± 1σ).

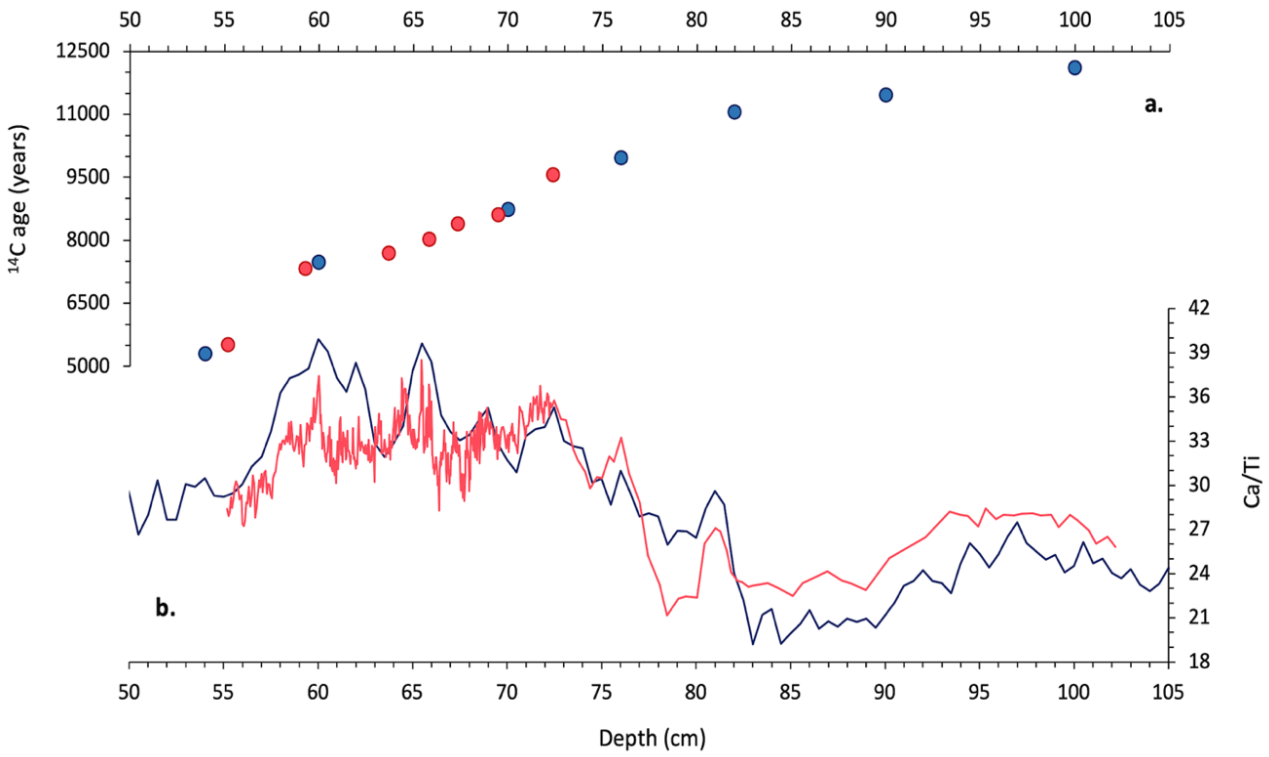

Fig. 6.5: Alignment of the SHAK06-5K and MD01-2444 records on the SHAK06-5K depth scale (cm), produced by the automated stratigraphical alignment method, highlighting the synchronisation of: **a.** the seven ^{14}C ages (years) from MD01-2444 (red) with those of SHAK06-5K (blue); and **b.** the Ca/Ti records of MD01-2444 (red) with SHAK06-5K (blue). 151, 232 and 238 cm are not used in the production of the age model.

6.3.3. Master age model

47 samples (40 from SHAK06-5K and seven from MD01-2444) create the age-depth model presented in Fig. 6.6, which spans the last 27.4 kyr and will be referred to, hereafter, as the 'master age model'. The ^{14}C age estimates have relatively high precision (Table 6.4), which generally increase up the core. The confidence intervals of the ^{14}C ages are quoted at 68.3% (±1σ) and range from ± 200 years at 329 cm to ± 50 years at 30 cm. The precision, however, declines at the very top of the core, with a value of ±150 years at both 0 and 4 cm. The calibrated age uncertainties (calculated in Oxcal and quoted at 95% confidence values; ±2σ) are all ≤ ±420 years. The uncertainty of the seven MD01-2444 ^{14}C dates and calibrated ages are similar to those of the closely aligned SHAK06-5K samples.

Core	Lab Code	Master depth (cm)	Radiocarbon age (^{14}C yr BP)	± 1σ	Calendar age (cal yr BP)	± 2σ
SHAK06-5K	82182.2.1	0	790	± 150	255	± 228
SHAK06-5K	82183.2.1	4	1,010	± 150	433	± 210
SHAK06-5K	72979.2.1	10	1,250	± 70	662	± 148
SHAK06-5K	82185.2.1	14	1,450	± 70	834	± 165
SHAK06-5K	72981.2.1	20	1,820	± 55	1,202	± 159
SHAK06-5K	72983.2.1	30	2,300	± 50	1,749	± 181
SHAK06-5K	72985.2.1	40	3,090	± 65	2,731	± 217
SHAK06-5K	75040.1.1	44	3,620	± 75	3,334	± 208
SHAK06-5K	70397.1.1	48	3,760	± 60	3,542	± 193
SHAK06-5K	75041.1.1	54	5,300	± 80	5,514	± 202
MD01-2444	102679.1.1	55	5,500	± 65	5,655	± 195
MD01-2444	102678.1.1	59	7,320	± 80	7,649	± 170
SHAK06-5K	72987.2.1	60	7,470	± 60	7,714	± 151
MD01-2444	102676.1.1	64	7,680	± 95	7.990	± 231
MD01-2444	102675.1.1	66	8,010	± 85	8,306	± 244

MD01-2444	102674.1.1	67	8,380	± 95	8,741	± 303
MD01-2444	102673.1.1	69	8,600	± 90	9,108	± 229
SHAK06-5K	72989.2.1	70	8,740	± 70	9,175	± 197
MD01-2444	102672.1.1	72	9550	± 95	10,261	± 300
SHAK06-5K	75042.1.1	76	9,960	± 80	10,821	± 283
SHAK06-5K	72991.2.1	82	11,050	± 85	12,336	± 287
SHAK06-5K	72993.2.1	90	11,450	± 90	12,795	± 201
SHAK06-5K	70400.1.1	100	12,100	± 110	13,404	± 248
SHAK06-5K	72995.2.1	110	12,400	± 100	13,848	± 276
SHAK06-5K	72997.2.1	120	13,250	± 95	15,050	± 309
SHAK06-5K	70403.1.1	130	13,600	± 110	15,581	± 313
SHAK06-5K	72999.2.1	140	14,100	± 100	16,209	± 285
SHAK06-5K	75043.1.1	146	14,300	± 100	16,527	± 295
SHAK06-5K	73001.2.1	152	14,900	± 100	17,063	± 256
SHAK06-5K	73002.2.1	160	14,900	± 110	17,291	± 269
SHAK06-5K	73003.2.1	172	15,350	± 110	17,839	± 306
SHAK06-5K	73005.2.1	180	15,950	± 140	18,394	± 304
SHAK06-5K	75044.1.1	196	16,650	± 120	19,274	± 303
SHAK06-5K	75016.1.1	200	17,100	± 120	19,596	± 285
SHAK06-5K	75018.1.1	210	17,300	± 120	19,964	± 281
SHAK06-5K	75020.1.1	220	17,400	± 140	20,298	± 321
SHAK06-5K	75022.1.1	230	18,600	± 180	21,381	± 420
SHAK06-5K	75024.1.1	240	18,750	± 140	21,839	± 352
SHAK06-5K	70406.1.1	260	20,000	± 180	23,098	± 373
SHAK06-5K	75028.1.1	270	20,400	± 150	23,556	± 304
SHAK06-5K	75030.1.1	280	20,700	± 150	23,988	± 284
SHAK06-5K	75048.1.1	284	21,000	± 160	24,229	± 332
SHAK06-5K	75032.1.1	290	21,300	± 160	24,621	± 376
SHAK06-5K	75033.1.1	300	22,100	± 170	25,432	± 339
SHAK06-5K	75034.1.1	310	22,600	± 180	25,965	± 318
SHAK06-5K	75036.1.1	320	23,000	± 180	26,506	± 407
SHAK06-5K	75038.1.1	329	24,100	± 200	27,395	± 358

Table 6.4: The master age-depth model based on 40 monospecific planktonic foraminifera *G. bulloides* samples from SHAK06-5K and seven from MD01-2444. The alignment of the cores produced using an automated stratigraphical alignment method. Ages and associated error have been rounded according to convention.

Based on the SAR calculated for the depths of the high-resolution XRF records, the mean SAR of the master sequence is 13 cm kyr^{-1}, ranging between 2 and 35 cm kyr^{-1} (shown in Fig. 6.6). The largest SAR occurs between 27.4 and 12.4 cal ka BP (329 - 83 cm), with the highest SAR (35 cm kyr^{-1}) reached at 17.2 cal ka BP (158 cm). The SAR declines between 12.4 and 3.5 cal ka BP (83 – 48 cm), reaching the minimum value of the record (2 cm kyr^{-1}) at 6.6 cal ka BP (57 cm). While the master age model uses the SHAK06-5K stratigraphy, the incorporation of ^{14}C dates from core MD01-2444 in the master age model means that the original SAR of core SHAK06-5K is modified. Consequently, the SAR between 8.2 and 7.7 cal ka BP is higher in the master sequence than for the same period in the SHAK06-5K record, with a mean SAR of 10.7 cm kyr^{-1} in the former, compared to 5.7 cm kyr^{-1} in the latter (Appendix 13). This increase is due to the inclusion of MD01-2444 in the master sequence which demonstrates a considerably higher SAR than the SHAK06-5K sequence for the same period, averaging 49 cm kyr^{-1} between 9.1 and 7.6 cal ka BP (Appendix 13). Towards the top of the master sequence, the SAR increases, reaching 23 cm kyr^{-1} at 0.3 cal ka BP (0 cm).

Applying the master chronology to both cores records demonstrates that the pollen record has a mean sampling resolution of 165 years for the SHAK06-5K pollen record and 218 years for the MD01-2444 pollen record. The *n*-alkane $\delta^{13}C$ record from SHAK06-5K has a lower mean sampling resolution of 421 years. When applying our master age model to the SHAK06-5K and MD01-2444 records and comparing the climate events in these records to those in the NGRIP $\delta^{18}O$ ice core record, the following age ranges have been applied to the key climate events of the last 28 kyr. HS2 spans 25.7 – 23.6 cal ka BP, while the LGM is dated between 23.6 – 19 cal ka BP and HS1 occurs from 18.2 – 15.4 cal ka BP. The BA proceeds this, lasting until 13.2 cal ka BP, followed by the YD which ends at 12 cal ka BP. The early Holocene ensues until 8.2 cal ka BP, followed by the mid-Holocene which continues until 4.2 cal ka BP, moving thereafter to the late Holocene (Nesje & Dahl, 1993; Walker *et al.,* 2018).

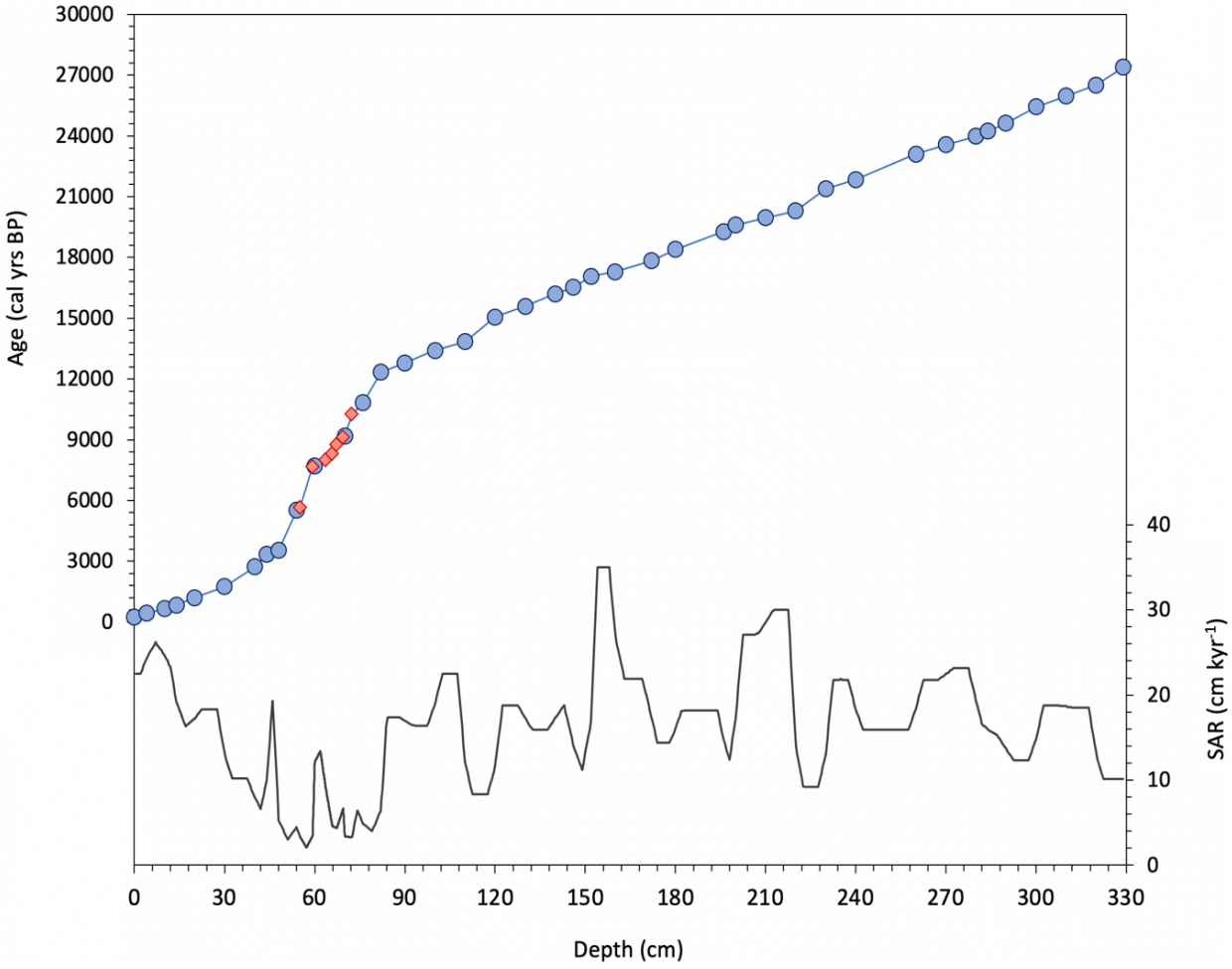

Fig. 6.6: Master calibrated age-depth model (cal yrs BP), created using 40 AMS ^{14}C dates from SHAK06-5K (blue dots) and seven from MD01-2444 (red diamonds). Black line shows sediment accumulation rate (SAR; cm kyr^{-1}). Both the age-depth model and SAR produced using a *P_sequence* depositional model in OxCal.

6.4. Conclusion

Here, a master Bayesian *P_sequence* chronology has been created and presented using 47 ^{14}C dates from cores SHAK06-5K and MD01-2444. The synchronisation of the records was conducted using an automated stratigraphical alignment method algorithm (Muschitiello *et al.,* 2020), simultaneously aligning the Ca/Ti and ^{14}C records of both cores. The resulting master age-model (0 – 329 cm) is based on 40 ^{14}C dates from SHAK06-5K and seven from MD01-2444 and spans 0 – 27.4 cal ka BP. This chronology will be applied to our pollen and biomarker records to assist in the palaeoclimatic interpretation of the glacial-interglacial and millennial to centennial-scale abrupt changes in SW Iberian vegetation over the past 27.4 kyr.

7.1. Introduction:

Significant uncertainty surrounds the dominant environmental signal of leaf-waxes in sediment records, as discussed in section 5.1. Consequently, the interpretation of fossil *n*-alkane records relies on a strong understanding of the production of these lipids in modern plants, variations between species, and their physiological and environmental controls. Existing research into the drivers of leaf-wax composition in present-day Mediterranean vegetation is limited in terms of species and locations (Damesin *et al.,* 1997; Schäfer *et al.,* 2016; Norström *et al.,* 2017). Thus, improving our understanding of the complex climatic and ecological controls of leaf-wax distribution and isotopic composition in SW Iberian vegetation is urgently required. To assess potential interspecies differences and the dominant biological/climatic drivers of *n*-alkane distribution and *n*-alkane $\delta^{13}C$ ($\delta^{13}C_{n\text{-alkane}}$) in SW Iberian vegetation, modern leaf samples were collected from within the Tagus basin, the dominant supplier of plant biomass from to core site SHAK06-5K. The aim is to then use these findings to assist with the interpretation of our fossil *n*-alkane records from core SHAK06-5K.

7.1.1. Understanding the dominant control of leaf-wax ACL

As discussed in section 5.1, leaf-wax ACL in sediment archives is used as a tool for palaeoenvironmental reconstruction. While it has been suggested that ACL is primarily driven by photosynthetic pathway and can therefore be used to distinguish C_3 from C_4 vegetation (Rommerskirchen *et al.,* 2006), other studies have concluded that ACL is influenced by plant type and can identify arboreal from herbaceous taxa (Cranwell, 1973; Meyers & Ishiwatari, 1993; Schwark *et al.,* 2002; Meyers, 2003). ACL has also been linked to temperature (Hoffmann *et al.,* 2013; Tipple & Pagani, 2013; Bush & McInerney, 2015), and water availability (Huang *et al.,* 2000; Schefuss *et al.,* 2003), but despite decades of research on this topic, there is little scientific consensus over the dominant physiological and environmental controls of leaf-wax ACL.

One area, however, that has received little attention from the palaeoclimatic community is the relationship between the crystalline structure of leaf cuticular wax lipids and its ACL. A plant's cuticle performs a number of functions including: repelling water from the cuticle surface, and acting as a barrier against water permeability, UV radiation, and contamination from harmful

chemicals and microorganisms. The cuticle is composed of a number of layers (Fig. 7.1). The cuticular layer (CL), located above the epidermal cells primarily consists of cutin, carbohydrates and waxes (Von Mohl, 1847; Heredia, 2003; Jeffree, 2006) and plays a significant role in determining the mechanical integrity and the thermal susceptibility of the transpiration barrier (Khanal & Knoche, 2017). The cuticle proper (CP) is the outermost layer, composed of intracuticular and epicuticular waxes. The intracuticular layer is embedded in the cutin matrix of the CL (Jeffree, 2006), while in many plant species, the epicuticular wax film is impregnated with epicuticular wax crystals (De Bary, 1871; Jeffree *et al.,* 1975; Barthlott *et al.,* 1998). While both layers are composed of a mixture of aliphatic compounds and can also contain cyclic compounds (Von Mohl, 1847; Baker, 1982), the composition of each layer is chemically distinct, performing different functions (Jetter *et al.,* 2000; Buschhaus & Jetter, 2011; Jetter & Reiderer, 2016). The epicuticular layer plays an important role in water repellence and protection against UV radiation and pathogens (Cameron, 1970; Neinhuis & Barthlott, 1997; Holmes and Keiller, 2002; Müller & Reiderer, 2005), with the quantity and composition of these waxes shown to change over time (Jetter & Schäffer, 2001). There appears to be little temporal change in the composition and quantity of intracuticular waxes (Jetter & Schäffer, 2001), with this layer acting as the dominant water permeability barrier (Jetter & Reiderer, 2016; Zeisler & Schreiber, 2016; Zeisler-Diehl *et al.,* 2018). Aliphatic compounds are the primary contributor to the transpiration barrier while cyclic compounds demonstrate very little (if any) barrier to water permeability (Jetter & Reiderer, 2016), but increase the plasticity and tensile strength of the wax (Edwards, 1958; Reiderer & Schneider, 1990).

The cuticular permeability is primarily determined by the physical molecular structure of the waxes, rather than just by the chemicals it is composed of, or delivery method of waxes to the leaf surface, or its thickness/coverage (Jeffree *et al.,* 1975; Riederer & Schönherr, 1985; Reiderer & Schneider, 1990; Jetter & Reiderer, 2016). No correlation has been found between cuticular transpiration and wax amounts or cuticle thickness (Becker *et al.,* 1986; Schreiber & Riederer, 1996; Jetter & Riederer, 2016; Zeisler-Diehl *et al.,* 2018).

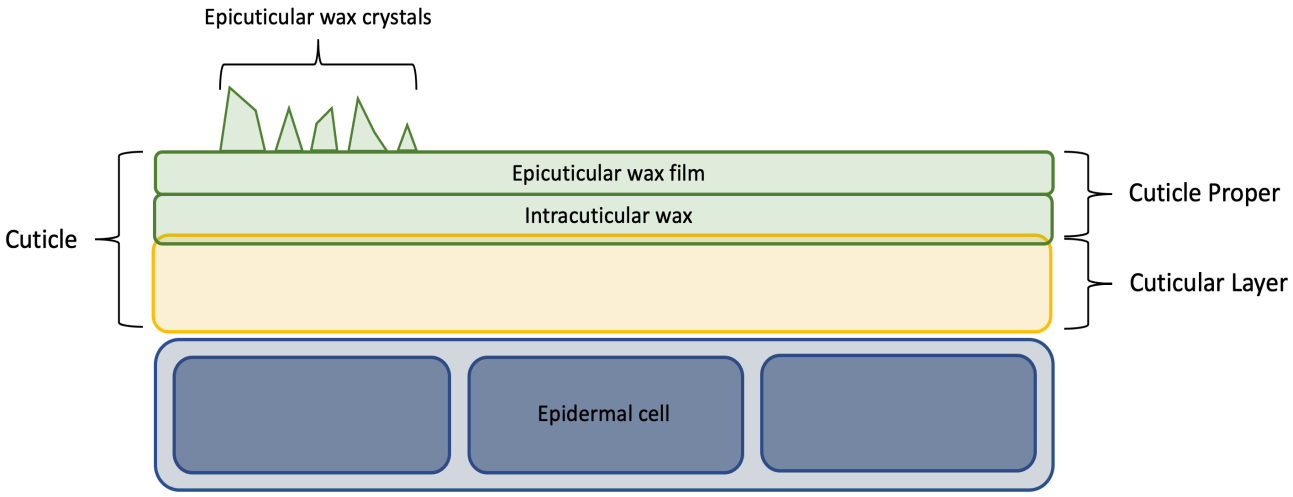

Fig. 7.1: Schematic diagram of a plant's cuticle structure (not to scale). The cuticle is separated into two major layers, described by von Mohl (1947). The cuticle proper (CP), which includes the epicuticular and intracuticular wax layers, and the cuticular layer (CL).

The aliphatic components are composed of both long (≥ C_{40}; alkyl esters) and shorter (C_{20} – C_{38}; *n*-alkanes, *n*-alkanols, *n*-alkanoic acids, and *n*-alkanals) chain lipids, although these 'shorter chained lipids' are favoured (Riederer & Schneider, 1990; Reynhardt & Riederer, 1994). These compounds form crystalline and amorphous zones, as shown in the Fig. 7.2 schematic, with the long axes of the molecules primarily anticlinal orientated (Basson & Reynhardt, 1988a; 1988b; Riederer & Schneider, 1990; Reynhardt & Riederer, 1994). The crystalline zone has an orthorhombic structure, transforming into a hexagonal structure just below its melting point (Reynhardt, 1986; Basson & Reynhardt, 1991). Molecules within the crystalline zone are of differing chain-lengths and form a staggered, irregular arrangement, while the amorphous zone does not have discrete structural order and contains chain ends (Lourens & Reynhardt, 1979). The range of molecules in cuticular waxes produces steric hindrances between the chains. This disrupts the geometric homogeneity of the wax structure and contributes to the amorphous layer (Riederer & Schneider, 1990; Reynhardt, 1997). Consequently, the larger the chain-length distribution, the greater the steric hindrances and the lower the crystallinity of the wax (Riederer & Schneider, 1990; Reynhardt, 1997).

While the crystalline zone prevents molecules from permeating across it, the disorder of the amorphous zone makes it accessible to permeating molecules (Riederer & Schneider, 1990; Reynhardt & Riederer, 1994). Due to their anticlinal orientation, this pathway is perpendicular to the flow of water and plays a minor role in movement of water from inside the leaf (Riederer & Schneider, 1990). Groups of these lipids form 'flake' structures which can form layers parallel to the surface of the leaf (Riederer & Schneider, 1990). Water then permeates primarily through the amorphous zone between the flakes (Riederer & Schneider, 1990). As the amorphous domain is determined by: i) the volume fraction of crystallites, and ii) the flake size and distance from each other, these factors influence the water permeability of the membrane (Riederer & Schneider, 1990).

Thermal stress can change the structure of the cuticle (Schönherr *et al.,* 1979; Eckl & Gruler, 1980; Schreiber & Schönherr, 1990; Reiderer & Schreiber, 2001). While permeability doubles on average when the leaf surface rises from 15 to 35°C (Reiderer & Schreiber, 2001) temperatures above 45°C can cause irreversible structural changes, such as hydrophilic holes, which increase permeability (Eckl & Gruler, 1980; Schreiber & Schönherr, 1990). The cuticular waxes melt over a wide temperature range; below this range, the wax is solid, but within it, a mobile amorphous zone forms, firstly within the solid amorphous zone, then outside of this zone (shown in Fig. 7.2; Basson & Reynhardt, 1992; Reynhardt & Riederer, 1994). Higher temperatures correspond with higher chain-lengths in the mobile amorphous zone (Reynhardt & Riederer, 1994). Just below the melting point, the orthorhombic structure transforms into a hexagonal structure, with chains rotating around their long axes (Reynhardt, 1986; Basson & Reynhardt, 1991; Reynhardt & Riederer, 1994). With rising temperatures, the mobile amorphous zone increases, which increases the cuticular permeability (Schreiber & Schönherr, 1990; Reynhardt & Riederer, 1994). At melting point, all of the wax is within the mobile amorphous zone. Due to the mixture of components forming the cuticular wax, its melting point is lower than that predicted by the melting point of its isolated lipid components (Patel *et al.,* 2001).

Despite this, the structure of the cuticular wax acts as mechanical reinforcement, enabling it to withstand significant thermal stress before entering this transition phase (Reynhardt, 1997; Bueno *et al.,* 2019). While *n*-alkanes have weak interchain forces, the presence of hydrogen bonds in n-alkanols, n-alkanoic acids, and n-esters prevent phase separation of long chain lipids (≥ C_{40}) and

shorter chain lipids (C_{20} – C_{38}), and the long-chain lipids bridge the amorphous gap to increase the melting point of the cuticular wax (Reynhardt & Riederer, 1994; Reynhardt, 1997). Despite this apparent critical role that the molecular structure of a leaf's cuticle plays in its permeability, little research has connected this to the distribution of a plant's cuticular *n*-alkanes and the surrounding environmental conditions. Consequently, while *n*-alkane ACL may not represent a species, a plant functional group, or surrounding environmental conditions in a predictable way, it may reflect a genetic adaptation of a species to heat or drought stress. This is, therefore, an area of research that requires further exploration.

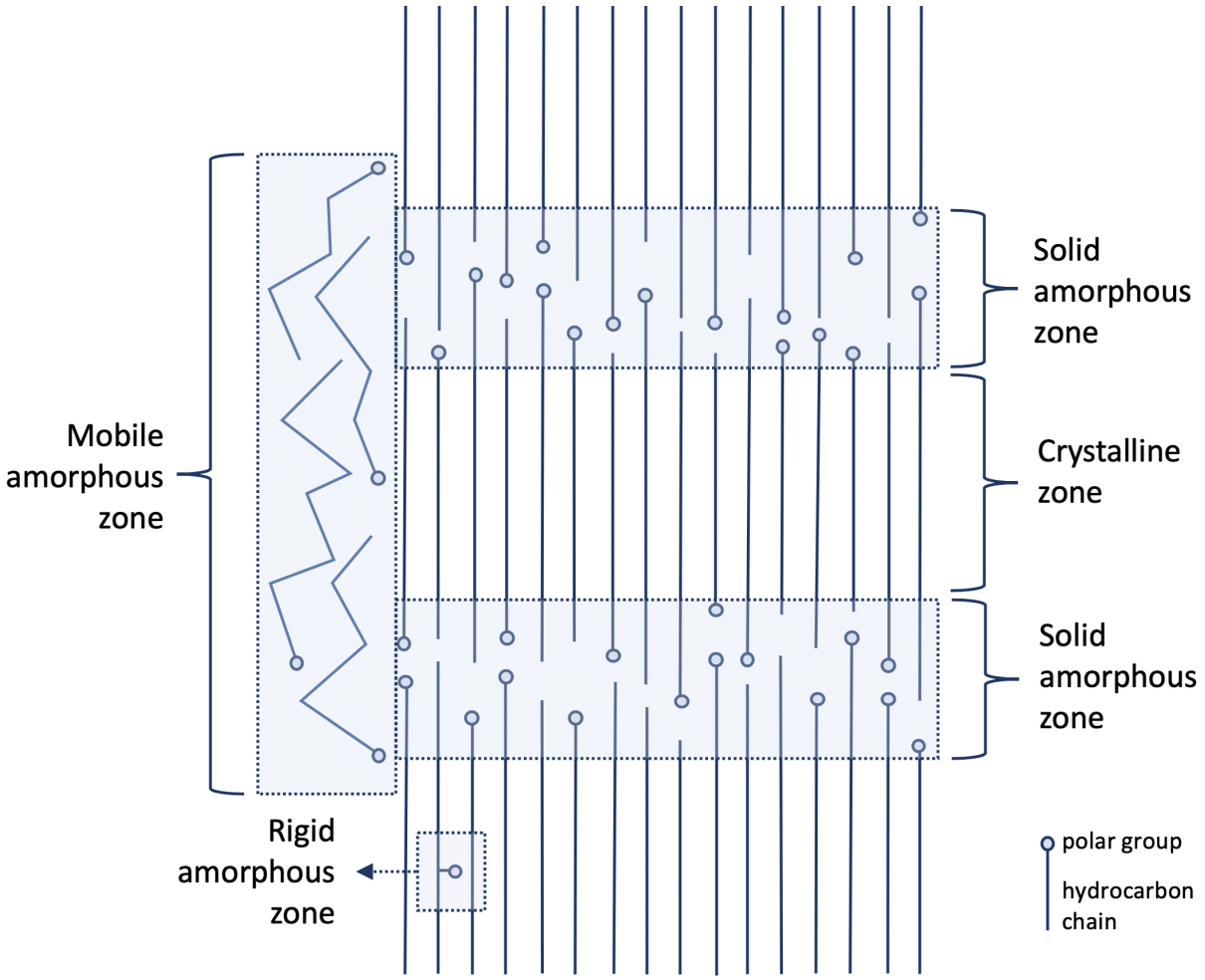

Fig. 7.2: Schematic diagram of the molecular structure of the cuticular layer (not to scale), including the crystalline zone and the solid, rigid amorphous zone, and the mobile amorphous zone (which occurs during crystallisation, only forming outside the solid amorphous zone when this void has been filled). Adapted from: (Riederer & Schneider, 1990; Reynhardt & Riederer, 1994).

7.1.2. Understanding the dominant control of a plant's $\delta^{13}C$

As discussed in section 5.1 and illustrated in Fig. 5.2, there are various physiological and environmental controls of cuticular carbon isotope fractionation. A plant's biomass is depleted in ^{13}C compared to the atmosphere as a result of carbon isotope fractionation associated with CO_2 uptake and photosynthetic carbon fixation (Farquhar *et al.,* 1982; 1989; Cernusak *et al.,* 2013; Freeman & Pancost, 2013). Further fractionation then occurs during lipid biosynthesis, causing cuticular *n*-alkanes to be further depleted in ^{13}C relative to the plant's biomass (Collister *et al.,* 1994; Chikaraishi *et al.,* 2004; Pancost & Boot, 2004; Diefendorf & Friemuth, 2017). Numerous environmental and biological factors drive this carbon isotope fractionation, as explained in section 5.1, and to enable accurate interpretation of terrestrial *n*-alkane signals in fossil records, it is important to understand the dominant drivers of ^{13}C discrimination in plants and how this may vary at a taxonomic level.

While the $\delta^{13}C$ of a plant's biomass ($\delta^{13}C_{plant}$) varies between C_3, C_4, and CAM vegetation, and also between C_3 angiosperms and gymnosperms (Collister *et al.,* 1994; Chikaraishi & Naraoka, 2003; Diefendorf *et al.,* 2010; Norström *et al.,* 2017), carbon isotope fractionation during lipid biosynthesis also varies between C_3 trees, graminoids, forbs and shrubs, (Diefendorf & Friemuth, 2017), between angiosperms and gymnosperms (Chikaraishi & Naraoka, 2003), and between gymnosperm families (Diefendorf *et al.,* 2015a).

Water availability is also a key driver of $\delta^{13}C_{plant}$ across large spatial scales, with C_3 plants demonstrating a significant negative correlation with mean annual precipitation (Diefendorf *et al.,* 2010; Liu & An, 2020). Enhanced water stress increases stomatal closure which reduces the plant's discrimination against ^{13}C, which in turn increases $\delta^{13}C_{plant}$ (Madhavan *et al.,* 1991; Ehleringer *et al.,* 1992; Diefendorf *et al.,* 2010; Prentice *et al.,* 2011). Research has suggested that the fractionation response to declining moisture availability is similar within and between angiosperm species, plant functional groups, and communities (Wittmer *et al.,* 2008; Prentice *et al.,* 2011). Temperature has shown little influence on $\delta^{13}C_{plant}$ over large spatial scales (Diefendorf *et al.,* 2010; Liu & An, 2020), but $\delta^{13}C_{plant}$ has shown considerable variation with altitude, although the mechanisms behind this relationship are yet to be constrained (Diefendorf *et al.,* 2010; Wu *et al.,* 2017). With regards to the association between atmospheric pCO_2 concentration and $\delta^{13}C_{plant}$, no significant correlation has yet been shown between these variables in C_3 vegetation (Arens *et al.,*

2000), and $\delta^{13}C_{plant}$ has shown a significantly stronger relationship with water availability and taxonomic group than with pCO_2 (Diefendorf *et al.,* 2015b).

7.1.3. Existing modern Mediterranean n-alkane records

Despite limited research on leaf-wax distributions and $\delta^{13}C$ in Mediterranean vegetation, there are existing modern records which document *n*-alkane concentrations, ACL, CPI and $\delta^{13}C$ in a number of Mediterranean species (Schäfer *et al.,* 2016; Norström *et al.,* 2017). Here, I aim to combine a new modern *n*-alkane record of Mediterranean vegetation with these two existing datasets to explore the principal environmental and physiological drivers of *n*-alkane concentrations, ACL, and $\delta^{13}C$ in Mediterranean vegetation.

As the *n*-alkane record from SHAK06-5K demonstrates the dominance of C_3 plants in SW Iberia over the past 27.4 kyr (Fig. 5.12), we aim use the new and existing modern *n*-alkane records of Mediterranean vegetation to explore the dominant controls of *n*-alkane properties in modern Mediterranean taxa and to disentangle physiological and environmental controls of ACL and carbon isotope fractionation in Mediterranean plants. The aim is to then use this to assist with the interpretation of the SHAK06-5K $\delta^{13}C_{n\text{-alkane}}$ record and provide some clarity on the climatic and/or biological signal of this fossil record over the last 27.4 kyr.

7.2. Materials and Methods

7.2.1. Sample collection

Samples were collected early in the growing season in May 2019, from sites in Portugal located within the Tagus basin (Fig. 7.3), the dominant supplier of terrestrial biomass to our core sites (Jouanneau *et al.,* 1998). Plant samples were taken from regions away from human activity (including irrigation, controlled burning, and natural wildfires) meaning, to the best of our knowledge, the vegetation sampled for this research was predominantly affected by regional environmental conditions. Sites 2 and 3 were located inland within national parks: removed from settlements, agriculture, and recent wildfires. Site 1 is a remote cliff location within the Sintra-Cascais Natural Park on the Atlantic coast. The species selected for our modern record were all Mediterranean C_3 vegetation present in the pollen records of SHAK06-5K and MD01-2444 (Table 7.1). For each taxon, 9 – 12 leaves were collected from three specimens closely situated to each other and then mixed to get an average *n*-alkane signal. New growth from the outer branches of isolated trees were selected to ensure equal light exposure. Hand collection of the leaves was avoided to prevent lipid contamination. In herbaceous and deciduous trees, we could be certain the growth was from this season, but the newest leaves were picked to ensure growth occurred over the past few weeks. In evergreen (*Quercus ilex, Juniperus turbinata, Pinus pinaster, Olea europaea*) and semi-evergreen species (*Quercus suber*), only obvious new growth was selected. Upon return to the UCL Department of Geography laboratory, samples were freeze-dried for 48 hours, then weighed (Table 7.1). The dataset collected in this study was compared with two existing leaf wax records from the Mediterranean. The first record contains 9 samples taken from El Paraíso, located in the western Mediterranean, in central Spain, within the Tagus catchment basin (Schäfer *et al.,* 2016). The second record is from the eastern Mediterranean and contains 21 samples, sourced from the Messenian Plain, Greece (Norström *et al.,* 2017). The sample locations are depicted in Fig. 7.3.

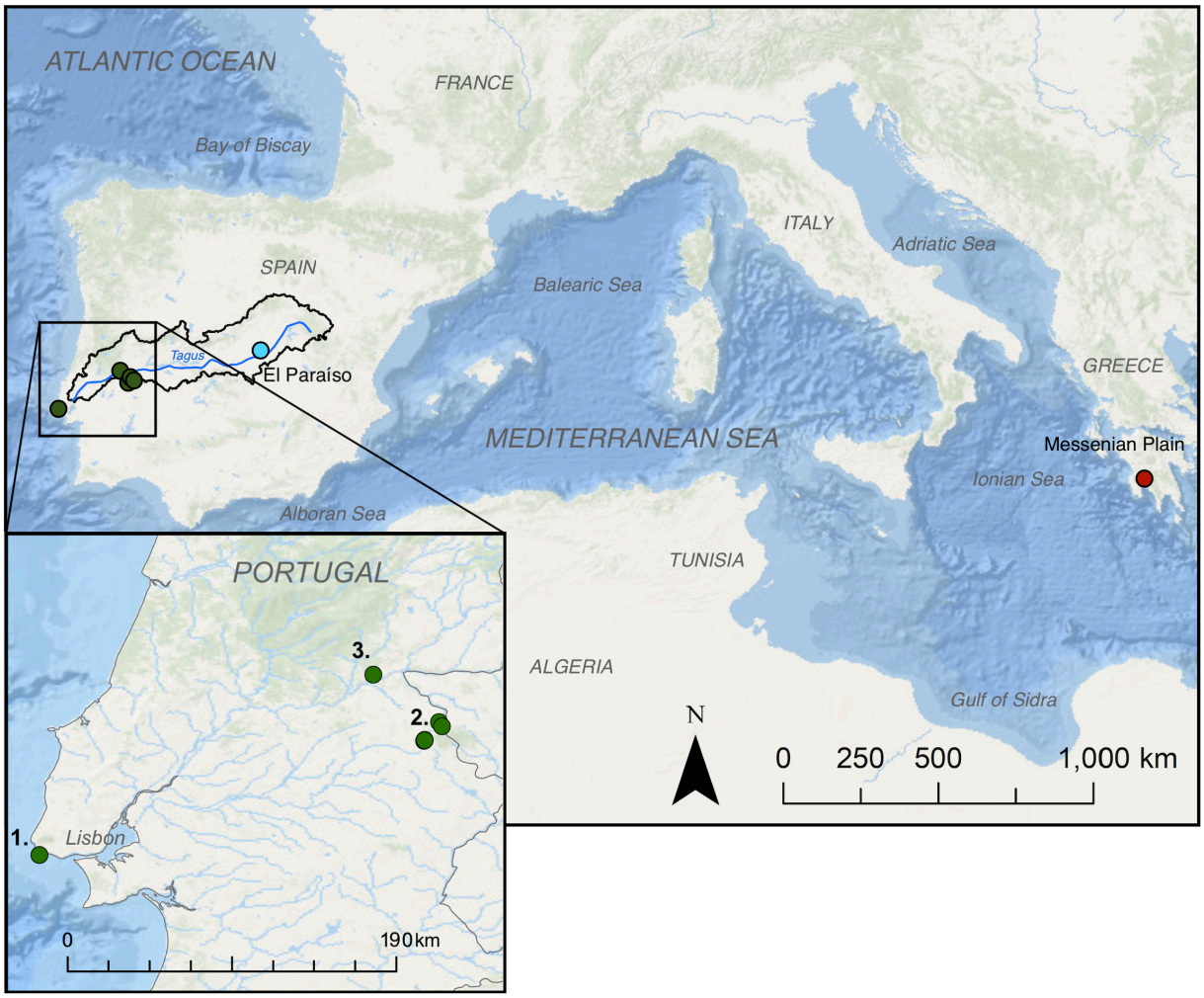

Fig. 7.3: Main map: Locations of modern leaf-wax samples from Portugal, (green; this study), El Paraíso, Central Spain (blue; Schäfer *et al.,* 2016), and the Messenian Plain, Greece (red; Norström *et al.,* 2017) also illustrating the Tagus River (blue line) and its catchment basin (black line). Inset: Sites from this study: 1. Sintra-Cascais Natural Park, Portuguese coast; 2. Serra de São Mamede; 3. Portas de Ródão.

Taxa	Pollen group	Plant functional group	Ecosystem	Site	Location		Dry weight of sample (g)
					Latitude	Longitude	
Quercus pyrenaica	Deciduous *Quercus*	WA	sM	2	39.30	-7.41	0.70
Quercus suber	*Quercus suber*	WA	M	2	39.38	-7.32	0.09
Quercus ilex	Evergreen *Quercus*	WA	M	3	39.65	-7.68	0.530
Olea europaea	*Olea*	WA	M	3	39.65	-7.68	0.26
Cistus salviifolius	*Cistus*	WA	G	2	39.30	-7.41	0.14
Cistus crispus	*Cistus*	WA	G	3	39.65	-7.68	0.07
Pinus pinaster	*Pinus*	WG	M	2	39.30	-7.41	0.49
Juniperus turbinata	*Juniperus*	WG	M	1	38.70	-9.45	0.50
Chenopodium album	Amaranthaceae	F	C	1	38.70	-9.45	0.06
Rumex acetosella A	Polygonaceae	F	C	1	38.70	-9.45	0.13
Rumex acetosella B	Polygonaceae	F	C	1	38.70	-9.45	0.11
Glebionis coronaria	Asteroideae	F	C	2	39.30	-7.41	0.08
Thapsia villosa	Apiaceae	F	sM	2	39.30	-7.41	0.31
Carduus pycnocephalus	Asteroideae	F	sM	2	39.38	-7.32	0.18
Leucanthemum vulgare	Asteroideae	F	sM	2	39.40	-7.34	0.03
Andryala integrifolia	Cichorioideae	F	sM	3	39.65	-7.68	0.11
Crepis vesicaria	Cichorioideae	F	sM	2	39.31	-7.41	0.14
Tolpis barbata	Cichorioideae	F	sM	3	39.65	-7.68	0.09
Briza maxima	Poaceae	Gr	GL	2	39.30	-7.41	0.08
Bromus diandrus	Poaceae	Gr	GL	2	39.40	-7.34	0.10
Lagurus ovatus	Poaceae	Gr	GL	1	38.70	-9.45	0.07

WA: Woody angiosperm; WG: Woody gymnosperm; Gr: Graminoid; F: Forb

C: cultivated; GL: grassland; G: garrigue; M: maquis; sM: sub-Mediterranean

1: Portuguese coast; 2. Serra de São Mamede; 3. Portas de Ródão

Table 7.1: Species collected from Portugal (this study), including pollen group, plant functional group, typical ecosystem, sample site and coordinates, and total dry weight of leaf sample (g).

7.2.2. Leaf-wax n-alkane extraction

Performed at the Biogeoscience Laboratory, ETH, Zürich, a two-step method was used to extract leaf-waxes from our samples, which is outlined below and illustrated in Fig. 7.4.

Stage 1. *Total Lipid Extraction:* Into a 40 ml glass centrifuge tube, 2 ml of methanol was added to the leaf sample to extract the lipids, before sonicating for 10 minutes to break cell walls. 18 ml of DCM was added to transfer lipids into the solvent, before reducing the DCM:Hex (9:1) using a heat block and nitrogen evaporator. 20 ml of Hex:DCM (4:1) was added to take any remaining hydrocarbons into the solvent; this was reduced and ~1 ml of Hexane added.

Stage 2. *Column Chromatography:* The chromatography column was set-up as outlined in section 4.3.1. Two drops of hexane were added to the samples, dissolving the *n*-alkanes within. A glass pipette transferred the solvent into the column, trapping all fractions in the silica gel bar the hexane and *n*-alkane solution which moved into the first 4 ml vial. The initial vial was cleaned twice with hexane, followed by a wash of the column, to ensure the complete transfer of all *n*-alkanes into the 4 ml vial. This was blown down and transferred into a 2 ml vial ready for quantification and distribution analysis on the GC-FID.

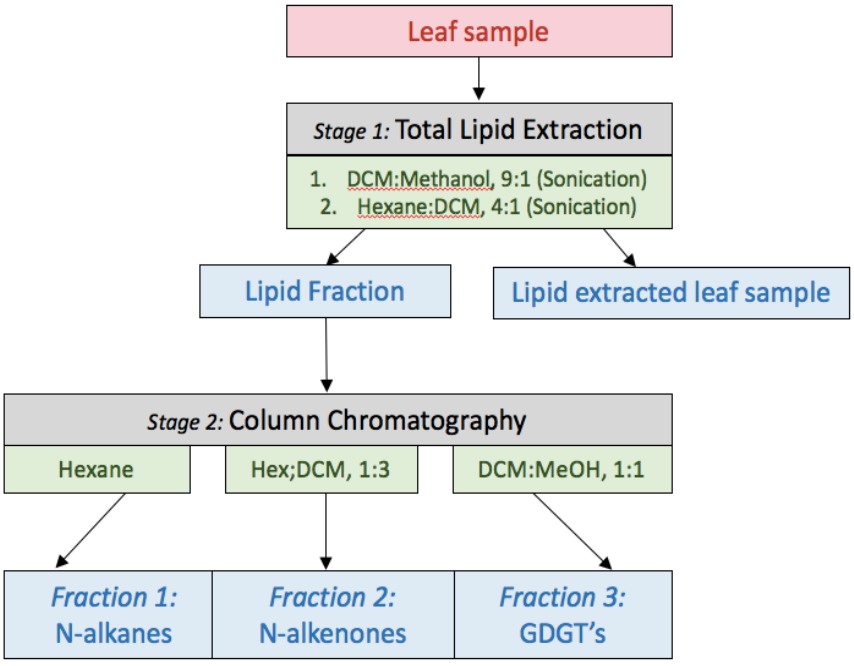

Fig. 7.4: *n*-Alkane extraction method from dried leaf sample (red), outlining the two method stages (black), chemicals used for extraction (green), and the fractions extracted from the sediment during the process (blue).

7.2.3. n-Alkane quantification

The concentration of each long-chain *n*-alkane homologue was quantified using the GC-FID (outlined in section 5.2.1.1) (Appendix 14 and 15). Each sequence was run with our external standard (outlined in section 5.1.2) to identify the retention time of each *n*-alkane homologue, and a number of blanks to monitor the working of the GC-FID and trace any artificial contamination. The typical sequence involved one hexane blank, one standard injection, then the *n*-alkane samples which were interposed by a hexane blank every three/four vials. The peak area of all odd and even long-chain *n*-alkane homologues in each sample was calculated on GC-FID 2 (Table 5.3). The *n*-alkane concentration per gram of dry leaf was calculated for odd and even homologues that were reflective of vascular plants (C_{25} to C_{35}). Equation. 5.2 was used to calculate the concentration of each homologue, which will hereafter be described in μg per gram of dry leaf weight (μg g^{-1}). Finally, the combined concentration of all odd long-chain *n*-alkanes (C_{25} – C_{35}) were calculated and will hereafter be referred to as the total concentration. The total concentration was calculated using the sum of all long-chain odd *n*-alkanes in the sample that were representative of vascular plants (C_{25} – C_{35}). The CPI and ACL were calculated for each taxon using Equations. 5.3a & b, respectively. The chromatograms showed clean peaks of the long-chain *n*-alkanes of interest meaning no further cleaning was required to remove highly-branched or cyclic structures.

7.2.4. Biomarker Isotope Analysis

Carbon isotope measurements were performed at the Lyell Centre, Heriot-Watt University (GC-MS details in Table 5.3). The methods are outlined in detail in section 5.2.3. All isotopic measurements are defined relative to a reference gas and calibrated to Vienna Pee Dee Belemnite (VPDB), with all values expressed in permil (‰) units. Each sample was measured in duplicates or triplicates. The standard deviation (± 1σ) for each sample did not exceed 0.74, with an average of 0.12 (Appendix 16). One exception was *Pinus pinaster*, where the isotopic composition of the dominant homologues could not be accurately measured; consequently, this sample is excluded from further analysis. As the leaf-wax of each species was composed of a range of *n*-alkane homologues, each with different concentrations, the weighted average of $\delta^{13}C$ was calculated for each taxon as follows (Equation. 7.1) and will be expressed hereafter as $\delta^{13}C_{n\text{-alkane}}$:

$$\delta^{13}C_{n-alkane} = (\delta^{13}C_{27} \times W_{27}) + (\delta^{13}C_{29} \times W_{29}) \ldots / (W_{27} + W_{29} \ldots)$$

Equation. 7.1: Formula for calculating *n*-alkane $\delta^{13}C$ weighted average ($\delta^{13}C_{n\text{-}alkane}$; ‰ VPDB) using the $\delta^{13}C$ of each *n*-alkane homologue present in the leaf-wax of the species, and the weight (W) given to each homologue, calculated using its dry leaf concentration (μg g^{-1}).

7.2.5. Statistical Analyses

Leaf-wax data from our Portugal record were analysed using Principal Component Analysis (PCA). PCA is based on a correlation matrix, with the aim of reducing the dimensions of the multivariate dataset, and ordinate taxa and variables on principal component axes in order to explore potential correlations between our variables. The PCA was performed using the code-based platform, R, utilising the packages 'factoextra' and 'FactoMineR'. Data were standardised to stabilise variance, enabling extraction and visualisation of the multivariate analyses. Measured leaf-wax *n*-alkane variables (continuous datasets) were used to explain the variations between the different species. These include ACL, CPI, $\delta^{13}C$ (‰ VPDB), and total *n*-alkane concentration (μg g^{-1}). Two quantitative supplementary variables (ordinal datasets) were also added to the PCA. These were heat tolerance and drought tolerance, with values assigned to each species based on resources from the literature (e.g. Baquedano & Castillo, 2007; Castillo *et al*., 2002; Lapidot *et al*., 2019). A value of 5 was assigned to the least tolerant vegetation, with 1 representing the most tolerant to extreme drought/heat (Appendix 17). While the supplementary variables are not used in the PCA computation, the aim is to use these variables to explore any potential correlations between the heat/drought tolerance of a plant and its leaf-wax *n*-alkane composition.

7.3. Results

7.3.1. N-alkane distributions

The taxa in our dataset (n = 21) show a considerable range of *n*-alkane concentrations (Table 7.2). *Olea europaea* demonstrates the highest total and dominant homologue concentration (C_{31}; 2,995.00 and 1,117.30 μg g^{-1}, respectively), while *Pinus pinaster* has the lowest (C_{29}; 8.40 and 3.24 μg g^{-1}, respectively). There is a strong positive correlation between the total *n*-alkane concentration and the dominant homologue concentration of individual species (r^2 = 0.74; p < 0.05). There is a large range in the CPI of taxa, which is skewed towards lower values (Table 7.2). *Carduus pycnocephalus* has the highest CPI (66.57), while *Andryala integrifolia* has the lowest (4.01). ACL varies considerably between taxa in the dataset (Table 7.2), with *Juniperus turbinata* demonstrating the highest ACL (33.27) and *Thapsia villosa* showing the lowest values (27.50). $\delta^{13}C_{n\text{-alkane}}$ ranges from -26.83 ‰ (*Juniperus turbinata*) to -40.22 ‰ (*Andryala integrifolia*), with a mean value of -35.93 ‰. Similar carbon isotope measurements were provided by two individual plants of same species (*Rumex acetosella*), while different *Quercus* species, all sampled from different locations, showed similar $\delta^{13}C_{n\text{-alkane}}$ values. The two *Cistus* species, however, displayed $\delta^{13}C_{n\text{-alkane}}$ values that differed by 1.6 ‰.

As highlighted by the ternary diagrams (Fig. 7.5), C_{29} and C_{31} are the most abundant chain-lengths in nearly all taxa in our dataset. In 15 of the 21 samples, C_{29} is the dominant homologue, as shown in Table 7.2. Fig. 7.5a. shows *Thapsia villosa* and *Crepis vesicaria* clearly separated from other taxa by the C_{27}homologue, which is their dominant chain-length. *Quercus pyrenaica* and *Pinus pinaster* also have a moderate proportion of C_{27}, but in both species the C_{29} homologue dominates. Fig. 7.5b and c show that few taxa are separated by high proportions of the shortest/longest homologues (C_{25} and C_{33}). *Thapsia villosa* alone demonstrates relatively high proportions of C_{25}, while all Poaceae species (in particular *Briza maxima*), *Olea europaea* and *Juniperus turbinata* are separated due to the high presence of C_{33}. *Juniperus turbinata* and *Briza maxima* show C_{33} to be their dominant homologue (Table 7.2).

Within each species, $\delta^{13}C_{n\text{-alkane}}$ varies between homologues (on average 0.87‰). While *Cistus crispus* demonstrates the greatest variation between homologues (2.45 ‰), *Leucanthemum vulgare* demonstrates the smallest difference (0.14 ‰). By max-min normalising the dataset (0-1)

(Fig. 7.6), it was possible to assess potential relationships between chain-length and $\delta^{13}C_{n\text{-alkane}}$ of each homologue. Unlike the SHAK06-5K fossil record, which demonstrates lower $\delta^{13}C_{n\text{-alkane}}$ with increasing chain-length, no clear trends are seen in the species of the modern record, with different taxa displaying different relationships between chain-length and homologue $\delta^{13}C_{n\text{-alkane}}$. Some taxa demonstrate a positive relationship between $\delta^{13}C_{n\text{-alkane}}$ and chain-length (ie. *Olea europaea* and *Carduus pycnocephalus*), others show a negative relationship (ie. *Quercus suber* and *Lagurus ovatus*), while many species show no relationship between these variables (i.e. *Quercus pyrenaica* and *Chenopodium album*). As the fossil record is an average of all the waxes of regional species, this could indicate that the fossil record is dominated by a small subset of species. Finally, $\delta^{13}C_{n\text{-alkane}}$ of each species' dominant chain-length (highlighted by square points in Fig. 7.6) demonstrates no consistent relationship with $\delta^{13}C_{n\text{-alkane}}$ of co-occurring homologues.

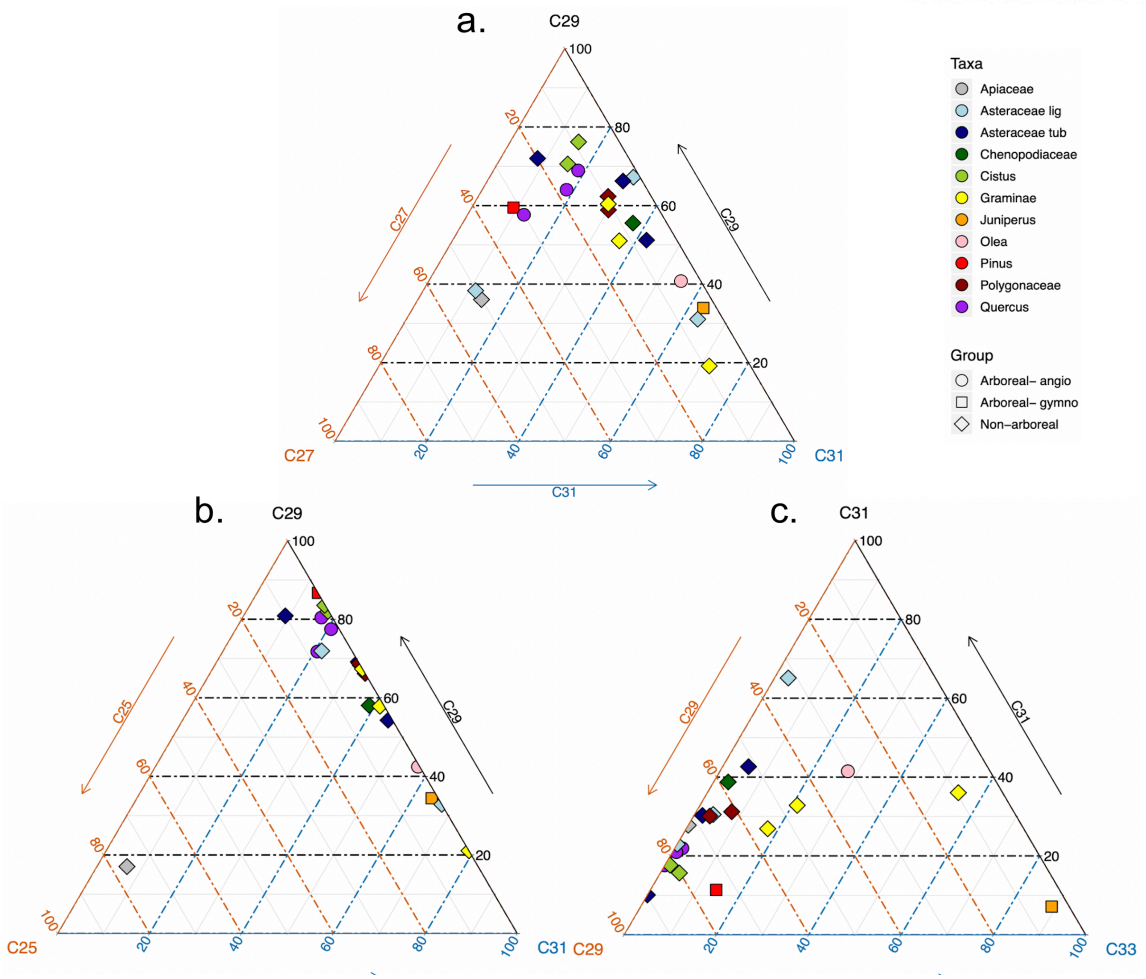

Fig. 7.5: Ternary diagram of *n*-alkane homologue abundance with taxa coloured either by genus or family. Diagrams show comparative proportions of homologues **a.** C_{27}, C_{29} and C_{31}; **b.** C_{25}, C_{29}, C_{31}; **c.** C_{29}, C_{31}, C_{33}

Taxon	Total amount of alkane in dry leaf (μg g^{-1})						Total amount C_{25}- C_{35} (μg g^{-1})	Dominant chain-length	ACL	CPI	$\delta^{13}C_{n\text{-alkane}}$ (‰ VPDB)
	C_{25}	C_{27}	C_{29}	C_{31}	C_{33}	C_{35}					
Juniperus turbinata	0.77	1.59	18.77	34.98	435.37	165.63	659.44	C_{33}	33.26	25.49	-26.83
Pinus pinaster	1.89	1.71	3.24	0.50	0.62	0.44	8.40	C_{29}	28.42	6.18	-32.00
Olea europaea	0.00	88.02	829.62	1117.30	747.21	212.85	2995.00	C_{31}	31.11	10.98	-33.04
Quercus pyrenaica	27.51	142.04	272.73	58.18	0.00	0.00	500.45	C_{29}	28.44	14.90	-33.42
Quercus suber	8.19	71.06	258.78	74.28	5.61	0.00	417.92	C_{29}	28.99	6.97	-33.77
Quercus ilex	2.26	18.02	98.60	26.41	1.06	0.00	146.35	C_{29}	29.08	9.85	-34.26
Cistus salviifolius	7.37	190.42	957.11	208.04	13.30	0.00	1376.23	C_{29}	29.04	17.43	-36.39
Cistus crispus	0.00	132.34	1135.12	221.88	58.52	0.00	1547.86	C_{29}	29.27	17.15	-38.06
Thapsia villosa	2.25	3.62	2.61	1.00	0.00	0.00	9.48	C_{27}	27.50	8.72	-35.34
Crepis vesicaria	11.69	52.83	40.31	12.03	0.00	0.00	116.86	C_{27}	27.90	7.34	-35.60
Andryala integrifolia	0.00	17.61	98.48	201.12	9.25	0.00	326.46	C_{31}	30.24	4.01	-40.22
Tolpis barbata	0.00	14.52	671.36	312.80	41.44	0.00	1040.13	C_{29}	29.73	15.19	-36.36
Leucanthemum vulgare	0.00	25.89	93.70	10.52	0.00	0.00	130.12	C_{29}	28.76	8.95	-36.33
Glebionis coronaria	4.75	19.76	313.14	139.60	8.43	0.00	485.67	C_{29}	29.52	22.74	-37.27
Carduus pycnocephalus	0.00	34.41	266.87	219.92	29.04	0.00	550.24	C_{29}	29.89	66.57	-35.34
Chenopodium album	11.64	44.68	335.71	224.02	18.29	0.00	634.33	C_{29}	29.61	14.60	-37.94
Rumex acetosella A	0.00	29.09	193.01	87.54	10.18	0.00	319.82	C_{29}	29.49	10.50	-39.72
Rumex acetosella B	3.69	15.79	84.16	42.97	10.61	0.00	157.23	C_{29}	29.52	9.56	-39.17
Bromus diandrus	0.00	34.83	203.72	98.77	64.81	3.17	405.29	C_{29}	30.00	51.76	-37.85
Lagurus ovatus	18.44	132.03	534.36	380.49	244.41	34.93	1344.67	C_{29}	30.20	9.84	-37.53
Briza maxima	8.75	9.77	20.85	78.20	118.05	8.02	243.64	C_{33}	31.55	19.77	-39.17

Table 7.2: For each taxon, the *n*-alkane concentration of each homologue, the total *n*-alkane concentration (C_{25}-C_{35}; μg g^{-1}), concentration of the dominant chain-length (μg g^{-1}), ACL, CPI, and $\delta^{13}C_{n\text{-alkane}}$ (weighted average; ‰ VPDB).

Fig. 7.6: $\delta^{13}C_{n\text{-alkane}}$ of long-chain homologues for each species in the modern record, (max-min normalised, 0-1, with 0 the more negative $\delta^{13}C$ values and 1 being less negative $\delta^{13}C$ values). Colour represents the chain-length, highlighting $\delta^{13}C_{C27}$ (yellow), $\delta^{13}C_{C29}$ (orange), $\delta^{13}C_{C31}$ (red), $\delta^{13}C_{C33}$ (dark red), $\delta^{13}C_{C35}$ (black), while squares represent the chain-length with the highest concentration.

Correlation analysis was applied to our data to assess relationships between the four *n*-alkane properties measured for each taxon (Fig. 7.7). The correlation coefficient (r) was calculated by applying Pearson product-moment correlation to normally distributed data (ACL and $\delta^{13}C_{n\text{-alkane}}$) and Spearman's Rank correlation to non-normal distributions (total *n*-alkane concentration and CPI). Although significant ($p < 0.05$), relatively weak correlations are shown between CPI and total concentration (r = 0.54), ACL and total concentration (r = 0.51), and ACL and CPI (r = 0.48). No significant correlation is shown between $\delta^{13}C_{n\text{-alkane}}$ and the other variables. All of the scatter plots are noisy and demonstrate a number of outlier values.

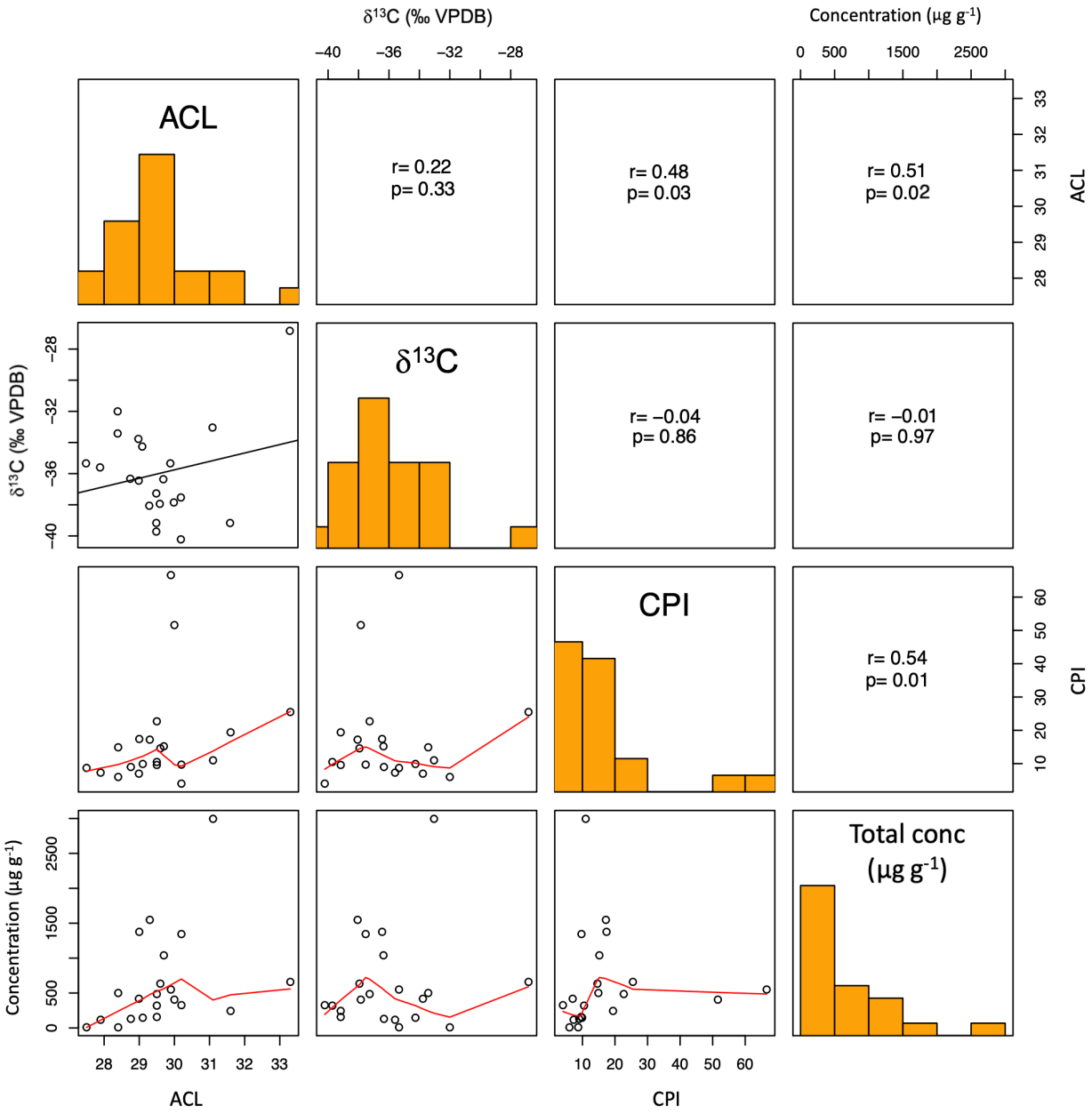

Fig. 7.7: Correlogram of the variables in our record. Diagonally central squares display histograms of each variable's distribution in the modern samples, while bottom squares show scatter plots of the data, including a linear regression curve for normally distributed data (black), and a local polynomial regression curve for non-parametric data (red). Upper squares illustrate the correlation between the variables (r ; applying Pearson product-moment correlation to normally distributed data and Spearman's Rank correlation to non-normal distributions), and the significance of the correlation ($p < 0.05$).

7.3.2. Plant functional groups

To assess potential differences in *n*-alkane concentration, homologue distribution, and isotope composition across plant functional groups (Fig. 7.8), taxa were grouped into woody angiosperms, woody gymnosperms, forbs, and graminoids, shown in Table 7.1. 'Woody angiosperms' encompasses all angiosperm trees and shrubs (n = 6), 'woody gymnosperms' includes gymnosperm trees and shrubs (n = 2), 'forbs' encompasses all angiosperm herbs, excluding grasses (n = 10), and 'graminoids' encompass all angiosperm grasses (n = 3). As shown in Fig. 7.8a, ACL varies between plant functional groups, with the lowest average shown in forbs (29.2), followed by woody angiosperms (29.3), graminoids (30.6), and woody gymnosperms (30.8). There is, however, considerable variation in the ACL of individual taxa within each plant group. Woody gymnosperms show the highest variation (4.8), followed by forbs (2.7), woody angiosperms (2.7), and graminoids (1.6). Fig. 7.8a shows two low ACL outlier values (*Thapsia villosa* (forb) and *Q. pyrenaica* (woody angiosperm)) and one high ACL outlier value (*Olea europaea* (woody angiosperm)). Fig. 7.8b shows the average CPI varies between groups, with woody angiosperms demonstrating the lowest average (12.9), followed by woody gymnosperms (15.7), forbs (16.8), and graminoids (26.9). Although CPI is skewed towards lower values (~10 – 20), there is significant variation within each group with forbs showing the highest range (62.6), followed by graminoids (41.9), gymnosperms (19.5), and angiosperms (10.5). The single outlier in Fig. 7.8b is *Carduus pycnocephalus* (forb) which demonstrates an exceptionally high CPI. Total *n*-alkane concentration varies considerably within and between plant functional groups. On average, woody angiosperms have the highest total *n*-alkane concentration (Fig. 7.8d; 1,164 $\mu g\ g^{-1}$) and dominant chain-length concentration (Fig. 7.8c; 640 $\mu g\ g^{-1}$) as well as a large range of values for each variable (2,849 $\mu g\ g^{-1}$ and 1,037 $\mu g\ g^{-1}$, respectively). Woody gymnosperms demonstrate the lowest mean and range of values for total *n*-alkane concentration (334 $\mu g\ g^{-1}$ and 651 $\mu g\ g^{-1}$), while graminoids have the lowest mean and range of values for dominant chain-length concentration (151 $\mu g\ g^{-1}$ and 86 $\mu g\ g^{-1}$, respectively). The single outlier in Fig. 7.8c is *Tolpis barbata* which demonstrates a high dominant chain-length concentration. The large range in the leaf wax *n*-alkane ACL, CPI and concentration within plant functional groups, suggests that plant type does not have a strong control on the composition of leaf wax *n*-alkanes.

Compared to the other variables, the range of $\delta^{13}C_{n\text{-alkane}}$ values within each plant functional group is relatively small (Fig. 7.8e). The two woody gymnosperm species demonstrate a higher $\delta^{13}C_{n\text{-alkane}}$

than all other angiosperm species in this record, with a mean of -29.4 ‰. Of our angiosperm plant functional groups, woody vegetation has the next highest mean value (-34.6 ‰), followed by forbs (-37.3 ‰), and graminoids (-38.2 ‰). The small range of values within each plant functional group and the variation between their means suggests that a relationship may exist between plant functional group and $\delta^{13}C_{n\text{-alkane}}$.

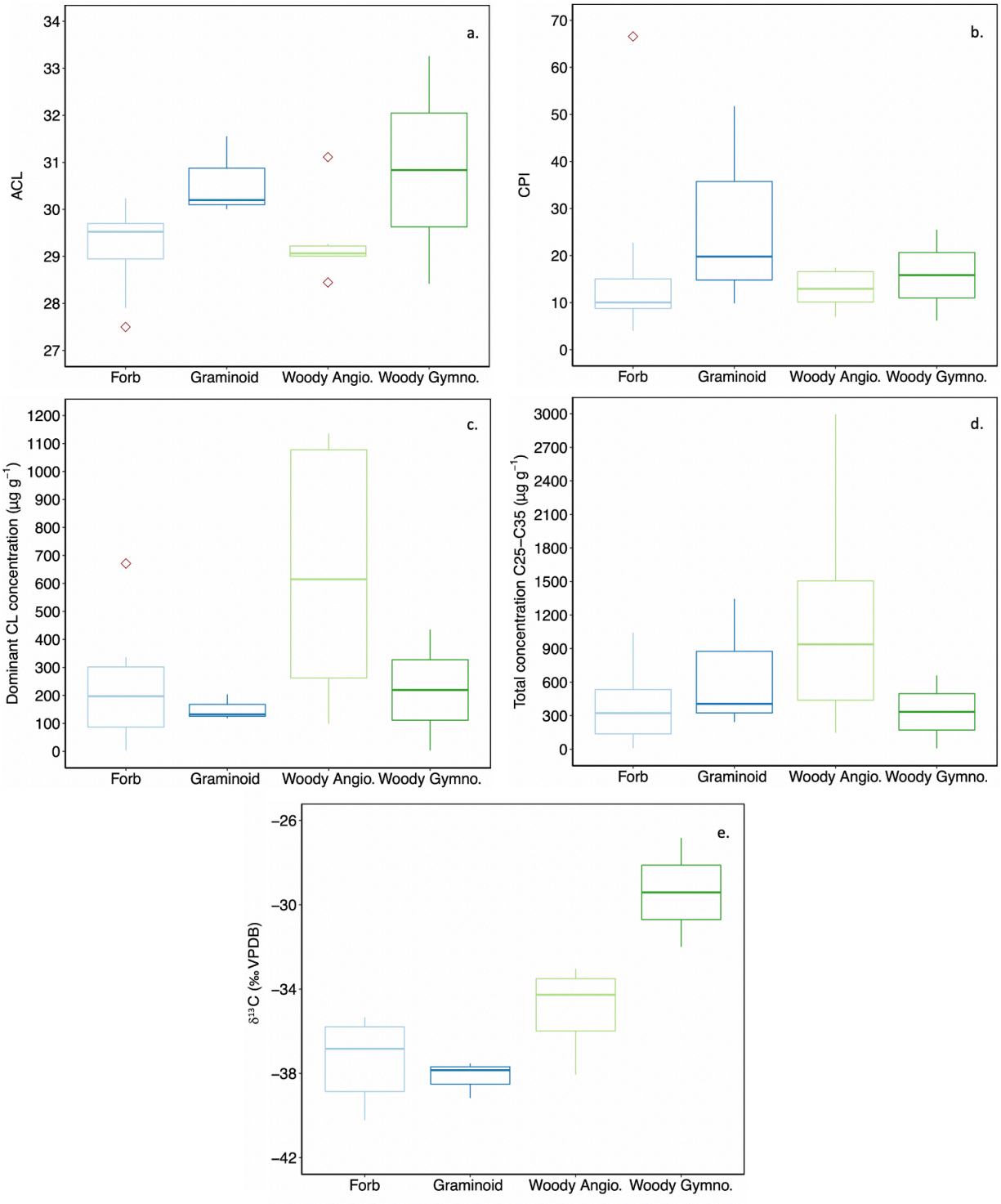

Fig. 7.8: Box plots split by plant functional group for **a.** ACL; **b.** CPI; **c.** dominant chain-length (CL) concentration (μg g^{-1}); **d.** total concentration C_{25}-C_{35} (μg g^{-1}); **e.** $\delta^{13}C_{n\text{-alkane}}$ (‰ VPDB). Each box represents the range of the middle 50% of the dataset, while the mid-line shows the mean value, and each whisker represents 25% of data. Red diamonds highlight outliers. Data from this study.

7.3.3. Principal Component Analysis

PCA was used to identify patterns and associations in the original data set by combining co-variables and highlighting relationships between leaf-wax *n*-alkane geochemical data and plant physiology (Table 7.3). This was conducted using leaf-wax *n*-alkane ACL, CPI, total concentration (μg g^{-1}), and $\delta^{13}C_{n\text{-alkane}}$ as the variables (Fig. 7.9; light blue vectors), and heat resistance and drought tolerance as supplementary variables (dark blue, dashed vectors). The results show that 64% of the variance between the species can be explained by the first two eigenvalues (Table 7.3). Principal component 1 (PC1) explains 39% of the total variation in the dataset, with all leaf-wax variables demonstrating a positive loading to PC1. ACL has the most positive loading followed by total concentration. Forbs generally show a negative loading to PC1, while graminoids primarily demonstrate a positive loading. PC2 explains 25% of the variance, with CPI demonstrating a high positive loading to PC2, and total concentration and $\delta^{13}C_{n\text{-alkane}}$ showing a negative loading. Woody angiosperms generally show a negative loading to PC2. With the angle between vectors signifying the correlation between variables, heat resistance and drought tolerance display a strong positive correlation with each other and a positive correlation with ACL.

	PC1	PC2	PC3	PC4
Correlation dimension				
ACL	0.83	0.07	-0.12	-0.54
$\delta^{13}C_{n\text{-alkane}}$	0.51	-0.31	0.79	0.14
CPI	0.47	0.83	0.02	0.31
Total concentration	0.63	-0.47	-0.50	0.37
Eigenvalue	1.57	1.00	0.89	0.54
Cumulative % of variance	39.18	64.12	86.40	100.00

Table 7.3: Principal component analysis of leaf-wax *n*-alkane measurements. Data from this study.

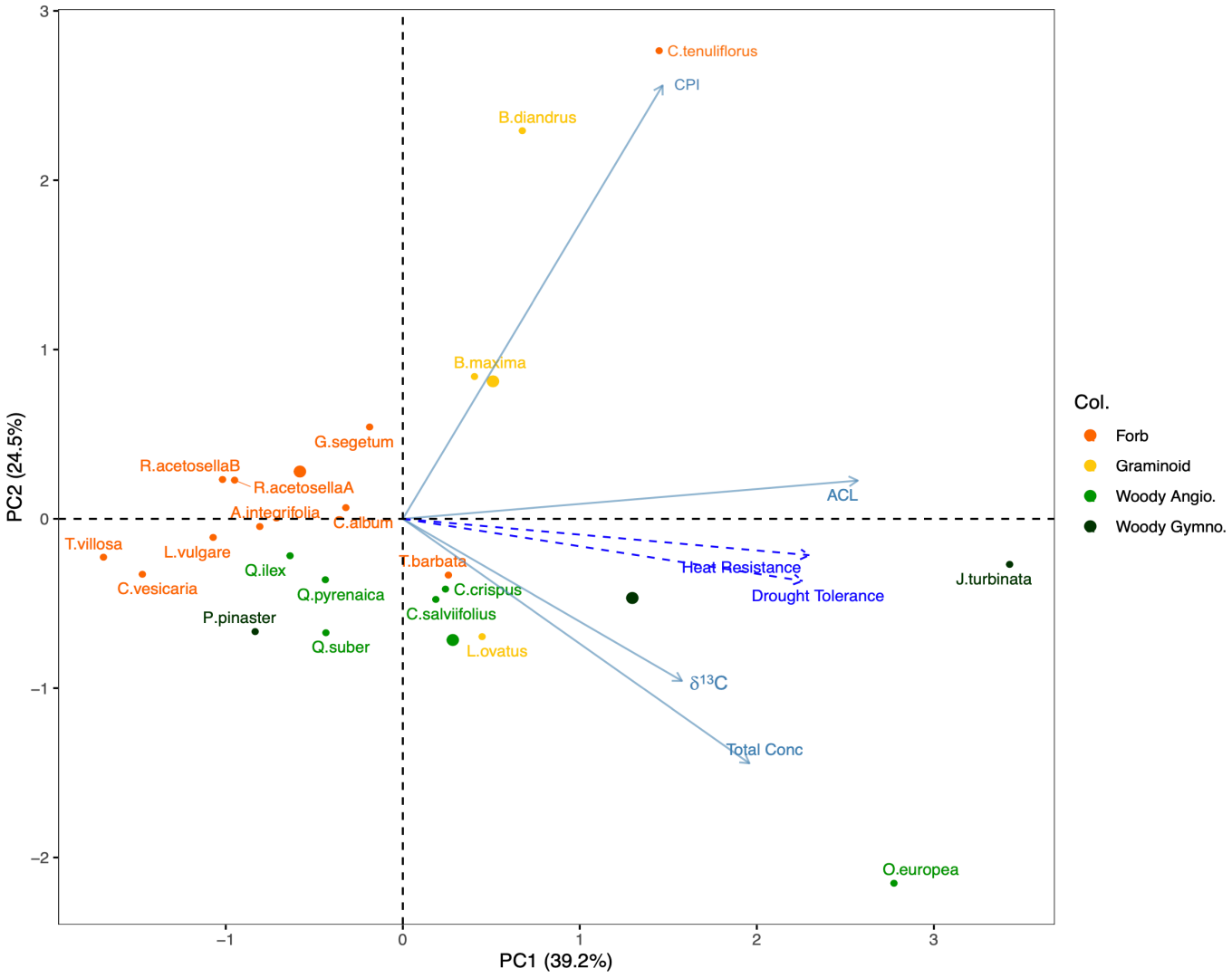

Fig. 7.9: Biplot of the species collected in this study, showing the vectors of the leaf-wax *n*-alkane variables ACL, CPI, $\delta^{13}C_{n\text{-alkane}}$ (‰ VPDB), total concentration (µg g^{-1}) (solid light blue lines). The vectors of the supplementary variables, heat resistance and drought tolerance, are also shown (dashed dark blue lines). The small dots represent each plant species, coloured according to their plant functional group, while the large dots represent the plant functional group.

7.3.4. Comparison to existing modern Mediterranean leaf-wax n-alkane records

To further explore the leaf-wax *n*-alkane homologue distributions and isotopic composition of Mediterranean taxa, the dataset from this study has been combined with two existing leaf-wax records from the Mediterranean (Schäfer *et al.,* 2016; Norström *et al.,* 2017). While the research sites are shown in Fig. 7.3, the species sampled at both locations are detailed in Table 7.4.

Taxa	Pollen group	Plant functional group	Ecosystem	Site	ACL	Total *n*-alkane concentration C_{25}-C_{35} (μg g^{-1})	$\delta^{13}C_{bulk}$	Author
Juniperus phoenicea	*Juniperus*	WG	M	El Paraíso	32.89	78.87	-	Schäfer *et al*., 2016
Juniperus thurifera	*Juniperus*	WG	M	El Paraíso	32.65	113.70	-	Schäfer *et al*., 2016
Olea europaea	*Olea*	WA	M	El Paraíso	32.17	112.03	-	Schäfer *et al*., 2016
Olea europaea	*Olea*	WA	M	El Paraíso	29.14	122.02	-	Schäfer *et al*., 2016
Pinus halepensis	*Pinus*	WG	M	El Paraíso	30.04	2.39	-	Schäfer *et al*., 2016
Pinus nigra	*Pinus*	WG	Mo	El Paraíso	31.71	5.35	-	Schäfer *et al*., 2016
Quercus ilex	Evergreen *Quercus*	WA	M	El Paraíso	29.25	90.32	-	Schäfer *et al*., 2016
Stipa tenacissima	Poaceae	Gr	GL	El Paraíso	30.97	284.50	-	Schäfer *et al*., 2016
Thymus vulgaris	Lamiaceae	WA	G	El Paraíso	31.82	352.29	-	Schäfer *et al*., 2016
Arundo donax	*Poaceae*	Gr	sM	Messenian Plain	28.06	273.34	-28.44	Norström *et al*., 2017
Acer sempervirens	*Acer*	WA	Mo	Messenian Plain	29.95	222.94	-28.28	Norström *et al*., 2017
Ceratonia siliqua	*Ceratonia*	WA	M	Messenian Plain	30.56	70.62	-28.89	Norström *et al*., 2017
Calicotome spinosa	*Fabaceae*	WA	M	Messenian Plain	29.70	36.11	-30.08	Norström *et al*., 2017
Daucus carota	*Apiaceae*	F	sM	Messenian Plain	28.53	59.47	-29.45	Norström *et al*., 2017
Ficus carica	*Ficus*	WA	sM	Messenian Plain	29.18	122.19	-26.99	Norström *et al*., 2017
Juniperus phoenicea	*Juniperus*	WG	M	Messenian Plain	33.38	499.83	-25.53	Norström *et al*., 2017
Nerium oleander	*Nerium*	WA	G	Messenian Plain	32.60	607.74	-26.36	Norström *et al*., 2017
Olea europaea	*Olea*	WA	M	Messenian Plain	31.11	452.41	-26.31	Norström *et al*., 2017

Phillyrea latifolia	*Phillyrea*	WA	M	Messenian Plain	30.49	148.88	-28.60	Norström *et al*., 2017
Pistacia lentiscus	*Pistacia*	WA	M	Messenian Plain	30.65	79.75	-29.24	Norström *et al*., 2017
Platanus orientalis	*Platanus*	WA	sM	Messenian Plain	30.84	870.48	-31.93	Norström *et al*., 2017
Pistacia terebinthus	*Pistacia*	WA	M	Messenian Plain	27.38	21.16	-29.02	Norström *et al*., 2017
Phlomis fruticosa	Lamiaceae	F	G	Messenian Plain	31.37	4915.77	-27.29	Norström *et al*., 2017
Quercus coccifera	Evergreen *Quercus*	WA	M	Messenian Plain	29.24	152.08	-28.65	Norström *et al*., 2017
Quercus ilex	Evergreen *Quercus*	WA	M	Messenian Plain	29.43	182.17	-29.60	Norström *et al*., 2017
Rosmarius officinalis	Lamiaceae	WA	G	Messenian Plain	31.79	2202.80	-26.56	Norström *et al*., 2017
Sarcopoterium spinosum	Rosaceae	WA	M	Messenian Plain	31.47	1194.90	-27.68	Norström *et al*., 2017
Salvia triloba	Lamiaceae	F	M	Messenian Plain	32.59	1581.00	-29.05	Norström *et al*., 2017
Thymus capitatus	Lamiaceae	WA	G	Messenian Plain	30.81	588.99	-28.69	Norström *et al*., 2017
Vitex agnus castus	Lamiaceae	WA	G	Messenian Plain	33.15	1797.97	-27.11	Norström *et al*., 2017

WA: Woody angiosperm; WG: Woody gymnosperm; Gr: Graminoid; F: Forb

GL: grassland; G: garrigue; M: maquis; sM: sub-Mediterranean; Mo: Montane

Table 7.4: Species collected from El Paraíso, Spain (Schäfer *et al*., 2016) and the Messenian Plain, Greece (Norström *et al*., 2017) including pollen group, plant functional group, typical ecosystem, sample site, ACL, total *n*-alkane concentration and leaf bulk $\delta^{13}C$.

The relationship between total *n*-alkane concentration and wider ecological variables is explored in Fig. 7.10. Of the plant functional groups, forbs show the highest mean total *n*-alkane concentration (348 μg g^{-1}) with two high outlier values (*P. fructicosa and S. triloba;* 1,581 and 4,916 μg g^{-1}, respectively), while woody gymnosperms have the lowest mean total concentration (467 μg g^{-1}). On average, graminoids and woody angiosperms have similar mean total *n*-alkane concentrations, but the latter displays two high outlier values (*O. europaea and R. officinalis;* > 2000 μg g^{-1}). When assessing the relationship between total *n*-alkane concentration and ecosystem, cultivated, grassland, montane and sub-Mediterranean species show a low distribution of values as well as a low mean, although this is likely influenced by small sample sizes (n = < 4) in the first three groups. Maquis vegetation, on average, has a low total *n*-alkane concentration, contrary to the high mean of garrigue species, but both demonstrate a wide range of values. In more heat tolerant vegetation, the mean and range of total *n*-alkane concentration values appear to be higher than in less heat tolerant vegetation. This pattern is also shown between total *n*-alkane concentration and drought tolerance. When assessing the variation in total *n*-alkane concentration according to sampling site, the highest mean is seen in samples from Portas de Ródão, while vegetation from El Paraíso has the smallest mean and a small distribution in total *n*-alkane concentration values.

Potential relationships between the ACL of Mediterranean species and wider ecological variables are explored in Fig. 7.11. It is, however, acknowledged that the limited sample size of some variable groups may have led to some sampling bias. When assessing the relationship between ACL and plant functional group, woody gymnosperms have a higher ACL, on average than woody angiosperms, but both groups cover a similar wide range of values. Graminoids have a similar mean ACL to woody angiosperms, but much smaller range, while forbs show the lowest mean ACL, but a wider distribution of values. When assessing the ACL of different species within the same genus, there is significant interspecies variation. While the four species of *Pinus* and two species of *Pistacia* (Table 7.1 and 7.4) show a considerable range in ACL (28.4 – 31.7 in the former, and 27.4 – 30.7 in the latter), other genera, such as the four species of *Quercus*, three species of *Juniperus*, and two species of *Cistus*, have ACL's that vary by < 1. Considerable variability is shown in the mean ACL of vegetation from different ecosystems. While garrigue taxa demonstrate the largest mean ACL (31.2), sub-Mediterranean vegetation has the lowest (29.0). There is high variation in the distribution of values within each ecosystem, but the low range of ACL values within cultivated, montane, and grassland vegetation is likely influenced by the small sample sizes. ACL appears to increase with higher

heat resistance; the largest mean ACL occurs in species with the highest tolerance to high temperatures, while the lowest values are in those with the least resistance. The ACL of taxa with middle resistance levels, however, show a large range with numerous outliers (n = 7). ACL shows a similar relationship with drought tolerance, with the highest mean ACL occurring in species with the greatest tolerance of water stress and the lowest values in those with the lowest tolerance. Similar to the PCA results using the data from Portugal (Fig. 7.9), there appears to be a relationship between the heat resistance and drought tolerance of a plant and its ACL. ACL does not show a strong relationship with site of sample collection, with the most westerly site (the Messenian Plain) demonstrating an extremely large range of values, likely reflective of the large sample size. Plants from El Paraíso have the largest mean ACL (31.2), while vegetation from the Serra de São Mamede site have the lowest mean ACL (29.2).

While the carbon isotope record from Portugal documents $\delta^{13}C_{n\text{-alkane}}$, the Messenian Plain $\delta^{13}C$ record analyses the carbon isotope composition of leaf tissue ($\delta^{13}C_{bulk}$). As we are unable to constrain lipid biosynthesis fractionation, these records cannot be directly compared. Two sclerophyllous species, *Olea europaea* and *Quercus ilex*, analysed by both studies show lower $\delta^{13}C_{n\text{-alkane}}$ than $\delta^{13}C_{bulk.}$ In *O. europaea*, $\delta^{13}C_{n\text{-alkane}}$ values are 6.8 ‰ lower than $\delta^{13}C_{bulk}$, while in *Q. ilex*, they are 5.2 ‰ lower. These values are similar to previous research which showed $\delta^{13}C_{n\text{-alkane}}$ in C_3 plants to be more depleted in ^{13}C compared to the leaf tissue by ~5.9 ‰ (Collister *et al.,* 1994).

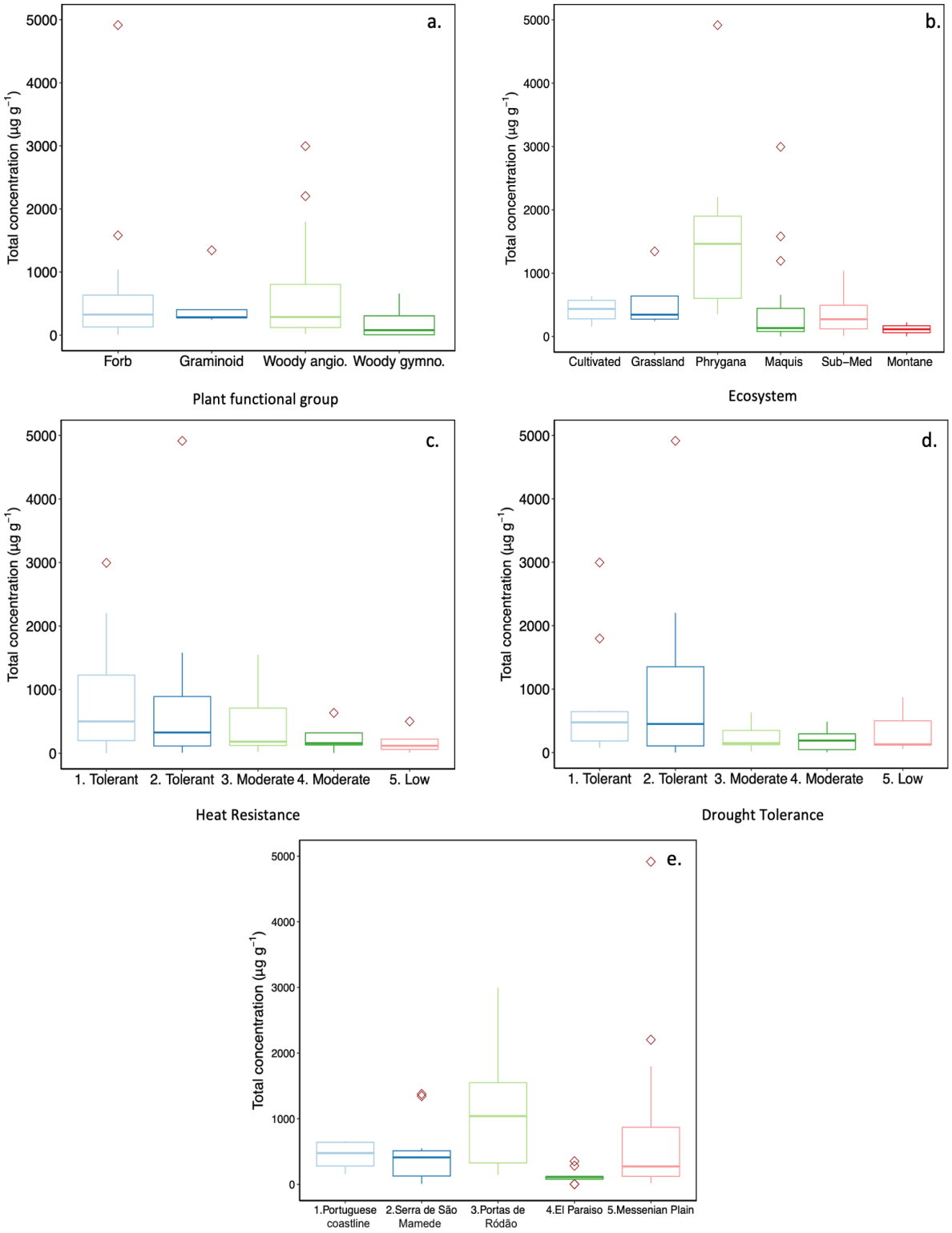

Fig. 7.10: Box plots for total concentration (µg g^{-1}) split by: **a.** plant functional group; **b.** ecosystem; **c.** heat resistance; **d.** drought tolerance; and **e.** site of sample collection. Each box represents the range of the middle 50% of the dataset, while the mid-line shows the mean value, and each whisker represents 25% of data. Red diamonds highlight outliers. Data from this study, Schäfer *et al.* (2016), and Norström *et al.* (2017).

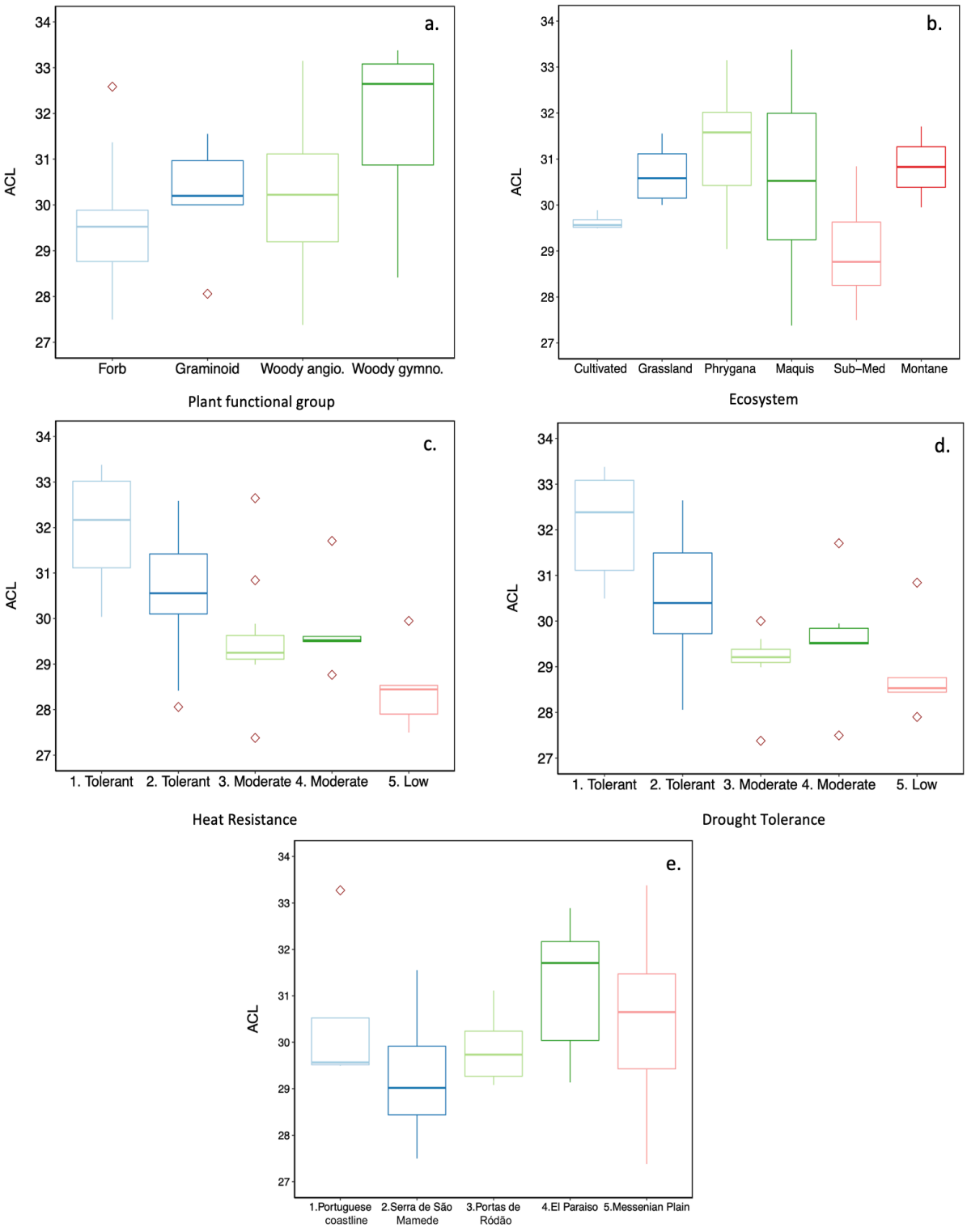

Fig. 7.11: Box plots for ACL split by: **a.** plant functional group; **b.** ecosystem; **c.** heat resistance; **d.** drought tolerance; and **e.** site of sample collection. Each box represents the range of the middle 50% of the dataset, while the mid-line shows the mean value, and each whisker represents 25% of data. Red diamonds highlight outliers. Data from this study, Schäfer *et al.* (2016), and Norström *et al.* (2017).

7.3.5. n-Alkane distribution in the fossil record

So as to use these modern leaf-wax records in the interpretation of the SHAK06-5K *n*-alkane records (see next section), these fossil records are presented here against age (Fig. 7.12), applying the chronology presented in Chapter 6. *n*-Alkane $\delta^{13}C$ ($\delta^{13}C_{C31}$) in the fossil record varies over the last 27.4 kyr (Fig. 7.12c), ranging from -30.2 to -32.9‰. While the highest $\delta^{13}C_{31}$ values occur during the Holocene, the lowest values are reached during HS1. During HS2 and the LGM, values remain steady and low, averaging ~-32.3‰. During HS1, there is considerably more variability, and although the lowest levels of the record (-33.0‰) are reached at 15.96 cal ka BP, higher values are seen at ~17.47 and 16.53 cal ka BP. Over the BA, $\delta^{13}C_{31}$ rises from -32.7‰ at the start of the stadial to -31.3‰ at the transition into the YD. The YD sees a slight decline in $\delta^{13}C_{31}$, averaging ~-31.5‰. From the transition into the Holocene, $\delta^{13}C_{31}$ rises from -31.36‰ to a peak of -30.3‰ at 8.36 cal ka BP. After this, $\delta^{13}C_{31}$ continues to decline through the mid-Holocene, reaching -32.0‰ at 5.19 cal ka BP. $\delta^{13}C_{31}$ then rises into the late Holocene, with increasing variability shown over this period, ranging from -30.2‰ at 2.54 cal ka BP to -31.83 at 0.6 cal ka BP.

Comparatively, $\delta^{13}C$ of atmospheric CO_2 ($\delta^{13}C_{atmos}$) (Fig. 7.12b) demonstrates a much smaller variation, ranging between -6.3 and -6.7‰ (Eggleston *et al.,* 2016). During MIS 2 the lowest values occur during the YD (-6.7‰) and HS1 (-6.7‰), while during the LGM (~-6.5‰) and BA higher values are reached (~-6.5 and ~-6.7‰, respectively). $\delta^{13}C_{atmos}$ gradually rises in the early Holocene, reaching the highest values of the record in the mid-Holocene (-6.3‰) and remaining high thereafter. The concentration of CO_2 in the atmosphere (pCO_2) (Fig. 7.12a) increases significantly over the deglaciation, rising rapidly from ~184 ppmv during the LGM to ~263 ppmv at 11.11 cal ka BP and rising more gradually thereafter to pre-industrial levels of 280 ppmv (Monnin *et al.,* 2004).

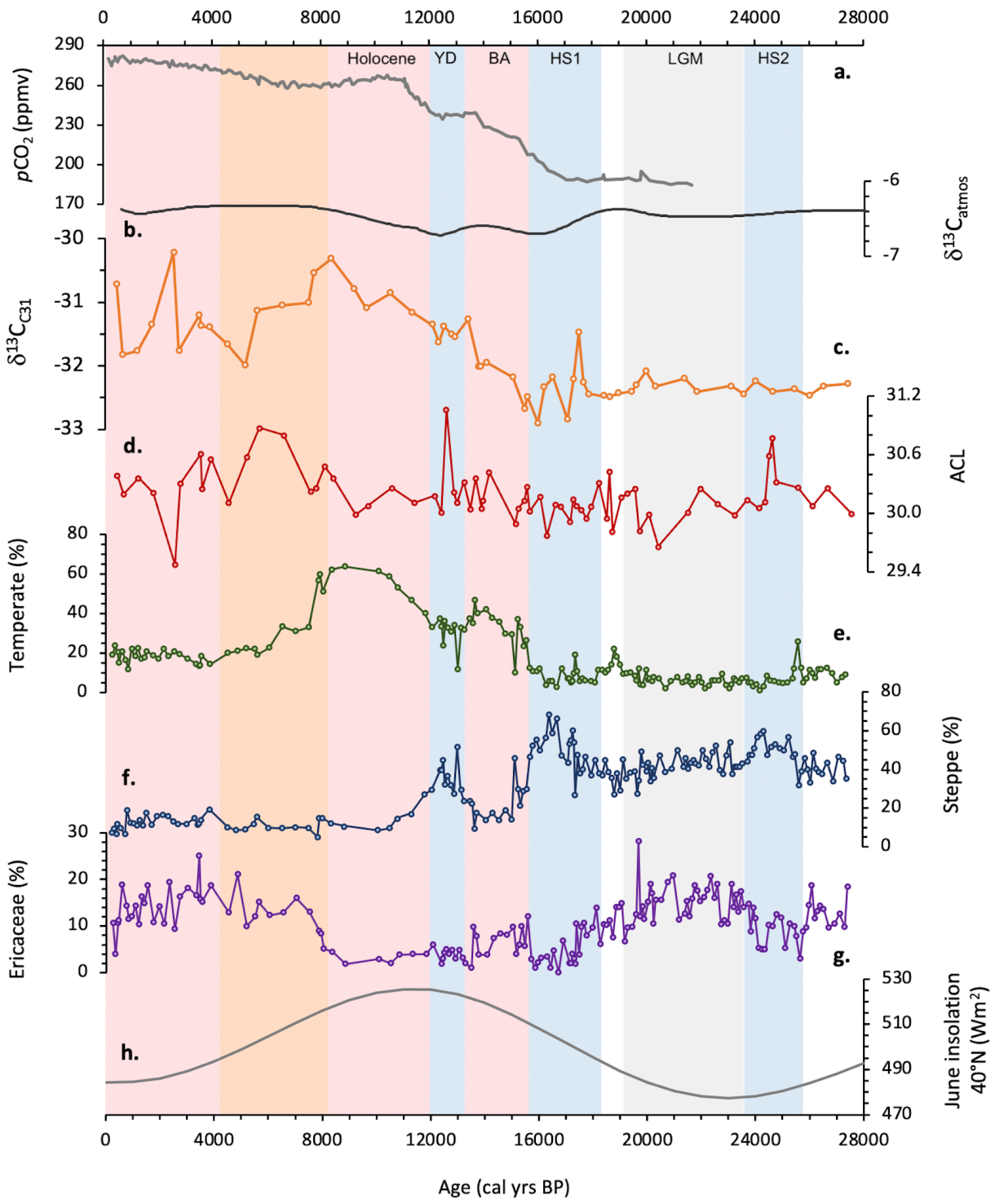

Fig. 7.12: Changes over time (cal yrs BP) in **a.** atmospheric CO_2 concentration (pCO_2) (ppmv) (Monnin *et al.,* 2004); **b.** $\delta^{13}C$ of atmospheric CO_2 ($\delta^{13}C_{atmos}$) (Eggleston *et al.,* 2016); **c.** *n*-alkane $\delta^{13}C_{C31}$ from SHAK06-5K (‰ VPDB); **d.** *n*-alkane ACL from SHAK06-5K; **e.** temperate pollen (%) from SHAK06-5K; **f.** steppe pollen (%) from SHAK06-5K; **g.** Ericaceae pollen (%) from SHAK06-5K; **h.** June boreal insolation (40°N; Wm^2) (Berger, 1978).

7.4. Discussion

7.4.1. Controls of total n-alkane concentration

All three Mediterranean datasets show significantly higher total *n*-alkane concentrations per gram of dry leaf mass in woody angiosperms than in woody gymnosperms, mirroring the findings of existing studies across other regions (Chikaraishi *et al.,* 2004; Diefendorf *et al.,* 2011; Bush & McInerney, 2013). Herbaceous taxa (forbs and graminoids) from this region also demonstrated larger total *n*-alkane concentrations than woody gymnosperms. These findings are significant for fossil records for two reasons. Firstly, sediments with terrestrial proxies sourced primarily from gymnosperms will have significantly lower *n*-alkane concentrations than regions dominated by angiosperm elements. This means that without supporting proxies such as pollen or macrofossils, total *n*-alkane concentration in the sediment record cannot be used as an indicator of regional biomass density, as it is heavily controlled by the composition of the source vegetation. Secondly, where *n*-alkanes are sourced from mixed vegetation containing gymnosperms, woody angiosperms and herbaceous elements, the gymnosperm signal will be underrepresented relative to that of the angiosperm taxa (Diefendorf *et al.,* 2011; Bush & McInerney, 2013). A parallel can be drawn to the treatment of some gymnosperm species in marine fossil pollen records. *Pinus* grains must be removed from palaeoclimatic reconstructions due to its over representation in marine sediments (Heusser & Balsam, 1977; Heusser, 1983), and as a consequence, neither leaf-wax *n*-alkane or marine pollen records can be reliably used to indicate the regional presence of gymnosperm vegetation compared to that of angiosperms.

7.4.2. Controls of CPI

Although the CPI in the Portuguese record demonstrates a significant correlation with both ACL and total *n*-alkane concentration, both relationships are weak (0.48 and 0.51, respectively; $p < 0.05$). Furthermore, no relationship is apparent between CPI and plant functional group showing that this variable cannot be used in the fossil record to signal the presence or dominance of a particular plant group. Although there is considerable variation in the CPI of species in the Portuguese record, no species demonstrates a CPI value under 4. This indicates that CPI remains a useful quantitative tool for assessing the degradation of *n*-alkanes in marine sediments in SW Iberia, as values < 1 indicate a significant input from petrogenic or degraded material (Bray & Evans, 1961; Eglinton & Hamilton, 1967; Kennicutt *et al.,* 1987). Further research on a greater range of species from this region, however, is required to support this conclusion.

7.4.3. Controls of ACL

The three Mediterranean datasets show ACL varies considerably across Mediterranean vegetation. There is also significant variability in homologue distribution between species within the same genus (as demonstrated by *Pinus pinaster, Pinus halepensis, and Pinus nigra* and *Pistacia lentiscus* and *Pistacia terebinthus*), but within a single species (*Olea europaea, Quercus ilex, Juniperus phoenicea, and Rumex acetosella*), similar ACL values are demonstrated, despite being sampled in different locations. This finding has been shown in previous research (Eglinton *et al.,* 1962). No relationship is demonstrated between plant functional groups and ACL in any of the records, despite this relationship having been previously implied for vegetation in other regions (Cranwell, 1973; Schwark *et al.,* 2002; Zech *et al.,* 2010; 2012). Consequently, we conclude that certain *n*-alkane chain-lengths cannot be used to represent certain plant functional groups in the Mediterranean region, but within some Mediterranean species, the distribution of *n*-alkane homologues appears to be similar.

The species with the highest ACL values from the three datasets are the three *Juniperus* species, *Vitex, Nerium, Olea, Salvia, Rosmarinus, Briza, Sarcopoterium, Phlomis*, and both *Thymus* species. All are from garrigue, maquis, and grassland ecosystems which are found on the drier end of the moisture gradient compared to sub-Mediterranean and montane ecosystems (Margaris & Vokou, 1982). To further explore the potential relationship between heat/drought and ACL, every species in all three datasets were assessed for their heat resistance and drought tolerance, because many of these species can be found in multiple ecosystems and coexist in the same ecosystem despite different tolerance levels. As has already been shown by Norström *et al.* (2017) in the Messenian Plain dataset, the most drought tolerant and heat resistant species from all three locations demonstrate the highest ACL values. This relationship in the Portuguese dataset was further explored by PCA which demonstrated that drought resistance, heat tolerance and ACL are the key explanatory variables of the variation between these taxa. Furthermore, drought and heat tolerance show a strong positive relationship with ACL. Previous research has linked higher ACL of terrestrially sourced *n*-alkanes to lower latitudes and consequently increased temperatures/aridity (Poynter *et al.,* 1989; Tipple & Pagani, 2013; Bush & McInerney, 2015). Here, I suggest that the ACL of cuticular *n*-alkanes of Mediterranean vegetation is closely linked to the drought and heat tolerance of the plant and therefore, the climatic conditions it is exposed to.

7.4.4. Mechanisms driving ACL

It is acknowledged that increased crystallinity and a higher melting point lowers the permeability of the cuticular wax (Riederer & Schneider, 1990). Although cuticular waxes are composed of both long-chain lipids (≤ C_{40}) and shorter-chain lipids (C_{20}-C_{38}; which includes *n*-alkanes), steric hindrances form between chains of different lengths, meaning the greater the chain-length distribution, the larger the amorphous zone and the lower the crystallinity (Riederer & Schneider, 1990; Reynhardt, 1997). The higher the ratio of short chain lipids to long-chain lipids, the smaller the steric hindrances and chain-length distribution, which consequently increases the wax crystallinity (Reynhardt, 1997).

Here, we suggest that as a drought avoidance mechanism, some plants benefit from higher ACL of their *n*-alkanes which consequently increases the chain-length distribution of the 'shorter-chain lipids' (C_{20} – C_{38}). This increases the volume of crystallites as well as the melting point of the wax because the longer the lipid chain-length, the higher its melting point. This enables the wax to maintain a high proportion of 'shorter-chain' hydrocarbons which reduces steric hinderances by decreasing the chain-length distribution, whilst increasing the volume fraction of crystallites. This potentially explains why it is beneficial in Mediterranean environments for plants under extreme temperature and drought stress to produce longer 'shorter-chain' lipids in order to reduce cuticular permeability, despite the increased energy required to do so. With previous research showing lower cuticular permeability in species better adapted to drought conditions (Kirsch *et al.,* 1997), we suggest that ACL is a localised ecological adaptation at molecular level to the water availability of a species' habitat.

7.4.5. Dominant drivers of $\delta^{13}C$ variations in the modern record

When assessing $\delta^{13}C$ of *Juniperus*, the only gymnosperm genus which garnered accurate isotopic results, both $\delta^{13}C_{n\text{-alkane}}$ of *Juniperus turbinata* and $\delta^{13}C_{bulk}$ of *Juniperus phoenicea* demonstrate the highest values of the Portuguese and Greek datasets, respectively. Previous research has shown the extent of both photosynthesis carbon fractionation and lipid biosynthesis fractionation varies between angiosperms and gymnosperms (Brooks *et al.,* 1997; Chikaraishi & Naraoka, 2003; Diefendorf *et al.,* 2010), and while our work cannot draw any firm conclusions from a single gymnosperm genus, it does indicate an area of interest for future research. $\delta^{13}C_{n\text{-alkane}}$ and $\delta^{13}C_{bulk}$ varies between angiosperm plant functional groups, with woody taxa demonstrating higher $\delta^{13}C$ values than herbaceous taxa in both records. This

variation suggests that a significant proportion of carbon isotope fractionation in Mediterranean vegetation is driven by the plant's functional group.

While the Mediterranean vegetation in both the Portuguese and Messenian Plain datasets display a wide range of $\delta^{13}C_{n\text{-alkane}}$ and $\delta^{13}C_{bulk}$ values, plant samples from the same species/genus demonstrate similar $\delta^{13}C_{n\text{-alkane}}$ (*Rumex acetosella* and *Quercus*) and $\delta^{13}C_{bulk}$ values (*Pistacia* and *Quercus*). These similarities occur despite many of the plants having been sampled from different locations, and consequently, exposed to varying local geological, ecological, and climatic conditions. This suggests that internal biological mechanisms are the dominant driver of the carbon isotopic signature within a species/genus, rather than external environmental conditions. Within families, however, $\delta^{13}C_{n\text{-alkane}}$ can vary significantly (i.e. Asteraceae), as does $\delta^{13}C_{bulk}$ (i.e. Lamiaceae and Oleaceae), suggesting that the biological mechanisms controlling plant carbon isotope fractionation differ between genera within the same family. While moisture availability can significantly influence a plant's carbon isotope fractionation during CO_2 uptake (Madhavan *et al.,* 1991; Ehleringer *et al.,* 1992; Pancost & Boot, 2004; Diefendorf *et al.,* 2010; Prentice *et al.,* 2011; Freeman & Pancost, 2013), this fractionation is suggested to be similar within and between angiosperm species, plant functional groups, and communities (Wittmer *et al.,* 2008; Prentice *et al.,* 2011). Existing research on two Mediterranean *Quercus* species found similar $\delta^{13}C$ values within each species (with a total range of 4.4 and 3.1‰ for *Q. pubescens* and *Q. ilex*, respectively), despite samples having been taken across four Mediterranean sites with varied water availability (Damesin *et al.,* 1997). In the Portuguese record, different species at each site show a wide range of $\delta^{13}C_{n\text{-alkane}}$ values; similarly, the $\delta^{13}C_{bulk}$ values (all sampled from the Messenian Plain) also show a wide distribution. This supports the suggestion that the variations in carbon isotope fractionation between Mediterranean plants is primarily biologically controlled, as $\delta^{13}C_{n\text{-alkane}}$ and $\delta^{13}C_{bulk}$ varies considerably between genera despite these plants having grown in the same location, under similar local environmental conditions. Consequently, the plant function appears to drive significant differences in carbon isotope fractionation, while similar carbon isotope fractionation occurs within a species/genus.

Finally, PCA (Fig. 7.9) showed that $\delta^{13}C_{n\text{-alkane}}$ explained a minor proportion of the variability in the Portuguese dataset, with no significant relationship found between $\delta^{13}C_{n\text{-alkane}}$ and other leaf-wax *n*-alkane properties (ACL, CPI, and total *n*-alkane concentration) (Fig. 7.7). This suggests that the primary driver(s) of other leaf-wax *n*-alkane properties are not linked to the

dominant driver of $\delta^{13}C_{n\text{-alkane}}$ in Mediterranean plants. Consequently, $\delta^{13}C_{n\text{-alkane}}$ may be useful as an independent climate proxy, with the potential for interpretation without reference to the other leaf-wax properties.

7.4.5. Implications for palaeoclimate reconstructions using fossil leaf-wax n-alkanes

Due to the significant variation in total *n*-alkane concentration between species and plant functional groups across all three Mediterranean datasets, the total *n*-alkane concentration in the fossil record cannot be confidently used to indicate the vegetation density of the source area. CPI values < 1 in the fossil record remain a useable tool in this region for indicating the significant input of petrogenic or degraded material.

The three Mediterranean records demonstrate that ACL cannot be used as an indicator of dominant vegetation type (woody taxa vs herbaceous vegetation) in this region because ACL varies considerably between Mediterranean species and within plant functional groups. Although the modern Mediterranean datasets show a relationship between a plant's ACL and its drought tolerance/heat resistance, the fossil *n*-alkane ACL record from SHAK06-5K shows considerable noise over the last 27.4 kyr. Consequently, it is not possible to assess whether ACL changes in the fossil record are primarily driven by the tolerance of the dominant plant communities to drought/heat stress.

Considerable variation is shown in the SHAK06-5K fossil $\delta^{13}C_{C31}$ record over the last 27.4 kyr, signifying changes in carbon isotope fractionation in SW Iberian vegetation throughout MIS 2 and the Holocene. While $\delta^{13}C_{atmos}$ varied over this period (Fig. 7.12b), changes in SHAK06-5K $\delta^{13}C_{C31}$ are significantly higher (Fig. 7.12c). This shows that $\delta^{13}C_{C31}$ was influenced by factors other than $\delta^{13}C_{atmos}$ over the last 27.4 kyr. Additionally, while leaf $\delta^{13}C_{bulk}$ can increase during periods of low pCO_2 (Popp *et al.,* 1989), the SHAK06-5K record displays the opposite trend, with low $\delta^{13}C_{C31}$ values during the LGM and HS1, coinciding with low pCO_2 (Fig. 7.12a and c). Furthermore, existing research has shown atmospheric pCO_2 to have a weak association with $\delta^{13}C$ in C_3 plants compared to other environmental variables (Arens *et al.,* 2000; Diefendorf *et al.,* 2015b).

While the modern data show that internal biological mechanisms are a key driver of carbon isotope fractionation in Mediterranean vegetation, demonstrating similar $\delta^{13}C_{n\text{-alkane}}$ values within plant functional groups, the SHAK06-5K fossil record is the combined signal of plant

communities within the Tagus catchment basin. Across large spatial scales, research has suggested that moisture availability is the dominant driver of $\delta^{13}C_{n\text{-alkane}}$ (Diefendorf *et al.,* 2010). Consequently, the $\delta^{13}C_{n\text{-alkane}}$ signal of the SHAK06-5K fossil record could be driven by two possible mechanisms: i) the direct influence of regional moisture availability/water stress on carbon isotope fractionation in SW Iberian vegetation, or ii) the indirect influence of the climate on regional vegetation structure leading to a change in dominant plant species with inherently different *n*-alkane $\delta^{13}C$ signatures.

The first hypothesis is that fossil $\delta^{13}C_{n\text{-alkane}}$ is directly driven by spring/summer climate conditions, particularly in relation to water availability/water stress. As previously mentioned, water availability can drive significant changes in carbon isotope fractionation during CO_2 uptake as plants modulate their stomata in response to changing moisture availability (Farquhar *et al.,* 1982; Farquhar & Sharkey, 1982; Ehleringer *et al.,* 1992; Diefendorf *et al.,* 2010; Kohn *et al.,* 2010; Liu & An, 2020). *n*-Alkane $\delta^{13}C$ in Mediterranean plants will primarily reflect spring/summer conditions as the greatest leaf-wax biosynthesis occurs during the growing season (Tipple *et al.,* 2013; Nelson *et al.,* 2018). Consequently, higher (lower) fossil $\delta^{13}C_{n\text{-alkane}}$ may document large-scale reduction (increase) in ^{13}C discrimination across SW Iberian vegetation in response to reduced (enhanced) Spring/Summer water availability.

The second hypothesis is that fossil $\delta^{13}C_{n\text{-alkane}}$ is driven by the isotopic signature of the dominant regional vegetation. The modern Mediterranean $\delta^{13}C_{n\text{-alkane}}$ records suggest that biological mechanisms are responsible for driving carbon isotope fractionation in Mediterranean vegetation, while in the SHAK06-5K record, $\delta^{13}C_{C31}$ is closely coupled with changes in temperate and steppe vegetation, signifying a close relationship between this proxy and SW Iberian vegetation composition. The highest $\delta^{13}C_{C31}$ occurs during the Holocene when thermophilous elements reached their peak expansion, while in the modern record, thermophilous woodland species demonstrate high $\delta^{13}C$ values between ~-33 and -34‰. Conversely, the lowest $\delta^{13}C_{C31}$ values are seen during the LGM and HS1 when steppe taxa reach their maximum expansion, while in the modern record, *Chenopodium* and graminoids (two major components of steppe taxa) show low $\delta^{13}C$ values around ~-38‰.

When assessing the likelihood of these two suggested $\delta^{13}C$ drivers, we are unable to deconvolve the signal in the fossil record. It is possible that the low $\delta^{13}C_{C31}$ during the LGM and HS1 represents the low water stress of steppe taxa (due to their adaptation to arid conditions),

while the peak in $\delta^{13}C_{C31}$ at ~8.36 cal ka BP reflects high spring/summer water stress of woodland taxa which reach their maximum expansion at this time. Based on the findings of the modern Mediterranean records, however, and the close relationship between the SHAK06-5K $\delta^{13}C_{C31}$ and temperate/steppe vegetation records, the fossil $\delta^{13}C_{n\text{-alkane}}$ signal could be driven primarily by changes in SW Iberian vegetation composition. In turn, these vegetation communities are influenced by regional climate conditions. Further research is required to disentangle the climate and biological controls of $\delta^{13}C_{n\text{-alkane}}$ in the fossil record. In particular, the production of a hydrogen isotope *n*-alkane ($\delta D_{n\text{-alkane}}$) record from SHAK06-5K would assist with the interpretation of the $\delta^{13}C$ signal by providing an independent precipitation signal (Sachse *et al*. 2004; Hou *et al*. 2008; Liu & Yang, 2008; Xia *et al.,* 2008; Garcin *et al*. 2012; Sachse *et al.,* 2012; Liu & An, 2018).

7.5. Conclusions

- All modern Mediterranean species in the Portuguese dataset demonstrate CPI values greater than 4. As CPI values > 1 are used to indicate no significant contribution of petrogenic or degraded material to the sedimentary record, our modern record suggests that CPI is a reliable tool to ensure that fossil n-alkanes in SW Iberian sedimentary sequences are sourced from terrestrial vegetation.
- The distribution of cuticular *n*-alkane ACL in modern Mediterranean vegetation varies between species within the same genus and within plant functional groups. This shows that *n*-alkane ACL cannot reliably indicate the dominant vegetation type (woody vs herbaceous taxa) in sediment records from this region.
- In modern Mediterranean vegetation, ACL appears to have a strong relationship with the plant's drought tolerance/heat resistance, with longer *n*-alkane chain-lengths occurring in species that are more tolerant of extreme drought/heat. I suggest this is an adaptive feature of Mediterranean vegetation at the molecular level, whereby the longer the chain-length of the 'shorter-chain lipids' (C_{20} – C_{38}; which includes n-alkanes), the higher the volume of crystallites and the higher melting point of the leaf-wax, which consequently reduces the cuticular permeability.
- In modern Mediterranean vegetation, $\delta^{13}C_{bulk}$ and $\delta^{13}C_{n\text{-alkane}}$ are both driven by physiological mechanisms, with similar carbon isotope fractionation within a species/genus, and similar values occurring within plant functional groups.
- We suggest that the fossil $\delta^{13}C_{n\text{-alkane}}$ record from SHAK06-5K could be driven by two key mechanisms: i) the direct influence of water availability on the carbon isotope fractionation of SW Iberian vegetation, and/or ii) the indirect influence of the climate on regional vegetation structure, as a carbon isotope fractionation may be primarily driven by a plant's physiology.
- Further research is required to produce a $\delta D_{n\text{-alkane}}$ record from SHAK06-5K; this will provide an independent precipitation signal, enabling the climatic and biological controls of $\delta^{13}C_{n\text{-alkane}}$ to be disentangled.

8.1. Introduction

This chapter presents the following palaeoclimatic records against the age model developed in Chapter 6: SW Iberian Margin pollen from SHAK06-5K and MD01-2444, leaf-wax *n*-alkane $\delta^{13}C$ from SHAK06-5K, and existing palaeoceanographic records from both cores, all spanning the past 27.4 kyr. The materials and methods used in the production and quantitative analysis of these datasets will be outlined followed by a discussion of the palaeoclimatic interpretations of these records. This will explore orbital and millennial-scale variability in SW Iberian vegetation over the past 27.4 kyr as well as changes in the deposition of terrestrial material at our core sites over the last deglaciation. Abrupt changes in the pollen records will be explored to assess both extrinsically and intrinsically mediated SW Iberian vegetation changes over the past 27.4 kyr in response to changing background conditions. An 'extrinsic' abrupt vegetation change is defined as a direct ecological response to an abrupt climate forcing, while an 'intrinsic' abrupt vegetation change is the result of a threshold/tipping point/non-linear feedback caused by a gradual climate forcing (Williams *et al.,* 2011).

8.2. Methodology

8.2.1. Bulk density and mass accumulation rates

The bulk density of samples along the length of core SHAK06-5K (n = 111) were calculated using Equation. 8.1a, maintaining a constant laboratory temperature (~24°C) during these measurements (Appendix 18). Samples were dried by placing in the oven for 12 hours at 50°C. Mass accumulation rates (MAR) were calculated for the SHAK06-5K terrestrial records: pollen (grains cm^{-2} kyr^{-1}) (Appendix 4) and *n*-alkanes (ng cm^{-2} kyr^{-1}), using bulk density, SAR, and proxy concentrations (Equation 8.1b) (Appendix 19). The calculation of pollen and *n*-alkane concentrations is explained in sections 4.2 and 5.2, respectively. As the SAR of the master sequence (Fig. 6.6; created using 40 AMS ^{14}C dates from SHAK06-5K and seven from MD01-2444) is higher between 8.2 and 7.7 cal ka BP than in core SHAK06-5K, due to the inclusion of MD01-2444 ^{14}C dates, the SAR used in the MAR calculations was produced using only SHAK06-5K ^{14}C dates, applying a Bayesian *P_sequence* model in Oxcal (Bronk Ramsey, 2007). This prevented the higher sedimentation rate of MD01-2444 from influencing the SHAK06-5K pollen and *n*-alkane MARs.

The bulk density record (n = 111) was linearly extrapolated to provide values for every depth of the pollen and *n*-alkane records (n = 162 and n = 71, respectively). While the MAR was calculated for every sample of the *n*-alkane record, three samples were excluded from the pollen record (96, 168 and 314cm); these depths displaying extreme pollen concentrations (shown in section 4.3). Their removal prevents the distortion of the figures and improves the subsequent analysis of the temporal changes in the mass flux of pollen to site SHAK06-5K. The pollen MAR record highlighted four additional extreme values (188, 202, 218 and 224 cm) which exceed 136,000 grains g^{-1}, with the largest of these outliers being 3.3x greater than the largest 'non-extreme' value. As all four outliers are single datapoints without corresponding *n*-alkane or bulk density measurements, it could not be determined whether these outliers resulted from a methodological error or an abrupt environmental change. Consequently, all four values were removed from the MAR dataset to improve the visualisation and interpretation of the record. This data allows for the analysis of temporal variations over the past 27.4 kyr in the deposition of pollen and n-alkanes at this location.

$$\text{a.} \quad BD = M_{dry} * V_{wet}$$

$$\text{b.} \quad MAR_{proxy} = C_{proxy} * SAR * BD$$

Equation. 8.1: Calculation of a sample's: **a.** bulk density (BD; g cm^{-3}) using the sample's dry sediment mass (M_{dry}; mg) and wet sediment volume (V_{wet}; mm^3); and **b.** mass accumulation rate of pollen and n-alkanes (MAR_{proxy}) (MAR_{pollen}, grains cm^{-2} kyr^{-1}; $MAR_{n\text{-}alkane}$, ng cm^{-2} kyr^{-1}) using the proxy concentration (C_{proxy}) (C_{pollen}, grains g^{-1}; $C_{n\text{-}alkane}$, ng g^{-1}), sediment accumulation rate (SAR; cm kyr^{-1}), and bulk density (BD; g cm^{-3}).

8.2.2. Intrinsic/extrinsic vegetation response

In order to quantitatively analyse the response of SW Iberian vegetation to abrupt climate events over the past 27.4 kyr, the rate of change (RoC) of the SHAK06-5K vegetation records was calculated and compared to the RoC of simulated and proxy climate records from this region. Temperate and steppe pollen records from SHAK06-5K were used to assess the rate of vegetation change, while $U^{K'}_{37}$- derived Iberian Margin SSTs from MD01-2444 (Martrat *et al.,* 2007), and simulated annual precipitation (cm yr^{-1}) and surface air temperature for December, January, and February (DJF SAT) (°C) over Iberia were used as regional climate forcings. Western Iberian DJF SAT and annual precipitation (9 – 2°W, 39 – 43°N) were extracted from transient experiments of the last glacial period (here 29.9 – 18 cal ka BP, Menviel *et al.,* 2014), subsequent deglaciation and Holocene (18 – 2 cal ka BP , Menviel *et al.,* 2011), performed with the Earth system model of intermediate complexity, LOVECLIM (Goosse *et al.,* 2010). The experiments were forced with time varying changes in orbital parameters (Berger, 1978), Northern Hemispheric ice-sheets topography, extent and albedo (Abe-Ouchi *et al.,* 2007), and atmospheric CO_2 concentration (Ahn & Brook, 2008). To mimic millennial-scale climate variability associated with Heinrich events and the YD, meltwater was added into the North Atlantic to induce AMOC variations. Reconstructed SW Iberian Margin SSTs ($U^{K'}_{37}$- derived) from MD01-2444 were aligned to the master age model using the automated proxy-to-proxy stratigraphical alignment method outlined in Chapter 4.

Gaussian interpolation was used to resample the simulated climate records and the SST and pollen timeseries every 200 years, although for the proxy data where the SAR in the master age model is extremely low, linear interpolation was used (~50 – 83 cm). The RoC was calculated

for the simulated and fossil climate records by taking the difference between consecutive samples every 200 years, then normalizing the data by subtracting the mean and dividing by the standard deviation, and finally transforming all values into positives (Table 8.1; Fig. 8.4). To define an abrupt event, the RoC in the simulated and fossil records had to meet the following criteria: a minimum of two datapoints in succession must exceed 1σ. One exception to this rule is the abrupt DJF SAT increase at the end of HS2, where one value falls slightly below 1σ (0.87). The RoC of its neighbouring samples, however, exceed the 1σ threshold as does the mean RoC of the three samples together; consequently, the rapid SAT increase at the end of HS2 was accepted as an abrupt event. The simulated and fossil records have different timescales and are therefore displayed separately in Fig. 8.4. As the timings of these abrupt changes in the simulated and fossil records do not always have the same age, only the RoC of abrupt climate transitions are analysed and compared.

8.2.3. Methods of published SW Iberian Margin palaeoceanographic records

While the following SW Iberian Margin palaeoceanographic records have been published elsewhere, a summary of the methods used to construct these records is provided below.

SHAK06-5K IRD measurements (Ausin et al., 2020):

A stereomicroscope was used to identify IRD from the sediment fraction > 300 µm. The measurements were made at a 2cm resolution for the depths of HS2 (308 – 262 cm), HS1 (170 – 114 cm) and the YD (96 – 78 cm). From the total IRD, detrital carbonate was then measured. The concentration of the total IRD and detrital carbonate IRD are expressed in grains per gram of dry sediment (grains g^{-1}; > 300 µm)

SHAK06-5K alkenone-derived SST (Ausin et al., 2019b):

Alkenones were extracted from the freeze-dried sediment of core SHAK06-5K at the Biogeoscience laboratory, ETH, Zurich. The method is similar to that outlined in section 5.2.2, with total lipid extraction, followed by saponification used to firstly isolate the neutral fraction. Silica gel column chromatography was then used to split the neutral fraction into three polarity fractions (explained in 5.2.2 and illustrated in Fig. 5.4), with fraction 2 (ketones and aldehydes) containing the alkenones. Abundances and $U^{k'}37$ ratios (Brassell *et al.,* 1986) were determined using GC-FID while $U^{k'}37$-derived SSTs were calculated using the latest global calibrations of Tierney and Tingley (2018).

MD01-2444 *alkenone-derived SST (Martrat et al., 2007):*

Alkenones were extracted from MD01-2444 sediment samples. Samples were first freeze dried and lipids extracted by sonification using DCM. Extracts were then hydrolysed with KOH (6%) in MeOH and derivatised using *bis*(trimethylsilyl)trifluoroacetamide. Samples were analysed using GC-FID and GC-MS. Absolute concentration errors were < 10%. The uncertainty of the $U^{k'}37$ determinations was < 0.015 (~ ±0.5oC). SST reconstructions were calculated using the relative composition of unsaturated C_{37} alkenones [$U^{k'}37$= $C_{37:2}/(C_{37:2}+C_{37:3})$] and calibrated following the method of Müller *et al.* (1998).

8.3. Results and Discussion:

8.3.1. Variation in the deposition of terrestrially sourced material

The pollen concentration and MAR, and the *n*-alkane MAR of SHAK06-5K is highest in the lower part of the core (the LGM, HS1, BA, and YD) (Fig. 8.1e-g). Between ~12 and 11 cal ka BP, the pollen MAR declines from 38,150 to 1,990 grains cm^{-2} ka^{-1}, while the pollen concentration declines from 3,070 to 680 grains g^{-1}, with both records remaining low thereafter. This decline coincides with a decrease in *n*-alkane MAR at ~12.3 cal ka BP and bulk density of the core at ~13 cal ka BP (Fig. 8.1b and d). A smaller but simultaneous decline is seen in the MD01-2444 pollen concentration record, reducing from 924 to 274 grains g^{-1} between ~12 and 11 cal ka BP (Fig. 8.1h). In contrast to our MAR and concentration records, lacustrine pollen records from Charco da Candieira (van der Knaap & van Leuween, 1997) show a prominent increase in total pollen concentration from the YD into the Holocene, indicating that vegetation density increased from the deglaciation into the warmer Holocene interglacial. The SHAK06-5K *ln(*Ca/Ti) reflects variations in the proportion of biogenic (Ca) to detrital (Ti) sediment (Fig. 8.1c) (Hodell *et al.,* 2013b). During warm interglacials/interstadials, Ti has been shown to decrease relative to Ca in the marine environment as a result of increased vegetation cover, reduced catchment erosion, reduced river transport of detrital material, and also increased carbonate productivity (Hodell *et al.,* 2013b). Our record demonstrates a slight rise in *ln(*Ca/Ti) during the BA and a significant increase throughout the Holocene, suggesting a decrease in terrigenous supply likely a result of increased vegetation cover, coinciding with the expansion of woodland. Conversely, during the LGM and subsequent deglaciation, *ln(*Ca/Ti) declined, indicating decreased carbonate productivity relative to the terrigenous supply, and by extension reduced vegetation cover which coincided with the expansion of steppe vegetation.

It would, therefore, be expected that the SHAK06-5K pollen and *n*-alkane MAR and concentration records would increase from the glacial into the Holocene. The pollen concentrations and MARs and the *n*-alkane MARs, however, show a significant decline from the middle of the YD into the Holocene, with the lowest values reached in the mid-Holocene (~6.1 cal ka BP in the pollen records and ~8 cal ka BP in the *n*-alkane MAR record). A similar pattern is also observed in the total pollen concentration record of nearby marine core MD95-2042 (Chabaud *et al.,* 2014), which shows an abrupt decline at ~12 cal ka BP and lowest values between ~8 – 5 cal ka BP. MD01-2444 also documents a significantly reduced pollen concentration from the YD into the Holocene, while core D13882 (Gomes *et al.,* 2020; Fig. 8.1i),

located on the continental shelf, near the mouth of the Tagus, shows lower pollen concentrations after 10.6 ka which remain low until 5.5 cal ka BP, increasing gradually until a significant increase at 2.3 cal ka BP.

I suggest that the decline in mass flux and concentration of terrestrial vegetation proxies in cores SHAK06-5K and MD01-2444 is a consequence of altered terrestrial sediment deposition at our core sites. While the source area of pollen to this site remained relatively constant over the last 27.4 kyr, the depocenter of terrestrial material delivered from the continent by the Tagus River was altered by rising sea levels over the deglaciation (Jouanneau *et al.,* 1998; Vis *et al.,* 2008; 2016).

The decline in pollen concentration and pollen and *n*-alkane MARs at our site is coeval with the timing of the disconnection of the Tagus river from the Cascais and Sebutal-Lisbon canyons between 13 – 12 cal ka BP (Vis *et al.,* 2008; 2016; Vis & Kasse, 2009). Throughout MIS 2, the direct connection of the river to these canyons (illustrated in Fig. 2.3) meant that high volumes of sediment bypassed the continental shelf and were deposited in the deeper marine environment (Vis *et al.,* 2008; 2016; Vis & Kasse, 2009). Deglacial sea-level rise resulted in the landward movement of the depocenter, starting between 13 – 12 cal ka BP and lasting until 7 cal ka BP (Vis *et al.,* 2008; 2016; Vis & Kasse, 2009). This reduced the transport of pollen and leaf-wax n-alkanes to greater depths, including to sites SHAK06-5K and MD01-2444, both located on the Promontório do Príncipe de Avis spur. While these deeper cores show a decline in pollen concentration and MAR, and *n*-alkane MAR after the disconnection of the canyon with the Tagus river, the location of D13882, situated on the continental shelf close to the mouth of the river (shown in Fig. 2.3), meant high quantities of terrestrial sediment continued to be deposited until much later. The decline in pollen concentration at D13882 occurred between 10.6 – 5.1 cal ka BP, coeval with the trapping of large quantities of fluvial sediment in the Lower Tagus Valley, reducing transport to the marine environment (Vis *et al.,* 2016). Once the lower valley had been filled after 5.5 cal ka BP, sedimentation to the shelf increased, which is likely to have contributed to the increase in pollen concentration in core D13882 after this time. We therefore suggest, on a glacial-interglacial timescale, that the location of terrestrial sediment deposition in this region, and consequently the pollen and *n*-alkane MARs at sites SHAK06-5K and MD01-2444, is strongly controlled by relative sea level.

After 2.7 cal ka BP, there is a slight rise in pollen concentrations and MARs and *n*-alkane MARs which coincides with a significant rise in SAR and a decline in *ln(*Ca/Ti). Other records from this region also show a rise in sedimentation rates after ~2 cal ka BP, resulting from the impact of anthropogenic land-use change (Vis *et al.,* 2016; Gomes *et al.,* 2020). The D13882 record, located closer to the Tagus river, shows a considerable rise in pollen concentration after this time, indicating that a large proportion of terrestrial proxies over the last 2 cal ka BP did not reach the deep ocean but were instead deposited in high concentrations on the continental shelf. At the very top of the SHAK06-5K record, after 0.6 cal ka BP, SAR declined, coinciding with reduced pollen and *n*-alkane concentrations and MARs, a pattern also seen in the pollen concentration of core D13882. This likely reflects enhanced anthropogenic activities in the catchment after this time (including the intensification of agriculture, reduction of Mediterranean shrublands, establishment of *Pinus* plantations, and hydrological regulation) altering the hydrology and sediment dynamics of the Tagus river (Vis *et al.,* 2008; Fernandes *et al.,* 2020), and consequently altering the deposition of terrestrial material at our core sites.

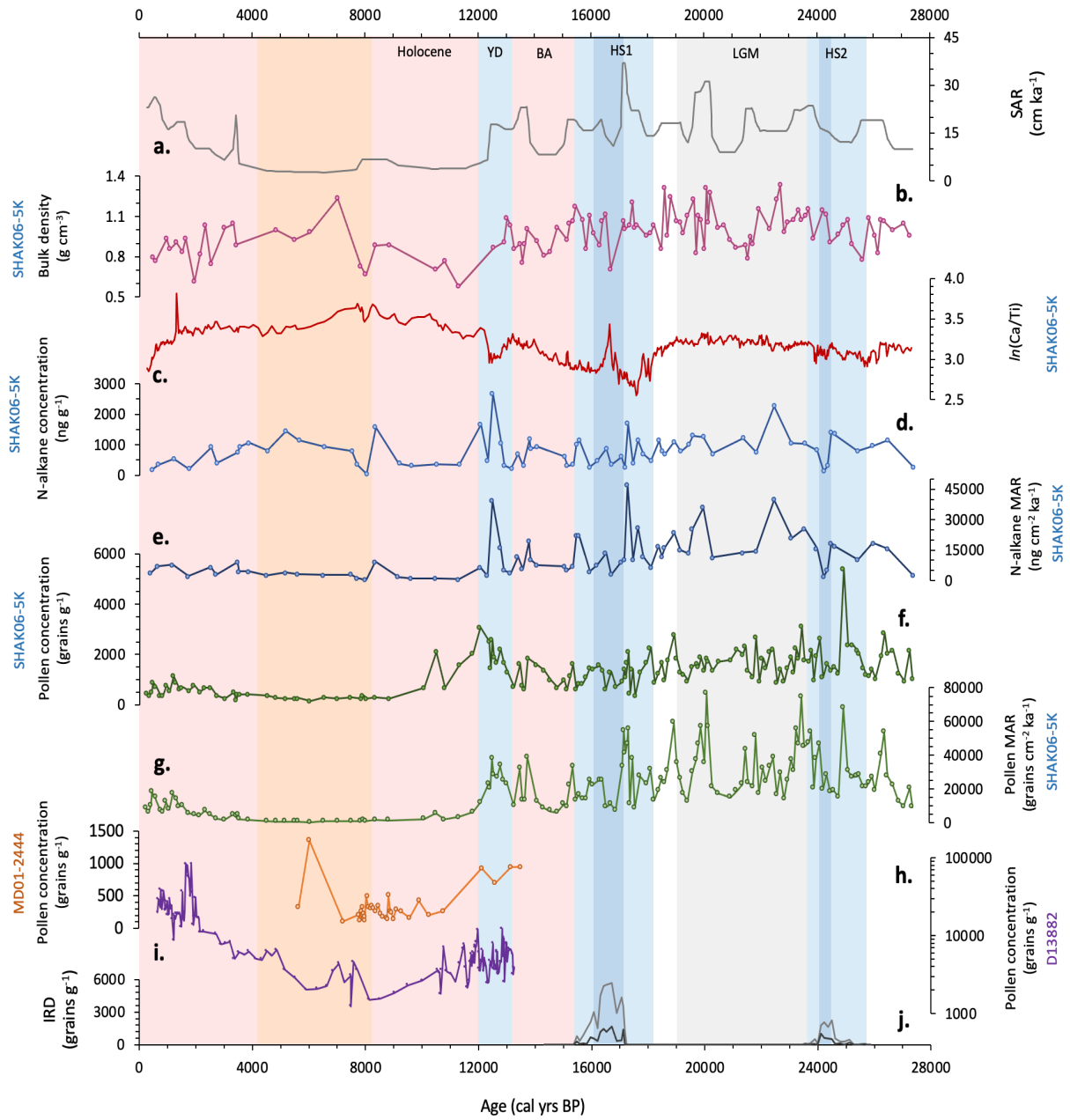

Fig. 8.1: a. Sediment accumulation rate (SAR) of core SHAK06-5K (cm ka^{-1}); **b.** bulk density of core SHAK06-5K (g cm^{-3}); **c.** *ln*(Ca/Ti) from SHAK06-5K; **d.** *n*-alkane concentration (C_{27} – C_{33}) of core SHAK06-5K (ng g^{-1}); **e.** *n*-alkane mass accumulation rate (C_{27} – C_{33}) of core SHAK06-5K ($MAR_{n\text{-}alkane}$; ng cm^{-2} ka^{-1}); **f.** pollen concentration of core SHAK06-5K (grains g^{-1}); **g.** pollen mass accumulation rate of core SHAK06-5K (MAR_{pollen}; grains cm^{-2} ka^{-1}); **h.** pollen concentration of core MD01-2444 (grains g^{-1}); **i.** pollen concentration of core D13882 (grains g^{-1}; Gomes *et al.,* 2020); **j.** ice rafted debris from core SHAK06-5K (grains g^{-1}; Ausin *et al.,* 2020).

8.3.2. Orbital-scale variability

8.3.2.1. MIS 2

Over MIS 2, the expansion of steppe vegetation, low SSTs (Ausin *et al.,* 2019b; Martrat *et al.,* 2007), and high $\delta^{18}O_{G.\ bulloides}$ values (Ausin *et al.,* 2019a) in core SHAK06-5K and high benthic foraminiferal $\delta^{18}O$ in MD95-2042 (Shackleton *et al.,* 2000) (Fig. 8.2), reflect the influence of low insolation, low pCO_2, and northern ice sheets on atmospheric circulation patterns, surface ocean and air temperatures, and the hydrological cycle (Pollard & Barron, 2003). In addition, the dominance of steppe taxa indicates the direct influence of low pCO_2 concentrations on the photosynthetic rate and water use efficiency of vegetation (Polley *et al.,* 1993; Cowling & Sykes, 1999; Ehleringer & Cerling, 1995; Monnin *et al.,* 2001; 2004; Marcott *et al.,* 2014). Research has suggested that the maximum ice volume extent of the LGM shifted the polar front southwards, intensifying the westerlies over Southern Europe and altering the transport of atmospheric heat and moisture (Bard *et al.,* 1987; Eynaud *et al.,* 2009). While some modelling studies have suggested that the westerlies strengthened and shifted southward, and precipitation over the Iberian Peninsula increased during the LGM (Laîné *et al.,* 2009; Beghin *et al.,* 2016; Ludwig *et al.,* 2016; Kutzbach *et al.,* 2020), other simulations show a drying (Braconnot *et al.,* 2007). Simulated cold/dry conditions are in line with the dominance of steppe in vegetation records from this region (Hooghiemstra *et al.,* 1992; Turon *et al.,* 2003; Oliveira *et al.,* 2018).

In the SHAK06-5K record, although steppe elements dominated throughout the LGM, there is a low (<12%) but continuous presence of thermophilous temperate pollen and an increase in Ericaceae pollen percentages which coincides with northern winter at perihelion ~22.5 ka (Fig. 8.2). Heathland expansion has been linked to reduced summer aridity as a result of precessional changes leading to reduced boreal summer insolation (Margari *et al.,* 2007; 2014; Fletcher & Sánchez Goñi, 2008).

While lower LGM temperatures and reduced winter precipitation favoured the expansion of steppe taxa, the reduced seasonality caused by the summer insolation minimum, combined with moderate Iberian Margin SSTs (Cayre *et al.,* 1999; Pailler & Bard, 2002; de Abreu *et al.,* 2003; Ausin *et al.,* 2019b) may have reduced summer evaporative conditions and allowed for moderate levels of effective moisture that were able to sustain heathland populations and some thermophilous elements. Simulated precipitation records from Western Iberia also show

reduced hydrological seasonality during the LGM compared to pre-industrial levels (Menviel *et al.,* 2011). At this time, $\delta^{13}C_{C31}$ displays the lowest values of the record, demonstrating high carbon isotope fractionation in SW Iberian vegetation, though it remains unclear whether this represents a direct or indirect climate control: the increased fractionation could reflect relatively low water stress or alternatively the physiology of the dominant vegetation.

8.3.2.2. Early Holocene

Following intermediate expansions and contractions during the Late Glacial (see next section), temperate tree pollen percentages gradually increased at the start of the Holocene, seeing an early expansion of pioneer taxa later replaced by thermophilous temperate elements, indicating an increasingly dense woodland environment and warmer/wetter conditions. Temperate tree taxa peaks in both SHAK06-5K and MD01-2444 between ~10.1 - 8.4 cal ka BP. This gradual forest expansion at the onset of the Holocene is in phase with the rise in $\delta^{13}C_{C31}$ which peaked at ~8.3 cal ka BP, and the gradual decline in $\delta^{18}O_{G.\ bulloides}$ and rise in SSTs. In parallel, Ericaceae percentages declined, reaching a minimum during the time of the summer insolation maximum, associated with enhanced hydrological seasonality and summer aridity, as indicated by the peak in Mediterranean sclerophylls. After ~7.8 cal ka BP temperate tree pollen values decreased while Ericaceae percentages increased and $\delta^{13}C_{C31}$ declined. Iberian Margin SSTs remained high (~18°C) (Martrat *et al.,* 2007; Rodrigues *et al.,* 2010; Ausin *et al.,* 2019b; Gomes *et al.,* 2020), but with an overall small gradual decreasing trend throughout the mid and late Holocene. Again, the increase in Ericaceae mirrors the decline in summer insolation, pointing to a shift in summer moisture availability.

What emerges is that while seasonality of precipitation in SW Iberia followed changes in summer insolation, the peak in temperate woodland values lags the insolation maximum by ~1 – 3 kyr. Comparison with the timing of vegetation changes during the Last Interglacial (LIG) at the same location (core MD01-2444) (Tzedakis *et al.,* 2018) reveals a distinct difference, with the peak in temperate tree pollen percentages occurring at ~128 ka, very close to the onset of the interglacial and ~1 kyr ahead of the insolation peak. One possible explanation for this difference might lie in the evolution of ice volume during the two interglacials, with sea level approaching present-day values at the onset of the LIG (Dutton *et al.,* 2015; Rohling *et al.,* 2019), while being 60 m below present values at the onset of the Holocene (Lambeck *et al.,* 2014). Thus, in the early Holocene, residual ice sheets still had a dominant influence over

regional temperatures and winter moisture availability (Baker *et al.,* 2017; Marsicek *et al.,* 2018), which delayed forest expansion, despite maximum boreal insolation.

A final consideration is the parallel evolution of the $\delta^{13}C_{C31}$ and temperate tree pollen records during the early Holocene. Following on from the suggestions in Chapter 7, the $\delta^{13}C_{C31}$ record could reflect a direct or indirect relationship with the changing climate. One possibility is that $\delta^{13}C_{C31}$ over the early Holocene was primarily driven by the changing vegetation structure. The increase in $\delta^{13}C_{C31}$ over this period coincided with the rise in thermophilous woodland which may indicate that the physiology of temperate taxa led to lower carbon isotope fractionation. Another possibility is that the $\delta^{13}C_{C31}$ record was directly influenced by changing climate conditions. As global ice volume reduced over the early Holocene, rising regional summer temperatures and evaporative conditions enhanced Spring/Summer water stress of the dominant taxa which led to higher $\delta^{13}C_{C31}$.

8.3.2.3. Early to Mid-Holocene transition

At the transition from the early to the mid-Holocene, MD01-2444 displays a brief decline in thermophilous woodland between 8.4 and 7.9 cal ka BP, with this contraction extending over the 8.2 ka event, which has been attributed to a catastrophic release of meltwater from Lake Agassiz/Ojibway that led to a perturbation of the AMOC (Barber *et al.,* 1999; Renssen *et al.,* 2001; Alley, 2003; Alley & Ágústsdóttir, 2005; LeGrande *et al.,* 2006) and a large-scale North Atlantic cooling (Von Grafenstein *et al.,* 1998; Tinner and Lotter, 2001; Thomas *et al.,* 2007). After a short recovery, a rapid and significant contraction of thermophilous woodland occurred, declining ~40% in < 500 cal yrs BP. Temperate woodland percentages remained low (between 19 - 33%) throughout the mid-Holocene, coinciding with an expansion of Ericaceae and heliophilous Cichorioideae. These changes follow the gradual decline in boreal insolation, suggesting that the associated increased summer water availability favoured the expansion of heathland over temperate woodland and provided a more open environment, allowing the expansion of heliophilous elements. While the mid-Holocene gradual expansion of heathland and heliophilous herbs is a relatively linear response to declining boreal insolation, the rapid decline of temperate taxa at ~7.8 cal ka BP signifies an abrupt response to the same gradual climate forcing. This abrupt ecological response will be further explored in section 8.3.4.

Similar to the temperate record, $\delta^{13}C_{C31}$ gradually increased over the early Holocene, peaking at 8.4 cal ka BP before declining and reaching the lowest values of the Holocene (-32‰) at 5.2

cal ka BP. The $\delta^{13}C_{C31}$ decline through the mid-Holocene is much more gradual than that of the temperate pollen record. While the Mid-Holocene $\delta^{13}C_{C31}$ decline may have been primarily influenced by the changing vegetation structure at this time, it is more likely reflecting the gradually decreasing Spring/Summer water stress of the dominant taxa over this period. The correspondence of the $\delta^{13}C_{C31}$ decline with the expansion of Ericaceae and declining boreal insolation indicates that the reduced hydrological seasonality may have lowered the spring/summer water stress of the dominant vegetation, and therefore increased carbon isotope fractionation in SW Iberian vegetation.

8.3.2.4. Late Holocene

Open woodland characterises the late Holocene, with low but increasing levels of thermophilous temperate woodland and high levels of heliophilous Cichorioideae and Ericaceae. The heathland expansion coincides with a boreal insolation minimum, associated with reduced precipitation seasonality and increased summer water availability. The SHAK06-5K pollen MAR record indicates that anthropogenic activities in the catchment significantly enhanced after 2.7 cal ka BP, while the sharp rise in *Pinus* after ~0.6 cal ka BP is likely linked to large-scale afforestation of this genus. The $\delta^{13}C_{C31}$ record shows significant variability, with an initial increase followed by a decline in values until ~0.6 cal ka BP. The vegetation composition of core SHAK06-5K, therefore, will have been heavily influenced after this time by the increasing intensification of agriculture and regulation of hydrology, with the latter making the interpretation of the $\delta^{13}C_{C31}$ record particularly difficult. Supporting data would be required to disentangle the anthropogenic, climatic and physiological controls of leaf-wax *n*-alkane $\delta^{13}C$ in SW Iberian vegetation during this period.

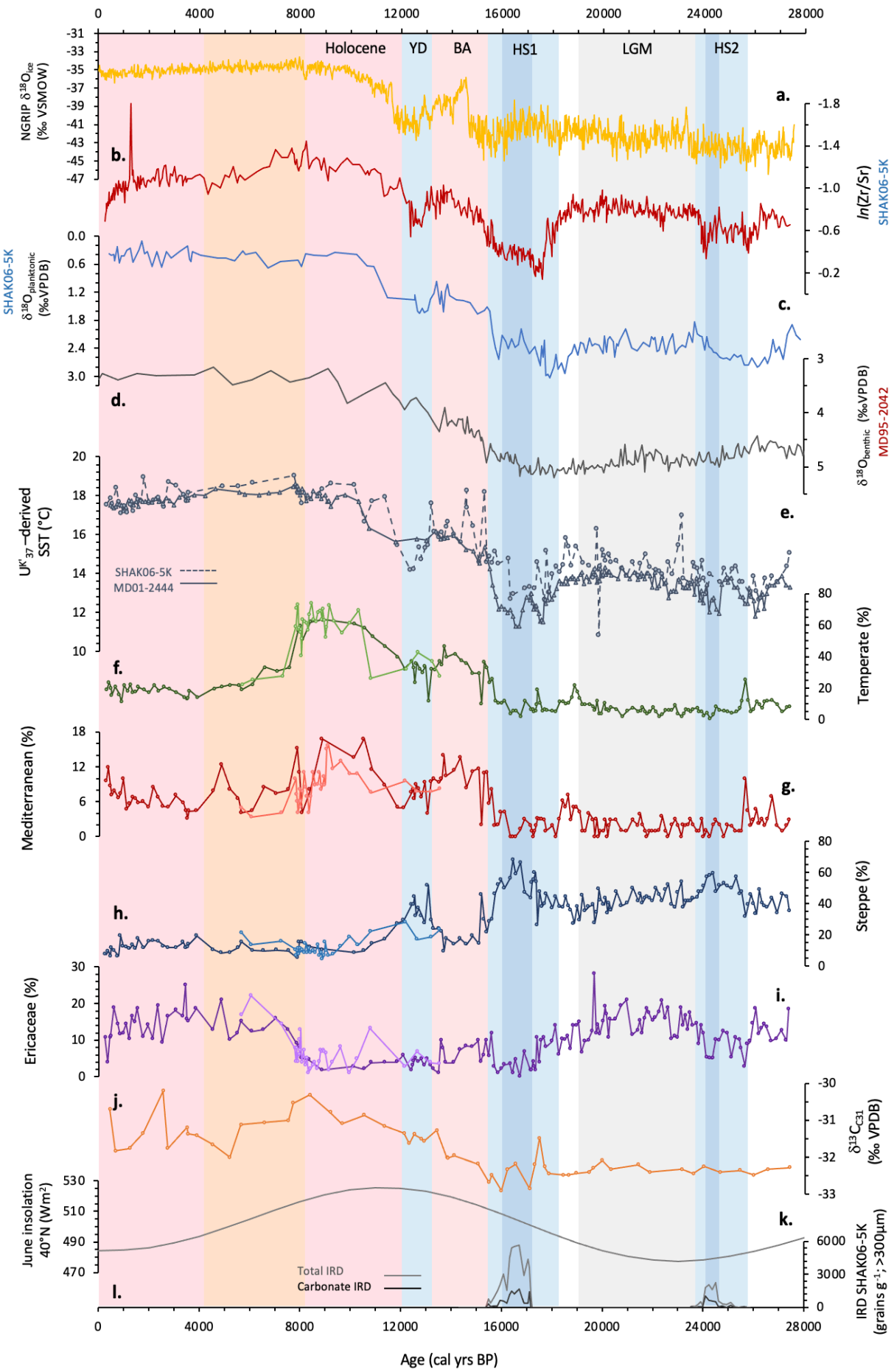
Holocene
YD
BA
HS1
LGM
HS2
NGRIP δ18Oice (‰ VSMOW)
a.
b.
ln(Zr/Sr) SHAK06-5K
SHAK06-5K δ18Oplanktonic (‰VPDB)
c.
d.
δ18Obenthic (‰VPDB) MD95-2042
U^K'37–derived SST (°C)
SHAK06-5K
MD01-2444
e.
f.
Temperate (%)
Mediterranean (%)
g.
h.
Steppe (%)
Ericaceae (%)
i.
j.
δ13C31 (‰ VPDB)
June insolation 40°N (Wm²)
k.
Total IRD
Carbonate IRD
l.
IRD SHAK06-5K (grains g-1; >300µm)
Age (cal yrs BP)

Fig. 8.2: Climate records over the past 27.4 kyr (cal yrs BP) of: **a.** North Greenland $\delta^{18}O_{ice}$ established by the Greenland Ice Core Chronology 2005 (VSMOW ‰; Rasmussen *et al*., 2006); **b.** *ln*(Zr/Sr) from SHAK06-5K (Ausin *et al.,* 2020); **c.** $\delta^{18}O$ of planktonic foraminifera from SHAK06-5K ($\delta^{18}O_{planktonic}$; ‰ VPDB; Ausin *et al.,* 2019a); **d.** $\delta^{18}O$ of benthic foraminifera from MD95-2042 ($\delta^{18}O_{benthic}$; ‰ VPDB; Shackleton *et al.,* 2000); **e.** UK'37 -derived sea surface temperature (SST; °C) from SHAK06-5K (Ausin *et al.,* 2019b) and MD01-2444 (Martrat *et al.,* 2007); **f.** temperate pollen from SHAK06-5K (dark green) and MD01-2444 (light green) (%); **g.** Mediterranean pollen from SHAK06-5K (red) and MD01-2444 (light red) (%); **h.** steppe pollen from SHAK06-5K (dark blue) and MD01-2444 (light blue); **i.** Ericaceae pollen from SHAK05-5K (dark purple) and MD01-2444 (light purple) (%); **j.** *n*-alkane $\delta^{13}C_{C31}$ from SHAK06-5K (‰ VPDB); **k.** boreal insolation at 40°N (Wm^2; Berger, 1978); **l.** ice-rafted debris (IRD; grains g^{-1}; Ausin *et al.,* 2020). Note different scales in pollen percentages.

8.3.3. Abrupt climate variability

8.3.3.1. Heinrich Stadials 1 & 2

Following Margari *et al.* (2020), HS2 and HS1 are defined in core SHAK06-5K by changes in lithology: the XRF *ln*(Ca/Ti) and *ln*(Zr/Sr) ratios (Figs. 8.1c and 8.2b) reflect variations in the relative proportion of detrital (Zr, Ti) and biogenic (Sr, Ca) sediment; this is governed by both dilution by terrigenous sediment and carbonate production. Carbonate productivity during stadial periods declined relative to the supply of terrigenous material; however transient increases in Ca reflect the input of detrital carbonate IRD, presumably originating from the Hudson Strait (Hodell *et al.,* 2013b).

During HS2, (25.7 – 23.6 cal ka BP) the pollen spectra are dominated by cryoxerophytic steppe taxa, primarily *Artemisia*, with some open woodland elements, indicating cold/dry conditions. Early in HS2, an expansion of steppe taxa with the presence of temperate and pioneer vegetation signifies cool temperatures and moderate moisture availability. Within HS2, a small peak in IRD, including detrital carbonate, occurs between ~24.6 - 24.1 cal ka BP (Ausin *et al.,* 2020) (Fig. 8.3) coeval with a local maximum in steppe taxa, while arboreal taxa and Ericaceae declined, indicating the coldest, driest conditions of the stadial.

HS1 (23.6 – 19.1 cal ka BP) is a complex interval characterized by lower SSTs and an increase in $\delta^{18}O_{G.\ bulloides}$ and high steppe pollen percentages. Early in HS1 (18.2 – 17.2 cal ka BP) SSTs and pollen percentages of temperate trees and pioneer taxa fluctuate, while Ericaceae remained

relatively high. The most extreme conditions of the entire 27.4 kyr record are documented within the second part of HS1, coeval with a peak in IRD, including detrital carbonate (17.2 – 16.1 cal ka BP): SSTs reached a minimum of 11.3°C (Fig. 8.3c), while the pollen record shows the greatest expansion of steppe taxa alongside minimal levels of temperate and pioneer vegetation and low levels of Ericaceae, signifying the coldest, driest conditions of the stadial and entire deglaciation. In the final section of HS1 (16.1 – 15.4 cal ka BP), IRD concentrations declined while SSTs and temperate tree pollen percentages gradually recovered, reflecting an interval of slowly evolving conditions before the onset of the BA interstadial.

A complex structure, with a double IRD peak and attendant cooling, has been identified in North Atlantic records of HS1 (Bond & Lotti, 1995; Bard *et al.,* 2000; Marcott *et al.,* 2011; Hodell *et al.,* 2017). This has also been observed in SW Iberian Margin SSTs (Pailler & Bard, 2002; Martrat *et al.,* 2007) and primary productivity (Ausin *et al.,* 2020), and in NW Iberian vegetation records (Naughton *et al.,* 2007; 2009). Our records also show two SST minima at 17.5 and 16.6 cal ka BP, with the first SST decline and SW Iberian steppe expansion occurring prior to the deposition of IRD at our core site. The IRD layer is associated with the second and more extensive SST and steppe maximum, indicating that the penetration of iceberg meltwater at the SW Iberian margin altered surface ocean conditions and regional hydrology (Bard *et al.,* 2000; Pailler & Bard, 2002; Voelker *et al.,* 2009; Salgueiro *et al.,* 2014; Ausin *et al.,* 2020), leading to the coldest/driest land conditions in SW Iberia. Although the low North Atlantic SSTs during HSs have been linked to the southward shift in the polar front and strengthened winds over SW and Central Iberia (Costas *et al.,* 2016; Wolf *et al.,* 2018; 2019), I suggest that despite the strengthened westerlies, lower regional temperatures reduced evaporative moisture in SW Iberia which favoured the expansion of steppe taxa during both HS2 and HS1. During both Heinrich Stadials, changes in steppe taxa are in phase with SSTs, $\delta^{18}O_{G.\ bulloides}$ and IRD (Fig. 8.2), demonstrating a close coupling of land-sea conditions in SW Iberia during these extreme cold North Atlantic events.

8.3.3.2. BA

The BA (15.4 – 13.2 cal ka BP) is defined by a change in lithology, with lower XRF *ln*(Zr/Sr) values and characterized by a shift in SSTs, $\delta^{18}O_{G.\ bulloides}$, and pollen percentages to an interstadial state, indicating warmer and wetter conditions. After a rapid expansion of arboreal vegetation and decline in $\delta^{18}O_{G.\ bulloides}$ at the transition from HS1, temperate taxa briefly declined at 15.2 cal ka BP, coeval with a small decrease in SSTs. Temperate tree values then gradually increased,

signifying progressively warmer/wetter conditions, and coinciding with declining $\delta^{18}O_{\textit{G. bulloides}}$. The peak in percentages of thermophilous elements occurred at 13.7 cal ka BP (47%), coeval with a decline in steppe values and rise in SSTs. Ericaceae pollen percentages expanded at the onset of the BA before gradually decreasing, while values of Mediterranean sclerophylls show an opposite trend, suggesting a gradual rise in summer aridity. All arboreal elements declined after 13.7 cal ka BP, along with a contraction of heathland and expansion of steppe, indicating a cooling/drying. During this interstadial, $\delta^{13}C_{C31}$ increased from -32.2‰ at 15.1 cal ka BP to -31.3‰ at 13.4 cal ka BP, indicating that carbon isotope fractionation in SW Iberian vegetation declined over the BA. This could reflect the changing vegetation structure of this period, with the temperate arboreal elements that expanded over the BA having lower carbon isotope fractionation than the steppe elements that preceded them. It may, however, be primarily influenced by enhanced Spring/Summer water stress of SW Iberian vegetation as hydrological seasonality increased, caused by the rising boreal insolation over the course of the interstadial.

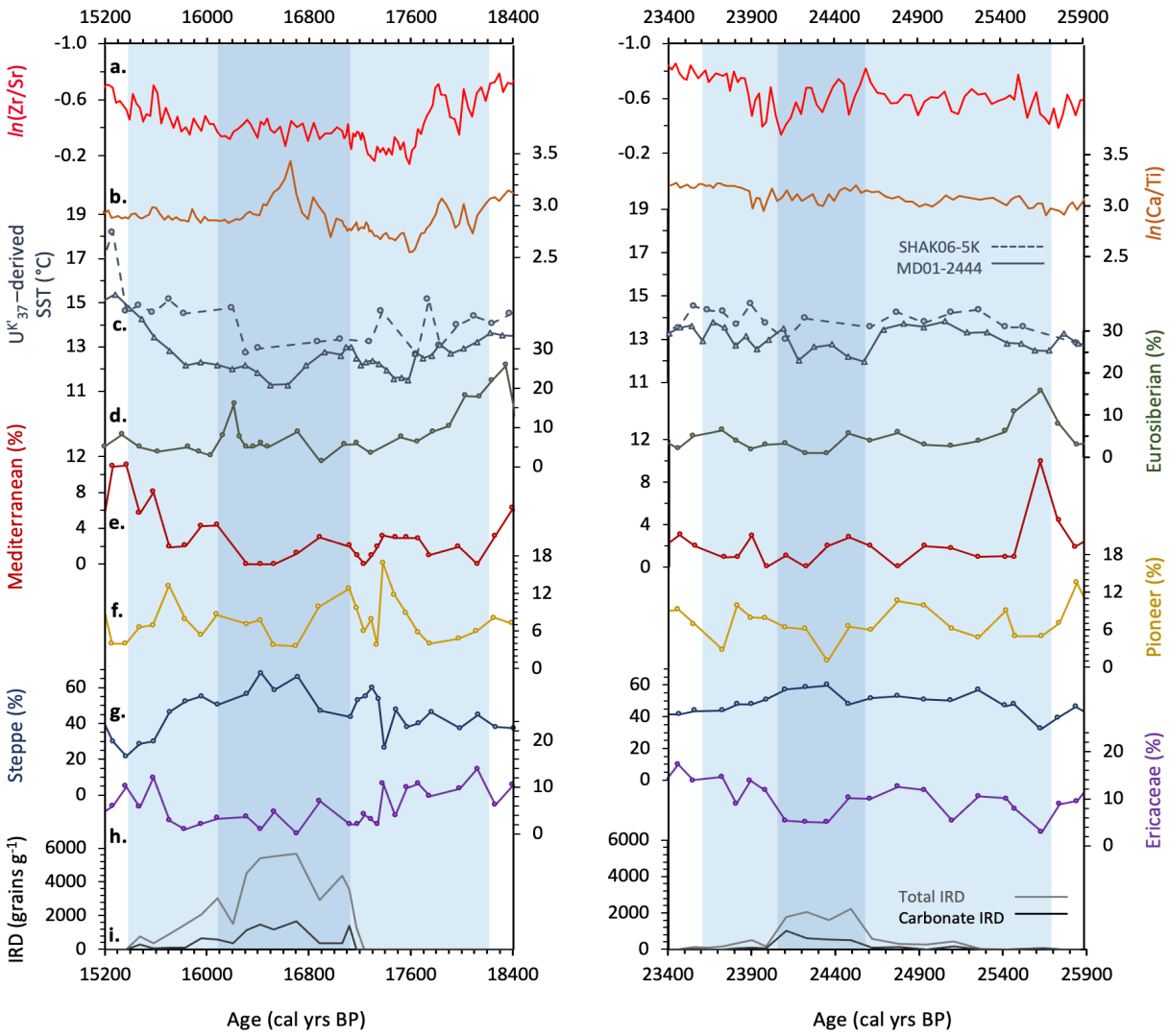

Fig. 8.3: In SW Iberian Margin cores over HS1 and HS2, changes in: **a.** *ln*(Zr/Sr) from SHAK06-5K (Ausin *et al.,* 2020); **b.** *ln*(Ca/Ti) from SHAK06-5K (Ausin *et al.,* 2020); **c.** UK'37 -derived sea surface temperature (SST; °C) from SHAK06-5K (Ausin *et al.,* 2019b) and MD01-2444 (Martrat *et al.,* 2007); **d.** Eurosiberian pollen from SHAK06-5K (%); **e.** Mediterranean pollen from SHAK06-5K (%); **f.** pioneer pollen from SHAK06-5K (%); **g.** steppe pollen from SHAK06-5K (%); **h.** Ericaceae pollen from SHAK06-5K (%); and **i.** ice rafted debris (IRD; grains g^{-1}; Ausin *et al.,* 2020).

8.3.3.3. YD

A shift in XRF *ln*(Zr/Sr) and *ln*(Ca/Ti) values demarcates the YD stadial in both cores SHAK06-5K and MD01-2444 (13.2 -12 cal ka BP), with the stadial characterized by a drop in SSTs. Pollen records document the expansion of steppe communities throughout this period, with a moderate presence of mixed open woodland, indicating cooler/drier conditions than the preceding interstadial. The pollen values of steppe taxa, however, do not reach those of HS2

and HS1 and the low but continuous presence of Mediterranean vegetation suggests that winter temperatures were moderate enough to sustain these elements. At the onset of the YD, steppe taxa rapidly expanded in < 250 years, coinciding with a decline in SSTs and a rise in $\delta^{18}O_{G.\ bulloides}$.

8.3.4. Intrinsic/Extrinsic vegetation change

For each climate transition (the onset and end of HS2, HS1, and the YD) and the HS1 IRD event, the criteria for abrupt change are met by at least one of the three regional climate records (simulated DJF SAT and annual precipitation, and $U^{K'}_{37}$- derived SSTs from MD01-2444); additionally, while not always having two consecutive samples above the threshold for inclusion, some of the records had one datapoint above 1σ at these transitions (highlighted by blue markers in Fig. 8.4). This demonstrates that all these climate changes can be defined as abrupt. In the vegetation records, however, the criteria for an abrupt change were not met for all transitions; notably at the onset of HS1 and the transition from the YD into the Holocene. At the onset of HS1 and the Holocene, an abrupt decline is seen in the climate records, while the vegetation records demonstrate a more gradual change.

The highest RoC values for the climate forcing and inferred vegetation response that meet the criteria for abrupt change are shown in Table 8.1. At the onset of HS2, the RoC of simulated annual precipitation qualifies as an abrupt event, coinciding with an abrupt change in both temperate and steppe pollen. At the end of HS2, the RoC of the declining simulated DJF SAT qualifies as an abrupt event, with the steppe pollen record also demonstrating an abrupt reduction at this time. The onset of HS1 sees an abrupt decline in DJF SAT and SSTs with the latter demonstrating the largest RoC. The pollen records, however, demonstrate a more gradual change at this transition, with the RoC of the temperate and steppe pollen not exceeding the 1σ threshold. The rapid decline in SSTs in the middle of HS1 qualifies as an abrupt event, coinciding with the maximum IRD deposition at this site. In parallel, steppe abruptly increased. Neither of the simulated records show this event, likely due to the timing of the freshwater fluxes applied in the model (Fig. 8.4a) which does not resolve the complex double peak structure of meltwater at this site, demonstrated by SW Iberian Margin palaeoceanographic records during HS1 (Bard *et al.,* 2000; Pailler & Bard, 2002; Martrat *et al.,* 2007; Ausin *et al.,* 2020). At the end of HS1, all regional climate variables show an abrupt change, with the SST record having the largest RoC. This coincides with an abrupt increase in temperate pollen and abrupt decline in steppe taxa, with the highest RoC shown by the latter.

At the onset of the YD, an abrupt decline is shown in both the simulated annual precipitation and DJF SAT records, with the former having the highest RoC. At this transition, an abrupt decline is apparent in the temperate pollen record, which coincides with an abrupt rise in steppe taxa. At the end of the YD, an abrupt decline is shown in both simulated variables, however, no abrupt change is shown in the SST or vegetation records. Instead, SSTs and temperate pollen show a gradual rise from the YD into the Holocene, while steppe taxa gradually decline. In the mid-Holocene, the rapid decline in thermophilous woodland between 7 – 7.6 cal ka BP meets the abrupt change criteria. The regional climate records, however, show no abrupt change at this time; while the RoC of SW Iberian SSTs does not exceed the threshold between 9.2 cal ka BP and the Late Holocene, the RoC of simulated annual precipitation and DJF SAT does not exceed 1σ for the entire early and mid-Holocene.

In the glacial part of the record, all qualifying abrupt pollen changes in core SHAK06-5K occur either at the transition between stadial and interstadial conditions or at the start/end of the HS1 IRD event. At all these transitions (the onset and end of HS2, the IRD event during HS1, the end of HS1, and the onset of the YD), these abrupt pollen changes coincide with an abrupt change in one or more of the regional climate records (Fig. 8.4 and Table 8.1), indicating that these vegetation changes were an ecological response to extrinsic climate changes. The abrupt decline in temperate tree pollen percentages during the mid-Holocene (7 – 7.6 cal ka BP), however, does not correspond with an abrupt climate change in any of the climate records. This suggests the rapid decline in thermophilous woodland was an intrinsically-mediated response, whereby temperate woodland crossed an ecological threshold resulting from regional feedbacks to external conditions. I propose that this is likely to be the gradual decline in boreal insolation and its influence on precipitation seasonality.

		Climate variable			Pollen change		
		Age (ka BP)	RoC (normalised)	Forcing	Age (ka BP)	RoC pollen (normalised)	Inferred vegetation type
HS2	Onset	25-25.2	1.18	Precipitation	25.2-25.4	2.24	Temperate
	End	23-23.4	1.41	DJF SAT	23.8-24	1.23	Steppe
HS1	Onset	17.2-18	1.89	DJF SAT	-	-	-
	IRD event	16.6-16.8	2.45	SST	16.6-16.8	1.86	Steppe
	End	15.2-15.6	2.83	SST	15.4-15.6	2.76	Steppe
YD	Onset	12.6-12.8	3.74	Precipitation	13-13.4	1.76	Temperate
	End	11.6-11.8	2.87	Precipitation	-	-	-
Holocene		-	-	-	7-7.6	2.04	Temperate

Table 8.1: Rate of change (RoC) of regional climate forcings (simulated annual precipitation (cm yr^{-1}) and DJF SAT (°C) over western Iberia, and SW Iberian Margin SSTs from MD01-2444 (°C)), and SW Iberian vegetation (steppe/temperate taxa) at the transitions of the millennial-scale climate events over the past 27.4 kyr.

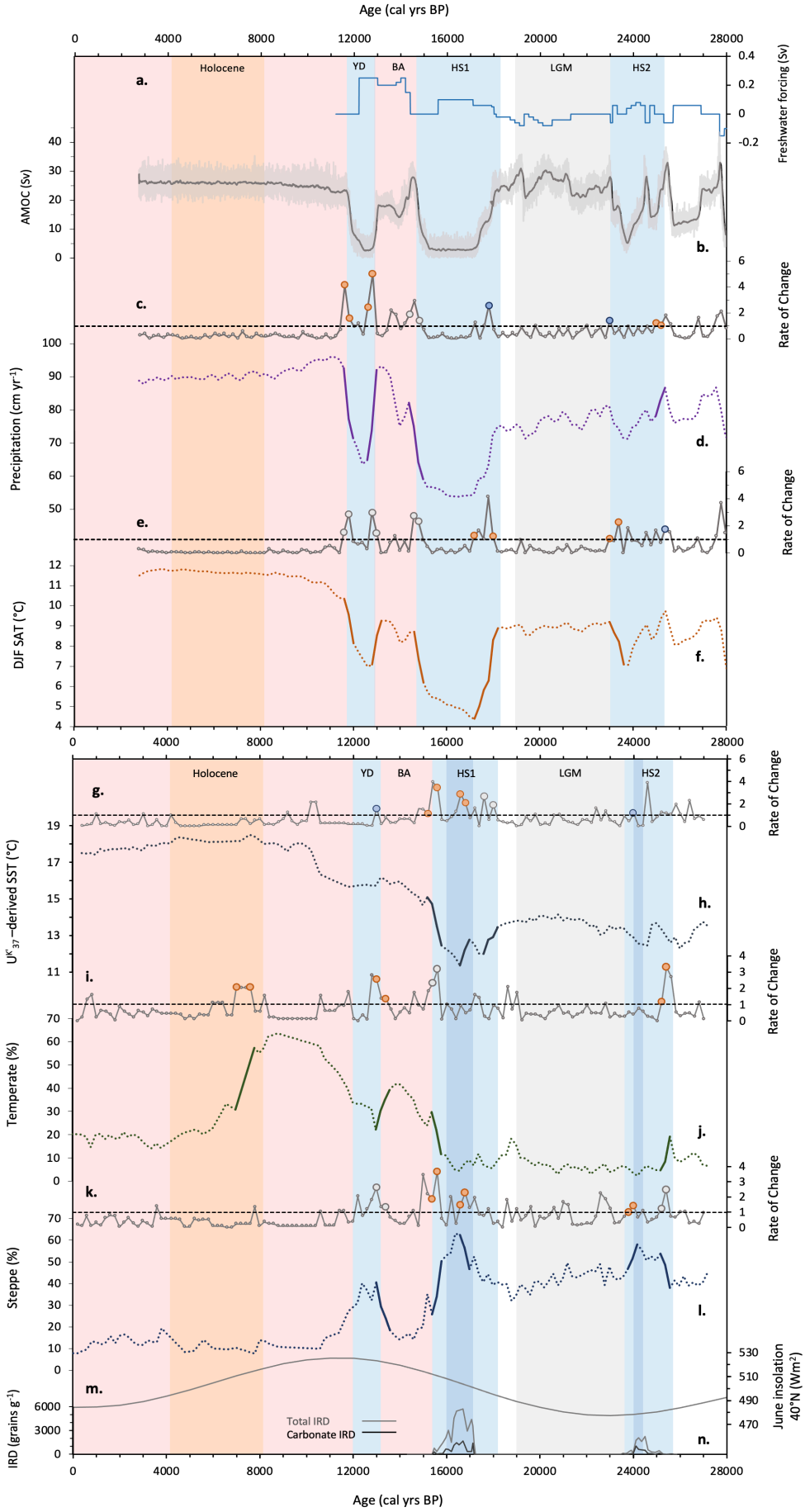
Age (cal yrs BP)
Holocene
YD
BA
HS1
LGM
HS2
a.
b.
c.
d.
e.
f.
g.
h.
i.
j.
k.
l.
m.
n.
Freshwater forcing (Sv)
AMOC (Sv)
Rate of Change
Precipitation (cm yr⁻¹)
DIF SAT (°C)
U^K'37–derived SST (°C)
Temperate (%)
Steppe (%)
IRD (grains g⁻¹)
Total IRD
Carbonate IRD
June insolation 40°N (Wm²)

Fig. 8.4: Changes over time (cal ka BP) in: **a.** freshwater forcing added into the North Atlantic (Sv) in the LOVECLIM model (Menviel *et al.,* 2011; 2014); and **b.** AMOC (Sv) (grey) simulated by LOVECLIM, smoothed with 100-year running mean (black line) (Menviel *et al.,* 2011; 2014). Changes over time in the normalised rates of change and resampled climate and vegetation records of: **c. & d.** annual precipitation simulated by LOVECLIM (cm yr^{-1}) (Menviel *et al.,* 2011; 2014); **e. & f.** December to February surface air temperature simulated by LOVECLIM (DJF SAT; °C) (Menviel *et al.,* 2011; 2014); **g. & h.** $U^{K'}_{37}$-derived sea surface temperatures from MD01-2444 (SST; °C) (Martrat *et al.,* 2007); **i. & j.** temperate taxa from SHAK06-5K (%); and **i. & j.** steppe taxa from SHAK06-5K (%). Changes over time of **m.** boreal insolation at 40°N (Wm^2; Berger, 1978); and **n.** ice-rafted debris (IRD; grains g^{-1}; Ausin *et al.,* 2020). Orange and grey markers highlight the values of RoC for the climate forcing and inferred vegetation response that meet the criteria for abrupt change; the former demonstrates the climate/pollen record with the highest RoC. Blue markers highlight single datapoints at the transitions that exceed 1σ, but do not meet the criteria for abrupt change.

8.3.5. Comparison to existing vegetation records

Here, we compare four existing high-resolution SW Iberian pollen records, covering various stages of the last 18 cal ka BP, to those of SHAK06-5K and MD01-2444 (Fig. 8.5). Three of these are marine cores located close to the mouth of the Tagus River, while one is a lacustrine record from Charco da Candieira in the Serra da Estrela, Portugal (van der Knaap & van Leuween, 1995; 1997), located 1400 m above sea level, bordering the Tagus catchment basin (all locations are shown in Fig. 3.1). While the marine records display large-scale vegetation change across this region, the terrestrial record documents a local signal, and provides a sense of spatial heterogeneity in the region. It must be noted that pollen percentages from the marine and terrestrial cores are not directly comparable. This is because in marine records, *Pinus* is excluded from the pollen sum, and herbaceous pollen percentages are significantly higher, likely a reflection of riparian and coastal vegetation communities.

The pollen records from marine cores SHAK06-5K and U1385 (Oliveira *et al.,* 2018) cover HS1 and demonstrate the dominance of steppe taxa, reaching 68% in SHAK06-5K and 50% in U1385, indicating cold/dry conditions. Temperate forest and Ericaceae values remained low, while *Pinus* percentages were high over this stadial. The BA is covered in both SHAK06-5K and U1385, while MD95-2042 (Chabaud *et al.,* 2014) begins in the mid-BA. The Charco da Candieira pollen record was plotted against a new age model, using the 24 ^{14}C bulk dates from the same record

(van der Knaap & van Leuween, 1995; 1997) and calibrated in Oxcal using the Intcal20 calibration curve (Reimer *et al.,* 2020). According to this, the record covers the interval 14.3 to 0.4 cal ka BP and shows high percentages of temperate taxa during the BA (~22%), signifying warmer/wetter conditions (Fig. 8.5). The other records also show high levels of temperate taxa throughout the BA, averaging ~45% in U1385 and ~34% in SHAK06-5K. A small rise in Ericaceae is documented in both SHAK06-5K and the Charco da Candieira record, indicating a slight rise in year-round moisture availability coinciding with high lake levels in the Serra da Estrela region (van der Knaap & van Leuween, 1997). An abrupt decline in temperate taxa and rise in steppe vegetation is seen in all cores at the transition from the BA into the YD, signifying a rapid regional cooling/drying. Lake levels are low in the Serra da Estrela region (van der Knaap & van Leuween, 1997), while on average, steppe percentages are ~36% in SHAK06-5K, ~24% in MD95-2042, ~24% in U1385, ~3% in Charco da Candieira, and ~20% in D13882 (Gomes *et al.,* 2020). All records document a gradual expansion of thermophilous temperate forest during the Early Holocene, with the peak in these elements occurring between 9.7 – 8.8 ka BP in the SHAK06-5K, MD95-2042, U1385, and Charco da Candieira records. The timing of this maximum woodland expansion coincides with increased lake levels in the Serra da Estrela region (van der Knaap & van Leuween, 1997). In core D13882, the peak in temperate woodland occurs later, at ~7.6 cal ka BP. The maximum percentage of these elements ranges between 64% in SHAK06-5K to 88% in the Charco da Candieira core, with all records indicating that optimal conditions for forest expansion occurred around ~2 cal ka BP after the peak in insolation. After the peak in woodland, thermophilous elements in cores SHAK06-5K, MD01-2444, and MD95-2042 briefly decline. Dated at ~8.6 cal ka BP in MD95-2042, it is likely that this event is aligned with the 8.2 cal ka BP decline displayed in cores SHAK06-5K and MD01-2444. These three cores, therefore, demonstrate the response of SW Iberian vegetation to regional cooling associated with feedbacks resulting from the 8.2 ka event. The lower resolution of the other regional pollen records at this time prevents this event from being assessed.

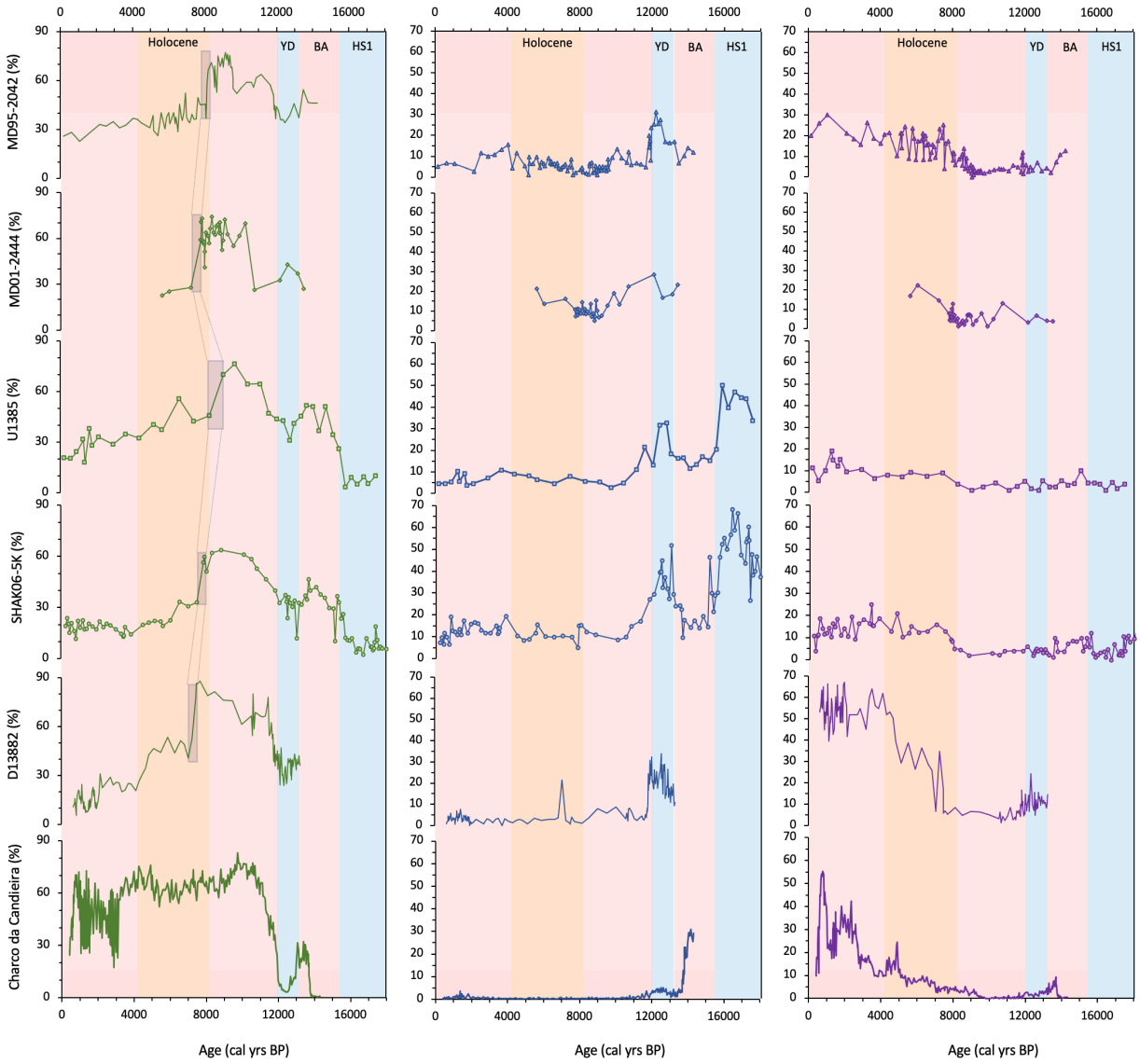

Fig. 8.5: SW Iberian pollen records of temperate tree (green), steppe (blue), and Ericaceae (purple) vegetation change over the past 17 kyr from cores MD95-2042 (Chabaud *et al.,* 2014), MD01-2444 (this study), U1385 (Oliveira *et al.,* 2018), SHAK06-5K (this study), D13882 (Gomes *et al.,* 2020), and Charco da Candieira (Van der Knaap & van Leeuwen, 1997).

All SW Iberian Margin marine cores analysed here display a rapid and significant decline in thermophilous woodland at the start of the mid-Holocene, with temperate elements declining to 30-45 % in under 500 years. The North Atlantic climate does not display any abrupt changes of this magnitude at this time, therefore, vegetation records from this region support the suggestion of an abrupt, intrinsic, non-linear response of SW Iberian thermophilous woodland to the gradual forcing of declining boreal insolation. The Charco da Candieira record, does not demonstrate this abrupt woodland contraction. This could be because the local vegetation signal is influenced by high altitude climate conditions, meaning the ecological threshold was not reached. Another possibility is that this is related to the problem of closure in percentages,

where significant changes in the size of tree populations are barely discernible when arboreal pollen values are high (Magri, 1994).

All Late Holocene marine records from this region document low levels of temperate taxa compared to the early interglacial. The high-resolution D13882 and Charco da Candieira records demonstrate significant multi-centennial variability in temperate woodland after 2.2 and 3.2 cal ka BP, respectively, likely due to the increasing intensification of anthropogenic pressures on this region's land-use, hydrology, and vegetation (van der Knaap & van Leeuwen, 1995; Gomes *et al.,* 2020). A rise in Ericaceae is seen in all cores over the Late Holocene, coinciding with the declining boreal insolation, demonstrating the response of heathland to the associated rise summer water availability, although the final peak in the Charco da Candieira record at 0.8 cal ka BP is likely caused by anthropogenic activities (van der Knaap & van Leeuwen, 1995; Tzedakis, 2010). In the SHAK06-5K, U1385, and Charco da Candieira records, a sharp rise in *Pinus* can be seen after ~0.6 cal ka BP, possibly linked to the large-scale plantation of this genus.

In summary, the pollen records discussed here provide support for the presence of extrinsic ecological responses of SW Iberian vegetation to rapid climate regime shifts during HS2, HS1, and the YD as well as the intrinsic abrupt vegetation response at ~7.8 cal ka BP to gradual climate change.

8.4. Conclusions

1. Over the course of the deglaciation, the deposition of terrestrial sediment at our core site is strongly influenced by changes in relative sea level. Until ~12 cal ka BP, the pollen concentration and MAR in SHAK06-5K is relatively high, abruptly declining thereafter as a result of the disconnection of the Tagus River from the Cascais and Sebutal-Lisbon canyons and the consequential landward movement of the terrestrial sediment depocenter.
2. Comparing the temperate and steppe records from core SHAK06-5K with SSTs, $\delta^{18}O_{G.\ bulloides}$, and *ln*(Ca/Ti) from the same core, a clear synchroneity is apparent in the timing of orbital and millennial-scale changes in all records. Additionally, when comparing our pollen records with existing SW Iberian vegetation records, a clear correlation can be seen in the timing and magnitude of abrupt vegetation changes in response to the abrupt climate events of HS2, HS1, the BA and the YD.
3. On orbital timescales, over MIS 2 and onset of the Holocene, temperate and steppe records from SHAK06-5K document a close coupling with Iberian Margin SSTs, $\delta^{18}O_{G.\ bulloides}$, and benthic $\delta^{18}O$, underscoring the influence of North Atlantic conditions and global ice volume on SW Iberian thermophilous and steppe elements over this period. The influence of residual high-latitude ice-sheets continues at the onset of the Holocene, causing the thermophilous woodland peak to lag boreal insolation maxima by ~2 kyr. This pattern is also apparent in existing SW Iberian vegetation records.
4. On orbital timescales, $\delta^{13}C_{C31}$ is closely coupled with the temperate and steppe records, displaying low values during MIS 2 as steppe elements dominated, increasing over the deglaciation as thermophilous woodland expanded, and documenting the same gradual increase over the early Holocene as temperate vegetation, lagging the boreal insolation maxima by ~2 kyr. While the close coupling of these records on orbital timescales is clear, this relationship could result from the direct influence of climate on both proxies, or it could be driven by physiological differences in carbon isotope fractionation between different dominant taxa groups, meaning $\delta^{13}C_{C31}$ is indirectly linked to changing regional climate conditions through its influence on SW Iberian vegetation structure.
5. On millennial timescales, the rapid changes in thermophilous and steppe elements in SHAK06-5K and MD01-2444 (at the onset and end of HS2, the IRD event and end of HS1, and the onset of the YD) are synchronous with abrupt North Atlantic events. This tight coupling and the RoC of the pollen and regional climate records suggests these abrupt ecosystem changes were extrinsically forced by abrupt climate regime shifts. At ~7.8 cal ka

BP, our pollen records show an abrupt and significant decline in thermophilous woodland, a pattern that is also documented across existing pollen records from this region. Occurring whilst boreal insolation is in gradual decline and North Atlantic conditions are relatively stable, this demonstrates an intrinsically mediated abrupt vegetation response, signifying that temperate taxa crossed an ecological threshold, possibly as a result of changes in moisture availability resulting from altered precipitation seasonality.

This research generated new continuous pollen and leaf-wax *n*-alkane records from deep-sea cores SHAK06-5K and MD01-2444 from the SW Iberian Margin, spanning the last glacial-interglacial transition. A new high-resolution master age model was created and applied to these records, based on 47 Accelerator Mass Spectrometry ^{14}C ages of monospecific samples of the planktonic foraminifera *G. bulloides*, measured from SHAK06-5K (n = 40) and MD01-2444 (n = 7), and aligned using an automated stratigraphical alignment method. The SHAK06-5K pollen and *n*-alkane records span the past 27.4 kyr, documenting the changing climate of MIS 2 and the Holocene and includes numerous abrupt North Atlantic climate events: HS2, HS1, the onset of the BA, the YD, and 8.2 cal ka BP. The MD01-2444 pollen record documents the transition from the YD into the Holocene, covering 5.7 to 13.5 cal ka BP. Consequently, these records provide insights into the changing depocenter of terrestrial sediment on the SW Iberian Margin over the last deglaciation, the potential use of the $\delta^{13}C_{n\text{-alkane}}$ record as a climate signal, and the ecological responses and sensitivity of SW Iberian vegetation to orbital and millennial-scale climate changes over the past 27.4 kyr.

9.1. The changing depocenter of terrestrial material at the SW Iberian Margin

The high-resolution pollen and *n*-alkane concentration and MAR records combined with existing SW Iberian Margin pollen concentration records, demonstrate the changing depocenter of terrestrial material on the SW Iberian Margin over the last deglaciation and Holocene. While the source area of pollen and n-alkanes to the SW Iberian Margin remained relatively constant over the last 27.4 kyr, the deposition of terrestrial sediment to the deep-sea environment, which had remained relatively high over the LGM, abruptly declined during the YD as the Tagus river became disconnected from the Cascais and Sebutal-Lisbon canyons due to sea level rise. This led to the landward movement of the terrestrial depocenter, resulting in the reduced transport of terrestrial material to the deep-ocean over the Holocene. Consequently, these vegetation records indicate the significant influence of marine transgression on the location of terrestrial sediment deposition on the SW Iberian Margin over the last 27.4 kyr.

9.2. The use of $\delta^{13}C_{n\text{-alkane}}$ as a climate signal

The production of the SHAK06-5K leaf-wax $\delta^{13}C_{n\text{-alkane}}$ record in combination with a pollen record from the same core, and leaf-wax $\delta^{13}C_{n\text{-alkane}}$ measurements on modern samples from

SW Iberia, enabled the dominant driver of $\delta^{13}C_{n\text{-alkane}}$ in the fossil record within a C_3 vegetation environment to be explored. While we conclude that $\delta^{13}C_{n\text{-alkane}}$ in SHAK06-5K cannot be used here as an independent climate signal, this proxy is likely to be driven directly or indirectly by SW Iberian climate, with two potential mechanisms proposed here. Firstly, $\delta^{13}C_{n\text{-alkane}}$ may be primarily controlled by regional moisture availability which influences the water stress of the plant, in turn affecting its stomatal conductance and consequently carbon isotope fractionation. Secondly, $\delta^{13}C_{n\text{-alkane}}$ may be primarily driven by the regional vegetation structure, with different taxa demonstrating inherently different *n*-alkane $\delta^{13}C$ signatures, as shown by the modern records presented in Chapter 7. With the vegetation structure driven by the regional climate, $\delta^{13}C_{n\text{-alkane}}$ would therefore be indirectly influenced by these conditions. In conclusion, this research has enabled further exploration of the use of this geochemical proxy as a climate/vegetation signal in a C_3 vegetation environment, outside of its traditional role as a C_3/C_4 vegetation signal. Although the dominant driver of $\delta^{13}C_{n\text{-alkane}}$ cannot be disentangled by this research alone, the close relationship displayed with the pollen record from within the same core indicates that, whether directly or indirectly, climate plays a key role in driving $\delta^{13}C_{n\text{-alkane}}$ in the fossil record. While $\delta^{13}C_{n\text{-alkane}}$ is likely to be a convolved signal, there is significant potential to disentangle the climate/physiological drivers of $\delta^{13}C_{n\text{-alkane}}$ using complementary palaeohydrological records (such as leaf-wax *n*-alkane δD). In future, it may be possible to use this proxy as an indicator of the dominant vegetation type or changes in regional water availability.

9.3. Orbital and millennial-scale vegetation change over the past 27.4 kyr

The pollen records indicate rapid responses of SW Iberian vegetation to orbital and millennial-scale climate events over the past 27.4 kyr, demonstrating clear synchroneity with SW Iberian palaeoceanographic records from within the same cores. On orbital timescales, there is a close coupling between the temperate tree and steppe pollen records from SHAK06-5K and Iberian Margin SSTs and planktonic and benthic $\delta^{18}O$ over MIS 2, indicating the strong influence of North Atlantic conditions and global ice volume on SW Iberian vegetation at this time. This coupling continues at the onset of the Holocene demonstrating that the continued influence of residual high-latitude ice-sheets on SW Iberian vegetation likely caused the peak in thermophilous woodland to lag boreal insolation maxima by ~2 kyr. On millennial timescales there is also a tight temporal coupling between rapid changes in temperate tree and steppe pollen percentages, SSTs, planktonic $\delta^{18}O$, and lithological variations during HS2, HS1, the onset of the BA, the YD, and the 8.2 ka event. This tight coupling and the RoC of the pollen and

regional climate records demonstrates that the abrupt vegetation changes at the onset and end of HS2, the IRD event and end of HS1, and the onset of the YD are extrinsically-forced ecosystem responses to abrupt climate shifts. In contrast, the abrupt decline in thermophilous elements at ~7.8 cal ka BP indicates an intrinsically-mediated abrupt vegetation response to the gradually declining boreal insolation, whereby temperate taxa crossed an ecological threshold, likely resulting from altered precipitation seasonality.

Consequently, this research shows that SW Iberian vegetation changed abruptly in response to both gradual and abrupt climate changes over the past 27.4 kyr, demonstrating that vegetation in this region can respond both linearly and non-linearly to climate forcings, depending on background conditions. This highlights the need for further exploration into the sensitivity and thresholds of dominant Mediterranean ecosystems to various abrupt and gradual climate forcings. With this research concluding that changes in hydrological seasonality may have played a key role in the intrinsic vegetation response at the early to mid-Holocene transition, and in light of projections of enhanced drought stress across the western Mediterranean in future (Giorgi, 2006; Giorgi & Lionello, 2008; Lionello, 2012; Lionello *et al.,* 2014), better understanding of the role of water availability and moisture stress on abrupt changes in western Mediterranean vegetation is required.

9.4. SW Iberian hydrology over the LGM

The continued discrepancies between the interpretations of SW Iberian hydrology over the LGM from proxy and simulated data highlight the need for better understanding of hydrological conditions in this region over MIS 2. Our pollen record shows that the hydrological conditions during the LGM were much more complex than just increased or reduced precipitation comparative to pre-industrial levels. The lower temperatures and reduced winter precipitation during the LGM favoured the dominance of steppe vegetation, while the reduced seasonality caused by the summer insolation minimum in combination with moderate Iberian Margin SSTs may have reduced summer evaporative moisture leading to moderate levels of effective moisture that were able to sustain heathland populations and some thermophilous elements. Reduced hydrological seasonality over western Iberia during the LGM compared to pre-industrial levels is also shown in the simulated precipitation records presented in this study (Menviel *et al.,* 2011; 2014).

9.5. Future directions

- With this thesis having focused on the response and sensitivity of SW Iberian vegetation to changing background conditions during the transition from the Last Glacial into the current interglacial (Termination I), there is potential to explore the response and sensitivity of SW Iberian vegetation to changing background conditions under different climate regimes. One period that could provide such insight is the transition from the Penultimate Glacial to Last Interglacial transition (Termination II), which also demonstrated complex climate changes with similar greenhouse gas forcings, but stronger boreal insolation and a different sea level and ice volume evolution (Berger *et al.,* 1978; Dutton *et al.,* 2015; Marino *et al.,* 2015; Tzedakis *et al.,* 2018). Comparing our records to new and/or existing high-resolution SW Iberian vegetation and palaeoceanographic records spanning Termination II (Tzedakis *et al.,* 2018) would provide further insight into the sensitivity and intrinsic/extrinsic responses of SW Iberian vegetation to different background conditions.

- While this research compared the RoC of abrupt events in vegetation and palaeoceanographic records, and simulated climate variables from SW Iberia, the production of an independent palaeohydrology record from within the same core would allow for the analysis of leads and lags between changes in vegetation and climate components.

- As shown in Chapter 8, with the addition of the new pollen records from SHAK06-5K and MD01-2444, there are a number of SW Iberian Margin marine pollen records spanning the past 27.4 kyr that provide a strong understanding of large-scale vegetation changes across SW Iberia. Conversely, few terrestrial pollen records from this region currently exist, but these records can provide valuable insight into the spatial heterogeneity of vegetation change across a region. The production of more long terrestrial pollen records from SW Iberia, spanning different altitudes and ecosystems, would provide valuable insight into the response and sensitivity of different Mediterranean ecosystems to changing background conditions. This would enhance the interpretations made here and allow for a more detailed investigation into SW Iberian vegetation change over the last 27.4 kyr.

- One of the original objectives of this research was to produce a complementary $\delta D_{n\text{-alkane}}$ record from SHAK06-5K as an independent proxy of SW Iberian hydrological change over the past 27.4 kyr. The national lockdowns, laboratory closures, and travel restrictions resulting from the Covid-19 pandemic prevented these measurements from being made

within the PhD timeframe. The production of a high-resolution leaf-wax $\delta D_{n\text{-alkane}}$ record from this core would enable a more robust interpretation of palaeoclimatic changes in SHAK06-5K, as this proxy is a useful tool for reconstructing hydrological changes over time (Sauer *et al.,* 2001; Sachse *et al.,* 2004; 2006; 2012; Polissar & D'Andrea, 2014; Sessions, 2016). There is every intention to complete these measurements when restrictions are lifted, and the $\delta D_{n\text{-alkane}}$ record will be combined with the climate records presented in this thesis to further explore the dominant $\delta^{13}C_{n\text{-alkane}}$ signal in the fossil record and aid the reconstruction of orbital and millennial-scale hydrological changes in SW Iberia over the past 27.4 kyr.

- As there are limited existing terrestrial biomarker studies from the western Mediterranean region, the contribution of pre-aged terrestrial n-alkanes to SW Iberian margin sediments has not previously been quantified. Research from other regions has shown that pre-aged leaf-wax material from intermediate reservoirs can significantly contribute to the fossil record (Huang *et al.,* 1996; Eglinton *et al.,* 1997; Pearson & Eglinton, 2000; Smittenberg *et al.,* 2006; Mollenhauer & Eglinton, 2007; Kusch *et al.,* 2010; French *et al.,* 2018), therefore, further research is required to quantify this potential contribution at our core site in order to better understand the factors influencing the fossil *n*-alkane signal.

- While the number of species sampled for our modern *n*-alkane record was limited by both time and financial constraints, it would be beneficial to build on this work and expand on the existing modern Mediterranean leaf-wax *n*-alkane records to include more plant species spanning a range of plant functional groups, ecosystems, and climates. This would enable further exploration into the role of external climate conditions and plant physiology on leaf-wax *n*-alkane distribution and isotope fractionation. In turn, this will assist with the interpretation of future fossil leaf-wax *n*-alkane records.

- This research demonstrated a relationship in modern Mediterranean vegetation between a plant's leaf-wax *n*-alkane ACL and its tolerance to heat and drought stress, suggesting that a higher ACL is an adaptive feature of Mediterranean taxa at the molecular level to increased drought and heat stress. The proposed mechanism behind this relationship is that longer *n*-alkane homologues increase the volume of crystallites and leaf-wax melting point, which in turn reduces cuticular permeability and reduces potential water loss. This relationship, however, has not been widely investigated and further research is required to explore this in more detail.

References

Abe-Ouchi, A., Segawa, T and Saito, F. 2007. Climatic Conditions for modelling the Northern Hemisphere ice sheets throughout the ice age cycle. *Climate of the Past*, **3**, 423–438.

Abrantes, F. 1992. Palaeoproductivity oscillations during the last 130 ka along the Portuguese and NW African margins. *Geological Society*, **64**, 499-510.

Adkins, J.F and Boyle, E.A. 1997. Changing atmospheric $\Delta^{14}C$ and the record of deep water paleoventilation ages. *Paleoceanography and Paleoclimatology*, **12**, 337-344.

Adkins, J. F., McIntyre, K and Schrag, D. P. 2002. The salinity, temperature, and $\delta^{18}O$ of the Glacial Deep Ocean. *Science*, **298**, 1769–1773.

Aguiar, F.C., Ferreira, M.T., Moreira, I.S and Albuquerque, A. 2000. Riparian types on a Mediterranean basin. *Aspects of Applied Biology*, **58**, 221-232.

Aguiar, F.C and Ferreira, M.T. 2005. Human-disturbed landscapes: effects on composition and integrity of riparian woody vegetation in the Tagus River basin, Portugal. *Environmental Conservation*, **32**, 30-41.

Ahn, J and Brook, E.J. 2008. Atmospheric CO_2 and Climate on Millennial Time Scales During the Last Glacial Period. *Science*, **322**, 83-85.

Alcara Ariza, F., Asensi Marfil, A., de Bolos y Capdevilla, O., Costa Tales, M., Arco Aguilar, M., Diaz Gonzales, T.E., Diez Garretas, B., Fernandez Prieto, J.A., Fernandez Gonzales, F., Izco Sevillando, J., Loidi Arregui, J., Martinez Parras, J.M., Navarro Andres, F., Ninot I Sugranes, J.M., Peinado Lorca, M., Rivas Martinez, S., Sanchez Mata, D., Valle Guitierrez, C., Vigo I Bonada, J and Wildpret de la Torre, W. 1987. *La vegetation de Espana*. Madrid: Universidad de Alcala de Henares, 544 pp.

Allen, J.R.M., Huntley, B and Watts, W.A. 1996. The vegetation and climate of northwest Iberia over the last 14,000 years. *Journal of Quaternary Science*, **11**, 125-147.

Allen, J. R., Brandt, U., Brauer, A., Hubberten, H. W., Huntley, B., Keller, J. Kraml, M., Mackensen, A., Mingram, J., Negendank, J.F.W., Nowaczyk, N.R., Oberhansli, H., Watts, W.A., Wulf, S and Zolitschka, B. 1999. Rapid environmental changes in southern Europe during the last glacial period. *Nature*, **400**, 740-743.

Alley, R.B., Mayewski, P.A., Sowers, T., Stuiver, M., Taylor, K. C and Clark, P. U. 1997. Holocene climatic instability: A prominent, widespread event 8200 yr ago. *Geology,* **25**, 483.

Alley, R.B., Marotzke, J., Nordhaus, W. D., Overpeck, J. T., Peteet, D. M., Pielke Jr., R. A., Pierrehumbert, R.T., Rhines, P. B., Stocker, T. F., Talley, L. D and Wallace, J. M. 2003. Abrupt Climate Change. *Science*, **299**, 2005-2010.

Alley, R.B and Ágústsdóttir, A.M. 2005. The 8k event: cause and consequences of a major Holocene abrupt climate change. *Quaternary Science Reviews*, **24**, 1123-1149.

Alt-Epping, U., Mil-Homens, M., Hebbeln, D., Abrantes, F and Schneider, R.R. 2007. Provenance of organic matter and nutrient conditions on a river- and upwelling influenced shelf: A case study from the Portuguese Margin. *Marine Geology*, **243**, 169-179.

Alt-Epping, U., Stuuta, J-B.W., Hebbelna, D and Schneider, R. 2009. Variations in sediment provenance during the past 3000 years off the Tagus River, Portugal. *Marine Geology*, **261**, 82-91.

Alvarez-Solas, J., Charbit, S., Ritz, C., Paillard, D., Ramstein, G and Dumas, C. 2010. Links between ocean temperature and iceberg discharge during Heinrich events. *Nature Geoscience*, **3**, 122-126.

Ambar, I and Fiúza, A. 1994. Some features of the Portugal current system: a poleward slope undercurrent, an upwelling-related summer southward flow and an autumn-winter poleward surface current. *In:* Katsaros, K.B., Fiúza, A. and Ambar, I. (eds.), Proceedings of the second international conference on air-sea interaction and on meteorology and oceanography of the coastal zone. Boston: American Meteorological Society, 286-287 pp.

Andersen, S.T. 1970. The relative pollen productivity and pollen representation of north European trees, and correction factors for tree pollen spectra. *Danm Geol Unders II*, **96**, 1–99.

Andersen, K.K., Svensson, A., Johnsen, S.J., Rasmussen, S.O., Bigler, M., Röthlisberger, R., Ruth, U., Siggaard-Andersen, M.-L., Steffensen, J.P., Dahl-Jensen, D., Vinther, B.M., Clausen, H.B. 2006. The Greenland Ice Core Chronology 2005, 15–42 ka. Part 1: constructing the time scale. *Quaternary Science Reviews*, **25**, 3246-3257.

Anderson, R.F., Ali, S., Bradtmiller, L.I., Nielsen, S.H.H., Fleisher, M.Q., Anderson, B.E and Burckle, L.H. 2009. Wind-Driven Upwelling in the Southern Ocean and the Deglacial Rise in Atmospheric CO_2. *Science*, **323**, 1143-1448.

Arens, N.C, Jahren, A.H and Amundson, R. 2000. Can C_3 Plants Faithfully Record the Carbon Isotopic Composition of Atmospheric Carbon Dioxide? *Paleobiology*, **26**, 137-164.

Armbruster, D.A and Pry, T. 2008. Limit of Blank, Limit of Detection and Limit of Quantitation. *The Clinical Biochemist Reviews*, **29**, 49-52.

Arz, H.W., Pätzold, J and Wefer, G. 1998. Correlated Millennial-Scale Changes in Surface Hydrography and Terrigenous Sediment Yield Inferred from Last-Glacial Marine Deposits off Northeastern Brazil. *Quaternary Research,* **50**, 157-166.

Arzola, R.G., Wynn, R.B., Lastras, G., Masson, D.G and Weaver, P.P.E. 2008. Sedimentary features and processes in the Nazaré and Setúbal submarine canyons, west Iberian margin. *Marine Geology*, **250**, 64-88.

Ausin, B., Haginpour, N., Wacker, L., Voelker, A.H.L., Hodell, D., Magill, C., Looser, N., Bernasconi, S.M and Eglinton, T.I. 2019a. Radiocarbon age offsets between two surface dwelling planktonic foraminifera species during abrupt climate events in the SW Iberian Margin. *Paleoceanography & Paleoclimatology*, **34**, 63-78.

Ausin, B., Magill, C., Haghipour, N., Fernández, A., Wacker, L., Hodell, D., Baumann, K-H and Eglinton, T.I. 2019b. (In)coherent multiproxy signals in marine sediments: Implications for high-resolution paleoclimate reconstruction. *Earth & Planetary Science Letters*, **515**, 38-46.

Ausin, B., Hodell, D.A., Cutmore, A and Eglinton, T.I. 2020. The impact of abrupt deglacial climate variability on productivity and upwelling on the southwestern Iberian Margin. *Quaternary Science Reviews*, **230**, 1-13.

Bai, Y., Fang, X., Nie, J., Wang, Y and Wu, F. 2009. A preliminary reconstruction of the paleoecological and paleoclimatic history of the Chinese Loess Plateau from the application of biomarkers. *Palaeogeography, Palaeoclimatology, Palaeoecology,* **271,** 161–169.

Baker, E.A., 1982. *Chemistry and morphology of plant epicuticular waxes. In:* Cutler, D.F., Alvin, K.L., Price, C.E (eds.), The *Plant* Cuticle. London: Academic Press, 139-165 pp.

Baker, J.L., Lachniet, M.S., Chervyatsova, O., Asmerom, Y and Polyak, V.J. 2017. Holocene warming in western continental Eurasia driven by glacial retreat and greenhouse forcing. *Nature Geoscience*, **10**, 430–435.

Baldini, L.M., McDermott, F., Baldini. J.U.L., Arias, P., Cueto, M., Fairchild, I.J., Hoffmann, D.L., Mattey, D.P., Müller, W., Nita, D.C., Ontanon, R., Garcia-Monco, C., Richards, D.A. 2015. Regional temperature, atmospheric circulation, and sea-ice variability within the Younger Dryas Event constrained using a speleothem from northern Iberia. *Earth & Planetary Science Letters*, **419**, 101–110.

Baldini, L.M., Baldini. J.U.L., McDermott, F., Arias, P., Cueto, M., Fairchild, I.J., Hoffmann, D.L., Mattey, D.P., Müller, W., Nita, D.C., Ontanon, R., Garcia-Monco, C., Richards, D.A. 2019. North Iberian temperature and rainfall seasonality over the Younger Dryas and Holocene. *Quaternary Science Reviews*, **226**, 1-22.

Baquedano, F.J and Castillo, F.J. 2007. Drought tolerance in the Mediterranean species Quercus coccifera, Quercus ilex, Pinus halepensis, and Juniperus phoenicea. *Photosynthetica*, **45**, 229-238.

Bao, R., Uchida, M., Zhao, M., Haghipour, N., Montlucon, D., McNichol, A., Wacker, L., Hayes, J.M and Eglinton, T.I. 2018. Organic carbon aging during across-shelf transport. *Geophysical Research Letters*, **45**, 8425-8434.

Barber, D.C., Dyke, A., Hillaire-Marcel, C., Jennings, A.E., Andrews, J.T., Kerwin, M.W., Bilodeau, G., McNeely, R, Southon, J., Morehead, M.D and Gagnon, J.M. 1999. Forcing of the cold event of 8,200 years ago by catastrophic drainage of Laurentide lakes. *Nature*, **400**, 344–348.

Bard, E., Arnold, M., Maurice, P., Duprat, J., Moyes, J and Duplessy, J. C. 1987. Retreat velocity of the North Atlantic polar front during the last deglaciation determined by ^{14}C accelerator mass spectrometry. *Nature*, **328**, 791-794.

Bard, E. 1988. Correction of accelerator mass spectrometry ^{14}C ages measured in planktonic foraminifera: Paleoceanographic implications. *Paleoceanography & Paleoclimatology*, **3**, 635-645.

Bard, E., Hamelin, B., Fairbanks, R.G and Zindler, A. 1990. Calibration of the ^{14}C timescale over the past 30,000 years using mass spectrometric U–Th ages from Barbados corals. *Nature*, **345**, 405-410.

Bard, E., Arnold, M., Hamelin, B., Tisnerat-Laborde, T and Cabioch, G. 1998. Radiocarbon Calibration by Means of Mass Spectrometric 230Th/234U and ^{14}C Ages of Corals: An Updated Database Including Samples from Barbados, Mururoa and Tahiti. *Radiocarbon*, **40**, 1085-1092.

Bard, E., Rostek, F., Turin, J-.L and Gendreau, S. 2000. Hydrological Impact of Heinrich Events in the Subtropical Northeast Atlantic. *Science*, **289**, 1321-1324.

Bard, E., Rostek, F and Menot-Combes, G. 2004. Radiocarbon calibration beyond 20,000 ^{14}C yr B.P. by means of planktonic foraminifera of the Iberian Margin. *Quaternary Research*, **61**, 204-214.

Bard, E. 2010. Paleoceanographic implications of the difference in deep-sea sediment mixing between large and fine particles. *Paleoceanography & Paleoclimatology*, **16**, 235-239.

Bard, E., Ménot, G., Rostek, F., Licari, L., Böning, P., Edwards, R.L., Cheng, H., Wang, Y and Heaton, T.J. 2013. Radiocarbon Calibration/Comparison Records Based on Marine Sediments from the Pakistan and Iberian Margins. *Radiocarbon*, **55**, 1999-2019.

Bard, E., Tuna, T., Fagault, Y., Bonvalot, L., Wacker, L., Fahrni, S and Synal, H-A. 2015. AixMICADAS, the accelerator mass spectrometer dedicated to ^{14}C recently installed in Aix-en-Provence, France. *Nuclear Instruments and Methods in Physics Research B*, **361**, 80-86.

Barker, S., Diz, P., Vautravers, M. J., Pike, J., Knorr, G., Hall, I. R and Broecker, W. S. 2009. Interhemispheric Atlantic seesaw response during the last deglaciation. *Nature*, **457**, 1097-1102.

Barker, S., Knorr, G., Vautravers, M.J., Diz, P and Skinner, L.C. 2010. Extreme deepening of the Atlantic overturning circulation during deglaciation. *Nature Geoscience*, **3**, 567-571.

Barker, S., Chen, J., Gong, X., Jonkers, L., Knorr, G and Thornalley, D. 2015. Icebergs not the trigger for North Atlantic cold events. *Nature*, **520**, 333–336.

Barthlott, W., Neinhuis, C., Cutler, D., Ditsch, F., Meusel, I., Theisen, I and Wilhelmi, H. 1998. Classification and terminology of plant epicuticular waxes. *Botanical Journal of the Linnean Society*, **126**, 237-260.

Bassett, S.E., Milne, G.A. Mitrovica, J.X and Clark, P.U. 2005. Ice sheet and solid earth influences on far-field sea-level histories**.** *Science*, **309**, 925-928.

Bassis, J.N., Peterson, S.V and Mac Cathles, L. 2017. Heinrich events triggered by ocean forcing and modulated by isostatic adjustment. *Nature*, **542**, 332–334.

Basson, I and Reynhardt, E.C. 1988a. An investigation of the structures and molecular dynamics of natural waxes. I. Beeswax. *Journal of Physics D: Applied Physics*, **21**, 1421-1428.

Basson, I and Reynhardt, E.C. 1988b. An investigation of the structures and molecular dynamics of natural waxes. II. Carnauba wax. *Journal of Physics D: Applied Physics*, **21**, 1429-1433.

Basson, I and Reynhardt, E.C. 1991. Identification of defect chain motions in the low temperature orthorhombic phase of binary mixtures of n-alkanes by means of nuclear

magnetic resonance spin-lattice relaxation time measurements. *The Journal of Chemical Physics*, **95**, 1215-1222.

Basson, I and Reynhardt, E.C. 1992. The structure and melting of paraffinic Fischer-Tropsch waxes. *Chemical Physics Letters*, **198**, 367-37

Bateman, M.D and Diez Herrero, A. 2001. The timing and relation of aeolian sand deposition in central Spain to the aeolian sand record of NW Europe. *Quaternary Science Reviews*, **20**, 779-782.

Bates, C.D., Coxon, P., Gibbard, P.L. 1978. A New method for the preparation of clay rich sediment samples for palynological investigation. *New Phytologist,* **81**, 459-463.

Bauska, T.K., Baggenstos, D., Brook, E.J., Mix, A.C., Marcott, S.A., Petrenko, V.V., Schaefer, H., Severinghaus, J.P and Lee, J.E. 2016. Carbon isotopes characterize rapid changes in atmospheric carbon dioxide during the last deglaciation. *Proceedings of the National Academy of Sciences*, **113**, 3465-3470.

Beck, J.W., Richards, D.A., Edwards, R.L., Silverman, B.W., Smart, P.L., Donahue, D.J., Hererra-Osterheld, S., Burr, G.S., Calsoyas, L., Jull, T and Biddulph, D. 2001. Extremely Large Variations of Atmospheric ^{14}C Concentration During the Last Glacial Period George. *Science*, **292**, 2453-2458.

Becker, M., Kerstiens, G and Schönherr, J. 1986. Water permeability of plant cuticles: permeance, diffusion and partition coefficients. *Trees*, **1**, 54-60.

Beghin, P., Charbit, S., Kageyama, M., Combourieu-Nebout, N., Hatté, C., Dumas, C and Peterschmitt, J.-Y. 2016. What drives LGM precipitation over the western Mediterranean? A study focused on the Iberian Peninsula and northern Morocco. *Climate Dynamics*, **46**, 2611–2631.

Bell, B.A and Fletcher, W.J. 2016. Modern surface pollen assemblages from the Middle and High Atlas, Morocco: insights into pollen representation and transport. *Grana*, **55**, 286–301.

Bennett, K.D. 1986. The rate and spread of population increase of forest trees during the postglacial. *Philosophical Transactions of the Royal Society*, **314**, 523-531.

Bennett, K.D., Tzedakis, P.C and Willis, K.J. 1991. Quaternary refugia of north European trees. *Journal of Biogeography*, **18**, 103-115.

Bennett, K.D. 1996. Determination of the number of zones in a biostratigraphical sequence. *New Phytologist*, **132**, 155–170.

Bennett, K.D. 2011. *Psimpoll* and *pscomb* programs for plotting and analysis. http://chrono.qub.ac.uk/psimpoll/psimpoll.html

Berger A. 1978. Long-term variations of daily insolation and quaternary climatic changes. *Journal of Atmospheric Science*, **35**, 2362–2367.

Berglund, B.E and Ralska-Jasiewiczowa, M. 1986. Pollen analysis and pollen diagrams. *In:* Berglund, B.E (ed.), Handbook of Holocene palaeoecology and palaeohydrology. Chichester: Wiley, 455-484 pp.

Beug, H.J. 1968. Probleme der Vegetationsgeschichte in Siideuropa. *Berichte der Deutschen Botanischen Gesellschaft*, **80**, 682-689.

Beug, H.J. 2004. *Leitfaden der Pollenbestimmung fur Mitteleuropa und angrenzende Gebiete.* Munich: Verlag Friedrich Pfeil, 542 pp.

Birks, H.J.B. 1987. Recent methodological developments in quantitative descriptive biogeography. *Annales Zoologici Fennici*, **24**, 165-177.

Birks, H.J.B. 2019. Contributions of Quaternary botany to modern ecology and biogeography. *Plant Ecology & Diversity*, **12**, 189-385.

Birks, H.J.B and Birks, H.H. 1980. *Quaternary Palaeoecology*. London: Edward Arnold, 289 pp.

Birks, H.H and Birks, H.J.B. 2000. Future uses of pollen analysis must include plant macrofossils. *Journal of Biogeography*, **27**, 31-35.

Birks, H.J.B and Gordon, A.D. 1985. *Numerical Methods in Quaternary Pollen Analysis*. London: Gordon Publisher Academic Press, 317 pp.

Birks, H.J.B and Berglund, B.E. 2018. One hundred years of Quaternary pollen analysis 1916–2016. *Vegetation History and Archaeobotany*, **27**, 271–309.

Birks, H.J.B. 2019. Contributions of Quaternary botany to modern ecology and biogeography. *Plant Ecology & Diversity*, **12**, 189-385.

Bjorck, S., Kromer, B., Johnsen, S., Bennike, O., Hammarlund, D., Lemdahl, G., Possnert, G., Rasmussen, T.L., Wohlfarth, B., Hammer, C.U and Spurk, M. 1996. Synchronized Terrestrial-Atmospheric Deglacial Records Around the North Atlantic. *Science*, **274**, 1155-1160.

Blanco Castro, E., Casado Gonzalez, M.A., Costa Tenorio, M., Escribano Bombin, R., Garcia Anton, M., Genova Fuster, M., Gomez Manzaneque, A., Gomez Manzaneque, F., Moreno Saiz, J.C., Morla Juaristi, C., Regato Pajares, P. and Sainz Ollero, H. 1997. *Los bosques ibericos: Una interpretacion geobotanica*. Barcelona: Planeta, 572 pp.

Bliedtner, M., Schäfer, I.K., Zech, R and von Suchodoletz, H. 2018. Leaf wax n-alkanes in modern plants and topsoils from eastern Georgia (Caucasus) – implications for reconstructing regional paleovegetation. *Biogeosciences*, **15**, 3927-3936.

Blunier, T., Chappellaz, J., Schwander, J., Dällenbach, A., Stauffer, B., Stocker, T. F., Raynaud, D., Jouzel, J., Clausen, H.B., Hammer, C.U and Johnsen, S. J. 1998. Asynchrony of Antarctic and Greenland climate change during the last glacial period. *Nature*, **394**, 739-743.

Bond, G., Heinrich, H., Broecker, W., Labeyrie, L., McManus, J., Andrews, J., Huon, S., Jantschik, R., Clasen, S., Simet, C., Tedesco, K., Klas, M., Bonani, G and Ivy, S. 1992. Evidence for massive discharges of icebergs into the North Atlantic Ocean during the last glacial period. *Nature*, **360**, 245–249.

Bond, G., Broecker, W., Johnsen, S., McManus, J., Labeyrie, L., Jouzel, J and Bonani, G. 1993. Correlations between climate records from North Atlantic sediments and Greenland ice. *Nature*, **365**, 143-147.

Bond, G and Lotti, R. 1995. Iceberg discharges into the North Atlantic on millennial time scales during the last glaciation. *Science*, **267**, 1005.

Bond, G., Showers, W., Cheseby, M., Lotti, R., Almasi, P., deMenocal, P., Priore, P., Cullen, H., Hajdas, I., Bonani, G. 1997. A Pervasive Millennial-Scale Cycle in North Atlantic Holocene and Glacial Climates. *Nature*, **278**, 1257-1266.

Bond, G., Kromer, B., Beer, J., Muscheler, R., Evans, M.N., Showers, W., Hoffmann, S., Lotti-Bond, R., Hajdas, I and Bonani, G. 2001. Persistent Solar Influence on North Atlantic Climate During the Holocene. *Science*, **294**, 2130-2136.

Boessenkool, P., Brinkhuis, H., Schonfeld, J and Targarona, J. 2001. North Atlantic sea-surface temperature changes and the climate of western Iberia during the last deglaciation; a marine palynological approach. *Global and Planetary Change*, **30**, 33-39.

Braconnot, P., Otto-Bliesner, B., Harrison, S., Joussaume, S., Peterchmitt, J.-Y., Abe-Ouchi, A., Crucifix, M., Driesschaert, E., Fichefet, T., Hewitt, C. D., Kageyama, M., Kitoh, A., Laîné, A., Loutre, M.-F., Marti, O., Merkel, U., Ramstein, G., Valdes, P., Weber, S. L., Yu, Y and Zhao, Y. 2007. Results of PMIP2 coupled simulations of the Mid-Holocene and Last Glacial Maximum – Part 1: experiments and large-scale features. *Climate of the Past*, **3**, 261-277.

Bradshaw, R.H.W and Webb, T. 1985. Relationships between Contemporary Pollen and Vegetation Data from Wisconsin and Michigan, USA. *Ecology*, **66**, 721-737.

Brassell, S.C., Eglinton, G., Marlowe, I.T., Pflaumann, U and Sarnthein, M. 1986. Molecular stratigraphy: a new tool for climatic assessment. *Nature*, **320**, 129–133.

Bray, E.E and Evans, E.D. 1961. Distribution of *n*-paraffins as a clue to recognition of source beds. *Geochimica et Cosmochimica Acta*, **22**, 2-15.

Broadmeadow, M.S.J and Griffiths, H. 1993. Carbon isotope discrimination and the coupling of CO_2 fluxes within forest canopies**.** *In:* Ehleringer, J.R., Hall, A.E and Farquhar, G.D (eds.), Stable Isotopes and Plant Carbon–Water Relations. San Diego: Academic Press, 109-129 pp.

Bröder, L., Tesi, T., Andersson, A., Semiletov, I and Gustafsson, O. 2018. Bounding cross-shelf transport time and degradation in Siberian-Arctic land-ocean carbon transfer. *Nature Communications*, **9**, 1-8.

Broecker, W.S., Thurber, D.L., Goddard, J., Ku, T-L., Matthews, R.K and Mesolella, K.J. 1968. Milankovitch Hypothesis Supported by Precise Dating of Coral Reefs and Deep-Sea Sediments. *Science*, **159**, 297-300.

Broecker, W.S., Mix, A., Andree, M and Oeschger, H. 1984. Radiocarbon measurements on coexisting benthic and planktic foraminifera shells: potential for reconstructing ocean ventilation times over the past 20 000 years. *Nuclear Instruments and Methods in Physics Research Section B: Beam Interactions with Materials and Atoms*, **5**, 331-339.

Broecker, W. S., Peteet, D. M and Rind, D. 1985. Does the ocean-atmosphere system have more than one stable mode of operation? *Nature*, **315**, 21-26.

Broecker, W. S and Denton, G. H. 1989. The role of ocean-atmosphere reorganizations in glacial cycles. *Geochimica et Cosmochimica Acta*, **53**, 2465-2501.

Broecker, W. S., Kennett, J. P., Flower, B. P., Teller, J.T., Trumbore, S., Bonani, G and Wolfli, W. 1989. Routing of meltwater from the Lauren-tide Ice Sheet during the Younger Dryas cold episode. *Nature*, **341**, 318–321.

Broecker, W. S., Bond, G., Klas, M., Bonani, G and Wolfli, W. 1990. A salt oscillator in the glacial Atlantic? 1. The concept. *Palaeoceanography & Palaeoclimatology*, **5**, 469-477.

Broecker, W., Bond, G., Klas, M., Clark, E and McManus, J. 1992. Origin of the northern Atlantic's Heinrich events. *Climate Dynamics*, **6**, 265-273.

Broecker, W. S. 1994. Massive iceberg discharges as triggers for global climate change. *Nature*, **372**, 421.

Broecker, W.S., Barker, S., Clark, E., Hajdas, I., Bonani, G and Stott, L. 2004. Ventilation of the Glacial Deep Pacific Ocean. *Science*, **306**, 1169-1172.

Broecker, W. S. 2006. Was the Younger Dryas Triggered by a Flood? *Science*, **312**, 1146-1148.

Bronk Ramsey, C. 2007. Deposition models for chronological records. *Quaternary Science Reviews*, **27**, 42-60.

Bronk Ramsey, C. 2009. Bayesian Analysis of Radiocarbon Dates. *Radiocarbon*, **51**, 337-360.

Brooks, J.R., Flanagan, L.B., Buchmann, N and Ehleringer, J.R. 1997. Carbon isotope composition of boreal plants: functional grouping of life forms. *Oecologia*, **110**, 301-311.

Brush, G.S and Brush, L.M. 1972. Transport of pollen in a sediment-laden channel; a laboratory study. *American Journal of Science*, **272**, 359-381.

Bueno, A., Alfarhan, A., Arand, K., Burghardt, M., Deininger, A.C., Hedrich, R., Leide, J,. Seufert, P., Staiger, S and Riederer, M. 2019. Effects of temperature on the cuticular transpiration barrier of two desert plants with water-spender and water-saver strategies. *Journal of Experimental Botany*, **70**, 1613–1625.

Büntgen, U., Wacker, L., Galván, J.D., Arnold, S., Arseneault, D., Baillie, M., Beer, J., Bernabei, M., Bleicher, N., Boswijk, G., Bräuning, A., Carrer, M., Ljungqvist, F.C., Cherubini, P., Christl, M., Christie, D.A., Clark, P.W., Cook, E.R., D'Arrigo, R., Davi, N., Eggertsson, Ó., Esper, J., Fowler, A.M., Gedalof, Ze., Gennaretti, F., Grießinger, J., Grissino-Mayer, H., Grudd, H., Gunnarson, B.E., Hantemirov, R., Herzig, F., Hessl, A., Heussner, K.-U., Jull, A.J.T., Kukarskih, V., Kirdyanov, A., Kolář, T., Krusic, P.J., Kyncl, T., Lara, A., LeQuesne, C., Linderholm, H.W., Loader, N.J., Luckman, B., Miyake, F., Myglan, V.S., Nicolussi, K., Oppenheimer, C., Palmer, J., Panyushkina, I., Pederson, N., Rybníček, M., Schweingruber, F.H., Seim, A., Sigl, M., Sidorova, O.C., Speer, J.H., Synal, H.-A., Tegel, W., Treydte, K., Villalba, R., Wiles, G., Wilson, R., Winship, L.J., Wunder, J.,

Yang, B and Young, G.H.F. 2018. Tree rings reveal globally coherent signature of cosmogenic radiocarbon events in 774 and 993 CE. *Nature Communications*, **9**, 1-7.

Bush, R.T and McInerney, F.A. 2013. Leaf wax *n*-alkane distributions in and across modern plants: Implications for paleoecology and chemotaxonomy. *Geochimica et Cosmochimica Acta*, **117**, 161-179.

Bush, R.T and McInerney, F.A. 2015. Influence of temperature and C_4 abundance on *n*-alkane chain length distributions across the central USA. *Organic Geochemistry*, **79**, 65-73.

Bush, R.T., Wallace, J., Currano, E., Jacobs, B.F., McInerney, F.A., Dunn, R.E and Tabord, N.J. 2017. Cell anatomy and leaf $\delta^{13}C$ as proxies for shading and canopy structure in a Miocene forest from Ethiopia. *Palaeogeography, Palaeoclimatology, Palaeoecology,* **485**, 593-604.

Buschhaus, C and Jetter, R. 2011. Composition differences between epicuticular and intracuticular wax substructures: How do plants seal their epidermal surfaces? *Journal of Experimental Botany*, **62**, 841–853.

Cacho, I., Grimalt, J. O., Pelejero, C., Canals, M., Sierro, F. J., Flores, J. A and Shackleton, N. 1999. Dansgaard-Oeschger and Heinrich event imprints in Alboran Sea paleotemperatures. *Paleoceanography*, **14**, 698-705.

Cacho, I., Grimalt, J. O., Sierro, F.J., Shackleton, N and Canals, M. 2000. Evidence for enhanced Mediterranean thermohaline circulation during rapid climatic coolings. *Earth & Planetary Science Letters*, **183**, 417-429.

Cacho, I., Grimalt, J.O., Canals, M., Sbaffi, L., Shackleton, N.J., Schönfeld, N.J and Zahn, R. 2001. Variability of the western Mediterranean Sea surface temperature during the last 25,000 years and its connection with the Northern Hemisphere climatic changes**.** *Palaeoceanography & Palaeoclimatology*, **16**, 40-52.

Calov, R., Ganopolski, A., Petoukhov, V., Claussen, M and Greve, R. 2002. Large-scale instabilities of the Laurentide ice sheet simulated in a fully coupled climate-system model. *Geophysical Research Letters*, **24**, 1-4.

Cameron, R.J. 1970. Light intensity and the growth of *Eucalyptus* seedlings. II. The effect of cuticular waxes on light absorption in leaves of *Eucalyptus* species. *Australian Journal of Botany*, **18**, 275-284.

Camuera, J., Jiménez-Moreno, G., Ramos-Román, M.J., García-Alixa, A., Toney, J.L., Anderson, R.S., Jiménez-Espejo, F., Kaufman, D., Bright, B., Webster, C., Yanes, Y., Carrión, J.S., Ohkouchi, N., Suga, H., Yamame, M., Yokoyama, Y., Martínez-Ruizj, F. 2018. Orbital-scale environmental and climatic changes recorded in a new ~200,000-year-long multiproxy sedimentary record from Padul, southern Iberian Peninsula. *Quaternary Science Reviews*, **198**, 91-114.

Carlson, A.E. 2009. Geochemical constraints on the Laurentide Ice Sheet contribution to Meltwater Pulse 1A. *Quaternary Science Reviews*, **28**, 1625-1630

Carlson, A.E and Clark, P.U. 2012. Ice sheet sources of sea level rise and freshwater discharge during the last deglaciation. *Review of Geophysics*, **50**, 1-72.

Capano, M., Miramont, C., Shindo, L., Guibal, F., Marschal., C., Kromer, B., Tuna, T and Bard, E. 2020. Onset of the Younger Dryas recorded with ^{14}C at annual resolution in French subfossil trees. *Radiocarbon*, **62**, 1-18.

Castagnoli, G and Lal, D. 1980. Solar Modulation Effects in Terrestrial Production of Carbon-14. *Radiocarbon*, **22**, 133-158.

Castillo, J.M., Rubio Casal, A.E., Luque, C.J., Lugue, T and Figueroa, M.E. 2002. Comparative Field Summer Stress of Three Tree Species Co-occurring in Mediterranean Coastal Dunes. *Photosynthetica*, **45**, 49-56.

Cayre, O., Lancelot, Y., Vincent, E and Hall, M. A. 1999. Paleoceanographic reconstructions from planktonic foraminifera off the Iberian Margin: temperature, salinity, and Heinrich events. *Paleoceanography*, **14**, 384-396.

Cernusak, L.A., Ubierna, N., Winter, K., Holtum, J.A.M., Marshall, J.D and Farquhar, G.D. 2013. Environmental and physiological determinants of carbon isotope discrimination in terrestrial plants. *New Phytologist*, **200**, 950-965.

Chabaud, L., Sánchez Goñi, M.F., Desprat, S and Rossignol, L. 2014. Land–sea climatic variability in the eastern North Atlantic subtropical region over the last 14,200 years: Atmospheric and oceanic processes at different timescales. *The Holocene*, **24**, 787–797.

Cheddadi, R., 1988. Paleoclimats au nord de la M6diterranec orientale depuis 250 Kyr. Analyse pollinique et stratigraphie isotopique de quatre carottes marines. Thesis (PhD). Université de Montpellier.

Chibnall, A.C., Piper, S.H., Pollard, A., Williams, E.F and Sahai, P.N. 1934. The constitution of the primary alcohols, fatty acids and paraffins present in plant and insect waxes. *Biogeochemistry*, **28**, 2189–2208.

Chikaraishi, Y and Naraoka, H. 2003. Compound-specific δD–δ^{13}C analyses of *n*-alkanes extracted from terrestrial and aquatic plants. *Phytochemistry*, **63**, 361-371.

Chikaraishi, Y., Naraoka, H and Poulson, S.R. 2004. Hydrogen and carbon isotopic fractionations of lipid biosynthesis among terrestrial (C_3, C_4 and CAM) and aquatic plants. *Phytochemistry*, **65**, 1369-1381.

Chmura, G.L and Liu, K-B. 1990. Pollen in the lower Mississippi River. *Review of Palaeobotany and Palynology*, **64**, 253-261.

Clark, P.U., Alley, R.B., Keigwin, L.D., Licciardi. J.M., Johnsen, S.J and Wang, H. 1996. Origin of the first global meltwater pulse following the last glacial maximum. *Paleoceanography*, **11**, 563-577.

Clark, P. U., Marshall, S. J., Clarke, G. K., Hostetler, S. W., Licciardi, J. M and Teller, J. T. 2001. Freshwater forcing of abrupt climate change during the last glaciation. *Science*, **293**, 283-287.

Clark, P.U., Mitrovica, J.X., Milne, G.A and Tamisieam M.E. 2002. Sea-Level Fingerprinting as a Direct Test for the Source of Global Meltwater Pulse IA. *Science*, **295**, 2438-2441

Collister, J.W., Rieley, G., Stern, B., Eglinton, G., Fry, B. 1994. Compound-specific δ ^{13}C analyses of leaf lipids from plants with differing carbon dioxide metabolisms. *Organic Geochemistry*, **21,** 619-627.

Combourieu Nebout, N., Turon, J.L., Zahn, R., Capotondi, L., Londeix, L and Pahnke, K. 2002. Enhanced aridity and atmospheric high-pressure stability over the western Mediterranean during the North Atlantic cold events of the past 50 k.y. *Geology*, **30**, 863-866.

Combourieu Nebout, N., Peyron, O., Dormoy, I., Desprat, S., Beaudouin, C., Kotthoff, U and Marret, F. 2009. Rapid climatic variability in the west Mediterranean during the last 25,000 years from high resolution pollen data. *Climate of the Past*, **5**, 503-521.

Conte, M.H and Weber, J.C. 2002. Plant biomarkers in aerols record isotopic discrimination of terrestrial photosynthesis. *Nature*, **417**, 639-641.

Costas, S., Naughton, F., Goble, R and Renssen, H. 2016. Windiness spells in SW Europe since the last glacial maximum. *Earth & Planetary Science Letters*, **436**, 82-92.

Cowling, S.A and Sykes, M.T. 1999. Physiological Significance of Low Atmospheric CO_2 for Plant–Climate Interactions. *Quaternary Research*, **52**, 237-242.

Cramer, W., Guiot, J., Fader, M., Garrabou, J., Gattuso, J.-P., Iglesias, A., Lange, M.A., Lionello, P., Llasat, M.C., Paz, S., Penuelas, J., Snoussi, M., Toreti, A., Tsimplis, M.N and Xoplaki, E. 2018. Climate change and interconnected risks to sustainable development in the Mediterranean. *Nature Climate Change*, **8**, 972-980.

Cranwell, P.A. 1973. Chain-length distribution of *n*-alkanes from lake sediments in relation to post-glacial environmental change. *Freshwater Biology*, **3**, 259-265.

Cranwell, P.A. 1981. Diagenesis of free and bound lipids in terrestrial detritus deposited in a lacustrine sediment. *Organic Geochemistry*, **3**, 79-89.

Cuffey, K.M., Clow, G.D., Alley, R.B., Stuiver, M., Waddington, E.D and Saltus, R.W. 1995. Large Arctic Temperature Change at the Wisconsin-Holocene Glacial Transition. *Science*, **270**, 455-458

Cushing, E.J. 1967. Evidence for differential pollen preservation in late quaternary sediments in Minnesota. *Review of Palaeobotany and Palynology*, **4**, 87-101.

Damesin, C., Rambal, S and Joffre, R. 1997. Between-tree variations in leaf $\delta^{13}C$ of Quercus pubescens and Quercus ilex among Mediterranean habitats with different water availability. *Oecologia*, **111**, 26-35.

Damon, P.E., Lerman, J.C and Long, A. 1978. Temporal Fluctuations of Atmospheric ^{14}C: Causal Factors and Implications. *Annual Review of Earth and Planetary Science Letters*, **6**, 457-494.

Dansgaard, W., Clausen, H. B., Gundestrup, N., Hammer, C. U., Johnsen, S. F., Kristinsdottir, P. M and Reeh, N. 1982. A new Greenland deep ice core. *Science*, **218**, 1273-1277.

Dansgaard, W., Johnsen, S.J., Clausen, H.B., Hvidberg, C.S and Steffensen, J.P. 1993. Evidence for general instability of past climate from a 250-kyr. *Nature,* **364**, 218-220.

Davis, M.B. 2000. Palynology after Y2k—understanding the source area of pollen in sediments. *Annual Review of Earth & Planetary Science*, **28**, 1–18.

Davis, M.B and Shaw, R.G. 2001**.** Range Shifts and Adaptive Responses to Quaternary Climate Change. *Science*, **292**, 673-679.

de Abreu, L., Shackleton, N.J., Schönfeld, J., Hall, M and Chapman, M. 2003. Millennial-scale oceanic climate variability off the Western Iberian margin during the last two glacial periods. *Marine Geology*, **196**, 1-20.

De Bary, A. 1871. Über die Wachsüberzüge der Epidermis. *Botanishe Zeitschrift*, **29**, 130-176.

de Stigter, H.C., Jesus, C.C., Boer, W., Richter, T.O., Costa, A., van Weering, T.C.E. 2011. Recent sediment transport and deposition in the Lisbon–Setúbal and Cascais submarine canyons, Portuguese continental margin. *Deep-Sea Research II,* **58**, 2321–2344.

Debret, M., Bout-Roumazeilles, V., Grousset, F., Desmet, M., McManus, J. F., Massei, N., Sebag, D., Petit, J.-R., Copard, Y and Trentesaux, A. 2007. The origin of the 1500-year climate cycles in Holocene North-Atlantic records. *Climate of the Past*, **3**, 569–575.

Debret, M., Sebag, D., Crosta, X., Massei, N., Petit, J.-R., Chapron, E and Bout-Roumazeilles, V. 2009. Evidence from wavelet analysis for a mid-Holocene transition in global climate forcing. *Quaternary Science Reviews*, **28**, 2675–2688.

Denton, G.H., Broecker, W.S and Alley, R.B. 2006. The mystery interval 17.5 to 14.5 kyrs ago. *PAGES News,* **14**, 14– 6.

Deplazes, G., Lückge, A., Stuut, J-B.W., Pätzold, J., Kuhlmann, H., Husson, D., Fant, M and Haug, G.H. 2014. Weakening and strengthening of the Indian monsoon during Heinrich events and Dansgaard-Oeschger oscillations. *Paleoceanography & Paleoclimatology*, **29**, 99-114.

Deschamps, P., Durand, N., Bard, E., Hamelin, B., Camoin, G., Thomas, A. L., Henderson, G. M., Okuno, J and Yokoyama, Y. 2012. Ice-sheet collapse and sea-level rise at the Bølling warming 14,600 years ago. *Nature*, **483**, 559–564.

Dias, J.M.A. 1987. *Dinâmica sedimentar e evolução recente da plataforma continental portuguesa septentrional*. Thesis (PhD). University of Lisbon.

Dias, J.M.A., Boskia, T., Rodrigues, A and Magalhães, F. 2000. Coast line evolution in Portugal since the Last Glacial Maximum until present — a synthesis. *Marine Geology*, **170**, 177-186.

Diefendorf, A.F., Muller, K.E., Wing, S.L., Koch, P.L and Freeman, K.H. 2010. Global patterns in leaf ^{13}C discrimination and implications for studies of past and future climate. *Proceedings of the National Academy of Sciences*, **107**, 5738–5743.

Diefendorf, A.F., Freeman, K.H., Wing, S.L and Graham, H.V. 2011. Production of n-alkyl lipids in living plants and implications for the geologic past. *Geochimica et Cosmochimica Acta*, **75,** 7472-7485.

Diefendorf, A.F., Leslie, A.B and Wing., S.L. 2015a. Leaf wax composition and carbon isotopes vary among major conifer groups. *Geochimica et Cosmochimica Acta,* **170**, 145-156.

Diefendorf, A.F., Freeman, K.H., Wing, S.L., Currano, E.D and Mueller, K.E. 2015b. Paleogene plants fractionated carbon isotopes similar to modern plants. *Earth and Planetary Science Letters,* **429,** 33-44.

Diefendorf, A.F and Freimuth, E.J. 2017. Extracting the most from terrestrial plant-derived n-alkyl lipids and their carbon isotopes from the sedimentary record: A review. *Organic Geochemistry*, **103**, 1-21.

Diffenbaugh, N.S., Pal, J.S., Giorgi, F and Gao, X. 2007. Heat stress intensification in the Mediterranean climate change hotspot. *Geophysical Research Letters*, **34**, 1-6.

Dokken, T. M and Jansen, E. 1999. Rapid changes in the mechanism of ocean convection during the last glacial period. *Nature*, **401**, 458-461.

Dokken, T. M., Nisancioglu, K. H., Li, C., Battisti, D. S and Kissel, C. 2013. Dansgaard-Oeschger cycles: Interactions between ocean and sea ice intrinsic to the Nordic seas. *Paleoceanography*, **28**, 491-502.

Dorador, J and Rodríguez-Tovar, F.J. 2016. Stratigraphic variation in ichnofabrics at the "Shackleton Site" (IODP Site U1385) on the Iberian Margin: Paleoenvironmental implications. *Marine Geology*, **377**, 118-126.

Dormoy, I., Peyron, O., Combourieu Nebout, N., Goring, S., Kotthoff, U., Magny, M and Pross, J. 2009. Terrestrial climate variability and seasonality changes in the Mediterranean region between 15,000 and 4000 years BP deduced from marine pollen records. *Climate of the Past*, **5**, 615-632.

Drenzek, N.J., Montlucon, D.B., Yunker, M.B., Macdonald, R.W and Eglinton, T.I. 2007. Constraints on the origin of sedimentary organic carbon in the Beaufort Sea from coupled molecular ^{13}C and ^{14}C measurements. *Marine Chemistry*, **103**, 146-162.

Dubrovsky, M., Hayes, M., Duce, P., Trnka, M., Svoboda, M., Zara, P. 2014. Multi-GCM projections of future drought and climate variability indicators for the Mediterranean region. *Regional Environmental Change*, **14**, 1907-1919.

Dupont, L.M. 1999. Pollen and spores in marine sediments from the East Atlantic—a view from the oceans into the African continent. *In:* Fischer, G and Wefer, G (eds.), Use of Proxies in Palaeoceanography. Examples from the South Atlantic. Berlin: Springer-Verlag, 523-546 pp.

Dutton, A. Carlson, A.E., Long, A.J., Milne, G.A., Clark, P.U., DeConto, R., Horton, B.P., Rahmstorf, S., Raymo, M.E. 2015. Sea-level rise due to polar ice-sheet mass loss during past warm periods. *Science*, **349**, 153-165.

Eckl, K and Gruler, H. 1980. Phase transitions in plant cuticles. *Planta*, **150**, 102–113.

Edwards, R.T. 1958. Solid petroleum hydrocarbons and their effect on wax properties. *Journal of Technical Association of the Pulp & Paper Industry*, **41**, 267-274.

Edwards, R.L., Beck, J.W., Burr, G.S., Donahue, D.J., Chappell, J.M.A., Bloom, A.L., Druffel, E.R.M and Taylor, F.W. 1993. A Large Drop in Atmospheric $^{14}C/^{12}C$ and Reduced Melting in the Younger Dryas, Documented with ^{230}Th Ages of Corals. *Science*, **260**, 962-968.

Eggleston, S., Schmitt, J., Bereiter, B., Schneider, R and Fischer, H. 2016. Evolution of the stable carbon isotope composition of atmospheric CO_2 over the last glacial cycle. *Paleoceanography*, **31**, 434-452.

Eglinton, G., Gonzalez, G., Hamilton, R.J and Raphael, R.A. 1962. Hydrocarbon constituents of the wax coatings of plant leaves: A taxonomic survey. *Phytochemistry*, **1**, 89-102.

Eglinton, G and Hamilton, R.J. 1963. Chapter 8: The distribution of n-alkanes. *In:* Swain, T (ed.), Chemical plant Taxonomy. Cambridge: Academic Press, 187-217 pp.

Eglinton, G and Hamilton, R.J. 1967. Leaf Epicuticular Waxes. *Science*, **156**, 1322-1335.

Eglinton, G., Gonzalez, A.G., Hamilton, R.J and Raphael, R.A. 1962. Hydrocarbon constituents of the wax coatings of plant leaves: A taxonomic survey. *Phytochemistry*, **1**, 89-102.

Eglinton, T.I., Benitez-Nelson, B.C., Pearson, A., McNichol, A.P., Bauer, J.E and Druffel, E.R.M. 1997. Variability in Radiocarbon Ages of Individual Organic Compounds from Marine Sediments. *Science*, **277**, 796-799.

Eglinton, T.I., Eglinton, G., Dupont, L., Sholkovitz, E.R., Montlucon, D and Reddy, C.M. 2002. Composition, age, and provenance of organic matter in NW African dust over the Atlantic Ocean. *Geochemistry, Geophysics and Geosystems*, **3**, 1525-2027.

Eglinton, T.I and Eglinton, G. 2008. Molecular proxies for paleoclimatology. *Earth and Planetary Science Letters*, **275**, 1-16.

Ehleringer, J.R., Phillips, S.L and Comstock, J.P. 1992. Seasonal Variation in the Carbon Isotopic Composition of Desert Plants**.** *Functional Ecology*, **6**, 396-404.

Ehleringer, J.R and Cerling, T.E. 1995. Atmospheric CO_2 and the ratio of intercellular to ambient CO_2 concentrations in plants. *Tree Physiology*, **15**, 105–111.

El Amrani, M., Macaire, J-J., Zarki, H., Breheret, G., Fontugne, M. 2008. Contrasted morphosedimentary activity of the lower Kert River (northeastern Morocco) during the Late Pleistocene and the Holocene. Possible impact of bioclimatic variations and human action. *Comptes Rendus Geoscience*, **340**, 533-542.

Elsasser, W., Ney, E.P and Winckler, J.R. 1956. Cosmic-Ray Intensity and Geomagnetism. *Nature*, **178**, 1226–1227.

Eynaud, F., de Abreu, L., Voelker, A., Schönfeld, J., Salgueiro, E., Turon, J.-L., Penaud, A., Toucanne, S., Naughton, F., Sánchez Goñi, M.F., Malaizé, B and Cacho, I. 2009. Position of the

Polar Front along the western Iberian margin during key cold episodes of the last 45 ka. *Geochemistry, Geophysics, Geosystems*, **10**, 1-21.

Fægri, K and Iversen, J. 1950. *Text-book of modern pollen analysis*. Copenhagen: Munksgaard, 169 pp.

Fægri, K and Iversen, J. 1964. *Textbook of pollen analysis*. 2nd ed. Oxford: Blackwell, 295 pp.

Fairbanks, R.G. 1989. 17,000 glacio-eustatic sea level record: influence of glacial melting rates on the Younger Dryas event and deep-ocean circulation. *Nature*, **342**, 637-642.

Fairbanks, R.G., Mortlock, R.A., Chiu, T-C., Cao, L., Kaplan, A., Guilderson, T.P., Fairbanks, T.W., Bloom, A.L., Grootes, P.M and Nadeau, M-J. 2005. Radiocarbon calibration curve spanning 0 to 50,000 years BP based on paired $^{230}Th/^{234}U/^{238}U$ and ^{14}C dates on pristine corals. Quaternary Science Reviews, **24**, 1781-1796.

Fall, P. 1987. Pollen Taphonomy in a Canyon Stream. *Quaternary Research*, **28**, 393-406.

Farquhar, G.D., O'Leary, M.H and Berry, J.A. 1982. On the Relationship Between Carbon Isotope Discrimination and the Intercellular Carbon Dioxide Concentration in Leaves. *Australian Journal of Plant Physiology*, **9**, 121-137

Farquhar, G.D., Ehleringer, J.R and Hubick, K.T. 1989. Carbon Isotope Discrimination and Photosynthesis. *Annual Review of Plant Physiology and Plant Molecular Biology*, **40**, 503-537.

Farquhar, G.D and Sharkey, T.D. 1982. Stomatal Conductance and Photosynthesis. *Annual Reviews of Plant Physiology*, **33**, 317–345.

Fernandes, M.R., Aguiar, F.C., Martins, M.J., Rivaes and Ferreira, M.T. 2020. Long-term human-generated alterations of Tagus River: Effects of hydrological regulation and land-use changes in distinct river zones. *Catena*, **188**, 1-14.

Fick, S.E and Hijmans, R.J. 2017. WorldClim 2: new 1-km spatial resolution climate surfaces for global land areas. *International Journal of Climatology*, **37**, 4302-4315.

Firestone, R.B., West, A., Kennett, J. P., Becker, L., Bunch, T. E., Revay, Z. S., Schultz, P. H., Belgya, T., Kennett, D. J., Erlandson, J. M., Dickenson, O. J., Goodyear, A. C., Harris, R. S., Howard, G. A., Kloosterman, J. B., Lechler, P., Mayewski, P. A., Montgomery, J., Poreda, R., Darrah, T., Que Hee, S. S., Smith, A. R., Stich, A., Topping, W., Wittke, J. H and Wolbach, W. S. 2007. Evidence for an extra- terrestrial impact 12,900 years ago that con- tributed to the megafaunal extinctions and the Younger Dryas cooling. *Proceedings of the National Academy of Sciences of the United States of America*, **104**, 16016–16021.

Fiúza, A. F. D., DeMacedo, M. E and Guerreiro, M. R. 1982. Climatological space and time-variation of the Portuguese coastal upwelling. *Oceanologica Acta*, **5**, 31-40.

Fletcher, W.J and Sanchez Goñi, M.F. 2008. Orbital-and sub-orbital-scale climate impacts on vegetation of the western Mediterranean basin over the last 48,000 yr. *Quaternary Research*, **70**, 451-464.

Fletcher, W.J., Sanchez Goñi, M.F.S., Peyron, O and Dormoy, I. 2010. Abrupt climate changes of the last deglaciation detected in a Western Mediterranean forest record. *Climate of the Past*, **6**, 245–264.

Fletcher, W.J., Debret, M and Goñi, M.F.S. 2013. Mid-Holocene emergence of a low-frequency millennial oscillation in western Mediterranean climate: Implications for past dynamics of the North Atlantic atmospheric westerlies. *The Holocene*, **23**, 153-166.

Flückiger, J., Knutti, R and White, J.W.C. 2006. Oceanic processes as potential trigger and amplifying mechanisms for Heinrich events. *Paleoceanography,* **21**, 1-11.

Frank, M., Schwarz, B., Baumann, S., Kubik, P.W., Suter, M and Mangini, A. 1997. A 200 kyr record of cosmogenic radionuclide production rate and geomagnetic field intensity from ^{10}Be in globally stacked deep-sea sediments. *Earth and Planetary Science Letters*, **149**, 121-129.

Freeman, K.H and Colarusso, L.A. 2001. Molecular and isotopic records of C_4 grassland expansion in the late Miocene. *Geochimica et Cosmochimica Acta*, **65**, 1439-1454.

Freeman, K.H and Pancost, R.D. 2013. Biomarkers for Terrestrial Plants and Climate. *In:* Holland, H.D and Turekian, K.K (eds.), *Treatise on Geochemistry: Second Edition.* Amsterdam: Elsevier, 395-416 pp.

Freeman, E., Skinner, L.C., Waelbroeck, C and Hoell, D. 2016. Radiocarbon evidence for enhanced respired carbon storage in the Atlantic at the Last Glacial Maximum. *Nature Communications*, **7**, 1-8.

Friedrich, M., Remmele, S., Kromer, B., Hofmann, J., Spurk, M., Kaiser, K.F., Orcel, C and Küppers, M. 2004. The 12,460-year Hohenheim oak and pine tree-ring chronology from Central Europe- A unique annual record for radiocarbon calibration and paleoenvironment reconstructions. *Radiocarbon*, **46**, 1111-1122.

French, K.L., Hein, C.J., Haghipour, N., Wacker, L., Kudrass, H.R., Eglinton, T.I and Galy, V. 2018. Millennial soil retention of terrestrial organic matter deposited in the Bengal Fan. *Scientific Reports*, **8**, 1-8.

Frigola, J., Moreno, A., Cacho, I., Canals, M., Sierro, F. J., Flores, J. A., Grimalt, J. O., Hodell, D. A and Curtis, J.H. 2007. Holocene climate variability in the western Mediterranean region from a deepwater sediment record. *Paleoceanography*, **22**, 1-16.

Gagosian, R.B., Peltzer, E.T and Zafiriou, O.C. 1981. Atmospheric transport of continentally derived lipids to the tropical North Pacific. *Nature*, **291**, 312-314.

Gagosian, R.B and Peltzer, E.T. 1986. The importance of atmospheric input of terrestrial organic material to deep sea sediments. *Organic Geochemistry*, **10**, 661-669.

Galy, V., Eglinton, T., France-Lanord, C and Syla, S. 2011. The provenance of vegetation and environmental signatures encoded in vascular plant biomarkers carried by the Ganges-Brahmaputra rivers. *Earth & Planetary Science Letters*, **204**, 1-12.

Galy, V and Eglinton, T.I. 2011. Protracted storage of biospheric carbon in the Ganges–Brahmaputra basin. *Nature Geoscience*, **4**, 843-847.

Gamarra, B and Kahmen, A. 2015. Concentrations and δ2H values of cuticular n-alkanes vary significantly among plant organs, species and habitats in grasses from an alpine and a temperate European grassland. *Physiological Ecology,* **178**, 981–998.

Ganopolski, A and Rahmstorf, S. 2001. Rapid changes of glacial climate simulated in a coupled climate model. *Nature*, **409**, 153-158.

Garcia-Moreiras, I., Cartelle, V., Garcia-Gil, S and Muñoz-Sobrino, C. 2019. First high-resolution multi-proxy palaeoenvironmental record of the Late Glacial and Early Holocene transition in the Ria de Arousa (Atlantic margin of NW Iberia). *Quaternary Science Reviews*, **215**, 308-321.

Garcin, Y., Schwab, V.F., Gleixner, G., Kahmen, A., Todou, G., Sénée, O., Onana, M., Achoundong, G and Sachse, D. 2012. Hydrogen isotope ratios of lacustrine sedimentary n-alkanes as proxies of tropical African hydrology: Insights from a calibration transect across Cameroon. *Geochimica et Cosmochimica Acta*, **79**, 106-126.

Giraudeau, J., Grelaud, M., Solignac, S., Andrews, J.T., Moros, M., Jansen, E. 2010. Millennial-scale variability in Atlantic water advection to the Nordic Seas derived from Holocene coccolith concentration records. *Quaternary Science Reviews*, **29**, 1276-1287.

Giorgi, F. 2006. Climate Change Hot-spots. *Geophysical Research Letters*, **33**, 1-4.

Giorgi, F and Lionello, P. 2008. Climate change projections for the Mediterranean region. *Global and Planetary Change*, **63**, 90-104.

Godwin, H. 1962. Half-life of radiocarbon. *Nature*, **195**, 984.

Gomes, S.D., Flectcher, W.J., Rodrigues, T., Stone, A., Abrantes, F and Naughton, F. 2020. Time-transgressive Holocene maximum of temperate and Mediterranean forest development across the Iberian Peninsula reflects orbital forcing. *Palaeogeography, Palaeoclimatology, Palaeoecology*, **550**, 1-16.

Gómez-Orellana, L., Ramil-Rego, P and Muñoz-Sobrino, C. 1998. A new palynological and chronological sequence for the Pleistocene deposit of Mougas (NW of Iberian Peninsula). *Revue de Paleobiologie*, **17**, 35-47.

Goosse, H., Brovkin, V., Fichefet, T., Haarsma, R., Huybrechts, P., Jongma, J., Mouchet, A., Selten, F., Barriat, P.-Y., Campin, J.-M., Deleersnijder, E., Driesschaert, E., Goelzer, H., Janssens, I., Loutre, M.-F., Morales Maqueda, M. A., Opsteegh, T., Mathieu, P.-P., Munhoven, G., Pettersson, E. J., Renssen, H., Roche, D. M., Schaeffer, M., Tartinville, B., Timmermann, A and Weber, S. L. 2010. Description of the Earth system model of intermediate complexity LOVECLIM version 1.2. *Geoscientific Model Development*, **3**, 603-633.

Gordon, A.D and Birks, H.J.B. 1972. Numerical Methods in Quaternary Palaeoecology I. Zonation of Pollen Diagrams. *New Phytologist*, **71**, 961-979.

Goslar, T., Bard, E., Kuc, T., Pazdur, M.F., Ralska-Jasiewiczowa, M., Tisnerat, N., Róañski, K., Walanus, A., Wicik, B and Wiêckowski, K. 1995. High concentration of atmospheric ^{14}C during the Younger Dryas cold episode. *Nature,* **377**, 414-7.

Goslar, T., Arnold, M., Tisnerat-Laborde, N., Hatté, C., Paterne, M and Ralska-Jasiewiczowa, M. 2000. Radiocarbon calibration by means of varves versus ^{14}C ages of terrestrial macrofossils from Lake Gosciaz and Lake Perespilno, Poland. *Radiocarbon*, **42**, 335-348.

Gouveia, C., Trigo, R.M., DaCamara, C.C., Libonati, R and Pereira, J.M.C. 2008. The North Atlantic Oscillation and European vegetation dynamics. *International Journal of Climatology*, **28**, 1835-1847.

Gouveia C and Trigo R.M. 2011. The Impacts of the NAO on the Vegetation Activity in Iberia. *In:* Vicente-Serrano S., Trigo R. (eds.), Hydrological, Socioeconomic and Ecological Impacts of the North Atlantic Oscillation in the Mediterranean Region. Dordrecht: Springer, 236 pp.

Gove, H.E. 1992. The History of AMS, its Advantages over Decay Counting: Applications and Prospects. *In:* Taylor, R.E, Long, A and Kra, R.S (eds), Radiocarbon after four decades. New York: Springer, 214-229.

Gregoire, L.J., Payne, A.J and Valdes, P.J. 2012. Deglacial rapid sea level rises caused by ice-sheet saddle collapses. *Nature*, **487**, 219–222.

Greuter, W. 1991. Botanical diversity, endemism, rarity, and extinction in the Mediterranean area: an analysis based on the published volumes of Med-Checklist. *Botanika Chronika*, **10**, 63-79.

Grimm, E.C. 1987. CONISS: a FORTRAN 77 program for stratigraphically constrained cluster analysis by the method of incremental sum of squares. *Computers & Geosciences*, **13**, 13-35.

Grinstead, M. J. 1977. *A study of the relationships between climate and stable isotope ratios in tree rings*. Ph.D. Thesis. University of Waikato.

Grootes, P. M., Stuiver, M., White, J. W. C., Johnsen, S and Jouzel, J. 1993. Comparison of oxygen isotope records from the GISP2 and GRIP Greenland ice cores. *Nature*, **366**, 552-554.

Grousset, F., Labeyrie, L., Sinko, J.A., Cremer, M., Bond, G., Duprat, J., Cortijo, E and Huon, S. 1993. Patterns of ice-rafted detritus in the glacial North Atlantic. *Paleoceanography*, **8**, 175–192.

Guerzoni, S., Molinaroli, E and Chester, R. 1997. Saharan dust inputs to the western Mediterranean Sea: depositional patterns, geochemistry and sedimentological implications. *Deep-Sea Research*, **44**, 631-654.

Haggi, C., Sawakuchi, A.A., Chiessi, C.M., Mulitza, S., Mollenhauer, G., Sawakuchi, H.O., Baker, P.A., Zabel, M and Scehuss, E. 2016. *Geochimica et Cosmochimica Acta*, **192**, 149-165.

Hall, V. 1989. A comparison of grass foliage, moss polsters and soil surfaces as pollen traps in modern pollen studies. *Circaea*, **6**, 63-69.

Harrison, S. P., Prentice, I. C and Bartlein, P. J. 1992. Influence of insolation and glaciation on atmospheric circulation in the North Atlantic sector: Implications of general circulation model experiments for the Late Quaternary climatology of Europe. *Quaternary Science Reviews,* **11**, 283-299.

Hartz, N and Milthers, V. 1901. Det senglaciale ler I Allerod Teglvaerksgrav. *Meddelelser fra Dansk Geologisk Forening*, **2**, 31-60.

Havinga, A.J. 1967. Palynology and pollen preservation**.** *Review of Palaeobotany and Palynology*, **2**, 81-98.

Hayes, J.M. 1993. Factors controlling ^{13}C contents of sedimentary organic compounds: Principles and evidence. *Marine Geology*, **113**, 111-125.

Hays, J. D., Imbrie, J and Shackleton, N. J. 1976. Variations in the Earth's orbit: pacemaker of the ice ages. *Science*, **194**, 1121-1132.

Haywood, A.M., Ridgwell, A., Lunt, D.J., Hill, D.J., Pound, M.J., Dowsett, H.J., Dolan, A.M., Francis, J.E and Williams, M. 2011. Are there pre-Quaternary geological analogues for a future greenhouse warming? *Philosophical Transactions of the Royal Society A,* **369**, 933-956.

Heaton, T.J., Köhler, P., Butzin, M., Bard, E., Reimer, R.W., Austin, W.E.N., Bronk Ramsey, C., Grootes, P.M., Hughen, K.M., Kromer, B., Reimer, P.J., Adkins, J., Burke, A., Cook, M.S., Olsen, J and Skinner, L.C. 2020a. Marine20—The Marine Radiocarbon Age Calibration Curve (0–55,000 Cal BP). *Radiocarbon*, **62**, 1-42.

Heaton, T.J., Blaauw, M., Blackwell, P.G., Bronk Ramsey, C., Reimer, P.J and Scott, E.M. 2020b. The Intcal20 Approach to Radiocarbon Calibration Curve Construction: A New Methodology using Bayesian Splines and Errors-in-variables. *Radiocarbon*, **62**, 1-43.

Heinrich, H. 1988. Origin and consequences of cyclic ice rafting in the northeast Atlantic Ocean during the past 130,000 years. *Quaternary research*, **29**, 142-152.

Heiri, O., Koinig, K.A., Spötl, C., Barrett, S., Brauer, A., Drescher-Schneider, R., Gaar, D., Ivy-Ochs, S., Kerschner, H., Luetscher, M., Moran, A., Nicolussi, K., Preusser, F., Schmidt, R., Schoeneich, P., Schwörer, C., Sprafke, T., Terhorst, B and Tinner, W. 2014. Palaeoclimate records 60–8 ka in the Austrian and Swiss Alps and their forelands. *Quaternary Science Reviews*, **106**, 186-205.

Heredia, A. 2003. Biophysical and biochemical characteristics of cutin, a plant barrier biopolymer. *Biochimica et Biophysica Acta*, **1620**, 1-7.

Hessler, I., Dupont, L., Bonnefille, R., Behling, H., Gonzalex, C., Helmens, K.F., Hooghiemstra, H., Lebamba, J., Ledru, M.-P., Lexine, A.-M., Maley, J., Marret, F and Vincens, A. 2010. Millennial-scale changes in vegetation records from tropical Africa and South America during the last glacial. *Quaternary Science Reviews*, **29**, 2882-2899.

Heusser, L and Balsam, W.L. 1977. Pollen Distribution in the Northeast Pacific Ocean. *Quaternary Research*, **7**, 45-62.

Heusser, L. 1983. Pollen distribution in the bottom sediments of the western North Atlantic Ocean. *Marine Micropaleontology*, **8**, 77-88

Hevly, R.H. 1981. Pollen Production, Transport and Preservation: Potentials and Limitations in Archaeological Palynology. *Journal of Ethnobiology*, **1**, 39-54.

Higginson, M.J., Altabet, M.A., Murray, D.W., Murray, R.W., Herbert, T.D. 2004. Geochemical evidence for abrupt changes in relative strength of the Arabian monsoons during a stadial/interstadial climate transition. *Geochimica et Cosmochimica Acta*, **68**, 3807-3826.

Hochuli, P.A and Feist-Burkhardt, S. 2013. Angiosperm-like pollen and Afropollis from the Middle Triassic (Anisian) of the Germanic Basin (Northern Switzerland). *Frontiers in Plant Science*, **4**, 1-14.

Hoetzel, S., Dupont, L., Schefuss, E., Rommerskirchen, F and Wefer, G. 2013. The role of fire in Miocene to Pliocene C_4 grassland and ecosystem evolution. *Nature Geoscience*, **6**, 1027–1030.

Hodell, D., Crowhurst, S., Skinner, L., Tzedakis, P. C., Margari, V., Channell, J. E., Kamenov, G., MacLacklan, S and Rothwell, G. 2013a. Response of Iberian Margin sediments to orbital and suborbital forcing over the past 420 ka. *Paleoceanography*, **28**, 185-199.

Hodell, D.A., Lourens, L., Stow, D. A. V., Hernández-Molina, J., Alvarez Zarikian, C. A. and the Shackleton Site Project Members. 2013b. The “Shackleton Site” (IODP Site U1385) on the Iberian Margin. *Scientific Drilling*, **16**, 13-19.

Hodell, D.A., Elderfield, H., Greaves, M., McCave, I.N., Skinner, L., Thomas, A., White, N., and the JC089 Scientific Party. 2014. JC089 Cruise Report- IODP Site Survey of the Shackleton Sites, SW Iberian Margin, British Ocean Data Centre. Available at: https://www.bodc.ac.uk/data/information_and_inventories/cruise_inventory/report/13392/.

Hodell, D., Lourens, L., Crowhurst, S., Konijnendijk, T., Tjallingii, R., Jimenez-Espejo, F., Skinner, L., Tzedakis, P.C and Shackleton Site Project Members. 2015. A reference time scale for Site U1385 (Shackleton Site) on the SW Iberian Margin. *Global & Planetary Change*, **133**, 49-64.

Hodell, D.A., Tomaso, N., Bontognali, R. R., Danino, S., Dorador, J., Dowdeswell, J.A., Einsle, J., Kuhlmann, H., Martrat, B., Mleneck-Vautravers, M.J., Rodríguez-Tovar, F.J and Röhl, U. 2017. Anatomy of Heinrich Layer 1 and its role in the last deglaciation. *Paleoceanography & Paleoclimatology*, **32**, 284-303.

Hoffmann, D.L., Beck, J.W., Richards, D.A., Smart, P.L., Singarayer, J.S., Ketchmark, T., Hawkesworth, C.J. 2010. Towards radiocarbon calibration beyond 28 ka using speleothems from the Bahamas. Earth and Planetary Science Reviews, **289**, 1-10.

Hoffmann, B., Kahmen, A., Cernusak, L.A., Arndt, S.K and Sachse, D. 2013. Abundance and distribution of leaf wax n-alkanes in leaves of Acacia and Eucalyptus trees along a strong humidity gradient in northern Australia. *Organic Geochemistry*, **62**, 62-67.

Hogg, A., Southon, J., Turney, C., Palmer, C., Bronk Ramsey, C., Fenwick, P., Boswijk, G., Büntgen, U., Friedrich, M., Helle, G., Hughen, K., Jones, R., Kromer, B., Noronha, A., Reinig, F., Reynard, L., Staff, R and Wacker, L. 2016. Decadally-resolved Lateglacial radiocarbon evidence from New Zealand kauri. *Radiocarbon*, **58**, 709-733.

Hogg, A., Heaton, T.J., Hua, Q., Palmer, J.G., Turney, C.S.M., Southon, J., Bayluss, A., Blackwell, P.G., Boswijk, G., Bronk Ramsey, C., Pearson, C., Petchey, F., Reimer, P., Reimer, R and Wacker, L. 2020. SHCal20 Southern Hemisphere Calibration, 0–55,000 years cal BP. *Radiocarbon*, **62**, 1-20.

Holmes, P.L. 1990. Differential transport of spores and pollen: A laboratory study. *Review of Palaeobotany and Palynology*, **64**, 289-296.

Holmes, M.G and Keiller, D.R. 2002. Effects of pubescence and waxes on the reflectance of leaves in the ultraviolet and photosynthetic wavebands: a comparison of a range of species. *Plant, Cell & Environment*, **25**, 85-93.

Hooghiemstra, H. 1988. Palynological records from northwest African marine sediments: A general outline of the interpretation of the pollen signal. *Philosophical Transactions of the Royal Society B*, **318**, 431-449.

Hooghiemstra, H., Stalling, H., Agwu, C.O.C and Dupont, LM. 1992. Vegetational and climatic changes at the northern fringe of the sahara 250,000–5000 years BP: evidence from 4 marine pollen records located between Portugal and the Canary Islands. *Review of Palaeobotany & Palynology*, **74**, 1-53.

Hopkins, J.S. 1950. Differential Flotation and Deposition of Coniferous and Deciduous Tree Pollen. *Ecology*, **31**, 633–641.

Hou, J., D'Andrea, W.J and Huang, Y. 2008. Can sedimentary leaf waxes record D/H ratios of continental precipitation? Field, model, and experimental assessments. *Geochimica et Cosmochimica Acta*, **72**, 3503-3517.

House, S., 1985. Australian rainforests: what is their value? University of Canberra: Centre for Resource and Environmental Studies. CRES working paper 1985/22, 11 pp.

Huang, Y., Bol, R., Harkness, D.D., Ineson, P and Eglinton, G. 1996. Post-glacial variations in distributions, 13C and ^{14}C contents of aliphatic hydrocarbons and bulk organic matter in three types of British acid upland soils. *Organic Geochemistry*, **24**, 273-287.

Huang, Y., Street-Perrott, A., Perrot, A., Metzger, P and Eglinton, G. 1999. Glacial–interglacial environmental changes inferred from molecular and compound-specific $\delta^{13}C$ analyses of sediments from Sacred Lake, Mt. Kenya. *Geochimica et Cosmochimica Acta*, **63**, 1383-1404

Huang, Y., Dupont, L., Sarnthein, M., Hayes, J. M., and Eglinton, G. 2000. Mapping of C_4 plant input from North West Africa into North East Atlantic sediments. *Geochimica et Cosmochimica Acta*, **64**, 3505-3513.

Hughen, K., Southon, J.R., Lehman, S.L and Overpeck, J.T. 2000. Synchronous Radiocarbon and Climate Shifts During the Last Deglaciation. *Science*, **290**, 1951-1954.

Hughen, K., Lehman, L., Southon, J., Overpeck, J., Marchal, O., Herring, C and Turnbull, J. 2004; ^{14}C Activity and Global Carbon Cycle Changes over the Past 50,000 Years. *Science*, **303**, 202-207.

Hughen, K.A., Southon, J.A., Lehman, S.J., Bertrand, C.J.H and Turnbull, J. 2006. Marine-derived ^{14}C calibration and activity record for the past 50,000 years updated from the Cariaco Basin. *Quaternary Science Reviews*, **25**, 3216–3227.

Hughen, K.A and Heaton, T.J. 2020. Updated Cariaco Basin ^{14}C Calibration Dataset From 0–60 Cal kyr BP. *Radiocarbon*, **62**, 1-43.

Hulbe, C. L., MacAyeal, D. R., Denton, G. H., Kleman, J and Lowell, T. V. 2004. Catastrophic ice shelf breakup as the source of Heinrich event icebergs. *Paleoceanography*, **19**, 1-15.

Huntley, B and Birks, H.J.B. 1983. *An Atlas of Past and Present Pollen Maps for Europe: O-13,000 years ago.* Cambridge University Press: Cambridge, 667 pp.

Hurrell, J.W. 1995. Decadal Trends in the North Atlantic Oscillation: Regional Temperatures and Precipitation. *Science*, **269**, 676-679.

Imbrie, J., Hays, J.D., Martinson, D.G., McIntyre, A., Mix, A.C., Morley, J.J., Pisias, N.G., Prell, W.L and Shackleton, N.J. 1984. The orbital theory of Pleistocene climate: Support from a revised chronology of the marine $\delta^{18}0$ record. *In*: Berger, A., Imbrie, J., Hays, J. D., Kukla, G and Saltzman, B. Milankovitch and Climate. Springer: Berlin, 269–305 pp.

Ingram, B.L and Kennett, J.P. 1995. Radiocarbon Chronology and Planktonic-Benthic Foraminiferal ^{14}C Age Differences in Santa Barbara Basin Sediments, Hole 893A. *In:* Kennett,

J.P., Baldauf, J.G and Lyle, M (eds), *Proceedings of the Ocean Drilling Program, Scientific Results.* Vol. 146. Texas: Integrated Ocean Drilling Program, 19-27 pp.

Itambi, A.C., von Dobeneck, T., Mulitza, S., Bickert, T and Heslop, D. 2009. Millennial-scale northwest African droughts related to Heinrich events and Dansgaard-Oeschger cycles: Evidence in marine sediments from offshore Senegal. *Palaeoceanography & Palaeoclimatology*, **24**, 1-16.

Ivy-Ochs, S., Kerschner, H., Kubik, P.W and Schlüchter, C. 2006. Glacier response in the European Alps to Heinrich Event 1 cooling: the Gschnitz stadial. *Journal of Quaternary Science*, **21**, 115-130.

Jacobson, G.L and Bradshaw, R.H.W. 1981. The Selection of Sites for Paleovegetational Studies. *Quaternary Research*, **16**, 80-96.

Jarvis, D.I., Leopold, E.B and Liu, Y. 1992. Distinguishing the pollen of deciduous oaks, evergreen oaks, and certain rosaceous species of southwestern Sichuan Province, China. *Review of Palaeobotany and Palynology*, **75**, 259-271.

Jeffree, C.E., Baker, E.A and Holloway, P.J. 1975. Ultrastructure and recrystallisation of plant epicuticular waxes. *New Phytologist*, **75**, 539-549.

Jeffree, C.E. 2006. The fine structure of the plant cuticle. *In:* Riederer, M and Müller, C (eds.), Biology of the Plant Cuticle. Oxford: Blackwell, 11-125 pp.

Jeng, Q. 2006. Higher plant *n*-alkane average chain length as an indicator of petrogenic hydrocarbon contamination in marine sediments. *Marine Chemistry*, **102**, 242-251.

Jetter, R., Schäffer, S and Riederer, M. 2000. Leaf cuticular waxes are arranged in chemically and mechanically distinct layers: evidence from *Prunus laurocerasus* L. *Plant Cell and Environment*, **23**, 619-628.

Jetter, R and Schäffer, S. 2001. Chemical Composition of the *Prunus laurocerasus* Leaf Surface. Dynamic Changes of the Epicuticular Wax Film during Leaf Development. *Plant Physiology*, **126**, 1725–1737.

Jetter, R., Kunst, L and Samuels, L.G. 2008. Annual Plant Reviews, Biology of the Plant Cuticle. *In:* Markus Riederer, M and Muller, C (eds.), Composition of Plant Cuticular Waxes. New Jersey, Wiley-Blackwell.

Jetter, R and Reiderer, M. 2016. Localization of the Transpiration Barrier in the Epi- and Intracuticular Waxes of Eight Plant Species: Water Transport Resistances Are Associated with Fatty Acyl Rather Than Alicyclic Components. *Plant Physiology*, **170**, 921–934.

Jiang, W., Wu, H., Li, Q., Lin, Y and Yu, Y. 2019. Spatiotemporal changes in C_4 plant abundance in China since the Last Glacial Maximum and their driving factors. *Palaeogeography, Palaeoclimatology, Palaeoecology*, **518**, 10-21.

Jongma, J.I., Prange, M., Renssen, H and Schulz, M. 2007. Amplification of Holocene multicentennial climate forcing by mode transitions in North Atlantic overturning circulation. *Geophysical Research Letters*, **34**, 1-4.

Jorge da Silva, A. 1992. Dependence of upwelling related circulation on wind forcing and stratification over the Portuguese northern shelf. ICES CM2/C 17. Copenhagen: Hydrography Committee, 1-12 pp.

Jost, A., Lunt, D., Kageyama, M., Abe-Ouchi, A., Peyron, O., Valdes, P.J and Ramstein, G. 2005. High-resolution simulations of the last glacial maximum climate over Europe: a solution to discrepancies with continental palaeoclimatic reconstructions? *Climate Dynamics*, **24**, 577–590.

Jouanneau, J. M., Garcia, C., Oliveira, A., Rodrigues, A., Dias, J. A and Weber, O. 1998. Dispersal and deposition of suspended sediment on the shelf off the Tagus and Sado estuaries, SW Portugal. *Progress in Oceanography*, **42**, 233-257.

Jouzel, J., Masson-Delmotte, V., Cattani, O., Dreyfus, G., Falourd, S., Hoffmann, G., Minster, B., Nouet, J., Barnola, J. M., Chappellaz, J., Fischer, H., Gallet, J. C., Johnsen, S., Leuenberger, M., Loulergue, L., Luethi, D., Oerter, H., Parrenin, F., Raisbeck, G., Raynaud, D., Schilt, A., Schwander, J., Selmo, E., Souchez, R., Spahni, R., Stauffer, B., Steffensen, J. P., Stenni, B., Stocker, T. F., Tison, J. L., Werner, M and Wolff, E. W. 2007. Orbital and Millennial Antarctic Climate Variability over the Past 800,000 Years. *Science*, **317**, 793-796.

Jull, A.J.T., Burr, G.S., Hodgins, G.W.L. 2013. Radiocarbon dating, reservoir effects, and calibration. *Quaternary International*, **299**, 64-71.

Kageyama, M., Valdes, P.J., Ramstein, G., Hewitt, C., Wyputta, U. 1999. Northern hemisphere storm tracks in present day and last glacial maximum climate simulations: a comparison of the European PMIP models**.** *Journal of Climatology*, **12**, 742-760.

Keigwin, L. D., Jones, G.A., Lehman, S.J and Boyle, E.A. 1991. Deglacial meltwater discharge, North Atlantic deep circulation, and abrupt climate change. *Journal of Geophysical Research*, **96**, 811-816.

Keigwin, L.D., Klotsko, S., Zhao, N., Reilly, B., Giosan, L., Driscoll, N.W. 2018. Deglacial floods in the Beaufort Sea proceeded Younger Dryas Cooling. *Nature Geoscience*, **11**, 599–604.

Kennicutt, M.C., Barker, C., Brooks, J.M., De Freitas, D.A and Zhu, G.H. 1987. Selected organic matter source indicators in the Orinoco, Nile and Changjiang deltas. *Organic Geochemistry*, **11**, 41-51.

Kershaw, A.P and Strickland, K.M. 1990. A 10 year pollen trapping record from rainforest in northeastern Queensland, Australia. *Review of Palaeobotany and Palynology*, **64**, 281-288.

Khanal, B.P and Knoche, M. 2017. Mechanical properties of cuticles and their primary determinants. *Journal of Experimental Botany*, **68**, 5351–5367.

Kindler, P., Guillevic, M., Baumgartner, M., Schwander, J., Landais, A and Leuenberger, M. 2014. Temperature reconstruction from 10 to 120 kyr b2k from the NGRIP ice core. *Climate of the Past*, **10**, 887–902.

Kirsch, T., Kaffarnik, F., Riederer, M and Schreiber, L. 1997. Cuticular permeability of the three tree species Prunus laurocerasus L., Ginkgo biloba L. and Juglans regia L.: comparative investigation of the transport properties of intact leaves, isolated cuticles and reconstituted cuticular waxes. *Journal of Experimental Botany*, **48**, 1035–1045.

Kitagawa, H and Van Der Plicht, J. 1997. A 40,000-Year Varve Chronology from Lake Suigetsu, Japan: Extension of the ^{14}C Calibration Curve. *Radiocarbon*, **40**, 505-515.

Knorr, G and Lohmann, G. 2007. Rapid transitions in the Atlantic thermohaline circulation triggered by global warming and meltwater during the last deglaciation. *Geochemistry, Geophysics, Geosystems*, **8**, 1-22.

Kohn, M.J. 2010. Carbon isotope compositions of terrestrial C_3 plants as indicators of (paleo)ecology and (paleo)climate. *Proceedings of the National Academy of Science*, **107**, 19691-19695.

Kotthoff, U., Müller, U.C., Pross, J., Schmiedl, G., Lawson, I.T., van de Schootbrugge, B and Schulz, H. 2008. Lateglacial and Holocene vegetation dynamics in the Aegean region: an integrated view based on pollen data from marine and terrestrial archives. *The Holocene*, **18**, 1019–1032.

Kusch, S., Rethemeyer, J., Schefuss, E and Mollenhauer, G. 2010. Controls on the age of vascular plant biomarkers in Black Sea sediments. *Geochimica et Cosmochimica Acta*, **74**, 7031-7047.

Kutzbach, J.E., Guan, J., He, F., Cohen, A.S., Orland, J and Chen, G. 2020. African climate response to orbital and glacial forcing in 140,000-y simulation with implications for early modern human environments. *Proceedings of the National Academy of Sciences*, **117**, 2255-2264.

Laîné, A., Kageyama, M., Salas-Mélia, D., Voldoire, A., Rivière, G., Ramstein, G., Planton, S and Tyteca, S. 2009. Northern hemisphere storm tracks during the last glacial maximum in the PMIP2 ocean-atmosphere coupled models: energetic study, seasonal cycle, precipitation. *Climate Dynamics*, **32**, 593–614.

Lamb, H.F and van der Kaars, S. 1995. Vegetational response to Holocene climatic change: pollen and palaeolimnological data from the Middle Atlas, Morocco. *The Holocene*, **5**, 400-408.

Lambeck, K and Chappell, J. 2001. Sea Level Change Through the Last Glacial Cycle. *Science*, **292**, 679-686.

Lambeck, K., Rouby, H., Purcell, A., Sun, Y and Sambridge, M. 2014. Sea level and global ice volumes from the Last Glacial Maximum to the Holocene. *Proceedings of the National Academy of Sciences*, **111**, 15296-15303.

Lapidot, O., Ignat, T., Rud, R., Rog, I., Alchanatis, V and Klein, T. 2019. Use of thermal imaging to detect evaporative cooling in coniferous and T broadleaved tree species of the Mediterranean maquis. *Agricultural and Forest Meteorology*, **271**, 285-294.

Larrasoaña, J.C., Roberts, A. P., Rohling, E. J., Winklhofer, M and Wehausen, R. 2003. Three million years of monsoon variability over the northern Sahara. *Climate Dynamics*, **21**, 689–698.

Lastras, G., Arzola, R.G., Masson, D.G., Wynn, R.B., Huvenne, V.A.I., Hühnerbach, V., Canals, M. 2009. Geomorphology and sedimentary features in the Central Portuguese submarinecanyons, Western Iberian margin. *Geomorphology*, **103**, 310-329.

Lea, D.W. 2015. Climate sensitivity in a warmer world. *Nature*, **518**, 46-47.

Lebreiro, S.M., Voelker, A.H.L., Vizcaino, A., Abrantes, F.G., Alt-Epping, U., Jung, S., Thouveny, N and Gràcia, E. 2009. Sediment instability on the Portuguese continental margin under abrupt glacial climate changes (last 60 kyr). *Quaternary Science Reviews*, **28**, 3211-3223.

LeGrande, A.N., Schmidt, G.A., Shindell, D.T., Field, C.V., Miller, R.L., Koch, D.M., Faluvegi, G and Hoffmann, G. 2006. Consistent simulations of multiple proxy responses to an abrupt climate change event. *Proceedings of the National Academy of Sciences*, **103**, 837-842.

Leuenberger, M., Siegenthaler, U and Langway, C. 1992. Carbon isotope composition of atmospheric CO_2 during the last ice age from an Antarctic ice core. *Nature*, **357**, 488-490.

Li, C and Born, A. 2019. Coupled atmosphere-ice-ocean dynamics in Dansgaard-Oeschger events. *Quaternary Science Reviews*, **203**, 1-20.

Libby, W.F. 1946. Atmospheric Helium Three and Radiocarbon from Cosmic Radiation. *Physical Review*, **69**, 671-672.

Libby, W.F., Anderson, E.C and Arnold, J.R. 1949. Age Determination by Radiocarbon Content: World-Wide Assay of Natural Radiocarbon. *Science*, **109**, 227-228.

Lichtfouse, E and Eglinton, T.I. 1995. ^{13}C and ^{14}C evidence of pollution of a soil by fossil fuel and reconstruction of the composition of the pollutant. *Organic Geochemistry*, **23**, 969-973.

Lionello, P. 2012. *The Climate of the Mediterranean Region. From the Past to the Future.* Elsevier: Amsterdam, 1-592 pp.

Lionello, P., Abrantes, F., Gacic, M., Planton, S., Trigo, R and Ulbrich, U. 2014. The climate of the Mediterranean region: research progress and climate change impacts. *Regional Environmental Change*, **14**, 1679-1684.

Lisiecki, L.E and Raymo, M.E. 2005. A Pliocene-Pleistocene stack of 57 globally distributed benthic δ18O records. *Paleoceanography and Paleoclimatology*, **20**, 1-17.

Liu, W and Yang, H. 2008. Multiple controls for the variability of hydrogen isotopic compositions in higher plant n-alkanes from modern ecosystems. *Global Change Biology*, **14**, 2166–2177.

Liu, J and An, Z. 2018. A hierarchical framework for disentangling different controls on leaf wax $\delta D_{n\text{-alkane}}$ values in terrestrial higher plants. *Quaternary Science Reviews*, **201**, 409-417.

Liu, J and An, Z. 2020. Leaf wax *n*-alkane carbon isotope values vary among major terrestrial plant groups: Different responses to precipitation amount and temperature, and implications for paleoenvironmental reconstruction. *Earth Science Reviews*, **202**, 1-11.

Liu, Z., Otto-Bliesner, B., He, F., Brady, E., Tomas, R., Clark, P. U., Carlson, A., Lynch-Stieglitz, J., Curry, W., Brook, E., Erickson, D., Jacob, R., Kutzbach, J and Cheng, J. 2009. Transient Simulation of Last Deglaciation with a New Mechanism for Bølling-Allerød Warming. *Science*, **325**, 310-314.

Lockheart, M.J., Van Bergen, P.F and Evershed, R.P. 1997. Variations in the stable carbon isotope compositions of individual lipids from the leaves of modern angiosperms: implications for the study of higher land plant-derived sedimentary organic matter. *Organic Geochemistry*, **26**, 137-153.

López-Sáez, J.A., Carrasco, R.M., Turu, V., Ruiz-Zapata, B., Gil-García, M.J., Luelmo-Lautenschlaeger, R., Pérez-Díaz, S., Alba-Sánchez, F., Abel-Schaad, D., Ros, X and Pedraza, J. 2020. Late Glacial-early Holocene vegetation and environmental changes in the western Iberian Central System inferred from a key site: The Navamuño record, Béjar range (Spain). *Quaternary Science Reviews*, **230**, 1-22.

Loureiro, J.J., Machado, M.L., Macedo, M.E., Nunes, M.N., Botelho, O.F., Sousa, M.L., Almeida, M.C and Martins, J.C. 1986. *Monografias hidrológicas dos principais cursos de água de Portugal continental.* Lisbon: Direcção Geral dos Serviços Hidraulicos, 569 pp.

Lourens, J.A.J and Reynhardt, E.C. 1979. NMR investigation in Fischer-Tropsch waxes. *Journal of Physics, D: Applied Physics*, **12**, 1963-1972.

Lourens, L.J., Hilgen, F.J., Gudjonsson, W.J and Zachariasse, W.J. 1992. Late Pliocene to early Pleistocene astronomically forced sea surface productivity and temperature variations in the Mediterranean. *Marine Micropaleontology*, **19**, 49-78.

Lourens, L.J., Antonarankou, A., Hilgen, F.J and Van Hoof, A.M.M. 1996. Evaluation of the Plio-Pleistocene astronomical timescale. *Paleoceanography*, **11**, 391-413.

Ludwig, P., Schaffernicht, E.J., Shao, Y and Pinto, J.G. 2016. Regional atmospheric circulation over Europe during the Last Glacial Maximum and its links to precipitation. *JGR Atmospheres*, **121**, 2130-2145.

Mabberley, D.J. 2017. *Mabberley's Plant-book: A Portable Dictionary of Plants, their Classification and Uses*. 4th ed. Cambridge: Cambridge University Press.

MacAyeal, D. R. 1993. Binge/purge oscillations of the Laurentide ice sheet as a cause of the North Atlantic's Heinrich events. *Paleoceanography*, **8**, 775-784.

Madhavan, S., Treichel, I and O'Leary, M.H. 1991. Effects of relative humidity on carbon isotope fractionation in plants. *Botanica Acta*, **104**, 292-294.

Magill, C.R., Ausín, B., Wenk, P., McIntyre, C., Skinner, L., Martínez-García, A., Hodell, D.A., Haug, G.H., Kenney, W and Eglinton, T.I. 2018. Transient hydrodynamic effects influence organic carbon signatures in marine sediments. *Nature Communications*, **9**, 1-8.

Magny, M., Thew, N and Hadorn, P. 2003a. Late-glacial and early Holocene changes in vegetation and lake-level at Hauterive/Rougest-Terres, lake Neuchâtel (Switzerland). *Journal of Quaternary Science*, **18**, 31-40.

Magny, M., Bégeot, C., Guiot, J and Peyron, O. 2003b. Contrasting patterns of hydrological changes in Europe in response to Holocene climate cooling phases. *Quaternary Science Reviews*, **22**, 1589-1596.

Magri, D. 1994. Late-quaternary changes of plant biomass as recorded by pollen-stratigraphical data: a discussion of the problem at Valle di Castiglione, Italy. *Review of Palaeobotany and Palynology*, **81**, 313-325.

Magri, D and Parra, I. 2002. Late Quaternary western Mediterranean pollen records and African winds. *Earth and Planetary Science Letters*, **200**, 401-408.

Maher Jr, L.J., 1981. Statistics for microfossil concentration measurements employing samples spiked with marker grains. *Review of Palaeobotany and Palynology*, **32**, 153-191.

Manabe, S and Stouffer, R.J. 1997. Coupled ocean-atmosphere model response to freshwater input: Comparison to Younger Dryas Event. *Paleoceanography & Paleoclimatology*, **12**, 321-336.

Marcott, S.A., Clark, P.U., Padman, L., Klinkhammer, G.P., Springer, S.R., Liu, Z., Otto-Bliesner, B.L., Carlson, A.E., Ungerer, A., Padman, J., He, F., Cheng, J and Schmittner, A. 2011. Ice-shelf collapse from subsurface warming as a trigger for Heinrich events. *Proceedings of the National Academy of Sciences*, **108**, 13415-13419.

Marcott, S.A., Bauska, T.K., Buizert, C., Steig, E.J., Rosen, J.L., Cuffey, K.M., Fudge, T. J., Severinghaus, J.P., Ahn, J., Kalk, M.K., McConnell, J.R., Sowers, T., Taylor, K.C., White, J.W.C and Brook, E.J. 2014. Centennial-scale changes in the global carbon cycle during the last deglaciation. *Nature*, **514**, 616–619.

Margari, V., Tzedakis, P.C., Shackleton, N.J and Vautravers, M. 2007. Vegetation response in SW Iberia to abrupt climate change during MIS 6: Direct land-sea comparisons. *Quaternary International*, **167–168**, Supplement 1, 267–268.

Margari, V., Skinner, L. C., Tzedakis, P. C., Ganopolski, A., Vautravers, M and Shackleton, N. J. 2010. The nature of millennial-scale climate variability during the past two glacial periods. *Nature Geoscience*, **3**, 127-131.

Margari, V., Skinner, L. C., Hodell, D. A., Martrat, B., Toucanne, S., Grimalt, J. O., Gibbard, P.L., Lunkka, J.P and Tzedakis, P. C. 2014. Land-ocean changes on orbital and millennial time scales and the penultimate glaciation. *Geology*, **42**, 183-186.

Margari, V. 2016. *Pollen Preparation Protocol for Marine Fossil Pollen.* [Online]. Available from: http://www.geog.ucl.ac.uk/about-the-department/supportservices/laboratory/laboratory-methods/lake-sediment-analysis/pollen-preparation-protocol-for-marine-fossil-pollen [Accessed 12th January 2018].

Margari, V., Skinner, L.C., Menviel, L., Capron, E., Rhodes, R.H., Mleneck-Vautravers, M.J., Ezat, M.M., Martrat, B., Grimalt, J.O., Hodell, D.A and Tzedakis, P.C. 2020. Fast and slow components of interstadial warming in the North Atlantic during the last glacial. *Communications Earth & Environment*, **1**, 1-9.

Margaris, N.S and Vokou, D. 1982. Structural and physiological features of woody plants in phryganic ecosystems related to adaptive mechanisms. *Ecologia Mediterranea Année*, **8**, 449-459.

Marino, B.D., McElroy, M.B., Salawitch, R.J and Spaulding, W.G. 1992. Glacial-to-interglacial variations in the carbon isotopic composition of atmospheric CO2. *Nature*, **357**, 461-466.

Marino, G., Rohling, E.J., Rodriguez-Sanz, Grant, K.M., Heslop, D., Roberts, A.P., Stanford, J.D and Yu, J. 2015. Bipolar seesaw control on last interglacial sea level. *Nature*, **522**, 197-201.

Marotzke, J *and* Willebrand, J. 1991. Multiple Equilibria of the Global Thermohaline Circulation. *Journal of Oceanography*, **21**, 1372-1385.

Marsicek, J., Shuman, B., Bartlein, P.J., Shafer, S.L and Brewer, S. 2018. Reconciling divergent trends and millennial variations in Holocene temperatures. *Nature*, **554**, 92-96.

Marzi, R., Torkelson, B.E and Olson, R.K. 1993. A revised carbon preference index. *Organic Geochemistry*, **20**, 1303-1306.

Martrat, B., Grimalt, J. O., Shackleton, N. J., de Abreu, L., Hutterli, M. A and Stocker, T. F. 2007. Four climate cycles of recurring deep and surface water destabilizations on the Iberian margin. *Science*, **317**, 502-507.

Maslin. M.A., Ettwein, V.J., Boot, C.S., Bendle, J and Pancost, R.D. 2012a. Against the refuge hypothesis. *Journal of Quaternary Science*, **27**, 451-460.

Maslin, M.A., Pancost, R.D., Wilson, K.E., Lewis, J and Trauth, M.H. 2012b. Three and half million year history of moisture availability of South West Africa; Evidence from ODP site 1085 biomarker records. *Palaeogeography, Palaeoclimatology, Palaeoecology*, **317-318**, 41-47.

Matthews, J. 1969. The assessment of a method for the determination of absolute pollen frequencies. *New Phytologist*, **68**, 161–166.

Mayer, L.M. 1994. Relationships between mineral surfaces and organic carbon concentrations in soils and sediments. *Chemical Geology*, **114**, 347-363.

Mayewski, P.A., Rohling, E.E., Stager, J.C., Karlen, W., Maasch, K.A., Meeker, L.D., Meyerson, E.A., Gasse, F., van Kreveld, S., Holmgren, K., Lee-Thorp, J., Rosqvist, G., Rack, F., Staubwasser, M., Scheider, R.R., Steig, E.J. 2004. Holocene climate variability. *Quaternary Research*, **62**, 243-255.

McCave, I.N and Hall, I.R. 2002. Turbidity of waters over the Northwest Iberian continental margin. *Progress in Oceanography*, **52**, 299-313.

McManus, J.F., Oppo, D.W and Cullen, J.L. 1999. A 0.5-Million-Year Record of Millennial-Scale Climate Variability in the North Atlantic. *Science*, **283**, 971-975.

McManus, J.F., Francois, R., Gherardi, J.M., Keigwin, L.D and Brown-Leger, S. 2004. Collapse and rapid resumption of Atlantic Meridional Circulation linked to deglacial climate changes. *Nature*, **428**, 834 – 837.

Médail, F and Quezel, P. 1997. Hot-Spots Analysis for Conservation of Plant Biodiversity in the Mediterranean Basin. *Annals of the Missouri Botanical Garden*, **84**, 112-127.

Médail, F., Monnet, A-C., Pavon, D., Nikolic, T., Dimopoulos, P., Bacchetta, G., Arroyo, J., Barina, Z., Albassatneh, M.C., Domina, G., Fady, B., Matevski, V., Mifsud, S and Leriche, A. 2019. What is a tree in the Mediterranean Basin hotspot? A critical analysis. *Forest Ecosystems*, **6**, 1-19.

Mekik, F. 2014. Radiocarbon dating of planktonic foraminifer shells: A cautionary tale. *Paleoceanography*, **29**, 13-29.

Melander, L and Saunders, W.H. 1979. *Reaction Rates of Isotopic Molecules.* New York: Wiley.

Menviel, L., Timmermann, A., Elison Timm, O and Mouchet, A. 2011. Deconstructing the Last Glacial termination: the role of millennial and orbital-scale forcings. *Quaternary Science Reviews*, **30**, 1155-1172.

Menviel, L., Timmerman, A., Friedrich, T., England, M. H. 2014. Hindcasting the continuum of Dansgaard–Oeschger variability: mechanisms, patterns and timing. *Climate of the Past*, **10**, 63–77.

Mesolella, K.J., Matthews, R.K., Broecker, W.S and Thurber, D.L. 1969. The Astronomical Theory of Climatic Change: Barbados Data. *The Journal of Geology*, **77**, 250-274.

Metcalfe, L.D., Schmitz, A.A and Pelka, J.R. 1966. Rapid Preparation of Fatty Acid Esters from Lipids for Gas Chromatographic Analysis. *Analytical Chemistry*, **38**, 514-515.

Meyers, P.A and Eadie, B.J. 1993. Sources, degradation and recycling of organic matter associated with sinking particles in Lake Michigan. *Organic Geochemistry*, **20**, 47-56.

Meyers, P.A and Ishiwatari, R. 1993. Lacustrine organic geochemistry: an overview of indicators of organic matter sources and diagenesis in lake sediments. *Organic Geochemistry*, **20**, 867-900.

Meyers, P.A. 2003. Applications of organic geochemistry to paleolimnological reconstructions: a summary of examples from the Laurentian Great Lakes. *Organic Geochemistry*, **34**, 261-289.

Mignot, J., Ganopolski, A and Levermann, A. 2007. Atlantic Subsurface Temperatures: Response to a Shutdown of the Overturning Circulation and Consequences for Its Recovery. *Journal of Climate,* **20**, 4884–4898.

Miyake, F., Nagaya, K., Masuda, K and Nakamura, T. 2012. A signature of cosmic-ray increase in AD 774–775 from tree rings in Japan. *Nature*, **486**, 240–242.

Miyake, F., Masuda, K and Nakamura, T. 2013. Another rapid event in the carbon-14 content of tree rings. *Nature Communications*, **4**, 1-5.

Mollenhauer, G and Eglinton, T.I. 2007. Diagenetic and sedimentological controls on the composition of organic matter preserved in California Borderland Basin sediments. *Limnology & Oceanography*, **52**, 558-576.

Mollenhauer, G., Kienast, M., Lamy, F., Meggers, H., Schneider, R.R., Hayes, J.R and Eglinton, T.I. 2005. An evaluation of ^{14}C age relationships between co-occurring foraminifera, alkenones, and total organic carbon in continental margin sediments. *Paleoceanography & Paleoclimatology*, **20**, 1-12.

Monges Soares, A M., Gutiérrez-Zugasti, I., González-Morales, M., Matos Martins, J.M., Cuenca-Solana, D., Bailey, G.N. 2016. Marine Radiocarbon Reservoir Effect in Late Pleistocene and Early Holocene Coastal Waters off Northern Iberia. *Radiocarbon*, **58**, 869-882.

Monnin, E., Indermühle, A., Dällenbach, A., Flückiger, J., Stauffer, B., Stocker, T.F., Raynaud, D and Barnola, J.-M. 2001. Atmospheric CO_2 Concentrations over the Last Glacial Termination. *Science*, **291**, 112-114.

Monnin, E., Steig, E.J., Siegenthaler, U., Kawamura, K., Schwander, J., Stauffer, B., Stocker, T.F., Morse, D.L., Barnola, J.-M., Bellier, B., Raynaud, D and Fischer, H. 2004. Evidence for substantial accumulation rate variability in Antarctica during the Holocene, through synchronization of CO^2 in the Taylor Dome, Dome C and DML ice cores. *Earth and Planetary Science Letters*, **224**, 45-54.

Montgomery, D.D and Montgomery, C.G. 1939. The Intensity of Neutrons of Thermal Energy in the Atmosphere at Sea Level. *Physical Review*, **56**, 10-12.

Moore, P.D., Webb, J.A., Collinson, M.E. 1991. *Pollen Analysis* (2nd ed). Oxford: Blackwell Science Publications, 216 pp.

Morales-Molino, C., Devaux, L., Georget, M., Hanquiez, V and Sánchez Goñi, M.F. 2020. Modern pollen representation of the vegetation of the Tagus Basin (central Iberian Peninsula). *Review of Palaeobotany and Palynology*, **276**, 1-15.

Morellón, M., Aranbarri, J., Moreno, A., González-Sampériz, P and Valero-Garcés, B.L. 2018. Early Holocene humidity patterns in the Iberian Peninsula reconstructed from lake, pollen and speleothem records. *Quaternary Science Reviews*, **181**, 1-18.

Moreno, A., Stoll, H., Jiménez-Sánchez, M., Cacho, I., Valero-Garcés, B., Ito, E and Edwards, R.L. 2010a. A speleothem record of glacial (25–11.6 kyr BP) rapid climatic changes from northern Iberian Peninsula. *Global & Planetary Change*, **71**, 218–231.

Moreno, A., Valero-Garcés, B., Jiménez-Sánchez, M., Dominguez-Cuesta, M.J., Pilarmata, M., Navas, A., Gonzalez-Samperiz, P., Stoll, H., Farias, P., Morellon, M., Corella, J.P and Rico, M. 2010b. The last deglaciation in the Picos de Europa National Park (Cantabrian Mountains, northern Spain). *Journal of Quaternary Science*, **25**, 1076–1091.

Moreno, A., Gonzalez-Samperiz, P., Morellon, M., Valero-Garcés, B., Fletcher, W.J. 2012. Northern Iberian abrupt climate change dynamics during the last glacial cycle: A view from lacustrine sediments. *Quaternary Science Reviews*, **36**, 139-153.

Moros, M., Lloyd, J.M., Perner, K., Krawczyk, D., Blanz, T., de Vernal, A., Ouellet-Berniere, M-M., Kuijpers, A., Jennings, A.E., Witkowski, A., Schneider, R., Janseni, E. 2016. Surface and sub-surface multi-proxy reconstruction of middle to late Holocene palaeoceanographic changes in Disko Bugt, West Greenland. *Quaternary Science Reviews*, **132**, 146-160.

Mott, R.J., Grant, D.R., Stea, R and Ocheitti, S. 1986. Late-glacial climatic oscillation in Atlantic Canada equivalent to the Allerød/Younger Dryas event**.** *Nature*, **323**, 247-250.

Müller, J. 1959. Palynology of Recent Orinoco Delta and Shelf Sediments: Reports of the Orinoco Shelf Expedition; Volume 5. *Micropaleontology*, **5**, 1-32.

Müller, P.J., Kirst, G., Ruhl, G., von Storch, I and Rosell-Melé, A. 1998. Calibration of the alkenone paleotemperature index $U37^{K'}$ based on core-tops from the eastern South Atlantic and the global ocean (60°N-60°S). *Geochimica et Cosmochimica Acta*, **62**, 1757-1772.

Müller, C and Reiderer, M. 2005. Plant surface properties in chemical ecology. *Journal of Chemical Ecology*, **31**, 2621-2641.

Monnin, E., Steig, E.J., Siegenthaler, U., Kawamura, K., Schwander, J., Stauffer, B., Stocker, T.F., Morse, D.L., Barnola, J.-M., Bellier, B., Raynaud, D and Fischer, H. 2004. Evidence for substantial accumulation rate variability in Antarctica during the Holocene, through synchronization of CO^2

in the Taylor Dome, Dome C and DML ice cores. *Earth and Planetary Science Letters*, **224**, 45-54.

Muñoz-Sobrino, C., Ramil-Rego, P and Rodríguez Guitián, M.A. 2001. Vegetation in the mountains of northwest Iberia during the last glacial-interglacial transition. *Vegetation History & Archaeobotany,* **10**, 7-21.

Muñoz-Sobrino, C., Ramil-Rego, P and Gómez-Orellana, L. 2004. Vegetation of the Lago de Sanabria area (NW Iberia) since the end of the Pleistocene: a palaeoecological reconstruction on the basis of two new pollen sequences. *Vegetation History & Archaeobotany*, **13**, 1–22.

Murton, J.B., Bateman, M.D., Dallimore, S.R., Teller, J.T and Yang, Z. 2010. Identification of Younger Dryas outburst flood path from Lake Agassiz to the Arctic Ocean. *Nature*, **464**, 740–743.

Muscheler, R., Beer, J., Wagner, G and Finkel, R.C. 2000. Changes in deep-water formation during the Younger Dryas event inferred from ^{10}Be and ^{14}C records. *Nature*, **408**, 567–570.

Muscheler, R., Beer, J., Kubik, P.W and Synal, H.A. 2005. Geomagnetic field intensity during the last 60,000 years based on ^{10}Be and ^{36}Cl from the Summit ice cores and ^{14}C. *Quaternary Science Reviews*, **24**, 1849-1860.

Muschitiello, F., Pausata, F.S., Watson, J.E., Smittenberg, R.H., Salih, A.A., Brooks, S.J., Whitehouse, N.J., Karlatou- Charalampopoulou, A. and Wohlfarth, B. 2015. Fennoscandian freshwater control on Greenland hydroclimate shifts at the onset of the Younger Dryas. *Nature Communications*, **6**, 1-18.

Muschitiello, F., D'Andrea, W.J., Schmittner, A., Heaton, T.J., Balascio, N.L., de Roberts, N., Caffee, M.W., Woodruff, T.E., Welten, K.C., Skinner, L.C., Simon, M.H and Dokken, T.M. 2019. Deep-water circulation changes lead North Atlantic climate during deglaciation. *Nature Communications*, **10**, 1-10.

Muschitiello, F., O'Regan, M., Martens, J., West, G., Gustafsson, O and Jakobsson, M. 2020. A new 30 000-year chronology for rapidly deposited sediments on the Lomonosov Ridge using bulk radiocarbon dating and probabilistic stratigraphic alignment. *Geochronology*, **2**, 81-91.

Naughton, F., Goñi, M. S., Desprat, S., Turon, J. L., Duprat, J., Malaizé, B, Joli, C., Cortijo, E., Drago, T and Freitas, M. C. 2007. Present-day and past (last 25000 years) marine pollen signal off western Iberia. *Marine Micropaleontology*, **62**, 91-114.

Naughton, F., Sánchez Goñi, M.F., Kageyama, M., Bard, E., Duprat, J., Cortijos, E., Desprat, S., Malaizé, B., Joly, C., Rostek, F and Turon, J.L. 2009. Wet to dry climatic trend in north-western Iberia within Heinrich events. *Earth & Planetary Science Letters*, **284**, 329-342.

Naughton, F., Sánchez Goñi, M.F., Rodrigues, T., Salgueiro, E., Costas, S., Desprat, S., Duprat, J., Michel, E., Rossignol, L., Zaragosi, S., Voelker, L and Abrantes, F. 2016. Climate variability across the last deglaciation in NW Iberia and its margin. *Quaternary International*, **414**, 9-22.

Naughton, F., Costas, S., Gomes, S.D., Desprate, S., Rodrigues, T., Sanchez Goñi, M.F., Renssen, H., Trigo, R., Bronk-Ramsey, C., Oliveira, D., Salgueiro, E., Voelker, A.H.L and Abrantes, F. 2019. Coupled ocean and atmospheric changes during Greenland stadial 1 in southwestern Europe. *Quaternary Science Reviews*, **212**, 108-120.

NEEM Community Members, Dahl-Jensen, D., Albert, M., Aldahan, A *et al.,* 2013. Eemian interglacial reconstructed from a Greenland folded ice core. *Nature*, **493,** 489–494.

Neinhuis, C and Barthlott, W. 1997. Characterization and Distribution of Water-repellent, Self-cleaning Plant Surfaces. *Annals of Botany*, **79**, 667-677.

Nelson, D.B., Ladd, S.N., Schubert, C.J and Kahmen, A. 2018. Rapid atmospheric transport and large-scale deposition of recently synthesized plant waxes. *Geochimica et Cosmochimica Acta*, **222**, 599-617.

Nesje, A and Dahl, S.O. 1993. Lateglacial and Holocene glacier fluctuations and climate variations in western Norway: A review. *Quaternary Science Reviews*, **12**, 255-261.

NGRIP Members, Andersen, K. K., Azuma, N., Barnola, J. M., Bigler, M., Biscaye, P., Caillon, N., Flückiger, J., Fritzsche, D., Fujii, Y., Goto-Azuma, K. Grønvold, K., Gundestrup, N. S., Hansson, M., Huber, C., Hvidberg, C.S., Johnsen, S.J., Jonsell, U., Jouzel, J., Kipfstuhl, S., Landais, A., Leuenberger, M., Lorrain, R., Masson-Delmotte, V., Miller, H., Motoyama, H., Narita, H., Popp, T., Rasmussen, S.O., Raynaud, D., Rothlisberger, R., Ruth, U., Samyn, D., Schwander, J., Shoji, H., Siggard-Andersen, M.L., Steffensen, J.P., Stocker, T., Sveinbjörnsdóttir A.E., Svensson, A., Takata, M., Tison, J.L., Thorsteinsson, T., Watanabe, O., Wilhelms, F and White, J.W.C. 2004. High-resolution of Northern Hemisphere climate extending into the last interglacial period. *Nature*, **431**, 147-151.

Norström, E., Katrantsiotis, C., Smittenberg, R.H and Kouli, K. 2017. Chemotaxonomy in some Mediterranean plants and implications for fossil biomarker records. *Geochimica et Cosmochimica Acta*, **219**, 96-110.

O'Hare, P., Mekhaldi, F., Adolphi, F., Raidbeck, G., Aldahan, A., Anderberg, E., Beer, J., Christl, M., Fahrni, S., Synal, H.-A., Park, J., Possnert, G., Southon, J., Bard, E., ASTER Team and Muscheler, R. 2019. Multiradionuclide evidence for an extreme solar proton event around 2,610 B.P. (~660 BC). *Proceedings of the National Academy of Sciences*, **116**, 5961-5966.

O'Leary, M.H. 1981. Carbon isotope fractionation in plants. *Phytochemistry*, **20**, 553-567.

Ohkouchi, N., Eglinton, T.I., Keigwin, L.D and Hayes, J.M. 2002. Spatial and Temporal Offsets Between Proxy Records in a Sediment Drift. *Science*, **298**, 1224-1227.

Oliveira, D. 2012. *Vegetation response to Holocene climate variability in South-Western Europe.* Thesis (PhD). Universidade de Lisboa.

Oliveira, A., Vitorino, J., Rodrigues, A., Jouanneau, J.M., Dias, J.M and Weber, O. 2002. Nepheloid layer dynamics in the northern Portuguese shelf. *Progress in Oceanography*, **52**, 195–213.

Oliveira, D., Desprat, S., Yin, Q., Naughton, F., Trigo, R., Rodrigues, T., Abrantes, F., Sánchez Goñi, M.F. 2018. Unraveling the forcings controlling the vegetation and climate of the best orbital analogues for the present interglacial in SW Europe. *Climate Dynamics*, **51**, 667-686.

Oschlies, A. 2001. NAO-induced long-term changes in nutrient supply to the surface waters of the North Atlantic. *Geophysical Research Letters*, **28**, 1751-1754.

Pacini, E. 1992. Tranpsort mechanisms of pollen- a short review. *In:* Cresti, M and Tiezzi, A (eds.), *Sexual Plant Reproduction.* Berlin: Springer, 69-79 pp.

Pailler, D and Bard, E. 2002. High frequency palaeoceanographic changes during the past 140 000 yr recorded by the organic matter in sediments of the Iberian Margin. *Palaeogeography, Palaeoclimatology, Palaeoecology*, **181**, 431-452.

Paillard, D. 1998. The timing of Pleistocene glaciations from a simple multiple-state climate model. *Nature,* **391,** 378–381.

Pancost, R.D and Boot, C.S. 2004. The palaeoclimatic utility of terrestrial biomarkers in marine sediments. *Marine Chemistry*, **92**, 239-261.

Papa, B.D., Mysak, L.A and Wang, Z. 2006. Intermittent ice sheet discharge events in northeastern North America during the last glacial period. *Climate Dynamics*, **26**, 201–216.

Patel, S., Nelson, D.R., Gibbs, A.G., 2001. Chemical and physical analyses of wax ester properties. *Journal of Insect Science*, **1**, 1-7.

Pearson, A and Eglinton, T.I. 2000. The origin of *n*-alkanes in Santa Monica Basin surface sediment: a model based on compound-specific $\Delta^{14}C$ and $\delta^{13}C$ data. *Organic Geochemistry*, **31**, 1103-1116.

Pedro, J.B., Jochum, M., Buizert, C., He, F., Barker, S and Rasmussen, S.O. 2018. Beyond the bipolar seesaw: Toward a process understanding of interhemispheric coupling. *Quaternary Science Reviews*, **192**, 27-46.

Peck, J.A., Green, R.R., Shanahan, T., King, J.W., Overpeck, J.T and Scholz, C.A. 2004. A magnetic mineral record of Late Quaternary tropical climate variability from Lake Bosumtwi, Ghana. *Palaeogeography, Palaeoclimatology, Palaeoecology***, 215**, 37-57.

Peck, V.L., Hall. I.R, Zahn, R., Scourse, J.L. 2007. Progressive reduction in NE Atlantic intermediate water ventilation prior to Heinrich events: Response to NW European ice sheet instabilities? *Geochemistry, Geophysics, Geosystems*, **8**, 1-11.

Peltier, W.R**.** 2005. On the hemispheric origins of meltwater pulse 1a. *Quaternary Science Reviews*, **24**, 1655-1671.

Pérez, F.F., Castro, C.G., Álvarez–Salgado, X.A and Ríos, A.F. 2001. Coupling between the Iberian basin — scale circulation and the Portugal boundary current system: a chemical study. *Deep Sea Research Part I: Oceanographic Research Papers*. **48**, 1519-1533.

Petit, J. R., Jouzel, J., Raynaud, D., Barkov, N. I., Barnola, J. M., Basile, I., Bender, M., Chappellaz, J., Davis, M., Delaygue, G., Delmotte, M., Kotlyakov, V.M., Legrand, M., Lipenkov, V.Y., Lorios, C., Pepin, L., Ritz, C., Saltzmann, E., and Stievenard, M. 1999. Climate and atmospheric history of the past 420,000 years from the Vostok ice core, Antarctica. *Nature*, **399**, 429-436.

Pimental, N.M and Azevedo, T.M. 1994. Alpine controlan sedimentation at Sado basin (SW Portugal). *Cuaderno Lab Xeolóxico de Laxe*, **19**, 229-238.

Pimental, N.L. 2002. Pedogenic and early diagenetic processes in Palaeogene alluvial fan and lacustrine deposits from the Sado Basin (S Portugal). *Sedimentary Geology*, **148**, 123-138.

Polissar, P.J and D'Andrea, W.J. 2014. Uncertainty in paleohydrologic reconstruction from molecular δD values. *Geochimica et Cosmochimica Acta,* **129**, 146-156.

Pollard, D and Barron, E.J. 2003. Causes of model–data discrepancies in european climate during oxygen isotope stage 3 with insights from the last glacial maximum. *Quaternary Research*, **59**, 108-113.

Polley, H.W., Johnson, H.B., Marinot, B.D and Mayeux, H.S. 1993. Increase in C_3 plant water-use efficiency and biomass over Glacial to present CO_2 concentrations. *Nature*, **361**, 61–64.

Polunin, O and Smithies, B.E. 1973. *Flowers of South-West Europe.* London: Oxford University Press, 496 pp.

Pons, A and Reille, M. 1988. The Holocene and Upper Pleistocene pollen records from Padul (Granada, Spain): A new study. *Palaeogeography, Palaeoclimatology, Palaecology*, **66**, 243-263.

Popp, B.N., Takigiku, R., Hayes, J. M., Louda, J. W and Baker, E.W. 1989. The post-Paleozoic chronology and mechanism of ^{13}C depletion in primary marine organic matter. *American Journal of Science*, **289**, 436-454.

Poynter, J.G and Eglinton, G. 1990. Molecular composition of three sediments from hole 717c: The Bengal fan. *In:* Cochran, JR; Stow, DAV; et al. (eds.), Proceedings of the Ocean Drilling Program, Scientific Results, College Station, TX (Ocean Drilling Program), **116**, 155-161.

Poynter, J.G., Farrimond, P., Robinson, N and Eglinton, G. 1989. Aeolian-Derived Higher Plant Lipids in the Marine Sedimentary Record: Links with Palaeoclimate. *In:* Leinen M., Sarnthein M (eds.), Paleoclimatology and Paleometeorology: Modern and Past Patterns of Global Atmospheric Transport. NATO ASI Series (Series C: Mathematical and Physical Sciences). Dordrecht: Springer.

Prentice, I.C. 1985. Pollen representation, source area, and basin size: toward a unified theory of pollen analysis. *Quaternary Research*, **23**, 76–86.

Prentice, I.C. 1988. Records of vegetation in time and space: the principles of pollen analysis. *In*: Huntley, B and Webb, T (eds.), *Vegetation History.* Dordrecht: Kluwer Academic Press, 17-42 pp.

Prentice, I.C., Guit, J., Huntley, B., Jolly, D and Cheddadi, R. 1996. Reconstructing biomes from palaeoecological data: a general method and its application to European pollen data at 0 and 6. *Climate Dynamics*, **12**, 185–194.

Prentice, I.C., Meng, T., Wang, H., Harrison, S.P., Ni, J and Wang, G. 2011. Evidence of a universal scaling relationship for leaf CO_2drawdown along an aridity gradient. *New Phytologist*, **190**, 169-180.

Quenea, K., Derenne, S., Largeau, C., Rumpel, C and Mariotti, A. 2004. Variation in lipid relative abundance and composition among different particle size fractions of a forest soil. *Organic Geochemistry*, **35**, 1355-1370.

Quezel, P. 1985. Definition of the Mediterranean region and the origin of its flora. *In:* Gomez-Campo, C (ed.), Plant conservation in the Mediterranean area. Dordrecht: Junk, 9-24 pp.

Rahmstorf, S. 2002. Ocean circulation and climate during the past 120,000 years. *Nature*, **419**, 207–214.

Raicich, F., Pinardi, N and Navarra, A. 2003. Teleconnections between Indian monsoon and Sahel rainfall and the Mediterranean. *International Journal of Climatology*, **23**, 173-186.

Railsback, L.B., Liang, F., Romani, J.R.V., Grandal-d'Anglade, A., Rodriguez, M.V., Fidalgo, L.S., Mosquera, D.F. Cheng, H. Edwards, R.L. 2011. Petrographic and isotopic evidence for Holocene long-term climate change and shorter-term environmental shifts from a stalagmite from the Serra do Courel of northwestern Spain, and implications for climatic history across Europe and the Mediterranean. *Palaeogeography, Palaeoclimatology, Palaeoecology*, **305**, 172–184.

Ramos-Roman, M.J., Jiménez-Moreno, G., Camuera, J., García-Alix, A., Anderson, R.S., Jiménez-Espejo, F.J., Sachse, D., Toney, J.L., Carrión, J.S., Webster, C and Yanes, Y. 2018a. Millennial-scale cyclical environment and climate variability during the Holocene in the western Mediterranean region deduced from a new multi-proxy analysis from the Padul record (Sierra Nevada, Spain). *Global & Planetary Change*, **168**, 35-53.

Ramos-Roman, M.J., Jiménez-Moreno, G., Camuera, J., García-Alix, A., Anderson, R.S., Jiménez-Espejo, F.J and Carrión, J.S. 2018b. Holocene climate aridification trend and human impact interrupted by millennial- and centennial-scale climate fluctuations from a new sedimentary record from Padul (Sierra Nevada, southern Iberian Peninsula). *Climate of the Past*, **14**, 117-137.

Rasmussen, S.O., Andersen, K.K., Svensson, A.M., Steffensen, J.P., Vinther, B.M., Clausen, H.B., Siggaard-Andersen, M.L., Johnsen, S.L., Larsen, L.B., Dahl-Jensen, D., Bigler, M., Röthlisberger, R., Fischer, H., Goto-Azuma, K., Hansson, M.E and Ruth, U. 2006. A new Greenland ice core chronology for the last glacial termination. *Journal of Geophysical Research*, **111**, 1-16.

Rasmussen, S.O., Bigler, M., Blockley, S.P., Blunier, T., Buchardt, S.L., Clausen, H.B., Cvijanovic, I., Dahl-Jensen, D., Johnsen, S.J., Fischer, H., Gkinis, V., Guillevic, M., Hoek, W.Z., Lowe, J., Pedro, J.B., PoppaInger, T., Seierstad, K., Steffensen, J.P., Svensson, A.M., Vallelonga, P., Vinther, B.M., Walker, M.J.C., Wheatley, J.J and Winstrup, M. 2014. A stratigraphic framework for abrupt climatic changes during the Last Glacial period based on three synchronized Greenland ice-core records: refining and extending the INTIMATE event stratigraphy. *Quaternary Science Reviews,* **106**, 14-28

Rao, Z., Wu, Y and Zhu, Z. 2011. Is the maximum carbon number of long-chain *n*-alkanes an indicator of grassland or forest? Evidence from surface soils and modern plants. *Chinese Science Bulletin*, **56**, 1714-1720.

Raymo, M.E. 1997. The timing of major climate terminations. *Paleoceanography and Paleoclimatology*, **12**, 577-585.

Rebollal, M.B and Pérez-González, A. 2007. Inland aeolian deposits of the Iberian Peninsula: Sand dunes and clay dunes of the Duero Basin and the Manchega Plain. Palaeoclimatic considerations. *Geomorphology*, **102**, 207–220.

Reiderer, M and Schneider, G. 1990. The effect of the environment on the permeability and composition of Citrus leaf cuticles. *Planta*, **180**, 154-165.

Riederer, M and Schreiber, L. 2001. Protecting against water loss: analysis of the barrier properties of plant cuticles. *Journal of Experimental Botany*, **52**, 2023-2032.

Riederer, M and Schönherr, J. 1985. Accumulation and transport of (2,4-dichlorophenoxy) acetic acid in plant cuticles: II. Permeability of the cuticular membrane. *Ecotoxicology and Environmental Safety*, **9**, 196-208.

Reille, M. 1999. *Pollen et spores d'Europe et d'Afrique du Nord.* Marseille: Laboratoire de Botanique Historique et Palynologie, 543 pp.

Reille, M and Lowe, J.J. 1993. A re-evaluation of the vegetation history of the eastern Pyrenees (France) from the end of the last glacial to the present. *Quaternary Science Reviews*, **12**, 47-77.

Reimer, P.J., Brown, T.A and Reimer, R.W. 2004. Discussion: Reporting and Calibration of Post-Bomb 14C Data. *Radiocarbon*, **46**, 1299-1304.

Reimer, P. J., Bard, E., Bayliss, A., Beck, J. W., Blackwell, P. G., Bronk Ramsey, C., Grootes, P. M., Guilderson, T. P., Haflidason, H., Hajdas, I., HattŽ, C., Heaton, T. J., Hoffmann, D. L., Hogg, A. G., Hughen, K. A., Kaiser, K. F., Kromer, B., Manning, S. W., Niu, M., Reimer, R. W., Richards, D. A., Scott, E. M., Southon, J. R., Staff, R. A., Turney, C. S. M., & van der Plicht, J. 2013. IntCal13 and Marine13 Radiocarbon Age Calibration Curves 0-50,000 Years cal BP. *Radiocarbon,* **55**, 1869–1887.

Reimer, P.J., Austin, W.E.N., Bard, E., Bayliss, A., Blackwell, P.G., Bronk Ramsey, C., Butzin, M., Cheng, H., Edwards, R.L., Friedrich, M., Grootes, P.M., Guilderson, T.P., Hajdas, I., Heaton, T.J., Hogg, A.G., Hughen, K.A., Kromer, B., Manning, S.W., Muscheler, R., Palmer, J.G., Pearson, C., van der Plicht, J., Reimer, R.W., Richards, D.A., Scott, W.M., Southon, J.R., Turney, C.S.M., Wacker, L., Adolphi, F., Büntgen, U., Capano, M., Fahrni, S.M., Fogtmann-Schulz, A., Friedrich, R., Köhler, P., Kudsk, S., Miyake, F., Olsen, J., Reinig, F., Sakamoto, M., Sookdeo, A and Talamo, S. 2020. The INTCAL20 Northern Hemisphere radiocarbon age calibration curve (0–55 CAL kBP) Part of: IntCal 20. *Radiocarbon*, **62**, 1-33.

Relvas, P., Barton, E.D., Dubert, J., Oliveira, P.B., Peliz, A., da Silva, J.C.B and Santos, A.M.P. 2007. Physical oceanography of the western Iberia ecosystem: Latest views and challenges. *Progress in Oceanography*, **74**, 149-173.

Renssen, H., Goosse, H., Fichefet, T and Campin, J.M. 2001. The 8.2 kyr BP event simulated by a global atmosphere–sea-ice–ocean model. *Geophysical Research Letters*, **28**, 1567-1570.

Renssen, H., Mairesse, A., Goose, H., Mathiot, P., Heiri, O., Roche, D.M., Nisancioglu, K.H and Valdes, P.J. 2015. Multiple causes of the Younger Dryas cold period. *Nature Geoscience*, **8**, 946–949.

Reynhardt, E.C. 1986. Temperature dependence of the cell parameters of Fischer-Tropsch waxes: hard wax and oxidised hard wax. *Journal of Physics D: Applied Physics*, **19**, 1925-1938.

Reynhardt, E.C. 1997. The role of hydrogen bonding in the cuticular wax of Hordeum vulgare L. *European Biophysics Journal*, **26**, 195–201.

Reynhardt, E.C and Riederer, M. 1994. Structures and molecular dynamics of plant waxes. *European Biophysics Journal*, **23**, 59-70.

Rieley, G., Collier, R.J., Jones, D.M and Eglinton, G. 1991a. The biogeochemistry of Ellesmere Lake, UK- I: source correlation of leaf wax inputs to the sedimentary lipid record. *Organic Geochemistry*, **17**, 901-912.

Rieley, G., Collier, R.J., Jones, D.M and Eglinton, G., Eakin, P.A and Fallick, A.E. 1991b. Sources of sedimentary lipids deduced from stable carbon-isotope analyses of individual compounds. Nature, **352**, 425–427.

Rieley, G., Welker, J.M., Callaghan, T.V., Eglinton, G. 1995. Epicuticular waxes of two arctic species: Compositional differences in relation to winter snow cover. *Phytochemistry*, **38**, 45-52.

Rind, D., Demenocal, P., Russell, G. L., Sheth, S., Collins, D., Schmidt, G. A and Teller, J. 2001. Effects of glacial meltwater in the GISS coupled atmosphere-ocean model: Part I: North Atlantic Deep Water response. *J. Geophysical Research*, **106**, 335-27.

Robinson, L.F., Adkins, J.F., Keigwin, L.D., Southon, J., Fernandez, D.P., Wang, S-L and Scheirer, D.S. 2005. Radiocarbon Variability in the Western North Atlantic During the Last Deglaciation. *Science*, **310**, 1469-1473.

Roche, D.M., Renssen, H., Weber, S.L and Goosse, H. 2007. Could meltwater pulses have been sneaked unnoticed into the deep ocean during the last glacial? *Geophysical Research Letters*, **34**, 1-6.

Roche, D.M and Wiersma, A.P. 2010. A systematic study of the impact of freshwater pulses with respect to different geographical locations. *Climate Dynamics*, **34**, 997–1013.

Rodríguez, S., Querol, X., Alastuey,A., Kallos, G and Kakaliagou, O. 2001. Saharan dust contributions to PM10 and TSP levels in Southern and Eastern Spain**.** *Atmospheric Environment*, **35**, 2433-2447.

Rodríguez-Rajo, F.J., Méndez, J And Jato, V. 2005. Airborne Ericaceae Pollen Grains in the Atmosphere Of Vigo (Northwest Spain) and its Relationship with Meteorological Factors. *Journal of Integrative Plant Biology*, **47**, 792-800.

Rodrigues, T., Grimalt, J.O., Abrantes, F.G., Flores, J.A and Lebreiro, S.M. 2009. Holocene interdependences of changes in sea surface temperature, productivity, and fluvial inputs in the Iberian continental shelf (Tagus mud patch). *Geochemistry, Geophysics & Geosystems*, **10**, 1-17.

Rodrigues, T., Voelker, A.H.L., Grimalt, J.O, Abrantes, F and Naughton, F. 2010. Iberian Margin sea surface temperature during MIS 15 to 9 (580–300 ka): Glacial suborbital variability versus interglacial stability. *Palaeoclimatology and Palaeoceanography*, **26**, 1-16.

Rogerson, M., Rohling, E. J and Weaver P.P.E. 2006. Promotion of meridional overturning by Mediterranean-derived salt during the last deglaciation. *Paleoceanography*, **21**, 1-8.

Rogge, W.F., Hildemann, L.M., Mazurek, M.A., Cass, G.R and Simoneit, B.R.T. 1993. Sources of fine organic aerosol. 4. Particulate abrasion products from leaf surfaces of urban plants. *Environmental Science and Technology,* **27**, 2700-2711.

Rohling, E.J., Fenton, M., Jorissen, F.J., Bertrand, P., Ganssen, G and Caulet, J.P. 1998. Magnitudes of sea-level low-stands of the past 500,000 years. *Nature,* **394**, 162-165.

Rohling, E.J., Mayewski, P., Abu-Zied, R., Casford, J and Hayes, A. 2002. Holocene atmosphere-ocean interactions: records from Greenland and the Aegean Sea. *Climate Dynamics*, **18**, 587-593.

Rohling, E.J. Marino, G and Grant, K.M. 2015. Mediterranean climate and oceanography, and the periodic development of anoxic events (sapropels). *Earth-Science Reviews*, **143**, 62-97.

Rohling, E.J., Hibbert, F.D., Grant, K.M., Galaasen, E.V., Irvali, N., Kleiven, H.F., Marino, G., Ninnemann, U., Roberts, A.P., Rosenthal, Y., Schulz, H., Williams, F.H and Y, J. 2019. Asynchronous Antarctic and Greenland ice-volume contributions to the last interglacial sea-level highstand. *Nature Communications*, **10**, 1-9.

Rommerskirchen, F., Eglinton, G., Dupont, L., Güntner, U., Wenzel, C and Rullkötter, J. 2003. A north to south transect of Holocene southeast Atlantic continental margin sediments: Relationship between aerosol transport and compound-specific $\delta^{13}C$ land plant biomarker and pollen records. *Geochemistry, Geophysics, Geosystems,* **4**, 1-29.

Rommerskirchen, F., Plader, A., Eglinton, G., Chikaraishi, Y., Rullkötter, J. 2006. Chemotaxonomic significance of distribution and stable carbon isotopic composition of long-chain alkanes and alkan-1-ols in C_4 grass waxes. *Organic Geochemistry*, **37**, 1303-1332.

Rooth, C. 1982. Hydrology and ocean circulation. *Progress in Oceanography*, **11**, 131-149.

Rossignol-Strick, M. 1973. Pollen analysis of some sapropel layers from the deep-sea floor of the Eastern Mediterranean. *Initial Report, Deep Sea Drilling Project*, **13**, 971-991.

Rossignol-Strick, M., Nesteroff, W., Olive, P and Vergnaud-Grazzini, C. 1982. After the deluge: Mediterranean stagnation and sapropel formation. *Nature*, **295**, 105–110.

Rossignol-Strick, M. 1983. African monsoons, an immediate climate response to orbital insolation. *Nature*, **304**, 46-49.

Roucoux, K.H., de Abreu, L., Shackleton, N.J and Tzedakis, P.C. 2005. The response of NW Iberian vegetation to North Atlantic climate oscillations during the last 65 kyr. *Quaternary Science Reviews*, **24**, 1637-1653.

Roucoux, K.H., Tzedakis, P.C., de Abreu, L and Shackleton, N.J. 2006. Climate and vegetation changes 180,000 to 345,000 years ago recorded in a deep-sea core off Portugal. *Earth and Planetary Science Letters*, **249**, 307-325.

Roucoux, K.H., Tzedakis, P.C., Lawson, I.T and Margari, V. 2011. Vegetation history of the penultimate glacial period (Marine Isotope Stage 6) at Ioannina, north-west Greece. *Journal of Quaternary Science*, **6**, 616-626.

Ruddiman, W.F and McIntyre, A. 1981. The North Atlantic Ocean during the last deglaciation. *Palaeogeography, Palaeoclimatology, Palaeoecology*, **35**, 145-214.

Ruddiman, W.F., Raymo, M and A. McIntyre, A. 1986. Matuyama 41,000-year cycles: North Atlantic Ocean and northern hemisphere ice sheets. *Earth and Planetary Science Letters*, **80**, 117-129.

Ruddiman, W.F., Raymo, M.E., Martinson, D.G., Clement, B.M and Backman, J. 1989. Pleistocene evolution: Northern hemisphere ice sheets and North Atlantic Ocean. *Paleoceanography and Paleoclimatology,* **4,** 353-412.

Sabino, M., Schefuss, E., Natalicchio, M., Pierre, F.D., Birgel, D., Bortels, D., Schnetger, B and Peckmann, J. 2020. Climatic and hydrologic variability in the northern Mediterranean across the onset of the Messinian salinity crisis. *Palaeogeography, Palaeoclimatology, Palaeoecology,* **545**, 1-12.

Sachse, D., Radke, J and Gleixner, G. 2004. Hydrogen isotope ratios of recent lacustrine sedimentary n-alkanes record modern climate variability. *Geochimica et Cosmochimica Acta*, **68**, 4877-4889.

Sachse, D., Radke, J and Gleixner, G. 2006. δD values of individual n-alkanes from terrestrial plants along a climatic gradient – Implications for the sedimentary biomarker record. *Organic Geochemistry*, **37**, 469-483.

Sachse, D., Billault, I., Bowen, G.K., Chikaraishi, Y., Dawson, T.E., Feakins, S.J., Freeman, K.H. Magill, C.R. McInerney, F. A., Van der Meer, M.T.J., Polissar, P., Robins, R.J., Sachs, J.P., Schmidt, H-L., Sessions, A.L., White, J.W.C., West, J.B and Kahmen, A. 2012. *Molecular Paleohydrology: Interpreting the Hydrogen-Isotopic Composition of Lipid Biomarkers from Photosynthesizing Organisms. Annual Review of Earth and Planetary Sciences*, **40**, 221-249.

Sachse, D., Dawson, T.E and Kahmen, A. 2015. Seasonal variation of leaf wax *n*-alkane production and δ^2H values from the evergreen oak tree, *Quercus agrifolia. Isotopes in Environmental and Health Studies*, **51**, 124-142.

Salgueiro, E., Naughton, F., Voelker, A.H.L., de Abreu, L., Alberto, A., Rossignol, L., Duprat, J., Magalhães, V.H., Vaqueiro, S., Turon, J.-L and Abrantes, F. 2014. Past circulation along the western Iberian margin: a time slice vision from the Last Glacial to the Holocene. *Quaternary Science Reviews*, **106**, 316-329.

Sanchez Goñi, M. S., Eynaud, F., Turon, J. L and Shackleton, N. J. 1999. High resolution palynological record off the Iberian margin: direct land-sea correlation for the Last Interglacial complex. *Earth and Planetary Science Letters*, **171**, 123-137.

Sanchez Goñi, M. S., Turon, J.L., Eynaud, F and Gendreau, S. 2000. European Climatic Response to Millennial-Scale Changes in the Atmosphere–Ocean System during the Last Glacial Period. *Quaternary Research*, **54**, 394-403.

Sánchez Goñi, M. F and Harrison, S. P. 2010. *Millennial-scale climate variability and vegetation changes during the last glacial: concepts and terminology. Quaternary Science Reviews*, **29**, 2823-2827.

Santos, L., Romani, J.R.V and Jalut, G. 2000. History of vegetation during the Holocene in the Courel and Queixa Sierras, Galicia, northwest Iberian Peninsula. *Journal of Quaternary Science*, **15**, 621–632.

Sarnthein, M., Winn, K., Jung, S.J.A., Duplessy, J-C., Labeyrie, L., Erlenkeuser, H and Ganssen, G. 1994. Changes in East Atlantic Deepwater Circulation over the last 30,000 years: Eight time slice reconstructions. *Palaeoceanography and Palaeoclimatology,* **9**, 209-267.

Sarnthein, M., 2000. Fundamental Modes and Abrupt Changes in North Atlantic Circulation and Climate over the last 60 ky — Concepts, Reconstruction and Numerical Modeling. *In:* Schäfer, P., Ritzrau, W., Schlüter, M and Thiede, J (eds.), The Northern North Atlantic. Berlin: Springer-Verlag, 365-410 pp.

Sauer, P. E., Eglinton, T. I., Hayes, J. M., Schimmelmann, A and Sessions, A. L. 2001. Compound-specific D/H ratios of lipid biomarkers from sediments as a proxy for environmental and climatic conditions. *Geochimica et Cosmochimica Acta*, **65**, 213-222.

Schäfer, I.K., Bliedtner, M., Wolf, D., Faust, D and Zech, R. 2016. Evidence for humid conditions during the last glacial from leaf wax patterns in the loessepaleosol sequence El Paraíso, Central Spain. *Quaternary International*, **407**, 64-73.

Schäfer, I.K., Bliedtner, M., Wolf, D., Kolb, T., Zech, H., Faust, D and Zech, R. 2018. A $\delta^{13}C$ and $\delta^{2}H$ leaf wax record from the Late Quaternary loess-paleosoil sequence El Paraíso, Central Spain. *Palaeogeography, Palaeoclimatology, Palaeoecology,* **507**, 52-59.

Schefuss, E., Ratmeyer, V., Stuut, J-B.W., Jansen, J.H.F., Damsté, J.S.S. 2003. Carbon isotope analyses of *n*-alkanes in dust from the lower atmosphere over the central eastern Atlantic. *Geochimica et Cosmochimica Acta*, **67**, 1757-1767.

Schirrmacher, J., Weinelt, M., Blanz, T., Andersen, N., Salgueiro, E and Schneider, R.R. 2019. Multi-decadal atmospheric and marine climate variability in southern Iberia during the mid- to late-Holocene. *Climate of the Past*, **15**, 617–634.

Schmittner, A and Galbraith, E.D. 2008. Glacial greenhouse-gas fluctuations controlled by ocean circulation changes. *Nature*, **456**, 373–376.

Schönherr,J., Eckl, K and Gruler, H. 1979. Water permeability of plant cuticles: the effect of temperature on diffusion of water. *Planta*, **147**, 21-26.

Schreiber, L and Schönherr, J. 1990. Phase transitions and thermal expansion coefficients of plant cuticles: The effects of temperature on structure and function. *Planta*, **182**, 186-193.

Schreiber, L and Riederer, M. 1996. Ecophysiology of cuticular transpiration: comparative investigation of cuticular water permeability of plant species from different habitats. *Oecologia*, **107**, 426-443.

Schulz, H., von Rad, U and Erlenkeuser, H. 1998. Correlation between Arabian Sea and Greenland climate oscillations of the past 110,000 years. *Nature*, **393**, 54-57.

Schulz, M., Prange, M and Klocker, A. 2007. Low-frequency oscillations of the Atlantic Ocean meridional overturning circulation in a coupled climate model. *Climate of the Past*, **3**, 97-107.

Schwark, L., Zink, K and Lechterbeck, J. 2002. Reconstruction of postglacial to early Holocene vegetation history in terrestrial Central Europe via cuticular lipid biomarkers and pollen records from lake sediments. *Geology*, **30**, 463-466.

Seppa, H and Bennett, K.D. 2003. Quaternary pollen analysis: recent progress in palaeoecology and palaeoclimatology. *Progress in Physical Geography*, **27**, 548-579.

Sessford, E.G., Jensen, M.F., Tisserand, A.A., Muschitiello, F., Dokken, T., Nisancioglu, K.H., Jansen, E. 2019. Consistent fluctuations in intermediate water temperature off the coast of Greenland and Norway during Dansgaard-Oeschger events. *Quaternary Science Reviews*, **223**, 1-16.

Sessions, A.L. 2016. Factors controlling the deuterium contents of sedimentary hydrocarbons. *Organic Geochemistry*, **96**, 43-64.

Shackleton, N.J and Opdyke, N.D. 1973. Oxygen Isotope and Palaeomagnetic Stratigraphy of Equatorial Pacific Core V28-238: Oxygen Isotope Temperatures and Ice Volumes on a 10^5 Year and 10^6 Year Scale. *Quaternary Research*, **3**, 39-55.

Shackleton, N., Berger, A and Peltier, W. 1990. An alternative astronomical calibration of the lower Pleistocene timescale based on ODP Site 677. *Transactions of the Royal Society of Edinburgh: Earth Sciences*, **81**, 251-261.

Shackleton, N. J., Hall, M. A and Vincent, E. 2000. Phase relationships between millennial-scale events 64,000–24,000 years ago. *Paleoceanography*, **15**, 565-569.

Shackleton, N. J., Sánchez Goñi, M.F., Paillerm D and Lancelot, Y. 2003. Marine Isotope Substage 5e and the Eemian Interglacial. *Global and Planetary Change*, **36**, 151-155.

Shackleton, N.J., Fairbanks, R.G., Chiu, T.-C and Parrenin, F. 2004. Absolute calibration of the Greenland time scale: implications for Antarctic time scales and for ^{14}C. *Quaternary Science Reviews*, **23**, 1513-1522.

Shakun, J.D and Carlson, A.E. 2010. A global perspective on Last Glacial Maximum to Holocene climate change. *Quaternary Science Reviews*, **29**, 1801-1816.

Shaffer, G., Olsen, S.M and Bjerrum, C.J. 2004. Ocean subsurface warming as a mechanism for coupling Dansgaard-Oeschger climate cycles and ice-rafting events. *Geophysical Research Letters,* **31**, 1-4.

Shepherd, T and Wynne Griffiths, D. 2006. The effects of stress on plant cuticular waxes. *New Phytologist*, **171**, 469-499.

Sierro, F.J., Hodell, D.A., Curtis, J.H., Flores, J.A., Requera, I., Colmenero-Hidalgo, E., Bárcena, M.A., Grimalt, J.O., Cacho, I., Frigola, J., Canals, M. 2005. Impact of iceberg melting on Mediterranean thermohaline circulation during Heinrich events. *Palaeoceanography and Palaeoclimatology*, **20**, 1-13.

Sikes, E.L., Samson, C.R., Guilderson, T.P and Howard, W.R. 2000. Old radiocarbon ages in the southwest Pacific Ocean during the last glacial period and deglaciation. *Nature*, **405**, 555-559.

Sikes, E.L., Medeirosa, P.M., Augustinus, P., Wilmshurst, J.M and Freeman, K.H. 2013. Seasonal variations in aridity and temperature characterize changing climate during the last deglaciation in New Zealand. *Quaternary Science Reviews*, **74**, 245-256.

Sikes, E.L., Cook, M.S and Guilderson, T.P. 2016. Reduced deep ocean ventilation in the Southern Pacific Ocean during the last glaciation persisted into the deglaciation. *Earth and Planetary Science Letters*, **438**, 130-138.

Sikes, E.L and Guilderson, T.P. 2016. Southwest Pacific Ocean surface reservoir ages since the last glaciation: Circulation insights from multiple-core studies. *Paleoceanography and Paleoclimatology,* **31**, 298-310.

Skinner, L.C., Shackleton, N.J and Elderfield, H. 2003. Millennial-scale variability of deep-water temperature and $\delta^{18}O_{dw}$ indicating deep-water source variations in the Northeast Atlantic, 0–34 cal. ka BP. *Geochemistry, Geophysics, Geosystems*, **4**, 1-17.

Skinner, L.C and Shackleton, N.J. 2004. Rapid transient changes in northeast Atlantic deep-water ventilation age across Termination I. *Paleoceanography and Paleoclimatology*, **19**, 1-11.

Skinner, L.C and Shackleton, N.J. 2005. An Atlantic lead over Pacific deep-water change across Termination I: implications for the application of the marine isotope stagestratigraphy. *Quaternary Science Reviews*, **24**, 571–580.

Skinner, L. C., Elderfield, H and Hall, M. 2007. Phasing of Millennial Climate Events and Northeast Atlantic Deep-Water Temperature Change Since 50 Ka Bp. *In:* Schmittner, A., Chiang, J.C.H and Hemming, S.R. (eds.), Ocean Circulation: Mechanisms and Impacts-Past and Future Changes of Meridional Overturning. Washington DC: American Geophysical Union, 197-208 pp.

Skinner, L.C. 2008. Revisiting the absolute calibration of the Greenland ice-core age-scales. *Climate of the Past*, **4**, 295–302.

Skinner, L.C., Fallon, S., Waelbroeck, C., Michel, E., Barker, S. 2010. Ventilation of the Deep Southern Ocean and Deglacial CO_2 Rise. *Science*, **328**, 1147-1151.

Skinner, L.C., Waelbroeck, C., Scrivner, A.E and Fallon, S. 2014. Radiocarbon evidence for alternating northern and southern sources of ventilation of the deep Atlantic carbon pool during the last deglaciation. *Proceedings of the National Academy of Sciences*, **111**, 5480-5484.

Skinner, L.C., McCave, I.N., Carter, L., Fallon, S., Scrivner, A.E., Primeau, F. 2015a. Reduced ventilation and enhanced magnitude of the deep Pacific carbon pool during the last glacial period. *Paleoceanography and Paleoclimatology*, **411**, 45-52.

Skinner, L.C., Waelbroeck, Scrivner, A.E and Fallon, S.J. 2015b. Radiocarbon evidence for alternating northern and southern sources of ventilation of the deep Atlantic carbon pool during the last deglaciation. *Proceedings of the National Academy of Sciences*, **111**, 5480–5484.

Skinner, L.C., Muschitiello, F and Scrivner, A.E. 2019. Marine Reservoir Age Variability Over the Last Deglaciation: Implications for Marine Carbon Cycling and Prospects for Regional Radiocarbon Calibrations. *Paleoceanography and Paleoclimatology*, **34**, 1807-1815.

Smit, A. 1973. A scanning electron microscopical study of the pollen morphology of the genus Quercus. *Acta Botanica Neerlandica*, **22**, 655-665.

Smittenberg, R. H., Eglinton, T. I., Schouten, S and Sinninghe Damsté, J. S. 2006. Ongoing Buildup of Refractory Organic Carbon in Boreal Soils During the Holocene. *Science*, **314**, 1283-1286.

Southon, J., Kashgarian, M., Fontugne, M., Metivier, B and Yim, W.W.-S. 2002. Marine Reservoir Corrections for the Indian Ocean and Southeast Asia. *Radiocarbon*, **44**, 167-180.

Southon, J., Noronha, A.L., Cheng, H., Edwards, R.L., and Wang, Y. 2012. A high-resolution record of atmospheric ^{14}C based on Hulu Cave speleothem H82. *Quaternary Science Reviews*, **33**, 32-41.

Stanley, E.A. 1966. The problem of reworked pollen and spores in marine sediments. *Marine Geology*, **4**, 397-408.

Stanley, D.J and Wear, C.M. 1978. The "mud-line": An erosion—Deposition boundary on the upper continental slope. *Marine Geology*, **28**, 19-29.

Stenni, B., Buiron, D., Frezzotti, M., Albani, S., Barbante, C., Bard, E., Barnola, J.M., Baroni, M., Baumgartner, M., Bonazza, M., Capron, E., Castellano, E., Chappellaz, J., Delmonte, B., S. Falourd, S., Genoni, L., Lacumin, P., Jouzel, J., Kipfstuhl, S., Landais, A., Lemieux-Dudon, B., Maggi, V., Masson-Delmotte, V., Mazzola, C., Minster, B., Montagnat, M., Mulvaney, R., B. Narcisi, B., H. Oerter, H., F. Parrenin, F., J. R. Petit, J,R., Ritz, C., Scarchilli, C., Schilt, A., Schüpbach, S., Schwander, J., Selmo, E., Severi, M., Stocker, T.F and Udisti, R. 2011. Expression of the bipolar see-saw in Antarctic climate records during the last deglaciation. *Nature Geoscience*, **4**, 46–49.

Stern, J.V and Lisiecki, L.E. 2013. North Atlantic circulation and reservoir age changes over the past 41,000 years. *Geophysical Research Letters*, **40**, 3693-3697.

Stocker, T. F. and Wright, D. G. 1991. Rapid transitions of the ocean's deep circulation induced by changes in surface water fluxes. *Nature*, **351**, 729.

Stocker, T.F and Wright, D.G. 1996. Rapid changes in ocean circulation and atmospheric radiocarbon. *Paleoclimatology and Paleoceanography*, **11**, 773-795.

Stocker, T.F and Johnsen, S.J. 2003. A minimum thermodynamic model for the bipolar seesaw. *Paleoceanography*, **18**, 1-11.

Stockmarr, J. 1971. Tablets with spores used in absolute pollen analysis. *Pollen et Spores,* **13**, 615-621.

Stoll, H.M., Moreno, A., Mendez-Vicente, A., Gonzalez-Lemos, S., Jimenez-Sanchez, M., Dominguez-Cuesta, M.J., Edwards, R.L., Cheng, H., Wang, X. 2013. Paleoclimate and growth rates of speleothems in the northwestern Iberian Peninsula over the last two glacial cycles. *Quaternary Research*, **80**, 284–290.

Stuiver, M. 1961. Variations in radiocarbon concentration and sunspot activity. *Journal of Geophysical Research*, **66**, 273-276.

Stuiver, M. 1982. A high-precision calibration of the AD radiocarbon time scale: *Radiocarbon*, **24**, 1-26.

Stuiver, M., Pearson, G.W and Pearson and Tom Braziunas, T. 1986. Radiocarbon age calibration of marine samples back to 9000 cal yr BP. *Radiocarbon*, **28**, 980-1021.

Stuiver, M., Reimer, P.J and Braziunas, T.F. 1998. High-Precision Radiocarbon Age Calibration for Terrestrial and Marine Samples. *Radiocarbon*, **40**, 1127-1151.

Stuiver, M and Braziunas, T.F. 1993. Sun, ocean, climate and atmospheric $^{14}CO_2$: an evaluation of causal and spectral relationships. *The Holocene*, **3**, 289-305**.**

Stuiver, M and Polach, H.A. 1977. Discussion Reporting of ^{14}C Data. *Radiocarbon*, **19**, 355-363.

Stuiver, M and Quay, P.D. 1980. Changes in Atmospheric Carbon-14 Attributed to a Variable Sun. *Science*, **207**, 11-19.

Sugita, S. 1993. A model of pollen source area for an entire lake surface. *Quaternary Research,* **39**, 239–44.

Sugita, S. 1994. Pollen representation of vegetation in quaternary sediments: theory and method in patchy vegetation. *Journal of Ecology*, **82**, 881–897.

Sugita, S., Hicks, S and Sormunen, H. 2010. Absolute pollen productivity and pollen–vegetation relationships in northern Finland. *Journal of Quaternary Science*, **25**, 724-736.

Svensson, A., Andersen, K.K., Bigler, M., Clausen, H.B., Dahl-Jensen, D., Davies, S.M., Johnsen, S.J., Muscheler, R., Rasmussen, S.O., Röthlisberger, R., Steffensen, J.P., Vinther, B.M. 2006. The Greenland Ice Core Chronology 2005, 15–42 ka. Part 2: comparison to other records. *Quaternary Science Reviews*, **25**, 3258-3267.

Synal, H-A., Stocker, M and Suter, M. 2007. MICADAS: A new compact radiocarbon AMS system. *Nuclear Instruments and Methods in Physics Research Section B: Beam Interactions with Materials and Atoms,* **259**, 7-13.

Tabel, J., Khater, C., Rhoujjati, A., Dezileau, L., Bouimetarhan, I., Carre, M., Vidal, L., Benkaddour, A., Nourelbait, M and Cheddadi, R. 2016. Environmental changes over the past 25 000 years in the southern Middle Atlas, Morocco. *Journal of Quaternary Science*, **31**, 93-102.

Tarasov, L and Peltier, W.R. 2005. Arctic freshwater forcing of the Younger Dryas cold reversal. *Nature*, **435**, 662–665.

Thomas, E.R., Wolff, E.W., Mulvaney, R., Steffensen, J.P., Johnsen, S.J., Arrowsmith, C., White, J.W.C., Vaughn, B and Popp, T. 2007. The 8.2 ka event from Greenland ice cores. *Quaternary Science Reviews*, **26**, 70-81.

Thomas, E.R., Wolff, E.W., Mulvaney, R., Johnsen, S.J., Steffensen, J.P and Arrowsmith, C. 2009. Anatomy of a Dansgaard-Oeschger warming transition: High-resolution analysis of the North Greenland Ice Core Project ice core. *Journal of Geophysical Research*, **114**, 1-9.

Thornalley, D. J., Elderfield, H and McCave, I.N. 2009. Holocene oscillations in temperature and salinity of the surface subpolar North Atlantic. *Nature*, **457**, 711–714.

Thornalley, D. J., McCave, I. N and Elderfield, H. 2010. Freshwater input and abrupt deglacial climate change in the North Atlantic. *Paleoceanography*, **25**, 1-16.

Thornalley, D.J.R., Barker, S., Broecker, W., Elderfield, H and McCave, I.N. 2011. The Deglacial Evolution of North Atlantic Deep Convection. *Science*, **331**, 202-205.

Thornalley, D.J.R., Bauch, H.A., Gebbie, G., Guo, W., Ziegler, M., Bernasconi, S.M., Barker, S., Skinner, L.C and Yu, J. 2015. A warm and poorly ventilated deep Arctic Mediterranean during the last glacial period. *Paleoceanography*, **349**, 706-710.

Tierney, J.E and Tingley, M.P. 2018. BAYSPLINE: A New Calibration for the Alkenone Paleothermometer. *Paleoceanography & Paleoclimatology*, **33**, 281-301.

Tipple, B.J., Berke, M.A., Doman, C.E., Khachaturyan, S and Ehleringer, J.R. 2013. Leaf-wax *n*-alkanes record the plant–water environment at leaf flush. *Proceedings of the National Academy of Science*, **110**, 2659–2664.

Tipple, B.J and Pagani, M. 2013. Environmental control on eastern broadleaf forest species' leaf wax distributions and D/H ratios. *Geochimica et Cosmochimica Acta*, **111**, 64-77.

Tinner, W and Lotter, A.F. 2001. Central European vegetation response to abrupt climate change at 8.2 ka. *Geology*, **29**, 551–554.

Toggweiler, J. R., Dixon, K and Broecker, W. S. 1991. The Peru upwelling and the ventilation of the south Pacific thermocline. *Journal of Geophysical Research*, **96**, 20467-20497.

Traverse, A. 2007. *Paleopalynology*. 2nd ed. Berlin: Springer, 813 pp.

Trigo, R.M., Pozo-Vazquez, D., Osborn, D., Castro-Diez, Y., Gamiz-Fortis, S and Esteban-Parra, M.J. 2004. North Atlantic oscillation influence on precipitation, river flow and water resources in the Iberian Peninsula. *International Journal of Climatology*, **24**, 925-944.

Tuenter, E., Webera, S.L., Hilgen, F.J and Lourens, L.J. 2003. The response of the African summer monsoon to remote and local forcing due to precession and obliquity. *Global & Planetary Change*, **36**, 219-235.

Tuniz, C., Kutschera, W., Fink, D., Herzog, D.F and Bird, J.R. 1998. *Accelerator Mass Spectrometry: Ultrasensitive Analysis for Global Science*. Florida: CRC Press, 371 pp.

Turon, J.L., Lézine, A.M and Denèfle, M. 2003. Land–sea correlations for the last glaciation inferred from a pollen and dinocyst record from the portuguese margin. *Quaternary Research*, **59**, 88-96.

Tzedakis, P.C. 1993. Long-term tree populations in northwest Greece through multiple Quaternary climatic cycles. *Nature*, **364**, 437–440.

Tzedakis, P.C., Roucoux, K.H., de Abreu, L and Shackleton, N.J. 2004. The Duration of Forest Stages in Southern Europe and Interglacial Climate Variability. *Geology*, **306**, 2231-2235.

Tzedakis, P. C. 2007. Seven ambiguities in the Mediterranean palaeoenvironmental narrative. *Quaternary Science Reviews*, **26**, 2042-2066.

Tzedakis, P.C., Pälike, H., Roucoux, K.H and de Abreu, L. 2009. Atmospheric methane, southern European vegetation and low-mid latitude links on orbital and millennial timescales. *Earth & Planetary Science Letters*, **277**, 307-317.

Tzedakis, P.C., Crucifix, M., Mitsui, T and Wolff, E.W. 2017. A simple rule to determine which insolation cycles lead to interglacials. *Nature*, **542,** 427–432.

Tzedakis, P.C., Drysdale, R.N., Margari, V., Skinner, L.C., Menviel, L., Rhodes, R. H., Taschetto, A. S., Hodell, D. A., Crowhurst, S. J., Hellstrom, J. C., Fallick, A. E., Grimalt, J. O., McManus, J. F., Martrat, B., Mokeddem, Z., Parrenin, F., Regattieri, E., Roe, K and Zanchetta, G. 2018. Enhanced climate instability in the North Atlantic and southern Europe during the Last Interglacial. *Nature Communications,* **9**, 1-14.

Vale, C. 1990. Temporal variations of particulate metals in the Tagus River Estuary. *Science of the Total Environment*, **97-98**, 137-154.

Vale, C and Sundby, B. 1987. Suspended sediment fluctuations in the Tagus estuary on semi-diurnal and fortnightly time scales. *Estuarine, Coastal and Shelf Science*, **25**, 495-508.

Vale, C., Cortesão, C., Castro, O and Ferreira, A.M. 1993. Suspended-sediment response to pulses in river flow and semidiurnal and fortnightly tidal variations in a mesotidal estuary. *Marine Chemistry*, **43**, 21-31.

van Aken, H.M. 2000a. The hydrography of the mid-latitude Northeast Atlantic Ocean: II: The intermediate water masses. *Deep Sea Research Part I: Oceanographic Research Papers*, **47**, 789-824.

van Aken, H.M. 2000b. The hydrography of the mid-latitude northeast Atlantic Ocean: I: The deep water masses. *Deep Sea Research Part I: Oceanographic Research Papers*, **47**, 757-788.

Van Benthem, F., Clarke, G.C.S. and Punt, W. 1984. The Northwest European Pollen Flora, 33: Fagaceae. *Review of Palaeobotany, Palynology*, **42**, 87-110.

Van der Hammen, T., Wijmstra, T.A and Zagwijn, H. 1971. The floral record of the Late Cenozoic of Europe. *In*: Turekian, K.K. (ed.), The Late Cenozoic Glacial Ages. New Haven: Yale University Press, 391–424 pp.

Van der Knaap, W.O and van Leeuwen, J.F.N. 1995. Holocene vegetation succession and degradation as responses to climatic change and human activity in the Serra de Estrela, Portugal. *Review of Palaeobotany & Palynology*, **89**, 153-211.

Van der Knaap, W.O and van Leeuwen, J.F.N. 1997. Late Glacial and early Holocene vegetation succession, altitudinal vegetation zonation, and climatic change in the Serra da Estrela, Portugal. *Review of Palaeobotany & Palynology*, **97**, 239-285.

van der Knaap, W.O., van Leeuwen, J.F.N and Ammann, B. 2001. Seven years of annual pollen influx at the forest limit in the Swiss Alps studied by pollen traps: relations to vegetation and climate. *Review of Palaeobotany and Palynology*, **117**, 31-52.

Vanney, J.R and Mougenot, D. 1981. *La plate-forme continentale du Portugal et les provinces adjacentes: analyse géomorphologique.* Lisbon: Serviços Geológicos de Portugal, 86 pp.

Vautravers, M.J and Shackleton, N.J. 2006. Centennial-scale surface hydrology off Portugal during marine isotope stage 3: Insights from planktonic foraminiferal fauna variability. *Paleoclimatology and Paleoceanography*, **21**, 1-13.

Vegas, J., Ruiz-Zapata, B., Ortiz, J.E., Galan, L., Torres, T., Garcia-Cortes, A., Gil-Garcia, M.J., Perez-Gonzalez, A and Gallardo-Milla, J.L. 2010. Identification of arid phases during the last 50 cal. ka BP from the Fuentillejo maar-lacustrine record (Campo de Calatrava Volcanic Field, Spain). *Journal of Quaternary Science*, **25**, 1051-1062.

Vicente-Serrano, S. M and Heredia-Laclaustra, A. 2004. NAO influence on NDVI trends in the Iberian peninsula (1982–2000). *International Journal of Remote Sensing*, **25**, 2871-2879.

Vinther, B.M., Clausen, H.B., Johnsen, S.J., Rasmussen, S.O., Andersen, K.K., Buchardt, S.L., Dahl-Jensen, D., Seierstad, I.K., Siggaard-Andersen, M.-L., Steffensen, J.P., Svensson, A., Olsen, J and Heinemeier, J. 2006. A synchronized dating of three Greenland ice cores throughout the Holocene. *Journal of Geophysical Research*, **111**, 1-11.

Vis, G-J., Kasse, C and Vandenberghe, J. 2008. Late Pleistocene and Holocene palaeogeography of the Lower Tagus Valley (Portugal): effects of relative sea level, valley morphology and sediment supply. *Quaternary Science Reviews*, **27**, 1682-1709.

Vis, G-J and Kasse, C. 2009. Late Quaternary valley-fill succession of the Lower Tagus Valley, Portugal. *Sedimentary Geology*, **221**, 19-39.

Vis, G-J., Kasse, C., Kroon, D., Vandenberghe, J., Jung, S., Lebreiro, S.M and Rodrigues, T. 2016. Time-integrated 3D approach of late Quaternary sediment-depocentermigration in the Tagus depositional system: From river valley to abyssal plain. *Earth Science Reviews*, **153**, 192-211.

Vitorino, J., Oliveira, A., Jouanneau, J.M and Drago, T. 2002. Winter dynamics on the northern Portuguese shelf. Part 1: physical processes. *Progress in Oceanography*, **52**, 129-153.

Voelker, A.H.J., Grootes, P.M., Nadeau, M-J and Sarnthein, M. 2000. Radiocarbon Levels in the Iceland Sea from 25-53 kyr and their Link to the Earth's Magnetic Field Intensity. *Radiocarbon*, **42**, 437-452.

Voelker, A.H.L., Lebreiro, S.M., Schönfeld, J., Cacho, I., Erlenkeuser, H., Abrantes, F. 2006. Mediterranean outflow strengthening during northern hemisphere coolings: A salt source for the glacial Atlantic? *Earth & Planetary Science Letters*, **245**, 39–55.

Voelker, A. H., de Abreu, L., Schönfeld, J., Erlenkeuser, H and Abrantes, F. 2009. Hydrographic conditions along the western Iberian margin during marine isotope stage 2. *Geochemistry, Geophysics, Geosystems*, **10**, 1-30.

Voelker, A. H and de Abreu, L. 2011. A review of abrupt climate change events in the northeastern Atlantic Ocean (Iberian Margin): Latitudinal, longitudinal, and vertical gradients. *In:* Rashid, H., Polyak, L and Mosley-Thompson, E (eds.), Abrupt Climate Change: Mechanisms, Patterns, and Impacts. Washington DC: *Geophysical Monograph Series,* 15-37 pp.

Vogts, A., Mossen, H., Rommerskirchen, F and Rullkötter, J. 2009. Distribution patterns and stable carbon isotopic composition of alkanes and alkan-1-ols from plant waxes of African rain forest and savanna C_3species. *Organic Geochemistry*, **40**, 1037-1054.

Von Grafenstein, U., Erlenkeuser, H., Müller, J., Jouzel, J and Johnsen, S. 1998. The cold event 8200 years ago documented in oxygen isotope records of precipitation in Europe and Greenland. *Climate Dynamics*, **14**, 73-81.

Von Mohl, H. 1847. Untersuchungen der Frage: bildet die cellulose die grundlage sammtlicher vegetabilischen membranen. *Botanische Zeitung,* **5**, 497–505.

Vonk, J.E., Drenzek, N.J., Hughen, K.A., Stanley, R.H.R., McIntyre, C., Montluçon, D.B., Giosan, L., Southon, J.R., Santos, G.M., Druffel, E.R.M., Andersson, A.A., Sköld, M and Eglinton, T.I. 2019. Temporal deconvolution of vascular plant-derived fatty acids exported from terrestrial watersheds. *Geochimica et Cosmochimica Acta*, **244**, 502-521.

von Post L. 1916. Mötet den 2 November 1916. *Geologiska Föreningens i Stockholm Förhandlingar*, **38**, 383–394.

Wacker, L., Christl, M and Synal, H.A. 2010. Bats: A new tool for AMS data reduction. *Nuclear Instruments and Methods in Physics Research Section B: Beam Interactions with Materials and Atoms,* **269**, 976-979.

Wacker, L., Lippold, J., Molnár, M and Schulz, H. 2013. Towards radiocarbon dating with single foraminifera with a gas ion source. *Nuclear Instruments and Methods in Physics Research B*, **294**, 307-310.

Waelbroeck, C., Duplessy, J-C., Michel, E., Labeyrie, L., Paillard, D and Duprat, J. 2001. The timing of the last deglaciation in North Atlantic climate records. *Nature*, **412**, 724-727.

Waelbroeck, C., Labeyriea, L., Michel, E., Duplessy, J.C., McManus, J.F., Lambeck, K., Balbon, E., Labracherie, M. 2002. Sea-level and deep water temperature changes derived from benthic foraminifera isotopic records. *Quaternary Science Reviews*, **21**, 295-305.

Wagner, G., Masarik, J., Beer, J., Baumgartner, S., Imboden, B., Kubik, P.W., Synal, H.A and Suter, M. 2000. Reconstruction of the geomagnetic field between 20 and 60 kyr BP from cosmogenic radionuclides in the GRIP ice core. *Nuclear Instruments and Methods in Physics Research Section B: Beam Interactions with Materials and Atoms*, **172**, 597-604.

WAIS Divide Project Members, 2015. Precise interpolar phasing of abrupt climate change during the last ice age. *Nature*, **520**, 661-665.

Walczak, I. W., Baldini, J.U.L., Baldini, L.M., McDermott, F., Marsden, S., Standish, C.D., Richards, D.A., Andreo, B., Slater, J. 2015. Reconstructing high-resolution climate using CT scanning of unsectioned stalagmites: A case study identifying the mid-Holocene onset of the Mediterranean climate in southern Iberia. *Quaternary Science Reviews*, **127**, 117-128.

Walker, M., Head, M.J., Berkelhammer, M., Björck, S., Cheng, H., Cwynar, L., Fisher, D., Gkinis, V., Long, A., Lowe, J., Newnham, R., Rasmussen, S.O and Weiss, H. 2018. Formal ratification of the subdivision of the Holocene Series/Epoch (Quaternary System/Period): two new Global Boundary Stratotype Sections and Points (GSSPs) and three new stages/subseries. *Episodes*, **41**, 1-11.

Wakeham, S.G., Hedges, J.I., Lee, C., Peterson, M.L and Hernes, P.J. 1997. Compositions and transport of lipid biomarkers through the water column and surficial sediments of the equatorial Pacific Ocean. *Deep Sea Research Part II: Topical Studies in Oceanography*, **44**, 131-2162.

Wang, M., Zhang, W and Hou, J. 2015. Is average chain length of plant lipids a potential proxy for vegetation, environment and climate changes? *Biogeosciences*, **12**, 1-25.

Wang, Y.J., Cheng, H., Edwards, R.L., An, Z.S., Wu, J.Y., Chen, C.C and Dorale, J.A. 2001. A High-Resolution Absolute-Dated Late Pleistocene Monsoon Record from Hulu Cave, China. *Science*, **294**, 2345-2348.

Wang, Y.J., Auler, A.S., Edwards, L., Cheng, H., Ito, E., Solheid, M. 2006. Interhemispheric anti-phasing of rainfall during the last glacial period. *Quaternary Science Reviews*, **25**, 3391-3403.

Wanner, H., Beer, J., Butikofer, J., Crowley, T.J., Cubasch, U., Fluckiger, J., Goosse, H., Grosjean, M., Joos, F., Kaplan, J.O., Kuttel, M., Muller, S.A., Prentice, C., Solomina, O., Stocker, T.F., Tarasov, P., Wagner, M and Widmann, M. 2008. Mid- to Late Holocene climate change: an overview. *Quaternary Science Reviews*, **27**, 1791-1828.

Watts, W.A. 1977. The Late Devensian vegetation of Ireland. *Philosophical Transactions of the Royal Society of London B*, **280**, 273-293

Watts, W.A. 1980. Regional variation in the response of vegetation to Lateglacial climatic events in Europe. *In:* Lowe, J., Gray, J and Robinson, J.E (eds.), Studies in the Late Glacial of North–West Europe. Oxford: Pergamon Press, 1-21 pp.

Weaver, A.J., Saenko, O.A., Clark, P.U and Mitrovica, J.X. 2003. Meltwater pulse 1a from Antarctica as a trigger of the Bølling–Allerød warm interval. *Science*, **299**, 1709-1713.

Weltje, G.J and Tjallingii, R. 2008. Calibration of XRF core scanners for quantitative geochemical logging of sediment cores: Theory and application. *Earth and Planetary Science Letters*, **274**, 423-438.

West, G., Kaufman, D.S., Muschitiello, F., Forwick, M., Matthiessen, J., Wollenburg, J and O'Regan, M. 2019. Amino acid racemization in Quaternary foraminifera from the Yermak Plateau, Arctic Ocean. *Geochronology*, **1**, 53-67.

Williams, J.W., Blois, J.L and Shuman, B.N. 2011. Extrinsic and intrinsic forcing of abrupt ecological change: case studies from the late Quaternary. *Journal of Ecology*, **99**, 664-677.

Wittmer, M.H.O.M., Auerswald, K., Tungalag, R., Bai, Y.F., Schäufele, R and Schnyder, H. 2008. Carbon isotope discrimination of C_3 vegetation in Central Asian grassland as related to long-term and short-term precipitation patterns. *Biogeosciences*, **5**, 913-924.

Wohlfarth, B., Luoto, T.P., Muschitiello, F., Väliranta, M., Björck, S., Davies, S.M., Kylander, M., Ljung, K., Reimer, P.J and Smittenberg, R.H. 2018. Climate and environment in southwest Sweden 15.5–11.3 cal. ka BP. *Boreas*, **47**, 687-710.

Wolff, E.W., Chappellaz, J., Blunier, T., Rasmussen, S.O., Svensson, A. 2010. Millennial-scale variability during the last glacial: The ice core record. *Quaternary Science Reviews*, **29**, 2828-2838.

Wolf, D., Kolb, T., Alcaraz-Castaño, M., Heinrich, S., Baumgart, P., Calvo, R., Sánchez, J., Ryborz, K., Schäfer, I., Bliedtner, M., Zech, R., Zöller, L and Faust, D. 2018. Climate deteriorations and Neanderthal demise in interior Iberia. *Scientific Reports*, **8**, 1-10.

Wolf, D., Ryborz, K., Kolb, T., Zapata, R.C., Vizcaino, J.S., Zöller, L and Faust, D. 2019. Origins and genesis of loess deposits in central Spain, as indicated by heavy mineral compositions and grain-size variability. *Sedimentology*, **66**, 1139-1161.

Wright, D. G and Stocker, T. F. 1991. A zonally averaged ocean model for the thermohaline circulation. Part I: Model development and flow dynamics. *Journal of Physical Oceanography*, **21**, 1713-1724.

Wu, M.S., Feakins, S.K., Martin, R.E., Shenkin, A., Bentley, L.P., Bloner, B., Salinas, N., Asner, G.P and Malhi, Y. 2017. Altitude effect on leaf wax carbon isotopic composition in humid tropical forests. *Geochimica et Cosmochimica Acta*, **206**, 1-17.

Xia, Z-H., Xu, B-Q., Mügler, I., Wu, G-J., Gleixner, G., Sachse, D., Zhy, L-P. 2008. Hydrogen isotope ratios of terrigenous *n*-alkanes in lacustrine surface sediment of the Tibetan Plateau record the precipitation signal. *Geochemical Journal*, **42**, 331-338.

Xu, Q., Li, Y., Yang, X and Zheng, Z. 2007. Quantitative relationship between pollen and vegetation in northern China. *Science in China Series D: Earth Sciences*, **50**, 582-599.

Xu, Q. Zhang, S., Gaillard, M-J., Li, M., Cao, X.Y., Tian, F and Li, F. 2016. Studies of modern pollen assemblages for pollen dispersal- deposition-preservation process understanding and for pollen- based reconstructions of past vegetation, climate, and human impact: a review based on case studies in China. *Quaternary Science Reviews*, **149**, 151–166.

Yamada, K and Ishiwatari, R. 1999. Carbon isotopic compositions of long-chain n-alkanes in the Japan Sea sediments: implications for paleoenvironmental changes over the past 85 kyr. *Organic Geochemistry*, **30**, 367-377.

Yokoyama, Y., Lambeck, K., De Deckker, P., Johnston, P and Fifield, L.K. 2000. Timing of the Last Glacial Maximum from observed sea-level minima. *Nature*, **405**, 713-716.

Zech, M., Buggle, B., Leiber, K., Marković, S., Glaser, B., Hambach, U., Huwe, B., Stevens, T., Sümegi, P., Wiesenberg, G and Zöller, L. 2010. Reconstructing Quaternary vegetation history in the Carpathian Basin, SE-Europe, using *n*-alkane biomarkers as molecular fossils: Problems and possible solutions, potential and limitations. *E&G Quaternary Science Journal*, **58**, 148–155.

Zech, M., Rass, S., Buggle, B., Löscher, M and Zöller, L. 2012. Reconstruction of the late Quaternary paleoenvironments of the Nussloch loess paleosol sequence, Germany, using *n*-alkane biomarkers. *Quaternary Research*, **78**, 226-235.

Zeisler-Diehl, V.V., Barthlott, W and Schreiber, L. 2018. Plant cuticular waxes: composition, function, and interactions with microorganisms. *Journal of Experimental Botany*, **68**, 5281–5291.

Zeisler, V and Schreiber, L. 2016. Epicuticular wax on cherry laurel (*Prunus laurocerasus*) leaves does not constitute the cuticular transpiration barrier. *Planta*, **243**, 65–81.

Zhang, X., Knorr, G., Lohmann, G and Barker, S. 2017. Abrupt North Atlantic circulation changes in response to gradual CO_2 forcing in a glacial climate state. *Nature Geoscience*, **10**, 518-524.

Zhao, M., Eglinton, G., Haslett, S.K., Jordan, R.W., Sarnthein, M and Zhang, Z. 2000. Marine and terrestrial biomarker records for the last 35,000years at ODP site 658C off NW Africa. *Organic Geochemistry*, **31**, 919-930.

Zhu, Y., Xie, Y., Cheng, B., Chen, F and Zhang, J. 2003. Pollen transport in the Shiyang River drainage, arid China. *Chinese Science Bulletin*, **48**, 1499 1506.

Zielhofer, C., Fletcher, W.J., Mischke, S., De Batist, M., Campbell, J.F.E., Joannin, S., Tjallinggii, R., El Amouti, N., Junginger, A., Stele, A., Bussmann, J., Schneider, B., Lauer, T., Spitzer, K., Strupler, M., Brachert, T and Mikdad, A. 2017. Atlantic forcing of Western Mediterranean winter rain minima during the last 12,000 years. *Quaternary Science Reviews*, **157**, 29-51.

Zielhofer, C., Köhler, A., Mischke, S., Benkaddour, A., Mikdad, A and Fletcher, W.J. 2018. Western Mediterranean hydro-climatic consequences of Holocene iceberg advances (Bond events). *Climate of the Past*, **15**, 463–475.

Appendices

Appendix 1: Reworked calcareous nannofossils (%).

Appendix 2: Pollen percentages (%) of main taxa groups from core SHAK06-5K.

Appendix 3: Pollen percentages (%) of main taxa groups from core MD01-2444.

Appendix 4: Pollen concentration (grains g^{-1}) and mass accumulation rate (grains cm^{-2} kyr^{-1}) of SHAK06-5K samples.

Appendix 5: Pollen concentration (grains g^{-1}) in samples from MD01-2444.

Appendix 6: For the small sediment aliquots from SHAK06-5K the peak areas and concentrations (ng g^{-1}) of odd homologues C_{25}-C_{35} for each sample.

Appendix 7: For the small sediment aliquots from SHAK06-5K, the peak areas and concentrations (ng g^{-1}) of even homologues C_{26}-C_{34} for each sample.

Appendix 8: For the large sediment aliquots from SHAK06-5K the peak areas and concentrations (ng g^{-1}) of odd homologues C_{25}-C_{35} for each sample.

Appendix 9: For the large sediment aliquots from SHAK06-5K, the peak areas and concentrations (ng g^{-1}) of even homologues C_{26}-C_{34} for each sample.

Appendix 10: The *n*-alkane recovery rate (%) of the zeolite cleaning method.

Appendix 11: The recovery rate (%) of the urea adduction cleaning method.

Appendix 12: For SHAK06-5K samples, the mean $\delta^{13}C_{n\text{-alkane}}$ values of the multiple runs for each homologue, showing the standard deviation (± 1σ) of the duplicate/triplicate runs.

Appendix 13: Sediment accumulation rate (cm kyr^{-1}) in cores SHAK06-5K and MD01-2444.

Appendix 14: For the modern leaf samples, the concentrations (ng g^{-1}) of odd homologues.

Appendix 15: For the modern leaf samples, the concentrations (ng g^{-1}) of even homologues.

Appendix 16: For the modern leaf samples, the mean $\delta^{13}C_{n\text{-alkane}}$ values of the multiple runs for each homologue, showing the standard deviation (± 1σ) of these duplicate/triplicate runs.

Appendix 17: Value assigned to each species (1-5) for both drought tolerance and heat resistance. 1 represents the most tolerant, 5 represents the least tolerant. Values used in PCA.

Appendix 18: Bulk density (g cm^{-3}) of SHAK06-5K samples.

Appendix 19: *n*-Alkane concentration (grains g^{-1}) and mass accumulation rate (grains cm^{-2} kyr^{-1}) of SHAK06-5K samples.

Depth (cm)	Age (cal yrs BP)	Reworked (%)
0	414	2.3
2	503	1.5
4	591	0.4
5	628	0.7
8	740	1.6
10	815	0.8
12	908	1.3
14	1001	1
16	1123	1.8
18	1245	3.4
22	1478	2.5
24	1588	1
26	1699	1.8
28	1809	0.8
30	1920	1.5
32	2112	1.7
34	2304	1.8
36	2495	0.6
38	2687	1
40	2879	2
42	3197	0.6
44	3514	0
46	3608	1.1
48	3702	0.3
52	5014	0.3
54	5670	1.8
56	6421	0.6
58	7172	2.2
62	8219	0.4
64	8515	0.9
66	8812	1.9
68	9108	1.3
70	9404	0.5
72	9911	0.2
74	10418	0.8
76	10925	1.2
78	11472	1.1
82	12566	2.5
86	12740	1.8

88	12826	3
90	12913	4.5
92	13034	3.6
94	13155	4.3
96	13275	1.1
98	13396	0.7
100	13517	3.3
102	13595	1.1
106	13752	3.1
108	13831	1.1
112	14182	2.8
114	14456	3.4
116	14729	1.9
118	15003	3.9
120	15276	6.6
122	15396	5.2
124	15516	6.7
126	15635	7.2
128	15755	5
130	15875	9
132	16004	5.9
134	16134	4.5
136	16263	9.3
138	16393	13
140	16522	15.7
142	16636	9.4
144	16750	19
146	16864	10.9
148	17085	8.9
150	17306	9.9
152	17527	13.8
154	17581	6
156	17635	16.7
158	17688	10.6
160	17742	7.7
162	17822	9.3
164	17901	12.4
166	17981	12.5
168	18060	8.9
170	18140	3.1
172	18219	9.1
174	18362	6.3
176	18505	5
178	18648	4.4

180	18791	4.2
182	18897	3
184	19004	2.4
186	19110	8.2
188	19217	3.1
190	19323	3.8
192	19429	2.4
194	19536	5.5
196	19642	4
198	19816	6.8
200	19989	6.2
202	20061	7.9
204	20132	5.3
206	20204	4.7
208	20275	5.9
222	20923	5.7
246	22630	4.8

Appendix 1: Reworked calcareous nannofossils (Magill et al., 2019).

Sample depth	Steppe	Ericaceae	Pioneer	Mediterranean	Eurosiberian	Temperate	AP	Pinus
0	7	11	4	10	10	19	23	55
2	10	4	1	12	12	24	25	39
4	7	11	3	9	12	20	23	20
5	12	11	2	7	8	15	17	13
8	10	19	4	8	13	21	25	17
12	7	14	1	7	10	16	17	20
14	19	12	1	7	4	12	13	14
16	13	12	4	10	12	22	26	15
18	12	14	4	5	13	18	22	13
20	11	10	5	6	17	22	27	9
22	14	16	2	7	11	17	19	6
24	11	15	4	6	11	18	21	14
26	17	19	2	6	15	21	23	10
30	12	11	3	6	13	19	22	14
32	16	14	2	5	12	17	19	21
34	17	10	1	9	13	22	23	10
36	16	19	2	7	12	18	20	13
38	13	9	2	5	15	21	23	13
40	12	16	2	5	14	19	21	15
42	12	18	3	7	10	17	20	21

44	15	17	5	6	9	15	19	25
46	12	25	2	4	9	13	15	32
47	12	16	3	3	10	14	17	16
48	14	15	5	4	14	18	24	16
49	19	19	5	4	10	14	20	16
51	10	13	4	8	12	20	24	16
52	9	21	1	12	9	21	22	34
53	9	10	4	8	14	22	26	18
54	12	12	4	7	15	22	26	21
55	15	15	8	4	15	19	27	18
56	10	12	7	4	18	22	29	30
57	10	13	4	9	25	33	38	22
58	10	16	4	7	23	31	35	30
59	10	13	5	8	25	33	38	24
62	5	9	8	15	41	57	65	63
63	15	8	0	11	49	60	60	66
64	15	5	5	4	47	51	56	65
66	12	5	1	8	54	62	63	56
68	11	2	5	17	47	64	68	69
72	9	3	6	14	48	61	67	49
74	10	2	6	17	42	58	64	64
76	15	4	7	12	41	53	60	70
78	17	4	10	9	38	47	56	65
80	27	4	6	5	35	40	46	73
81	29	6	6	5	28	33	39	74
83	39	2	4	8	30	37	41	75
84	40	3	7	8	25	33	40	74
85	45	4	3	6	17	24	27	75
86	32	5	5	9	27	36	41	76
88	37	4	6	8	24	33	39	76
90	32	5	5	7	24	30	35	71
92	28	3	5	9	25	34	39	75
94	52	5	5	4	8	12	17	77
96	30	3	8	9	23	33	41	83
98	24	2	9	10	22	32	41	75
102	24	1	6	9	28	37	43	71
104	23	10	9	10	25	35	44	79
106	10	8	8	14	33	47	54	83
108	18	4	10	10	30	40	50	71
112	14	4	9	11	30	42	50	68
114	17	7	9	14	24	38	47	73
116	14	8	9	8	27	36	45	82
118	19	8	3	11	18	30	33	84
120	14	10	6	12	18	29	35	69
122	46	4	13	2	8	10	23	93

124	30	6	4	11	26	37	41	72
126	22	10	4	11	22	33	37	80
128	29	6	7	6	18	24	30	84
130	30	12	7	8	18	26	33	87
132	46	3	13	2	10	12	25	92
134	52	1	8	2	9	11	19	92
136	55	2	5	4	6	11	16	89
138	50	3	9	4	8	12	20	90
142	57	4	7	0	4	4	11	92
144	68	1	8	0	6	6	14	91
146	59	5	4	0	6	6	9	93
148	66	0	4	1	1	2	6	92
150	47	7	10	3	9	12	22	94
154	44	2	13	2	5	7	20	91
156	53	2	10	1	6	7	17	90
158	55	4	6	0	5	5	11	93
160	60	3	8	1	5	6	14	89
161	54	2	4	2	8	10	13	87
162	27	11	17	3	16	19	36	83
164	48	4	12	3	8	11	23	85
166	38	10	9	3	3	6	15	90
168	40	11	6	3	4	7	13	89
170	47	8	4	1	5	6	10	79
174	37	10	5	2	4	6	11	78
176	45	14	6	0	5	5	11	84
178	38	6	8	3	8	11	19	88
180	37	10	7	6	5	11	19	82
182	45	10	3	5	5	10	13	51
184	39	11	7	7	4	11	18	86
186	36	8	10	3	11	14	25	73
188	27	14	11	5	17	22	33	81
190	38	14	7	5	13	18	25	84
192	29	15	13	4	10	14	27	81
194	45	7	17	1	8	9	26	79
196	35	10	12	1	9	10	21	74
198	38	10	12	4	6	10	22	84
200	39	13	14	3	6	9	23	83
202	28	28	4	0	6	6	10	90
204	34	12	10	3	9	12	22	87
206	49	14	6	0	4	4	10	80
208	43	12	13	1	3	4	17	73
212	39	15	6	1	10	11	17	77
214	44	19	6	3	4	7	12	75
216	34	17	7	0	7	7	14	87
218	41	11	13	2	4	6	18	84

220	36	16	13	3	5	8	20	77
222	47	16	12	3	4	7	18	75
224	39	19	10	1	1	2	12	76
226	41	21	6	1	5	6	11	76
228	50	11	6	3	5	8	13	72
230	42	13	17	2	3	5	22	76
232	46	15	9	4	2	6	14	66
234	41	12	9	2	6	8	17	75
236	44	16	6	1	4	5	11	78
238	45	19	7	0	4	4	10	66
240	43	17	9	1	4	5	14	66
242	42	15	10	1	7	8	17	74
244	50	16	6	1	4	5	10	67
246	46	18	6	1	1	2	8	64
248	42	21	9	3	0	3	13	73
250	49	16	5	1	5	6	11	74
252	52	19	0	0	6	6	6	74
254	40	10	7	2	4	6	13	66
256	37	11	8	3	6	9	17	71
258	47	11	4	2	2	4	8	66
260	54	19	3	0	2	2	5	70
262	38	14	9	2	2	4	13	64
264	42	17	6	2	5	7	13	64
266	42	13	9	2	4	6	15	56
268	41	17	9	3	2	5	14	62
270	43	14	7	2	5	7	14	68
274	44	15	3	1	6	7	10	65
276	48	9	10	1	4	5	15	58
278	48	14	8	3	2	5	13	68
280	51	12	8	0	3	3	11	71
282	57	5	6	1	3	4	11	64
284	58	5	6	0	1	1	7	61
286	60	5	1	2	1	3	4	55
288	48	10	6	3	6	8	15	53
290	52	10	6	2	4	6	12	72
292	53	13	11	0	6	6	16	53
294	51	12	10	2	3	5	15	75
296	50	5	6	2	3	4	11	71
298	57	11	5	1	4	5	10	70
300	47	10	9	1	6	7	16	75
301	48	8	5	1	11	12	17	70
304	32	3	5	10	16	26	31	77
306	39	9	7	4	8	12	19	63
308	46	10	13	2	3	5	18	63
310	40	15	8	3	4	7	15	77

312	33	19	11	5	7	11	22	66
314	49	12	10	2	7	10	19	79
316	40	13	10	3	4	7	17	69
318	39	14	9	2	10	12	20	69
320	38	14	7	3	9	12	19	75
322	44	10	8	7	6	13	21	65
324	34	10	11	2	8	10	21	68
326	47	13	11	1	4	5	16	75
328	44	10	6	2	6	8	14	71
329	35	18	10	3	6	9	18	79

Appendix 2: Pollen percentages (%) of main taxa groups from core SHAK06-5K.

Sample depth	Steppe	Ericaceae	Pioneer	Mediterranean	Eurosiberian	Temperate	AP	Pinus
121	21	17	2	5	18	23	25	34
124	14	22	1	3	22	26	27	38
133	16	14	2	4	24	28	30	37
145	11	8	2	10	50	59	61	56
148	7	4	2	7	64	71	73	63
151	10	8	0	6	67	73	73	76
154	11	4	1	4	54	58	59	48
157	8	6	0	6	52	58	58	45
160	11	6	3	6	50	56	59	49
161	11	10	3	8	49	58	61	67
163	9	7	1	5	36	41	42	56
164	10	13	5	6	46	51	56	74
166	10	4	0	8	56	64	64	36
169	9	7	1	11	51	62	63	55
172	15	3	0	9	53	62	62	56
175	9	5	1	7	50	57	58	57
178	11	1	4	4	63	67	71	58
181	9	2	1	7	67	74	75	66
184	10	3	1	11	53	64	65	50
187	9	4	1	9	53	62	63	67
190	14	2	0	9	59	68	68	55
193	7	4	2	11	58	69	71	57
196	9	7	2	8	56	64	66	45
199	5	7	0	9	62	71	71	55
202	7	7	3	10	53	63	66	49
205	15	7	2	9	44	52	54	55

208	10	6	4	15	44	59	63	57
211	7	2	1	16	57	73	74	57
214	8	4	2	12	51	63	65	65
217	13	8	1	13	42	55	56	75
220	19	1	0	11	51	62	62	67
223	13	5	0	11	59	70	70	70
226	22	13	2	8	19	26	28	79
229	28	3	6	10	23	33	38	84
232	17	7	1	8	35	43	44	78
235	19	4	2	8	29	37	39	83
238	23	4	6	8	19	28	33	79

Appendix 3: Pollen percentages (%) of main taxa groups from core MD01-2444.

Depth	Pollen grains counted	Exotic grains counted	Total exotic grains	Sediment (g)	Total pollen concentration (grains g^{-1})	Bulk density (g cm^{-3})	SAR (cm kyr^{-1})	Mass flux total pollen (grains cm^{-2} kyr^{-1})
0	94	328	9666	6.145	451	0.84	22.40	8494
2	101	478	9666	6.114	334	0.82	22.50	6187
4	103	311	9666	6.112	524	0.81	24.20	10204
5	98	172	9666	6.104	902	0.80	24.90	17886
8	101	214	9666	6.208	735	0.77	25.70	14524
12	105	460	9666	6.075	363	0.85	23.30	7204
14	95	397	9666	6.658	347	0.89	19.20	5953
16	100	206	9666	6.136	765	0.93	17.30	12349
18	104	300	9666	6.081	551	0.86	16.60	7832
20	107	144	9666	6.344	1132	0.88	17.20	17135
22	104	186	9666	6.104	885	0.90	18.10	14484
24	108	286	9666	6.119	596	0.87	18.30	9514
26	102	235	9666	6.090	689	0.84	18.30	10582
30	101	277	9666	6.264	563	0.77	13.10	5707
32	99	204	9666	6.142	764	0.61	10.80	5058
34	105	380	9666	5.230	511	0.81	10.20	4232
36	103	243	9666	6.098	672	1.04	10.20	7103
38	97	228	9666	6.116	672	0.75	9.77	4932
40	98	407	9666	6.300	369	0.88	8.03	2617
42	99	653	9666	6.108	240	1.01	6.63	1613
44	103	335	9666	6.122	485	1.05	9.88	5013
46	92	737	9666	6.026	200	0.89	19.30	3441
47	96	372	9666	6.234	400	0.91	12.30	4470
48	92	352	9666	6.316	400	0.93	5.26	1949
49	91	325	9666	6.403	423	0.94	4.52	1803

51	101	440	9666	6.194	358	0.98	3.04	1067
52	81	473	9666	6.103	271	1.00	3.51	949
53	99	602	9666	6.431	247	0.96	3.99	948
54	92	567	9666	6.264	250	0.93	4.46	1034
55	99	563	9666	6.380	266	0.95	3.48	884
56	89	1045	9666	6.178	133	0.98	2.80	366
57	93	477	9666	6.356	296	1.11	2.20	722
58	94	623	9666	6.162	237	1.23	2.58	753
59	100	528	9666	6.102	300	1.11	3.27	1085
62	99	618	9666	6.197	250	0.72	13.10	2372
63	72	290	9666	6.413	374	0.69	10.60	2750
64	98	568	9666	6.880	242	0.66	8.32	1335
66	87	473	9666	6.147	289	0.88	4.57	1169
68	107	692	9666	6.149	243	0.89	5.07	1097
72	103	234	9666	6.232	683	0.76	3.28	1713
74	101	76	9666	6.118	2100	0.70	6.18	9110
76	104	240	9666	6.183	677	0.76	4.92	2545
78	101	102	9666	6.132	1561	0.57	4.28	3841
80	100	77	9666	6.090	2061	0.65	4.79	6392
81	101	68	9666	4.681	3067	0.68	5.63	11805
83	105	86	9666	4.675	2525	0.76	11.90	22713
84	99	109	9666	6.080	1444	0.79	17.40	19903
85	93	75	9666	4.633	2587	0.83	17.40	37293
86	100	82	9666	6.307	1869	0.86	17.40	28118
88	98	90	9666	6.183	1702	0.88	17.40	26031
90	102	70	9666	6.388	2205	0.89	16.90	33280
92	97	88	9666	6.345	1679	0.91	16.50	25143

94	102	117	9666	6.428	1311	1.09	16.40	23382
96	95	6	9666	6.108	25058	1.04	16.40	425440
98	101	217	9666	6.396	703	0.86	16.90	10225
102	97	95	9666	6.148	1605	0.90	21.80	31393
104	101	203	9666	6.413	750	0.76	22.50	12803
106	101	247	9666	6.156	642	0.90	22.50	12959
108	105	89	9666	6.186	1844	1.00	20.40	37756
112	105	103	9666	6.223	1583	0.92	9.09	13223
114	96	109	9666	6.225	1368	0.81	8.32	9173
116	95	153	9666	6.099	984	0.84	8.32	6853
118	98	214	9666	6.431	688	1.02	8.96	6288
120	102	157	9666	6.333	992	0.97	11.50	11112
122	99	260	9666	6.120	601	0.93	17.40	9724
124	101	137	9666	6.352	1122	1.04	18.80	22011
126	100	94	9666	6.365	1615	1.07	18.80	32486
128	106	262	9666	6.328	618	1.18	18.50	13468
130	100	182	9666	6.367	834	1.13	17.30	16240
132	106	199	9666	6.185	832	1.07	16.20	14464
134	101	147	9666	6.145	1081	0.85	15.90	14658
136	94	96	9666	6.423	1474	1.10	15.90	25883
138	93	100	9666	6.257	1437	0.97	16.20	22615
142	84	85	9666	6.172	1548	0.89	18.30	25138
144	103	118	9666	6.207	1359	1.07	17.30	25098
146	107	284	9666	6.139	593	1.12	14.10	9363
148	84	97	9666	6.369	1314	0.71	12.20	11367
150	101	221	9666	6.161	717	0.80	13.10	7490
154	102	174	9666	6.161	920	0.97	35.00	31368

156	103	118	9666	6.054	1394	1.06	35.00	51858
158	100	140	9666	6.169	1119	1.01	35.00	39415
160	102	93	9666	6.361	1667	1.02	27.00	45971
161	105	78	9666	6.191	2102	1.03	25.30	54739
162	95	331	9666	6.156	451	1.04	23.60	11030
164	102	114	9666	6.117	1414	1.21	21.90	37344
166	102	430	9666	6.128	374	1.02	21.90	8339
168	103	4	9666	6.128	40619	1.04	21.90	921127
170	100	116	9666	6.310	1320	1.01	20.40	27178
174	104	96	9666	6.157	1701	0.96	14.40	23406
176	101	70	9666	6.118	2279	0.98	14.40	32039
178	98	171	9666	6.151	901	1.04	14.40	13452
180	97	119	9666	6.215	1268	0.95	16.00	19189
182	98	81	9666	7.006	1669	0.85	18.10	25828
184	99	153	9666	6.307	992	1.31	18.20	23642
186	106	94	9666	6.161	1769	0.96	18.20	30884
188	100	21	9666	6.111	7532	1.25	18.20	170828
190	100	56	9666	6.142	2810	1.16	18.20	59105
192	94	80	9666	6.188	1835	1.06	18.20	35574
194	106	124	9666	6.193	1334	1.06	18.20	25650
196	104	137	9666	5.997	1224	0.97	14.80	17642
198	101	177	9666	5.797	951	1.11	12.40	13052
200	104	106	9666	6.219	1525	1.17	17.10	30448
202	99	22	9666	6.154	7068	1.23	25.10	218025
204	100	95	9666	6.251	1628	0.83	27.10	36555
206	99	103	9666	6.137	1514	1.11	27.10	45428
208	104	87	9666	6.182	1869	1.08	27.40	55211

212	99	114	9666	6.179	1359	0.86	29.70	34626
214	105	84	9666	6.477	1866	1.32	30.00	73687
216	88	80	9666	6.178	1721	1.06	30.00	54552
218	104	23	9666	6.149	7108	1.27	26.80	242408
220	103	117	9666	6.338	1343	1.15	14.10	21694
222	103	91	9666	6.372	1717	1.02	10.20	17849
224	93	10	9666	6.144	14631	1.04	9.23	140134
226	105	90	9666	6.300	1790	0.92	9.23	15230
228	105	74	9666	6.261	2191	0.87	9.98	19009
230	102	77	9666	6.357	2014	0.88	13.00	23000
232	104	92	9666	4.676	2337	0.89	20.10	41682
234	100	117	9666	6.126	1349	0.78	21.80	22968
236	101	N/A	9666	6.114	N/A	0.95	21.80	N/A
238	107	152	9666	6.194	1099	0.90	21.10	20822
240	103	59	9666	6.279	2687	1.03	18.30	50511
242	104	217	9666	4.995	927	1.16	16.40	17581
244	105	116	9666	4.716	1855	1.11	15.90	32621
246	96	100	9666	6.266	1481	1.06	15.90	24864
248	87	72	9666	5.609	2082	1.01	15.90	33304
250	100	71	9666	6.211	2192	1.12	15.90	38928
252	100	180	9666	6.154	873	1.23	15.90	17039
254	97	108	9666	6.149	1412	1.33	15.90	29896
256	99	171	9666	6.138	912	0.98	15.90	14247
258	104	112	9666	6.147	1460	1.05	16.40	25169
260	100	81	9666	6.254	1908	1.06	18.40	37366
262	100	117	9666	6.218	1329	1.08	21.10	30211
264	102	71	9666	6.200	2240	1.11	21.80	54276

266	100	83	9666	6.274	1856	1.15	21.80	46355
268	98	65	9666	4.656	3130	1.07	22.00	73994
270	100	85	9666	6.302	1804	1.09	22.50	44335
274	109	99	9666	6.114	1741	1.16	23.20	46661
276	101	74	9666	6.056	2179	1.04	23.20	52816
278	101	165	9666	6.094	971	0.93	22.40	20327
280	102	82	9666	6.189	1943	1.00	19.40	37805
282	94	54	9666	6.421	2620	1.07	16.60	46608
284	99	143	9666	6.167	1085	1.14	15.90	19668
286	100	100	9666	5.867	1647	1.11	15.50	28386
288	108	125	9666	6.097	1370	0.90	14.80	18329
290	100	102	9666	6.326	1498	0.93	13.70	19183
292	104	129	9666	6.083	1281	0.97	12.60	15579
294	101	29	9666	6.202	5428	1.03	12.30	68893
296	113	76	9666	6.127	2346	1.08	12.30	31057
298	104	70	9666	5.991	2397	0.89	12.80	27416
300	99	70	9666	6.313	2165	0.86	14.80	27411
301	101	76	9666	6.244	2057	0.84	16.40	28214
304	101	103	9666	6.449	1470	0.78	18.80	21523
306	113	147	9666	6.080	1222	0.93	18.80	21361
308	104	132	9666	6.546	1163	1.08	18.70	23506
310	103	114	9666	6.226	1403	1.02	18.70	26670
312	107	160	9666	6.069	1065	0.95	18.50	18780
314	94	4	9666	6.162	36864	0.82	18.50	560801
316	98	78	9666	6.157	1972	1.07	18.50	39097
318	104	55	9666	6.399	2856	1.06	17.40	52849
320	102	76	9666	6.254	2074	1.03	13.10	28016

322	72	52	9666	6.235	2147	1.00	10.50	22511
324	105	134	9666	5.977	1267	1.02	10.10	13101
326	103	171	9666	6.199	939	1.05	10.10	9946
328	102	72	9666	6.314	2169	0.96	10.10	20991
329	103	155	9666	6.274	1024	0.91	10.10	9443

Appendix 4: Pollen concentration (grains g^{-1}) and mass accumulation rate (grains cm^{-2} kyr^{-1}) in samples from SHAK06-5K

Depth	Pollen grains counted	Exotic grains counted	Total exotic grains	Sediment (g)	Total concentration (grains g^{-1})
121	101	679	13911	6.448	321
124	90	161	13911	5.7313	1357
133	97	2300	13911	5.5774	105
145	101	1068	13911	6.2085	212
148	96	1482	13911	6.9195	130
151	101	764	13911	6.8428	269
154	99	627	13911	6.8735	320
157	101	1004	13911	6.6311	211
160	100	1464	13911	6.366	149
161	99	1311	13911	4.4733	235
163	98	1637	13911	7.2293	115
164	101	1699	13911	4.4189	187
166	103	452	13911	6.4068	495
169	100	643	13911	6.672	324
172	94	607	13911	6.9387	311
175	100	660	13911	5.9072	357
178	99	871	13911	5.024	315
181	100	793	13911	6.6308	265
184	100	565	13911	7.1121	346
187	101	931	13911	6.9275	218
190	100	997	13911	7.8653	177
193	100	1194	13911	6.8802	169
196	100	1289	13911	7.7168	140
199	102	522	13911	5.3227	511
202	98	693	13911	7.1735	274
205	101	792	13911	7.0146	253
208	80	1725	13911	4.6661	138
211	102	732	13911	6.7343	288
214	102	977	13911	5.5182	263
217	100	1500	13911	5.7548	161
220	102	525	13911	6.4061	422
223	102	1142	13911	6.2019	200
226	106	932	13911	5.9294	267
229	104	316	13911	4.9221	930
232	103	381	13911	5.405	696
235	103	184	13911	8.274	941
238	109	265	13911	6.0561	945

Appendix 5: Pollen concentration (grains g^{-1}) in samples from MD01-2444.

Depth (cm)	Dry weight (g)	GC-FID	Standard injection (µl)	Solvent in vial (µl)	Sample injection (µl)	Peak area of homologue						Total *n*-alkane concentration in dry sediment (ng g^{-1})					
						C_{25}	C_{27}	C_{29}	C_{31}	C_{33}	C_{35}	C_{25}	C_{27}	C_{29}	C_{31}	C_{33}	C_{35}
0	2.40	1	2	50	5	20.30	42.40	110.00	130.60	72.70	57.30	9.44	19.71	51.13	60.71	33.79	26.64
2	3.20	1	2	25	5	1.90	18.00	22.80	22.10	33.20	5.50	0.61	5.76	7.30	7.07	10.62	1.76
4	1.20	2	2	50	5	LR	LR	LR	LR	LR	LR	LR	LR	LR	LR	LR	LR
5	2.22	2	1	100	5	17.70	33.40	76.70	90.90	36.50	12.50	10.40	19.63	45.08	53.43	21.45	7.35
8	2.45	1	2	25	5	7.50	19.00	41.60	51.20	26.50	15.30	3.14	7.96	17.42	21.44	11.10	6.41
10	2.85	1	2	50	5	1.30	6.20	14.90	18.50	7.50	2.30	0.47	2.23	5.36	6.66	2.70	0.83
12	2.26	1	1	100	5	16.70	22.70	84.50	97.30	57.20	34.50	5.62	7.64	28.44	32.74	19.25	11.61
14	1.30	2	1	100	5	27.90	47.40	119.10	148.20	49.50	11.20	28.00	47.58	119.54	148.75	49.68	11.24
16	1.25	1	1	100	5	11.90	21.70	48.70	55.60	31.00	15.70	8.67	15.82	35.50	40.53	22.60	11.45
18	2.34	1	1	100	5	15.40	25.30	68.80	82.60	28.80	8.90	5.60	9.21	25.03	30.05	10.48	3.24
20	2.76	1	2	50	5	5.50	14.90	29.40	35.30	18.90	9.70	2.22	6.02	11.88	14.27	7.64	3.92
22	2.37	2	1	100	5	30.40	38.60	94.40	115.00	46.70	16.30	16.77	21.30	52.08	63.45	25.77	8.99
24	1.20	1	1	100	1	4.70	11.60	25.10	31.70	11.30	2.80	16.95	41.84	90.54	114.35	40.76	10.10
26	1.25	1	2	50	5	4.70	13.00	34.60	44.10	14.50	3.00	3.85	10.65	28.34	36.12	11.88	2.46
28	2.37	2	3	100	5	17.30	31.60	61.60	65.60	21.10	4.50	8.37	15.28	29.79	31.73	10.20	2.18
30	2.55	1	2	100	5	5.60	12.80	25.30	26.50	12.80	4.40	2.00	4.56	9.02	9.45	4.56	1.57
32	2.22	2	2	50	5	23.30	38.60	78.90	96.40	34.50	10.80	13.66	22.63	46.25	56.51	20.22	6.33
34	2.45	1	1	100	5	16.90	46.40	110.40	130.80	52.50	13.20	5.26	14.43	34.34	40.69	16.33	4.11
36	1.25	1	1	100	5	9.10	18.40	43.30	51.50	19.10	8.60	6.63	13.41	31.57	37.54	13.92	6.27
38	2.29	1	1	100	5	13.10	30.70	77.40	93.20	37.90	11.20	4.87	11.41	28.78	34.65	14.09	4.16
40	2.74	1	2	50	5	6.50	11.90	24.60	29.10	19.70	7.00	2.65	4.85	10.03	11.87	8.04	2.86
42	2.52	2	3	100	5	26.70	42.40	90.90	104.40	30.90	7.20	12.14	19.29	41.35	47.49	14.06	3.27
44	1.25	1	1	100	5	26.50	56.20	140.10	179.80	57.00	12.00	19.32	40.97	102.13	131.07	41.55	8.75
46	2.16	2	1	100	5	5.10	17.10	32.40	40.20	15.90	5.90	3.08	10.33	19.57	24.28	9.60	3.56
48	2.81	1	2	25	5	21.20	40.00	89.30	110.30	38.30	11.50	7.74	14.60	32.60	40.26	13.98	4.20
52	2.20	1	2	25	5	17.30	34.00	84.50	112.10	40.50	11.10	8.05	15.82	39.33	52.17	18.85	5.17
54	1.25	2	1	100	5	8.10	15.60	34.00	42.80	13.90	4.50	8.46	16.28	35.49	44.68	14.51	4.70

56	1.30	2	2	50	5	24.00	47.90	117.60	144.80	47.00	9.90	24.02	47.95	117.72	144.94	47.05	9.91
58	2.49	1	2	50	5	1.70	7.80	17.40	23.40	8.80	2.80	0.70	3.21	7.15	9.62	3.62	1.15
60	2.67	1	2	25	5	11.74	24.17	28.34	35.20	10.52	15.58	2.82	5.81	6.82	8.47	2.53	3.75
62	2.50	1	1	100	5	5.90	19.80	41.80	50.10	21.60	10.50	1.79	6.02	12.72	15.24	6.57	3.19
64	1.20	2	1	100	5	LR	LR	LR	LR	LR	LR	LR	LR	LR	LR	LR	LR
66	2.34	1	2	100	5	8.60	20.50	44.90	52.20	18.90	5.00	3.34	7.97	17.45	20.28	7.34	1.94
68	2.49	1	2	50	5	12.20	30.60	75.90	94.40	33.40	7.00	5.47	13.71	34.01	42.30	14.96	3.14
70	2.78	2	2	25	5	11.30	23.60	42.30	49.50	20.90	7.00	3.00	6.27	11.23	13.15	5.55	1.86
72	1.25	1	1	100	5	22.60	55.10	131.60	160.60	56.40	12.50	16.48	40.17	95.93	117.08	41.11	9.11
74	1.25	2	2	50	5	LR	LR	LR	LR	LR	LR	LR	LR	LR	LR	LR	LR
76	2.28	1	1	100	5	5.70	16.50	38.80	43.50	16.60	7.10	1.91	5.52	12.97	14.54	5.55	2.37
78	2.48	1	2	100	5	11.30	31.30	62.50	58.00	21.10	6.40	4.15	11.50	22.96	21.31	7.75	2.35
80	1.30	2	2	50	5	97.70	89.70	149.40	122.20	114.30	59.00	97.80	89.79	149.55	122.32	114.41	59.06
82	2.70	1	2	50	5	5.40	15.10	23.40	21.20	8.80	6.40	2.05	5.73	8.87	8.04	3.34	2.43
84	1.58	2	1	100	5	2.20	12.40	21.40	22.00	10.40	4.10	1.82	10.24	17.67	18.17	8.59	3.39
86	2.80	1	1	100	5	35.70	68.30	120.20	109.60	50.20	26.00	9.71	18.58	32.71	29.82	13.66	7.07
88	1.20	1	2	50	5	6.50	17.90	28.80	26.90	12.20	6.00	6.04	16.64	26.78	25.01	11.34	5.58
90	2.70	1	2	50	5	8.20	18.50	32.90	30.60	13.40	8.90	3.11	7.02	12.48	11.60	5.08	3.37
92	5.11	2	2	50	5	87.40	203.50	374.20	365.80	128.60	34.10	22.26	51.82	95.29	93.15	32.75	8.68
94	4.77	1	1	100	1	4.50	14.60	27.50	25.40	13.90	5.00	4.08	13.25	24.95	23.05	12.61	4.54
96	1.25	1	2	25	5	3.00	17.70	37.10	41.10	13.70	3.20	2.46	14.50	30.39	33.66	11.22	2.62
98	5.07	2	1	100	5	13.40	33.20	71.70	78.90	33.00	7.70	3.45	8.55	18.47	20.33	8.50	1.98
100	2.98	2	2	50	5	8.60	14.20	22.80	22.50	13.90	7.90	3.76	6.20	9.96	9.83	6.07	3.45
102	1.15	1	1	100	5	16.00	57.50	125.10	126.70	45.70	11.90	10.58	38.03	82.73	83.79	30.22	7.87
104	1.30	2	4	25	5	9.70	27.80	37.10	35.70	15.20	5.10	8.20	23.52	31.38	30.20	12.86	4.31
106	4.74	1	1	100	5	16.20	41.40	85.80	92.00	38.20	13.90	3.11	7.96	16.49	17.69	7.34	2.67
108	2.26	1	1	100	5	15.70	34.10	70.10	72.00	31.00	11.10	5.28	11.48	23.59	24.23	10.43	3.74
110	2.91	1	2	50	5	5.10	12.90	26.10	25.50	11.00	4.60	1.96	4.95	10.01	9.78	4.22	1.76
112	4.59	1	2	100	5	18.90	50.90	113.00	131.50	67.40	24.10	3.75	10.09	22.41	26.08	13.37	4.78
114	4.93	1	1	100	1	8.30	24.80	50.60	54.60	27.00	8.80	7.29	21.80	44.47	47.99	23.73	7.73
116	1.30	1	1	100	5	17.00	39.80	71.70	64.60	27.90	9.90	9.95	23.28	41.95	37.79	16.32	5.79
118	1.30	2	2	25	5	10.40	22.00	37.00	33.40	14.80	5.20	5.90	12.47	20.98	18.93	8.39	2.95

120	2.83	2	2	50	5	5.70	13.70	24.50	24.90	11.50	4.40	2.62	6.30	11.27	11.45	5.29	2.02
122	1.15	1	2	25	5	1.00	5.00	6.90	6.30	3.30	LR	0.89	4.45	6.14	5.61	2.94	LR
124	1.15	1	2	50	5	12.10	26.80	49.30	44.40	16.60	5.80	11.74	26.00	47.83	43.07	16.10	5.63
126	1.20	2	4	25	5	7.00	18.30	28.90	24.80	10.80	3.30	6.41	16.77	26.48	22.73	9.90	3.02
128	4.69	1	1	100	5	24.00	78.20	171.90	180.60	107.80	31.50	4.66	15.19	33.40	35.09	20.94	6.12
130	2.97	1	2	50	5	5.90	16.50	30.20	28.30	13.00	3.50	2.03	5.69	10.41	9.76	4.48	1.21
132	2.98	1	2	25	5	34.33	110.49	212.51	182.28	85.99	23.61	7.41	23.85	45.87	39.34	18.56	5.10
134	4.79	2	1	100	5	32.90	91.70	171.60	155.00	68.70	14.80	8.96	24.98	46.74	42.22	18.71	4.03
136	1.10	1	2	100	5	13.60	43.90	71.80	51.60	28.50	5.90	11.24	36.29	59.35	42.66	23.56	4.88
138	5.14	1	1	100	5	38.40	60.10	60.80	34.40	12.10	19.70	5.69	8.90	9.00	5.09	1.79	2.92
140	2.72	2	1	100	5	18.30	41.50	60.30	40.50	18.00	3.60	8.78	19.91	28.93	19.43	8.63	1.73
142	1.05	1	1	100	5	7.90	23.80	39.40	31.70	11.90	3.30	6.86	20.65	34.19	27.51	10.33	2.86
144	1.25	2	2	50	5	33.00	82.60	137.70	117.40	50.50	12.20	34.35	85.99	143.35	122.22	52.57	12.70
146	4.85	1	1	100	1	4.40	12.70	21.40	21.40	12.10	3.90	3.93	11.33	19.10	19.10	10.80	3.48
148	1.10	1	2	50	5	5.30	14.90	23.80	23.40	10.80	3.30	4.93	13.87	22.15	21.78	10.05	3.07
150	1.05	1	2	50	5	75.20	214.40	337.90	250.60	52.90	81.20	79.90	227.80	359.02	266.26	56.21	86.28
152	2.98	2	1	100	5	14.10	17.60	24.00	17.30	11.50	6.90	6.18	7.72	10.53	7.59	5.04	3.03
154	4.71	1	1	100	5	23.90	56.30	103.60	100.90	62.00	44.50	4.63	10.90	20.06	19.54	12.01	8.62
156	5.11	2	2	25	5	14.20	18.90	20.00	16.90	8.10	3.60	2.05	2.73	2.88	2.44	1.17	0.52
158	4.45	1	1	100	5	80.30	25.70	101.40	78.30	50.30	35.70	13.72	4.39	17.33	13.38	8.60	6.10
160	2.95	1	1	100	5	119.30	315.30	586.60	536.20	228.10	60.20	36.91	97.56	181.50	165.91	70.58	18.63
162	1.15	1	1	100	5	5.20	16.30	26.00	18.10	6.20	2.10	3.85	12.07	19.25	13.40	4.59	1.55
164	1.20	1	2	50	5	4.70	18.50	32.70	30.40	13.60	3.60	4.37	17.20	30.40	28.26	12.64	3.35
166	5.18	1	2	100	5	5.30	53.40	106.20	112.10	57.30	15.30	0.37	3.76	7.47	7.89	4.03	1.08
168	1.10	2	2	50	5	44.90	116.50	223.20	211.70	88.90	17.30	26.56	68.91	132.02	125.22	52.58	10.23
170	1.15	2	2	50	5	6.80	17.20	31.60	31.60	15.40	3.80	4.36	11.02	20.25	20.25	9.87	2.44
172	2.79	1	2	50	5	3.15	10.85	18.82	15.70	6.04	1.37	0.73	2.50	4.33	3.61	1.39	0.32
174	1.15	1	2	50	5	15.40	47.00	82.30	66.80	29.20	12.40	14.94	45.60	79.84	64.80	28.33	12.03
176	4.58	2	2	50	5	92.60	197.50	362.40	372.40	191.20	64.70	26.34	56.18	103.08	105.92	54.38	18.40
178	1.15	1	2	100	5	12.80	36.30	58.90	42.00	37.20	22.90	4.06	11.51	18.67	13.32	11.79	7.26
180	2.83	1	1	100	5	12.00	28.90	52.20	36.70	16.30	4.60	3.87	9.32	16.84	11.84	5.26	1.48
182	1.25	1	2	50	5	19.70	53.70	87.80	69.50	29.80	10.90	17.58	47.93	78.36	62.03	26.60	9.73

184	1.15	2	1	100	5	10.40	21.10	33.60	24.30	8.70	2.00	11.80	23.94	38.12	27.57	9.87	2.27
186	1.00	2	2	50	5	147.60	346.10	632.90	604.10	260.40	81.90	96.04	225.19	411.79	393.06	169.43	53.29
188	2.86	1	2	50	5	3.80	13.10	26.20	24.50	10.70	4.50	0.85	2.95	5.89	5.51	2.41	1.01
194	1.00	1	1	100	5	60.50	169.50	319.70	286.70	132.30	37.40	55.13	154.45	291.32	261.25	120.56	34.08
196	2.50	1	2	25	5	11.30	50.00	90.10	86.30	45.20	16.10	4.63	20.48	36.90	35.34	18.51	6.59
198	2.23	1	1	100	5	7.60	46.20	82.50	68.10	26.50	7.80	2.90	17.64	31.50	26.00	10.12	2.98
200	2.88	1	2	50	5	49.90	141.00	248.90	200.80	82.10	28.10	19.36	54.71	96.58	77.92	31.86	10.90
202	1.05	1	1	100	5	54.40	185.10	361.00	337.00	148.10	32.80	47.21	160.64	313.29	292.46	128.53	28.47
204	2.25	1	2	100	5	2.30	13.20	25.10	26.10	13.80	4.70	0.37	2.14	4.07	4.23	2.24	0.76
206	1.00	2	2	50	5	29.80	66.50	103.70	81.50	30.20	8.30	38.78	86.54	134.94	106.06	39.30	10.80
208	2.19	2	1	100	5	9.30	23.50	39.00	34.30	12.00	3.90	5.54	14.00	23.24	20.44	7.15	2.32
210	2.79	2	2	50	5	17.10	39.10	50.00	36.50	23.70	13.40	4.55	10.40	13.30	9.71	6.31	3.57
212	2.20	1	2	50	5	29.90	82.80	161.60	136.90	77.90	33.80	13.92	38.53	75.21	63.71	36.25	15.73
214	2.58	1	1	100	5	18.90	64.00	119.50	108.10	47.80	12.50	6.69	22.65	42.29	38.25	16.92	4.42
216	1.05	1	2	50	5	2.90	8.80	16.60	16.00	8.60	2.70	1.77	5.38	10.15	9.79	5.26	1.65
218	1.00	1	2	50	5	12.40	35.00	60.10	46.70	17.20	5.50	13.83	39.05	67.05	52.10	19.19	6.14
220	2.87	2	4	25	5	6.10	18.50	32.30	30.30	11.60	1.50	2.34	7.09	12.38	11.61	4.44	0.57
222	2.53	2	2	50	5	78.00	121.20	193.90	167.40	88.90	43.60	40.20	62.46	99.93	86.27	45.82	22.47
224	1.25	1	2	100	5	32.10	129.60	234.50	205.70	200.90	21.60	9.36	37.80	68.40	60.00	58.60	6.30
226	1.05	2	1	100	5	19.30	39.40	70.60	57.90	26.50	8.20	23.98	48.96	87.73	71.95	32.93	10.19
228	1.15	1	2	50	5	11.30	40.00	76.10	73.10	28.30	7.70	10.06	35.61	67.75	65.08	25.20	6.86
230	2.71	2	2	25	5	10.00	22.80	39.30	36.40	17.40	5.70	2.72	6.20	10.69	9.90	4.73	1.55
232	3.45	1	2	50	5	72.60	195.30	302.60	237.40	116.80	39.40	23.48	63.15	97.85	76.77	37.77	12.74
236	1.20	1	1	100	5	5.70	24.00	44.30	38.60	17.10	5.10	4.33	18.22	33.64	29.31	12.99	3.87
238	2.79	1	2	50	5	4.80	15.90	29.10	30.60	15.10	3.90	1.10	3.66	6.70	7.04	3.48	0.90
240	2.74	2	2	50	5	6.20	13.30	23.10	22.50	9.80	4.30	1.67	3.58	6.22	6.06	2.64	1.16
242	2.67	1	2	50	5	11.20	44.40	85.10	91.00	56.70	22.00	4.29	17.03	32.63	34.90	21.74	8.44
244	1.15	2	2	50	5	39.20	78.90	145.20	135.40	61.50	19.60	44.36	89.28	164.30	153.21	69.59	22.18
246	1.10	2	2	25	5	16.20	34.30	65.90	63.10	35.70	11.60	10.85	22.98	44.15	42.28	23.92	7.77
248	1.15	1	1	100	5	13.40	36.50	77.30	76.90	33.70	8.30	10.62	28.92	61.25	60.93	26.70	6.58
250	2.80	1	2	50	5	3.90	7.90	19.60	21.90	9.80	2.80	0.89	1.81	4.50	5.02	2.25	0.64
252	2.88	1	2	50	5	3.90	7.90	19.60	21.90	9.80	2.80	0.87	1.76	4.38	4.89	2.19	0.63

254	1.00	1	2	25	5	3.20	33.90	32.90	34.90	15.90	6.00	3.28	34.71	33.69	35.73	16.28	6.14
256	2.85	2	1	100	5	18.80	23.30	35.60	37.60	7.70	10.60	8.62	10.69	16.33	17.24	3.53	4.86
258	4.53	2	2	50	5	34.80	81.50	177.50	205.60	106.40	26.60	10.00	23.41	50.99	59.06	30.56	7.64
260	2.73	1	1	100	5	151.70	297.50	536.10	512.50	327.30	154.80	50.73	99.48	179.27	171.38	109.45	51.76
262	1.48	1	2	100	5	7.10	24.80	48.60	42.60	16.40	6.90	1.75	6.11	11.97	10.49	4.04	1.70
264	2.49	1	1	100	5	50.00	116.60	209.20	186.80	88.00	27.30	18.30	42.67	76.56	68.36	32.20	9.99
266	1.10	1	2	50	5	35.30	69.50	150.20	142.40	63.80	20.20	35.80	70.49	152.33	144.42	64.71	20.49
268	1.10	2	2	25	5	15.30	31.10	60.40	59.40	25.50	7.30	10.25	20.84	40.47	39.80	17.08	4.89
270	2.94	1	1	100	5	47.00	113.20	262.90	261.50	123.10	35.90	14.57	35.09	81.48	81.05	38.15	11.13
272	1.10	2	1	100	5	11.60	27.30	51.90	52.00	19.90	4.30	13.76	32.38	61.56	61.68	23.61	5.10
274	1.15	1	2	50	5	4.30	8.40	21.00	22.30	19.30	3.60	2.40	4.69	11.73	12.45	10.78	2.01
276	1.15	1	2	50	5	15.20	36.40	71.50	74.00	23.60	6.70	14.75	35.31	69.36	71.79	22.89	6.50
278	2.72	2	2	50	5	17.20	25.80	37.70	32.80	19.90	8.20	4.69	7.03	10.27	8.94	5.42	2.23
280	2.71	2	1	100	5	80.00	140.10	273.60	276.20	129.00	43.40	38.52	67.46	131.73	132.99	62.11	20.90
282	1.10	2	2	50	5	17.90	37.80	75.00	79.30	33.30	10.80	21.18	44.72	88.72	93.81	39.39	12.78
284	1.20	1	2	25	5	5.50	20.90	45.20	45.70	20.40	5.80	4.69	17.83	38.57	38.99	17.41	4.95
286	2.55	2	2	50	5	187.00	302.80	582.50	558.50	228.20	82.10	54.34	87.99	169.27	162.30	66.31	23.86
288	2.94	1	2	100	5	33.80	77.20	124.20	105.60	65.70	41.90	4.19	9.57	15.40	13.10	8.15	5.20
290	5.30	2	1	100	5	86.70	49.40	65.90	69.70	77.10	56.90	21.34	12.16	16.22	17.16	18.98	14.01
292	4.29	1	2	50	5	113.40	207.00	427.50	434.60	255.80	91.10	29.52	53.89	111.30	113.15	66.60	23.72
294	1.20	2	1	100	5	8.60	12.80	23.90	24.20	11.50	4.00	9.35	13.92	25.99	26.31	12.50	4.35
296	1.00	2	2	25	5	13.50	30.20	58.40	54.10	22.20	5.20	9.95	22.26	43.04	39.87	16.36	3.83
298	1.00	1	2	100	5	11.90	28.30	69.20	70.30	39.50	7.70	4.34	10.32	25.23	25.63	14.40	2.81
304	2.83	1	2	100	5	21.80	66.00	120.20	112.60	59.60	24.40	2.81	8.52	15.51	14.53	7.69	3.15
306	1.15	2	1	100	5	7.80	13.80	20.30	17.70	8.60	3.50	8.85	15.66	23.03	20.08	9.76	3.97
308	1.10	2	2	50	5	14.30	32.00	63.60	63.40	29.60	9.80	9.63	21.56	42.84	42.71	19.94	6.60
310	5.18	2	2	50	5	13.40	22.00	22.90	13.30	14.50	5.70	1.92	3.15	3.28	1.90	2.07	0.82
312	1.25	1	2	100	5	14.40	50.30	106.20	97.60	44.50	10.90	4.20	14.67	30.98	28.47	12.98	3.18
314	1.20	2	2	50	5	17.20	36.60	63.30	54.20	23.80	6.70	18.65	39.69	68.64	58.78	25.81	7.27
316	2.70	2	2	50	5	9.70	16.00	22.90	19.80	7.90	2.90	2.66	4.39	6.28	5.43	2.17	0.80
318	1.15	1	2	50	5	24.70	62.40	127.80	117.90	54.80	16.60	23.96	60.54	123.98	114.38	53.16	16.10
320	5.12	1	2	100	5	13.40	22.20	30.60	18.70	7.60	8.40	0.95	1.58	2.18	1.33	0.54	0.60

322	1.15	1	2	25	5	89.20	253.90	537.30	534.10	249.90	80.40	79.42	226.05	478.37	475.52	222.49	71.58
324	1.10	2	2	50	5	9.80	21.00	38.30	46.00	25.10	7.50	11.59	24.84	45.31	54.42	29.69	8.87
326	3.00	2	1	100	5	54.30	74.80	136.10	127.70	70.10	40.50	23.62	32.53	59.20	55.54	30.49	17.62
328	1.30	1	2	50	5	6.00	11.80	24.60	25.60	14.10	5.90	2.96	5.83	12.15	12.65	6.96	2.91
329	5.14	2	2	25	5	59.00	29.40	47.70	40.30	30.40	26.10	8.46	4.22	6.84	5.78	4.36	3.74

Appendix 6: For the small sediment aliquots from SHAK06-5K (n = 160), the dry sediment weight, standard injection (µl), solvent in vial (µl) for each sample, with the peak areas and concentrations (ng g^{-1}) of odd homologues C_{25}-C_{35} for each sample. 'LR' is where the detection limit measuring the retention time of long-chain homologues was reached.

Depth (cm)	Dry weight (g)	GC-FID	Standard injection (µl)	Solvent in vial (µl)	Sample injection (µl)	Peak area of homologue					Total *n*-alkane concentration in dry sediment (ng g^{-1})				
						C_{26}	C_{28}	C_{30}	C_{32}	C_{34}	C_{26}	C_{28}	C_{30}	C_{32}	C_{34}
0	2.40	1	2	50	5	9.60	16.00	27.00	25.20	32.90	4.46	7.44	12.55	11.71	16.10
2	3.20	1	2	25	5	1.40	2.00	5.70	1.30	0.99	0.45	0.64	1.82	0.42	0.34
4	1.20	2	2	50	5	LR	LR	LR	LR	LR	LR	LR	LR	LR	LR
5	2.22	2	1	100	5	10.30	12.40	10.70	7.20	3.20	6.05	7.29	6.29	4.23	6.53
8	2.45	1	2	25	5	2.30	3.60	6.00	6.40	3.90	0.96	1.51	2.51	2.68	1.75
10	2.85	1	2	50	5	1.20	3.70	3.10	1.80	LR	0.43	1.33	1.12	0.65	LR
12	2.26	1	1	100	5	13.00	8.50	19.50	10.60	4.20	4.37	2.86	6.56	3.57	1.49
14	1.30	2	1	100	5	12.70	14.80	15.40	12.90	3.90	12.75	14.85	15.46	12.95	13.60
16	1.25	1	1	100	5	3.80	5.30	11.90	6.30	4.10	2.77	3.86	8.67	4.59	3.12
18	2.34	1	1	100	5	5.40	6.50	11.10	5.70	2.30	1.96	2.37	4.04	2.07	0.90
20	2.76	1	2	50	5	1.70	5.10	4.20	4.20	1.20	0.69	2.06	1.70	1.70	0.51
22	2.37	2	1	100	5	17.20	15.60	13.20	8.40	6.70	9.49	8.61	7.28	4.63	12.84
24	1.20	1	1	100	1	3.40	4.00	5.40	3.00	0.10	12.26	14.43	19.48	10.82	0.39
26	1.25	1	2	50	5	2.30	3.80	4.30	2.20	1.20	1.88	3.11	3.52	1.80	1.05
28	2.37	2	3	100	5	8.10	9.30	7.80	4.80	2.40	3.92	4.50	3.77	2.32	5.59
30	2.55	1	2	100	5	3.00	4.10	4.30	3.00	1.40	1.07	1.46	1.53	1.07	0.51
32	2.22	2	2	50	5	9.70	15.10	10.20	7.90	3.20	5.69	8.85	5.98	4.63	8.64
34	2.45	1	1	100	5	7.90	12.10	21.50	10.70	6.10	2.46	3.76	6.69	3.33	2.00
36	1.25	1	1	100	5	3.80	5.00	10.50	5.40	1.20	2.77	3.64	7.65	3.94	0.91
38	2.29	1	1	100	5	14.30	6.20	13.20	7.90	3.00	5.32	2.31	4.91	2.94	1.20
40	2.74	1	2	50	5	2.30	3.80	4.20	2.60	1.70	0.94	1.55	1.71	1.06	0.73
42	2.52	2	3	100	5	12.80	16.20	12.10	8.90	3.00	5.82	7.37	5.50	4.05	6.57
44	1.25	1	1	100	5	14.60	19.40	17.00	11.30	4.30	10.64	14.14	12.39	8.24	3.28
46	2.16	2	1	100	5	2.80	4.30	3.50	3.90	1.60	1.69	2.60	2.11	2.36	3.36
48	2.81	1	2	25	5	8.50	13.10	17.20	10.70	3.20	3.10	4.78	6.28	3.91	1.25
52	2.20	1	2	25	5	7.50	9.20	11.10	7.60	3.70	3.49	4.28	5.17	3.54	1.84
54	1.25	2	1	100	5	4.10	4.40	4.80	2.30	1.60	4.28	4.59	5.01	2.40	5.80

56	1.30	2	2	50	5	12.90	15.70	13.50	10.50	3.70	12.91	15.72	13.51	10.51	17.05
58	2.49	1	2	50	5	1.90	2.40	2.60	2.70	0.98	0.78	0.99	1.07	1.11	0.43
60	2.67	1	2	25	5	3.63	4.54	2.95	2.69	1.01	0.87	1.09	0.71	0.65	0.25
62	2.50	1	1	100	5	3.80	5.40	9.20	7.00	3.60	1.16	1.64	2.80	2.13	1.15
64	1.20	2	1	100	5	LR	LR	LR	LR	LR	LR	LR	LR	LR	LR
66	2.34	1	2	100	5	5.60	6.40	7.10	4.20	2.20	2.18	2.49	2.76	1.63	0.88
68	2.49	1	2	50	5	6.50	9.10	14.20	5.20	2.50	2.91	4.08	6.36	2.33	1.18
70	2.78	2	2	25	5	3.30	5.10	4.00	2.60	1.50	0.88	1.35	1.06	0.69	0.70
72	1.25	1	1	100	5	11.50	13.90	20.10	9.60	3.20	8.38	10.13	14.65	7.00	2.44
74	1.25	2	2	50	5	LR	LR	LR	LR	LR	LR	LR	LR	LR	LR
76	2.28	1	1	100	5	3.70	3.40	8.60	5.00	3.30	1.24	1.14	2.87	1.67	1.16
78	2.48	1	2	100	5	7.00	8.70	8.00	5.20	2.70	2.57	3.20	2.94	1.91	1.02
80	1.30	2	2	50	5	3.10	21.00	8.10	5.10	6.40	3.10	21.02	8.11	5.11	29.50
82	2.70	1	2	50	5	2.00	2.40	4.70	3.20	1.10	0.76	0.91	1.78	1.21	0.45
84	1.58	2	1	100	5	1.40	2.50	3.30	2.50	1.10	1.16	2.06	2.73	2.06	3.16
86	2.80	1	1	100	5	12.20	23.70	15.70	11.10	10.40	3.32	6.45	4.27	3.02	2.98
88	1.20	1	2	50	5	2.00	3.20	3.60	2.40	1.90	1.86	2.98	3.35	2.23	1.86
90	2.70	1	2	50	5	2.70	2.10	6.90	2.40	LR	1.02	0.80	2.62	0.91	LR
92	5.11	2	2	50	5	35.10	41.60	29.80	29.40	15.70	8.94	10.59	7.59	7.49	18.41
94	4.77	1	1	100	1	0.47	3.20	4.80	2.70	1.30	0.43	2.90	4.36	2.45	1.28
96	1.25	1	2	25	5	2.60	4.70	5.50	4.20	1.90	2.13	3.85	4.51	3.44	1.66
98	5.07	2	1	100	5	7.60	10.30	7.50	6.60	1.60	1.96	2.65	1.93	1.70	1.43
100	2.98	2	2	50	5	4.80	4.80	2.50	2.80	3.20	2.10	2.10	1.09	1.22	6.43
102	1.15	1	1	100	5	9.70	13.50	19.90	11.10	4.60	6.41	8.93	13.16	7.34	3.21
104	1.30	2	4	25	5	2.20	5.60	3.90	2.20	1.40	1.86	4.74	3.30	1.86	1.99
106	4.74	1	1	100	5	6.90	9.00	14.30	8.10	3.80	1.33	1.73	2.75	1.56	0.76
108	2.26	1	1	100	5	6.90	9.10	11.40	5.20	2.30	2.32	3.06	3.84	1.75	0.82
110	2.91	1	2	50	5	2.50	2.80	4.00	3.00	1.70	0.96	1.07	1.53	1.15	0.69
112	4.59	1	2	100	5	8.30	9.70	21.00	15.30	10.60	1.65	1.92	4.16	3.03	2.17
114	4.93	1	1	100	1	4.10	4.60	8.30	3.90	2.30	3.60	4.04	7.29	3.43	2.20
116	1.30	1	1	100	5	7.50	6.20	16.20	7.20	5.60	4.39	3.63	9.48	4.21	3.45
118	1.30	2	2	25	5	3.40	5.00	3.10	2.70	2.50	1.93	2.83	1.76	1.53	2.48

120	2.83	2	2	50	5	LR	3.50	2.80	2.10	2.10	LR	1.61	1.29	0.97	4.45
122	1.15	1	2	25	5	1.80	1.90	1.30	LR	LR	1.60	1.69	1.16	LR	LR
124	1.15	1	2	50	5	5.10	5.60	9.00	5.20	1.40	4.95	5.43	8.73	5.04	1.43
126	1.20	2	4	25	5	1.20	4.50	2.80	2.40	LR	1.10	4.12	2.57	2.20	0.00
128	4.69	1	1	100	5	9.40	13.50	27.50	15.70	9.60	1.83	2.62	5.34	3.05	1.95
130	2.97	1	2	50	5	2.50	3.30	2.70	2.80	1.20	0.86	1.14	0.93	0.97	0.44
132	2.98	1	2	25	5	15.25	24.88	25.96	14.00	5.97	3.29	5.37	5.60	3.02	1.33
134	4.79	2	1	100	5	14.20	19.50	14.80	12.50	4.60	3.87	5.31	4.03	3.41	4.35
136	1.10	1	2	100	5	10.00	10.10	13.50	5.00	2.10	8.27	8.35	11.16	4.13	1.79
138	5.14	1	1	100	5	10.80	8.90	11.80	3.30	3.90	1.60	1.32	1.75	0.49	0.61
140	2.72	2	1	100	5	7.20	7.70	4.90	3.70	2.10	3.45	3.69	2.35	1.77	3.50
142	1.05	1	1	100	5	3.70	4.90	5.20	3.50	1.30	3.21	4.25	4.51	3.04	1.18
144	1.25	2	2	50	5	17.00	20.00	15.40	11.70	7.30	17.70	20.82	16.03	12.18	34.99
146	4.85	1	1	100	1	2.60	2.20	4.10	2.90	1.30	2.32	1.96	3.66	2.59	1.26
148	1.10	1	2	50	5	1.50	3.50	3.70	4.50	1.10	1.40	3.26	3.44	4.19	1.09
150	1.05	1	2	50	5	33.50	44.10	60.20	31.00	15.40	35.59	46.86	63.96	32.94	17.23
152	2.98	2	1	100	5	5.40	3.90	3.80	2.50	2.00	2.37	1.71	1.67	1.10	3.05
154	4.71	1	1	100	5	5.20	11.10	19.20	13.20	6.00	1.01	2.15	3.72	2.56	1.21
156	5.11	2	2	25	5	3.60	6.00	2.20	1.40	1.50	0.52	0.87	0.32	0.20	0.38
158	4.45	1	1	100	5	4.70	4.90	24.10	19.80	12.30	0.80	0.84	4.12	3.38	2.22
160	2.95	1	1	100	5	43.80	52.40	78.90	32.70	26.80	13.55	16.21	24.41	10.12	8.67
162	1.15	1	1	100	5	7.70	2.10	3.70	1.30	1.00	5.70	1.55	2.74	0.96	0.79
164	1.20	1	2	50	5	2.40	4.40	5.50	3.40	1.50	2.23	4.09	5.11	3.16	1.47
166	5.18	1	2	100	5	6.90	11.10	15.60	6.70	4.40	0.49	0.78	1.10	0.47	0.33
168	1.10	2	2	50	5	19.80	29.10	23.40	17.40	5.80	11.71	17.21	13.84	10.29	15.80
170	1.15	2	2	50	5	3.30	5.30	2.30	2.90	1.00	2.11	3.40	1.47	1.86	1.12
172	2.79	1	2	50	5	1.24	1.85	1.99	1.71	LR	0.29	0.43	0.46	0.39	LR
174	1.15	1	2	50	5	5.60	8.90	14.60	9.10	3.80	5.43	8.63	14.16	8.83	3.88
176	4.58	2	2	50	5	63.00	60.90	40.60	35.60	24.00	17.92	17.32	11.55	10.13	31.43
178	1.15	1	2	100	5	2.20	20.10	9.40	6.40	1.90	0.70	6.37	2.98	2.03	0.64
180	2.83	1	1	100	5	3.00	5.80	7.00	3.80	1.20	0.97	1.87	2.26	1.23	0.40
182	1.25	1	2	50	5	7.40	11.10	11.70	5.50	2.40	6.60	9.91	10.44	4.91	2.26

184	1.15	2	1	100	5	3.60	5.10	2.60	2.50	LR	4.08	5.79	2.95	2.84	LR
186	1.00	2	2	50	5	49.80	92.80	63.90	61.50	25.30	32.40	60.38	41.58	40.01	75.79
188	2.86	1	2	50	5	2.20	2.90	3.20	2.90	1.60	0.49	0.65	0.72	0.65	0.37
194	1.00	1	1	100	5	18.70	22.70	42.30	27.10	10.00	17.04	20.68	38.55	24.69	9.53
196	2.50	1	2	25	5	4.70	8.10	12.70	12.30	3.00	1.92	3.32	5.20	5.04	1.31
198	2.23	1	1	100	5	6.00	8.90	11.40	2.00	2.10	2.29	3.40	4.35	0.76	0.86
200	2.88	1	2	50	5	14.50	29.50	33.70	14.70	8.50	5.63	11.45	13.08	5.70	3.47
202	1.05	1	1	100	5	21.70	31.40	52.20	19.90	15.20	18.83	27.25	45.30	17.27	13.79
204	2.25	1	2	100	5	1.20	1.90	4.50	2.70	1.40	0.19	0.31	0.73	0.44	0.24
206	1.00	2	2	50	5	11.20	13.20	10.70	9.00	2.40	14.57	17.18	13.92	11.71	14.38
208	2.19	2	1	100	5	3.50	4.90	3.60	3.00	1.20	2.09	2.92	2.14	1.79	2.48
210	2.79	2	2	50	5	11.00	11.10	3.70	2.80	LR	2.93	2.95	0.98	0.75	LR
212	2.20	1	2	50	5	5.60	13.60	26.90	14.50	4.60	2.61	6.33	12.52	6.75	2.29
214	2.58	1	1	100	5	6.90	9.40	15.10	9.10	3.60	2.44	3.33	5.34	3.22	1.33
216	1.05	1	2	50	5	1.60	1.30	2.70	2.50	1.60	0.98	0.80	1.65	1.53	1.01
218	1.00	1	2	50	5	4.40	5.30	10.40	4.50	1.30	4.91	5.91	11.60	5.02	1.53
220	2.87	2	4	25	5	1.50	4.30	1.00	2.50	LR	0.57	1.65	0.38	0.96	LR
222	2.53	2	2	50	5	8.30	49.30	26.40	6.60	9.20	4.28	25.41	13.61	3.40	21.83
224	1.25	1	2	100	5	19.10	22.20	28.10	16.00	13.70	5.57	6.48	8.20	4.67	4.27
226	1.05	2	1	100	5	7.50	10.40	6.50	6.30	2.30	9.32	12.92	8.08	7.83	9.93
228	1.15	1	2	50	5	5.00	7.20	16.30	5.90	3.10	4.45	6.41	14.51	5.25	2.95
230	2.71	2	2	25	5	2.40	5.30	3.30	4.60	1.40	0.65	1.44	0.90	1.25	0.67
232	3.45	1	2	50	5	29.20	34.00	56.90	38.60	11.90	9.44	10.99	18.40	12.48	4.05
236	1.20	1	1	100	5	3.30	4.90	5.70	3.20	1.10	2.51	3.72	4.33	2.43	0.87
238	2.79	1	2	50	5	2.60	2.20	3.00	3.70	LR	0.60	0.51	0.69	0.85	LR
240	2.74	2	2	50	5	2.20	3.90	2.20	2.60	1.20	0.59	1.05	0.59	0.70	0.57
242	2.67	1	2	50	5	5.10	8.80	13.60	10.20	4.90	1.96	3.37	5.22	3.91	2.01
244	1.15	2	2	50	5	19.20	17.70	13.80	14.40	5.50	21.73	20.03	15.62	16.29	28.65
246	1.10	2	2	25	5	8.50	9.80	6.80	7.20	3.60	5.69	6.57	4.56	4.82	4.22
248	1.15	1	1	100	5	6.60	10.70	11.40	5.90	2.00	5.23	8.48	9.03	4.68	1.66
250	2.80	1	2	50	5	1.10	1.70	1.90	1.90	1.10	0.25	0.39	0.44	0.44	0.26
252	2.88	1	2	50	5	1.50	1.70	1.90	1.90	1.10	0.34	0.38	0.42	0.42	0.25

254	1.00	1	2	25	5	2.50	4.70	5.80	3.80	1.90	2.56	4.81	5.94	3.89	0.52
256	2.85	2	1	100	5	7.00	4.70	3.20	2.00	2.90	3.21	2.16	1.47	0.92	4.62
258	4.53	2	2	50	5	14.30	22.20	16.80	20.50	8.00	4.11	6.38	4.83	5.89	10.58
260	2.73	1	1	100	5	32.00	66.90	97.40	41.50	59.00	10.70	22.37	32.57	13.88	20.63
262	1.48	1	2	100	5	3.90	5.00	8.40	1.70	1.00	0.96	1.23	2.07	0.42	0.26
264	2.49	1	1	100	5	10.90	23.20	30.80	19.30	8.40	3.99	8.49	11.27	7.06	3.21
266	1.10	1	2	50	5	11.30	16.90	25.80	12.80	4.90	11.46	17.14	26.17	12.98	5.23
268	1.10	2	2	25	5	2.70	9.40	5.50	6.10	2.60	1.81	6.30	3.68	4.09	3.05
270	2.94	1	1	100	5	20.20	30.60	41.30	16.90	6.10	6.26	9.48	12.80	5.24	1.98
272	1.10	2	1	100	5	5.70	7.40	5.30	5.50	1.80	6.76	8.78	6.29	6.52	7.42
274	1.15	1	2	50	5	2.00	2.60	7.00	2.70	LR	1.12	1.45	3.91	1.51	LR
276	1.15	1	2	50	5	6.50	8.80	14.70	5.00	2.40	6.31	8.54	14.26	4.85	2.45
278	2.72	2	2	50	5	5.70	7.10	4.10	6.60	4.20	1.55	1.93	1.12	1.80	1.63
280	2.71	2	1	100	5	50.60	46.90	31.70	23.70	15.20	24.36	22.58	15.26	11.41	25.42
282	1.10	2	2	50	5	8.00	10.20	8.10	6.90	3.30	9.46	12.07	9.58	8.16	17.97
284	1.20	1	2	25	5	4.00	6.70	8.20	3.80	1.90	3.41	5.72	7.00	3.24	1.73
286	2.55	2	2	50	5	113.70	99.60	72.60	50.00	12.10	33.04	28.94	21.10	14.53	5.01
288	2.94	1	2	100	5	13.00	13.90	32.50	10.20	4.70	1.61	1.72	4.03	1.26	0.62
290	5.30	2	1	100	5	10.10	19.70	26.30	9.00	6.70	2.49	4.85	6.47	2.22	5.73
292	4.29	1	2	50	5	24.60	43.80	87.60	46.30	29.00	6.40	11.40	22.81	12.05	7.95
294	1.20	2	1	100	5	4.90	3.50	2.80	3.20	1.00	5.33	3.81	3.04	3.48	3.78
296	1.00	2	2	25	5	2.10	8.50	5.80	6.30	4.70	1.55	6.26	4.27	4.64	6.06
298	1.00	1	2	100	5	4.40	8.30	10.50	5.40	2.30	1.60	3.03	3.83	1.97	0.90
304	2.83	1	2	100	5	10.20	13.70	23.90	11.90	6.00	1.32	1.77	3.08	1.54	0.83
306	1.15	2	1	100	5	3.70	4.40	2.00	2.10	1.20	4.20	4.99	2.27	2.38	4.73
308	1.10	2	2	50	5	7.00	6.00	4.90	4.60	2.20	4.72	4.04	3.30	3.10	2.11
310	5.18	2	2	50	5	4.50	6.80	4.20	2.90	3.80	0.64	0.97	0.60	0.41	0.78
312	1.25	1	2	100	5	6.20	11.30	14.80	8.40	2.90	1.81	3.30	4.32	2.45	0.90
314	1.20	2	2	50	5	7.00	8.30	5.60	5.90	1.70	7.59	9.00	6.07	6.40	8.49
316	2.70	2	2	50	5	3.20	4.10	2.50	2.30	1.50	0.88	1.13	0.69	0.63	0.59
318	1.15	1	2	50	5	8.70	13.30	18.50	9.50	3.10	8.44	12.90	17.95	9.22	3.17
320	5.12	1	2	100	5	5.50	14.50	5.60	2.10	1.80	0.39	1.03	0.40	0.15	0.14

322	1.15	1	2	25	5	33.70	56.50	79.80	40.70	21.90	30.00	50.30	71.05	36.24	20.84
324	1.10	2	2	50	5	3.40	4.90	3.80	5.00	2.80	4.02	5.80	4.50	5.91	15.25
326	3.00	2	1	100	5	3.70	18.80	21.10	8.90	7.30	1.61	8.18	9.18	3.87	11.03
328	1.30	1	2	50	5	2.10	3.20	3.70	3.50	1.80	1.04	1.58	1.83	1.73	0.92
329	5.14	2	2	25	5	2.50	19.10	6.40	2.50	3.50	0.36	2.74	0.92	0.36	0.88

Appendix 7: For the small sediment aliquots from SHAK06-5K (n = 160), the dry sediment weight, standard injection (µl), solvent in vial (µl) for each sample, with the peak areas and concentrations (ng g^{-1}) of even homologues C_{26}-C_{34} for each sample. 'LR' is where the detection limit measuring the retention time of long-chain homologues was reached.

Depth (cm)	Dry weight (g)	GC-FID	Standard injection (µl)	Solvent in vial (µl)	Sample injection (µl)	Peak area of homologue						Total *n*-alkane concentration in dry sediment (ng g^{-1})					
						C_{25}	C_{27}	C_{29}	C_{31}	C_{33}	C_{35}	C_{25}	C_{27}	C_{29}	C_{31}	C_{33}	C_{35}
4	81.87	2	2	500	1	38.00	40.20	70.50	102.90	53.10	29.80	25.13	26.58	46.62	68.04	44.93	19.71
10	141.27	2	2	500	1	93.60	165.40	387.10	472.70	183.70	66.90	25.88	45.73	107.02	130.69	62.99	22.94
20	79.58	2	2	500	1	73.70	127.50	308.50	433.30	181.90	71.10	35.84	62	150.02	210.71	110.72	43.28
30	120.52	2	2	500	1	44.60	83.70	201.90	248.20	94.10	32.50	14.32	26.88	64.83	79.7	37.82	13.06
38	127.30	2	1	100	1	2864.00	3947.80	5043.00	7988.00	7113.00	2761.50	153.15	211.1	269.66	427.14	783.16	147.66
40	122.57	2	2	500	1	100.80	169.50	356.60	483.40	212.50	84.20	31.83	53.52	112.59	152.62	83.98	33.28
47	105.59	2	1	100	1	751.80	1219.10	2639.70	3637.60	1452.80	713.60	54.23	87.93	190.4	262.37	217.61	51.47
48	95.45	1	2	500	1	115.70	216.30	567.10	718.70	322.90	134.00	59.56	111.34	291.93	369.96	163.64	67.91
49	104.36	2	1	100	1	1219.10	1842.00	3715.90	4908.30	2001.20	1117.70	88.97	134.43	271.18	358.2	303.74	81.57
51	106.17	2	1	100	1	1388.30	2007.90	2943.30	4418.30	928.80	862.50	99.59	144.04	211.14	316.94	138.57	61.87
53	110.05	2	1	100	1	2663.20	3584.00	5252.70	7319.30	3599.70	2420.80	164.73	221.68	324.9	452.73	458.46	149.74
55	105.28	2	1	100	1	1484.90	2314.60	3492.00	4966.20	3402.30	2459.40	96.01	149.65	225.78	321.1	452.95	159.02
57	104.01	2	1	100	1	972.70	1874.40	2806.10	4485.80	2494.80	1462.70	63.66	122.67	183.65	293.58	336.19	95.73
59	32.70	2	2	500	1	32.90	75.10	193.30	253.80	85.70	24.50	41.45	94.62	243.54	319.76	133.66	38.21
60	123.74	1	2	500	1	57.90	113.40	257.80	330.10	165.90	92.80	22.78	44.62	101.43	129.88	64.85	36.28
64	61.77	2	2	500	1		4.10	8.10	11.10	6.60			5.15	10.18	13.95	10.65	
66	84.27	2	1	100	1	1558.00	2779.10	5764.60	5833.60	2495.30	1253.70	125.85	224.49	465.64	471.22	415.03	101.27
70	35.08	1	2	500	1	18.00	40.60	93.90	107.00	35.40	9.20	24.98	56.35	130.32	148.5	48.81	12.69
71	176.78	2	2	500	1	98.90	198.30	459.30	523.00	178.20	55.10	21.65	43.41	100.55	114.49	48.83	15.1
74	81.55	2	2	500	1	49.50	75.10	154.70	201.70	86.30	29.50	32.86	49.85	102.7	133.9	73.3	19.58
78	82.69	2	2	500	1	47.20	90.60	163.00	186.10	80.80	40.50	29.56	56.75	102.1	116.56	66.63	25.37
81	84.38	2	1	100	1	1414.30	3759.50	7447.60	7476.60	3128.10	1771.90	114.09	303.28	600.81	252.35	519.6	142.94
82	79.88	2	2	500	1	77.30	169.90	336.00	342.30	142.50	63.10	37.45	82.31	162.78	165.84	86.41	38.26
85	85.11	2	1	100	1	2204.30	3981.20	5628.10	9186.90	7113.10	3827.40	176.3	318.41	450.13	734.76	1171.4	306.11
90	63.41	1	2	500	1	115.40	206.00	447.20	438.30	308.20	210.50	88.6	158.16	343.35	336.52	235.11	160.58

92	62.62	2	2	500	1	29.70	58.60	118.10	131.60	55.00	35.30	25.68	50.66	102.1	113.77	60.84	30.52
96	62.12	2	2	500	1	15.90	24.10	47.20	66.20	29.40	13.10	19.69	29.85	58.46	82	47.19	16.23
100	84.22	1	2	500	1	95.60	182.80	396.20	415.80	195.00	93.20	55.26	105.67	229.03	240.36	112	53.53
104	61.75	2	2	500	1	19.00	36.00	66.30	87.60	47.70	21.60	23.89	45.27	83.38	110.16	77.03	27.16
109	179.94	2	2	500	1	302.80	821.00	1828.50	1979.10	720.80	93.90	65.12	176.57	393.25	425.64	194.03	25.28
110	116.43	2	2	500	1	174.10	426.20	825.50	857.80	444.00	183.40	57.87	141.67	274.39	285.13	184.72	76.3
112	82.15	2	2	500	1	82.50	185.90	414.40	521.40	281.70	121.70	52.01	117.21	261.27	328.73	233.82	76.73
120	79.45	1	2	500	1	66.90	170.90	353.70	331.10	144.70	52.10	40.99	104.72	216.74	202.89	88.1	31.72
122	61.18	2	2	500	1	30.80	43.20	73.00	77.50	36.90	22.20	38.74	54.33	91.81	97.47	60.14	27.92
126	81.66	2	2	500	1	81.10	128.50	93.10	202.70	94.00	48.70	53.77	85.19	61.72	134.38	79.74	32.29
128	85.27	2	1	100	1	1611.50	3270.90	4270.10	3938.50	3154.60	2414.80	99.65	202.25	264.04	243.54	301.9	149.32
130	108.04	2	2	500	1	215.30	560.10	1020.90	983.80	494.90	217.90	77.12	200.62	365.68	352.39	221.88	97.69
136	82.27	2	2	500	1	31.90	65.50	124.90	139.20	68.90	23.50	20.99	43.1	82.19	91.6	58.01	15.46
140	125.66	1	2	500	1	108.40	250.60	407.30	367.60	174.20	69.50	42	97.09	157.8	142.42	67.06	26.75
146	113.49	2	2	500	1	300.70	536.70	718.60	662.40	526.50	336.00	102.54	183.01	245.04	225.87	224.72	143.41
148	61.71	2	2	500	1	47.00	72.60	115.50	122.10	64.70	23.70	41.23	63.69	101.32	107.11	72.63	20.79
152	159.13	1	2	500	1	181.20	381.00	656.40	597.30	318.80	124.70	55.44	116.57	200.82	182.74	105.6	46.05
156	61.39	2	2	500	1	33.70	58.80	90.50	87.70	66.40	40.60	29.72	51.85	79.81	58.55	74.92	35.8
160	138.51	1	2	500	1	321.50	802.90	1547.80	1523.40	770.70	228.40	113	282.21	544.04	535.46	328.18	165.22
164	61.11	2	2	500	1	48.60	78.40	134.30	133.90	68.40	36.20	43.05	69.45	118.97	118.62	77.53	32.07
168	61.85	2	2	500	1	67.10	163.40	312.70	291.50	124.60	14.70	84.25	205.16	392.61	365.99	200.88	18.46
172	103.12	2	2	500	1	135.40	302.30	602.50	613.20	285.10	101.80	50.81	113.45	226.11	230.12	133.92	47.82
176	57.32	2	2	500	1	34.70	83.30	144.70	171.00	102.50	60.00	31.35	75.27	130.75	154.51	121.93	54.22
180	41.93	2	2	500	1	69.50	210.40	419.60	398.10	164.70	81.70	64.15	194.19	387.27	367.43	190.27	94.38
182	61.82	2	2	500	1	48.10	84.20	164.20	215.30	124.10	20.10	59.87	104.8	204.37	267.98	200.17	25.02
184	61.85	2	2	500	1	91.90	175.90	250.50	231.10	108.50	50.30	80.44	153.96	219.26	202.28	121.51	44.03
190	124.82	2	2	500	1	288.20	644.90	1061.00	1050.80	700.80	363.00	89.35	199.95	328.95	325.79	271.96	140.87
194	61.57	2	2	500	1	69.50	148.20	299.90	246.60	181.00	92.40	58.46	124.67	252.28	207.44	200.45	77.73
198	62.09	2	2	500	1	79.90	194.50	339.00	387.60	219.40	110.20	66.65	162.25	282.78	323.32	240.94	91.93

200	39.93	1	2	500	1	59.30	193.60	381.90	348.10	141.40	33.40	72.3	236.05	465.64	424.42	171.3	40.46
210	117.08	1	2	500	1	276.70	535.50	993.40	943.80	485.30	232.30	115.06	222.68	413.09	392.46	224.39	107.05
220	126.08	2	2	500	1	200.30	472.20	809.20	836.50	169.80	237.30	61.48	144.94	248.38	256.76	65.24	91.17
230	123.92	1	2	500	1	199.40	492.90	1061.50	996.70	531.60	167.70	78.34	193.65	417.04	391.59	207.52	65.46
240	99.68	2	2	500	1	126.40	299.40	593.70	616.60	381.70	166.50	49.07	116.24	230.5	239.39	185.48	80.91
250	49.69	2	2	500	1	211.80	476.70	923.00	951.10	467.60	175.70	164.95	371.26	718.85	740.73	455.82	171.28
260	83.65	1	2	500	1	113.70	295.00	628.50	611.20	290.20	73.00	66.17	171.69	365.79	355.72	167.82	42.21
270	37.46	2	2	500	1	52.00	138.00	306.40	328.90	146.70	56.70	56.67	150.38	333.9	358.42	199.72	77.19
280	79.78	1	2	500	1	70.90	205.40	440.10	473.30	221.20	69.10	43.27	125.35	268.57	288.83	134.12	41.9
284	82.62	2	2	500	1	11.40	17.30	84.00	39.50	30.90		7.15	10.85	52.66	24.76	25.5	0
286	30.92	2	2	500	1	13.80	22.60	43.40	60.80	40.80	29.40	23.12	37.86	72.7	101.84	89.97	49.25
288	57.29	2	2	500	1	87.30	204.20	322.70	460.50	438.30	250.60	78.92	184.61	291.74	416.32	521.66	226.56
290	57.42	2	2	500	1	119.50	249.70	547.40	655.00	349.70	129.00	85.74	179.16	392.76	469.96	310.59	114.57
300	144.58	2	2	500	1	176.50	376.00	907.60	937.40	514.60	197.70	49.83	106.16	256.25	264.67	181.52	69.73
310	59.27	2	2	500	1	79.40	214.50	461.30	455.30	210.60	69.90	55.19	149.09	320.63	316.46	181.2	60.14
320	105.81	2	2	500	1	198.10	441.30	936.90	893.30	593.80	312.90	76.43	170.25	361.46	344.64	286.2	150.81
329	83.67	1	2	500	1	82.00	76.10	156.80	159.40	75.70	16.30	47.71	44.28	91.24	92.75	43.77	9.42

Appendix 8: For the large sediment aliquots from SHAK06-5K (n = 71), the dry sediment weight, standard injection (µl), solvent in vial (µl) for each sample, with the peak areas and concentrations (ng g^{-1}) of odd homologues C_{25}-C_{35} for each sample. 'LR' is where the detection limit measuring the retention time of long-chain homologues was reached.

Depth (cm)	Dry weight (g)	GC-FID	Standard injection (µl)	Solvent in vial (µl)	Sample injection (µl)	Peak area of homologue					Total *n*-alkane concentration in dry sediment (ng g^{-1})				
						C_{26}	C_{28}	C_{30}	C_{32}	C_{34}	C_{26}	C_{28}	C_{30}	C_{32}	C_{34}
4	81.87	2	2	500	1	26.60	12.90	9.70	9.40	12.90	17.59	8.53	6.41	6.22	10.91
10	141.27	2	2	500	1	57.90	59.00	57.50	36.10	23.40	16.01	16.31	15.90	9.98	8.02
20	79.58	2	2	500	1	52.20	50.50	52.40	38.20	33.50	25.38	24.56	25.48	18.58	20.39
30	120.52	2	2	500	1	22.90	26.00	27.50	19.80	7.70	7.35	8.35	8.83	6.36	3.09
38	127.30	2	1	100	1	1913.70	1760.00	2309.00	1735.00	2093.20	102.33	94.11	123.47	92.77	230.47
40	122.57	2	2	500	1	65.70	63.30	64.60	48.10	40.70	20.74	19.99	20.40	15.19	16.08
47	105.59	2	1	100	1	440.60	495.90	564.00	476.20	355.50	31.78	35.77	40.68	34.35	53.25
48	95.45	1	2	500	1	42.20	62.10	80.40	45.80	16.20	21.72	31.97	41.39	23.58	8.56
49	104.36	2	1	100	1	470.20	750.70	823.50	674.90	637.60	34.31	54.78	60.10	49.25	96.77
51	106.17	2	1	100	1	1234.70	1014.10	865.80	674.20	576.00	88.57	72.75	62.11	48.36	85.93
53	110.05	2	1	100	1	2454.00	1919.80	1596.80	1284.20	1259.70	151.79	118.75	98.77	79.43	160.44
55	105.28	2	1	100	1	1009.50	1021.30	861.40	694.70	1380.00	65.27	66.03	55.70	44.92	183.72
57	104.01	2	1	100	1	331.20	1145.90	1096.30	891.10	994.00	21.68	74.99	71.75	58.32	133.95
59	32.70	2	2	500	1	15.70	23.30	24.50	16.90	7.10	19.78	29.36	30.87	21.29	11.07
60	123.74	1	2	500	1	22.70	31.90	23.30	25.10	15.80	8.93	12.55	9.17	9.88	6.44
64	61.77	2	2	500	1										
66	84.27	2	1	100	1	1021.20	1139.10	960.00	923.30	669.30	82.49	92.01	77.55	74.58	111.32
70	35.08	1	2	500	1	8.30	11.40	16.80	6.20	2.20	11.52	15.82	23.32	8.60	3.16
71	176.78	2	2	500	1	51.10	58.60	51.60	46.10	22.70	11.19	12.83	11.30	10.09	6.22
74	81.55	2	2	500	1	22.40	21.60	20.80	24.80	9.70	14.87	14.34	13.81	16.46	8.24
78	82.69	2	2	500	1	25.10	22.20	20.90	23.30	40.50	15.72	13.91	13.09	14.59	33.40
81	84.38	2	1	100	1	879.10	1221.50	1220.60	1325.80	1056.00	70.92	98.54	98.47	106.95	175.41
85	85.11	2	1	100	1	1530.80	1784.90	2531.00	2233.50	3005.00	122.43	142.76	202.43	178.63	494.87
82	79.88	2	2	500	1	58.80	52.40	47.20	32.60	23.00	28.49	25.39	22.87	15.79	13.95

90	63.41	1	2	500	1	26.80	53.70	84.50	54.10	26.10	20.58	41.23	64.88	41.54	20.75
92	62.62	2	2	500	1	8.40	16.40	13.50	12.60	7.30	7.26	14.18	11.67	10.89	8.08
96	62.12	2	2	500	1	7.60	6.10	4.30	5.30	4.10	9.41	7.56	5.33	6.56	6.58
100	84.22	1	2	500	1	28.40	39.70	63.10	32.30	25.50	16.42	22.95	36.48	18.67	15.26
104	61.75	2	2	500	1	5.10	9.90	5.90	7.30	5.40	6.41	12.45	7.42	9.18	8.72
109	179.94	2	2	500	1	150.80	219.10	218.50	204.70	93.90	32.43	47.12	46.99	44.02	25.28
110	116.43	2	2	500	1	123.20	141.20	138.50	134.20	98.50	40.95	46.93	46.04	44.61	40.98
112	82.15	2	2	500	1	52.10	64.40	72.40	71.30	61.50	32.85	40.60	45.65	44.95	51.05
120	79.45	1	2	500	1	27.40	48.90	105.10	36.00	24.70	16.79	29.96	64.40	22.06	15.67
122	61.18	2	2	500	1	14.30	11.10	6.70	8.40	5.50	17.98	13.96	8.43	10.56	8.96
126	81.66	2	2	500	1	39.90	30.90	17.70	25.80	22.00	26.45	20.49	11.73	17.10	18.66
128	85.27	2	1	100	1	1210.30	1458.50	866.30	922.30	436.70	74.84	90.19	53.57	57.03	41.79
130	108.04	2	2	500	1	150.90	170.00	194.50	152.70	182.30	54.05	60.89	69.67	54.70	81.73
136	82.27	2	2	500	1	23.90	17.50	14.40	15.50	13.30	15.73	11.52	9.48	10.20	11.20
140	125.66	1	2	500	1	39.70	56.20	97.20	37.70	30.00	15.38	21.77	37.66	14.61	12.03
146	113.49	2	2	500	1	280.70	279.70	144.60	214.70	212.20	95.72	95.38	49.31	73.21	90.57
148	61.71	2	2	500	1	23.20	17.40	15.00	15.80	11.40	20.35	15.26	13.16	13.86	12.80
152	159.13	1	2	500	1	59.30	89.10	138.80	77.30	60.00	18.14	27.26	42.47	23.65	19.01
156	61.39	2	2	500	1	25.10	20.00	11.40	10.30	11.50	22.13	17.64	10.05	9.08	12.98
160	138.51	1	2	500	1	127.00	239.80	324.70	206.30	217.60	44.64	84.29	114.13	72.51	79.19
164	61.11	2	2	500	1	20.50	17.60	15.11	15.20	7.70	18.16	15.59	13.39	13.47	8.73
168	61.85	2	2	500	1	33.90	40.30	35.50	23.90	14.70	42.56	50.60	44.57	30.01	23.70
172	103.12	2	2	500	1	63.80	85.00	94.50	73.80	61.10	23.94	31.90	35.46	27.70	28.70
176	57.32	2	2	500	1	11.80	25.60	22.40	19.30	37.80	10.66	23.13	20.24	17.44	44.97
180	41.93	2	2	500	1	36.20	47.00	45.30	49.30	31.20	33.41	43.38	41.81	45.50	36.04
182	61.82	2	2	500	1	48.10	22.80	15.60	22.10	20.10	59.87	28.38	19.42	27.51	32.42
184	61.85	2	2	500	1	48.70	38.20	14.80	29.20	17.10	42.63	33.44	12.95	25.56	19.15
190	124.82	2	2	500	1	230.70	274.30	230.40	220.60	198.70	71.53	85.04	71.43	68.40	77.11
194	61.57	2	2	500	1	23.70	33.80	32.80	33.00	26.30	19.94	28.43	27.59	27.76	29.13

198	62.09	2	2	500	1	40.20	54.50	40.60	56.40	60.80	33.53	45.46	33.87	47.05	66.77
200	39.93	1	2	500	1	22.90	34.60	58.50	21.60	9.30	27.92	42.19	71.33	26.34	11.74
210	117.08	1	2	500	1	67.50	128.20	204.60	107.20	41.00	28.07	53.31	85.08	44.58	17.65
220	126.08	2	2	500	1	139.30	146.80	197.70	155.60	169.80	42.76	45.06	60.68	47.76	65.24
230	123.92	1	2	500	1	67.10	118.60	146.00	83.10	45.00	26.36	46.60	57.36	32.65	18.31
240	99.68	2	2	500	1	77.90	88.70	112.90	101.30	86.80	30.24	34.44	43.83	39.33	42.18
250	49.69	2	2	500	1	105.90	123.00	129.60	128.10	93.70	82.48	95.79	100.93	99.77	91.34
260	83.65	1	2	500	1	51.10	79.30	95.20	65.50	26.20	29.74	46.15	55.41	38.12	15.79
270	37.46	2	2	500	1	27.00	35.70	33.30	34.80	16.80	29.42	38.90	36.29	37.92	22.87
280	79.78	1	2	500	1	28.10	53.10	95.00	40.80	17.70	17.15	32.40	57.97	24.90	11.18
284	82.62	2	2	500	1	4.30	5.20	5.70	8.20	LR	2.70	3.26	3.57	5.14	LR
286	30.92	2	2	500	1	5.20	8.00	4.80	6.40	5.70	8.71	13.40	8.04	10.72	12.57
288	57.29	2	2	500	1	26.20	126.60	114.00	135.40	157.30	23.69	114.45	103.06	122.41	187.22
290	57.42	2	2	500	1	65.90	79.80	93.40	79.20	35.40	47.28	57.26	67.01	56.83	31.44
300	144.58	2	2	500	1	100.90	126.30	171.70	126.60	43.00	28.49	35.66	48.48	35.74	15.17
310	59.27	2	2	500	1	38.90	57.60	50.40	42.10	21.50	27.04	40.04	35.03	29.26	18.50
320	105.81	2	2	500	1	145.60	156.90	232.70	188.60	160.80	56.17	60.53	89.78	72.76	77.50
329	83.67	1	2	500	1	21.70	17.20	19.10	15.20	7.60	12.63	10.01	11.11	8.84	4.58

Appendix 9: For the large sediment aliquots from SHAK06-5K (n = 71), the dry sediment weight, standard injection (µl), solvent in vial (µl) for each sample, with the peak areas and concentrations (ng g^{-1}) of even homologues C_{26}-C_{34} for each sample. 'LR' is where the detection limit measuring the retention time of long-chain homologues was reached.

Depth (cm)	Cleaning method	Run 1: Alkane concentration in vial (ng)				Run 2 clean: Alkane concentration in vial (ng)				Recovery rate (%)				
		C_{27}	C_{29}	C_{31}	C_{33}	C_{27}	C_{29}	C_{31}	C_{33}	C_{27}	C_{29}	C_{31}	C_{33}	Total (C_{27}-C_{33})
4	Zeolite	2176.29	3816.62	5570.64	3529.58	790.08	1752.15	2031.63	1055.77	36.30	45.91	36.47	29.91	37.30
10	Zeolite	6459.97	15118.82	18462.07	8538.67	4664.22	11450.38	13374.81	5964.36	72.20	75.74	72.44	69.85	72.98
20	Zeolite	4934.16	11938.74	16768.41	8455.00	1273.81	3210.53	4328.36	2263.88	25.82	26.89	25.81	26.78	26.31
30	Zeolite	3239.13	7813.39	9605.17	4373.92	2901.84	6755.77	8720.72	4030.96	89.59	86.46	90.79	92.16	89.52
40	Zeolite	6559.53	13800.17	18707.24	9877.34	2786.79	6369.06	7861.24	3997.32	42.48	46.15	42.02	40.47	42.94
48	Zeolite	10627.82	27864.25	35313.06	15619.53	6263.54	16155.68	22151.26	10541.98	58.94	57.98	62.73	67.49	61.63
59	Zeolite	3094.02	7963.70	10456.22	4194.00	1843.85	4733.92	6313.62	2623.80	59.59	59.44	60.38	62.56	60.35
60	Zeolite	5520.89	12551.02	16070.95	8025.02	1388.24	2855.30	3707.07	4246.53	25.15	22.75	23.07	52.92	28.93
70	Zeolite	1976.61	4571.53	5209.31	1712.39	1365.85	3018.26	3669.55	1617.04	69.10	66.02	70.44	94.43	71.80
74	Zeolite	4065.65	8374.91	10919.33	5736.39	3546.66	5742.74	6407.61	3514.34	87.23	68.57	58.68	61.26	66.03
78	Zeolite	4692.48	8442.32	9638.75	5286.86	4874.23	8353.08	9337.73	5301.07	103.87	98.94	96.88	100.27	99.31
82	Zeolite	6575.01	13002.97	13246.77	6623.63	2407.24	4993.86	4611.72	2125.20	36.61	38.41	34.81	32.09	35.84
90	Zeolite	10029.13	21771.98	21338.68	14908.45	3944.95	8343.94	8195.07	4145.77	39.33	38.32	38.40	27.81	36.19
92	Zeolite	3172.40	6393.52	7124.36	3655.87	1590.91	3396.80	3294.68	1604.23	50.15	53.13	46.25	43.88	48.59
96	Zeolite	1854.37	3631.80	5093.75	2813.16	0.00	1341.45	1595.24	752.46	0.00	36.94	31.32	26.75	27.55
100	Zeolite	8899.64	19289.04	20243.26	9432.67	5697.85	12132.58	12776.42	6607.33	64.02	62.90	63.11	70.05	64.31
109	Zeolite	31772.13	70761.68	76589.79	33503.94	25379.30	55068.83	59883.56	28006.17	79.88	77.82	78.19	83.59	79.17
110	Zeolite	16493.64	31946.27	33196.26	20637.83	12800.83	28075.45	29890.47	14310.70	77.61	87.88	90.04	69.34	83.19
112	Zeolite	9628.39	21463.19	27005.08	18432.04	2937.67	6934.39	8413.87	5185.24	30.51	32.31	31.16	28.13	30.67
120	Zeolite	8320.28	17219.92	16119.64	6999.52	4800.93	8809.14	8265.78	4150.57	57.70	51.16	51.28	59.30	53.49
126	Zeolite	6956.54	5040.10	10973.46	6248.22	2601.35	3805.28	3488.17	1967.58	37.39	75.50	31.79	31.49	40.60
130	Zeolite	21675.48	39508.12	38072.37	23003.75	8165.26	15505.71	14027.14	7617.90	37.67	39.25	36.84	33.12	37.07
136	Zeolite	3545.94	6761.64	7535.80	4579.81	1112.56	2090.75	1994.01	1165.47	31.38	30.92	26.46	25.45	28.38

140	Zeolite	12200.49	19829.44	17896.64	8426.52	4458.54	6806.90	5597.36	3046.95	36.54	34.33	31.28	36.16	34.12
146	Zeolite	20769.92	27809.32	25634.42	24472.57	6899.09	11754.11	10148.64	5859.36	33.22	42.27	39.59	23.94	35.12
148	Zeolite	3930.31	6252.76	6610.06	4300.63	2069.26	3224.81	3111.95	1912.73	52.65	51.57	47.08	44.48	48.92
152	Zeolite	18549.02	31956.90	29079.61	16804.66	5292.19	8310.44	6989.26	4107.39	28.53	26.01	24.03	24.44	25.62
156	Zeolite	3183.22	4899.35	4747.77	4413.63	995.19	1692.35	1615.19	1169.26	31.26	34.54	34.02	26.49	31.73
160	Zeolite	40910.09	80432.65	81878.60	45455.78	12264.22	24729.89	23814.61	32769.15	29.98	30.75	29.09	72.09	37.63
164	Zeolite	4244.30	7270.53	7248.87	4546.57	1258.62	2030.29	2064.88	1467.79	29.65	27.92	28.49	32.28	29.26
168	Zeolite	12688.90	24282.85	22636.55	11922.44	1585.77	3062.35	2737.40	1646.77	12.50	12.61	12.09	13.81	12.63
172	Zeolite	11698.80	23316.33	23730.41	13251.91	5842.57	11533.43	11045.17	6007.13	49.94	49.47	46.54	45.33	47.82
176	Zeolite	4314.39	7494.51	8856.67	6706.72	1458.19	2546.51	2456.04	1695.24	33.80	33.98	27.73	25.28	29.80
182	Zeolite	6478.76	12634.36	16566.25	11874.60	1372.53	2895.25	3268.16	2028.38	21.18	22.92	19.73	17.08	20.11
184	Zeolite	9522.60	13561.18	12510.94	7212.04	2714.15	3791.83	3195.78	2096.84	28.50	27.96	25.54	29.07	27.56
190	Zeolite	24957.18	41059.96	40665.23	32574.31	12573.39	24611.63	23364.77	13455.10	50.38	59.94	57.46	41.31	53.14
194	Zeolite	7675.78	15532.84	12772.25	11843.09	851.92	1150.09	1078.21	1114.66	11.10	7.40	8.44	9.41	8.77
198	Zeolite	10073.82	17557.96	20075.12	14355.66	3703.18	6615.67	6442.63	4280.59	36.76	37.68	32.09	29.82	33.90
200	Zeolite	9425.43	18592.84	16947.28	6839.89	4964.68	9553.47	8786.81	4932.70	52.67	51.38	51.85	72.12	54.51
210	Zeolite	26070.87	48363.78	45949.00	26271.19	11202.16	20856.12	20052.25	12883.57	42.97	43.12	43.64	49.04	44.32
220	Zeolite	18273.81	31315.48	32371.97	7892.58	7414.94	13414.75	12165.13	7170.88	40.58	42.84	37.58	90.86	44.70
230	Zeolite	23996.88	51679.23	48524.44	25714.90	6043.96	11987.43	12084.20	7773.33	25.19	23.20	24.90	30.23	25.27
240	Zeolite	11586.57	22975.78	23861.99	17742.03	5151.44	10537.15	10672.93	6684.42	44.46	45.86	44.73	37.68	43.39
250	Zeolite	18447.96	35719.46	36806.91	21734.80	7880.24	15166.79	14871.28	9526.28	42.72	42.46	40.40	43.83	42.09
260	Zeolite	14362.10	30598.58	29756.33	14037.74	8217.40	17514.08	17927.19	10589.96	57.22	57.24	60.25	75.44	61.12
270	Zeolite	5633.40	12507.77	13426.26	7179.23	4029.53	9022.41	9726.80	5371.92	71.53	72.13	72.45	74.83	72.65
280	Zeolite	9999.92	21426.31	23042.66	10700.03	4748.82	9750.72	10156.38	6151.48	47.49	45.51	44.08	57.49	47.27
288	Zeolite	10576.21	16713.73	23850.86	28678.61	2502.51	4981.05	6101.86	4864.63	23.66	29.80	25.58	16.96	23.11
290	Zeolite	10287.30	22552.14	26985.11	17113.67	7437.53	17034.85	19236.07	11699.14	72.30	75.54	71.28	68.36	72.02
300	Zeolite	15348.96	37049.79	38266.27	25183.57	9959.87	22830.53	25725.78	15697.01	64.89	61.62	67.23	62.33	64.06

310	Zeolite	8837.11	19004.93	18757.74	10306.37	4635.51	9757.88	9379.78	5385.01	52.46	51.34	50.00	52.25	51.24
320	Zeolite	18014.62	38245.86	36466.03	29059.47	6213.08	13336.03	13866.35	9932.63	34.49	34.87	38.03	34.18	35.59
329	Zeolite	3704.94	7633.82	7760.40	3661.81	3736.54	8306.72	8730.99	5417.34	100.85	108.81	112.51	147.94	115.07
									MEAN	46.64	48.39	46.17	49.31	47.07

Appendix 10: The *n*-alkane recovery rate (%) of the zeolite cleaning method, outlining the *n*-alkane concentration before (Run 1) and after cleaning (Run 2).

Depth (cm)	Cleaning method	Run 1: *n*-Alkane concentration in vial (ng)				Run 2 clean: *n*-Alkane concentration in vial (ng)				Recovery rate (%)				
		C_{27}	C_{29}	C_{31}	C_{33}	C_{27}	C_{29}	C_{31}	C_{33}	C_{27}	C_{29}	C_{31}	C_{33}	Total (C_{27}-C_{33})
38	Urea	26872.83	34327.90	54374.63	99696.27	7659.02	15386.22	19586.49	10588.80	28.50	44.82	36.02	10.62	24.72
47	Urea	9284.71	20104.04	27704.08	22977.06	5972.56	12246.45	14522.10	7583.38	64.33	60.92	52.42	33.00	50.36
49	Urea	14028.73	28300.42	37381.78	31698.28	6641.49	15057.18	19786.46	4514.31	47.34	53.20	52.93	14.24	41.29
51	Urea	15292.23	22416.27	33649.92	14711.85	6036.02	13092.22	16616.52	8317.68	39.47	58.40	49.38	56.54	51.19
53	Urea	24396.43	35755.34	49822.76	50453.63	7529.78	14558.87	18996.70	11075.18	30.86	40.72	38.13	21.95	32.51
55	Urea	15755.57	23770.18	33805.12	47686.86	6634.96	14932.04	18328.99	9515.16	42.11	62.82	54.22	19.95	40.83
57	Urea	12759.12	19101.23	30535.02	34967.28	4646.50	10343.03	12421.11	6883.31	36.42	54.15	40.68	19.68	35.22
66	Urea	18917.44	39239.86	39709.55	34974.29	4475.95	8455.57	10294.12	5912.83	23.66	21.55	25.92	16.91	21.93
81	Urea	25591.07	50696.11	21293.10	43843.65	7526.82	14477.79	13017.78	7077.36	29.41	28.56	61.14	16.14	29.77
85	Urea	27100.19	38310.70	62535.59	99697.67	12705.36	23283.87	22102.80	12148.90	46.88	60.78	35.34	12.19	30.86
128	Urea	17246.27	22514.69	20766.29	25743.31	9959.20	16272.90	13168.47	8708.38	57.75	72.28	63.41	33.83	55.77
									MEAN	40.61	50.74	46.33	23.19	37.68

Appendix 11: The recovery rate (%) of the urea adduction cleaning method, outlining the *n*-alkane concentration before (Run 1) and after cleaning (Run 2).

	C_{27}		C_{29}		C_{31}		C_{33}	
Depth	$\delta^{13}C$ mean	± 1σ	$\delta^{13}C$ mean	± 1σ	$\delta^{13}C$ mean	± 1σ	$\delta^{13}C$ mean	± 1σ
4			-30.31	0.12	-30.72	0.13	-30.59	0.10
10			-31.88	0.16	-31.83	0.02	-32.08	0.28
20			-31.36	0.36	-31.77	0.54	-31.30	0.60
30			-31.82	0.13	-31.35	0.01	-31.69	0.04
38	-30.17	0.01	-30.57	0.11	-30.22	0.02	-31.74	0.06
40			-31.36	0.36	-31.77	0.54	-31.30	0.60
47	-30.52	0.06	-31.59	0.05	-31.20	0.07	-32.45	0.04
48	-30.40	0.09	-31.73	0.12	-31.37	0.19	-30.94	0.34
49	-30.93	0.09	-32.10	0.06	-31.40	0.11	-32.26	0.11
51	-31.21	0.12	-32.64	0.14	-31.66	0.04	-31.73	0.06
53	-31.38	0.09	-32.50	0.09	-32.00	0.07	-32.68	0.18
55	-30.14	0.05	-31.18	0.06	-31.13	0.08	-32.05	0.03
57	-29.85	0.04	-30.95	0.12	-31.05	0.08	-30.72	0.07
59			-31.72	0.16	-31.01	0.06	-30.03	0.35
60	-29.80	0.35	-31.10	0.10	-30.53	0.15	-29.45	0.18
66	-30.04	0.03	-30.73	0.11	-30.31	0.13	-30.43	0.03
70	-30.71	0.11	-31.37	0.15	-30.78	0.31	-30.65	0.55
71	-30.48	0.32	-31.30	0.28	-31.09	0.15	***-29.28***	
74			-31.83	0.52	-30.86	0.05	-31.51	0.03
78			-31.60	0.00	-31.15	0.01	-31.99	0.19
81	-30.89	0.05	-31.15	0.02	-31.36	0.08	-31.99	0.10
82			-31.72	0.01	-31.63	0.00	-31.39	0.04

85	-29.98	0.77	-30.44	0.63	-31.38	0.11	-32.08	0.16
90	-30.77	0.03	-31.47	0.02	-31.51	0.03	-31.36	0.08
92			-31.76	0.14	-31.55	0.18	-31.82	0.16
96			*-30.34*	*1.15*	*-30.91*	*1.13*	*-29.73*	*1.22*
100	-30.45	0.09	-31.49	0.03	-31.27	0.11	-31.24	0.15
109	-31.14	0.23	-32.07	0.40	-32.01	0.53	-32.12	0.45
110			-32.00	0.06	-32.02	0.06	-31.65	0.06
112			-31.90	0.10	-31.96	0.16	-32.15	0.89
120	-30.92	0.13	-31.91	0.09	-32.18	0.07	-32.37	0.52
126			*-30.37*	*1.70*	*-30.91*	*1.45*	*-30.61*	*1.55*
128	-30.87	0.06	-32.04	0.14	-32.68	0.15	-33.65	0.12
130			-31.94	0.07	-32.48	0.03	-33.05	0.19
136	-31.13	0.06	-32.07	0.09	-32.90	0.09	***-32.03***	
140	-30.67	0.19	-31.88	0.05	-32.33	0.09	-32.22	0.86
146			-31.75	0.07	-32.18	0.02	-31.66	0.10
148			*-29.77*	*0.03*	*-30.35*	*0.37*	*-29.79*	*0.36*
152	-30.89	0.02	-31.79	0.06	-32.85	0.10	-32.59	1.20
156			*-33.34*	*0.26*	*-34.87*	*0.53*	*-35.16*	*0.02*
160	-30.27	0.11	-31.63	0.03	-32.22	0.00	-32.53	0.22
164			-30.73	0.12	-31.47	0.22	-31.19	0.23
168			-32.32	0.10	-32.26	0.47	-32.44	0.63
172			-32.02	0.04	-32.44	0.10	-31.97	0.09
176			*-32.88*	*0.53*	*-34.18*	*1.62*	*-34.10*	*1.99*
180	-30.52	0.08	-32.02	0.21	-32.48	0.23	-33.07	0.08

184			-32.27	0.10	-32.48	0.16	-32.66	0.51
190			-32.03	0.04	-32.44	0.03	-32.88	0.09
194			*-30.31*	*1.31*	*-31.03*	*1.86*	*-30.64*	*2.23*
198			-32.10	0.14	-32.40	0.08	-33.31	0.22
200	-30.67	0.17	-32.02	0.10	-32.31	0.02	-31.96	0.11
210	-31.02	0.38	-32.12	0.24	-32.09	0.24	-31.92	0.47
220			-31.95	0.02	-32.32	0.10	-32.63	0.00
230	-30.63	0.00	-32.05	0.00	-32.20	0.00	-31.91	0.42
240			-31.88	0.03	-32.41	0.11	-32.83	0.05
250			*-31.34*	*0.82*	*-32.05*	*1.08*	*-31.87*	*0.88*
260	-30.63	0.10	-32.12	0.09	-32.32	0.09	-31.96	0.09
270	-30.90	0.50	-32.32	0.18	-32.44	0.13	-32.16	0.23
280	-30.60	0.24	-32.05	0.15	-32.24	0.06	-31.85	0.15
288			*-33.90*	*3.22*	*-33.87*	*2.74*	*-33.66*	*2.14*
290	-30.36	0.27	-32.07	0.06	-32.40	0.24	-32.22	0.05
300	-30.65	0.24	-32.23	0.12	-32.36	0.14	-31.93	0.03
310	-30.99	0.52	-32.43	0.37	-32.47	0.20	-31.79	0.10
320			-32.05	0.06	-32.32	0.04	-32.09	0.10
329	-30.70	0.18	-32.08	0.16	-32.28	0.09	-31.75	0.15

Appendix 12: For SHAK06-5K samples (n = 65), the mean $\delta^{13}C_{n\text{-alkane}}$ values of the multiple runs for each homologue, showing the standard deviation (± 1σ) of these duplicate/triplicate runs. Values highlighted in red were removed due to concern around sample contamination, with many of these samples showing high std dev. Values highlighted in grey only had one run and were removed from final analysis. Blank boxes indicate where homologue concentrations were too low to measure the isotope composition.

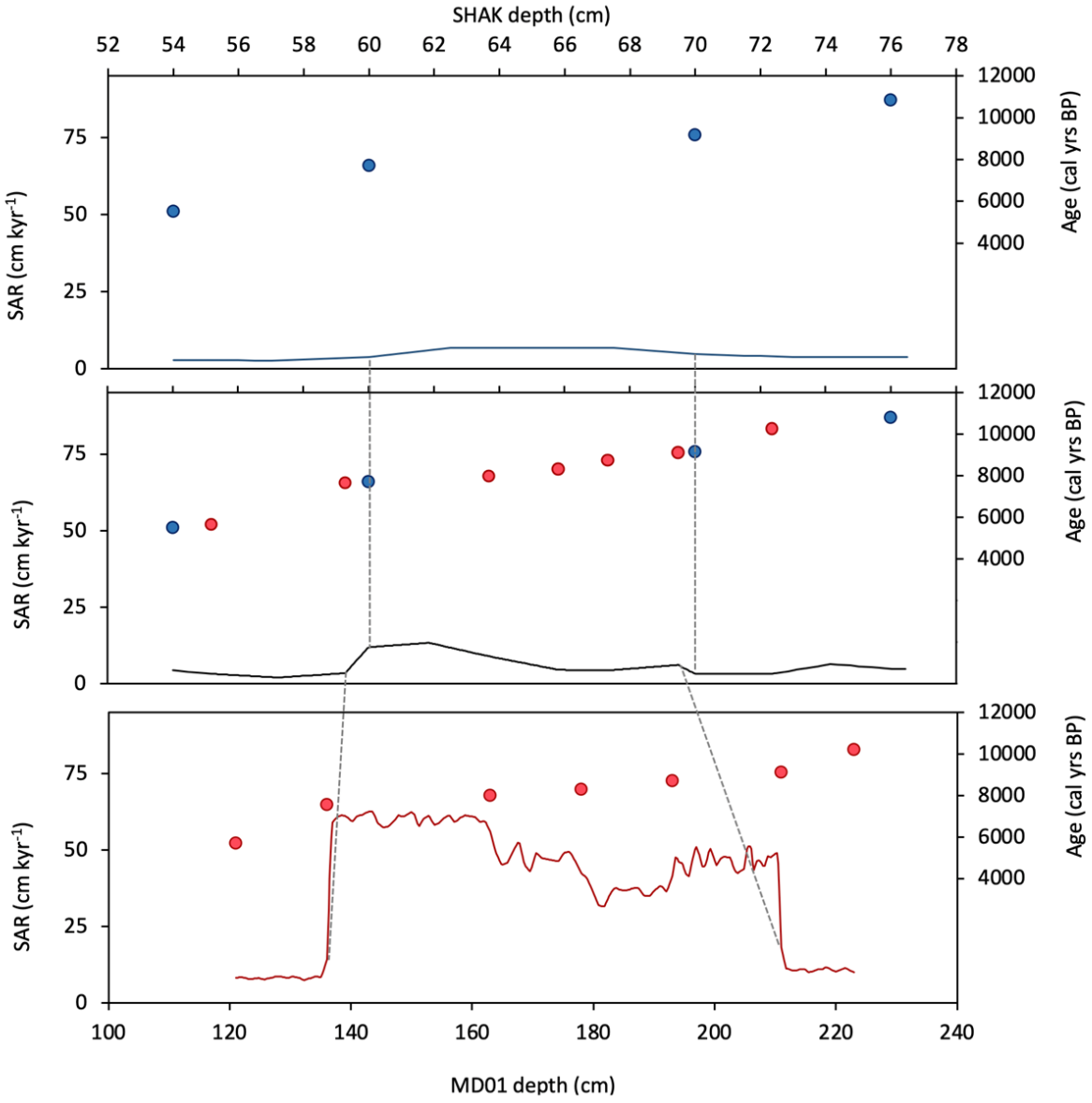

Appendix 13: Sediment accumulation rate (SAR; cm kyr^{-1}) in cores SHAK06-5K and MD01-2444. Note that the SHAK06-5K SAR (blue line) and Master sequence SAR (black line) are on the SHAK06-5K depth scale, while MD01-2444 SAR (red line) is on its own depth scale.

Taxa	Dry weight (g)	GC-FID	Standard injection (µl)	Solvent in vial (µl)	Sample injection (µl)	Peak area of homologue							Total amount of alkane in dry leaf (ng g^{-1})						
						C_{25}	C_{27}	C_{29}	C_{31}	C_{33}	C_{35}	C_{37}	C_{25}	C_{27}	C_{29}	C_{31}	C_{33}	C_{35}	C_{37}
J. turbinata	0.50	2	1	500	1	11.10	22.90	269.60	502.40	6330.00	2408.10	33.60	772.92	1594.57	18772.80	34983.15	435374.49	165628.01	2310.99
O. europea	0.26	2	1	500	1	0.00	566.40	5338.80	7190.10	4262.20	1214.10	0.00	0.00	88015.63	829621.90	1117304.34	747213.00	212845.78	0.00
C. salviifolius	0.14	2	1	500	1	28.90	746.80	3753.70	815.90	52.80	12.10	0.00	7368.83	190416.81	957107.11	208035.72	13297.96	3047.45	0.00
Q. suber	0.09	2	1	500	1	17.80	154.40	562.30	161.40	10.80	0.00	0.00	8191.94	71058.16	258782.41	74279.71	5607.44	0.00	0.00
Q. pyrenaica	0.70	2	1	500	1	473.30	2444.00	4692.70	1001.00	39.90	0.00	0.00	27507.26	142040.44	272730.43	58176.14	0.00	0.00	0.00
Q. ilex	0.53	2	1	500	1	34.60	276.30	1511.90	404.90	15.60	0.00	0.00	2256.58	18020.01	98604.61	26407.17	1059.06	0.00	0.00
T. villosa	0.31	2	1	500	1	20.20	32.50	23.40	9.00	0.00	0.00	0.00	2251.01	3621.67	2607.60	1002.92	0.00	0.00	0.00
P. pinaster	0.48	2	1	500	1	26.70	24.10	45.70	7.00	8.40	5.90	0.00	1893.48	1709.09	3240.89	496.42	621.23	436.34	0.00
C. vesicaria	0.14	2	1	500	1	31.10	140.50	107.20	32.00	0.00	0.00	0.00	11693.54	52827.75	40307.01	12031.94	0.00	0.00	0.00
R. acetosella 2	0.13	2	1	500	1	9.50	40.60	216.40	110.50	17.30	0.00	0.00	3694.60	15789.57	84159.18	42974.07	10610.08	0.00	0.00
C. crispus	0.07	2	1	500	1	0.00	167.60	1437.60	281.00	47.00	0.00	0.00	0.00	132336.33	1135123.57	221876.55	58523.62	0.00	0.00
L. vulgare	0.03	2	1	500	1	0.00	15.50	56.10	6.30	0.00	0.00	0.00	0.00	17742.67	64217.03	7211.54	0.00	0.00	0.00
C. album	0.06	2	1	500	1	15.00	57.60	432.80	288.80	19.00	0.00	0.00	11635.14	44678.93	335712.55	224015.21	18291.40	0.00	0.00
B. diandrus	0.10	2	1	500	1	9.60	80.50	470.90	228.30	120.70	5.90	0.00	4153.13	34825.72	203719.67	98766.62	64807.41	3167.89	0.00
G. coronaria	0.08	2	1	500	1	8.60	35.80	567.30	252.90	12.30	0.00	0.00	4747.02	19760.85	313137.76	139595.52	8426.38	0.00	0.00
L. ovatus	0.07	2	1	500	1	27.20	194.70	788.00	561.10	290.40	41.50	0.00	18444.91	132030.28	534359.83	380494.04	244409.08	34927.61	0.00
C. pycnocephalus	0.18	2	1	500	1	0.00	171.10	1327.10	1093.60	66.90	0.00	0.00	0.00	34407.18	266871.78	219916.34	29042.24	0.00	0.00
R. acetosella 1	0.11	2	1	500	1	0.00	90.10	597.70	271.10	14.60	0.00	0.00	0.00	29094.55	193005.68	87541.98	10177.58	0.00	0.00
A .integrifolia	0.11	2	1	500	1	0.00	56.30	314.90	643.10	13.70	0.00	0.00	0.00	17606.96	98480.11	201119.59	9249.14	0.00	0.00
B. maxima	0.08	2	1	500	1	31.80	35.50	75.80	284.30	198.80	13.50	0.00	8747.48	9765.27	20850.91	78204.66	118053.02	8016.68	0.00
T. barbata	0.09	2	1	500	1	0.00	59.90	2769.60	1290.40	79.20	0.00	0.00	0.00	14520.04	671363.93	312798.97	41444.90	0.00	0.00

Appendix 14: For the modern leaf samples (n = 21), the dry leaf weight, standard injection (µl), solvent in vial (µl) for each sample, with the peak areas and concentrations (ng g^{-1}) of odd homologues C_{25}-C_{35} for each sample.

Taxa	Dry weight (g)	GC-FID	Standard injection (µl)	Solvent in vial (µl)	Sample injection (µl)	Peak area of homologue						Total amount of alkane in dry leaf (ng g^{-1})					
						C_{26}	C_{28}	C_{30}	C_{32}	C_{34}	C_{36}	C_{26}	C_{28}	C_{30}	C_{32}	C_{34}	C_{36}
J. turbinata	0.50	2	1	500	1	13.70	171.50	110.10	28.10	0.00	0.00	953.96	11941.90	7666.49	1956.66	0.00	0.00
O. europea	0.26	2	1	500	1	0.00	204.20	462.70	694.20	294.80	274.70	0.00	31731.62	71901.19	107875.09	51681.85	48158.09
C. salviifolius	0.14	2	1	500	1	9.60	172.60	110.20	16.50	0.00	0.00	2447.78	44009.03	28098.46	4207.12	0.00	0.00
Q. suber	0.09	2	1	500	1	0.00	21.10	17.90	60.20	26.40	0.00	0.00	9710.67	8237.96	27705.32	13707.07	0.00
Q. pyrenaica	0.70	2	1	500	1	57.20	272.20	112.40	86.50	30.00	0.00	3324.35	15819.72	6532.47	5027.21	1967.01	0.00
Q. ilex	0.53	2	1	500	1	0.00	68.70	90.00	48.80	17.80	0.00	0.00	4480.55	5869.71	3182.69	1208.42	0.00
T. villosa	0.31	2	1	500	1	0.00	8.60	0.00	0.00	0.00	0.00	0.00	958.35	0.00	0.00	0.00	0.00
P. pinaster	0.48	2	1	500	1	4.90	6.40	5.70	0.00	0.00	0.00	347.49	453.87	404.23	0.00	0.00	0.00
C .vesicaria	0.14	2	1	500	1	19.20	16.40	4.60	0.00	0.00	0.00	7219.17	6166.37	1729.59	0.00	0.00	0.00
R. acetosella 2	0.13	2	1	500	1	7.30	12.20	16.50	5.80	0.00	0.00	2839.01	4744.65	6416.94	2255.65	0.00	0.00
C. crispus	0.07	2	1	500	1	0.00	66.10	41.50	6.70	0.00	0.00	0.00	52192.31	32768.24	5290.29	0.00	0.00
L. vulgare	0.03	2	1	500	1	0.00	8.70	0.00	0.00	0.00	0.00	0.00	14531.61	0.00	0.00	0.00	0.00
C. album	0.06	2	1	500	1	4.60	10.80	36.00	4.10	0.00	0.00	3568.11	8377.30	27924.33	3180.27	0.00	0.00
B. diandrus	0.10	2	1	500	1	0.00	7.40	5.90	4.80	0.00	0.00	0.00	3201.37	2552.44	2076.56	0.00	0.00
G. coronaria	0.08	2	1	500	1	0.00	10.50	28.00	0.00	0.00	0.00	0.00	5795.78	15455.42	0.00	0.00	0.00
L. ovatus	0.07	2	1	500	1	0.00	39.50	84.00	55.20	17.30	0.00	0.00	26785.80	56962.22	37432.31	14560.18	0.00
C. pycnocephalus	0.18	2	1	500	1	0.00	10.60	25.20	5.30	0.00	0.00	0.00	2131.60	5067.57	1065.80	0.00	0.00
R. acetosella 1	0.11	2	1	500	1	10.50	28.00	46.00	9.80	0.00	0.00	3390.60	9041.59	14854.04	3164.56	0.00	0.00
A .integrifolia	0.11	2	1	500	1	0.00	14.70	48.70	197.00	0.00	0.00	0.00	4597.20	15230.17	61608.71	0.00	0.00
B. maxima	0.08	2	1	500	1	5.00	4.60	8.20	8.60	0.00	0.00	2292.32	2108.93	3759.40	3942.78	0.00	0.00
T. barbata	0.09	2	1	500	1	0.00	18.20	131.00	20.30	0.00	0.00	0.00	7352.94	52925.02	8201.36	0.00	0.00

Appendix 15: For the modern leaf samples (n = 21), the dry leaf weight, standard injection (µl), solvent in vial (µl) for each sample, with the peak areas and concentrations (ng g^{-1}) of even homologues C_{26}-C_{34} for each sample.

Taxa	C_{27}		C_{29}		C_{31}		C_{33}		C_{35}	
	$\delta^{13}C$ mean	± 1σ	$\delta^{13}C$ mean	± 1σ	$\delta^{13}C$ mean	± 1σ	$\delta^{13}C$ mean	± 1σ	$\delta^{13}C$ mean	± 1σ
J. turbinata			-27.71	0.14	-27.82	0.18	-26.72	0.15		
B. maxima					-38.81	0.09	-39.41	0.09		
O.europea	-33.63	0.07	-33.09	0.03	-33.04	0.15	-32.84	0.09	-32.78	0.04
A. integrifolia			-39.66	0.04	-40.49	0.12				
L. ovatus	-36.85	0.09	-37.43	0.06	-37.52	0.01	-38.15	0.02		
B. diandrus	-36.84	0.09	-37.92	0.08	-37.90	0.06	-38.09	0.01		
C. pycnocephalus	-35.83	0.12	-35.38	0.11	-35.21	0.06				
T. barbata			-36.21	0.04	-36.69	0.06				
C. album	-37.54	0.09	-38.17	0.03	-37.66	0.04				
G. coronaria			-37.37	0.08	-37.03	0.06				
R. acetosella 2			-39.32	0.02	-38.88	0.15				
R. acetosella 1	-38.76	0.12	-40.02	0.05	-39.36	0.08				
C. crispus	-35.92	0.19	-38.37	0.09	-37.71	0.25				
Q. ilex	-34.44	0.57	-34.14	0.74	-34.60	0.28				
C. salviifolius	-35.94	0.15	-36.67	0.03	-35.93	0.16				
Q. suber	-33.37	0.10	-33.68	0.07	-34.45	0.08				
L. vulgare	-36.35	0.16	-36.32	0.08	-36.46	0.07				
Q. pyrenaica	-33.60	0.17	-33.26	0.23	-33.76	0.37				
P. pinaster			-32.00	0.07						
C. vesicaria	-34.79	0.02	-36.67	0.14						
T. villosa	-35.35	0.13	-35.20	0.08	-35.57	0.06				

Appendix 16: For the modern leaf samples (n=21), the mean $\delta^{13}C_{n\text{-alkane}}$ values of the multiple runs for each homologue, showing the standard deviation (± 1σ) of these duplicate/triplicate runs

Taxa	Site	Heat resistance	Drought tolerance
Quercus pyrenaica	2	1	1
Quercus suber	2	3	3
Quercus ilex	3	3	3
Olea europaea	3	5	5
Cistus salviifolius	2	4	3
Cistus crispus	3	4	3
Pinus pinaster	2	4	4
Juniperus turbinata	1	5	5
Chenopodium album	1	3	2
Rumex acetosella A	1	2	2
Rumex acetosella B	1	2	2
Glebionis coronaria	2	2	3
Thapsia villosa	2	2	1
Carduus pycnocephalus	2	4	3
Leucanthemum vulgare	2	1	2
Andryala integrifolia	3	4	4
Crepis vesicaria	2	1	1
Tolpis barbata	3	4	3
Briza maxima	2	4	4
Bromus diandrus	2	3	4
Lagurus ovatus	1	4	4

Appendix 17: Value assigned to each modern species (1-5) for both drought tolerance and heat resistance. 1 represents the most tolerant, 5 represents the least tolerant. Values used in PCA.

Depth (cm)	Sediment volume (mm^3)	Dry sediment mass (mg)	Bulk density ($g\ cm^{-3}$)
5	500	398.05	0.80
8	500	384.54	0.77
16	500	466.76	0.93
18	500	428.09	0.86
22	500	451.87	0.90
26	500	419.70	0.84
28	500	467.62	0.94
32	500	306.60	0.61
34	500	406.19	0.81
36	500	518.21	1.04
38	500	375.38	0.75
42	500	506.94	1.01
44	500	522.59	1.05
46	500	445.22	0.89
52	500	498.68	1.00
54	500	463.02	0.93
56	500	490.42	0.98
58	500	616.78	1.23
62	500	362.34	0.72
64	500	330.95	0.66
66	500	442.25	0.88
68	500	445.02	0.89
74	500	351.04	0.70
76	500	381.76	0.76
78	500	287.49	0.57
86	500	432.32	0.86
92	500	453.70	0.91
94	500	543.73	1.09
96	500	517.63	1.04
98	500	430.06	0.86
102	500	448.51	0.90
104	500	379.37	0.76
106	500	448.56	0.90
108	500	501.96	1.00
112	500	459.32	0.92
114	500	403.06	0.81
116	500	418.49	0.84
118	500	509.83	1.02
122	500	464.61	0.93
124	500	521.84	1.04

126	500	534.82	1.07
128	500	588.99	1.18
132	500	536.30	1.07
134	500	426.52	0.85
136	500	552.33	1.10
138	500	485.86	0.97
142	500	443.80	0.89
144	500	533.60	1.07
146	500	559.65	1.12
148	500	354.45	0.71
156	500	531.53	1.06
158	500	503.08	1.01
162	500	518.53	1.04
164	500	603.01	1.21
166	500	508.88	1.02
168	500	517.74	1.04
174	500	477.87	0.96
176	500	488.03	0.98
178	500	518.63	1.04
182	500	427.40	0.85
184	500	654.94	1.31
186	500	479.54	0.96
188	500	623.09	1.25
192	500	532.46	1.06
194	500	528.16	1.06
196	500	487.13	0.97
198	500	553.13	1.11
202	500	614.47	1.23
204	500	414.37	0.83
206	500	553.68	1.11
208	500	539.06	1.08
212	500	429.08	0.86
214	500	658.33	1.32
216	500	528.28	1.06
218	500	636.30	1.27
222	500	509.58	1.02
224	500	518.85	1.04
226	500	460.88	0.92
228	500	434.72	0.87
232	500	443.71	0.89
234	500	390.59	0.78

236	500	474.32	0.95
238	500	449.15	0.90
242	500	577.93	1.16
248	500	502.98	1.01
252	500	614.04	1.23
254	500	665.85	1.33
256	500	491.45	0.98
258	500	525.53	1.05
262	500	538.81	1.08
266	500	572.80	1.15
268	500	537.24	1.07
272	500	554.79	1.11
274	500	577.68	1.16
278	500	467.28	0.93
284	500	569.98	1.14
286	500	555.82	1.11
288	500	452.06	0.90
292	500	482.59	0.97
294	500	515.95	1.03
296	500	538.19	1.08
298	500	446.74	0.89
304	500	389.50	0.78
308	500	540.23	1.08
312	500	476.53	0.95
314	500	411.15	0.82
316	500	535.72	1.07
318	500	531.67	1.06
322	500	499.35	1.00
326	500	524.24	1.05
328	500	479.17	0.96

Appendix 18: Bulk density (g cm^{-3}) of SHAK06-5K samples, calculated by volume wet sample (mm^3) * dry sediment mass (mg).

Depth	C_{29} concentration (ng g^{-1})	C_{31} concentration (ng g^{-1})	Total concentration C_{27}-C_{33} (ng g^{-1})	Bulk density (g cm^{-3})	SAR (cm kyr^{-1})	Mass flux C_{29} (ng cm^{-2} kyr^{-1})	Mass flux C_{31} (ng cm^{-2} kyr^{-1})	Mass flux C_{27}-C_{33} (ng cm^{-2} kyr^{-1})
4	46.62	68.04	184.35	0.805	24.1	904.5	1320.2	3577.0
10	107.02	130.69	343.88	0.810	24.6	2133.0	2604.7	6853.7
20	150.02	210.71	528.98	0.880	17.2	2270.6	3189.2	8006.3
30	64.83	79.70	207.70	0.774	13.1	657.5	808.3	2106.5
38	269.66	427.14	907.90	0.751	9.74	1971.9	3123.4	6638.9
40	112.59	152.62	399.32	0.882	8.02	796.7	1080.0	2825.6
47	190.40	262.37	758.31	0.908	12.3	2127.0	2931.1	8471.5
48	291.93	369.96	936.87	0.926	5.27	1424.7	1805.6	4572.4
49	271.18	358.20	1067.55	0.944	4.53	1159.5	1531.6	4564.7
51	211.14	316.94	810.68	0.980	3.05	630.8	946.9	2422.0
53	324.90	452.73	1457.78	0.962	3.97	1240.5	1728.5	5565.7
55	225.78	321.10	1149.48	0.953	3.45	742.7	1056.2	3781.1
57	183.65	293.58	936.09	1.107	2.19	445.3	711.9	2269.8
59	243.54	319.76	786.18	1.106	3.28	883.8	1160.4	2852.9
60	101.43	129.88	340.78	0.979	12	1191.8	1526.0	4004.0
64	10.18	13.95	39.52	0.662	8.35	56.3	77.1	218.4
66	465.64	471.22	1576.38	0.885	4.57	1882.2	1904.7	6372.0
70	130.32	148.50	383.98	0.827	3.27	352.6	401.8	1038.9
71	100.55	114.49	305.30	0.796	3.27	261.7	298.0	794.7
74	102.70	133.90	356.79	0.702	6.16	444.1	579.1	1543.1
78	102.10	116.56	339.34	0.575	4.28	251.2	286.9	835.1
81	600.81	252.35	1676.04	0.684	5.63	2312.3	971.2	6450.5
82	162.78	165.84	493.85	0.720	6.46	756.9	771.1	2296.4

85	450.13	734.76	2674.71	0.828	17.4	6488.5	10591.4	38555.1
90	343.35	336.52	1073.15	0.893	16.9	5182.6	5079.5	16198.3
92	102.10	113.77	324.91	0.907	16.5	1528.7	1703.4	4864.7
96	58.46	82.00	215.60	1.035	16.4	992.6	1392.2	3660.5
100	229.03	240.36	687.06	0.879	19	3823.2	4012.3	11469.1
104	83.38	110.16	312.73	0.759	22.4	1417.1	1872.3	5315.1
109	393.25	425.64	1181.66	0.983	16.3	6298.5	6817.2	18925.9
110	274.39	285.13	878.44	0.961	12.1	3191.6	3316.4	10217.6
112	261.27	328.73	931.57	0.919	9.09	2181.7	2745.0	7779.0
120	216.74	202.89	612.45	0.974	11.6	2449.9	2293.4	6922.9
122	91.81	97.47	301.32	0.929	17.4	1484.4	1575.9	4871.9
126	61.72	134.38	357.80	1.070	18.8	1241.2	2702.3	7195.2
128	264.04	243.54	1011.73	1.178	18.5	5754.1	5307.3	22048.3
130	365.68	352.39	1131.62	1.125	17.3	7118.9	6860.2	22029.7
136	82.19	91.60	272.56	1.105	16	1452.6	1619.0	4817.3
140	157.80	142.42	464.37	0.930	17.3	2538.0	2290.6	7468.6
146	245.04	225.87	869.56	1.119	14.1	3867.2	3564.8	13723.5
148	101.32	107.11	341.82	0.709	12.2	876.3	926.4	2956.3
152	200.82	182.74	605.73	0.886	17	3024.7	2752.4	9123.3
156	79.81	58.55	262.11	1.063	34.6	2935.5	2153.7	9640.9
160	544.04	535.46	1689.89	1.022	26.9	14950.9	14715.2	46440.4
164	118.97	118.62	381.45	1.206	21.9	3142.3	3133.0	10074.7
168	392.61	365.99	1156.52	1.035	21.9	8903.2	8299.6	26226.4
172	226.11	230.12	698.19	0.982	17.4	3864.7	3933.4	11933.7
176	130.75	154.51	477.53	0.976	14.5	1850.5	2186.8	6758.5
180	387.27	367.43	1131.46	0.946	16.1	5898.5	5596.3	17233.4

182	204.37	267.98	769.23	0.855	18.2	3179.5	4169.0	11967.2
184	219.26	202.28	692.11	1.310	18.1	5198.4	4795.8	16409.0
190	328.95	325.79	1115.66	1.156	18.2	6918.2	6851.7	23463.5
194	252.28	207.44	776.74	1.056	18.1	4823.4	3966.2	14850.8
198	282.78	323.32	999.56	1.106	12.5	3910.4	4471.0	13822.1
200	465.64	424.42	1297.41	1.168	17.1	9296.9	8474.0	25904.0
210	413.09	392.46	1252.62	0.968	28.4	11358.0	10790.9	34441.1
220	248.38	256.76	712.67	1.146	14.2	4041.5	4177.8	11596.3
230	417.04	391.59	1209.80	0.878	13	4762.5	4471.7	13815.4
240	230.50	239.39	764.11	1.027	18.3	4332.3	4499.4	14361.9
250	718.85	740.73	2268.25	1.117	15.9	12767.1	13155.8	40285.4
260	365.79	355.72	1061.03	1.064	18.4	7163.6	6966.5	20779.0
270	333.90	358.42	1034.35	1.092	22.4	8167.6	8767.4	25301.7
280	268.57	288.83	816.87	1.003	19.3	5199.1	5591.3	15813.3
284	52.66	24.76	112.74	1.140	15.9	954.5	448.8	2043.4
286	72.70	101.84	298.74	1.112	15.5	1252.6	1754.8	5147.4
288	291.74	416.32	1393.25	0.904	14.8	3903.8	5570.7	18643.1
290	392.76	469.96	1339.92	0.935	13.7	5029.1	6017.7	17157.3
300	256.25	264.67	801.27	0.855	14.9	3265.8	3373.0	10211.5
310	320.63	316.46	960.05	1.017	18.5	6031.0	5952.6	18058.6
320	361.46	344.64	1150.99	1.031	13.1	4882.0	4654.8	15545.7
329	91.24	92.75	272.04	0.913	10.2	849.9	864.0	2534.1

Appendix 19: *n*-Alkane concentration (grains g^{-1}) and mass accumulation rate (grains cm^{-2} kyr^{-1}) of SHAK06-5K samples